COMPUTATIONAL MODELING AND SIMULATION OF QUADRUPEDAL ANIMAL MOVEMENT

EDITED BY: Gina Bertocci, John R. Hutchinson, Denis J. Marcellin-Little and Marcus G. Pandy

PUBLISHED IN: Frontiers in Bioengineering and Biotechnology and Frontiers in Veterinary Science

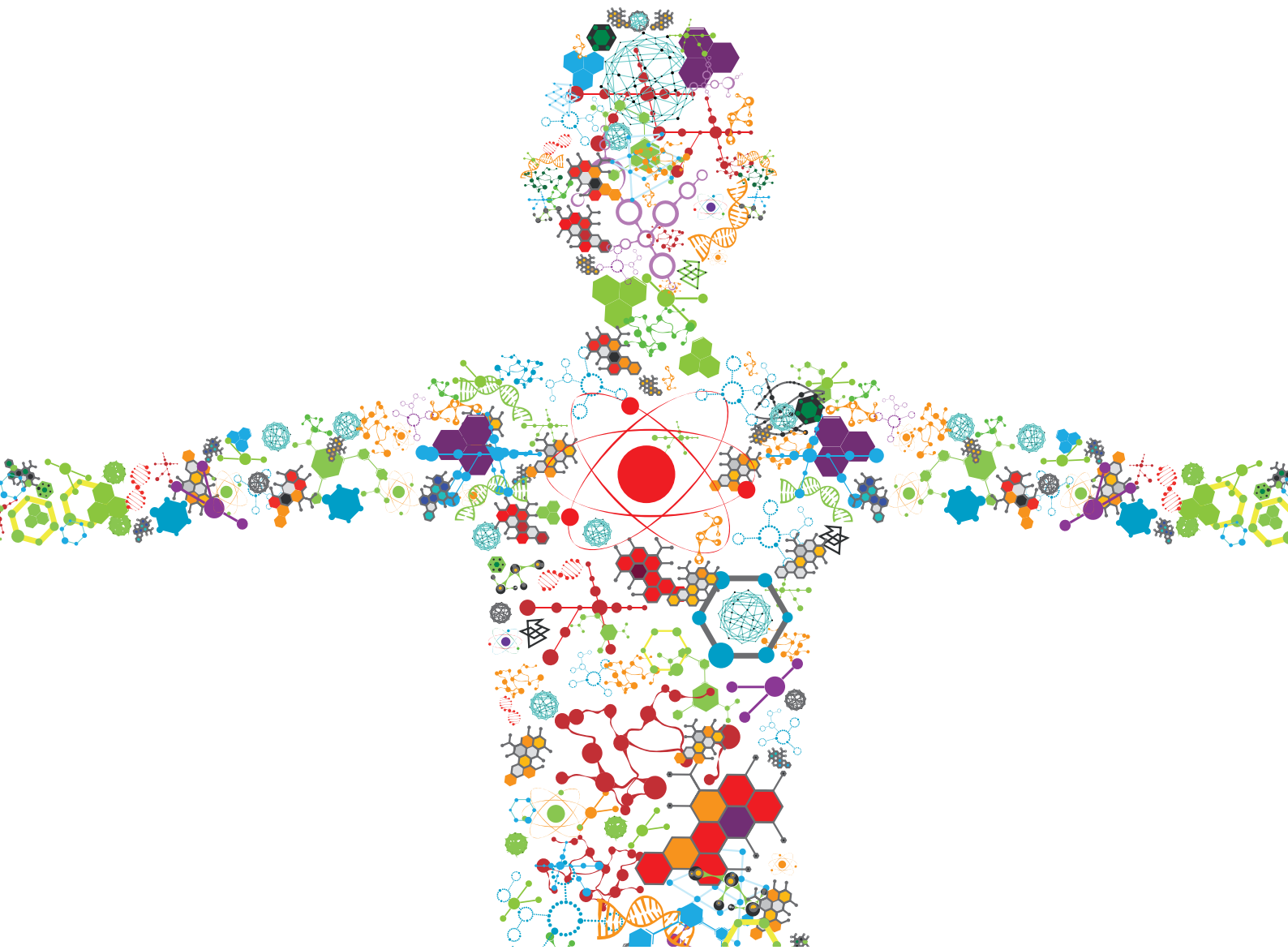

frontiers Research Topics

frontiers

ISSN 1664-8714
ISBN 978-2-88976-781-6
DOI 10.3389/978-2-88976-781-6

About Frontiers

Frontiers is more than just an open-access publisher of scholarly articles: it is a pioneering approach to the world of academia, radically improving the way scholarly research is managed. The grand vision of Frontiers is a world where all people have an equal opportunity to seek, share and generate knowledge. Frontiers provides immediate and permanent online open access to all its publications, but this alone is not enough to realize our grand goals.

Frontiers Journal Series

The Frontiers Journal Series is a multi-tier and interdisciplinary set of open-access, online journals, promising a paradigm shift from the current review, selection and dissemination processes in academic publishing. All Frontiers journals are driven by researchers for researchers; therefore, they constitute a service to the scholarly community. At the same time, the Frontiers Journal Series operates on a revolutionary invention, the tiered publishing system, initially addressing specific communities of scholars, and gradually climbing up to broader public understanding, thus serving the interests of the lay society, too.

Dedication to Quality

Each Frontiers article is a landmark of the highest quality, thanks to genuinely collaborative interactions between authors and review editors, who include some of the world's best academicians. Research must be certified by peers before entering a stream of knowledge that may eventually reach the public - and shape society; therefore, Frontiers only applies the most rigorous and unbiased reviews.
Frontiers revolutionizes research publishing by freely delivering the most outstanding research, evaluated with no bias from both the academic and social point of view. By applying the most advanced information technologies, Frontiers is catapulting scholarly publishing into a new generation.

What are Frontiers Research Topics?

Frontiers Research Topics are very popular trademarks of the Frontiers Journals Series: they are collections of at least ten articles, all centered on a particular subject. With their unique mix of varied contributions from Original Research to Review Articles, Frontiers Research Topics unify the most influential researchers, the latest key findings and historical advances in a hot research area! Find out more on how to host your own Frontiers Research Topic or contribute to one as an author by contacting the Frontiers Editorial Office: frontiersin.org/about/contact

COMPUTATIONAL MODELING AND SIMULATION OF QUADRUPEDAL ANIMAL MOVEMENT

Topic Editors:
Gina Bertocci, University of Louisville, United States
John R. Hutchinson, Royal Veterinary College (RVC), United Kingdom
Denis J. Marcellin-Little, University of California, Davis, United States
Marcus G. Pandy, The University of Melbourne, Australia

Citation: Bertocci, G., Hutchinson, J. R., Marcellin-Little, D. J., Pandy, M. G., eds. (2022). Computational Modeling and Simulation of Quadrupedal Animal Movement. Lausanne: Frontiers Media SA. doi: 10.3389/978-2-88976-781-6

Table of Contents

frontiers | Frontiers in Bioengineering and Biotechnology

TYPE Editorial
PUBLISHED 19 July 2022
DOI 10.3389/fbioe.2022.943553

OPEN ACCESS

EDITED AND REVIEWED BY
Markus O. Heller,
University of Southampton,
United Kingdom

*CORRESPONDENCE
Gina Bertocci,
g.bertocci@louisville.edu

†These authors have contributed equally to this work

SPECIALTY SECTION
This article was submitted to Biomechanics, a section of the journal Frontiers in Bioengineering and Biotechnology

RECEIVED 13 May 2022
ACCEPTED 29 June 2022
PUBLISHED 19 July 2022

CITATION
Bertocci G, Hutchinson JR, Marcellin-Little DJ and Pandy MG (2022), Editorial: Computational modeling and simulation of quadrupedal animal movement. *Front. Bioeng. Biotechnol.* 10:943553. doi: 10.3389/fbioe.2022.943553

Editorial: Computational modeling and simulation of quadrupedal animal movement

Gina Bertocci[1*†], John R. Hutchinson[2†], Denis J. Marcellin-Little[3†] and Marcus G. Pandy[4†]

[1]Department of Bioengineering, University of Louisville, Louisville, KY, United States, [2]Department of Comparative Biomedical Sciences, The Royal Veterinary College, University of London, London, United Kingdom, [3]Department of Surgical and Radiological Sciences, University of California, Davis, Davis, CA, United States, [4]Department of Mechanical Engineering, University of Melbourne, Parkville, VIC, Australia

KEYWORDS

modeling, simulation, dynamics, motion, animal, quadruped, biomechanics

Editorial on the Research Topic
Computational modeling and simulation of quadrupedal animal movement

Computational modeling and simulation used to study movement and function in healthy humans, as well as in those with clinical pathologies, is a well-developed field. Computational models of movement can provide objective insights into skeletal motion, muscle/ligament and joint loading, muscle activation patterns, coordination of multi-joint movement, injury mechanisms, compensatory locomotion, and other dynamic anatomical functions. Anatomically accurate models developed from medical imaging in combination with biomechanical properties can provide a window into *in vivo* function that would otherwise not be possible without subject experimentation or invasive testing. Modeling and simulation enable the investigation of the dynamic interaction between musculoskeletal and neuromuscular systems needed to generate motion and can be used to study pathologies, injury mechanisms, joint replacement/implants, rehabilitation, prosthetics/orthotics, and sports medicine. Additionally, the predictive capabilities of *validated* models can answer "what if" questions, and through sensitivity analysis can determine the influence of parameters on outcomes. Only recently has computational modeling been used to study animal movement and function. Such models seek to not only understand functional movement of healthy quadrupeds, but also to advance our understanding of clinical pathologies to improve animal health.

In this Research Topic, researchers from the fields of bioengineering, robotics, mathematics, veterinary medicine, comparative biology and zoology, and kinesiology have advanced our understanding of quadrupedal animal movement and function using various types of computational models. Manuscripts in this Research Topic describe a wide range of models including anatomical/morphological models to explore musculoskeletal function, musculoskeletal models developed from advanced XROMM

and diceCT imaging technologies and used to describe locomotor stability and dynamics or to enhance locomotor performance, hydrodynamics models to investigate the influence of surface properties on impact loading of the forelimb, neuromuscular models to study afferent feedback in locomotion, multibody models to evaluate the effects of uncertainties on microscale motion simulations, evolutionary models to characterize muscle morphology, kinematic models to evaluate spinal motion, and models of adaptive motion to advance robotic design. These computational models have been applied to a diverse array of quadrupeds ranging from Chihuahuas to Labrador Retrievers, cats to fossil crocodile relatives, and rodents to horses. A brief description of these leading-edge manuscripts follows.

Three papers in the Research Topic focus on the area of pathology in quadrupeds. A paper by Schaub et al. describes 3D motion of the lower lumbar spine and pelvis in German Shepherd dogs at a walk and trot evaluated using cineradiography. Intervertebral motion was small overall, under 3° of rotation and under 2 mm of translation. Surprisingly, however, intervertebral motion varied among strides within a dog and among dogs. The paper by Schikowski et al. describes 3D atlantooccipital and atlantoaxial kinematic motion of the craniocervical junction in Chihuahuas compared to Labrador Retrievers at a walk, which was also evaluated using cineradiography. Maximal sagittal, lateral, and axial rotation at the atlantooccipital and atlantoaxial joints ranged from 16° to 30° and was slightly larger in Chihuahuas than Labrador Retrievers. Computational modeling can also be used to improve our understanding of injury mechanisms. The paper by Harrison et al. focused on a coupled biomechanical-smoothed particle hydrodynamics model for horse racing tracks and describes the development and validation of a 3D computational model of an equine hoof interacting with a dirt surface and a synthetic track. This model describes the interaction of track surface properties and limb loading, and has the potential to provide insight into distal limb injuries in horse racing.

Several studies in this Research Topic used musculoskeletal models to better understand muscle morphological measures during dynamic motion. Regnault et al. used anatomical, kinematic and dynamic analyses in experimentally manipulated echidna (monotreme mammal) cadaveric forelimbs, while simultaneously capturing estimates of muscle moment arms around major joints. They used the moment arms to estimate maximal muscle moments, and tested whether using moment arms alone vs. joint moments (dependent on muscle size) yielded different conclusions about overall limb mechanics. This approach helped to evaluate the 3D musculoskeletal model, showing which assumptions were reasonable vs. where detailed inputs might be needed. In another study, Löffler et al. also investigated mammalian muscle moment arms in 3D, of hindlimb gluteus medius, but in caviomorph rodents across a broad evolutionary span. They tested how locomotor adaptations (e.g., digging, climbing, and running) related to leverage, finding support for their hypotheses that climbing caviomorphs tended to have larger moment arms, whereas diggers had smaller ones. Furthermore, the authors reconstructed the evolution of locomotor styles, showing how running adaptation was ancestral, with climbing and digging evolving independently, their muscle leverages promoted by natural selection. To investigate the mechanics of walking in frogs, Collings et al. conducted a "Functional analysis of anuran pelvic and thigh anatomy using musculoskeletal modeling of the *Phlyctimantis maculatus.*" In this study, a 3D musculoskeletal model demonstrated that lateral pelvic rotation influenced muscle moment arm in most hindlimb muscles. Findings indicated that pelvic influence was dependent upon femoral angle, which can further alter muscle function.

Lumped-parameter, rigid body biomechanical models were also used to investigate locomotor performance in quadrupedal gait. Ding et al., studying jerboa rodents, combined experimental data on locomotor dynamics with a Spring-Loaded Inverted Pendulum model, applying optimal control theory in simulations predicting where gait transitions should occur. They successfully predicted these transitions across a wide speed range and discovered two different bipedal gaits that were previously undescribed, producing a total of five different locomotor modes. The simulations revealed two major limb-control mechanisms used, involving angular displacement of limbs in swing phase. Using a 2D model with simple springlike limbs, but adding a flexible back joint, Yamada et al. simulated how body center of mass position in horses influenced gait selection. Their simulations used Poincaré maps identifying periodic solutions corresponding to six gait patterns, optimizing gait stability across a range of speeds. They found that the "real" center of mass position corresponds to the optimum for the transverse galloping gait, as opposed to the other five gait patterns. Adachi et al. used a similar modeling approach, varying model geometry to produce a more short-necked (dog-like) vs. long-necked (horse-like) morphology, adopting a quasi-3D approach (e.g., torsional joint allowing body roll). They investigated which periodic solutions for trotting gaits were optimal in terms of stability across a Poincaré map for nine gait patterns. Three patterns were favored, but varying the asymmetry of the model improved stability, demonstrating how horse morphology and forelimb stiffness promote gait differences from trotting dogs. Kamimura et al. also used Poincaré maps to obtain periodic solutions characterizing galloping mechanics in the fastest land animal on Earth: cheetah. A 2D model with rigid torso segments actuated by massless spring-like legs showed that only one periodic solution properly identified the three most distinctive features of cheetah galloping–limited vertical displacements of the mass center, small pitching movements of the torso, and appreciable bending of the spine–which in turn enable these animals to maximize running speed. Polet and Hutchinson used a trajectory

optimization approach and 2D model, applied to a different species: the quadrupedal extinct archosaur *Batrachotomus*, from the Triassic Period. Their simulations predicted at which speeds gait transitions should occur, with good success when applied to experimental data from dogs which supported this methodology. For the fossil, the simulations suggested that there were two gait transitions, with gaits unlike those of extant trotting crocodiles. Importantly, they compared their results with fossilized trackways from similar Triassic archosaurs, obtaining reasonable agreement. Various metrics have been proposed for quantifying mechanical work in quadrupedal locomotion. Pelot and Bertram evaluated the ability of three such measures–Net COM Work, Individual Limbs COM Work, and Limb Extension Work–to predict the four-beat walking strategy commonly observed in cursorial quadrupedal mammals. Applying each of these metrics as cost functions, they solved a series of parameter optimization problems to find that only Limb Extension Work coupled with a model of distributed body mass predicted a walking gait that matches the stereotypical quadruped pattern. The number of legs used to propel the body during locomotion has a decisive effect on the motion of the center of mass and gait stability. Using a Leg Force Interference Model, Wiehmann sought to explain why terrestrial animals change the number of propulsive legs as running speed increases. His analysis showed that as running speed increases, the magnitude of the ground reaction force decreases consonant with the number of legs propelling the body forward. However, one caveat of these findings is that the results do not appear to apply to bipedal locomotion.

Neuromuscular control and force feedback are critical during dynamic activities. Two studies in this Research Topic incorporated these elements into feline models investigating locomotion and landing following descent. Kim et al. included cat hindlimb muscles and a neural network into a neuromusculoskeletal modeling framework to test how feedback influences locomotor dynamics during walking and perturbation via stepping into a hole. The model included Hill-type muscles causing forces to have length- and velocity-dependence. Simulations then used optimization to characterize walking dynamics, and dynamical systems theory to investigate how perturbations were addressed. Their experimental vs. simulation results exhibited good agreement, illustrating how feedback rapidly changes dynamics to compensate for perturbations. Xu et al. employed a feline model to study adaptive strategies in landing following descents from different heights using experimental forelimb dynamic data, finite element analysis (FEA) and machine learning. The FE model demonstrated agreement with experimental data and indicated that maximal limb/bone stress occurs at the joints. Considering force feedback, they determined that with increasing ground reaction force, loading shifts progressively from the distal limb joint to the middle joint and up proximal joint. This information can be used in the design of bionic robots to increase service life of mechanical limbs and reduce wear by strengthening materials used in joints.

Sensitivity analyses are often performed using musculoskeletal models to evaluate the influence of various relevant parameters on outcome. Arroyave-Tobón et al. used 3D skeletal modeling applied to the entire body of seed-collecting ants to quantify locomotor kinematics and to determine the sensitivity of outcomes to marker positions. Their analysis combined specimen geometry with raw locomotor kinematics data, then integrated via modelled inverse kinematic analysis. Monte Carlo simulations showed that marker positions displayed more sensitivity than joint angle inputs. While ants use hexapedal rather than quadrupedal locomotion, the principles applied here are the same and may inspire cross-fertilization of ideas.

Together, these studies in this Research Topic demonstrate the wide array of computational modeling applications addressing research questions related to quadrupedal locomotion and dynamics. With increasing parallel computing and graphics processing capabilities, dynamic optimization of advanced anatomical models and more realistic simulation of motion can further advance our understanding of functional movement in quadrupedal animals in future studies.

Author contributions

All authors have made substantial, direct and intellectual contributions to this work, and approved it for publication.

Conflict of interest

The authors declare that the research was conducted in the absence of any commercial or financial relationships that could be construed as a potential conflict of interest.

Publisher's note

frontiers in Veterinary Science

ORIGINAL RESEARCH
published: 20 August 2021
doi: 10.3389/fvets.2021.709967

Three-Dimensional Kinematic Motion of the Craniocervical Junction of Chihuahuas and Labrador Retrievers

Lisa Schikowski[1]*, *Nele Eley*[1], *Nicola Kelleners*[1], *Martin J. Schmidt*[2] and *Martin S. Fischer*[3]

[1] Department of Veterinary Clinical Sciences, Small Animal Clinic—Surgery, Justus-Liebig-University, Giessen, Germany, [2] Department of Veterinary Clinical Sciences, Small Animal Clinic—Neurosurgery, Neuroradiology and Clinical Neurology, Justus-Liebig-University, Giessen, Germany, [3] Institute of Zoology and Evolutionary Research, Friedrich-Schiller-University, Jena, Germany

All vertebrate species have a distinct morphology and movement pattern, which reflect the adaption of the animal to its habitat. Yet, our knowledge of motion patterns of the craniocervical junction of dogs is very limited. The aim of this prospective study is to perform a detailed analysis and description of three-dimensional craniocervical motion during locomotion in clinically sound Chihuahuas and Labrador retrievers. This study presents the first *in vivo* recorded motions of the craniocervical junction of clinically sound Chihuahuas ($n = 8$) and clinically sound Labrador retrievers ($n = 3$) using biplanar fluoroscopy. Scientific rotoscoping was used to reconstruct three-dimensional kinematics during locomotion. The same basic motion patterns were found in Chihuahuas and Labrador retrievers during walking. Sagittal, lateral, and axial rotation could be observed in both the atlantoaxial and the atlantooccipital joints during head motion and locomotion. Lateral and axial rotation occurred as a coupled motion pattern. The amplitudes of axial and lateral rotation of the total upper cervical motion and the atlantoaxial joint were higher in Labrador retrievers than in Chihuahuas. The range of motion (ROM) maxima were 20°, 26°, and 24° in the sagittal, lateral, and axial planes, respectively, of the atlantoaxial joint. ROM maxima of 30°, 16°, and 18° in the sagittal, lateral, and axial planes, respectively, were found at the atlantooccipital joint. The average absolute sagittal rotation of the atlas was slightly higher in Chihuahuas (between 9.1 ± 6.8° and 18.7 ± 9.9°) as compared with that of Labrador retrievers (between 5.7 ± 4.6° and 14.5 ± 2.6°), which corresponds to the more acute angle of the atlas in Chihuahuas. Individual differences for example, varying in amplitude or time of occurrence are reported.

Keywords: dog locomotion, scientific rotoscoping, craniocervical motion, three-dimensional kinematics, cervical spine

OPEN ACCESS

Edited by:
Denis J. Marcellin-Little, University of California, Davis, United States

Reviewed by:
Shinichi Kanazono, Veterinary Specialists and Emergency Center, Japan
Angela Fadda, Langford Vets Small Animal Referral Hospital, United Kingdom

***Correspondence:**
Lisa Schikowski
lisa.schikowski@googlemail.com

Specialty section:
This article was submitted to Veterinary Neurology and Neurosurgery, a section of the journal Frontiers in Veterinary Science

Received: *14 May 2021*
Accepted: *29 July 2021*
Published: *20 August 2021*

Citation:
Schikowski L, Eley N, Kelleners N, Schmidt MJ and Fischer MS (2021) Three-Dimensional Kinematic Motion of the Craniocervical Junction of Chihuahuas and Labrador Retrievers. Front. Vet. Sci. 8:709967. doi: 10.3389/fvets.2021.709967

INTRODUCTION

Each vertebrate species has a distinct morphology and movement pattern, which reflect the adaption of the animal to its habitat (1). Little is known about the actual motion pattern and ranges of the craniocervical junction during natural locomotion in dogs. Scientific insight is largely limited to data derived from cadaver studies on spinal column specimens or studies performed under standard clinical conditions with sedated animals (2–4). Aberrations of the cervical spine,

including those of vertebral body morphology, may have an influence on locomotion, movement patterns, and ranges of motion. For this purpose, two different breeds, a toy breed dog and a large breed dog with no predisposition to craniocervical abnormalities, were selected. Scientific insight about movement patterns may have implications for the understanding, diagnosis, and treatment of "craniocervical junction abnormalities," which encompass several conditions (5–7).

Our research group was able to record preliminary data on the upper cervical spine to begin with four clinically sound Chihuahuas at a walk and a trot (8). Four additional Chihuahuas and a comparison group of three Labrador retrievers allowed us to establish baseline data on *in vivo* three-dimensional (3D) craniocervical motions.

The aim of this prospective study was to perform a detailed analysis and description of 3D craniocervical non-invasive *in vivo* motion analysis during locomotion in clinically sound Chihuahuas (Ch) and Labrador retrievers (L). Data analysis was focused on gait-cycle-related movements during walking as well as naturally occurring active head and neck motion during locomotion. We were especially interested to evaluate whether body size (Ch vs. L) would have any impact on the timing or range of motion (ROM) of stride-cycle-dependent motions of the cranial cervical spine.

MATERIALS AND METHODS

Animals

A total of 15 Chihuahuas and 14 Labrador retrievers were examined first clinically and later in locomotion on a treadmill. The exclusion criteria were abnormal findings on clinical, orthopedic, or neurological examination or dogs with insufficient habituation on treadmill or movements. Eight Chihuahuas with an average age of 38.5 ± 16.3 months were included. The subjects had an average body weight of 2.8 ± 0.6 kg and a withers size of 19.9 ± 2.3 cm at the time of the study. The gender distribution was 1:1 (**Table 1**).

Three Labrador retrievers with an average age of 26.3 ± 5.7 months were examined as the reference breed. At the time of the examination, the average body weight was 37.6 ± 3.5 kg, and the withers size was 59.3 ± 2.6 cm. The gender distribution was 2:1 with two males to one female. All dogs were privately owned (**Table 1**).

This study was conducted with the owners' consent. All experiments were reviewed and approved by the Ethics Commission of the German states of Thuringia and Hesse. The registration number of the application is (TLV Reg. No.: 22-2684-04-02-075/14).

TABLE 1 | Details of the study population: Chihuahuas (Ch), Labrador retrievers (L).

Dog	Sex	Age (months)	Body weight (kg)	Height at withers (cm)
Ch1	Female	59	2.8	21
Ch2	Female	11	3.7	25
Ch3	Male	35	2.1	20
Ch4	Female	46	2.1	20
Ch5	Male	35	2.4	25
Ch6	Female	25	2.5	21
Ch7	Male	33	3.7	26
Ch8	Male	64	3.0	24
L1	Male	33	41.7	58
L2	Female	19	33.0	57
L3	Male	27	38.0	63

XROMM/Scientific Rotoscoping

Scientific rotoscoping, a markerless, non-invasive method of the XROMM methodology (X-Ray Reconstruction of Moving Morphology) (9), was used for kinematic analysis. The scientific rotoscoping workflow is composed of a large number of individual work steps, from which the movement data are subsequently generated. For this purpose, a bony marionette with articular joints is constructed on the basis of computed tomography (CT) data. Biplanar fluoroscopy and high-speed cameras are used to record the dog's movements on the treadmill. Essentially, the bone marionette is matched with the bony silhouette of the X-ray videos. This procedure results in a 3D spinal column that virtually reflects the real movement patterns of the bony structures during locomotion and enables 3D movement measurements with high accuracy (see (10) for a more detailed description).

Study Design

After inconspicuous general clinical as well as orthopedic and neurological examinations, a CT examination was performed under general anesthesia. Only subjects with an unremarkable neurological and orthopedic examinations were approved for the study. CT scans (Brilliance, Philips, Best, Netherlands, 16-slice helical scanner) of the head, complete spine, and pelvis of each dog were obtained. Settings of 120 kV and 200 mA were used for the investigation. In addition, an MRI scan of the spine was conducted to rule out cervical conditions which potentially may cause gait alterations. For study subjects examined before December 2016, MRI (MRI 1.0 Tesla superconducting system Intera Philips, Netherlands) was used. After that date, the MRI (MRI 3.0 Tesla Magnetom Verio Siemens, Germany) was used in combination with the Syn-spine-coil. Sagittal T2-weighted images of the cervical, thoracic and lumbar spine and transversal T2-weighted images at the craniocervical and lumbosacral junction were acquired. No dogs included in the study did show any signs of craniocervical junction disease or degenerative lumbosacral stenosis at the time of the investigation.

All subjects were individually habituated to treadmill locomotion. Chihuahuas showed an average walking speed of 0.44 ± 0.09 m/s and Labrador retrievers 0.98 ± 0.2 m/s (**Table 2**). A horizontal motorized treadmill (**Figures 1**, **2**) was used. The respective duty factor for each dog during walking on the treadmill was calculated (**Table 2**).

Abbreviations: SR, scientific rotoscoping; TUCM, total upper cervical motion; ROM, range of motion; TOO, time of occurrence; Ch, Chihuahua; L, Labrador retriever; C1, first cervical spine, atlas; C2, second cervical spine, axis; C3, third cervical spine; 3D, three-dimensional.

TABLE 2 | Overview of Chihuahuas (Ch) and Labrador retrievers (L) regarding the treadmill speed and duty factor in relation to the left hind limb.

Dog	Treadmill speed (m/s)	Duty-factor (%)	Phase normalization
Ch1	0.39	66.8 ± 0.8	70/30
Ch2	0.52	63.9 ± 2.0	60/40
Ch3	0.38	62.7 ± 2.2	60/40
Ch4	0.32	63.0 ± 1.3	60/40
Ch5	0.45	65.7 ± 1.5	70/30
Ch6	0.38	67.3 ± 2.7	70/30
Ch7	0.50	58.7 ± 1.1	60/40
Ch8	0.60	62.4 ± 1.3	60/40
Total Ch	**0.44 ± 0.09**	**63.8 ± 1.6**	
L1	0.77	62.6 ± 1.7	60/40
L2	0.98	65.3 ± 0.9	70/30
L3	1.20	63.4 ± 0.8	60/40
Total L	**0.98 ± 0.2**	**63.8 ± 1.1**	

Phase normalization of Chihuahuas and Labrador retrievers based on the respective averaged duty factor with respect to the left hind limb.

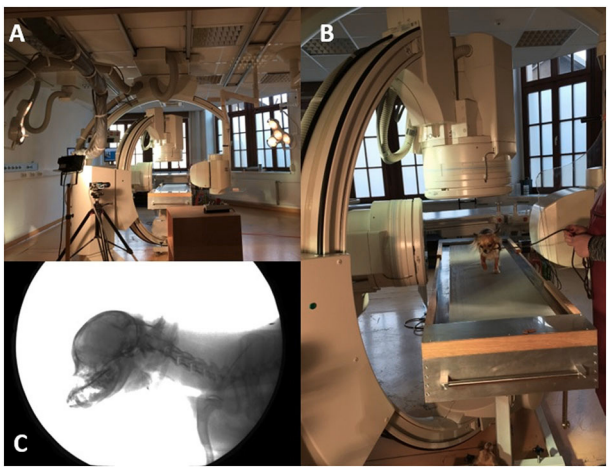

FIGURE 1 | Fluoroscopy 90° experimental setup. **(A)**: 90° fluoroscopy setting to record the-laterolateral and ventrodorsal beam path. The treadmill is located in the center. **(B)**: Chihuahua walking on the treadmill located in the beam path. **(C)**: X-ray video view of the laterolateral beam path.

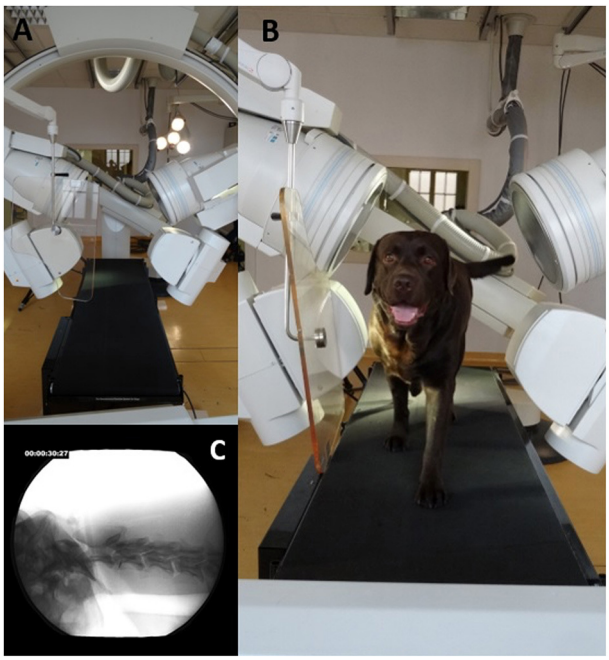

FIGURE 2 | Fluoroscopy 63° experimental setup. **(A)**: 63° fluoroscopy setting to record the oblique-laterolateral beam path. The treadmill is located in the center. **(B)**: Labrador retriever walking on the treadmill located in the beam path. **(C)**: X-ray video view of the oblique-laterolateral beam path.

Biplanar X-ray videos of each dog during walking were recorded using a digital high-speed videography system. Biplanar fluoroscopy (Neurostar Siemens AG, Munich) consists of two image intensifier systems (diameters 40 cm) as well as high-speed cameras (Visario Speedcam, Weinberger GmbH, Nuremberg). Image resolution is 1,536 × 1,024 pixels at a frame rate of 500 Hz. The C-arms were adjusted in relation to the size of the study subjects, either as a ventrodorsal and a laterolaterale beam (Ch) or in a right and left oblique beam (L) at an angle of 63° (**Figures 1**, **2**) X-ray-settings depended on the dog's size (Chihuahua: 80 kV, 40 mAs; Labrador retriever: 100 kV, 75 mAs). The frame rate was 500 frames per second, and a shutter speed of 500 μs was used to prevent motion blur. The X-ray videos can be viewed in the **Supplementary Material**.

Data Analysis

From the recorded trials, consecutive walking strides ($n = 6$) were selected for scientific rotoscoping except for one Labrador retriever ($n = 3$). C3 represents the first animated vertebrae on the hierarchical joint marionette. Because of this hierarchical order C3 reflect the movement of the spine and dog in space and is further called as total upper cervical spine motion (TUCM). The transitional and rotational movements of the TUCM (C3), intervertebral joints (C3/2), the atlantoaxial joint (C2/C1), and the atlantooccipital joint (C1/skull) were analyzed in six degrees of freedom (tx—ty—tz, rx—ry—rz). Due to the individual differences in the duration of the stance and swing phases, a phase normalization (11) with reference to the footfall events had to be performed for all dogs and strides. This allows a comparison of the angular movements across dogs and strides. Time normalization was performed using MATLAB® (TheMathWorks). The duty factor, defined as "the fraction of the duration of a stride for which each foot remains on the ground," (12) is used for classifying different types of gait. Values >0.5 (contact time >50%) characterize walking (13–15). For each dog and stride, the duty factor was calculated, based on the synchronously recorded high-speed live videos, showing the up and downtimes of the left pelvic limb. The duty factor of

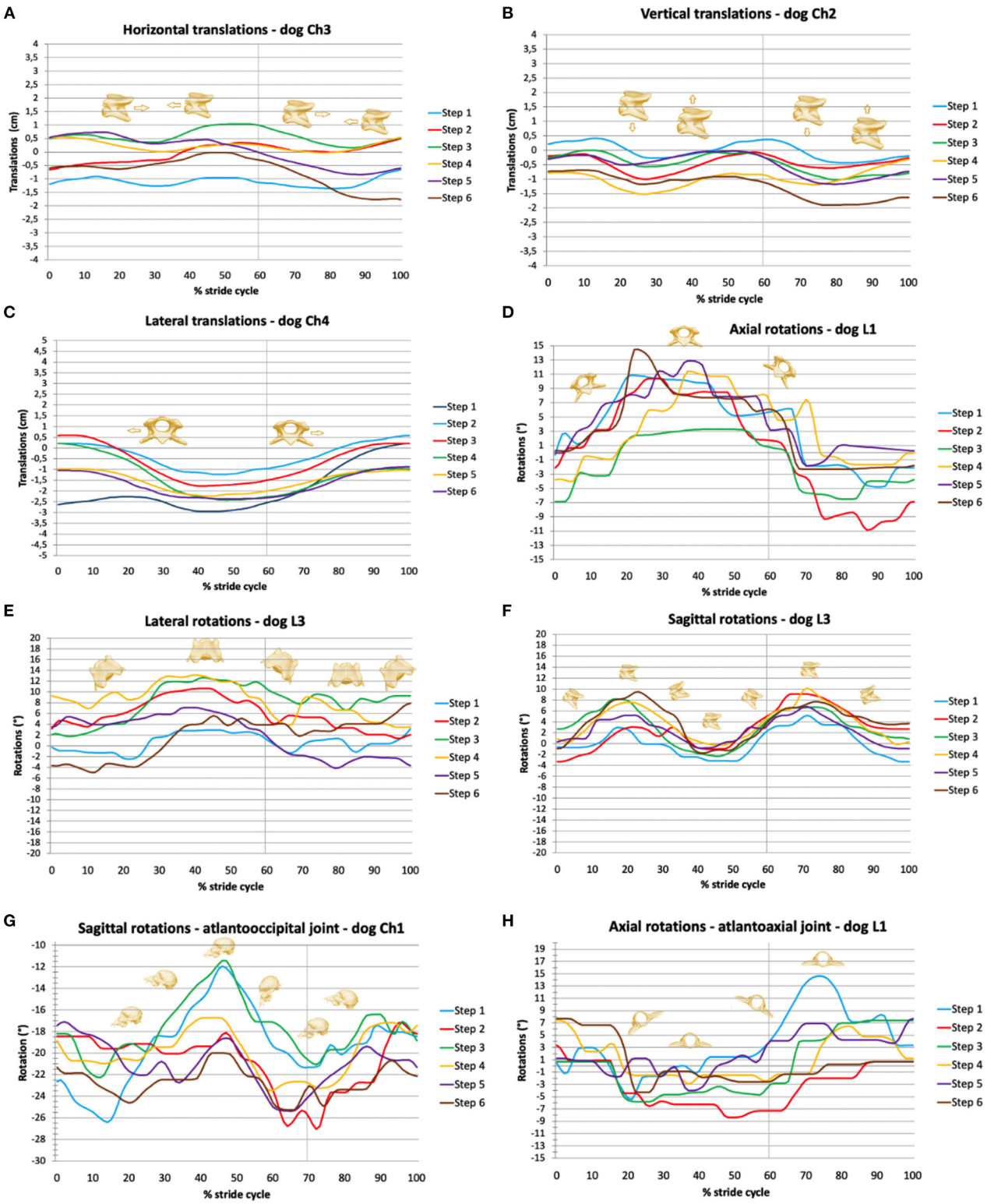

FIGURE 3 | Stride-phase-normalized gait-cycle-dependent movements of the total upper cervical motion (TUCM), atlantoaxial joint, and atlantooccipital joint. Six walking stride cycles (step 1 to step 6) for each dog are presented. X-axes represent the stride cycle from touch-down (0%) to subsequent touch-down of the reference limb (100%). The vertical line indicates the duty factor. **(A)** Horizontal, **(B)** vertical, and **(C)** lateral translations of the TUCM. **(D)** Axial, **(E)** lateral, and **(F)** sagittal rotations of the TUCM. **(G)** Axial rotations of the atlantoaxial joint, **(H)** sagittal rotations of the atlantooccipital joint.

Chihuahuas is 63.8 ± 1.6, and that of Labrador retrievers is 63.8 ± 1.1 (**Table 2**).

The 3D movements of the intervertebral joints and the atlantoaxial and atlantooccipital joint were defined as follows: axial rotations occurred along the horizontal axis, lateral rotations along the vertical axis, and sagittal rotations along the latero-medial axis. The translational movements were only described for the TUCM, which determines the movements in space. Transitional movement could not be detected in the intervertebral joints (C3/2), the atlantoaxial joint (C2/C1), and the atlantooccipital joint (C1/skull). Horizontal translation is translation in the craniocaudal direction; vertical translation, in the dorsal and ventral directions; and lateral translation, in the laterolateral direction.

The arithmetic means and standard deviations of the individual movements, as well as the range of motion (ROM) of each joint, were determined. The movements of the virtual joints of each dog were evaluated and correlated with the stride cycle or other movements that were synchronously observable on the high-speed video. This correlation, the percentage time of occurrence to the stride cycle, is called the time of occurrence (TOO). The movements of the Chihuahuas were compared with each other and with those of the Labrador retrievers. The movements of Labrador retrievers were also correlated.

RESULTS

Gait Analysis Using High-Speed Video

Walking speed varied individually between 0.32 m/s and 0.6 m/s for Chihuahuas and between 0.77 m/s and 1.2 m/s for Labrador retrievers. On average, the comfortable treadmill speed of Chihuahuas was 0.44 ± 0.09 m/s, and that of Labrador retrievers was 0.98 ± 0.2 m/s (**Table 2**). Chihuahuas made an average of 6.19 ± 0.9 strides per minute and Labrador retrievers 4.67 ± 0.3 strides per minute. According to the footfall pattern, the tripod support typically alternated with a parallel or diagonal bipod support during walking.

Three-Dimensional Movements With Stride Cycle Dependency

All movements related to the total movements during locomotion were correlated with the stride cycle. Locomotion-dependent movements can be superimposed by active head movements or by position changes on the treadmill. Individual values of TOO and ROM are reported in the **Supplementary Tables 3–7**. Exemplary stride-cycle-dependent movements are shown in **Figure 3**.

Data Analysis of the Total Upper Cervical Motion

Horizontal translation in the craniocaudal direction (**Figures 3**, **4**) showed a biphasic pattern in both breeds. The amplitude and average ROM of Chihuahuas was 0.5 ± 0.7 cm, which was slightly lower than the ROM 0.8 ± 0.9 cm of Labrador retrievers. The highest amplitude was similar in both breeds (5 and 5.2 cm in Chihuahuas and Labrador retrievers, respectively). Horizontal translation in Chihuahuas changed direction on average after 16.3 ± 10.5%, 36.0 ± 6.6%, 60.7 ± 7.3%, and 87.9 ± 6.1% of the stride cycle of the reference limb and in Labrador retrievers after 28.8 ± 0.3%, 40.8 ± 7.5%, 72.1 ± 8.3%, and 91.0 ± 9.9. A change in position of the bony marionette in the cranial direction is associated with lift-off events of the pelvic limbs. A caudal displacement is visible at mid-stance of the pelvic limbs or at the beginning of the second half, at the level of the ipsilateral forelimb lift-off.

A biphasic pattern of vertical translation (**Figures 3**, **4**) was recognized in both breeds. In comparison with horizontal translation, vertical translation showed greater differences with respect to the footfall pattern. The average ROM of Chihuahuas (0.7 ± 0.9 cm) was slightly lower than that of Labrador retrievers (0.9 ± 1.0 cm). The greatest ROM of Chihuahuas (5.8 cm) was

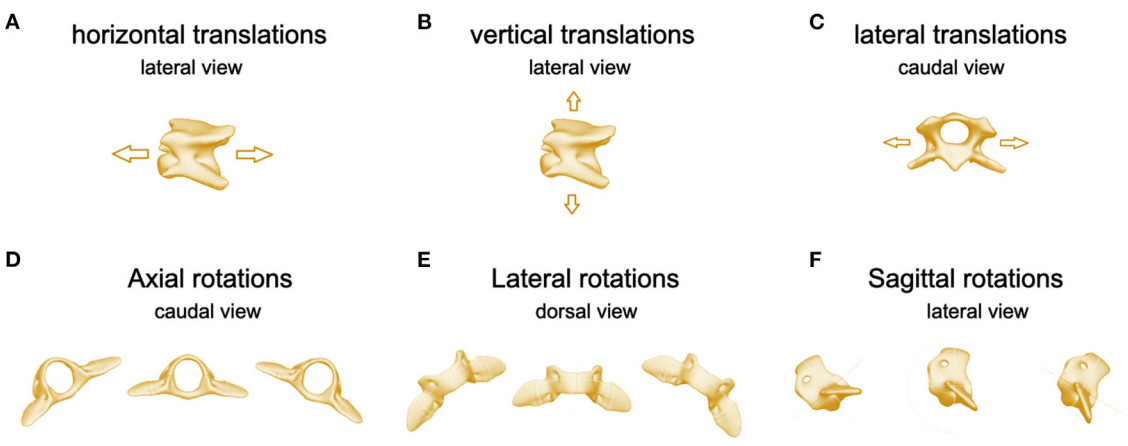

FIGURE 4 | Images of C3 illustrating **(A)** horizontal translations, lateral perspective, **(B)** vertical translations, lateral perspective, **(C)** lateral translations, cranial perspective. Images of C2 illustrating **(D)** axial, **(E)** lateral, and **(F)** sagittal rotations.

approximately the same as that of Labrador retrievers (5.9 cm). Vertical translation in Chihuahuas changed direction on average after 17.6 ± 7.3%, 39.3 ± 10.6%, 67.6 ± 6.5%, and 89.2 ± 6.6% of the stride cycle of the reference limb and in Labrador retrievers after 11.8 ± 8.6%, 36.4 ± 7.9% 60.6 ± 9.3%, and 81.5 ± 9.4%. A vertical translation in the dorsal direction is visible in the swing phase of the anterior limbs. A ventral vertical translation occurs at the beginning of the stance phase of the respective anterior limbs.

A monophasic pattern of lateral translation (**Figures 3**, **4**) was visible in both breeds. The average ROM of Chihuahuas (1.0 ± 1.0 cm) was equal to that of Labrador retrievers (1.0 ± 1.9 cm). The maximum values were significantly smaller for Chihuahuas (4.6 cm) than for Labrador retrievers (12.9 cm). With a weight shift at the beginning of the respective forelimb stance phase, the change in motion direction was associated with right- and left-lateral translation. The direction of translation corresponded to the limb in the stance phase.

Axial rotation is the rotation around the horizontal axis (**Figures 3**, **4**). Multiple movements that cause axial rotation complicate the identification of stride cycle-associated axial rotation. All Labrador retriever showed a correlation to the stride cycle with a monophasic pattern. A correlation of axial rotation to the stride cycle was only visible in four of eight Chihuahuas. The average ROM of the axial rotation of the TUCM was slightly lower in Chihuahuas (2.6 ± 2.9°) than in Labrador retrievers (3.5 ± 3.9°). The maximal values were 16.4 and 18.2 ° in Chihuahuas and Labrador retrievers, respectively. The axial rotation was associated with the forelimb stance phase and reached its maximum in the last third. The change in motion direction was associated with forelimb lift-off. The direction of rotation was related to the corresponding limb in the stance phase. The monophasic pattern was only suggestively visible in one Chihuahua. At the time of lifting-off, the other three dogs with stride cycle dependency show only curve deflections. The entire amplitude of the monophasic pattern of Labrador retrievers was on average at least two to four times larger.

Lateral rotation describes rotation around the vertical axis (**Figures 3**, **4**). Average ROM was 2.3 ± 2.7° for Chihuahuas and 2.7 ± 3.6° for Labrador Retrievers. The greatest amplitude was 17.4° for Chihuahuas and 21.8° for Labrador retrievers. Overall, both breeds showed a monophasic pattern. Among Chihuahuas, this pattern could only be partially observed due to the small entire amplitude. The entire amplitude of the monophasic pattern of Labrador retrievers is greater in comparison to Chihuahuas. Concerning footfall events, greater variation was observed in lateral rotation. Lateral rotation changed direction on average after 53.1 ± 9.4% and 78.0 ± 9.8% of the stride cycle of the reference limb in Chihuahuas and after 42.0 ± 3.1% and 65.6 ± 4.6% in Labrador retrievers. Rotation to the right/left occurred in conjunction with neck movement and weight shift to the right or left during locomotion. The extent of movement and the starting point of the direction of movement varied among dogs but not between the two breeds.

Sagittal rotation describes rotation about the lateral axis (**Figures 3**, **4**). The average ROM of Chihuahuas was 4.0 ± 5.4° and that of Labrador retrievers was 4.8 ± 4.4°. The maximum value was significantly greater in Chihuahuas than in Labrador retrievers (50.9 and 22.0°, respectively). If a stride cycle-associated pattern of the sagittal rotation was observable, it was biphasic. Sagittal rotation changed direction on average after 22.9 ± 6.2%, 41.5 ± 4.0%, 73.6 ± 10.7%, and 90.5 ± 3.6% of the stride cycle of the reference limb in Chihuahuas and after 24.5 ± 7.1%, 48.1 ± 2.8%, 75.7 ± 6.4%, and 93.4 ± 3.7% in Labrador retrievers. Concerning the stride cycle, dorsal sagittal rotation occurs when the neck is raised at the end of the swing phase. Likewise, ventral sagittal rotation is associated with lowering of the neck at the beginning of the forelimb stance phase. Sagittal rotation is related to vertical translation and both occur together.

Rotational Movements of the Atlantoaxial Joint and Atlantooccipital Joint

The rotational movements in the atlantoaxial joint are predominantly independent of the stride cycle. However, for all Labrador retrievers and one Chihuahua (Ch2) axial rotation of the atlantoaxial joint showed a stride-cycle-associated monophasic pattern. The average ROM of Ch2 was 3.3 ± 2.0°, and that of Labrador retrievers was 3.8 ± 3.6°. The maximum ROM was 24.3° in Chihuahuas and 15.8° in Labrador retrievers. A correlation with the stride cycle existed in the stance phase of the forelimb with a downward/side-to-side movement of the neck/head. The direction of axial rotation was opposite to that of the forelimb in stance. The overall extent of curve deflection varied with respect to the action of the limb and may be primarily punctate or may occur during the course of the stance phase. However, the maximum curve deflection was visible in all dogs in the last third of the stance phase. The amplitude of the stride-cycle dependent pattern of Labrador retrievers was equal to or slightly larger than that of Chihuahuas, but the entire pattern was easier to follow.

The sagittal rotation of the head was linked to the sagittal rotation of the neck but occurred in opposite rotational direction. A relationship between sagittal head rotation to forelimb action during the stride cycle, and sagittal rotation of the TUCM, was likely based on the coupled occurrence. The average ROM of sagittal rotation of the atlantooccipital joint was 3.09 ± 3.5° in Chihuahuas and 3.8 ± 2.9° in Labrador retrievers. The greatest amplitude was 30.2° in Chihuahuas and in 16.8° Labrador retrievers.

Three-Dimensional Movements During Active Head Movements

When the dog is in motion, sagittal, lateral, and axial rotation can be detected in both the atlantoaxial and the atlantooccipital joint during head movements. Lateral and axial rotation occurs as a coupled motion pattern. In locomotion, mainly lateral movements, as well as extension and flexion movements of the head, become visible. During active head movements in locomotion, sagittal rotation in the atlantoaxial and atlantooccipital joints is related to flexion and extension movements. When the head is moved actively to the left, lateral rotation to the left and axial rotation to the right occurs in

the atlantoaxial joint. In the atlantooccipital joint, this head movement results in lateral and axial rotation to the left.

At the atlantoaxial joint, the widest measured ROM were Ch: 20° and L: 9.7° in sagittal rotation, Ch: 26° and L: 7.8° in lateral rotation, and Ch: 24° L: 15.8° in axial rotation. The average ROM of the atlantoaxial joint in all three directions of rotational movement was greater in Chihuahuas than in Labrador retrievers (axial rotation Ch: 4.2 ± 3.7°, L: 3.8 ± 3.6°, lateral rotation: Ch: 2.8 ± 2.8°, L: 2.1 ± 1.7°, Ch: 2.0 ± 2.1°, L: 1.4 ± 1.8°). Axial rotation of the atlantoaxial joint is inferential and, as expected, the rotation with the greatest motion.

In the atlantooccipital joint, the greatest ROM was Ch: 16° and L: 11.7° in lateral rotation, Ch: 18° and L:12.0° in axial rotation, and Ch: 30° and L:16.8° in sagittal rotation. The average ROM of Chihuahuas was 2.7 ± 2.5 ° in axial rotation and 1.8 ± 1.8° in lateral rotation. The average ROM of Labrador retrievers was 2.9 ± 2.3° in axial rotation and 2.4 ± 2.5° in lateral rotation. In conclusion, the sagittal rotation of the atlantooccipital joint is the rotation with the greatest movement during locomotion.

The positioning during CT examination in dorsal recumbency is the reference position and starting position for scientific rotoscoping, set to 0°. Comparing the absolute position of the atlas of Chihuahuas and Labrador retrievers to the reference position Chihuahuas show a slightly higher absolute average value of the sagittal rotation of the atlas (between 9.1 ± 6.8° and 18.7 ± 9.9°) than Labrador retrievers (between 5.7 ± 4.6° and 14.5 ± 2.6°). Regarding the absolute position of the head Chihuahuas showed overall average absolute values between −22.4 ± 16.4° and −42.9 ± 15.1° in sagittal rotation of the head and Labrador retrievers between −33.3 ± 5.5° and −54.1 ± 3.8°.

DISCUSSION

Influence of the Treadmill on Gait Pattern

A long discussion on how gait patterns might be influenced by a treadmill [for a review, see Bockstahler, Skalicky [16]] is of no importance in this study as it is not possible to record biplanar fluoroscopy of the cervical spine without using a treadmill. Although the dogs used in our study were well-trained, the dog itself is the greatest factor influencing the variability of the gait pattern (16). The treadmill speed was individually adjusted to the subject to achieve a consistent gait pattern. The selection of a comfortable speed for each individual is very important, as this is the only way to maintain subject compliance, which also leads to a lower variability of steps among them (16). A steady stride was achieved at an average speed of 0.44 ± 0.09 m/s in Chihuahuas and at 0.98 ± 0.2 m/s in Labrador retrievers. The average treadmill speed in Chihuahuas was similar those reported by Kelleners (8) and Fischer, Lilje (13) (0,41 m/s). For Labrador retrievers, the average treadmill speed was in line with the values of the different treadmill speeds (range from 0,77 to 1,22 m/s) used in the literature of Bockstahler, Skalicky (17), Gustås, Pettersson (18), Wachs, Fischer (19), Kopp (20).

Relationships Between Movements

Biphasic horizontal translation and monophasic lateral translation each show a relationship to position changes during locomotion. The vertical translation, the sagittal and axial rotation of the TUCM as well as the sagittal rotation of C3/C2, the atlantooccipital joint, and the axial rotation of the atlantoaxial joint show a relation to the stance phase and swing phase of the forelimbs. However, the stride-cycle-dependent movements are only visible if the pattern is not "disturbed" by active head movements. Chihuahuas and Labrador retrievers have the same basic pattern of movements with individually varying amplitude and slightly varying TOO.

There is a positive correlation between stride-cycle-dependent horizontal translation and vertical translation as well as between vertical translation and sagittal rotation of the TUCM. Lateral rotation of the TUCM occurs simultaneously with lateral translation in the same direction. At the end of lateral translation, axial rotation occurs in opposite direction. In comparison with Chihuahuas, Labrador retrievers show a significantly greater amplitude of axial rotation of the TUCM. The stride-cycle-associated axial rotation of the TUCM and the axial rotation of the atlantoaxial joint show an opposite direction of rotation. The stride-cycle-associated sagittal rotation of C3/C3 and C3/C2 have the same direction of rotation with an opposite sagittal rotation of the head.

Three-Dimensional Movements of the Upper Cervical Spine With Stride-Cycle Dependence

Regarding the greater amplitude of the horizontal translation of Labrador retrievers in comparison with that of Chihuahuas, its greater advance due to its larger size or the variations in its position on the treadmill are possible explanations. The amplitude of lateral rotation of the TUCM in the Labrador retriever is significantly greater than that in the Chihuahua. This is consistent with observations by Loscher and Meyer (21) that the amplitude of head-neck movements decreases with relatively short necks.

The axial rotation of the TUCM follows the rolling motion over the trunk in connection with the action of the forelimbs as well as a coupling to lateral and vertical translation during locomotion. In comparison with Chihuahuas, Labrador retrievers show a clearly monophasic axial pattern. This entire amplitude is on average at least two to four times larger. Looking at the gait pattern of Labrador retrievers subjectively, a more ponderous gait with a further out-stepping and reaching of the forelimbs is evident in comparison with that of Chihuahuas. Fischer et al. (13) examined the kinematic parameters of Chihuahuas. In a comparison of both breeds, the forelimbs of Chihuahuas were found to be deflected a very short distance to touch down and lift off at a walk. In stride, the hindlimb deflection to the rear is very small, but the hindlimb is guided far forward for lifting off (13). The rolling motion over the trunk is possibly influenced by limb chiseling out and reaching out. Further chiseling out and reaching out results in greater diagonal motion and, consequently, greater axial rotation. Therefore, because of the greater amplitude, this is easier to identify in Labrador retrievers. Locomotion-associated rotations have

already been published for the pelvis and lumbar spine (19, 20, 22, 23).

The magnitude and timing of sagittal rotation, that is, up and down movements of the head and neck during locomotion, are influenced by the neck-trunk ratio, stride frequency, and locomotion speed (21). Additionally, in horses, there is evidence of energetic benefits of the cycle-associated up-and-down movement of the head/neck (21, 24). As the neck oscillates, weight force is transferred to the forelimbs, and energy expenditure is minimized by a phase shift between head-neck oscillation and trunk oscillation (21). Carrier et al. (25), Carrier et al. (26) addressed the EMG pattern of the shoulder girdle muscles and the EMG pattern of the muscles responsible for forelimb protraction and retraction during locomotion in two studies. Both studies were performed on the trotting dog after treadmill habituation. The protractor muscles showed a different pattern of activity, but the main movement of all muscles as a whole was visible toward the end of the stance phase of the forelimb (26). Associating the biphasic pattern of vertical translation and sagittal rotation of the TUCM with the stance phase of the respective forelimb, instead of the swing phase a curve increase is evident from the first third of the forelimb stance phase. This is coincident with lift-off of the contralateral anterior limb. The maximum curve deflection is traceable in the last third of the stance phase. When sagittal rotation and vertical translation are considered together with the activity pattern of the forelimb protractors, dorsal rotation as well as translation of the neck is found to be related to the activity of the forelimb protractors. These findings emphasize the relationship between head and neck motion during locomotion.

The amplitude of the stride-cycle-dependent pattern of axial rotation of the atlantoaxial joint of Labrador retrievers is equally to or slightly larger than that of Chihuahuas, but the overall pattern is easier to follow. Another possible reason is a greater protrusion and extension of the forelimb (13) as well as a larger amplitude of head and neck movement during locomotion (21).

Comparison of Chihuahuas and Labrador Retrievers Concerning Anomalies of the Craniocervical Junction

The present study involved random head movements with varying degrees of movement between individuals, and no standardized movements were provoked and measured. Therefore, the average values of ROM and ROM_{max} between breeds cannot be used to assume greater mobility within a direction of rotation of a breed. However, in locomotion, the absolute measured values of the atlas and the skull in comparison with the reference position, the CT position, can indicate different angulations of the vertebral bodies between both breeds of dogs. When sagittal rotation of the atlas is examined, Chihuahuas show overall average absolute values between 9.1 ± 6.8 and $18.7 \pm 9.9°$ and Labrador retrievers between $5.7 \pm 4.6°$ and $14.5 \pm 2.6°$. Thus, the average value of sagittal rotation of the atlas in Chihuahuas was slightly higher than that in Labrador retrievers, which corresponds to a more acute angle of the atlas. However, the high standard deviation of the Chihuahua indicated a large variance. In a comparison of ROM between large and small dogs, similar ROM values would be expected if the vertebral bodies were scaled, but this would not be due to differences in the morphology of the vertebral bodies (27–29). The results are consistent with subjective observations of gait analysis on the treadmill, whereas Chihuahuas, in comparison with Labrador retrievers, showed a more upright neck posture during locomotion. The large inter-individual variance within Chihuahuas may be due to a different neck posture during locomotion. This may also be caused, to a different extent, individually by different degrees of treadmill habituation, but may also be due to a large variance in the morphology of the vertebral bodies and their rotational position relative to each other, which could be a predisposition of individual dogs to pathologies of the craniocervical junction. However, the standard deviation of Labrador retrievers may be lower than that of Chihuahuas only because of the smaller study population. Due to the more acute angle of the atlas of Chihuahuas, an atlantooccipital overlap during locomotion is less likely.

The positioning during CT examination in dorsal recumbency is the reference position and starting position for scientific rotoscoping, set to 0°. When considering the sagittal rotation of the head, Chihuahuas showed overall average absolute values between -22.4 ± 16.4 and $-42.9 \pm 15.1°$ and Labrador retrievers between -33.3 ± 5.5 and $-54.1 \pm 3.8°$. Thus, in comparison with Chihuahuas, Labrador retrievers have a more negative sagittal rotational position of the head during locomotion relative to the CT position. The morphology of the head represents a possible cause. The skull of Labrador retrievers is flatter and can therefore be stretched more during positioning for CT, which could explain the more negative sagittal rotational position.

Comparing the absolute position of the atlas of Chihuahuas and Labrador retrievers to the reference position, Chihuahuas show a slightly higher absolute average value of the sagittal rotation of the atlas (between 9.1 ± 6.8 and $18.7 \pm 9.9°$) than Labrador retrievers (between $5.7 \pm 4.6°$ and $14.5 \pm 2.6°$). Considering the position of the atlantoaxial and atlantooccipital joint at CT and during surgical treatment in the context of fixation techniques, it is important to recognize that this position does not correspond to the physiological position during locomotion.

Comparison of the Results at Walk With the Results at Trot, Focusing on Stride-Cycle-Dependent Movements

The stride-cycle-dependent movements at a trot differ from those at a walk, especially in their amplitude. Horizontal and vertical translation of the TUCM in space are larger at trot than at walk (0.7 ± 0.5 cm horizontal translation and 0.8 ± 0.4 cm vertical translation). The larger values of the above mentioned movements can be explained by the oscillating character of the trot (30, 31). Both movements showed a biphasic motion pattern and a correlation with each other during walking and during trotting. Lateral translation of the TUCM is, however, smaller at a trot than at a walk (0.5 ± 0.6 cm), most likely

due to the diagonal limb action while trotting, which minimizes this motion pattern. Sagittal rotation of the TUCM is smaller at a trot, too (2.8 ± 2.8°), thus validating the findings that the oscillating character of the trot originates mainly from the trunk while fixing the head (21). Axial rotation of the TUCM has a similar extent and correlation at a walk and at a trot.

CONCLUSION

The results of this study confirm the correlation between head and neck movements and locomotion. Chihuahuas and Labrador retrievers have the same basic pattern of movements with individually varying amplitude and slightly varying TOO. For the first time, a similar pattern of these movements is shown in Labrador retrievers and Chihuahuas. General cyclical position changes at a walk as well as movements of the forelimbs affect the head–neck movement in locomotion when the craniocervical junction is not actively moved.

Biphasic horizontal translation and monophasic lateral translation each show a relationship to position changes during locomotion. Vertical translation and sagittal and axial rotation of the TUCM, as well as sagittal rotation of C3/C2 and the atlantooccipital joint and the axial rotation of the atlantoaxial joint, show a relation to the stance and swing phase of the forelimbs. In the atlantoaxial joint, the widest measured ranges of motion are 20° sagittal rotation, 26° lateral rotation, and 24° axial rotation. In the atlantooccipital joint, the widest measured ranges of motion are 16° lateral rotation, 18° axial rotation, and 30° sagittal rotation. Chihuahuas show a slightly higher absolute average value of the sagittal rotation of the atlas (between 9.1 ± 6.8 and 18.7 ± 9.9°) than Labrador retrievers (between 5.7 ± 4.6 and 14.5 ± 2.6°), which corresponds to a more acute angle of the atlas. When moving, the sagittal, lateral, and axial rotation can be detected in both the atlantoaxial and the atlantooccipital joint during head movements. The lateral and axial rotation occurs as a coupled motion pattern. In comparison with Chihuahuas, Labrador retrievers show a greater entire amplitude of axial and lateral rotation of the TUCM as well as of the atlantoaxial joint.

Physiological measured values of the range of motion during locomotion were determined for the sagittal, lateral, and axial rotation in both breeds of dogs. The present study gives insights into the 3D kinematics of the craniocervical joints in locomotion and in active head movements of Chihuahuas and Labrador retrievers. It provides a basis for further comparative studies and contributes to a better understanding of the physiological conditions and variations between the two breeds of dogs studied. The influence of positioning should be included in any sectional imaging and surgical technique.

DATA AVAILABILITY STATEMENT

The raw data supporting the conclusions of this article will be made available by the authors, without undue reservation.

ETHICS STATEMENT

The animal study was reviewed and approved by the Committee on the Ethics of Animal Experiments of the Justus Liebig University as well as from the Regierungspräsidium Hessen and Thuringia (Permit No.: 22-2684-04-02-075/14). Written informed consent was obtained from the owners for the participation of their animals in this study.

AUTHOR CONTRIBUTIONS

LS, NK, NE, MS, and MF conceived the study. LS, NK, and MF conducted the experiments. LS and NK prepared X-ray data and generated the digital bone models from animal data. LS and NK performed the rotoscoping and analyzed the experimental data. LS, NK, and MF drafted the manuscript. All authors contributed to the interpretation of the results and revised the manuscript.

FUNDING

The study was partially funded by AOVET. The funding body did not had influence on the design of the study, on the collection, analysis, and interpretation of the data or in writing the manuscript.

ACKNOWLEDGMENTS

We would like to thank Rommy Petersohn and Ella Wenz for technical assistance during experiments, Bettina Hesse for program skills in MATLAB and Dr. Sebastian Schaub for technical support. This manuscript represents a part of the Doctoral thesis submitted by the first author in partial fulfillment of the requirements of a Dr. med. vet. Degree (32).

SUPPLEMENTARY MATERIAL

The Supplementary Material for this article can be found online at: https://www.frontiersin.org/articles/10.3389/fvets.2021.709967/full#supplementary-material

REFERENCES

1. Arnold P. Evolution of the mammalian neck from developmental, morpho-functional, and paleontological perspectives. *J Mamm Evol.* (2020) 28:1–11. doi: 10.1007/s10914-020-09506-9
2. McLear RC, Saunders HM. Atlantoaxial mobility in the dog. *Vet Radiol Ultrasound.* (2000) 41:558.
3. Morgan J, Miyabayashi T, Choy S. Cervical spine motion: radiographic study. *Am J Vet Res.* (1986) 47:2165–9.
4. Penning L, Badoux DM. Radiological study of the movements of the cervical spine in the dog compared with those in man. *Anat Histol Embryol.* (1987) 16:1–20. doi: 10.1111/j.1439-0264.1987.tb00720.x
5. Cerda-Gonzalez S, Dewey CW. Congenital diseases of the craniocervical junction in the dog. *Vet Clin North Am Small Anim Pract.* (2010) 40:121–41. doi: 10.1016/j.cvsm.2009.10.001

6. Cerda-Gonzalez S, Dewey CW, Scrivani P, Kline K. Imaging features of atlanto-occipital overlapping in dogs. *Vet Radiol Ultrasound.* (2009) 50:264–8. doi: 10.1111/j.1740-8261.2009.01531.x
7. Cummings K, Vilaplana G, Moore G, Rochat M, Thomovsky S, Bentley R. Radiographic indices for the diagnosis of atlantoaxial instability in toy breed dogs [corrected]. *Vet Radiol Ultrasound.* (2018) 59:667. doi: 10.1111/vru.12668
8. Kelleners N. *Kinematik des kraniozervikalen Übergangs beim Chihuahua: eine Untersuchung mittels biplanarer Röntgenvideographie und Scientific Rotoscoping* (dissertation). Justus-Liebig-Universität, Gießen (2019).
9. Gatesy SM, Baier DB, Jenkins FA, Dial KP. Scientific rotoscoping: a morphology-based method of 3-D motion analysis and visualization. *J Exp Zool A Ecol Genet Physiol.* (2010) 313:244–61. doi: 10.1002/jez.588
10. Fischer MS, Lehmann SV, Andrada E. Three-dimensional kinematics of canine hind limbs: in vivo, biplanar, high-frequency fluoroscopic analysis of four breeds during walking and trotting. *Sci Rep.* (2018) 8:1–22. doi: 10.1038/s41598-018-34310-0
11. Deban S, Schilling N, Carrier D. Activity of extrinsic limb muscles in dogs at walk, trot and gallop. *J Exp Biol.* (2012) 215:287–300. doi: 10.1242/jeb.063230
12. McNeill A. R. Energetics and optimization of human walking and running: the 2000 Raymond Pearl memorial lecture. *Am J Hum Biol.* (2002) 14:641–8. doi: 10.1002/ajhb.10067
13. Fischer M, Lilje K, Lauströer J, Andikfar A. *Hunde in Bewegung*. Dortmund: Franckh-Kosmos-Verlag (2011). p. 207.
14. Hildebrand M. Analysis of the symmetrical gaits of tetrapods. *Folia Biotheor.* (1966) 6:9–22.
15. Hildebrand M. Symmetrical gaits of dogs in relation to body build. *J Morphol.* (1968) 124:353–9. doi: 10.1002/jmor.1051240308
16. Fanchon L, Valette J-P, Sanaa M, Grandjean D. The measurement of ground reaction force in dogs trotting on a treadmill. *Vet Comp Orthop Traumatol.* (2006) 19:81–6. doi: 10.1055/s-0038-1632979
17. Bockstahler B, Skalicky M, Peham C, Müller M, Lorinson D. Reliability of ground reaction forces measured on a treadmill system in healthy dogs. *Vet J.* (2007) 173:373–8. doi: 10.1016/j.tvjl.2005.10.004
18. Gustås P, Pettersson K, Honkavaara S, Lagerstedt A, Byström A. Kinematic and spatiotemporal assessment of habituation to treadmill walking in Labrador retrievers. *Acta Vet Scand.* (2016) 58:87. doi: 10.1186/s13028-016-0265-9
19. Wachs K, Fischer M, Schilling N. Three-dimensional movements of the pelvis and the lumbar intervertebral joints in walking and trotting dogs. *Vet J.* (2016) 210:46–55. doi: 10.1016/j.tvjl.2015.12.009
20. Kopp K. *Kinematik des Beckens und der kaudalen Lendenwirbelsäule beim Deutschen Schäferhund: eine Untersuchung mittels biplanarer Röntgenvideographie und Scientific Rotoscoping* (dissertation). Justus-Liebig-Universität, Gießen (2018).
21. Loscher DM, Meyer F, Kracht K, Nyakatura JA. Timing of head movements is consistent with energy minimization in walking ungulates. *Proc Biol Sci.* (2016) 283. doi: 10.1098/rspb.2016.1908
22. Jenkins FA, Camazine SM. Hip structure and locomotion in ambulatory and cursorial carnivores. *J Zool.* (1977) 181:351–70. doi: 10.1111/j.1469-7998.1977.tb03249.x
23. Layer A. *Ganganalytische untersuchung der rückenbewegung von gesunden hunden der rassen dackel und labrador retriever* [dissertation]. Ludwig-Maximilians- Universität, Müchen (2012).
24. Gellman KS, Bertram J. The equine nuchal ligament 2: passive dynamic energy exchange in locomotion. *Vet Comp Orthop Traumatol.* (2002) 15:7–14. doi: 10.1055/s-0038-1632706
25. Carrier D, Deban S, Fischbein T. Locomotor function of the pectoral girdlemuscular sling'in trotting dogs. *J Exp Biol.* (2006) 209:2224–37. doi: 10.1242/jeb.02236
26. Carrier D, Deban S, Fischbein T. Locomotor function of forelimb protractor and retractor muscles of dogs: evidence of strut-like behavior at the shoulder. *J Exp Biol.* (2008) 211:150–62. doi: 10.1242/jeb.010678
27. Angermann M. *Vergleichende biometrische und funktionsanalytische Auswertung von Röntgenaufnahmen des Kopf-Hals-Überganges klinisch gesunder Hunde* (dissertation). Veterinärmedizinische Fakultät Leipzig, Leipzig (2006).
28. Schlegel K, Parry AT, Lamb CR, Kneiss S, Probst A, Tichy A, et al. X-ray and CT morphology of atlas variants in the dog. *Berl Munch Tierarztl Wochenschr.* (2010) 123:425–30.
29. Spörl I. *Zur okzipitalen Dysplasie des Foramen magnum und Morphometrie des Atlas beim Hund* (dissertation). Ludwig-Maximilians-Universität, München (2014).
30. Blickhan R. The spring-mass model for running and hopping. *J Biomech.* (1989) 22:1217–27. doi: 10.1016/0021-9290(89)90224-8
31. Cavagna GA, Heglund NC, Taylor CR. Mechanical work in terrestrial locomotion: two basic mechanisms for minimizing energy expenditure. *Am J Physiol Regul Integr Comp Physiol.* (1977) 233:R243–R61. doi: 10.1152/ajpregu.1977.233.5.R243
32. Schikowski L. *Kinematik des kraniozervikalen Übergangs beim Chihuahua im Vergleich zum Labrador Retriever—eine Untersuchung mittels biplanarer Fluoroskopie und Scientific* (dissertation). Justus-Liebig-Universität, Gießen (2020).

Conflict of Interest: The authors declare that the research was conducted in the absence of any commercial or financial relationships that could be construed as a potential conflict of interest.

Publisher's Note: All claims expressed in this article are solely those of the authors and do not necessarily represent those of their affiliated organizations, or those of the publisher, the editors and the reviewers. Any product that may be evaluated in this article, or claim that may be made by its manufacturer, is not guaranteed or endorsed by the publisher.

frontiers in Veterinary Science

ORIGINAL RESEARCH
published: 26 August 2021
doi: 10.3389/fvets.2021.709966

Three-Dimensional Kinematics of the Pelvis and Caudal Lumbar Spine in German Shepherd Dogs

Katharina I. Schaub[1]*, *Nicola Kelleners*[1], *Martin J. Schmidt*[2], *Nele Eley*[1] and *Martin S. Fischer*[3]

[1] Department of Veterinary Clinical Sciences, Small Animal Clinic—Surgery, Justus-Liebig-University, Giessen, Germany, [2] Department of Veterinary Clinical Sciences, Small Animal Clinic—Neurosurgery, Neuroradiology and Clinical Neurology, Justus-Liebig-University, Giessen, Germany, [3] Institute of Zoology and Evolutionary Research, Friedrich-Schiller-University, Jena, Germany

OPEN ACCESS

Edited by:
Denis J. Marcellin-Little, University of California, Davis, United States

Reviewed by:
Shinichi Kanazono, Veterinary Specialists and Emergency Center, Japan
Sam Long, Veterinary Referral Hospital, Australia

***Correspondence:**
Katharina I. Schaub
katharinakopp88@gmail.com

Specialty section:
This article was submitted to Veterinary Neurology and Neurosurgery, a section of the journal Frontiers in Veterinary Science

Received: 14 May 2021
Accepted: 29 July 2021
Published: 26 August 2021

Citation:
Schaub KI, Kelleners N, Schmidt MJ, Eley N and Fischer MS (2021) Three-Dimensional Kinematics of the Pelvis and Caudal Lumbar Spine in German Shepherd Dogs. Front. Vet. Sci. 8:709966. doi: 10.3389/fvets.2021.709966

Lumbosacral vertebral motion is thought to be a factor in the development of degenerative lumbosacral stenosis in German shepherd dogs. So far, few studies exist describing natural canine lumbosacral movement *in vivo*. Therefore, this investigation aims to achieve a detailed *in vivo* analysis of bone movement of the lumbosacral region to gain a better understanding of the origin of degenerative lumbosacral stenosis using three-dimensional non-invasive *in vivo* analysis of canine pelvic and caudal lumbar motion (at L6 and L7). Biplanar cineradiography of the pelvis and caudal lumbar spine of four clinically sound German shepherd dogs at a walk and at a trot on a treadmill was recorded. Pelvic and intervertebral motion was virtually reconstructed and analyzed with scientific rotoscoping. The use of this technique made possible non-invasive measurement of physiological vertebral motion in dogs with high accuracy. Furthermore, the gait patterns of the dogs revealed a wide variation both between individual steps and between dogs. Pelvic motion showed a common basic pattern throughout the stride cycle. Motion at L6 and L7, except for sagittal rotation at a trot, was largely asynchronous with the stride cycle. Intervertebral motion in all dogs was small with approximately 2–3° rotation and translations of approximately 1–2 mm. The predominant motion of the pelvis was axial rotation at a walk, whereas lateral rotation was predominant at a trot. L7 showed a predominance of sagittal rotation (with up to 5.1° at a trot), whereas lateral rotation was the main component of the movement at L6 (about 2.3° in both gaits). During trotting, a coupling of various motions was detected: axial rotation of L7 and the pelvis was inverse and was coupled with craniocaudal translation of L7. In addition, a certain degree of compensation of abnormal pelvic movements during walking and trotting by the caudal lumbar spine was evident.

Keywords: dog locomotion, scientific rotoscoping, lumbosacral motion, pelvic motion, three-dimensional kinematics

INTRODUCTION

Diseases of the lumbosacral junction belong to the most common disorders of the musculoskeletal system in German shepherd dogs (GSDs) (1), which is why degenerative lumbosacral stenosis is a focus of clinical research. In dogs, degenerative lumbosacral stenosis (DLS) is known as the main cause of cauda equina syndrome (2). In DLS, degeneration and protrusion of the lumbosacral intervertebral disc and compression of the cauda equina nerves play an important role, with resulting pain and neurological failure (2–5). Large breed and working dogs seem to be particularly affected by DLS (2, 3); in fact, some authors have shown a breed predisposition for GSD, based on the particular morphology of the articular facets (6, 7). Despite many scientific studies, the true cause of DLS and the reasons for the predisposition of the GSD to it still remain uncertain. It was also stated that certain breeds, such as the GSD, are prone to premature intervertebral disc degeneration and DLS because of an abnormal movement pattern at the lumbosacral junction (5, 8, 9).

The complex motion of the canine lumbar spine has been the subject of several investigations, including range-of-motion studies on cadavers and kinematic studies using skin and bone markers. Each of these methods has certain limitations. Cadaver skeleton studies lack the influence of the surrounding soft tissue (8, 10–12). The highly invasive procedure of implanted bone markers is likely to interfere with natural movement (13, 14). Less invasive skin markers can only give an approximation of the motion of single vertebral bodies, due to the movement of the skin, which moves independently of the underlying skeletal elements (15, 16). One of the latest studies on canine lumbar kinematics was an investigation by Wachs examining lumbar and pelvic motion in three beagles by means of biplanar fluoroscopy and scientific rotoscoping (17). This method was also used in the current study due to its high measurement accuracy and low invasiveness.

The aim of the study was to perform a detailed, three-dimensional, non-invasive *in vivo* analysis of pelvic and caudal lumbar motion in healthy GSD at a walk and a trot. Furthermore, the study attempted to evaluate the benefit and accuracy of scientific rotoscoping, a markerless XROMM (X-ray Reconstruction of Moving Morphology) (18) method for the examination of canine lumbar vertebral kinematics.

MATERIALS AND METHODS

Animals

Four healthy adult GSDs (one female, three male) of the working line were examined. The dogs had an average age of 22 ± 6 months, an average height of 61 ± 4 cm, an average weight of 34 ± 5 kg, and an average body condition score 4–5/9. All examined dogs came from private and breeding sectors and were active in sports.

Abbreviations: DF, duty factor; FCI, federation cynologique internationale; GSD, German shepherd dog; L6, sixth lumbar vertebra; L7, seventh lumbar vertebra; LH, left hindlimb (reference leg); ROM, range of motion; rx, axial rotation; ry, lateral rotation; rz, sagittal rotation; S1, first sacral vertebra; TOO, time of occurrence; tx, craniocaudal translation; ty, ventrodorsal translation; tz, laterolateral translation; XROMM, X-ray reconstruction of moving morphology.

Ethics statement

The prospective part of the study was carried out in strict accordance with the recommendations in the Guidelines for the Care and Use of Laboratory Animals of the German Animal Protection Law. The protocol was approved by the Committee on the Ethics of Animal Experiments of the Justus Liebig University as well as from the Regierungspräsidium Hessen and Thuringia (Permit No.: 22-2684-04-02-075/14).

Study Design

Part 1: Clinical Examination and Cross-Sectional Imaging

The dogs underwent a complete clinical workup including general, orthopedic, and neurologic examinations, to rule out diseases that could influence the gait or vertebral motion. Anesthesia was induced using an anesthetic protocol with diazepam (0.5 mg/kg i.v.) and xylazine (0.03 mg/kg i.v.) in combination with ketamine (3 mg/kg i.v.). Propofol (2–4 mg/kg i.v.) was used if needed. Anesthesia was maintained by isoflurane (1.5–3 vol%) in 100% oxygen.

CT images of the complete spine and pelvis were acquired using a 16-slice helical scanner (Brilliance Philips, Best, Netherlands) under general anesthesia, to gain individual morphological data. CT scan settings were 120 kV, 200 mA, and a slice thickness of 1 mm. In addition, an MRI scan of the spine was conducted to rule out an early stage of DLS. An Intera 1.0T^{TM} MRI scanner (Philips) was used in combination with the Syn-spine-coil. Sagittal T2-weighted images of the lumbar spine and transversal T2-weighted images at the level of L5–S1 were acquired. No dogs included in the study showed any signs of DLS at the time of the investigation.

Part 2: Treadmill-Assisted Biplanar Cineradiography and Gait Analysis

The dogs were led on a horizontal mechanical treadmill at a walk and a trot. The speed of the treadmill depended on the comfort speed of the individual dog and was 0.8 ± 0.1 m/s for a walk and 2.4 ± 0.1 m/s for a trot. After an individual habituation time on the treadmill of about 10–20 min, biplanar X-ray high-speed videography (Neurostar Siemens AG, München and Visario Speedcam, Weinberger GmbH, Nürnberg) was performed. The biplanar X-ray videography system consisted of two C-arms with the treadmill in between. Depending on the size of the dog, the tube settings were 100 kV and 75 mA, and the shutter speed was set to 500 μs. The motion of the pelvis and caudal lumbar spine was recorded in two imaging planes at an angle of 63° at a walk and a trot for at least five steps. Simultaneously, the run was recorded with synchronous standard light high-speed live cameras (Standardlicht-Hochgeschwindigkeitkameras, Visario SpeedCam MiniVis®, High Speed Vision GmbH, Ettlingen, Germany) with 500 pics/s, to document the time when the feet rose and fell for evaluation of the duty factor and of disruptive movement (**Figure 1** and **Supplementary Videos 1, 2**).

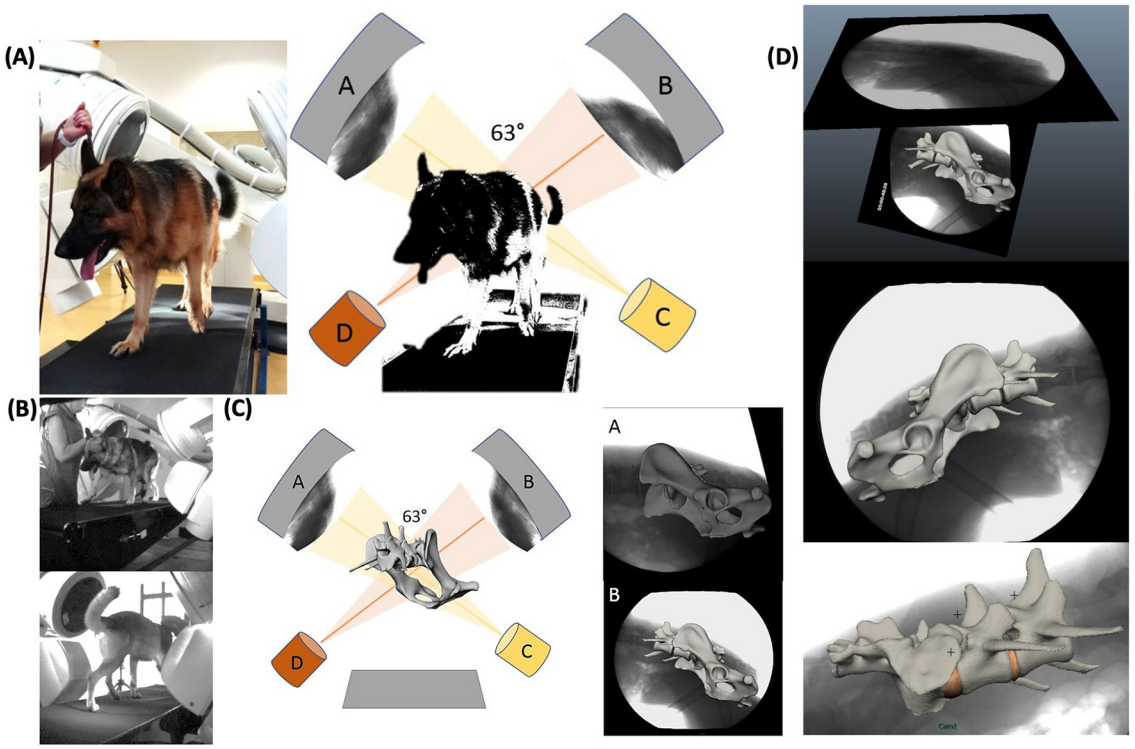

FIGURE 1 | Experimental setup of the treadmill-assisted biplanar cineradiography and scientific rotoscoping with the image intensifiers set at 63°. **(A)** Physical experimental setup. X-ray films of lumbosacral motion are recorded in two different oblique lateral views (63°). **(A, B)** X-ray image intensifier with high-speed cameras. **(C, D)** X-ray tubes. **(B)** Livecam videos, recording motion synchronous to the X-ray films to correlate later motion curves with the stride cycle. **(C)** Scientific rotoscoping: virtual model of the real-life experimental setup in Autodesk Maya®. Schematical experimental setup with virtual bone marionette. **(D)** X-ray films with virtually adjusted bone marionette. Adjustment of the virtual bones in scientific rotoscoping is comparable to a shadow play—the virtual bone is rotated and slid until the bone silhouette is exactly congruent with both X-ray films.

Part 3: Scientific Rotoscoping

Scientific rotoscoping is a non-invasive, markerless procedure of the XROMM method (18, 19) and a kinematic method to analyze natural skeletal motion in vertebrates *in vivo*. The detailed motion of the pelvis, sacrum, L6, and L7 was recorded using biplanar cineradiography. Based on individual CT scans of the spine and pelvis, a three-dimensional virtual bone marionette of the pelvis, sacrum, and the last two lumbar vertebrae was created, accurate in every detail, using the three-dimensional image processing program Amira 6® (Visage Imaging, Berlin, Germany). The experimental setup and the bone movement of the pelvis and vertebrae were virtually reconstructed by adjusting the virtual bone marionette to the biplanar X-ray videos using the graphic software Autodesk Maya 2014®. Since the two X-ray films were recorded from two different views, a moving three-dimensional virtual spine was created, virtually imitating the real three-dimensional bone movement with high precision (**Figure 1** and **Supplementary Videos 3, 4**). Afterwards, three-dimensional motion measurements were performed using virtual animation. To minimize individual measurement inaccuracy, scientific rotoscoping was carried out by a single person (the first author, KS), and measurements were made after a period of training of about 12 weeks.

Data Analysis

In the present study, consecutive strides at a walk (n = 6) and a trot (n = 9) of the four participating GSDs were analyzed and described in six degrees of freedom. The directions of three-dimensional pelvic and vertebral movements were defined according to Wachs: axial rotation (rx) describing rotating movement around the craniocaudal body axis. Lateral rotation (ry) illustrated rotation around the ventrodorsal body axis, and sagittal rotation (rz) was defined as rotation around the laterolateral body axis (17). In addition, translational movement of the pelvis, L6, and L7 was analyzed based on craniocaudal translation (tx), ventrodorsal translation (ty), and laterolateral translation (tz) (**Figure 2**). Bone movement was described in relation to the adjoining caudal bone (17, 20).

To compare steps with various stance and swing phases, a stride normalization (21) of the individual steps was performed, based on the duty factor (22–24) using MATLAB (MATLAB®, The MathWorks, Massachusetts). The duty factor describes the percentage of the stance phase of a reference leg during the entire stride cycle. The duty factor of each dog was determined by means of gait analysis of the synchronized LifeCams. In the present study, the duty factor of the reference leg (left hindlimb;

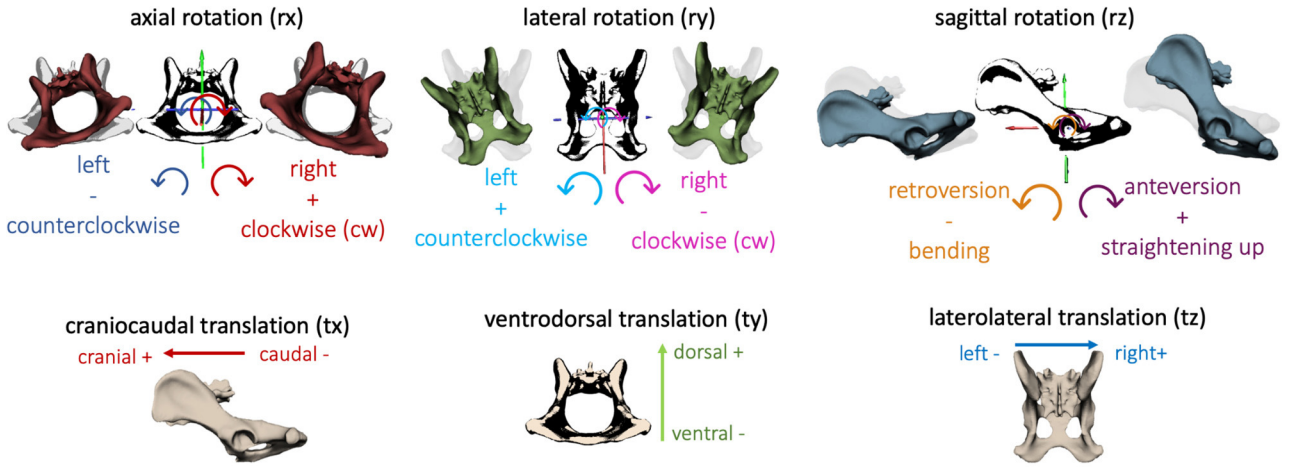

FIGURE 2 | Definition of the direction of rotation and translation of the pelvis and vertebrae: axial rotation (rx)—rotation about the craniocaudal body axis, lateral rotation (ry)—rotation about ventrodorsal body axis, sagittal rotation (rz)—rotation about the laterolateral body axis; craniocaudal translation (tx), ventrodorsal translation (ty), laterolateral translation (tz).

LH) was 0.7 ± 0.01 for a walk and 0.4 ± 0.01 for a trot (except for GSD 3: duty factor 0.5 ± 0.02).

Due to the minimal expected movements of the sacroiliac joint (25) and the overlap of the sacrum and pelvis in the X-ray videos, the sacrum was defined as a fixed connection with the pelvis. Therefore, in the following text, the motion of the pelvis simultaneously represents the movement of the sacrum.

Analyzed motion data included range of motion (ROM) of the facet joints and pelvis, time of occurrence (TOO) of maxima and minima within a stride cycle (15, 17), type of movement (dependent on the number of changes in motion direction), and dependence on the stride cycle. The collected data were compared between separate steps and individual dogs.

Data on pelvic and intervertebral motion were correlated between different steps, dogs, and anatomic locations using SPSS (SPSS®, Statistics for windows, Version 24.0, IBM Corp., Armonk, NY). Additionally, data were analyzed with the help of Fourier transformation with the command line interpreter Jupyter (Project Jupyter, www.jupyter.org). Due to the small number of patients and the high inter- and intraindividual variation in motion, even between individual steps of one dog, this study was limited to descriptive analysis. In the present study, a measurement accuracy of approximately 1.5° for rotation and approximately 0.1 cm for translational movements was achieved.

RESULTS

Pelvic Rotation and Translation

Axial pelvic rotation (rx) demonstrated a monophasic motion pattern with one minimum and one maximum both at a walk and at a trot. For single steps of GSD 2, an intermittent bi- to triphasic motion was noticed at a trot, due to ipsilateral limb interactions. Motion was stride cycle-dependent and followed a basic pattern. In both gaits, the pelvis tilted in the direction of the foot touching the ground, starting with the left hindlimb (reference leg). During the stance phase, the pelvis rotated clockwise (caudocranial view) until the middle of the stance phase and then changed direction, rotating counterclockwise up to the middle of the swing phase; afterwards, it changed again to clockwise rotation until the end of the stride cycle (**Figure 3**).

Change in the direction of the motion occurred at a walk at 29.0 ± 9.0% and 86.8 ± 10.1% and at a trot at 33.0 ± 10.7% and 85.5 ± 18.6% of the stride cycle of the reference limb (**Supplementry Table 1**). In both gaits, intermittent, small elevations of the curve in terms of momentary changes in rotational direction were noticed. These were associated with the touch-down of a hind paw. Axial pelvic rotation showed the greatest ROM at a walk (12.1 ± 4.7°) in comparison with lateral and sagittal rotation. At a trot, ROM only reached values approximately 6.1 ± 5.7° (**Supplementary Table 2**).

Lateral pelvic rotation (ry) was monophasic at a walk and a trot and followed a generally reproducible motion pattern (**Figures 4**, **5**). A change in the direction of motion occurred at the mid to second half of the stance phase and approximately at touch-down of the hind paws in both gaits (walk: 43.3 ± 3.9% and 96 ± 4.0% of the stride cycle; trot: 39.3 ± 10.6% and 91.9 ± 8.3% of the stride cycle). ROM was similar at a walk and a trot: 10.9 ± 0.8° (walk) and 9.0 ± 0.9° (trot). Compared with axial and sagittal rotation, at a trot, lateral pelvic rotation reached the greatest values.

Sagittal pelvic rotation (rz) showed a biphasic motion at a walk and a trot (**Figures 4**, **5**). Both maxima were associated with touch-down of the hindlimbs and represented maximal anteversion of the pelvis. Both minima occurred in mid stance and swing phase and expressed maximum retroversion of the pelvis (walk: maxima at 2.8 ± 1.5% and 54.3 ± 5.2%, minima at 30.6 ± 2.5% and 80.4 ± 3.6% of the stride cycle). ROM of the sagittal pelvis movement was 7.8 ± 2.5° for a walk and 6.7 ± 1.9° for a trot.

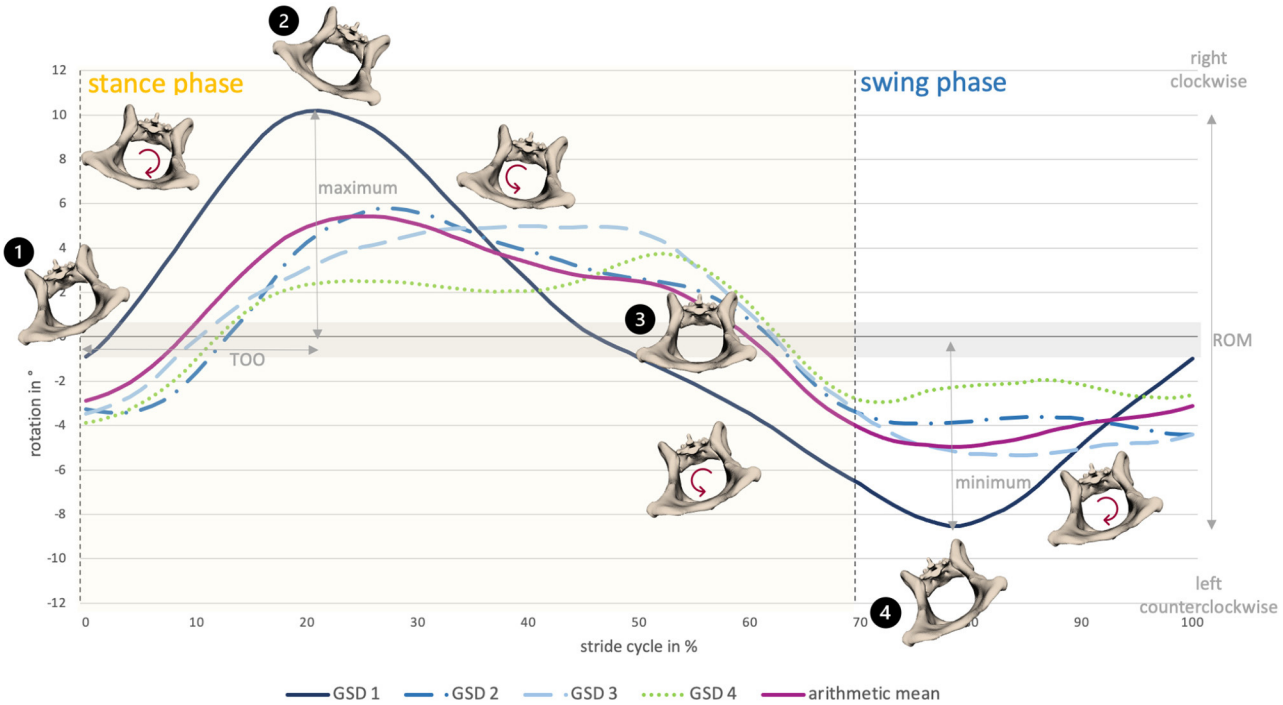

FIGURE 3 | Pelvic axial rotation of all dogs at a walk. The anatomical diagrams visualize pelvic axial rotation of GSD 1. 1) Stride cycle starts with footing of the left hindlimb with the pelvis slightly tilted to the left, followed by a right-sided rotation. 2) Around the middle of the stance phase, the pelvis is maximally right tilted. 3) Afterwards, it rotates to the left side, reaching a neutral position shortly before the end of the stance phase. 4) Around the middle of the swing phase, the pelvis is maximally left tilted, then it rotates to the right side until the end of the swing phase.

Translation of the pelvis was analyzed in the craniocaudal (tx), ventrodorsal (ty), and laterolateral (tz) directions (**Figures 4**, **5**). Craniocaudal translation (tx) in the study was mainly influenced by the treadmill with a nearly linear curve during a walk and an implied biphasic curve during a trot. Maximal cranial translation occurred shortly after touch-down of the hindlimbs reflecting a strengthened cranial pelvic movement. ROM was 2.6 ± 0.6 cm (walk) and 2.9 ± 0.6 cm (trot) matching the constant forward movement of the dogs on the treadmill.

Pelvic ventrodorsal translation (ty) presented a biphasic motion in both gaits with maxima at 3.6 ± 4.0% and 81.2 ± 4.3% (walk) and 43.5 ± 3.5% and 93.2 ± 6.2% (trot) of the stride cycle. Minima were noted at 7.2 ± 2.8% and 57.4 ± 3.2% (walk) and 17.5 ± 5.2% and 70.5 ± 5.3% (trot) of the stride cycle. ROM of ventrodorsal pelvis translation was similar in both gaits with 3.6 ± 0.8° (walk) and 3.6 ± 0.6° (trot). Laterolateral translation (tz) of the pelvis showed a nearly linear movement with ROM of 3.5 ± 1.6 cm (walk) and 2.6 ± 0.7 cm (trot) in both gaits and suggested a steady position on the treadmill.

Intervertebral Motion of L6 and L7

Intervertebral motion was measured at the level of the facet joints of L6–L7 and L7–S1. ROM was in most cases approximately 2–3° at the level of L6 and L7, whereas lateral rotation was the dominant motion at L6 [∼3.4° (walk) and 3.8° (trot)]. At L7, sagittal rotation achieved the greatest ROM in both gaits, with ∼5.1° while trotting. Axial intervertebral rotation (rx) (**Figures 4**, **5**) of L7 was partly biphasic and partly triphasic at a walk. No common stride dependency was found. Instead, a certain negative dependence of axial rotation of L7 and the pelvis was noted. ROM was similar in both gaits (walk: 3.0 ± 0.5°, trot: 3.0 ± 0.3°).

At the level of L6, no reproducible gait pattern-related motion could be found between the steps of one dog nor between those of different dogs. This was also reflected in the high standard deviations of the individual steps. ROM at the level of L6 was only slightly smaller than the lumbosacral ROM (walk: 2.5 ± 0.4°, trot: 2.3 ± 0.2°).

Lateral intervertebral rotation (ry) of L7 had a similar magnitude in both gaits, with a ROM of 3.6 ± 0.6° (walk) and 3.4 ± 1.0° (trot) and showed no gait–cycle relation. Whereas a bi-to-triphasic motion was seen in most dogs at a walk, lateral rotation of L7 at a trot was irregular biphasic (**Figures 4**, **5**). The motion pattern between the separate steps of one dog was inconstant and showed great variation, noticeable in the high standard deviation of the TOO. Interindividual variation between dogs was smaller than intraindividual variation between the steps of one dog. Lateral rotation of L7 differed clearly from lateral pelvic movement.

Lateral rotation of L6 was neither related to the TOO of L7 nor to pelvic rotation or stride cycle. The TOO of L6 differed greatly between dogs and between steps of individual dogs. ROM

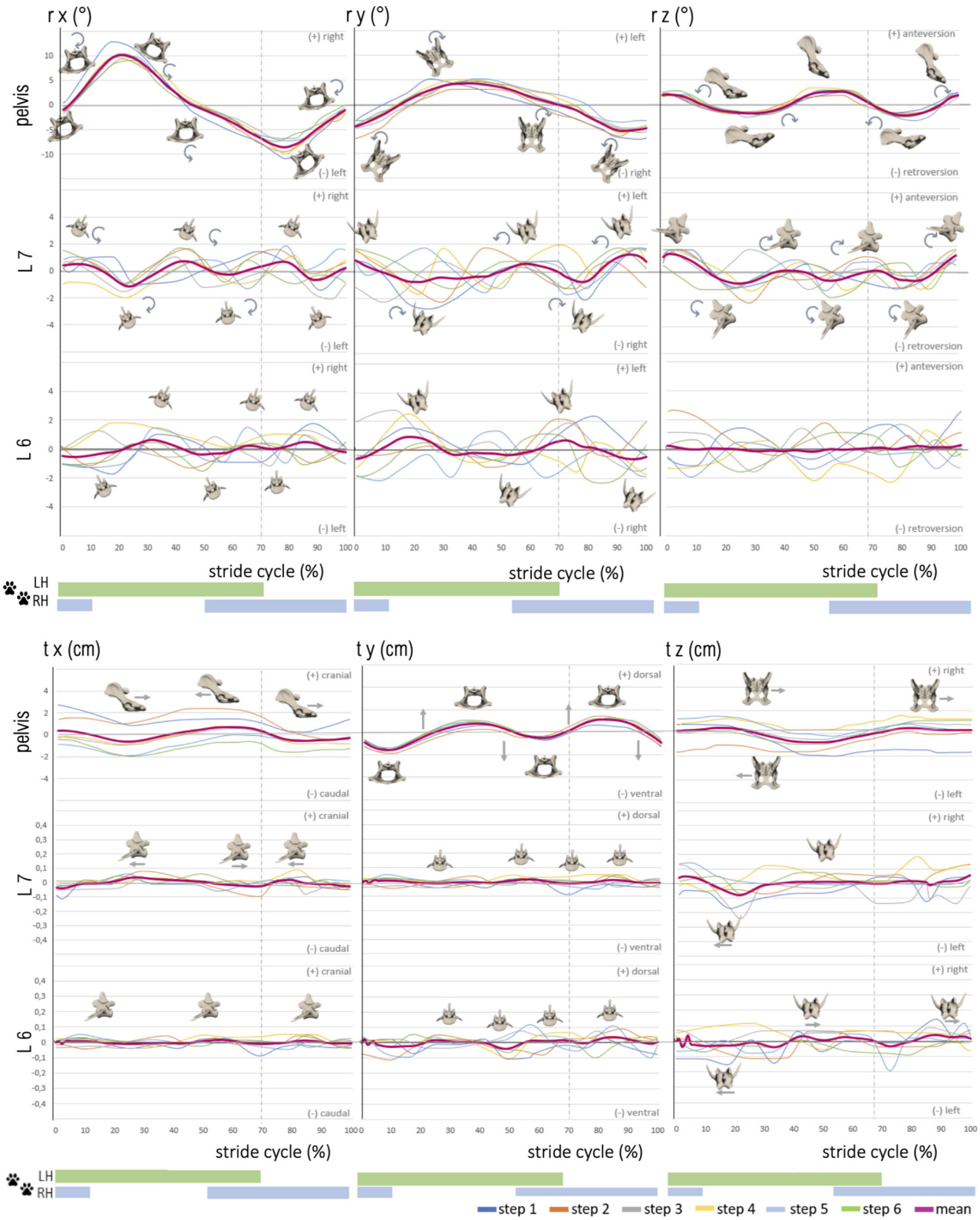

FIGURE 4 | Stride phase-normalized stride cycle-dependent motion of pelvic and caudal lumbar vertebrae (L7, L6) of GSD 1 at a walk. Listed are motions of the separate bones in six degrees of freedom: rx (axial rotation), ry (laterolateral rotation), rz (sagittal rotation), tx (craniocaudal translation), ty (dorsoventral rotation), and tz (laterolateral translation). The different colored curves present the six analyzed individual steps of dog 1, dependent on the stride cycle [duty factor 0.7; LH, left hindlimb (reference leg); RH, right hindlimb]. The pink line represents the mean value graph of all six strides with anatomical diagrams symbolizing the stride cycle-dependent bone movement.

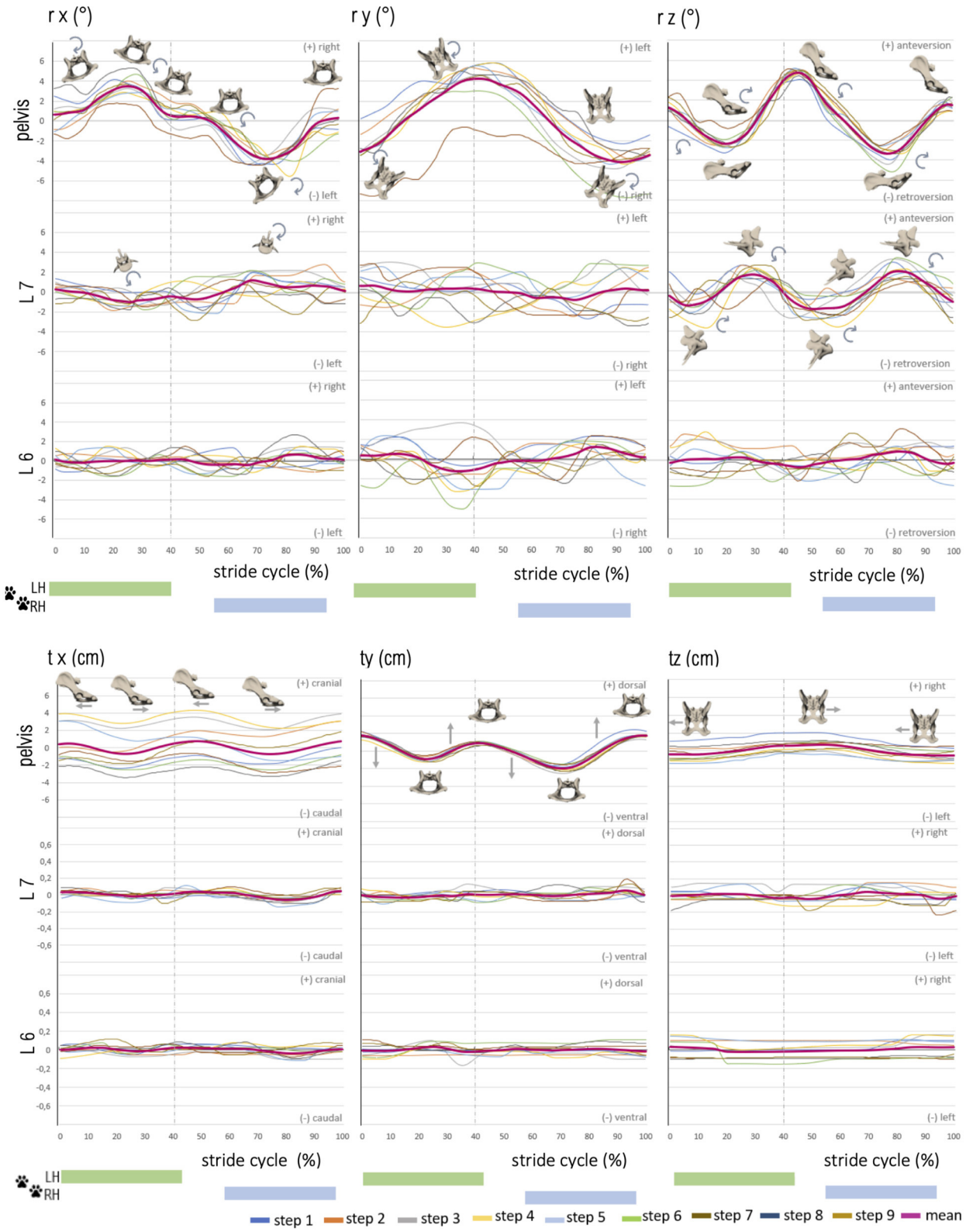

FIGURE 5 | Stride phase-normalized stride cycle-dependent motion of pelvic and caudal lumbar vertebrae (L7, L6) motion of GSD 1 at a trot. Listed are motions of the separate bones in six degrees of freedom: rx (axial rotation), ry (laterolateral rotation), rz (sagittal rotation), tx (craniocaudal translation), ty (dorsoventral rotation), and tz (laterolateral translation). The different colored curves present the nine analyzed steps of dog 1, dependent on the stride cycle [duty factor 0.4; LH, left hindlimb

(Continued)

FIGURE 5 | (reference leg); RH, right hindlimb]. The pink line represents the mean value graph of all nine strides with anatomical diagrams symbolizing the stride cycle-dependent bone movement. Rotation and translation of L6 and partly L7 are widely asynchronous to the stride cycle with a high variety in TOO except for sagittal rotation of L7, and vertebral translation is minimal.

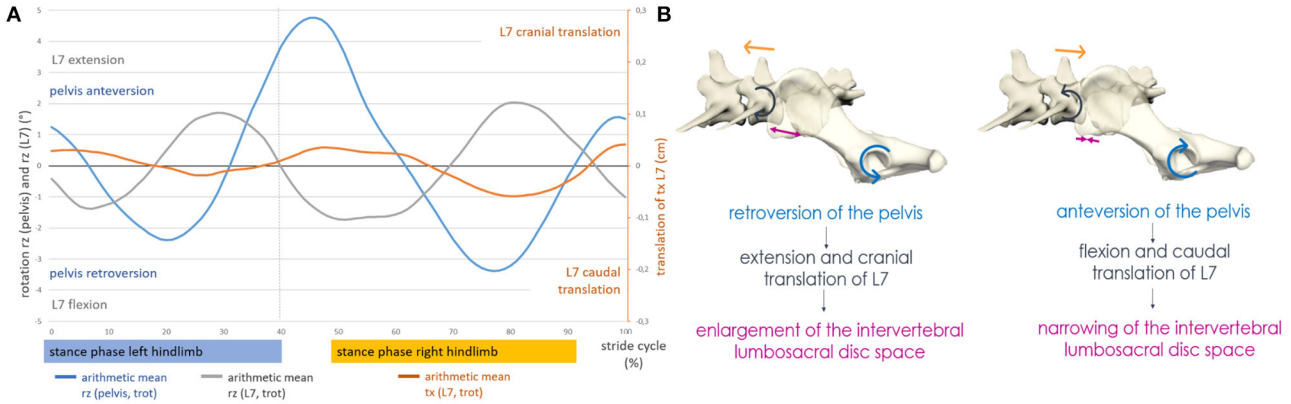

FIGURE 6 | (A) Motion of the lumbosacral junction at a trot of GSD 1: coupled motion of craniocaudal translation of L7 and sagittal rotation of the pelvis and L7. **(B)** Schematic illustration of the lumbosacral movement in GSDs during trotting. Lumbosacral motion in GSDs is complex and comparable with the motion of train couplers. The lumbosacral facet joints serve as a hinge, allowing deformation of the intervertebral disc space into a reverse V shape in case of retroversion of the pelvis. In case of anteversion of the pelvis, the hinge formed by the facet joints will only allow narrowing of the intervertebral disc space in the ventral aspect but prevent widening in the dorsal aspect by the limited translation within the facet joints.

of L6 was 3.4 ± 1.0° at a walk and 3.9 ± 0.4° at a trot. Lateral rotation was, at the level of L6, the dominating rotational motion in both gaits.

Sagittal intervertebral rotation (rz) at L6 and L7 at a walk was only mildly above the measurement limit. A uniform motion pattern with a greater ROM was only detected at a trot (**Figures 4**, **5**).

Sagittal rotation of L7 was irregular, biphasic, and sometimes triphasic at a walk, without any reproducible motion pattern. The TOO between separate steps and individual dogs demonstrated great variability. ROM was 3.6 ± 0.7° at a walk. At a trot, however, sagittal rotation of L7 in all dogs showed a strong dependence on the stride cycle with a reproducible motion pattern. GSD 1, 2, and 4 demonstrated a nearly concurrent motion pattern, whereas dog 3 had a similar motion pattern but with a delayed occurrence of the first maximum. TOO for sagittal intervertebral rotation of L7 for the maxima was 30.0 ± 5.7% and 83.8 ± 1.4%, and for the minima, it was 9.6 ± 1.5% and 57.7 ± 4.0% of the stride cycle. ROM was 5.1 ± 0.5° and, therefore, the dominant rotational motion at the level of L7.

At L6, at a walk, no dependence of sagittal intervertebral rotation on the stride cycle was detected. ROM reached a maximum level of 3.1 ± 0.9°. At a trot, a biphasic motion pattern with ROM of 3.3 ± 0.3° was noted. In comparison with L7, the motion of L6 was much more irregular. The TOO was less synchronic in a step pattern of singular steps and different dogs (maxima: 22.4 ± 5.9%, 70.7 ± 7.1%; minima: 36.3 ± 6.4%, 80.3 ± 10.9%).

Intervertebral translation of L6 and L7 was only minimal, 0.1–0.2 cm in all directions, and thus at the resolving limit of the research method. A reproducible biphasic stride cycle-dependent motion pattern was only noticed at a trot for craniocaudal translation of L7, with maxima at 6.0 ± 3.9% and 55.3 ± 5.5% and minima at 31.8 ± 4.5% and 81.5 ± 2.7% of the stride cycle (**Figures 4**, **5**).

General Lumbosacral Motion

Axial pelvic rotation and axial rotation of L7 were directed inverse. L6 followed the axial rotation of L7, but with a mild delay and a phase shift. Deviations in pelvic motion, resulting from ipsilateral limb interaction, flexion of the spine, or displacement of the caudal body axis, affected the motion of the caudal lumbar spine. In the case of deviating axial pelvic rotation, the caudal lumbar vertebrae showed a forced axial rotation in the opposite direction, although the basic motion remained and was only mildly affected. This context was also noticed in lateral and sagittal rotation but was less pronounced. Therefore, variant pelvic and hindlimb motions were compensated to a certain degree by opposing directed movements of the caudal lumbar spine (mostly L7 and sometimes L6) as well as by subsequent pelvic movement. When the lumbosacral motion was examined, an inverse sagittal rotation between the pelvis and L7 was observed, but only at a trot. In addition, at a trot, coupling of craniocaudal translation to sagittal rotation of L7 was evident (**Figure 6**).

Motion data were correlated using Spearman's correlation, with solitary bones, strides, and individual dogs to verify a common motion pattern. Pelvic rotation showed a strong correlation in all dogs and strides. In pelvic translation, only ventrodorsal translation reached high correlation values. L6 and L7 showed a mild correlation for rotation and translation between strides. Only sagittal rotation of L7 showed a moderate

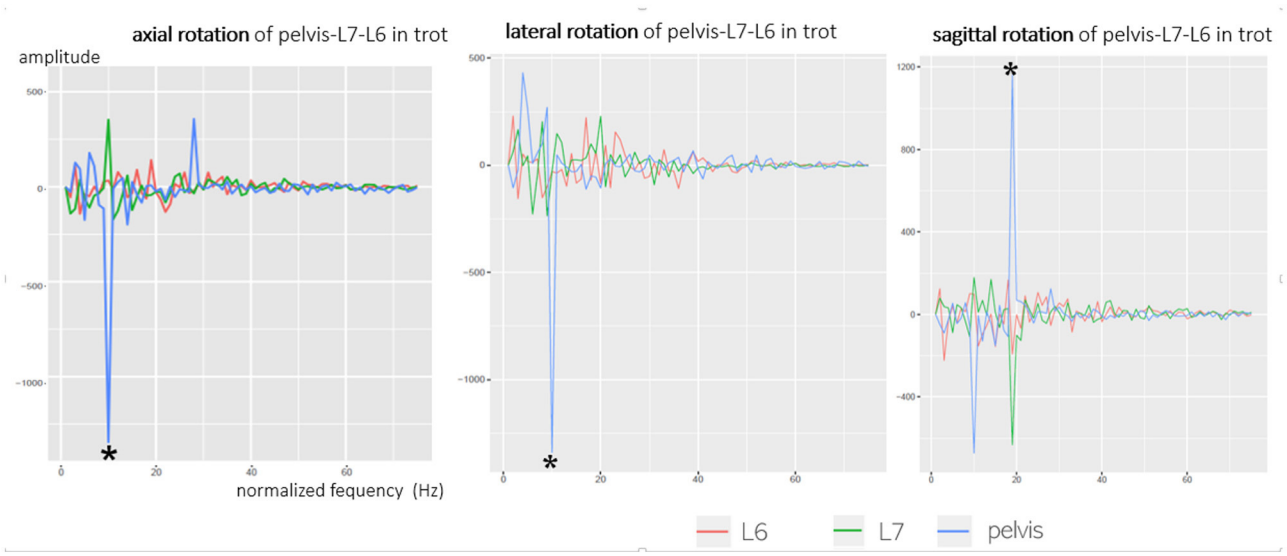

FIGURE 7 | Fourier transformation (cosine part) of axial, lateral, and sagittal rotation of the pelvis, L6, and L7, exemplary GSD 2 at a trot. Axial rotation shows one main frequency (*) and many smaller spurious oscillations. The main oscillations (*) of the axial rotation of the pelvis (blue line) are directed opposite to L6 (red line) and L7 (green line) as the pelvis shows a negative amplitude, whereas L6 and L7 show a positive amplitude. This means that the pelvis and caudal lumbar spine show an inverse axial oscillation.

stride correlation. Motion patterns between different dogs were more strongly correlated and thus more consistent than different strides of one dog. However, except for pelvic rotation, correlation was mild to moderate between dogs. Rotation of L6 and L7 was negatively correlated with pelvic rotation, above all at a trot.

Fourier transformation breaks down complex motion curves into their underlying frequencies for a better investigation of linkages. Peaks in the Fourier transformation indicate similar reproducible strides. A comparison of axial rotation of the pelvis, L6, and L7 confirmed the described observations: the main oscillation of axial rotation was based on the cosine function with one main frequency and multiple secondary frequencies in a different manner (**Figure 7**). At all main oscillations of the pelvis, an opposite direction of the vibration of L6 and L7 was proven, which also matches the negative pelvic–L7/L6 correlation. Fourier transformation verified that the pelvis and caudal lumbar spine oscillated inversely in the axial direction. The same context was found concerning sagittal rotation of the pelvis and L7/L6; however, this was only observed at a trot. While pelvic oscillations were similar in all dogs and had a clear main oscillation, oscillations of L6 and L7 had a relatively wide frequency spectrum and differed between individual dogs. Fourier analysis suggests that rotational motion of L6 and L7 is not only dependent on pelvic movement but also influenced by other motion factors—this fits with the significant inhomogeneity of the intervertebral rotation curves.

DISCUSSION

To the authors' knowledge, this is the first study providing a detailed insight into natural lumbosacral motion in GSD. To date, a similar investigation of lumbosacral kinematics has only been performed in three beagles, also using scientific rotoscoping (17).

Scientific rotoscoping offers outstanding measurement accuracy for investigations of canine lumbosacral motion *in vivo*, along with minimal invasiveness. However, even this method reaches the limits of spatial resolution when defining exceedingly small intervertebral movements. Despite the many advantages of scientific rotoscoping, it is a very time-consuming and complicated process. Therefore, only small numbers of patients can be examined with scientific rotoscoping at the moment. Thus, the method is reserved for research and is currently unsuitable for clinical examination due to the high cost and time requirement.

Pelvic axial and lateral rotation were monophasic in both gaits, whereas pelvic sagittal rotation revealed biphasic motion at a walk and a trot. Pelvic rotation showed strong stride cycle dependence and displayed a reproducible motion pattern with only mild individual variation. These observations are mostly consistent with studies conducted on beagles (17). The main motion of the caudal lumbar spine originated from the pelvis and, for the most part, followed pelvic motion passively. Isolated intervertebral motion on its own, however, was small. Pelvic rotation was mainly a result of hindlimb movement and thus showed a strong dependence on the stride cycle. As in research conducted on beagles, pelvic motion displayed a common reproducible basic gait pattern in all GSDs, which was, however, subject to individual variation (17).

In the present study, axial pelvic rotation dominated with 12.1 ± 4.7° at a walk, whereas at a trot, lateral rotation (ROM 9.0 ± 0.9°) was the predominant motion. In GSD, motion of the hindlimbs was mainly transferred to the spine as propulsion in trot, as lateral pelvic rotation dominated here. This is in contrast

to studies on horses (26, 27) and beagles (17). The GSD, beagle, and horse showed similar pelvic axial rotation ROM at a walk, whereas the beagle showed a higher ROM (10.9 ± 0.8°) at a trot than the GSD (6.1 ± 5.7°) and horse (5.7 ± 0.9°) (17, 26). Only GSD 3 showed a similar ROM to the beagle; both the beagle and GSD 3 showed an identical duty factor of 0.5 at a trot. A certain dependency of axial pelvic rotation on the duty factor is therefore likely.

Lateral pelvic rotation was monophasic and stride cycle-dependent with maxima and minima associated with the footing of the hindlimbs. This fits with the observations on beagle (17). ROM was only slightly greater at a walk than at a trot (10.9 ± 0.8 vs. 9.0 ± 0.9°) and was the dominant pelvic rotation at a trot. GSDs showed greater lateral pelvic rotation than horses and beagles (beagle 4.6 ± 1.1° walk/5.8° trot vs. horse 5.1 ± 1.7° walk/4.1 ± 1.0° trot) (17, 27, 28). The aforementioned results indicate that in GSD, hindlimb movement is mainly transferred to propulsion at a trot.

Sagittal pelvic rotation was biphasic in both gaits and stride cycle-dependent, as in previous studies in dogs (16, 17). In GSD, a ROM of 7.8 ± 2.5° at a walk and 6.7 ± 1.9° at a trot was documented for sagittal pelvic rotation. At a walk, similar values are known for beagles (approximately 8°) (17) and horses (∼7.3 ± 1.4°) (27). At a trot, however, sagittal pelvic rotation varied slightly at 8.2 ± 1.0° in beagles and at 4.3° in horses (17, 28). In GSD, sagittal pelvic rotation was the smallest at a walk and only slightly greater than axial rotation at a trot, probably resulting from muscular stabilization of the pelvis and sacrum in the sagittal plane (M. longissimus and M. multifidus) (29, 30).

Craniocaudal and laterolateral pelvic translation was mainly dependent on the position of the dog on the treadmill. Ventrodorsal pelvic translation was biphasic and described the up and down movement of the pelvis, caused by the hindlimbs pushing off the ground; ROM was similar at a walk and a trot, resulting from a relatively constantly maintained pelvic position despite larger, bouncy steps at a trot. This supports the thesis that in GSD, hindlimb motion is mainly transferred to propulsion of the trunk.

Only small intervertebral motion was detected in the caudal lumbar spine. ROM of intervertebral rotation at L6 and L7 reached ∼2–3° for rotation and approximately 1–2 mm for translation. This coincides with observations on the beagle that the main movement of the caudal lumbar spine originates from the pelvis (17). Nevertheless, this result contradicts the description of canine cadaver studies, in which sagittal rotation of up to 39° was observed (8). Thus, in natural motion of living dogs, only a fraction of the possible ROM is used in the symmetrical gaits at the lumbosacral junction. This supports the assumption of a stabilizing effect of the epaxial muscles on the spine (17, 30). In GSD, sagittal rotation was the predominant motion at the lumbosacral junction, with up to 5.1 ± 0.5° at a trot, while the lateral rotation was greatest in L6 at ∼3.8° trot at both a walk and a trot. This differs from observations on the beagle, where axial rotation was the dominant direction of movement at the lumbosacral junction (beagle: walk 3.8 ± 0.6°/trot 4.9 ± 0.4°) (17).

When the lumbosacral motion was examined, an inverse sagittal rotation between L7 and the pelvis was noted during trotting. This context was also described in the beagle (17). Furthermore, a coupling of craniocaudal translation and sagittal rotation of L7 was observed in all GSDs. However, this context was only found at a trot. During this motion coupling, retroflection of the pelvis caused simultaneous extension and cranial translation of L7, resulting in a widening of the lumbosacral intervertebral disc space. By contrast, anteversion of the pelvis during trot led to flexion and simultaneous caudal translation of L7 and thus resulted in increased narrowing of the lumbosacral intervertebral disc space. The widening and narrowing of the intervertebral lumbosacral disc space occurred twice per stride cycle. This context was already described in a canine cadaver study and was now confirmed for the first time in living dogs during natural locomotion (8). It should be noted, however, that in the present study, this motion coupling at the lumbosacral junction was only observed at a trot.

When pelvic and lumbar rotation was examined, it was conspicuous that deviations in pelvic movement affected the caudal lumbar spine to a certain degree. When the pelvis, for example, showed an increased negative (right-sided) lateral rotation, L7 simultaneously performed an increased movement in the opposite direction. This coherence was already described in dogs with lameness of one hindlimb that presented with an increased longitudinal axis of rotation from the back to the healthy side (31). In the present study, it can be assumed that even small deviations in pelvic movement caused, for example, by tripping or turning are compensated by the caudal lumbar spine to some extent and thus contribute to the balance of the trunk. This supports the assumption of Wachs that extreme movements during sports put increased strain on the lumbosacral intervertebral disc (29).

Besides proving an inverse axial and sagittal rotation of the pelvis and L7, Fourier transformation also showed that axial and sagittal rotation of the caudal lumbar spine consist of one main oscillation and many smaller secondary frequencies. It can be assumed that the significant main frequency of axial vertebral rotation in Fourier translation represents the monophasic main motion of the pelvis and caudal lumbar spine, induced by motion of the hindlimbs. Pelvic axial rotation showed a clear main frequency, whereas the main frequency of the caudal lumbar spine differed by much less from the secondary frequencies. This suggests that compared with pelvic axial rotation, axial rotation of L6 and L7 is more influenced by other movements. Based on synchronous live videos, an impact of tail motion and hindlimb touch-down seemed likely in the present study. A similar hypothesis was stated in a gait analysis of Labrador retrievers and Dachshunds, where a superposition of monophasic caudal lumbar and sacral motion with motion of the tail and resulting oscillation interferences was suspected (16). For further evaluation, a combination of scientific rotoscoping with skin markers would improve the evaluation of this context.

Both pelvic and intervertebral motion presented wide variation between dogs and between strides in both gaits. While pelvic motion was relatively stereotypical in individual dogs and followed the same basic gait pattern, a basic pattern was hardly recognized in intervertebral motion, except for sagittal rotation at a trot. Pelvic motion differed above all between dogs, whereas intervertebral motion showed more similarities between

dogs than between strides of one dog. Therefore, every stride, also within one dog, is unique, even if it follows the same basic motion pattern (23, 32). As every single step is influenced by several different factors (33), this explains the variation in intervertebral motion in the present study. Therefore, gaining reference values for kinematic gait analysis and lumbosacral motion is challenging, even in healthy dogs of a single breed. It can be assumed that this singularity of movement will play a central role in answering diagnostic questions in the future.

In the current literature, the canine lumbosacral junction is described as a spinal section of high mobility (8, 11, 34). The vertebral disc ensures stability between adjacent vertebrae (35–38), and therefore, lumbosacral disc degeneration seems to play an important role in the origin of canine DLS (2, 4, 5, 35). An increased lumbosacral vertebral translation, like the often-seen spondylolisthesis in X-rays (2, 4–6), an altered ROM, and an abnormal motion type are discussed as causes of DLS in GSDs (2, 4, 5, 11). This theory could not be confirmed in the present study, as all GSDs showed only minimal intervertebral translation and rotation in the caudal spine, comparable with those seen in the beagle (17). In GSD, sagittal rotation is the predominant motion at the lumbosacral junction, above all at a trot. The described coupling of sagittal rotation with craniocaudal translation increases the stretching and compression of the lumbosacral intervertebral disc during trotting. It can be assumed that the lumbosacral intervertebral disc in the GSD is exposed not only to repeated stress in the context of axial rotation, especially during trotting, but also to high stress from sagittal compression forces. A possible interpretation would be that this strong lumbosacral sagittal motion in GSD with compression of the intervertebral disc, in combination with the repeated shear movements as part of the axial rotation of L7, puts increased strain on the lumbosacral intervertebral disc, especially during trotting, thus contributing, in addition to extreme movements, for example, in sports, to early disc degeneration in this breed.

In GSDs, lumbosacral transmission of hindlimb and pelvic motion on L7 differs significantly from that in the beagle (17). Altered motion transmission in the GSD might be a consequence of the precipitous and flat lumbosacral facet joint geometry (9), making sagittal rotation the main lumbosacral motion component at a trot. It can be assumed that sagittal rotation is still sufficiently stabilized at a walk by the epaxial muscles resulting in a small ROM (29, 30, 39). At a trot, however, high lumbosacral sagittal rotation of GSDs suggests that muscular stabilization at the lumbosacral transition in faster gaits is no longer sufficient or has been reduced in favor of propulsion. The special lumbosacral motion transmission in the GSD in comparison with that in other breeds such as the beagle (17) indicates an increased strain on the lumbosacral intervertebral disc, probably resulting in early disc degeneration. An increased ventrodorsal vertebral translation, often associated with DLS, could not be observed in the GSDs in the present study. Therefore, it is possible that increased ventrodorsal lumbosacral translation in GSDs is not the cause but rather the consequence of lumbosacral disc degeneration in DLS and therefore could not be observed in the healthy dogs of the study (37, 38, 40, 41).

The distinct lumbosacral sagittal rotation combined with dominant pelvic lateral rotation at a trot suggests an optimal and effective propulsive motion transmission of hindlimb locomotion on the caudal lumbar spine in the GSD as a trotter (FCI guidelines). Probably, this effective propulsive lumbosacral motion transmission is associated with the special facet joint anatomy of GSD (9) but unfortunately seems to be at the expense of the lumbosacral vertebral disc. To further investigate this hypothesis, larger-scale studies of different dog breeds regarding lumbosacral *in vivo* kinematics and facet joint geometry are necessary.

CONCLUSION

The present study demonstrates that a non-invasive measurement of physiological vertebral motion in dogs was possible with high accuracy, by means of scientific rotoscoping. Additionally, it has become evident that the canine gait pattern shows great diversity and varies widely both between individual dogs and between strides. Pelvic motion was based on a fundamental gait pattern, depending on hindlimb locomotion. Caudal lumbar motion was largely asynchronous with the stride cycle and showed high variation in dogs and strides, except for sagittal rotation at a trot. The main motion of the caudal lumbar spine originated from the pelvis, whereas isolated intervertebral caudal lumbar motion was small with approximately 2–3° rotational and ∼1–2 mm translational ROM. Consequently, intervertebral motion is influenced by more factors than solely the movement of the hindlimbs.

The main direction of motion differed depending on the location. In pelvic motion, axial rotation was the dominant component at a walk, whereas lateral rotation was predominant at a trot. At L7, sagittal rotation was the highest (with up to 5.1° at a trot), whereas lateral rotation was the main component of the movement at L6. At a trot, coupling of various motions was detected. Sagittal rotation of the pelvis and L7 was directed inverse and presented coupling with craniocaudal translation. In addition, a compensation of abnormal pelvic movements by L7 and partially by L6 was demonstrated.

The study provides a first detailed insight into *in vivo* kinematics of the lumbosacral junction of GSDs, provides a basis for further comparative studies on other breeds and dogs with DLS, and therefore contributes to a better understanding of the cauda equina syndrome in GSDs.

DATA AVAILABILITY STATEMENT

The raw data supporting the conclusions of this article will be made available by the authors, without undue reservation.

ETHICS STATEMENT

The animal study was reviewed and approved by the Committee on the Ethics of Animal Experiments of the Justus Liebig University as well as from the Regierungspräsidium Hessen and Thuringia (Permit No.: 22-2684-04-02-075/14). Written

informed consent was obtained from the owners for the participation of their animals in this study.

AUTHOR CONTRIBUTIONS

KS, NK, NE, MS, and MF conceived the study. KS and NK conducted the experiments. KS prepared the X-ray data, generated the digital bone models from animal data, performed the rotoscoping, and analyzed the experimental data. KS, MS, and MF drafted the manuscript. All authors contributed to the interpretation of the results and revised the manuscript.

FUNDING

The study was partially funded by AOVET. The funding body did not have any influence on the design of the study; the collection, analysis, and interpretation of the data; or the writing of the manuscript.

ACKNOWLEDGMENTS

We would like to thank Rommy Petersohn and Ella Wenz for technical assistance during the experiments, Volkher Scholz for assistance with Fourier transformation, Bettina Hesse for the help with the stride normalization, Katja Wachs for helpful discussions and advice, and Sebastian Schaub for technical support with computer problems. This manuscript represents a part of the doctoral thesis submitted by the first author (KS, born Kopp) in partial fulfillment of the requirements of a Dr. med. vet. degree (42).

SUPPLEMENTARY MATERIAL

The Supplementary Material for this article can be found online at: https://www.frontiersin.org/articles/10.3389/fvets.2021.709966/full#supplementary-material

REFERENCES

1. Vilson Å, Bonnett B, Hansson-Hamlin H, Hedhammar Å. Disease patterns in 32,486 insured German shepherd dogs in Sweden: 1995–2006. *Vet Rec.* (2013) 5:116. doi: 10.1136/vr.101577
2. Suwankong N, Meij BP, Voorhout G, de Boer AH, Hazewinkel HA. Review and retrospective analysis of degenerative lumbosacral stenosis in 156 dogs treated by dorsal laminectomy. *Vet Comp Orthop Traumatol.* (2008) 3:285–93. doi: 10.1055/s-0037-16 17374
3. Danielsson F, Sjöström L. Surgical treatment of degenerative lumbosacral stenosis in dogs. *Vet Surg.* (1999) 2:91–8. doi: 10.1053/jvet.1999.0091
4. Oliver JE Jr, Selcer RR, Simpson S. Cauda equina compression from lumbosacral malarticulation and malformation in the dog. *J Am Vet Med Assoc.* (1978) 2:207–14.
5. Jaggy A, Lang J, Schawalder P. Cauda equina-Syndrom beim Hund [Cauda equina syndrome in the dog]. *Schweiz Arch Tierheilkd.* (1987) 4:171–92.
6. Amort KH, Ondreka N, Rudorf H, Stock KF, Distl O, Tellhelm B, et al. MR-imaging of lumbosacral intervertebral disc degeneration in clinically sound German shepherd dogs compared to other breeds. *Vet Radiol Ultrasound.* (2012) 3:289–95. doi: 10.1111/j.1740-8261.2011.01903.x
7. Flückiger MA, Damur-Djuric N, Hässig M, Morgan JP, Steffen F. A lumbosacral transitional vertebra in the dog predisposes to cauda equina syndrome. *Vet Radiol Ultrasound.* (2006) 1:39–44. doi: 10.1111/j.1740-8261.2005.00103.x
8. Benninger MI, Seiler GS, Robinson LE, Ferguson SJ, Bonél HM, Busato AR, et al. Three-dimensional motion pattern of the caudal lumbar and lumbosacral portions of the vertebral column of dogs. *Am J Vet Res.* (2004) 5:544–51. doi: 10.2460/ajvr.2004.65.544
9. Breit S, Künzel W. On biomechanical properties of the sacroiliac joint in purebred dogs. *Ann Anat.* (2001) 2:145–50. doi: 10.1016/S0940-9602(01)80036-4
10. Bürger R, Lang J. Kinetische Studie über die Lendenwirbelsäule und den lumbosakralen Übergang beim Deutschen Schäferhund. Teil 1: Funktionelle Anatomie und kinetische Grundlagen [Kinetic study of the lumbar vertebrae and the lumbosacral passage in German shepherd dogs. 1. Functional anatomy and kinetic foundation]. *Schweiz Arch Tierheilkd.* (1992) 9:411–6.
11. Bürger R, Lang J. Kinetische Studie über die Lendenwirbelsäule und den lumbosakralen Ubergang beim Deutschen Schäferhund. Teil 2: Eigene Untersuchungen [Kinetic studies of the lumbar vertebrae and the lumbosacral transition in the German shepherd dog. 2. Our personal investigations]. *Schweiz Arch Tierheilkd.* (1993) 2:35–43.
12. Benninger MI, Seiler GS, Robinson LE, Ferguson SJ, Bonél HM, Busato AR, Lang J. Effects of anatomic conformation on three-dimensional motion of the caudal lumbar and lumbosacral portions of the vertebral column of dogs. *Am J Vet Res.* (2006) 1:43–50. doi: 10.2460/ajvr.67.1.43
13. Wood KB, Schendel MJ, Pashman RS, Buttermann GR, Lewis JL, Ogilvie JW, Bradford DS. In vivo analysis of canine intervertebral and facet motion. *Spine.* (1976) 10:1180–6. doi: 10.1097/00007632-199210000-00009
14. Schendel MJ, Dekutoski MB, Ogilvie JW, Olsewski JM, Wallace LJ. Kinematics of the canine lumbar intervertebral joint. An in vivo study before and after adjacent instrumentation. *Spine.* (1995) 23:2555–64. doi: 10.1097/00007632-199512000-00015
15. Gradner G, Bockstahler B, Peham C, Henninger W, Podbregar I. Kinematic study of back movement in clinically sound malinois dogs with consideration of the effect of radiographic changes in the lumbosacral junction. *Vet Surg.* (2007) 5:472–81. doi: 10.1111/j.1532-950X.2007.00294.x
16. Layer AF. *Ganganalytische Untersuchung der Rückenbewegung von gesunden Hunden der Rassen Dackel und Labrador Retriever* (doctoral thesis). Ludwig Maximilian University of Munich, Munich, Germany (2012).
17. Wachs K, Fischer MS, Schilling N. Three-dimensional movements of the pelvis and the lumbar intervertebral joints in walking and trotting dogs. *Vet J.* (2016) 210:46–55. doi: 10.1016/j.tvjl.2015.12.009
18. Gatesy SM, Baier DB, Jenkins FA, Dial KP. Scientific rotoscoping: a morphology-based method of 3-D motion analysis and visualization. *J Exp Zool A Ecol Genet Physiol.* (2010) 5:244–61. doi: 10.1002/jez.588
19. Brainerd EL, Baier DB, Gatesy SM, Hedrick TL, Metzger KA, Gilbert SL, et al. X-ray reconstruction of moving morphology (XROMM): precision, accuracy and applications in comparative biomechanics research. *J Exp Zool A Ecol Genet Physiol.* (2010) 5:262–79. doi: 10.1002/jez.589
20. Haussler KK, Bertram JE, Gellman K, Hermanson JW. Segmental in vivo vertebral kinematics at the walk, trot and canter: a preliminary study. *Equine Vet J Suppl.* (2001) 33:160–4. doi: 10.1111/j.2042-3306.2001.tb05381.x
21. Deban SM, Schilling N, Carrier DR. Activity of extrinsic limb muscles in dogs at walk, trot and gallop. *J Exp Biol.* (2012) 215:287–300. doi: 10.1242/jeb.063230
22. Hildebrand M. Analysis of the symmetrical gaits of tetrapods. *Folia biotheoretica.* (1966) 6:9–22.
23. Hildebrand M. Symmetrical gaits of dogs in relation to body build. *J Morphol.* (1968) 3:353–60. doi: 10.1002/jmor.1051240308
24. Fischer MS, Lilje KE. *Hunde in Bewegung*. Stuttgart: Franckh-Kosmos-Verlag (2011). p. 34.
25. Gregory CR, Cullen JM, Pool R, Vasseur PB. The canine sacroiliac joint. Preliminary study of anatomy, histopathology, and biomechanics. *Spine.* (1976) 10:1044–8. doi: 10.1097/00007632-198612000-00019

26. Wennerstrand, J. *Clinical perspectives on equine back kinematics* (doctoral thesis). Department of Anatomy, Physiology and Biochemistry, Swedish University of Agricultural Sciences, Uppsala, Sweden (2008).
27. Faber M, Schamhardt H, van Weeren R, Johnston C, Roepstorff L, Barneveld A. Basic three-dimensional kinematics of the vertebral column of horses walking on a treadmill. *Am J Vet Res.* (2000) 4:399–406. doi: 10.2460/ajvr.2000.61.399
28. Faber M, Johnston C, Schamhardt H, van Weeren R, Roepstorff L, Barneveld A. Basic three-dimensional kinematics of the vertebral column of horses trotting on a treadmill. *Am J Vet Res.* (2001) 5:757–64. doi: 10.2460/ajvr.2001.62.757
29. Wachs, K. *Kinematische Analyse von 3D-rekonstruierten Bewegungen der Lendenwirbelsäule und des Beckens beim Beagle in Schritt und Trab* (doctoral thesis). Tierärztliche Hochschule Hannover, Hanover, Germany (2015).
30. Schilling N, Carrier DR. Function of the epaxial muscles during trotting. *J Exp Biol.* (2009) 7:1053–63. doi: 10.1242/jeb.020248
31. Fischer S, Nolte I, Schilling N. Adaptations in muscle activity to induced, short-term hindlimb lameness in trotting dogs. *PLoS ONE.* (2013) 8:11. doi: 10.1371/journal.pone.0080987
32. Nunamaker DM, Blauner PD. Normal and abnormal gait. In: Newton CD, Nunamaker DM, editors. *Textbook of Small Animal Orthopaedics*. Philadelphia, PA: JP Lippincott Company (1985). p. 1083–95.
33. DeCamp CE. Kinetic and kinematic gait analysis and the assessment of lameness in the dog. *Vet Clin North Am Small Anim Pract.* (1997) 4:825–40. doi: 10.1016/S0195-5616(97)50082-9
34. Braund KG, Taylor TK, Ghosh P, Sherwood AA. Spinal mobility in the dog. A study in chondrodystrophoid and non-chondrodystrophoid animals. *Res Vet Sci.* (1977) 1:78–82. doi: 10.1016/S0034-5288(18)33317-4
35. Adams MA, Roughley PJ. What is intervertebral disc degeneration, and what causes it? *Spine.* (2006) 18:2151–61. doi: 10.1097/01.brs.0000231761.73859.2c
36. Krismer M, Haid C, Ogon M, Behensky H, Wimmer C. Biomechanik der lumbalen Instabilität [Biomechanics of lumbar instability]. *Orthopade.* (1997) 6:516–20. doi: 10.1007/PL00003406
37. Adams MA, Hutton WC. The mechanical function of the lumbar apophyseal joints. *Spine.* (1983) 3:327–30. doi: 10.1097/00007632-198304000-00017
38. Cyron BM, Hutton WC, Stott JR. Spondylolysis: the shearing stiffness of the lumbar intervertebral joint. *Acta Orthop Belg.* (1979) 4:459–69.
39. Schilling N, Carrier DR. Function of the epaxial muscles in walking, trotting and galloping dogs: implications for the evolution of epaxial muscle function in tetrapods. *J Exp Biol.* (2010) 9:1490–502. doi: 10.1242/jeb.039487
40. Kirkaldy-Willis WH. The relationship of structural pathology to the nerve root. *Spine.* (1984) 1:49–52. doi: 10.1097/00007632-198401000-00010
41. Sukthankar A, Nerlich AG, Paesold G. Age-related changes of the spine. In: Boos N, Aebi M, editors. *Spinal Disorders*. Heidelberg: Springer (2008). p. 91–122.
42. Kopp, KI. *Kinematik des Beckens und der kaudalen Lendenwirbelsäule beim Deutschen Schäferhund: eine Untersuchung mittels biplanarer Röntgenvideographie und Scientific Rotoscoping* (doctoral thesis). Justus Liebig University of Giessen, Giessen, Germany (2019).

Conflict of Interest: The authors declare that the research was conducted in the absence of any commercial or financial relationships that could be construed as a potential conflict of interest.

Publisher's Note: All claims expressed in this article are solely those of the authors and do not necessarily represent those of their affiliated organizations, or those of the publisher, the editors and the reviewers. Any product that may be evaluated in this article, or claim that may be made by its manufacturer, is not guaranteed or endorsed by the publisher.

frontiers in Bioengineering and Biotechnology

ORIGINAL RESEARCH
published: 08 November 2021
doi: 10.3389/fbioe.2021.751518

Validation of an Echidna Forelimb Musculoskeletal Model Using XROMM and diceCT

Sophie Regnault[1,2]*, *Philip Fahn-Lai*[1,3] *and Stephanie E. Pierce*[1]*

[1]*Museum of Comparative Zoology and Department of Organismic and Evolutionary Biology, Harvard University, Cambridge, MA, United States,* [2]*Institute of Biological, Environment and Rural Sciences, Aberystwyth University, Aberystwyth, United Kingdom,* [3]*Concord Field Station and Department of Organismic and Evolutionary Biology, Harvard University, Bedford, MA, United States*

OPEN ACCESS

Edited by:
John R. Hutchinson, Royal Veterinary College (RVC), United Kingdom

Reviewed by:
John Alexander Nyakatura, Humboldt University of Berlin, Germany
Craig McGowan, University of Southern California, United States
Ashley Heers, California State University, United States

***Correspondence:**
Sophie Regnault
sor24@aber.ac.uk
Stephanie E. Pierce
spierce@oeb.harvard.edu

Specialty section:
This article was submitted to Biomechanics, a section of the journal Frontiers in Bioengineering and Biotechnology

Received: *01 August 2021*
Accepted: *04 October 2021*
Published: *08 November 2021*

Citation:
Regnault S, Fahn-Lai P and Pierce SE (2021) Validation of an Echidna Forelimb Musculoskeletal Model Using XROMM and diceCT. Front. Bioeng. Biotechnol. 9:751518. doi: 10.3389/fbioe.2021.751518

In evolutionary biomechanics, musculoskeletal computer models of extant and extinct taxa are often used to estimate joint range of motion (ROM) and muscle moment arms (MMAs), two parameters which form the basis of functional inferences. However, relatively few experimental studies have been performed to validate model outputs. Previously, we built a model of the short-beaked echidna (*Tachyglossus aculeatus*) forelimb using a traditional modelling workflow, and in this study we evaluate its behaviour and outputs using experimental data. The echidna is an unusual animal representing an edge-case for model validation: it uses a unique form of sprawling locomotion, and possesses a suite of derived anatomical features, in addition to other features reminiscent of extinct early relatives of mammals. Here we use diffusible iodine-based contrast-enhanced computed tomography (diceCT) alongside digital and traditional dissection to evaluate muscle attachments, modelled muscle paths, and the effects of model alterations on the MMA outputs. We use X-ray Reconstruction of Moving Morphology (XROMM) to compare *ex vivo* joint ROM to model estimates based on osteological limits predicted via single-axis rotation, and to calculate experimental MMAs from implanted muscles using a novel geometric method. We also add additional levels of model detail, in the form of muscle architecture, to evaluate how muscle torque might alter the inferences made from MMAs alone, as is typical in evolutionary studies. Our study identifies several key findings that can be applied to future models. 1) A light-touch approach to model building can generate reasonably accurate muscle paths, and small alterations in attachment site seem to have minimal effects on model output. 2) Simultaneous movement through multiple degrees of freedom, including rotations and translation at joints, are necessary to ensure full joint ROM is captured; however, single-axis ROM can provide a reasonable approximation of mobility depending on the modelling objectives. 3) Our geometric method of calculating MMAs is consistent with model-predicted MMAs calculated via partial velocity, and is a potentially useful tool for others to create and validate musculoskeletal models. 4) Inclusion of muscle architecture data can change some functional inferences, but in many cases reinforced conclusions based on MMA alone.

Keywords: muscle moment arm, range of motion, SIMM, joint, mobility, translation, biomechanics, muscle

INTRODUCTION

Three-dimensional musculoskeletal computer models have become widely used to test hypotheses of biomechanical function in both extant and extinct animals. Such models are increasingly used to infer species-specific functional parameters (e.g., Pierce et al., 2012; Demuth et al., 2020; Bishop et al., 2021b; Richards et al., 2021), as well as in larger scale comparative analyses to characterise trends in functional evolution (e.g., Bates et al., 2012; Allen et al., 2021; Molnar et al., 2021). Two fundamental parameters of interest to evolutionary and biomechanical researchers are joint range of motion (ROM) and muscle moment arms (MMAs). A major advantage of 3D models is that they allow analyses of these parameters through non-planar motions, and so expand the types of movements and animals that can be studied (e.g., Regnault and Pierce, 2018). Models also provide a means to collect difficult-to-acquire data in extant animals (e.g., due to specimen scarcity or requiring invasive collection techniques) and, more recently, to more rigorously explore functional reconstruction in extinct animals (e.g., Hutchinson, 2012; Brassey et al., 2017; Nyakatura et al., 2019; Bishop et al., 2021c). However, there is a recognised gap – particularly in paleobiology – between the number of modelling studies published versus validation studies (Brassey et al., 2017), despite acceptance that such validation is critical to evaluate model-building practices and appropriately interpret results.

ROM estimates in extinct animals can eliminate improbable poses to constrain hypotheses about the types of mobility achievable (Gatesy et al., 2009; Manafzadeh and Padian, 2018; Manafzadeh et al., 2021) and so can inform understanding of major evolutionary transitions (e.g., water-to-land in tetrapods; Pierce et al., 2012). Where experimental data are not available, model ROM estimates are usually made through digital manipulation of bones until bone-on-bone contact or probable joint disarticulation (e.g., Mallison, 2010; Pierce et al., 2012; Lai et al., 2018; Manafzadeh and Padian, 2018; Bishop et al., 2021a; Richards et al., 2021). Traditionally, this has been done for each rotational degree of freedom (DOF) independently i.e., flexion-extension, abduction-adduction, long-axis rotation. More recently, Manafzadeh and Padian (2018) developed a semi-automated workflow that allows simultaneous rotations through each DOF to calculate an "envelope" of movement. As well as interactions between rotational DOF, other factors have also been long-identified as relevant to model-predictions of ROM: the effect of missing soft tissues, joint spacing, and translation at joint surfaces. Soft tissues can limit ROM directly (e.g., ligament, joint capsule) or indirectly (e.g., muscle bulk, integument) and several studies have documented the effects of different soft tissues (e.g., Hutson and Hutson, 2012; Pierce et al., 2012; Arnold et al., 2014), but an explicit methodology for applying these observations to extinct animal reconstructions is lacking (Manafzadeh and Padian, 2018). Joint spacing can alter ROM estimates (e.g., Regnault and Pierce, 2018), and can be difficult to account for in disarticulated specimens; in fossils, estimates are often made from the intra-articular distances and cartilage morphologies of living relatives (e.g., Holliday et al., 2010; Molnar et al., 2021). Translations at joint surfaces can greatly increase ROM (Pierce et al., 2012; Manafzadeh and Gatesy, 2021) but can be difficult to implement simultaneously with rotational DOF, and are often excluded from models for simplicity. Previous studies that include joint translations have programmed it as a pre-defined function coupled to specific joint rotations (Pierce et al., 2012; Richards et al., 2021) or account for translation by iteratively adjusting the starting (reference) position of the distal bone prior to performing joint rotations (Arnold et al., 2014; Manafzadeh and Padian, 2018).

Moment arms give an indication of a muscle's leverage, or effectiveness at generating specific rotational forces at joints (Sherman et al., 2013). MMAs are crucial for understanding how muscles produce (or resist) movement (Brassey et al., 2017), from the level of individual muscle role (e.g., flexor vs. extensor; Regnault and Pierce, 2018) to whole animal function (Fujiwara and Hutchinson, 2012; Bates et al., 2012; Bishop et al., 2021c; Wiseman et al., 2021), to comparative function between animals (e.g., evolutionary trends; Maidment et al., 2014; Molnar et al., 2021; Allen et al., 2021). MMAs are also the basis for calculating further parameters of interest; for example, combined with muscle architecture and kinematic data to calculate muscle and joint torques. MMAs are known to change with joint position and limb orientation (An et al., 1984), and so 3D models are an ideal way to study functional consequences at multiple scale-levels previously mentioned (from individual muscles to evolutionary trends), provided that models have been well-validated in the context in which results are interpreted. In human clinical biomechanics, MMAs have been validated against experimental data but such validation studies are relatively rare outside of humans and other bipedal and parasagittal animals (Kargo and Rome, 2002), and for muscles crossing complex joints (for example, a single biological "joint" comprising several bony articulations, or exhibiting coupled motions; Sherman et al., 2013; Brassey et al., 2017). A further consideration for validation is the several ways to measure MMA: estimates are commonly made from either tendon-travel or geometric measurements, around fixed (anatomical) or moving (kinematic) joint centres and axes. The equivalence of different methods is unclear, and possibly a source of variation when attempting to validate MMAs acquired through different means. The use of several methods has been advocated as a cross-check, where possible (An et al., 1984). The scope of validation may differ depending on the purpose of the study; for example, absolute values for specific behaviours vs. relative trends across taxa.

In a previous study (Regnault and Pierce, 2018), we built a musculoskeletal model of a short-beaked echidna (Monotremata: *Tachyglossus aculeatus*) forelimb to investigate osteological joint ROM and MMAs. We took a traditional model-building approach, commonly used to model extinct animals, to identify learning opportunities that could be applied to future models of extinct synapsids in studying the evolution of the mammalian forelimb. Here, we aim to critically evaluate the behaviour and outputs from the initial echidna musculoskeletal

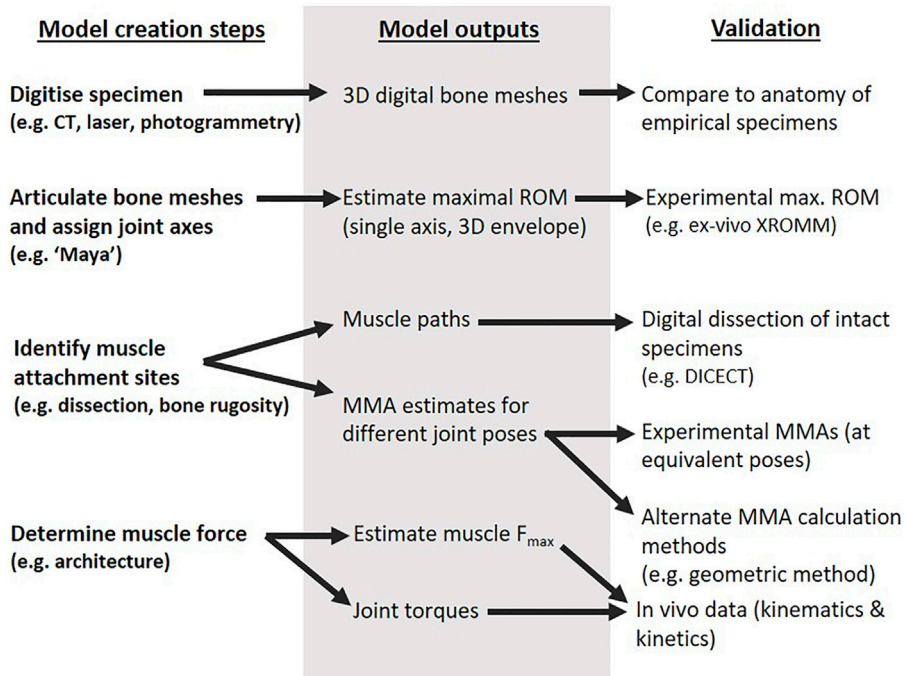

FIGURE 1 | Different components of the musculoskeletal modelling process as detailed in the text.

model against experimental data, taking into account some of the considerations for ROM and MMA predictions mentioned above. In the initial model, ROMs were predicted through 1 DOF independent rotations around an anatomical joint centre until bone-bone contact. Muscle geometry was modelled as lines of action between bony attachment sites, with the minimal 'wrapping' needed to prevent muscles from passing through bones. MMAs were calculated using a partial velocity method (equivalent to tendon travel) through each rotational DOF independently. In the current study, we now seek to validate and refine the model via several stages: 1) contrast stain (via diceCT) and digitally dissect the echidna specimen's forelimb muscles to evaluate the accuracy of a minimalist wrapping approach in replicating muscle geometry, and evaluate the effect of inaccuracies on predicted MMA; 2) collect maximal ROM data via passive manipulation of cadavers using bi-planar x-ray fluoroscopes and X-ray Reconstruction of Moving Morphology (XROMM; Brainerd et al., 2010) to evaluate single-axis rotational DOF model predictions against experimental joint excursions in both rotation and translation (up to 6 DOF); and 3) develop a geometric method of calculating MMA from markers implanted in cadaver muscles, to evaluate both model-predicted MMAs and different methods of calculating MMAs. We also combine MMA from the initial model with muscle architecture data (Regnault et al., 2020) to evaluate the functional interpretations that can be made from MMAs alone (typical outputs of extinct animal models) versus more holistic parameters (muscle torque).

MATERIALS AND METHODS

The typical components of the musculoskeletal modelling process are outlined in **Figure 1** (Bishop, 2021a), from model creation to outputs and validation using experimental data. The steps are often iterative, and validation of a previous step may feed into subsequent model creation and output (though care must be taken to avoid circularity or targeted results by specifying the methods, acceptable adjustments, and rationale for each *a priori*). The detailed methods for the creation steps of our echidna forelimb model (left column of **Figure 1**) are described in Regnault and Pierce (2018) and Regnault et al. (2020). In this study, we critically examine our model outputs through diceCT, *ex vivo* XROMM, and details of muscle architecture.

Digital Dissection and Evaluation of Muscle Paths

The initial musculoskeletal model (Regnault and Pierce, 2018) was built using the modelling software SIMM (Delp and Loan, 1995). The model was created following the steps of **Figure 1**: bone meshes were obtained from computed tomography (CT) scans of an echidna cadaver (first row of **Figure 1**), articulated with anatomical joint axes based on shape "primitives" fitted to joint surfaces (second row of **Figure 1**), and used muscle attachment sites identified from the qualitative descriptions of Gambaryan et al. (2015) (third row of **Figure 1**). To enable specimen-specific evaluation of muscle attachments and muscle paths in the model and ensure model accuracy (right column of **Figure 1**), the same echidna specimen underwent digital

dissection (Gignac et al., 2016). The specimen was contrast-stained with a 3% iodine potassium iodide solution, and micro-CT scanned a second time to visualise its soft-tissue anatomy. The muscles were digitally segmented, and three-dimensional muscle meshes created to identify muscle attachment regions on the bones. The full method and illustrations of attachment regions are detailed in Regnault et al. (2020). No overt pathological changes or other anomalies were evident in the shoulder and forelimb region of this specimen or the others used in this study; all specimens were evaluated to confirm skeletal maturity (fused epiphyses) and lack of injury/pathology via radiography, computed tomography, dissection, and (for the modelled specimen) diceCT/digital dissection.

Muscle origin and insertion coordinates from the initial model were compared with the diceCT-identified attachment regions. Where the model's muscle attachment coordinates did not fall within the diceCT-identified regions, model coordinates were adjusted within SIMM. The effects of adjusting muscle attachment coordinates on model-estimated MMAs are detailed in the Results.

The initial model's muscle pathways between origin and insertion were also compared to the diceCT muscle geometry. The digital bone and muscle meshes segmented from the diceCT scan were imported into SIMM, alongside the initial model. The initial model's forelimb position was aligned, via rotation around its joint centres, to the forelimb position of the specimen in the diceCT scan. In this way, the model's muscle lines of action could be compared to the actual muscle geometry for this position. Modelled muscles whose paths deviated appreciably from the digitally segmented muscle meshes were adjusted and the wrap objects associated with these muscles were edited. The effects of these adjustments on model-predicted MMAs are likewise reported in Results. The updated musculoskeletal model (with adjusted muscle attachments and pathways, based on diceCT) was used for all follow-on MMA and torque analyses.

Experimental Set-Up and Data Collection

Experimental data were collected to validate model estimates of maximal joint ROMs and MMAs at the scapulocoracoid-clavicle-interclavicle, glenohumeral, and humeroradioulnar joints (second and third rows of **Figure 1**). Data collection consisted of passive manipulation of three echidna cadavers, using marker-based X-ray Reconstruction of Moving Morphology (XROMM; Brainerd et al., 2010). The echidna cadavers were obtained from the University of Adelaide (as per descriptions in Regnault et al., 2020), stored frozen at −18°C, and thawed at 4°C prior to data collection.

To track bone positions and calculate joint kinematics, 1 mm tantalum markers were implanted into holes predrilled into bones, using a 0.96 mm tungsten carbide hand drill. Three markers were implanted into each of the following bones (both left and right forelimb bones): the fused clavicle-interclavicle, scapulocoracoid, humerus, radius, and ulna. Subsequent animation and analysis showed the radius markers to display error associated with co-linearity, due to the size, shape and accessibility of the radius constraining marker placement sites. Because of this, we chose to animate the antebrachium as one unit (i.e., radius taking on the rotations and translations of the ulna). The radius and ulna generally move as a unit in the echidna, though some lateral displacement of the radius is possible (Haines, 1946). Our analyses therefore could not verify radial movement relative to the ulna, but were sufficient to evaluate elbow ROM. Two markers were also implanted into the sternum and one marker in the vertebral column, so that the body position could be approximated as a "body plane".

To calculate experimental MMAs (third row of **Figure 1**), markers were also inserted into select muscles of each specimen based on their accessibility. A 16G needle was used to implant 0.8 mm tantalum markers into the following muscles: m. latissimus dorsi, m. pectoralis, m. triceps brachii (pars superficialis longus), m. biceps brachii, m. coracobrachialis (pars longus), and m. clavodeltoideus. Several other muscles were also implanted (m. triceps brachii pars lateralis and profundus, m. subscapularis), but later eliminated from analysis due to marker migration. A maximum of two muscles were implanted per specimen side (right or left) to facilitate muscle and marker identification on recordings. Markers were implanted proximally and distally in the muscle belly, as close to the origin and insertion as possible, so that a straight muscle line of action could be approximated. Due to their broad origins, multiple markers were implanted at the origins of m. latissimus dorsi (one at the scapular origin, plus one each at the cranial and caudal extremes of the fleshy vertebral origin) and m. pectoralis (one each at the cranial and caudal extremes of the sternal origin).

Veterinary tissue glue was used to secure all the bone and muscle markers and the forelimb and body was re-covered with the reflected skin and plastic wrap to prevent drying of the soft tissues during experiments.

Each echidna cadaver was secured to an angled, custom-made carbon fibre platform, in an orientation that allowed maximal mobility of the forelimb. Typically, this was achieved by securing the hindlimbs and abdomen to the platform with cable ties through pre-drilled holes in the platform, so that the thorax and forelimbs hung over the edge (**Figure 2**). One forelimb was manipulated at a time using a wooden pole, so that the operator could maintain distance from the x-ray source. The pole was attached to the echidna forelimb via either a cable tie around the carpus, and/or a metal screw eye inserted into the distal humerus. Each experimental trial incorporated several cycles of differing motion: the forelimb was manipulated through maximal abduction (X+), adduction (X−), internal rotation/pronation (Y+), external rotation/supination (Y−), flexion (Z+ or Z− depending on joint), and extension (Z− or Z+), at both the glenohumeral and humeroradioulnar joints. The manipulations attempted to achieve maximum possible excursions for each DOF, through the DOF itself and combined with other motions. For example, to attempt to achieve maximum glenohumeral extension, we manipulated the limb through cycles of flexion-extension at variously abduction-adduction and internally-externally rotated positions, including approximately "neutral" (mid-point) joint positions for abduction-adduction and long-axis rotation.

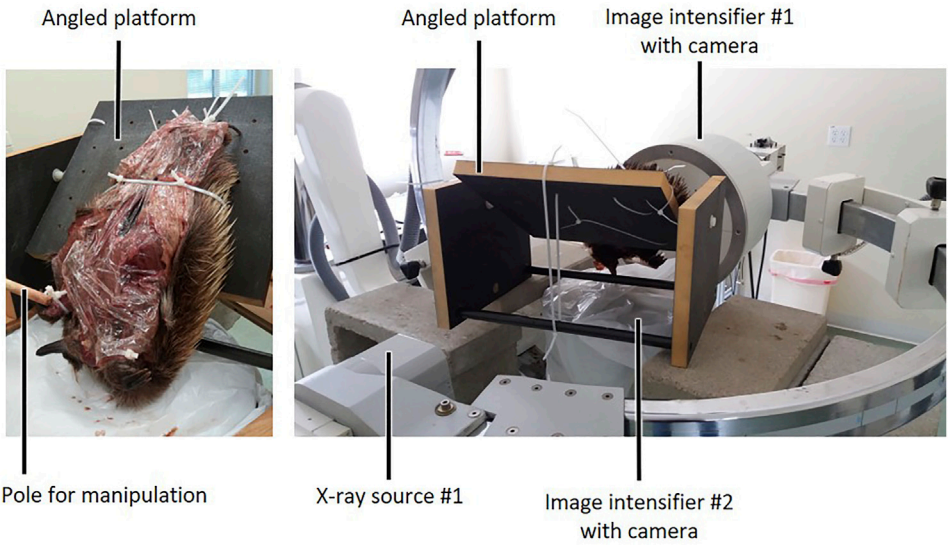

FIGURE 2 | Experimental set-up for *ex vivo* passive manipulation of echidna cadaver forelimbs. After markers were placed in bones and muscles, each animal was covered with plastic wrap to prevent drying out, tied to a custom-made carbon fibre platform oriented to allow limb manipulation, and placed in the field of view of two refurbished c-arm fluoroscopes for data collection.

Data were collected using two refurbished c-arm fluoroscopes (90–95 kV and 2–2.5 mA for 13.3 s), recorded using two high speed Photron Fastcam 1024 PCI cameras (Photron United States Inc., San Diego, CA, United States) at 60 frames per second. The relatively long recording times enabled each trial to contain several cycles of each type of limb manipulation. Between 7 and 10 trials were recorded for each side of each animal, and the best 3–5 trials (i.e., lowest error reported in XMALab, detailed below, and qualitatively judged to capture full range of motion) were selected from these for marker digitisation and analysis. In total, five trials were processed for mm. clavodeltoideus, coracobrachialis and biceps brachii, four trials for mm. pectoralis and latissimus dorsi, and three trials for m. triceps brachii superficialis longus.

Experimental Data Processing

Trials were processed using XMALab version 1.5.1 (Knörlein et al., 2016) to calculate the transformations of the bone and muscle markers. Transformation data were filtered using a cut-off frequency 5-10x of the passively manipulated motions; values varied from trial to trial but cut-off frequencies between 3 and 8Hz were used. Filtered transformations were checked in the rigid body plot window of XMALab to ensure data were not over-filtered (i.e., plotted rigid body transformations were smoothed without changing the shape of the curve).

To calculate the rigid body transformations of the bones during each trial, the XROMM workflow requires creation and animation of specimen-specific digital bone models containing bone marker locations. To generate these models, each experimental animal was scanned at the Harvard University Center for Nanoscale Systems using a HMXST225 micro-CT system (X-Tek, Amherst, NH, United States), with the following parameters: 120 kV, 120 mA, 1s exposure, 0.25 mm copper filter. The CT projections were converted to a TIFF image stack using CT Pro 3D software (Nikon Metrology Inc., Brighton, MI, United States), then imported into Mimics version 19.0 (Materialise, Leuven, Belgium), to segment three-dimensional surface meshes of the forelimb bones and implanted bone and muscle markers.

To enable comparison between the experimental XROMM data and the SIMM model's ROM and MMA estimates, the digital bone models of all experimental animals were aligned to the same joint coordinate system and "reference pose" as the initial model (Regnault and Pierce, 2018). The 3D bone meshes from the experimental cadavers were imported into 3ds Max 2017 (Autodesk, San Rafael, CA, United States) and the left and right-side pectoral girdle and forelimb bones of each animal were assigned anatomical joint axes and assembled into a kinematic hierarchy, as in the initial model [described in Regnault and Pierce (2018)]. The experimental animal models were then aligned via rotation around the joint axes to match the initial model specimen's reference pose.

Although the body masses of the animals differed somewhat (2.48–3.79 kg experimental animals vs. 3.31 kg initial model specimen), much of the difference was due to body condition/fat: the bones were similarly-proportioned when overlying each other and scaling of bone meshes was not necessary. All aligned and posed experimental animal bone models were then exported to Maya 2017 (Autodesk, San Rafael, CA, United States), along with their joint axes. The rigid body transformation data from each XROMM trial was used to animate the bone meshes. The translations and rotations of the joint axes at each frame were exported as .csv files using the "exp" function of the XROMM tool shelf.

Each echidna specimen was dissected after XROMM data collection, to assess whether muscle markers had remained *in*

situ during the trials, and also to collect muscle architecture data (detailed in Regnault et al. (2020). Muscles for which markers were found to have moved from the implantation site during data collection were eliminated from the analysis, and so are not reported in this study. The mm. pectoralis and latissimus dorsi muscles had broad origins, and were modelled as several lines of action. To enable valid comparison, the markers in the experimental animal specimens were implanted as close to the selected model muscle heads as possible and the position confirmed in dissection and imaging post data collection.

The muscle markers were digitised and filtered alongside bone markers in XMALab version 1.5.1 (described above). The muscle marker transformations throughout each experimental trial were then imported into Maya 2017 alongside the animated bones. The animated marker locations were used to calculate experimental MMAs, detailed below.

Experimental MMA Calculation and Comparison With Model MMA

MMAs were calculated for each implanted muscle at each joint pose, across the full range of experimental joint ROM. This was done using a geometric method based on the mechanical definition of a moment arm being the shortest perpendicular distance from the centre of rotation to the force line of action (Sherman et al., 2013); or in the echidna's case, the distance between the anatomical joint centre and vector running between implanted muscle markers. The 3D geometric MMAs were calculated using a custom Python script, in two steps described in detail below.

First, for each muscle-joint pairing (e.g., biceps-elbow), separate X, Y, and Z moment arms ($\overrightarrow{r_x}$, $\overrightarrow{r_y}$, and $\overrightarrow{r_z}$) were calculated as vectors spanning the shortest perpendicular distance between two skew lines: a unit vector representing one of the three joint axes ($\hat{x}$, $\hat{y}$, and $\hat{z}$), and a muscle vector running between the proximal and distal implanted muscle markers ($\vec{F}$) (**Supplementary Figure S9A**). Since the shortest distance between two skew lines is always perpendicular to both lines (**Supplementary Figure S9B**), this is equivalent to first finding the perpendicular 3D distance between the anatomical joint centre and the muscle's line of action, and then finding the 2D projection of that distance onto each axis' plane of rotation. The resulting moment arm $\vec{r}$ is a vector with both direction and magnitude. A joint moment $\vec{\tau}$ may then be determined by finding the cross product of $\vec{r}$ and a force vector $\vec{F}$, following the equation:

$$\vec{\tau} = \vec{r} \times \vec{F} \tag{1}$$

While this geometric method yields moment arms as vectors, musculoskeletal modelling programs such as SIMM use a different concept of moment arms that follows the general definition:

$$r_\theta = \frac{\tau_\theta}{F} \tag{2}$$

where r_θ, τ_θ, and F are all scalars and r_θ is specific to each axis of rotation (Sherman et al., 2013). To convert a vector moment arm $\vec{r}$ to the scalar form r_θ for comparison, it is not sufficient to simply take the magnitude of $\vec{r}$; once $\vec{r}$ has been computed for each joint axis, its magnitude $||\vec{r}||$ must then be scaled by the fraction of the muscle vector's magnitude that lies in the plane perpendicular to the axis, and thus capable of generating a moment about $\hat{x}$. In other words, the scalar magnitude of the vector projection of $\vec{F}$ from axis $\hat{x}$ is divided by $||\vec{F}||$. The intuition for this step is straightforward: **Eq. 1** contains spatial information in the form of the directions of vectors $\vec{r}$ and $\vec{F}$, both of which are necessary to calculate a moment since $\vec{r}$ is valid for an infinite number of possible force vectors of equal magnitude (e.g., $\vec{F}'$,$\vec{F}''$), all intersecting with $\vec{r}$ at point p (**Supplementary Figure S9C**). This issue does not arise in the 2D case, where $\vec{F}$ is constrained to lie entirely in the same plane as $\vec{r}$; its entire magnitude contributes to τ_θ. In 3D, it is possible for part or all of $\vec{F}$ to lie out of plane. For instance, the hypothetical $\vec{F}''$ runs antiparallel to axis $\hat{x}$, and obviously has no capacity to generate an x moment, yet using $||\vec{F}''||$ rather than $||\vec{F}||$ for F in **Eq. 2** yields the same value for τ_θ, rather than the expected 0. Hence, we preserved the spatial specificity of r_θ by scaling $||\vec{r}||$ based on the direction of $\vec{F}$.

To speed up analysis and increase user-friendliness by enabling quick visual inspection, the geometric moment arm script was incorporated into a Maya shelf tool. This allowed all calculations to be performed entirely within the Maya graphical interface. The tool has been made freely available as a GitHub repository, accessible at https://github.com/philsometimes/mayaMomentArms. The tool requires two sets of inputs: 1) the proximal and distal joint axes created by the jAx tool in XROMM MayaTools, and 2) a pair of animated objects representing the start and end points of a 3D muscle vector. In the present study, Maya locators animated to match implanted markers were used for the muscle points, but any arbitrary objects including "virtual" points placed directly on animated bones may be used instead.

To compare the experimentally-calculated MMAs with equivalent SIMM model estimations, MMAs from the SIMM model needed to be taken at the same poses as in each experimental trial. The rotations and translations of the joint axes at each frame of the experimental trials were used to create a SIMM motion (.mot) file with which to animate the SIMM model. An example trial is available as **Supplementary Video S1**.

The built-in Plot Maker function in SIMM was used to calculate muscle moment arms for comparison with the experimental MMAs. As a result, MMAs were calculated using two independent methods: the experimental MMAs are based on a geometric method of calculating MMAs described above, whilst the SIMM model uses a partial velocity method equivalent to tendon travel, using the model's muscle paths (determined by attachment points and wrap objects). As discussed in the Introduction, the use of two different methods is valuable in validating model MMA outputs.

In addition to visualising the similarities and differences between SIMM model and experimental MMAs, we also calculated Root Mean Square Error (RSME) with the mean_squared_error function in the scikit-learn Python package (Pedregosa et al., 2011). These results can be found in **Supplementary Table S2**. While this provides a more

quantitative perspective on the relative similarity/differences between experimental and model MMAs, RSMEs are generally employed to compare the performance of multiple models, and we caution that compared with the visual MMA plots presented here, RMSE values do not offer a more objective threshold on how well the MMA data agree.

Muscle Architecture and Functional Signal

As part of our evaluation of the traditional musculoskeletal model workflow (e.g., Bishop et al., 2021a), we collected muscle architectural parameters: muscle belly mass and length, external tendon length, fascicle length and pennation angle, and calculation of muscle physiological cross-sectional area [methods and results are reported in Regnault et al. (2020)]. Here we wanted to better understand how robust the overall conclusions drawn from the initial model (based on MMAs) were to additional levels of modelling detail through the calculation of muscle torques. To the initial SIMM model muscle (.msl) file, we added: 1) maximum force, calculated from muscle physiological cross-sectional area (PCSA) multiplied by a muscle stress value of $0.3 Nmm^{-2}$ (Zajac, 1989), 2) optimal fibre length (i.e., resting muscle fibre length), 3) tendon slack length, and 4) the pennation angle of inserting fibres. Four characteristic musculotendon curves (Millard et al., 2013) were also added to the SIMM .msl file: a tendon force-length curve, active and passive force-length curves, and a force-velocity curve. These are generalised curves which are not species-specific for the echidna, as those data are currently not available. Calculation of individual muscle torques around each joint for each rotational degree of freedom allowed comparison of model-calculated MMAs with muscle torques, and evaluation of how interpretations about individual muscles and whole limb function might (or might not) change with the inclusion of these additional data.

Data Visualisation

Data in this study are presented through several visualisation methods to explore different aspects of model evaluation. The detailed methods for presented figures are described here, and summarised in the figure captions, to ensure readers can interpret figures with relevant contextual information.

Experimental joint ROMs are presented as rotational ranges in both raw (uncorrected) Euler space (**Figure 3**) as well as cosine-corrected Euler space (**Figure 4**). Joint ROMs are often presented as maximum excursions per rotational DOF or plotted in uncorrected Euler space, but these visualisations can preclude comparisons amongst joints with different joint coordinate systems and distort comparisons between joint space volumes (for example, equally-different poses not being depicted equally far apart) (Manafzadeh and Gatesy, 2020). Cosine-correction is a method that has been recently developed and applied to 3D depictions of model pose-space, addressing these issues (Manafzadeh and Gatesy, 2020). Here, we have chosen to present both types of visualisation. For the uncorrected visualisation (**Figure 3**), the maximal joint angles achieved across each experimental animal's trials were pooled (i.e., the largest joint angle for each motion and joint taken for each animal) to be directly compared to the initial SIMM model-estimated maximal ROMs (Regnault and Pierce, 2018). For the cosine-corrected ROMs (**Figure 4**), all joint transformations (i.e., pose per frame of experimental trial) were imported into Python (Van Rossum and Drake, 1995) and cosine-correction performed on the axis of greatest variation (X-axis). The plotted points of cosine-corrected joint transformations were then wrapped in a concave hull (or alpha shape) to visualise ROM as a 3D "envelope" with an alpha threshold of 20. Uncorrected point clouds are presented alongside the hull envelopes to enable comparison with the initial SIMM model maximal ROM estimates, since both use the same joint coordinate system.

Experimentally-calculated 3D MMAs vs. SIMM model 3D MMAs for each joint pose are also presented as plots in cosine-corrected Euler space (**Figures 6–9**, **Supplementary Figure S5**). For these plots, the colour indicates whether the MMA is positive (purple) or negative (orange), with colour intensity indicating relative magnitude (normalised to maximum absolute value for each muscle, inclusive of the SIMM and experimental estimates). The sign (positive or negative) denotes the direction of the torque, according to the joint coordinate system. For example, a positive MMA at the glenohumeral X-axis would cause an abduction moment (torque) whilst a negative MMA would cause an adduction moment. The 3D MMA plots for the glenohumeral joint are provided in the main paper, while those for the humeroradioulnar joint can be found in the **Supplementary Figure S5**. Absolute (non-normalised) MMA magnitudes are also presented more traditionally for each rotational axis (**Figures 5**, **10**, **11**), as representative kinematic trials for each muscle and as frequency distribution boxplots to assess magnitudes and rank orders.

Finally, individual and summed MMAs and torques were determined at the glenohumeral joint and compared to evaluate inferred functions and muscle roles using the initial SIMM model's ROM (single-axis DOF rotations as is typical of traditional musculoskeletal models). To avoid over-representation of muscles with multiple modelled heads (e.g., mm. biceps brachii, m. latissimus dorsi), mean values were determined for these muscles before calculation of the summed MMAs [as described in Regnault and Pierce (2018)]. Comparisons between individual MMAs and their corresponding torques are presented in the **Supplementary Figures S1–S3, S6–S8**.

RESULTS

Muscle Pathways

Several muscle attachment points on the initial SIMM model were adjusted following diceCT and digital segmentation, to better reflect specimen-specific anatomy (see **Supplementary Table S1**). Many of the muscles that were adjusted were done so due to small or narrow attachment areas differing between Gambaryan et al. (2015), on which the initial model was based, and our specimen-specific attachment areas, but with negligible effects on the initial model-predicted MMAs

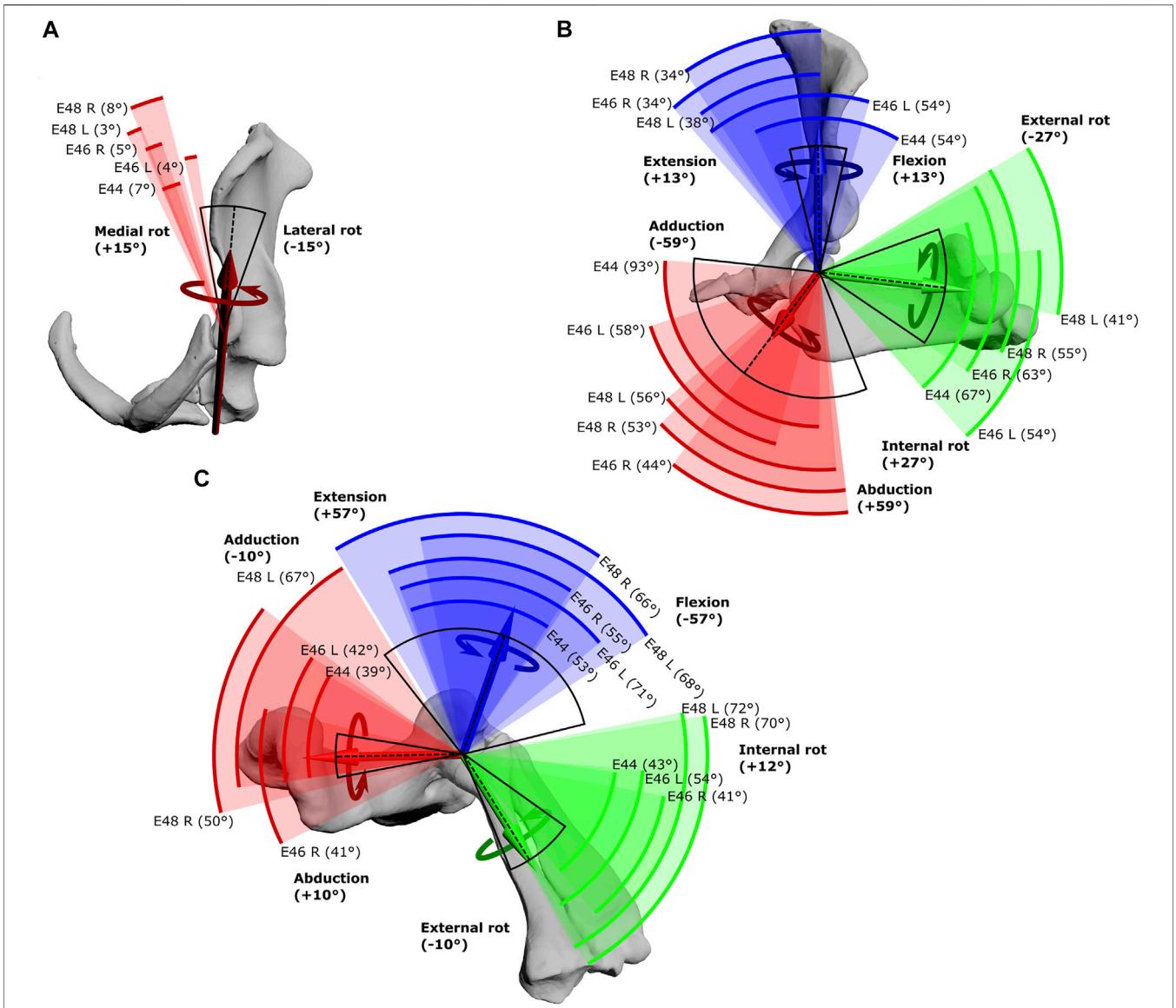

FIGURE 3 | Maximal Range of Motion (ROM) at the echidna forelimb joints. **(A)** scapulocoracoid-clavicle-interclavicle joint, **(B)** glenohumeral joint, **(C)** humeroradioulnar joint. Experimentally-estimated ROMs (pooled raw data) for each echidna specimen E44, E46 and E48 (coloured arcs, total ROM in parentheses) compared with initial model-predicted ROMs based on single DOF rotations (black arc, limits in bold text) about the X (red), Y (green) and Z (blue) axes. The dotted line represents the limb's reference position. See **Table 1** for more details.

(**Supplementary Figures S1–S3**). However, a few muscle attachments genuinely appeared to differ from Gambaryan et al. (2015), and thus more significant adjustments were deemed necessary, as noted below.

One muscle was m. pectoralis. The cranial-most extent of this muscle's origin ("part 1" in the initial model) was far more cranial in the literature reconstruction than in our contrast-stained and segmented specimen. Gambaryan et al. (2015) observed this muscle to originate from the interclavicle cranially, but our specimen's cranial-most border was the first sternal element (sometimes called the presternum; shown in **Figure 1B**, **2B** of Regnault et al., 2020). Moving parts 1 and 2 of m. pectoralis in the model (representing the cranial-most and middle body of the muscle origins) affected the resultant estimated MMAs for these parts of m. pectoralis (**Supplementary Table S1**, **Supplementary Figures S1, S2H**). At the scapulocoracoid-clavicle-interclavicle joint, the moment arms for parts 1 and 2 of m. pectoralis become less negative (**Supplementary Figure S1**): part 1 thus is interpreted to produce a much weaker lateral scapulocoracoid movement, whilst part 2's moment arms now cross zero with a negative slope, suggesting it may act as an intrinsic joint stabiliser (albeit weakly). Similarly, at the glenohumeral joint, m. pectoralis part 1 (cranial part) now has positive moment arm values in long-axis rotation; in other words, acting to internally rotate/pronate the humerus, similar to the other parts of m. pectoralis (**Supplementary Figure S2H**). Overall, at the glenohumeral joint, the MMAs for the parts of m. pectoralis appear more

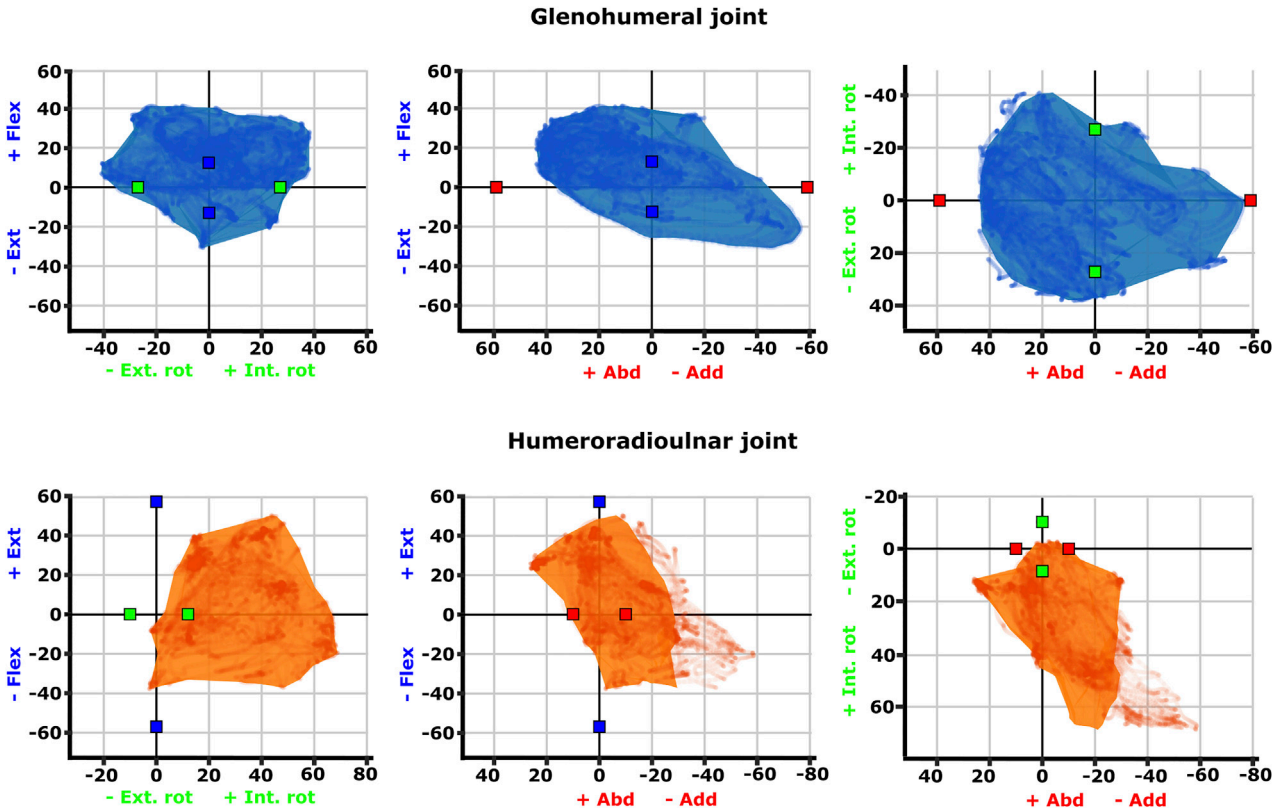

FIGURE 4 | Three-dimensional (3D) joint ROM at the glenohumeral joint (top row, blue) and humeroradioulnar joint (bottom row, orange). Note that axis scale differs between plots. The 3D envelopes encompass cosine-corrected experimental ROMs wrapped in a concave hull (alpha value 20), whilst the plotted points behind in the same colour show the uncorrected experimental ROMs. The initial model-predicted maximum ROMs for single DOF rotations from the zero (reference) position have been superimposed on the 3D plots as red (X), green (Y), and blue (Z) cubes (data from Regnault and Pierce (2018)). Individual specimen trial sets are illustrated in **Supplementary Figure S4**.

similar to one another compared with the initial model, indicating these muscle parts would produce similar actions when contracting.

The other muscle with greater discrepancy was m. biceps brachii longus. In the initial model, this head originated from the epicoracoid (following Gambaryan et al., 2015). In our diceCT specimen (and accompanying dissections of other specimens; Regnault et al., 2020), we confirmed an epicoracoid attachment, but note that the bulk of the muscle originated on the coracoid (alongside m. biceps brevis). Altering its origin from the more modest epicoracoid attachment site to the larger scapulocoracoid site resulted in m. biceps longus no longer crossing the scapulocoracoid-clavicle-interclavicle joint in the model, and so the small moment arm at this joint is removed (**Supplementary Figure S1**).

The muscle paths of mm. biceps brachii brevis and longus were also adjusted to better follow the centroid of 3D muscle meshes. Subsequent to the muscle origin and path adjustments in the revised model, the flexion-extension moment arms of mm. biceps at the glenohumeral joint changed signs, altering their interpreted action from external rotators/supinators to internal rotators/pronators. The flexion-extension moment arm for m. biceps brevis also switched from negative to positive, changing its interpreted action at the glenohumeral joint from an extensor to flexor. In a similar fashion, adjustment of muscle paths for parts of mm. deltoid resulted in the glenohumeral abduction moment arm for m. clavodeltoideus to switch sign at greater angles of adduction (i.e., becomes an adductor), and the mixed flexor-extensor moment arms of m. acromiodeltoideus to become wholly negative (i.e., only extensor).

Joint Range of Motion

The scapulocoracoid-clavicle-interclavicle joint possesses only a single rotational degree of freedom (**Figure 3A**). Pooled experimental data from all echidna trials encompass a ROM totalling 17° of motion around this rotational axis (**Table 1**). However, individual ranges for each animal are more limited (**Figure 3A**), and so the experimentally-estimated ROMs are much less than the initial model-predicted ROM of 30°.

Conversely, at the glenohumeral and humeroradioulnar joints, experimental ROMs approached and/or exceeded the model-predicted ranges (**Figures 3B,C** and **Table 1**). At the glenohumeral joint, abduction-adduction was greatest across all specimens and trials, totalling 101°, followed by long-axis rotation at 79° and flexion-extension at 72°. This is a similar pattern as predicted by the initial model using single-axis DOF

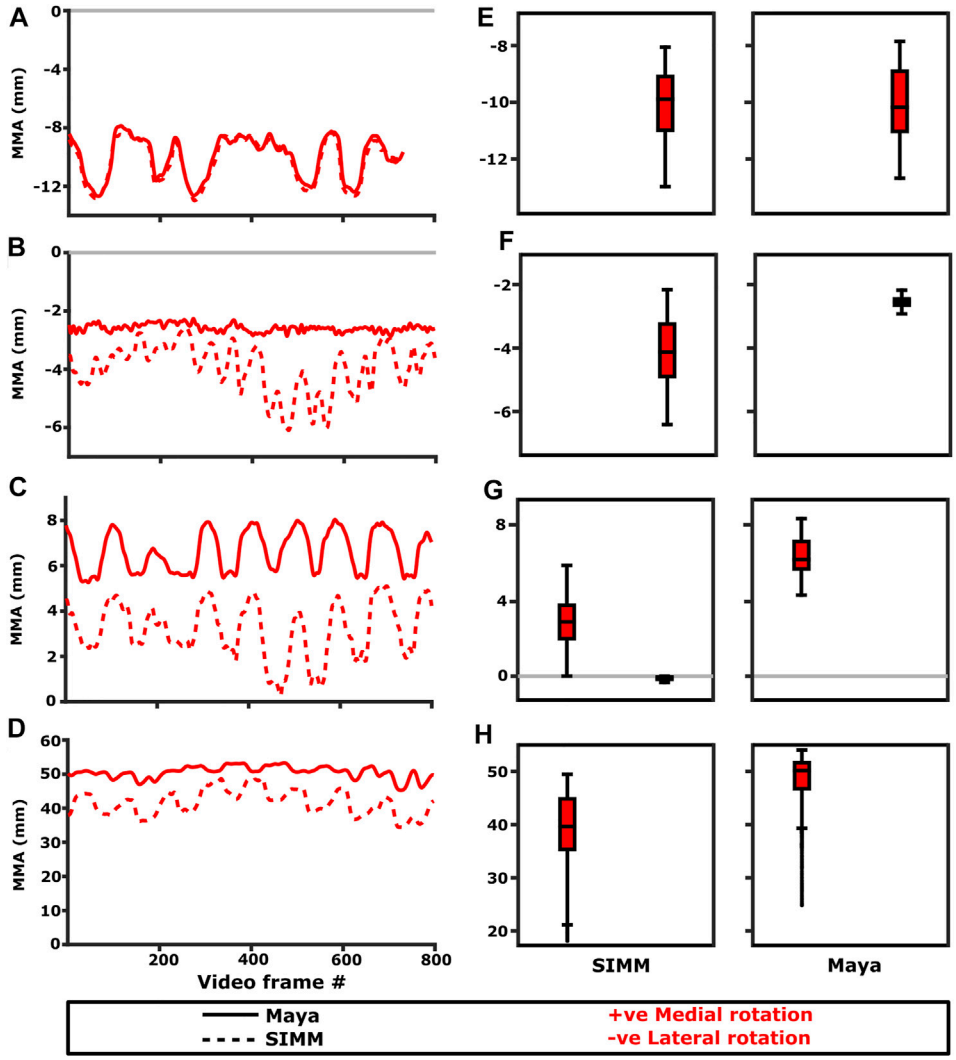

FIGURE 5 | Representative trials (left) and frequency distributions of MMAs for all kinematic trials (right) for muscles crossing the scapulocoracoid-clavicle-interclavicle joint. Representative trials for: **(A)** m. clavodeltoideus, **(B)** m. pectoralis cranial origin, **(C)** m. pectoralis caudal origin, **(D)** m. latissimus dorsi vertebral origin. The boxplots (**E–H)** show the distribution and median values of MMAs for all trials: **(E)** m. clavodeltoideus, **(F)** m. pectoralis cranial origin, **(G)** m. pectoralis caudal origin, **(H)** m. latissimus dorsi vertebral origin. Positive and negative MMAs are plotted as separate boxplots for each DOF. SIMM = model-predicted MMAs based on partial velocity; Maya = experimentally-calculated MMAs based on the geometric method.

rotations: total ROMs were 118° in abduction-adduction, 54° in long-axis rotation and 26° in flexion-extension (Regnault and Pierce, 2018). Of particular note here, flexion-extension ROM was much greater at the glenohumeral joint during the experimental trials. Experimental data also showed that translations at the joint surfaces occurred, the greatest being 10.4 mm along the X (craniocaudal) axis, with less translation along the other axes (**Table 1**).

At the humeroradioulnar joint, experimental ROM was similar around each of the rotational degrees of freedom (**Figure 3C**): flexion-extension was greatest, totalling 88°, followed by abduction-adduction at 85°, and then long-axis rotation at 72°. This contrasts with the initial model that predicted a predominance of flexion-extension (114° total) over the other two movements (20° and 22° for long-axis rotation and abduction-adduction respectively). Interestingly, the experimental data show long-axis rotation to consist almost completely of internal rotation (pronation) from the reference pose, with internal rotation accounting for 69° of the total 72° ROM. Joint translations were also evident at the humeroradioulnar joint, particularly along the Z (mediolateral) axis, recorded at up to 5.1 mm (**Table 1**).

Visualisation of the 3D glenohumeral and humeroradioulnar ROMs (**Figure 4**) shows the envelope of motion elicited experimentally, inclusive of simultaneous rotations and translations at the joints (up to 6 DOF). At the glenohumeral joint, these 3D plots (volume = 163,942 cubic degrees) show the initial model-predicted maximum ROMs using a single rotational

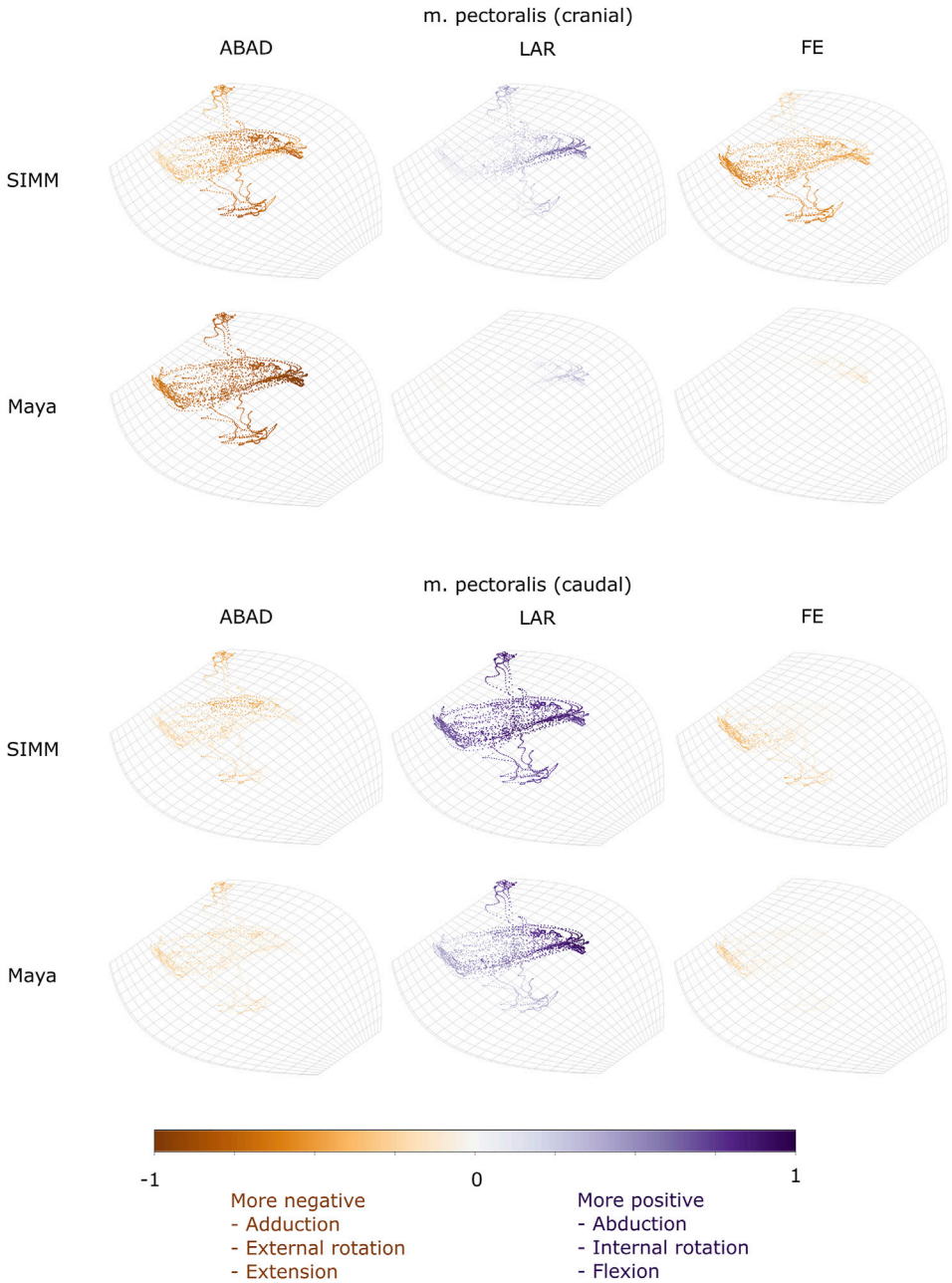

FIGURE 6 | Three-dimensional (3D) MMAs of m. pectoralis at the glenohumeral joint, plotted in cosine-corrected ROM space for the SIMM model (using partial velocity) and Maya experimental data (using the geometric method). MMA sign is indicated by point colour (positive values are purple, negative values are orange) with colour intensity scaled to relative MMA magnitude as described in the Methods. ABAD = abduction-adduction; LAR = long-axis rotation (internal-external rotation); FE = flexion-extension.

DOF were very close to the experimental ROMs in abduction-adduction and long-axis rotation. However, flexion-extension ROM in the initial model greatly underpredicts possible motion in this region of pose space. It can be seen from the 3D plot in **Figure 4** that the increased ROM achieved in glenohumeral flexion-extension experimental data is not wholly due to combined rotations, but more likely due to translations at the articular surface (especially along the craniocaudal axis, given the recorded translations and the elongated morphology of the echidna glenoid). In contrast, other motions, such as maximal humeral adduction, are achieved only alongside rotations in other axes (in this case, with concomitant maximum extension of the humerus; **Figure 4**). **Supplementary Figure S4** illustrates how each specimen/side contributes to the total pooled ROM.

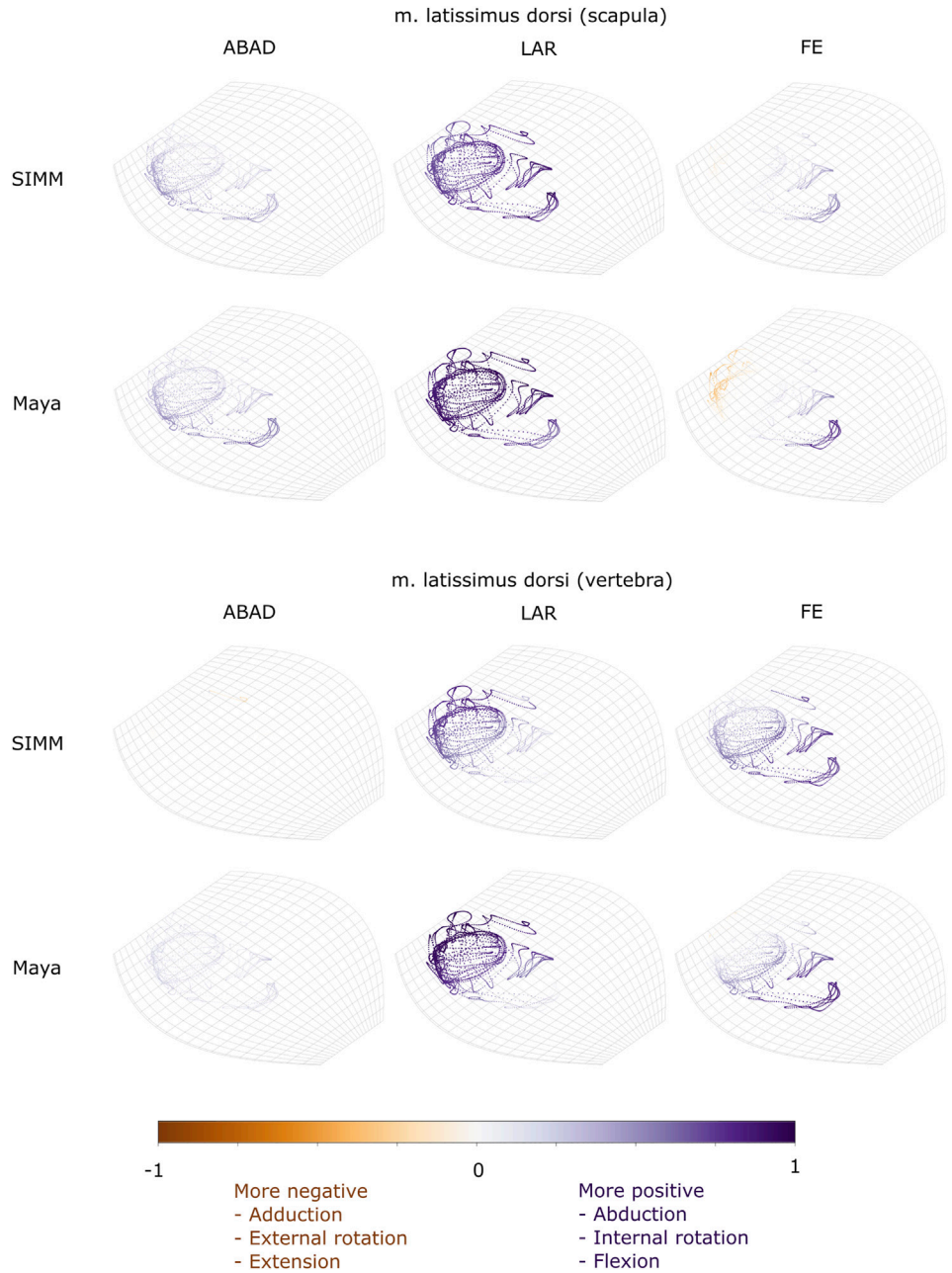

FIGURE 7 | Three-dimensional (3D) MMAs of m. latissimus dorsi at the glenohumeral joint, plotted in cosine-corrected ROM space for the SIMM model (using partial velocity) and Maya experimental data (using the geometric method). MMA sign is indicated by point colour (positive values are purple, negative values are orange) with colour intensity scaled to relative MMA magnitude as described in the Methods. ABAD = abduction-adduction; LAR = long-axis rotation (internal-external rotation); FE = flexion-extension.

The 3D envelope of experimental ROM at the humeroradioulnar joint (volume = 79,303 cubic degrees) more clearly shows the limitations of the single rotational DOF method in predicting ROM. The experimental ROM envelope only occupies some regions within the model-predicted limits. In particular, far more internal rotation (pronation) occurs than the initial model predicted, with peak internal rotation occurring concomitant with near-maximal joint adduction (**Figure 4**). Further, maximal humeroradioulnar joint abduction occurs at high extension angles and adduction at high flexion angles. Experimental flexion-extension ROM falls within model-predicted limits, though maximal extension only co-occurs with humeral internal rotation. As above,

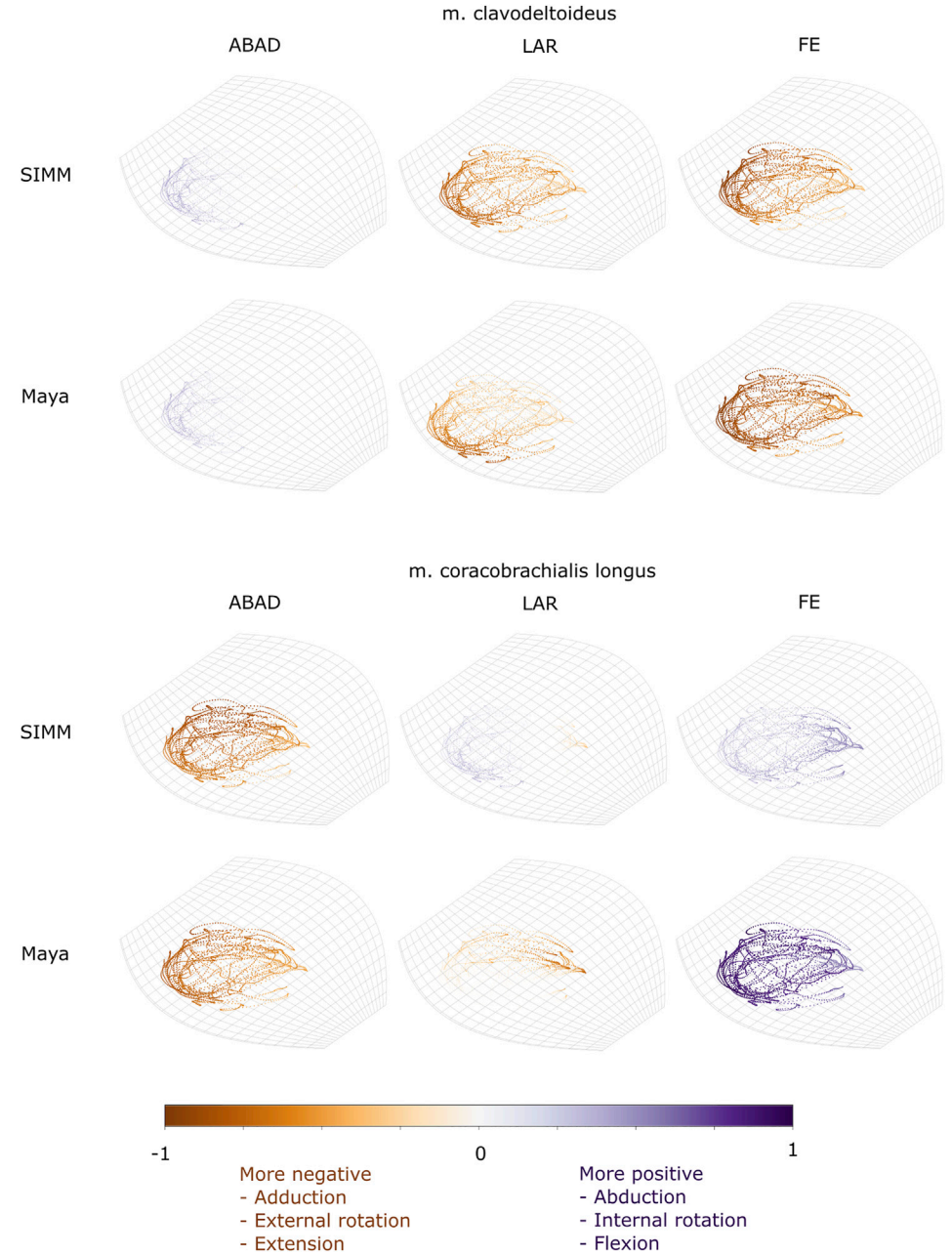

FIGURE 8 | Three-dimensional (3D) MMAs of m. clavodeltoideus and m. coracobrachialis longus at the glenohumeral joint, plotted in cosine-corrected ROM space for the SIMM model (using partial velocity) and Maya experimental data (using the geometric method). MMA sign is indicated by point colour (positive values are purple, negative values are orange) with colour intensity scaled to relative MMA magnitude as described in the Methods. ABAD = abduction-adduction; LAR = long-axis rotation (internal-external rotation); FE = flexion-extension.

individual specimen trial sets are illustrated in **Supplementary Figure S4**. These results highlight the importance of interactions between DOF in determining possible joint motions – a traditional single DOF approach in the echidna, as shown here, can miss joint poses that are achievable and include those which are not achievable in the real animal, but the degree of mismatch appears to be joint and direction dependent.

Muscle Moment Arms

Six muscles crossing the scapulocorcacoid-clavicle-interclavicle, glenohumeral and humeroradioulnar joints were successfully implanted with markers. These muscles were: m. clavodeltoideus, m. coracobrachialis (pars longus), m. triceps brachii (pars superficialis longus), m. biceps brachii, m. pectoralis, and m. latissimus dorsi. To evaluate MMAs, experimentally-estimated muscle moment arms using the geometric method were

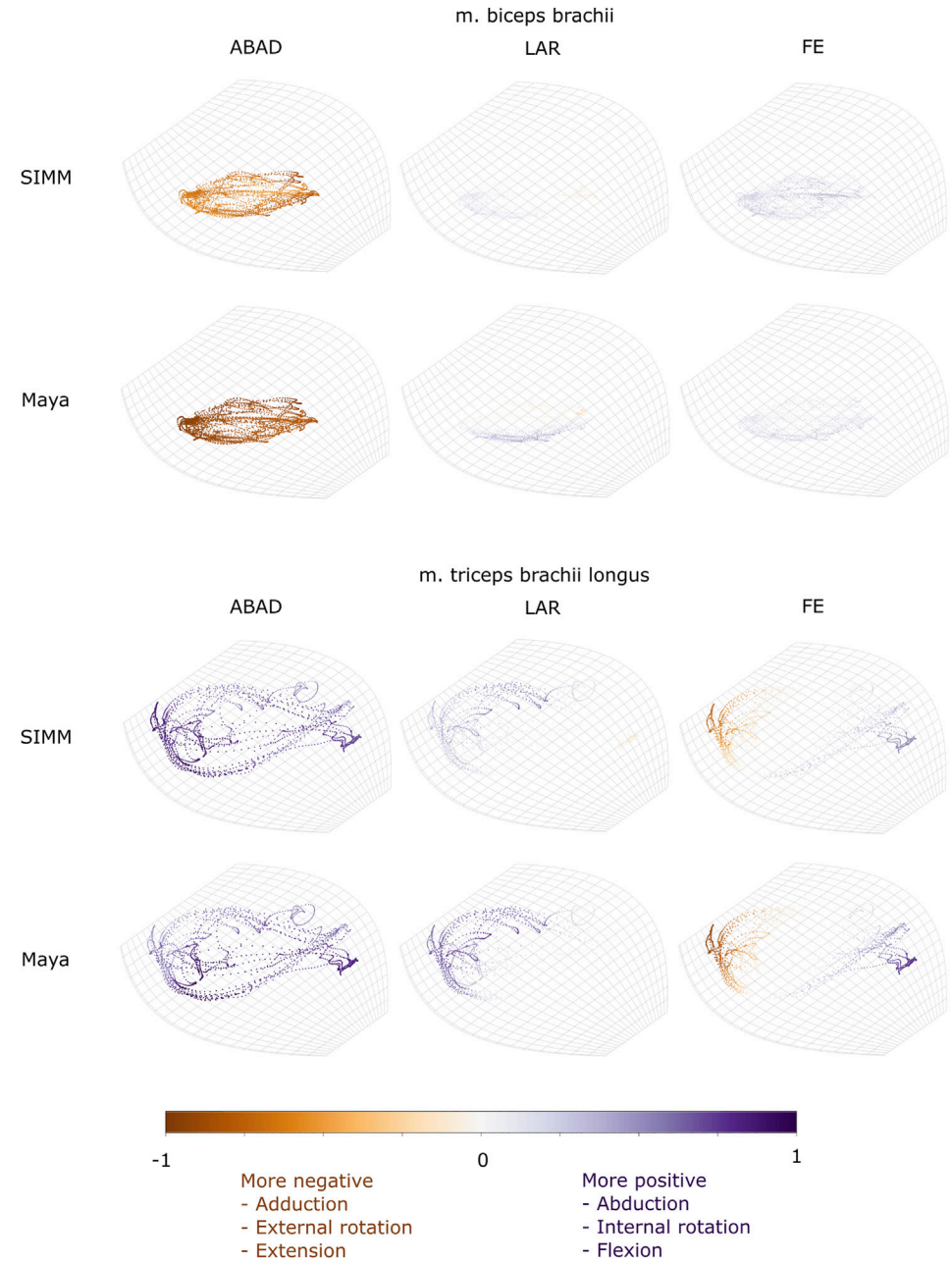

FIGURE 9 | Three-dimensional (3D) MMAs of m. biceps brachii and m. triceps brachii at the glenohumeral joint, plotted in cosine-corrected ROM space for the SIMM model (using partial velocity) and Maya experimental data (using the geometric method). MMA sign is indicated by point colour (positive values are purple, negative values are orange) with colour intensity scaled to relative MMA magnitude as described in the Methods. ABAD = abduction-adduction; LAR = long-axis rotation (internal-external rotation); FE = flexion-extension. Plot for these muscles MMAs at the humeroradioulnar joint can be found in **Supplementary Figure S5**.

compared to those predicted by the updated SIMM model animated with the experimental trial kinematics.

M. Clavodeltoideus

The m. clavodeltoideus crosses both the scapulocoracoid-clavicle-interclavicle and glenohumeral joints. At both joints, the experimentally-estimated MMAs and SIMM model-predicted MMAs agreed well. The MMAs were consistent in sign, magnitude, and rank order. At the scapulocoracoid-clavicle-interclavicle joint, both SIMM model and experimental MMAs show m. clavodeltoideus to laterally rotate the scapulocoracoid, assuming an unloaded limb (**Figures 5A,E**). At the glenohumeral joint, both consistently show this muscle (in order of largest to smallest MMA) to extend (i.e., protract), externally rotate (i.e., supinate), abduct, and minimally adduct the humerus (**Figure 8** and **Figures 10A,G**).

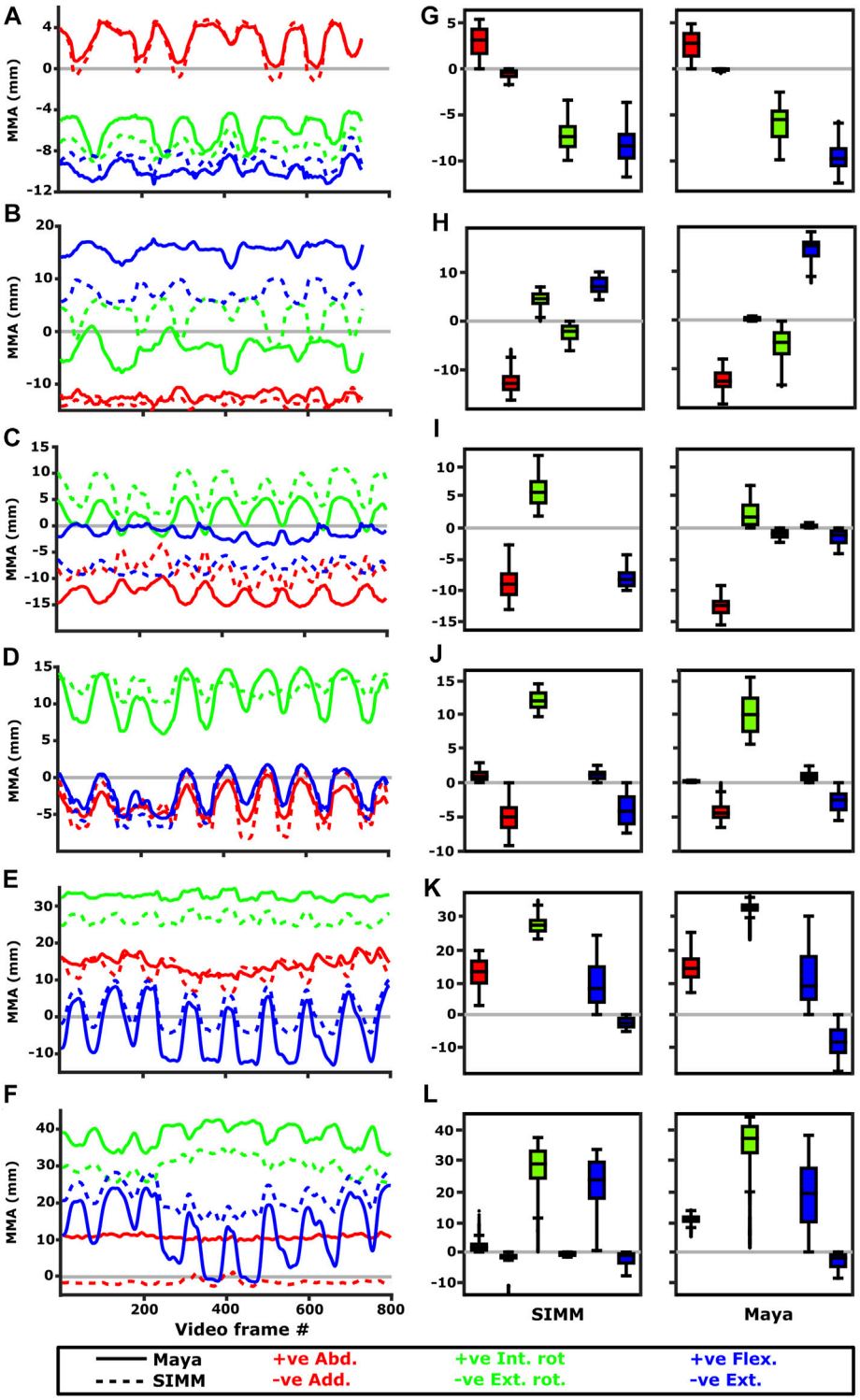

FIGURE 10 | Representative kinematic trials (left) and frequency distributions of MMAs for all kinematic trials (right) for muscles crossing the glenohumeral joint. Representative trials for **(A)** m. clavodeltoideus, **(B)** m. coracobrachialis, **(C)** m. pectoralis cranial origin, **(D)** m. pectoralis caudal origin, **(E)** m. latissimus dorsi scapular origin, **(F)** m. latissimus dorsi vertebral origin. The boxplots **(G–L)** show the distribution and median values of MMAs for all trials: **(G)** m. clavodeltoideus, **(H)** m. coracobrachialis, **(I)** m. pectoralis cranial origin, **(J)** m. pectoralis caudal origin, **(K)** m. latissimus dorsi scapular origin, **(L)** m. latissimus dorsi vertebral origin. Positive and negative MMAs are plotted as separate boxplots for each DOF. SIMM = model-predicted MMAs based on partial velocity; Maya = experimentally-calculated MMAs based on the geometric method.

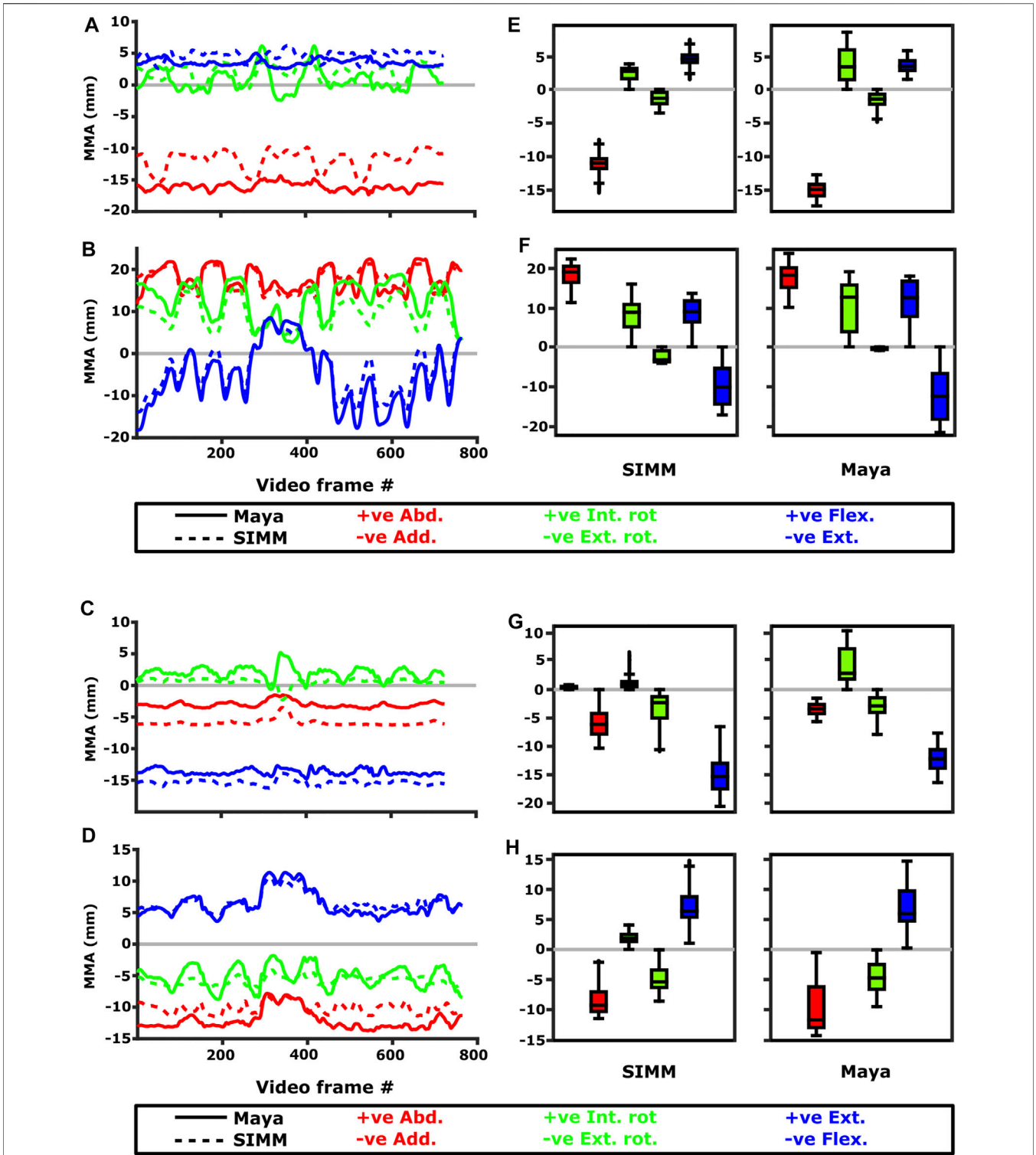

FIGURE 11 | Representative kinematic trials (left) and frequency distributions of MMAs for all kinematic trials (right) crossing the glenohumeral (top) and humeroradioulnar joints (bottom). Representative trials for **(A)** m. biceps brachii at glenohumeral joint, **(B)** m. triceps brachii at glenohumeral joint, **(C)** m. biceps brachii at humeroradioulnar joint, **(D)** m. triceps brachii at humeroradioulnar joint. The boxplots **(E–H)** show the distribution and median values of MMAs for all trials: **(E)** m. biceps brachii at glenohumeral joint, **(F)** m. triceps brachii at glenohumeral joint, **(G)** m. biceps brachii at humeroradioulnar joint, **(H)** m. triceps brachii at humeroradioulnar joint. Positive and negative MMAs are plotted as separate boxplots for each DOF. SIMM = model-predicted MMAs based on partial velocity; Maya = experimentally-calculated MMAs based on the geometric method.

TABLE 1 | Raw, un-cosine-corrected values of experimentally-estimated rotations and translations at the echidna forelimb joints. Total joint ROM is in parentheses.

Echidna #	E44	E46		E48		Total possible
Side: Left (L), Right (R)	L	L	R	L	R	
Scapulocoracoid-clavicle-interclavicle medial (X+) lateral (X–) rotation angle (°)	21 to 28 (7)	14 to 18 (4)	23 to 28 (5)	27 to 31 (3)	20 to 28 (8)	14 to 31 (17)
Glenohumeral abduction (X+) adduction (X–) angle (°)	–57 to 37 (93)	–35 to 23 (58)	0 to 44 (44)	–13 to 42 (56)	–9 to 44 (53)	–57 to 44 (100)
Glenohumeral internal (Y+) external (Y–) long-axis rotation angle (°)	–41 to 26 (67)	–41 to 13 (54)	–27 to 36 (63)	–3 to 38 (41)	–17 to 38 (55)	–41 to 38 (79)
Glenohumeral flexion (Z+) extension (Z–) angle (°)	–31 to 24 (54)	–17 to 37 (54)	7 to 41 (34)	–1 to 36 (38)	–1 to 33 (34)	–31 to 41 (72)
Glenohumeral cranial (X+) caudal (X–) translation (mm)	–5.9 to 4.5 (10.4)	–4.5 to 4.3 (8.8)	–5.4 to 1.7 (7.1)	–2.6 to 2.7 (5.3)	–2.5 to 3.6 (6.1)	–5.9 to 4.5 (10.4)
Glenohumeral proximal (Y–) distal (Y+) translation (mm)	–0.4 to 2.7 (3.1)	–0.9 to 2.4 (3.3)	–0.9 to 2.6 (3.5)	0.1 to 2.6 (2.5)	0.5 to 2.5 (2.0)	–0.9 to 2.7 (3.6)
Glenohumeral dorsal (Z+) ventral (Z–) translation (mm)	–3.8 to 0.1 (3.9)	–3.2 to 0.4 (2.8)	0.6 to 3 (2.4)	–2.9 to 0.4 (2.5)	0.3 to 2.7 (2.4)	–3.8 to 3.0 (6.8)
Humeroradioulnar abduction (X+) adduction (X–) angle (°)	–31 to 8 (39)	–34 to 8 (42)	–14 to 26 (41)	–59 to 8 (67)	–38 to 13 (50)	–59 to 26 (85)
Humeroradioulnar internal (Y+) external (Y–) long-axis rotation angle (°)	7 to 50 (43)	1 to 54 (54)	8 to 48 (41)	–3 to 69 (72)	–2 to 67 (70)	–3 to 69 (72)
Humeroradioulnar flexion (Z–) extension (Z+) angle (°)	–15 to 38 (53)	–32 to 39 (71)	–15 to 40 (55)	–38 to 30 (68)	–16 to 50 (66)	–38 to 50 (88)
Humeroradioulnar cranial (X+) caudal (X–) translation (mm)	–1.5 to 1.6 (3.1)	–1.0 to 1.8 (2.8)	–1.2 to 1.0 (2.2)	–2.4 to 0.5 (2.9)	–1.7 to 1.3 (3.0)	–2.4 to 1.8 (4.2)
Humeroradioulnar proximal (Y–) distal (Y+) translation (mm)	–1.2 to 0.2 (1.4)	–1.9 to 0.4 (2.3)	–2.0 to 1.6 (3.6)	–1.9 to 1.5 (3.4)	–1.9 to 0.4 (2.3)	–2.0 to 1.6 (3.6)
Humeroradioulnar pre (Z–) postaxial (Z +) translation (mm)	–2.3 to 1.5 (3.8)	–1.9 to 2.6 (4.5)	–0.9 to 3.0 (3.9)	–3.6 to 1.5 (5.1)	–1.3 to 4.0 (5.3)	–3.6 to 4.0 (7.6)

M. Coracobrachialis (Pars Longus)

The m. coracobrachialis (pars longus) crosses the glenohumeral joint only. The MMAs in abduction-adduction agreed well between the experimental estimates and model predictions, being consistent in sign (i.e., adduction) and magnitude (**Figure 8**), as well as pattern of MMA peaks and troughs (**Figure 10B**). The MMAs for flexion-extension agreed in sign (i.e., flexion), but deviated in magnitude, and MMAs for long-axis rotation did not agree well in either sign or magnitude (**Figure 8**). The rank order was somewhat consistent (**Figure 10H**), with abduction-adduction MMAs generally largest (although the large MMAs for flexion-extension equalled abduction-adduction in experimental trials), followed by flexion-extension and then long-axis rotation.

M. Biceps Brachii

Both long and short heads of m. biceps brachii cross the glenohumeral and humeroradioulnar joints. These two heads could not be distinguished separately at marker implantation, and so the SIMM modelled m. biceps brachii short head (pars brevis) was chosen to compare with the experimentally-estimated MMAs of m. biceps brachii. The modelled head of m. biceps longus was not chosen due to the large artefactual deviations in the muscle head's geometry when animated with the experimental trial kinematics, resulting from idiosyncratic interaction with its wrap object. The modelled m. biceps brevis showed similar MMA values to m. biceps longus (Regnault and Pierce, 2018), without such artefactual wrap object interactions.

At the glenohumeral joint, the MMAs were approximately consistent in sign and magnitude (**Figure 9**), though more negative adduction and internal rotation was evident in the experimental MMAs. In terms of rank order (**Figures 11A,E**), both the experimentally-estimated and model-predicted MMAs were largest in adduction. The comparatively smaller MMAs for flexion and internal/external rotation were less consistent: in the SIMM model, flexion-extension generally exceeded long-axis rotation whereas the experimental estimates overlapped in value. The patterns in MMA peaks and troughs during motion were not always consistent between model and experimental data (**Figure 11A**).

At the humeroradioulnar joint, there was also some agreement. The signs of MMAs were consistent, although long-axis rotation MMAs did fluctuate around zero and so were occasionally inconsistent in sign (**Supplementary Figure S5**). The magnitudes were generally consistent, though the SIMM model exhibited generally larger abduction and flexion MMAs (**Supplementary Figure S5**). In terms of rank order (**Figures 11C,G**), flexion MMAs were consistently the largest. Abduction-adduction and long-axis rotation MMAs were smaller, but their rank order sometimes varied inconsistently between the model and experimental MMAs, depending on the trial kinematics. Like the glenohumeral joint, during parts of some trials there were inconsistent patterns in MMA peak and troughs between model and experimental data (**Figure 11C**).

M. Triceps Brachii (Pars Superficialis Longus)

The long superficial head of m. triceps brachii crosses both the glenohumeral and humeroradioulnar joints. At both the joints, the experimentally-estimated MMAs and model-predicted MMAs agreed well. At the glenohumeral joint, the MMAs were consistent in sign and magnitude (**Figure 9**). The kinematic trial peaks/troughs and rank order (**Figures 11B,F**) were also consistent. Both the experimental and SIMM model MMAs show this muscle to adduct the humerus, with similar MMAs overall in flexion, extension and internal rotation, plus minimal external rotation. At the humeroradioulnar joint, results were similar (**Supplementary Figure S5** and **Figures 11D,H**); the experimental and SIMM model MMAs show m. triceps brachii to extend and adduct the antebrachium, with lower MMAs for external rotation. The model also predicts capability for internal rotation, not shown by the experimental MMAs.

M. Pectoralis

The m. pectoralis crosses both the scapulocoracoid-clavicle-interclavicle and glenohumeral joints. To capture this muscle's broad origin across the sternum, it was modelled with three origins (cranial, mid, and caudal). Only the cranial-most and caudal-most areas of m. pectoralis' origin were implanted experimentally. Therefore, in our comparisons, we compare the cranial and caudal origin points of m. pectoralis in the SIMM model and experimental data.

At the scapulocoracoid-clavicle-interclavicle joint, MMAs were generally consistent in sign for both the cranial-most and caudal-most origins (**Figures 5B,C**); the cranial origin is interpreted as drawing the scapulocoracoid laterally (due to negative MMAs) whilst the caudal origin is interpreted as drawing the scapulocoracoid medially (due to positive MMAs). However, the magnitudes of model-predicted MMAs were not in particularly close agreement with experimental estimates. The model-predicted MMAs of the cranial origin were generally larger, with peaks and troughs that did not correspond well with the pattern of the experimentally-estimated MMAs (**Figure 5B**). Conversely, the model-predicted MMAs of the caudal origin were generally smaller, but the pattern of kinematic peaks and troughs did usually correspond with the experimental pattern (**Figures 5C,G**).

At the glenohumeral joint (**Figure 6**), the cranial-most origin showed some consistency in sign: both SIMM model and experimental data estimated negative MMAs in abduction-adduction (i.e., adductor), generally negative MMAs in flexion-extension (i.e., extensor), and generally positive MMAs in long axis rotation (i.e., pronator). However, the experimental estimates for flexion-extension and long-axis rotation occasionally crossed zero (**Figure 10I**; i.e., some small moment arms for glenohumeral flexion and external rotation/supination). Magnitudes of the MMAs overlapped somewhat in abduction-adduction and long-axis rotation, and showed generally similar patterns of peaks and troughs (**Figure 10C**), but flexion-extension MMAs were more obviously dissimilar in both magnitude and general pattern. Rank orders of MMAs also did not agree: the largest peaks of experimentally-estimated MMAs were in adduction, then internal rotation, then extension, whilst the model-predicted MMAs were approximately similar (**Figure 10I**).

The glenohumeral joint MMAs of the caudal-most origin (**Figure 6**, **Figures 10D,J**) were consistent in sign, magnitude and rank order; i.e., this part of the muscle is interpreted in both model-predicted and experimental estimates as primarily a humeral internal rotator, with smaller MMAs for humeral adduction and extension.

M. Latissimus Dorsi

The m. latissimus dorsi partially originates from the scapula, and partially from a broad attachment along the thoracic vertebrae. The scapular head of m. latissimus dorsi only crosses the glenohumeral joint, whilst the remainder also crosses the scapulocoracoid-clavicle-interclavicle joint.

For the scapular head of m. latissimus dorsi at the glenohumeral joint, the experimentally-estimated MMAs and model-predicted MMAs agreed well (**Figure 7**). The MMAs were consistent in sign, though there was more negative (i.e., extension) MMAs seen in experimental data than in the model (**Figure 7**, and **Figures 10E,K**). The MMAs also agreed in approximate magnitude and rank order. Thus, the interpreted actions and absolute and relative leverages of m. latissimus dorsi (scapular head) are consistent between experimental and SIMM model methods; i.e., primarily a humeral internal rotator, but with large moment arms for humeral abduction and flexion.

The portion of m. latissimus dorsi originating from the thoracic vertebrae was implanted at the level of T6, and compared to the modelled muscle line of action also originating from this vertebra. At the scapulocoracoid-clavicle-interclavicle joint, experimentally-estimated and model-predicted MMAs were consistent in sign (acting to rotate the scapulocoracoid medially) and had similarly large magnitudes (**Figures 5D,H**). However, the pattern of kinematic peaks and troughs were not overtly consistent in every trial (**Figure 5D**).

For the vertebral origin of m. latissimus at the glenohumeral joint, MMAs agreed in sign for flexion-extension (positive; glenohumeral flexion) and long-axis rotation (positive; internal rotation). However, the smaller MMAs in abduction-adduction fluctuated either side of zero, with positive (abduction) experimental estimates but generally negative (adduction) SIMM model predictions (**Figure 7**, and **Figures 10F,L**). The magnitudes of flexion-extension and long-axis rotation MMAs were similar (**Figure 7** and **Figure 10L**), and the pattern of kinematic peaks and troughs (or lack thereof, for abduction-adduction) also agreed somewhat (**Figure 10F**). The rank order of peak MMAs was consistent, with the interpreted actions of m. latissimus (mid-vertebral portion) for both SIMM model and experimental data being primarily internal humeral rotation and glenohumeral flexion.

Muscle Architecture and Torque

Inclusion of muscle architectural parameters in the updated SIMM model to estimate muscle torque at different joint angles generally yielded similar patterns to MMAs on the individual muscle level (**Supplementary Figures S1–S3** vs. **Supplementary Figures S6–S8**). Occasionally, the differing physiological cross-sectional area (PCSA) of muscle parts with otherwise similar MMAs yielded differing, higher torques (e.g.,

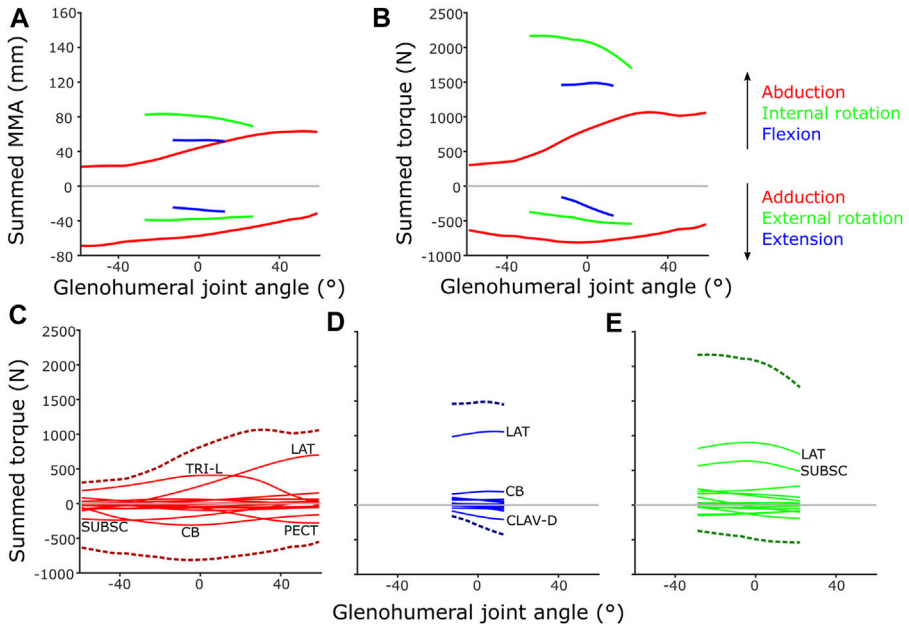

FIGURE 12 | Model-predicted MMAs and muscle torques at the glenohumeral joint, using the updated SIMM model muscle pathways from diceCT and for single-axis DOF rotations: **(A)** Summed MMAs, **(B)** Summed torques. Major muscles contributing to summed torque (dashed lines) are labelled for each rotational DOF: **(C)** Abduction-adduction, **(D)** Flexion-extension, **(E)** Internal-external rotation. LAT = m. latissimus dorsi, TRI-L = m. triceps brachii longus, SUBSC = m. subscapularis, CB = m. coracobrachialis, CLAV-D = m. clavodeltoideus. For details on individual muscles, see the **Supplementary Material**.

m. coracobrachialis longus compared to m. coracobrachialis brevis, **Supplementary Figure S2** vs. **Supplementary Figure S7**), as would be expected. Patterns between summed muscle MMAs and torques were also generally quite similar across the glenohumeral joint (**Figures 12A,B**). For instance, inclusion of architecture and calculation of muscle torque highlighted the predominance of some joint movements, compared with MMAs alone, e.g., the relative magnitude of internal humeral rotation, which is ranked largest in both summed MMAs and torques at the glenohumeral joint.

However, some patterns differed between summed MMAs and torques: across the abduction-adduction ROM, torque values peak around the middle of the glenohumeral abduction-adduction range (i.e., a neutrally-positioned glenohumeral joint), compared with MMAs which peak at extremes of abduction and adduction. This is likely due to the modelled fibre lengths exceeding the optimal length for force production at extreme joint angles. The rank order of peak summed MMAs and muscle torques at the glenohumeral joint also differ in some respects, too. Rank order was maintained in terms of peak MMA and torque, except adduction and flexion which swap position as second and fourth-ranked. MMAs suggested humeral adduction to be fairly important (with peak MMAs ranked second, below internal humeral rotation) due to the large-summed adduction MMAs in the -60° abducted joint (**Figure 12A**), but the summed peak adduction torque is relatively lower (ranked fourth) (**Figure 12B**).

If the torques of individual muscles are plotted against summed torque, the contributions of each muscle can be evaluated (**Figures 12C–E**). These show that MMA alone is occasionally not the best predictor of a muscle's contribution to limb function. For example, m. biceps brachii has large humeral adductor moment arms (**Supplementary Figure S2**) and might be anticipated to be a major contributor to adduction, but in terms of torque it is overshadowed by m. pectoralis, m. coracobrachialis and m. subscapularis due to their larger PCSAs (**Figure 12C**).

DISCUSSION

Here, we critically evaluate the behaviour and outputs of an echidna forelimb musculoskeletal model in terms of its predicted ranges of motion, muscle path accuracy, and muscle moment arms. The echidna's unusual body plan and resultant biomechanical/locomotory function provides an opportunity to validate established model-building practices beyond those applied to more "conventional" anatomical configurations [i.e., erect bipeds such as humans and avian/non-avian dinosaurs (e.g., Bishop et al., 2021a), sagittal/erect quadrupeds such as therian mammals (e.g., Stark et al., 2021)]. Our initial model was constructed using a traditional workflow, often used to model extinct animals, with our primary data consisting of bone morphology and muscle attachment points from the literature (Regnault and Pierce, 2018). In the present study, we aimed to 1) validate the modelling process and its outputs in a species with "unconventional" anatomy and posture, and 2) identify lessons that could be learned and applied to future models interpreting function in extant and extinct quadrupedal animals. We also explored whether the addition of a further level of anatomical

detail (muscle architecture; generally unavailable for extinct animals) alters the functional interpretations made from muscle moment arms alone.

A Light-Touch Approach can Generate Reasonably Accurate Muscle Paths

Our study identifies several key lessons that can be applied to future modelling studies. Firstly, a light-touch approach to muscle modelling – using only muscle attachment sites plus the fewest "wrap objects" necessary to avoid muscle-bone interactions through single-axis DOF rotations – can generate reasonably accurate muscle paths. In comparing the muscle pathways of the initial model (Regnault and Pierce, 2018) to the pose-matched digitally dissected specimen, we found representative muscle paths were generally well-reproduced. Where we found muscle paths to display inaccuracy compared with the 3D reconstructed soft tissues, correction of those inaccuracies shows the effects on predicted muscle moment arms to be generally minimal (see **Supplementary Figures S1–S3**).

The initial model's muscle attachment coordinates were estimated from images and descriptions of Gambaryan et al. (2015). Unsurprisingly these coordinates occasionally fell outside of our specimen's specific attachment areas (identified via diceCT; Regnault et al., 2020), usually due to small or narrow attachment sites, e.g., m. latissimus dorsi scapular origin. The adjustments made to either muscle attachment sites or wrap objects are summarised in **Supplementary Table S1**, and their impact on estimated MMAs (around a single rotational DOF) are shown in **Supplementary Figures S1–S3**. For most muscles, the effects of adjusting muscle paths were negligible: small changes in moment arm magnitude, or the pattern of moment arm change with joint angle. The signs of MMAs (i.e., positive or negative) and rank order of MMAs (i.e., whether abduction-adduction, flexion-extension, or long-axis rotation are largest or smallest) were unchanged for most muscles.

There were a few exceptions. M. pectoralis was originally modelled originating from the interclavicle to the third sternebra and interpreted to have regional variation in its action cranially vs. caudally (**Supplementary Figure S2**; see also Regnault and Pierce, 2018). Adjustment of its origin to a narrower site caudally, from the manubrium to the third sternebra, now shows it acting more homogenously (i.e., still a humeral pronator and extensor, but perhaps also intrinsic stabilisation of adduction-abduction). M. biceps brachii longus appeared to originate principally from the coracoid, rather than epicoracoid as originally described by Gambaryan et al. (2015); as a result, the small lateral-rotation moment arm contributed by this muscle at the scapulocoracoid-clavicle-interclavicle joint is no longer present in the revised model (**Supplementary Figure S1**). It is not clear whether this represents intraspecific variability; further sampling would be beneficial.

There were some adjustments to muscle paths (via their wrap objects) which could also change the inferences of functional aspects. At the glenohumeral joint, this altered the sign of some MMAs at certain joint angles and therefore aspects of the inferred muscle action: mm. biceps brachii brevis and longus changed from having minor action as humeral external rotators (supinators) to mostly internal rotation (pronation), and m. biceps brevis additionally from humeral extensor to flexor (**Supplementary Figure S2**); m. acromiodeltoideus changed from having flexor-extensor actions to just extensor; and m. clavodeltoideus changed from having action as an adductor to both abduction-adduction (**Supplementary Figure S2**). However, the affected moment arms were all relatively small (i.e., closer to zero) in both initial and adjusted versions of the model, as compared with the much larger humeral adductor moment arms (interpreted as the principal action of m. biceps brachii), extensor/external rotator moment arms (the principal action of m. clavodeltoideus) and extensor/abductor moment arms (the principal action of m. acromiodeltoideus).

For the majority of muscles, differences in paths generated by the initial "light-touch" model and real specimen's digitally-dissected muscle meshes were small, and any adjustments made had little impact on their leverage, interpreted action(s), and relative importance of each action. For future models – particularly fossils, where 3D muscle geometry is unknown – this means researchers can have reasonable confidence in a minimalist approach that uses osteological correlates of attachment and as few modifications (wrap objects) as necessary to generate realistic muscle paths.

Joint Translations and Multi-Axis Rotations Maximise Joint Range of Motion

A second key lesson of this study is that use of independent, single-axis DOF rotations to determine the limits of joint range of motion (ROM) is unlikely to capture the full picture, at least at some joints. In our initial model, the limits to joint ROM were first predicted by rotating around a single joint axis (e.g., flexion-extension) until bone-on-bone contact (Regnault and Pierce, 2018). This method of assessing ROM – single rotational DOF, with no joint translation – is customary within fossil modelling studies (see Bishop et al., 2021c), and used to exclude impossible poses when reconstructing extinct animals. Our experimental data show that, converse to expectations, some of the movements possible in a real, intact animal can exceed the model's osteological "limits" when predicted this way. Given that osteological limits predicted by such models are generally accepted to represent the maximum mobility possible – ligaments, muscles, and skin should all act to constrain mobility in the real specimen (Hutson and Hutson, 2012; Arnold et al., 2014) – our result was unexpected, however not without precedent (Hutson and Hutson, 2014, 2015).

More recently, automated and iterative workflows have been developed that evaluate ROM through multiple DOF simultaneously (Manafzadeh and Padian, 2018; Richards et al., 2021). Manual checking must be performed to ensure biologically implausible poses are not included (Regnault and Pierce, 2018; Bishop et al., 2021c), but these methods have the potential to more realistically represent mobility (since animal movement rarely occurs through pure rotation about a single axis), and allow

for interactions between DOF that could expand or limit ROM in an informative manner to researchers. These workflows (Manafzadeh and Padian, 2018; Richards et al., 2021), and several other studies (Pierce et al., 2012; Lai et al., 2018), include joint translation, but in general translations are usually not included in models (Bishop et al., 2021a; Wiseman et al., 2021) and there are even fewer experimental data examining the effects of joint translation on ROM (e.g., Baier and Gatesy, 2013; Tsai et al., 2020; Manafzadeh and Gatesy, 2021), even though they are vital to validate such models.

Our study suggests that joint translation is an important component of joint mobility, alongside simultaneous rotational DOF. Mobility measured experimentally exceeded the model's ROM predictions for glenohumeral flexion-extension and internal-external rotation, and antebrachial abduction-adduction and internal rotation, whilst other types of mobility were below model-predicted ROMs (glenohumeral abduction-adduction, humeroradioulnar flexion-extension). Other studies have also found that exclusion of joint translation from models can both under- and over-estimate true ROM (Hutson and Hutson, 2014, 2015; Manafzadeh and Gatesy 2021), though these studies examine only archosaur species and primarily find over-estimation only to be the case for specific joint morphologies (bi-condylar or gliding/planar: ostrich wrist, alligator knee and ankle, guineafowl knee and ankle).

The effect of translation on experimental ROM in our study can be inferred on the 3D plots by the width of envelope at the point where other rotational joint angles are zero. For example, at the hemi-sellar glenohumeral joint, it can be seen that the flexion-extension envelope is wider than the model predicted, even when long-axis rotation and abduction-adduction are zero (**Figure 4**). The almost tripling of flexion-extension ROM (from 26° in the initial model, to up to a possible maximum of 72° across all experimental trials; **Table 1**) can be explained by translation at the joint surface. Cranio-caudal translations at the glenohumeral joint (which would act to increase flexion-extension) were large: recorded up to a maximum of 10.4 mm (mean = 7.5 mm) and distributed relatively evenly between cranio-caudal movements, due to sliding along the echidna's elongate hemi-sellar glenoid morphology. For context, the cranio-caudal length of the glenoid in the modelled echidna is approximately 12.2 mm.

The effect of simultaneous rotations on experimental ROM can also be seen on the 3D plots (though the contributory effect of rotations cannot be separated from translations in these experimental data, and so other rotational axes could also be contributing here). For example, although the experimental data suggest glenohumeral abduction-adduction ranges close to the model's predicted limits, greatest humeral adduction could only be achieved concomitant with humeral extension (**Figure 4**); likewise, greatest humeral abduction appears to necessitate some flexion. An interesting secondary point is that the experimental data do support the very large glenohumeral joint abduction-adduction range predicted by the initial model. Therefore, even in cases where ROM is presumed to be highly constrained based on articular morphology, soft tissues, and available *in vivo* data, such as in the echidna (Jenkins, 1970; Luo, 2015; Regnault and Pierce, 2018), models and validation studies such as ours can be valuable in challenging our assumptions about what is (or is not) possible.

At the modified-condylar humeroradioulnar joint, the dramatic amount of antebrachial internal rotation seen experimentally as compared to the initial model (55% of the total long-axis rotation ROM in the initial model vs 96% experimentally) seems to be due, in part, to translation (**Figure 4**; **Table 1**) along the single, elongate ball-like humeral condyle. However, to achieve maximum internal rotation, adduction of the antebrachium is also required (**Figure 4**). The increase in abduction-adduction measured experimentally compared to the initial model's ROM "limit" appears similarly due to the interactions of multiple DOF: for instance, maximum abduction is only achieved experimentally alongside internal rotation and extension (**Figure 4**), and may be assisted by pre-postaxial translations up to a possible maximum of 7.6 mm along the ulnar articular surface (mean = 4.5 mm), again distributed relatively evenly between pre- and postaxial movements.

More expectedly, the experimentally-estimated ROM at the scapulocoracoid-clavicle-interclavicle joint was less than the initial SIMM model-predicted ROM (**Figure 3A**). This joint is comprised of two articulations in the echidna (between the acromion of the scapulocoracoid and the fused clavicle-interclavicle laterally, and between the coracoid and interclavicle ventrally), shown in **Figure 3A**. The effect is to essentially produce a single rotational axis, i.e., only a single DOF, unlike the glenohumeral and humeroradioulnar joints, which had opportunities for interactions between several DOF (including rotations and translations).

The experimental ROM at the scapulocoracoid-clavicle-interclavicle joint occupies a more medial range of rotations than the SIMM model "limit" (**Figure 3A**, black arc), suggesting additional factors are relevant in the intact animal compared with a digital model. For instance, loading of the forelimb in the intact echidna is likely to result in a dorsally- and medially-directed force at the glenoid (due to the lateral and ventral orientation of the humerus/glenoid; Pridmore, 1985), pulling the acromion-clavicle and coracoid-interclavicle joint surfaces apart. Alterations to model joint spacing can alter joint ROM estimates (e.g., Brassey et al., 2017), and increased spacing has been shown in the echidna model to increase estimated ROM (albeit at the glenohumeral joint; Regnault and Pierce, 2018).

Thus, future models may need to explore not only static joint spacing choices in the re-articulation of bones, but also consider how joint spacing may differ in a loaded limb (e.g., through sensitivity analyses). Interestingly, the recent study of Manafzadeh and Gatesy (2021) shows inclusion of a single translational DOF in distraction-compression (equivalent to increasing or decreasing joint spacing) results in great improvement of model-predicted osteological limits, to encompass most possible *ex vivo* and *in vivo* joint poses. Taken together, our results suggest translation to be a potentially important component to ROM estimates in addition to simultaneous rotational DOFs. However, the decision to include further translational DOF (beyond distraction-compression AKA appropriate joint spacing) is one

to be made case-by-case on a joint-morphology and species-specific basis, guided by data from extant animals.

Independently-Calculated Experimental MMAs Validate Model Predictions

We also found that under an identical kinematic regime, experimentally-derived MMAs calculated using a geometric method reasonably matched the model-predicted MMAs estimated using partial velocity. Of the six muscles evaluated (and eight muscle paths total), moment arms for five muscles/paths agreed well in sign, general kinematic pattern, magnitude and rank order, thus validating predicted muscle function: m. clavodeltoideus (**Figures 5A,E**, **8**, **10A,G**), m. triceps longus superficialis (**Figures 9**, **11B,D,F,H**, **Supplementary Figure S5**), m. biceps brevis (**Figures 9**, **11A,C,E,G**, **Supplementary Figure S5**), m. latissimus dorsi (scapular origin) (**Figures 7**, **10E, K**), and m. pectoralis (caudal origin) (**Figure 5C,G** and **Figures 6**, **10D,J**).

The MMAs for the remaining three muscle paths agreed less well crossing at the glenohumeral joint: m. latissimus dorsi (vertebral origin) (**Figure 10F**), m. coracobrachialis longus (**Figures 8**, **10B**), and m. pectoralis (cranial origin) (**Figure 10C**). However, despite discrepancies between experimentally-derived and model-predicted MMAs for some muscles, our data showed aspects of the model outputs that are still informative for the purposes of functional interpretation. The sign (positive or negative), approximate magnitude, and/or rank order of MMAs agreed for some of these muscles, even when the MMA kinematic patterns did not. These MMA parameters provide a useful guide for inferring muscle action(s) – for example, whether a muscle (such as m. latissimus dorsi, vertebral origin; **Figure 10F**) is interpreted as a glenohumeral flexor vs. extensor (MMA sign), its approximate leverage (MMA magnitude), and whether it is considered primarily an internal rotator vs. flexor vs. abductor (MMA rank order).

There is clear utility in understanding why some muscles agreed well between methods and others did not in order to build confidence in our interpretations of future models. Unfortunately, it is not clear from our data which factors are most relevant. Since the experimental method of calculating MMAs uses a straight line of action between implanted muscle markers, disagreement could presumably be related to muscles undergoing more complex trajectories within the model. However, MMA agreement does not appear to be related to the number of joints crossed by a muscle; uni- and bi-articular muscle paths did not clearly differ in degree of agreement. MMA agreement is also not clearly related to the complexity of muscle wrapping objects; although some muscles without wrap objects had better agreement (m. clavodeltoideus, m. triceps, m. latissimus scapular head, m. pectoralis caudal origin) others had worse (m. pectoralis cranial origin), and yet others with several wrap objects agreed fairly well (m. biceps brevis). Another plausible factor could be whether muscles change direction near to their attachment site or the joint of interest, but again examples for and against this are seen in the muscles evaluated here, and so a clear relationship cannot be established. A final possibility could be error related to marker placement: approximate marker locations were checked on micro-CT scans post-data collection (though the muscles could not themselves be visualised), and on subsequent dissection markers were noted if found to be displaced (as for the muscles discounted in this study due to obvious marker migration). However, dynamic marker migration during data collection may be possible and a potential source of error, despite steps taken to secure them (use of smallest gauge needle possible, tissue glue).

However, the very close agreement of many muscles between the experimentally-derived MMAs and the SIMM model-predicted MMAs provides important alternate validation for different conceptual methods of calculating MMAs, and the comparison of MMAs calculated using different methodologies. There are several ways to define and calculate MMAs, both by models (see Sherman et al., 2013) and experimentally (An et al., 1984). The SIMM model uses a partial velocity method (Delp and Loan, 1995), whilst the script we developed for processing experimental data uses a geometric method (based on the perpendicular distance between joint centre and muscle line of action). A substantial body of research suggests that model-predicted MMAs fall across similar ranges to experimental estimates (typically made via the "tendon travel" method) (see Brassey et al., 2017). Here, we find important confirmation that this is also the case for experimental estimates made via geometric calculation (particularly for muscles with straight lines of action), and apparently avoiding some potential pitfalls of experimental tendon travel estimates, such as kinematic cross-talk (Hutchinson et al., 2015). While there is room for refinement of the geometric method – most saliently, in accounting for less straightforward muscle paths – the broad agreement between multiple techniques can give researchers further confidence in 3D musculoskeletal models of animals with diverse morphologies.

Muscle Architecture can Alter Functional Inferences

Finally, addition of muscle architecture data alongside muscle moment arms has capacity to change aspects of the functional inferences made from a model at a finer scale (Bates and Falkingham, 2018). In a previous study, the short-beaked echidna was found to exhibit little variation in normalised architectural parameters of its forelimb muscles (Regnault et al., 2020). In this study, we therefore anticipated that inclusion of architectural data (to yield muscle torques) would not greatly affect our conclusions, compared to using MMAs alone. This was often the case – particularly at the individual muscle level, muscle torque vs. joint angle exhibited generally similar patterns to MMA vs joint angle (**Supplementary Figures S1–S3** vs. **Supplementary Figures S6–S8**).

However, when evaluating summed muscle torque or individual muscle contributions to summed muscle torque, inferences can differ compared with those made from MMAs

alone. From the initial model (Regnault and Pierce, 2018), m. biceps brachii was inferred to be particularly important in supporting the echidna's sprawling posture and locomotion, due to the large humeral adduction moment arms of this muscle. However, when architecture data are added as a model parameter, the inferred role of m. biceps brachii is diminished compared to other muscles (m. pectoralis, m. subscapularis) due to their large muscle volumes and resultantly large physiological cross-sectional areas. Further, while our summed muscle torques support the inference that the echidna's forelimb musculoskeletal anatomy is optimised for humeral internal rotation (**Figure 12B**), summed muscle torques in flexion outrank those for adduction, a pattern that differs from results based solely on MMAs (Regnault and Pierce, 2018). Aside from adduction and flexion, the rank orders of peak values for other movements (internal rotation, abduction, external rotation and extension) are the same between summed MMAs and muscle torques. The change in relative importance of adduction and flexion reflects the cumulative effect of smaller differences in individual muscles, particularly the combination of the large PCSA and large MMAs of m. latissimus in glenohumeral flexion (**Figure 12D**, **Supplementary Figures S2, S7**; see also Regnault et al., 2020).

In extinct animals, soft tissues, such as muscles, are not preserved in sufficient detail to allow direct measurement of these functionally-relevant parameters. In absence of detailed architectural parameters, less detailed parameters such as muscle volume (size) can still allow for some refinement of inferences based on MMA alone, such as for m. biceps brachii, discussed above. Diverse data from living animals can help to further guide estimates of architectural parameters (Bates and Falkingham, 2018; Bishop et al., 2021a) or even direct evidence-based reconstructions of these parameters for extinct species (Fahn-Lai et al., 2020). Here we have used generalised curves for muscle and tendon properties, and estimations of torque over the full ROM can be sensitive to these properties. Further work may be needed to evaluate the relationship between MMA and torque in modelling studies, ideally with species-specific values measured on fresh muscle tissue under controlled conditions. However, our findings in this study affirm the need to account for muscle architecture to some degree in musculoskeletal computer models (if possible) or to recognise architecture as a source of disparity in functional model outputs (where not possible).

CONCLUSIONS

Our study has several pertinent findings for the field of musculoskeletal computer modelling. Firstly, we find that a minimalist muscle-wrapping approach – in other words, one that minimises assumption or knowledge of muscle anatomy beyond attachment site – can approximate muscle geometry. Additionally, when further intervention is required, and muscle attachment or geometry is adjusted (as was occasionally the case in our echidna model), the resultant effect on MMAs appears minimal. This approach could be of particular utility in situations where muscle anatomy may not be clearly characterised, for example, in extinct or difficult-to-source extant animals.

We find joint ROMs from experimentally-manipulated cadavers to have similar ranges to those predicted using single-axis DOF osteological ROM in most directions, including the surprisingly wide range of humeral abduction-adduction initially predicted by the model. However, there are also several discrepancies, the biggest being ROM in flexion-extension at the glenohumeral joint and long-axis rotation at the humeroradioulnar joint, where the experimental ROM far exceeded the model-predicted ROM. These results further support the contention that simultaneous rotational and translational DOF can expand the envelope of possible joint poses in certain anatomical directions, and should be accounted for in model design, if possible. Importantly, the experimental data collected here provides important insights into joint function that can be used in the future to refine osteological ROM modelling assumptions and methodological development.

We also find high-level agreement for most muscles between experimentally-derived and SIMM model-predicted MMAs. Our geometric method of estimating experimental MMAs from implanted muscles appears equivalent to model-predictions made via the partial velocity method, particularly for muscles with straightforward paths. The geometric method and tools we have developed here may have further utility and application where other methods (such as tendon travel) fall short: for instance, proximal limb muscles, those with little tendon, and joints with 3D mobility (where kinematic cross-talk may be a concern) (e.g., Hutchinson et al., 2015; Brassey et al., 2017). The method allows for the creation of simplified musculoskeletal models in Maya or other software to calculate 3D MMAs, where previously such models may have explored only planar MMA calculation (e.g., Regnault et al., 2017).

Finally, we observe that inclusion of muscle architecture within models can change some functional interpretations of muscle roles, and MMAs alone may not yield a complete functional signal, echoing the caveats of other studies. However, for the muscles we model here, patterns of MMAs and muscle torques across joint angles are similar at an individual level. Their contributions to summed torques vs. summed MMA can differ, particularly for muscles with large PCSA, which could impact the rank order of peak summed values. Nonetheless, our addition of muscle architecture supports a major conclusion drawn from the initial study based on MMAs alone: that the forelimb musculoskeletal system of the echidna is specialised for humeral internal rotation, consistent with *in vivo* locomotion data.

DATA AVAILABILITY STATEMENT

The raw data supporting the conclusions of this article will be made available by the authors, without undue reservation.

AUTHOR CONTRIBUTIONS

SEP conceived the study. SEP, SR, and PF-L designed the study. SR and PF-L collected the experimental data. SR processed and analysed the experimental and modelling data. PF-L developed the geometric moment arm Maya shelf tool available on github. SR and PF-L visualised the data. SR and SEP interpreted and data and drafted the manuscript. All authors edited the manuscript and gave final approval for publication.

FUNDING

This work was supported by the National Science Foundation grants no. DEB-1754459 and EAR-1524523 to SEP.

ACKNOWLEDGMENTS

We would like to thank Rachel Norris and Anthony Wilkes (University of Adelaide) for donating the echidna specimens. Members of the Pierce and Biewener labs (Harvard University) contributed insightful and helpful discussion during the project, and especially Allison Arnold-Rife for exploration of methods in calculating MMAs.

SUPPLEMENTARY MATERIAL

The Supplementary Material for this article can be found online at: https://www.frontiersin.org/articles/10.3389/fbioe.2021.751518/full#supplementary-material

REFERENCES

Allen, V. R., Kilbourne, B. M., and Hutchinson, J. R. (2021). The Evolution of Pelvic Limb Muscle Moment Arms in Bird-Line Archosaurs. *Sci. Adv.* 7 (12), eabe2778. doi:10.1126/sciadv.abe2778

An, K. N., Takahashi, K., Harrigan, T. P., and Chao, E. Y. (1984). Determination of Muscle Orientations and Moment Arms. *J. Biomechanical Eng.* 106, 280–282. doi:10.1115/1.3138494

Arnold, P., Fischer, M. S., and Nyakatura, J. A. (2014). Soft Tissue Influence on *Ex Vivo* Mobility in the Hip of Iguana : Comparison with *In Vivo* Movement and its Bearing on Joint Motion of Fossil Sprawling Tetrapods. *J. Anat.* 225 (1), 31–41. doi:10.1111/joa.12187

Baier, D. B., and Gatesy, S. M. (2013). Three-dimensional Skeletal Kinematics of the Shoulder Girdle and Forelimb in Walking Alligator. *J. Anat.* 223 (5), 462–473. doi:10.1111/joa.12102

Bates, K. T., and Falkingham, P. L. (2018). The Importance of Muscle Architecture in Biomechanical Reconstructions of Extinct Animals: A Case Study Using Tyrannosaurus rex. *J. Anat.* 233 (5), 625–635.

Bates, K. T., Maidment, S. C. R., Allen, V., and Barrett, P. M. (2012). Computational Modelling of Locomotor Muscle Moment Arms in the Basal dinosaur *Lesothosaurus Diagnosticus*: Assessing Convergence between Birds and Basal Ornithischians. *J. Anat.* 220 (3), 212–232. doi:10.1111/j.1469-7580.2011.01469.x

Bishop, P. J., Cuff, A. R., and Hutchinson, J. R. (2021a). How to Build a dinosaur: Musculoskeletal Modeling and Simulation of Locomotor Biomechanics in Extinct Animals. *Paleobiology* 47 (1), 1–38. doi:10.1017/pab.2020.46

Bishop, P. J., Falisse, A., De Groote, F., and Hutchinson, J. R. (2021c). Predictive Simulations of Musculoskeletal Function and Jumping Performance in a Generalized Bird. *Integr. Organismal Biol.* 3, obab006. doi:10.1093/iob/obab006

Bishop, P. J., Michel, K. B., Falisse, A., Cuff, A. R., Allen, V. R., De Groote, F., et al. (2021b). Computational Modelling of Muscle Fibre Operating Ranges in the Hindlimb of a Small Ground Bird (*Eudromia elegans*), with Implications for Modelling Locomotion in Extinct Species. *Plos Comput. Biol.* 17 (4), e1008843. doi:10.1371/journal.pcbi.1008843

Brainerd, E. L., Baier, D. B., Gatesy, S. M., Hedrick, T. L., Metzger, K. A., Gilbert, S. L., et al. (2010). X-ray Reconstruction of Moving Morphology (XROMM): Precision, Accuracy and Applications in Comparative Biomechanics Research. *J. Exp. Zool A. Ecol. Genet. Physiol.* 313 (5), 262–279. doi:10.1002/jez.589

Brassey, C. A., Maidment, S. C. R., and Barrett, P. M. (2017). Muscle Moment Arm Analyses Applied to Vertebrate Paleontology: a Case Study Using Stegosaurus Stenops Marsh, 1887. *J. Vertebr. Paleontol.* 37 (5), e1361432. doi:10.1080/02724634.2017.1361432

Delp, S. L., and Loan, J. P. (1995). A Graphics-Based Software System to Develop and Analyze Models of Musculoskeletal Structures. *Comput. Biol. Med.* 25 (1), 21–34. doi:10.1016/0010-4825(95)98882-e

Demuth, O. E., Rayfield, E. J., and Hutchinson, J. R. (2020). 3D Hindlimb Joint Mobility of the Stem-Archosaur *Euparkeria Capensis* with Implications for Postural Evolution within Archosauria. *Sci. Rep.* 10 (1), 15357. doi:10.1038/s41598-020-70175-y

Fahn-Lai, P., Biewener, A. A., and Pierce, S. E. (2020). Broad Similarities in Shoulder Muscle Architecture and Organization across Two Amniotes: Implications for Reconstructing Non-mammalian Synapsids. *PeerJ* 8, e8556. doi:10.7717/peerj.8556

Fujiwara, S.-i., and Hutchinson, J. R. (2012). Elbow Joint Adductor Moment Arm as an Indicator of Forelimb Posture in Extinct Quadrupedal Tetrapods. *Proc. R. Soc. B.* 279 (1738), 2561–2570. doi:10.1098/rspb.2012.0190

Gambaryan, P. P., Kuznetsov, A. N., Panyutina, A. A., and Gerasimov, S. V. (2015). Shoulder Girdle and Forelimb Myology of Extant Monotremata. *Rus.J.Theriol.* 14 (1), 1–56. doi:10.15298/rusjtheriol.14.1.01

Gatesy, S. M., Bäker, M., and Hutchinson, J. R. (2009). Constraint-based Exclusion of Limb Poses for Reconstructing Theropod dinosaur Locomotion. *J. Vertebr. Paleontol.* 29 (2), 535–544. doi:10.1671/039.029.0213

Gignac, P. M., Kley, N. J., Clarke, J. A., Colbert, M. W., Morhardt, A. C., Cerio, D., et al. (2016). Diffusible Iodine-based Contrast-enhanced Computed Tomography (diceCT): an Emerging Tool for Rapid, High-resolution, 3-D Imaging of Metazoan Soft Tissues. *J. Anat.* 228, 889–909. doi:10.1111/joa.12449

Haines, R. W. (1946). A Revision of the Movements of the Forearm in Tetrapods. *J. Anat.* 80 (Pt 1), 1–11.

Holliday, C. M., Ridgely, R. C., Sedlmayr, J. C., and Witmer, L. M. (2010). Cartilaginous Epiphyses in Extant Archosaurs and Their Implications for Reconstructing Limb Function in Dinosaurs. *PLoS One* 5 (9), e13120. doi:10.1371/journal.pone.0013120

Hutchinson, J. R. (2012). On the Inference of Function from Structure Using Biomechanical Modelling and Simulation of Extinct Organisms. *Biol. Lett.* 8 (1), 115–118. doi:10.1098/rsbl.2011.0399

Hutchinson, J. R., Rankin, J. W., Rubenson, J., Rosenbluth, K. H., Siston, R. A., and Delp, S. L. (2015). Musculoskeletal Modelling of an Ostrich (*Struthio camelus*) Pelvic Limb: Influence of Limb Orientation on Muscular Capacity during Locomotion. *PeerJ* 3, e1001. doi:10.7717/peerj.1001

Hutson, J. D., and Hutson, K. N. (2014). A Repeated-Measures Analysis of the Effects of Soft Tissues on Wrist Range of Motion in the Extant Phylogenetic Bracket of Dinosaurs: Implications for the Functional Origins of an Automatic Wrist Folding Mechanism in Crocodilia. *Anat. Rec.* 297 (7), 1228–1249. doi:10.1002/ar.22903

Hutson, J. D., and Hutson, K. N. (2012). A Test of the Validity of Range of Motion Studies of Fossil Archosaur Elbow Mobility Using Repeated-Measures Analysis and the Extant Phylogenetic Bracket. *J. Exp. Biol.* 215 (12), 2030–2038. doi:10.1242/jeb.069567

Hutson, J. D., and Hutson, K. N. (2015). Inferring the Prevalence and Function of finger Hyperextension in Archosauria from finger-joint Range of Motion in the American alligator. *J. Zool* 296 (3), 189–199. doi:10.1111/jzo.12232

Jenkins, F. A. (1970). Limb Movements in a Monotreme (*Tachyglossus aculeatus*): a Cineradiographic Analysis. *Science* 168 (3938), 1473–1475. doi:10.1126/science.168.3938.1473

Kargo, W. J., and Rome, L. C. (2002). Functional Morphology of Proximal Hindlimb Muscles in the Frog *Rana pipiens*. *J. Exp. Biol.* 205 (14), 1987–2004. doi:10.1242/jeb.205.14.1987

Knörlein, B. J., Baier, D. B., Gatesy, S. M., Laurence-Chasen, J. D., and Brainerd, E. L. (2016). Validation of XMALab Software for Marker-Based XROMM. *J. Exp. Biol.* 219 (23), 3701–3711. doi:10.1242/jeb.145383

Lai, P. H., Biewener, A. A., and Pierce, S. E. (2018). Three-dimensional Mobility and Muscle Attachments in the Pectoral Limb of the Triassic Cynodont Massetognathus Pascuali (Romer, 1967). *J. Anat.* 232 (3), 383–406. doi:10.1111/joa.12766

Luo, Z. X. (2015). "Origin of the Mammalian Shoulder," in *Great Transformations: Major Events in the History of Vertebrate Life* (Chicago, Illinois: The University of Chicago Press), 167–187.

Maidment, S. C., Bates, K. T., and Barrett, P. M. (2014). *Three-dimensional Computational Modeling of Pelvic Locomotor Muscle Moment Arms in* Edmontosaurus *(Dinosauria, Hadrosauridae) and Comparisons with Other Archosaurs. Hadrosaurs*. Bloomington: Indiana University Press, 433–448.

Mallison, H. (2010). CAD Assessment of the Posture and Range of Motion of Kentrosaurus Aethiopicus Hennig 1915. *Swiss J. Geosci.* 103 (2), 211–233. doi:10.1007/s00015-010-0024-2

Manafzadeh, A. R., and Gatesy, S. M. (2020). A Coordinate-system-independent Method for Comparing Joint Rotational Mobilities. *J. Exp. Biol.* 223 (18), jeb227108. doi:10.1242/jeb.227108

Manafzadeh, A. R., and Gatesy, S. M. (2021). Paleobiological Reconstructions of Articular Function Require All Six Degrees of Freedom. *J. Anat.*. doi:10.1111/joa.13513

Manafzadeh, A. R., Kambic, R. E., and Gatesy, S. M. (2021). A New Role for Joint Mobility in Reconstructing Vertebrate Locomotor Evolution. *Proc. Natl. Acad. Sci.* 118 (7), e2023513118. doi:10.1073/pnas.2023513118

Manafzadeh, A. R., and Padian, K. (2018). ROM Mapping of Ligamentous Constraints on Avian Hip Mobility: Implications for Extinct Ornithodirans. *Proc. R. Soc. B.* 285 (1879), 20180727. doi:10.1098/rspb.2018.0727

Millard, M., Uchida, T., Seth, A., and Delp, S. L. (2013). Flexing Computational Muscle: Modeling and Simulation of Musculotendon Dynamics. *ASME. J. Biomech. Eng.* 135 (2), 021005. doi:10.1115/1.4023390

Molnar, J. L., Hutchinson, J. R., Diogo, R., Clack, J. A., and Pierce, S. E. (2021). Evolution of Forelimb Musculoskeletal Function across the Fish-To-Tetrapod Transition. *Sci. Adv.* 7 (4), eabd7457. doi:10.1126/sciadv.abd7457

Nyakatura, J. A., Melo, K., Horvat, T., Karakasiliotis, K., Allen, V. R., Andikfar, A., et al. (2019). Reverse-engineering the Locomotion of a Stem Amniote. *Nature* 565 (7739), 351–355. doi:10.1038/s41586-018-0851-2

Pedregosa, F., Varoquaux, G., Gramfort, A., Michel, V., Thirion, B., Grisel, O., et al. (2011). Scikit-learn: Machine Learning in Python. *J. machine Learn. Res.* 12, 2825–2830.

Pierce, S. E., Clack, J. A., and Hutchinson, J. R. (2012). Three-dimensional Limb Joint Mobility in the Early Tetrapod *Ichthyostega*. *Nature* 486 (7404), 523–526. doi:10.1038/nature11124

Pridmore, P. A. (1985). Terrestrial Locomotion in Monotremes (Mammalia: Monotremata). *J. Zool.* 205, 53–73. doi:10.1111/j.1469-7998.1985.tb05613.x

Regnault, S., Allen, V. R., Chadwick, K. P., and Hutchinson, J. R. (2017). Analysis of the Moment Arms and Kinematics of Ostrich (*Struthio camelus*) Double Patellar Sesamoids. *J. Exp. Zool.* 327 (4), 163–171. doi:10.1002/jez.2082

Regnault, S., Fahn-Lai, P., Norris, R. M., and Pierce, S. E. (2020). Shoulder Muscle Architecture in the Echidna (Monotremata: *Tachyglossus aculeatus*) Indicates Conserved Functional Properties. *J. Mamm. Evol.* 27, 591–603. doi:10.1007/s10914-020-09498-6

Regnault, S., and Pierce, S. E. (2018). Pectoral Girdle and Forelimb Musculoskeletal Function in the Echidna (*Tachyglossus aculeatus*): Insights into Mammalian Locomotor Evolution. *R. Soc. Open Sci.* 5 (11), 181400. doi:10.1098/rsos.181400

Richards, H. L., Bishop, P. J., Hocking, D. P., Adams, J. W., and Evans, A. R. (2021). Low Elbow Mobility Indicates Unique Forelimb Posture and Function in a Giant Extinct Marsupial. *J. Anat.* 238 (6), 1425–1441. doi:10.1111/joa.13389

Sherman, M. A., Seth, A., and Delp, S. L. (2013). "What Is a Moment Arm? Calculating Muscle Effectiveness in Biomechanical Models Using Generalized Coordinates," in Proceedings of the ASME 2013 International Design Engineering Technical Conferences & Computers and Information in Engineering Conference IDETC/CIE, Portland, Oregon, United States, August 4–7, 2013 (American Society of Mechanical Engineers (ASME)), V07BT10A052.

Stark, H., Fischer, M. S., Hunt, A., Young, F., Quinn, R., and Andrada, E. (2021). A Three-Dimensional Musculoskeletal Model of the Dog. *Sci. Rep.* 11 (1), 11335. doi:10.1038/s41598-021-90058-0

Tsai, H. P., Turner, M. L., Manafzadeh, A. R., and Gatesy, S. M. (2020). Contrast-enhanced XROMM Reveals *In Vivo* Soft Tissue Interactions in the Hip of *Alligator mississippiensis*. *J. Anat.* 236 (2), 288–304. doi:10.1111/joa.13101

Van Rossum, G., and Drake, F. L., Jr (1995). *Python Reference Manual*. Amsterdam: Centrum voor Wiskunde en Informatica.

Wiseman, A. L., Bishop, P. J., Demuth, O. E., Cuff, A. R., Michel, K. B., and Hutchinson, J. R. (2021). Musculoskeletal Modelling of the Nile Crocodile (*Crocodylus niloticus*) Hindlimb: Effects of Limb Posture on Leverage during Terrestrial Locomotion. *J. Anat.* 239, 424–444. doi:10.1111/joa.13431

Zajac, F. E. (1989). Muscle and Tendon: Properties, Models, Scaling, and Application to Biomechanics and Motor Control. *Crit. Rev. Biomed. Eng.* 17 (4), 359–411.

Conflict of Interest: The authors declare that the research was conducted in the absence of any commercial or financial relationships that could be construed as a potential conflict of interest.

Publisher's Note: All claims expressed in this article are solely those of the authors and do not necessarily represent those of their affiliated organizations, or those of the publisher, the editors and the reviewers. Any product that may be evaluated in this article, or claim that may be made by its manufacturer, is not guaranteed or endorsed by the publisher.

frontiers in Bioengineering and Biotechnology

ORIGINAL RESEARCH
published: 03 February 2022
doi: 10.3389/fbioe.2021.800311

Estimating Gaits of an Ancient Crocodile-Line Archosaur Through Trajectory Optimization, With Comparison to Fossil Trackways

Delyle T. Polet[*†] *and John R. Hutchinson*[*†]

Structure and Motion Lab, Comparative Biomedical Sciences, Royal Veterinary College, Hatfield, United Kingdom

Fossil trackways provide a glimpse into the behavior of extinct animals. However, while providing information of the trackmaker size, stride, and even speed, the actual gait of the organism can be ambiguous. This is especially true of quadrupedal animals, where disparate gaits can have similar trackway patterns. Here, predictive simulation using trajectory optimization can help distinguish gaits used by trackmakers. First, we demonstrated that a planar, five-link quadrupedal biomechanical model can generate the qualitative trackway patterns made by domestic dogs, although a systematic error emerges in the track phase (relative distance between ipsilateral pes and manus prints). Next, we used trackway dimensions as inputs to a model of *Batrachotomus kupferzellensis*, a long-limbed, crocodile-line archosaur (clade Pseudosuchia) from the Middle Triassic of Germany. We found energetically optimal gaits and compared their predicted track phases to those of fossil trackways of *Isochirotherium* and *Brachychirotherium*. The optimal results agree with trackways at slow speeds but differ at faster speeds. However, all simulations point to a gait transition around a non-dimensional speed of 0.4 and another at 1.0. The trackways likewise exhibit stark differences in the track phase at these speeds. In all cases, including when simulations are constrained to the fossil track phase, the optimal simulations after the first gait transition do not correspond to a trot, as often used by living crocodiles. Instead, they are a diagonal sequence gait similar to the slow tölt of Icelandic horses. This is the first evidence that extinct pseudosuchians may have exhibited different gaits than their modern relatives and of a gait transition in an extinct pseudosuchian. The results of this analysis highlight areas where the models can be improved to generate more reliable predictions for fossil data while also showcasing how simple models can generate insights about the behavior of extinct animals.

Keywords: locomotion, predictive simulation, Pseudosuchia, fossil trackways, energetics, Chirotheriidae

OPEN ACCESS

Edited by:
Bernardo Innocenti,
Université libre de Bruxelles, Belgium

Reviewed by:
Eudald Mujal,
Staatliches Museum für Naturkunde Stuttgart, Germany
Shinya Aoi,
Kyoto University, Japan

***Correspondence:**
Delyle T. Polet
dpolet@rvc.ac.uk
John R. Hutchinson
jhutchinson@rvc.ac.uk

†ORCID:
Delyle T. Polet
orcid.org/0000-0002-8299-3434
John R. Hutchinson
orcid.org/0000-0002-6767-7038

Specialty section:
This article was submitted to Biomechanics, a section of the journal Frontiers in Bioengineering and Biotechnology

Received: *22 October 2021*
Accepted: *30 December 2021*
Published: *03 February 2022*

Citation:
Polet DT and Hutchinson JR (2022) Estimating Gaits of an Ancient Crocodile-Line Archosaur Through Trajectory Optimization, With Comparison to Fossil Trackways. Front. Bioeng. Biotechnol. 9:800311. doi: 10.3389/fbioe.2021.800311

INTRODUCTION

Despite the incredible animal diversity of the present, the past contains forms with no ideal modern analogues. *Batrachotomus kupferzellensis* (Gower, 1999) is one such example. This long-limbed, crocodile-line archosaur (clade Pseudosuchia) from the Middle Triassic of Germany had a large head and a massive tail similar to modern crocodylians but a more erect (adducted) limb posture similar to

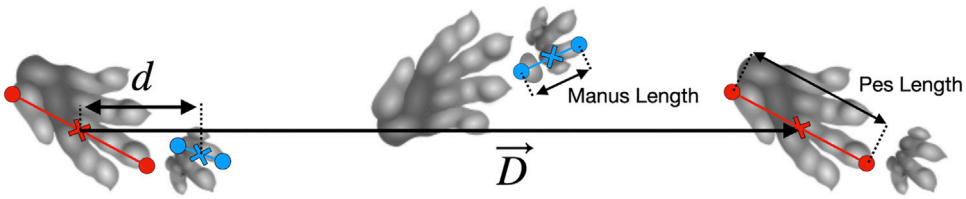

FIGURE 1 | Schematic of a *Brachychirotherium* trackway, showing definition of parameters. Footprints are measured from the caudal-most point to the tip of digit III, or to digit II in the case of *Brachychirotherium* manus. The caudal side of digit V was used (e.g., the second manus in the diagram) when available. The manus–pes distance is calculated between midpoints along the stride vector, $\vec{D}$; the track phase is then d/D. Trackway adapted from Wikimedia Commons (2010), used here under a CC BY-SA 3.0 license.

modern (cursorial) mammals (Gower and Schoch, 2009). Was *Batrachotomus* more similar to a mammal in its locomotion, to a modern crocodylian, or was it altogether different?

Bonaparte (1984) considered the erect limbs, and elongated pubis and ischium, of "rauisuchids" (a group containing *Batrachotomus*) to be adaptations for parasagittal locomotion that enabled them to survive a Middle–Late Triassic faunal replacement. Parrish (1986) postulated that the erect limbs of "rauisuchians" and other archosaurs gave them increased maneuverability on land as in mammals. While Parrish noted that their hindlimb plantigrady and crurotarsal ankle were more similar to those of modern crocodylians, reorganization of the ankle resulted in symmetrical pull of the plantarflexors, leading to simple plantarflexion of the ankle rather than lateral rotation with plantarflexion as seen in crocodylians and lizards. Nesbitt et al. (2013) interpreted plantigrady and the extended calcaneal tuber as adaptation to high power rather than high speed. Apart from a consensus that *Batrachotomus* used parasagittal and erect locomotion, and was quadrupedal (Bishop et al., 2020), there is as yet no analysis on the kind(s) of gait it may have employed.

Many aspects of gait choice in cursorial, quadrupedal mammals emerge from work-based optimization in simple parasagittal models. Trajectory optimization, in particular, allows for the numerical optimization of continuous motion through time. Xi et al. (2016) used trajectory optimization to recover the four-beat walk and trot typically used by mammals with a planar model. Galloping was later discovered as optimal when a compliant torso was added (Yesilevskiy et al., 2018). By minimizing mechanical work in parasagittal models, the body's pitch moment of inertia (when normalized to glenoacetabular distance and mass as the Murphy number), was shown to broadly determine which mammals do and do not trot (Usherwood, 2020; Polet, 2021b).

Precise anatomical details are often unnecessary for the biomechanical models to arrive at similar solutions to the animals they are based upon. For example, a model with one rigid body element, massless prismatic legs, and no elastic elements captured walking and trotting in dogs, matching the gait transition speed, changes in the duty factor with speed, ground reaction force shape, and limb phase with reasonable accuracy from minimizing a cost combining limb work with a penalty for rapid changes in force (Polet and Bertram, 2019). Such models may be useful in paleontological research, where soft-body details including musculature geometry, fiber length, and tendon length are not usually preserved. Indeed, the gaits of fossil organisms are often very difficult to be determined from trackways, although some attempts have been broadly successful (see Nyakatura et al., 2019; Vincelette, 2021).

Triassic pseudosuchian fossil trackways (referred to ichnotaxa *Isochirotherium* and *Brachychirotherium*) may belong to *Batrachotomus* or a close relative (Petti et al., 2009; Diedrich, 2015; Apesteguía et al., 2021; Klein and Lucas, 2021), and offer information on an approximate trackmaker size and gait parameters (e.g., track phase, defined as ipsilateral pes to manus displacement divided by the stride length, **Figure 1**). However, the precise gait employed by these trackmakers remains ambiguous.

A biomechanical model can provide quantitative predictions of the track phase given the stride length and trackmaker size. If the model adequately predicts the track phase, it offers not only evidence that a particular gait was used but also clues about other aspects of the trackmaker's locomotion not directly recorded in fossil trackways.

METHODS

Planar Model and Optimization Scheme

The parasagittal, planar model follows the study by Polet and Bertram (2019); Polet (2021b). It has a rigid trunk and massless legs that push along an axis connecting footfall location to acetabulum or glenoid through time (**Figure 2**). Feet are simple points, actuator force is instantaneously reflected in ground reaction force, and sliding friction is infinite. The center of mass (COM) lies along the glenoacetabular axis, and the pitch moment of inertia (MOI), stride length (D), and average horizontal speed are provided to the model.

The optimizations minimize an objective J combining the axial limb work, with a regularization penalizing rapid changes in force, as follows:

$$J = \sum_i \int_0^T F_i \dot{L} + c\dot{F}_i^2 dt\,, \tag{1}$$

where F_i is the axial force of the ith limb, L is the axial limb length, c is the force-rate penalty parameter, and $0 \leq t \leq \mathrm{T}$ is time during a stride. The penalty on the force rate ensures no discontinuity in force or velocity (i.e., no collisions). However, as force rates are decision variables, near-impulsive solutions (i.e., quasi-collisions

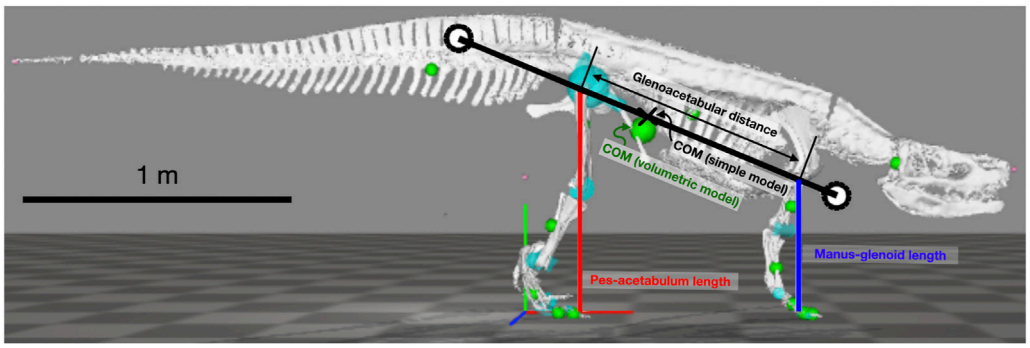

FIGURE 2 | Simple quadrupedal model used for simulations overlayed on the skeletal model used for length measurements. White circles show radius of gyration from the center of mass (x). Only two of four legs (red and blue lines) are shown in the figure.

with sharp peaks in force) are possible and emerge when force-rate penalties are low.

In the optimization scheme, c is normalized as $c' = c\frac{Mg}{L_B T}$, where L_B is the glenoacetabular distance, M is the body mass, and g is the acceleration due to gravity (Polet and Bertram, 2019). Note that throughout this paper, we use the prime symbol to denote dimensionless variables. Values of c' are reported here for $U'_H = 0.4$ ($U'_H = U/\sqrt{gH}$, where U is the average horizontal speed, g is the acceleration due to gravity, and H is the hip height) and were scaled appropriately according to T (corresponding to the same c).

Force rates are controls in the model, with forces, velocities, and positions serving as states. A leg-impulse state is added to prevent simultaneous cranial and caudal contact of a single leg. Footfall positions are parameters (and decision variables) for the optimization. Additional relaxation parameters and slack variables are added as controls to regularize complementarity conditions (see Polet and Bertram, 2019 for details).

As the gaits of interest are symmetrical, the simulation is over a half cycle (time from 0 to $T/2$). An initial and final COM horizontal position of 0 and $D/2$ is imposed. A periodicity constraint is enforced such that the body kinematics must be equal at $t = 0$ and $T/2$, and left-side forces at $t = 0$ must be equal to right-side forces at $t = T/2$. The vertical position of hips and shoulders are constrained to be above ground, and the orientation of the torso (relative to the horizontal) is restricted to $[-\pi/2, \pi/2]$. Bounds on the remaining parameters, states, and controls are left sufficiently large so as to be effectively unconstrained. Through this implementation, the optimizer can choose any symmetrical contact sequence and the duty factor for a given speed and stride length.

Optimal gaits are found by trajectory optimization with direct collocation using GPOPS-II (v. 2.3) (Patterson and Rao, 2014) and SNOPT (v. 7.5) (Gill et al., 2005; Gill et al., 2015) in MATLAB 2020b. For each parameter combination, we keep only the best local optimum from a minimum of 50 random initial guesses. The custom software used to generate symmetrical solutions is available on GitHub (Polet, 2021a).

In the baseline unconstrained case, we compared different force-rate penalties but allowed the optimizer to choose its own track phase. In the constrained case, we forced the optimizer to use the track phase to match the fossil trackway trends. We also performed a sensitivity analysis with increasing forelimb length, leaving the track phase unconstrained. In all cases, diagonal sequence and lateral sequence gaits are equivalent, as the model is planar. The ipsilateral limb phase (ϕ_L, the time from hindlimb contact to ipsilateral forelimb contact divided by the stride period) from optimization results for the dog model was modulated to the range $0 < \phi_L < 0.6$, while those for the *Batrachotomus* model were modulated to $0.4 < \phi_L < 1$.

Morphology: Domestic Dogs and *Batrachotomus*

Model track phase predictions were tested against gait and footfall data readily available for Belgian Malinois dogs (Maes et al., 2008), using the body proportions specified by Polet and Bertram (2019) and the MOI specified by Polet (2021b). *Batrachotomus* dimensions and inertial properties were determined from a volumetric model (Bishop et al., 2020). This in turn was based on the skeletal reconstruction at the Staatliches Museum für Naturkunde Stuttgart. As manus and pes material is fragmentary for this species, the autopodia were partially reconstructed by the museum staff based on closely related species, and we assumed that this autopodial morphology was sufficiently accurate for our purposes. Gower and Schoch (2009) noted that specimen SMNS 90018 preserves two fragmentary metacarpals and phalanges of the right manus, and then "four metatarsals, several phalanges, and a few distally incomplete unguals" of which only the fifth metatarsal's identity was certain. Yet what is preserved of the general autopodial morphology is consistent with the following: (1) the reconstructed, mounted museum display specimen's morphology, having a relatively small manus vs. the pes; and (2) the general autopodial morphology of other "rauisuchian"-grade Pseudosuchia (also with smaller manus vs. pes). The model was posed in an approximate standing posture to determine leg lengths and pitch MOI about the COM (**Figure 2**; **Table 1**). The distance from the hip to COM along the glenoacetabular axis, divided by L_B, was the "COM forelimb bias," presumed to represent percentage weight support in *Batrachotomus* (e.g., see Henderson, 2003; Willey et al., 2004). COM forelimb bias in dogs was derived from Griffin et al. (2004).

TABLE 1 | Body parameters used as inputs to the models.

Body Parameter	Symbol	Batrachotomus	Belgian Malinois dog
Pes-acetabulum length	L_H	0.76 m	0.48 m
Glenoacetabular distance (GAD)	L_B	0.80 m	0.48 m
Horizontal GAD	L_{Bx}	0.74 m	0.48 m
Manus-glenoid length	L_F	0.46 m	0.44 m
Pes length	L_P	0.26 m	N/A
Manus length	L_M	0.15 m	N/A
COM forelimb bias	M_F^*	0.31	0.63
Mass	M	142 kg	28 kg
Pitch MOI about COM	I	69 kg m^2	1.35 kg m^2
Murphy number	$\hat{\imath}$	3.0	0.84

Trackway Data

The ichnotaxa *Isochirotherium* and *Brachychirotherium* have usually been assigned to a large pseudosuchian trackmaker, possibly a "rauisuchian" such as *Batrachotomus* or a close relative (Diedrich, 2015; Apesteguía et al., 2021; Hminna et al., 2021; Klein and Lucas, 2021). Trackway data of interest include stride length, pes and manus length, and ipsilateral pes to manus distance within a footprint "set." For each trackway of interest, we aggregated all of the above trackway data. For example, all pes lengths were used to calculate mean pes length, even if some were not associated with a manus. These data were gathered from published sources. While these sources on occasion assigned trackways to ichnospecies, for the sake of this analysis, we grouped ichnotaxa to the ichnogenus level.

Data from Tables

Where available, published table data were used (Petti et al., 2009; Diedrich, 2012; Diedrich, 2015). The manus–pes distance was always reported as inter-print distance (IPD). In this case, we calculated midpoint–midpoint distance as (Pes Length + Manus Length)/2 + IPD.

Petti et al. (2009) assigned four trackways to *Brachychirotherium* (identified as BsZ-A, -D, -E, and -F). Only BsZ-A and BsZ-D included manus–pes distance, and so are included in the present study. Diedrich (2012) reported three *Isochirotherium* trackways in Table 1. We interpreted the values therein as means. No variational statistics were reported, apart from number of manus/pes sets. Diedrich (2015) reported a single *Isochirotherium* trackway in their Table 1 with data for each manus/pes set. Stride lengths were reported in this table for every third manus/pes set.

Data from figures

Additional trackway data were extracted from published orthogonal-view photographs or traces of trackways using ImageJ (Abramoff et al., 2004). In general, for each pes print, we digitized the tip of the third digit and the caudal-most point of the fifth digit, where the craniocaudal axis was defined to lie along the axis of the third digit (**Figure 1**). In the cases where the fifth digit was missing, the caudal-most point of the metatarsal pad was used instead. This process was repeated for the manus tracks, except in the case of *Brachychirotherium*. Because of the rotation of the manus in this latter ichnogenus, the second digit was used for the craniocaudal axis, and the tip was digitized accordingly.

The midpoints for each manus or pes were calculated, and the stride vector was defined as the displacement between midpoints of successive pes footfalls on the same side ($\vec{D}$). The midpoint was chosen as it likely represents the average center of pressure for footfalls and reduces the reliance on accurately measuring single points. The manus–pes midpoint vector is the displacement from pes to manus midpoint ($\vec{d}$). The manus–pes distance was then calculated as the length of the projection of this vector onto the average stride vector for the trackway ($\vec{d} \cdot \vec{D}_{av}/||\vec{D}_{av}||$).

Clark and Corrance (2009) presented photos of single manus–pes sets of *Isochirotherium*. These were digitized as shown above. The set from their Figure 7B was associated with trackway BWF_5 data in Table 1 of the study by Clark et al. (2002), where the trackway was at first assigned to *Chirotherium*. The trackway set from Figure 6C of Clark and Corrance (2009) was associated with trackway SLID_1 data in their Table 1. However, the digitized pes in this case had a much smaller length (0.13 m) than the smallest reported value in their Table 1 (0.21 m). Based on the trackway photo (Figure 6 in Clark et al., 2002), the pes was the sixth print of SLID_1 in their Table 1, and the caudal portion of the print may have been cropped out of the photo in Figure 6C of Clark and Corrance (2009). To correct this, we extended the caudal point by the length of pes 6 reported in their Table 1 (0.28 cm). As there were no orthogonal views of either trackway available, no projection to stride could be performed, and the absolute distance from pes to manus midpoint was used instead. The pes length data for the final print in BWF_5 were excluded, as it was poorly preserved.

Apesteguía et al. (2021) assigned four trackways to *Brachychirotherium*, identified as R1, R2-t1, -t5, and -t9, and presented them in their Figures 4A, 5B. Trackway R1 includes a trailing left manus with no associated pes. Therefore, a manus–pes midpoint distance to the next left pes was calculated, and it was subtracted from the stride length to get the pes–manus midpoint distance. The same left pes was used to calculate the pes–manus midpoint distance for the next left manus print. Trackway R2-t1 appears to include a slight turn at the start of the trackway, apparent in manus–pes sets 1 and 2. The remainder of the trackway appears steady and straight. Therefore, we omitted the first two manus–pes sets for the purposes of the track phase or stride length calculations, but included them for the trackmaker size. The prints in trackway R2-t5 are relatively poorly preserved, but with enough preservation to

allow identification of the ichnotaxon (*Brachychirotherium*). For this trackway, the cranial-most and caudal-most point of each print were digitized, where digits could not be discerned, with craniocaudal being defined as the trackway direction.

Klein et al. (2006) reported a single *Brachychirotherium* trackway in their Figure 7. As the digits of the first manus could not be discerned, the cranial-most portion of the print along the trackway direction was used instead.

Hminna et al. (2021) reported a single *Brachychirotherium* trackway in their Figure 4. There was only one set of well-preserved sequential ipsilateral pes footprints in this trackway. Therefore, sequential ipsilateral manus footprints were used to measure the stride length (total 4 in the trackway).

Calculation of Gait Parameters

Hip height of the trackmaker was determined as mean track pes length times the ratio between hip height and pes length of the *Batrachotomus* model. The non-dimensional speed ($U'_{\mathrm{H}} = U/\sqrt{gH}$) was estimated from the non-dimensional stride length ($D'_{\mathrm{H}} = D/H$, where D is the stride length) by Alexander's (1976) dynamic similarity relation, as follows:

$$U'_{\mathrm{H}} = 0.25 D'^{1.67}_{\mathrm{H}}. \quad (2)$$

The trackway stride length and speed were inputs of the model, while the track phase was compared to optimization predictions. An analytical approximation (Stevens et al., 2016) for the track phase (ϕ_T) as a function of the ipsilateral limb phase (ϕ_L), with L_{Bx} being the horizontal glenoacetabular distance, was performed as follows:

$$\Phi_T = \mathrm{mod}\left(\Phi_L + L_{\mathrm{Bx}}/D, 1\right). \quad (3)$$

This was also compared to trackway and optimization results. L_{Bx} is derived from L_B, the absolute glenoacetabular distance, as $L_{Bx} = \sqrt{L_B^2 - (L_H - L_F)^2}$ in standing (**Figure 2**).

L_{Bx} can be estimated directly from trackways if periods of quadruple stance are assumed (when all limbs are simultaneously in contact). For a trot, this parameter is given as the distance from the midpoint between left and right pes prints to the midpoint between subsequent left and right manus prints. For the present study, this is equivalent to the following:

$$L_{\mathrm{Bx}} = d + D/2. \quad (4)$$

See **Supplementary Figure S1** for a geometric proof. While Stevens et al. (2016) demonstrated how these estimates can be ambiguous for small stride lengths, the stride lengths in the present study are sufficiently large such that there is no ambiguity about which prints would be in simultaneous contact (assuming quadrupedal stance).

RESULTS

Belgian Malinois Dogs

For dogs, optimization predicts a lateral sequence gait with the limb phase $\phi_L = 0.25$ transitioning to a trot with $\phi_L = 0.5$, matching the natural behavior (**Figure 3**). The predicted track phase falls within natural variation (2 standard deviations, from Maes et al., 2008) and captures the trends of changing the track phase with speed but is consistently below the mean empirical value.

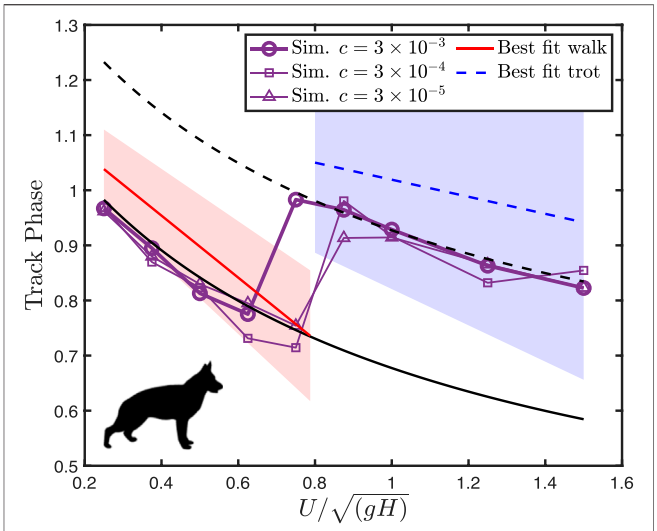

FIGURE 3 | Dog track phase decreases with speed, before exhibiting a jump at the walk-trot transition. The lines of best fit to empirical data are from Maes et al. (2008), with filled areas representing two standard deviations from the mean. Black solid and dotted lines indicate $\phi_L = 0.25$ and 0.5, respectively.

Varying the force-rate penalty c has little qualitative effect on the optimization results, except for the walk–trot transition point. The natural walk–trot transition point is at about $U'_{\mathrm{H}} = 0.8$. The transition point in simulation moves from about $U'_{\mathrm{H}} = 0.7$ at or the highest force-rate penalty ($c' = 3 \times 10^{-3}$) to $U'_{\mathrm{H}} = 0.8$ at the lowest ($c' = 3 \times 10^{-5}$). Overall, Polet and Bertram (2019) considered $c' = 3 \times 10^{-3}$ to best match dog duty factors and ground reaction force profiles at an intermediate walking speed. The ground reaction forces at this force-rate penalty (**Figure 4**) qualitatively match the double-humped profile of walking (Jayes and Alexander, 1978) and the single-humped profile of trotting (Bertram et al., 2000) in dogs.

Trackway Data

Trackways varied in size and length, with mean pes lengths varying in *Isochirotherium* from 0.22 to 0.34 m and in *Brachychirotherium* from 0.12 to 0.39 m (**Table 2**). *Isochirotherium* normalized speed (estimated *via* **Eq. 2**) varied from 0.40 to 0.79, typical for a moderate walk to fast walk or slow run. *Brachychirotherium* speeds varied more, from a slow walk at 0.31 to a fast run of 1.92. The mean manus to pes length ratio across all trackways was 0.35 ± 0.05 for *Isochirotherium* and 0.38 ± 0.09 for *Brachychirotherium* (±standard deviation).

Altogether, the fossil trackways exhibit a sharp reduction of the track phase with an increasing speed for slow speeds, following the analytical line for a trot (**Figure 5**). Above $U'_H = 0.6$, the track phase remains constant at about 0.15, until $U'_H = 1$, where it falls sharply to about 0.10.

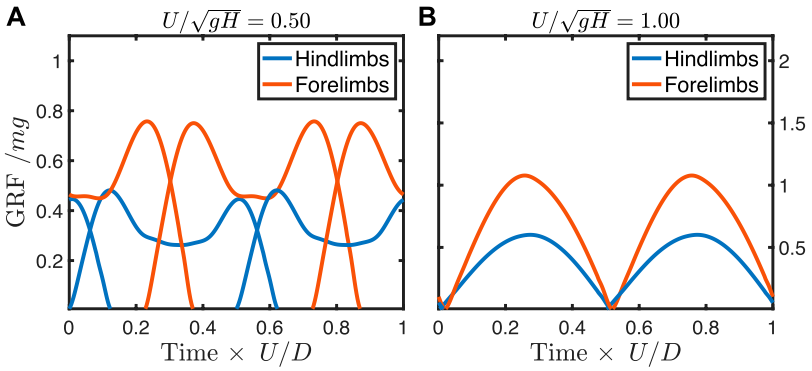

FIGURE 4 | Ground reaction forces from predictive simulation at a walking speed **(A)** and trotting speed **(B)** in a dog model with force-rate penalty c' of 3×10^{-3}. Note that any symmetrical profile is allowed, yet the simulation correctly predicts double-humped walking profiles at slow speeds and single-humped trotting profiles at faster speeds.

TABLE 2 | Summary data for *Isochirotherium* and *Brachychirotherium* trackways. Values are means ± standard deviation (sample size). Speed is normalized to presumed hip height. ET, Early Triassic; MT, Middle Triassic; LT, Late Triassic; A, Anisian; C, Carnian; N, Norian; S, "Scythian."

Source	Track ID in source	Epoch/ series, age/ stage	Pes length (m)	Manus length (m)	Manus–pes distance (m)	Stride length (m)	Track phase	Estimated speed
Isochirotherium								
Diedrich (2012), Table 1	12	MT, A	0.34	0.12	0.24	1.68	0.14	0.60
	1	MT, A	0.22	0.10	0.17	1.28	0.13	0.79
	-	MT, A	0.24	0.08	0.19	1.30	0.15	0.70
Diedrich (2015), Table 1	-	MT, A	0.34 ± 0.02 (34)	0.12 ± 0.01 (34)	0.23 ± 0.03 (34)	1.68 ± 0.03 (11)	0.14	0.60
Clark and Corrance (2009) Figure 6C and Table 1	SLID_1	ET/MT, S/A	0.29 ± 0.03 (14)	0.1 (1)	0.28 (1)	1.2 ± 0.07 (11)	0.23	0.45
Figure 7B and Clark et al. (2002) Table1	BWF_5	ET/MT, S/A	0.28 ± 0.02 (5)	0.08 (1)	0.51 (1)	1.08 ± 0.07 (4)	0.47	0.40
Brachychirotherium								
Petti et al. (2009), Table 1	BsZ-A	LT, C	0.32 ± 0.02 (10)	0.09 ± 0.01 (8)	0.24 ± 0.03 (8)	1.49 ± 0.04 (8)	0.16	0.54
	BsZ-D	LT, C	0.24 ± 0 (3)	0.12 ± 0.01 (3)	0.22 ± 0.01 (3)	1.41 (1)	0.16	0.80
Apesteguía et al. (2021) Figure 1A	R1	LT	0.39 ± 0.03 (3)	0.2 (2)	0.56 (2)	1.29 (1)	0.43	0.31
Figure 5B	R2-t1	LT	0.3 ± 0.03 (7)	0.11 ± 0.02 (6)	0.26 ± 0.04 (4)	1.23 ± 0.08 (3)	0.21	0.44
	R2-t5	LT	0.24 ± 0.03 (11)	0.08 ± 0.02 (9)	0.25 ± 0.03 (9)	0.91 ± 0.04 (8)	0.27	0.39
	R2-t9	LT	0.33 ± 0.07 (5)	0.12 (2)	0.33 (2)	1.29 ± 0.04 (4)	0.26	0.41
Klein et al. (2006) Figure 7	NMMNH P-48756	LT, N	0.15 ± 0.01 (3)	0.04 ± 0.01 (3)	0.09 ± 0.01 (3)	0.98 (1)	0.09	0.96
Hminna et al. (2021) Figure 4B	CDUE 802–808	LT, C	0.12 ± 0.01 (4)	0.05 ± 0.01 (5)	0.13 ± 0.01 (4)	1.19 ± 0.04 (4)	0.11	1.92

We estimated the horizontal glenoacetabular distance (L_{Bx}) from the trackways using **Eq. (4)** for estimated non-dimensional speeds less than 0.4 (where quadruple limb stance may have occurred). There are only two trackways that fit this criterion, both of *Brachychirotherium* (Apesteguía et al., 2021, trackways R1 and R2-t5), which yield estimates of L_{Bx}/L_P of 3.11 and 2.95, respectively (where L_P is the mean pes length). The reconstructed *Batrachotomus* model has $L_{Bx}/L_P = 2.85$ and $L_B/L_P = 3.08$.

Scaling the fossil trackways to the *Batrachotomus* reconstruction yields estimated L_{Bx} of 0.81 and 0.79 m. The reconstruction itself gives $L_{Bx} = 0.74$ m and $L_B = 0.80$ m.

Batrachotomus Simulation Results

Optimization predicts that *Batrachotomus* should have used a walking trot at slow speeds ($U_H^{'} \leq 0.4$), transitioning to a diagonal sequence gait at faster speeds (**Figure 5**). The walking trot corresponds to a sharp reduction in the track phase with an increasing speed. For relatively high force-rate penalties, the transition to a diagonal sequence, singlefoot gait corresponds to a discontinuity in the track phase around $U_H^{'} = 0.4$. For the lowest force-rate penalty ($c' = 3 \times 10^{-5}$), the track phase jumps to a plateau, with the track phase remaining constant at about 0.33, while the limb phase gradually increases. Just as the limb phase reaches a diagonal sequence in singlefoot ($\phi_L = 0.75$), the

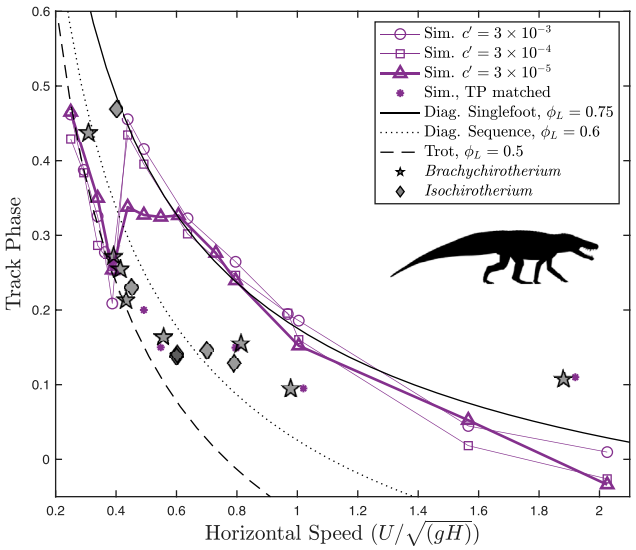

FIGURE 5 | Track phase plotted against speed for *Batrachotomus* vs. fossil chirotheriid trackways. Different levels of the force-rate penalty c' are shown as different symbols. The lowest force-rate penalty of 3×10^{-5} best fits trackway data. Both simulation and trackway data show a gradual reduction in the track phase at slow walking, corresponding to a trot based on the analytical curve (dashed line). This changes abruptly to a constant track phase with increasing speed, corresponding to the increased limb phase according to the analytical curves. Near $U_H^{'} = 1$, the theoretical upper limit for pendular walking, both simulation and trackway data exhibit a sharp reduction in the track phase, shifting toward a diagonal sequence singlefoot walk ($\phi_L = 0.75$). At intermediate speeds, the simulation consistently overestimates the trackway phase. Silhouette of *Batrachotomus* by Scott Hartman, used under a CC BY 3.0 license.

track phase decreases sharply again with an increasing speed, maintaining an approximately constant limb phase.

At the highest force-rate penalty, the walking trot exhibits typical "vaulting" double-humped ground reaction force profiles (**Figure 6A**), with simultaneous contacts between fore- and hindlimbs. As speed increases, the hindlimbs continue to vault, while the single-humped force profile in the forelimbs indicates a bouncing mode (**Figure 6B**). At the theoretical limit for vaulting in the hindlimbs ($U_H^{'} = 1$), the hindlimbs also shift to bouncing (**Figure 6C**) (see **Supplementary Video S1** for animations of these solutions). This same general shift in gait is also seen at the lowest force-rate penalty (**Figures 6D–F**), though the peak forces approach impulsivity, as is expected from work-minimizing optimization (Srinivasan, 2010). At walking speeds, the solutions can exhibit periods during stance where the hindlimbs are completely offloaded (**Figure 6D**).

When solutions are constrained to match the track phase trends of the fossil trackways, the ground reaction forces differ somewhat from the unconstrained case. Prior to the transition to a constant track phase, the optimal solution transitions away from a vaulting, walking trot, and exhibits vaulting hindlimbs with skewed ground reaction forces in the forelimbs indicating an asymmetrical (generative) bouncing mode (**Figure 7A**, see also **Supplementary Video S2**). This same gait is used at the transition to the constant track phase (**Figure 7B**), but gradually shifts to bouncing in both fore- and hindlimbs, similar to the unconstrained case (**Figure 7C**). As speed increases further, the solution remains the same, but with a lower duty factor and higher peak forces.

The constrained solutions exhibit higher costs than the unconstrained solutions (**Supplementary Figure S2A**). The difference in cost is largest at intermediate speeds and smaller at faster speeds. At $U_H^{'} = 0.55$, the cost of transport of the constrained case is 1.2 times that of the constrained case (**Supplementary Figure S2B**). At $U_H^{'} = 1.92$, this ratio diminishes to 1.01.

DISCUSSION

The simulation method predicts the canine track phase within natural variation, though predicted values are consistently below the mean empirical values (**Figure 3**). The model correctly predicts the symmetrical walking and running gaits used by dogs, the shape of their ground reaction forces (**Figure 4**), and the gait transition speed. This gives us some confidence in applying the model to forms where only the stride length, size, and shape can be estimated, and gait is unknown.

Brachychirotherium trackways follow a consistent pattern with the track phase and speed: a sharp reduction with increasing speeds below $U_H^{'} = 0.6$, followed by a constant track phase up to $U_H^{'} = 1$, at which point the track phase suddenly drops (**Figure 5**). *Isochirotherium* trackways also follow this pattern, except data are missing above dimensionless speeds of 0.8. This broad similarity in the track phase pattern with estimated speed justifies combining these ichnogenera for the analysis.

At all force-rate penalties, the simulation data correctly predict a walking trot at slow speeds, closely following the analytical curve. In all cases, the optimal gait transitions at around $U_H^{'} = 0.4$ and shifts to a higher track phase. Not only does this indicate an increase in the limb phase from a trot to a diagonal sequence gait but it also represents a fundamental shift in the gait type. While

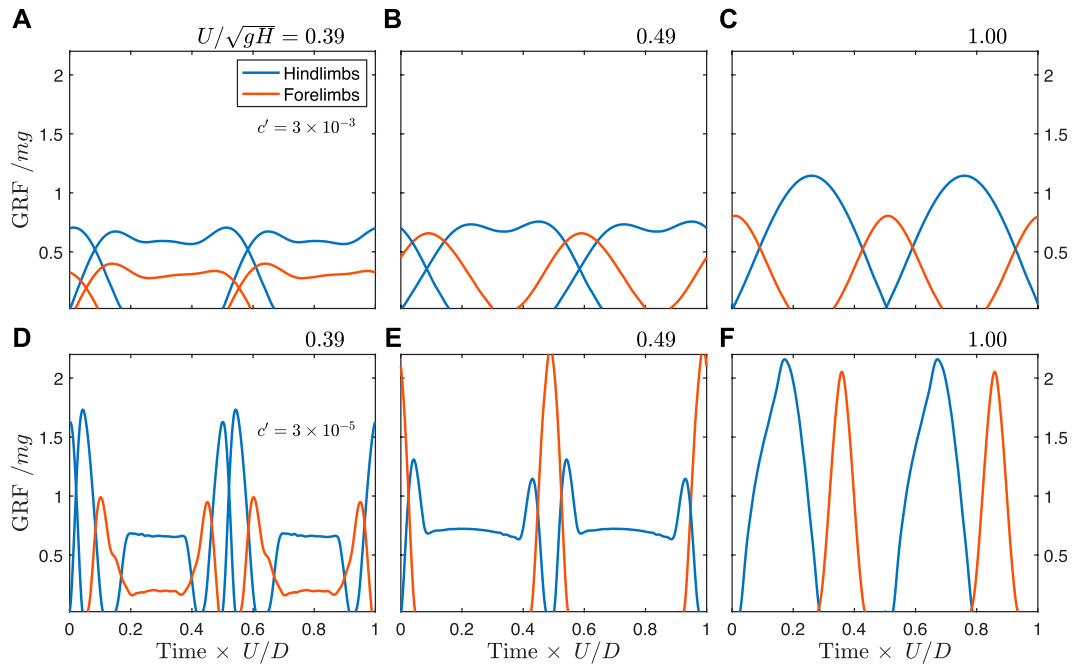

FIGURE 6 | Predicted ground reaction forces from simulation for the unconstrained *Batrachotomus* model with a force-rate penalty of 3×10^{-3} (upper row) and 3×10^{-5} (lower row). **(A)** At slow speeds, a walking trot pattern is observed, with double-humped profiles typical of vaulting. **(B)** At intermediate speeds, the forelimbs transition to a single-humped, bouncing mode. **(C)** At the fastest speeds, the hindlimbs also transition to bouncing. **(D–F)** Similar behavior is also seen at a higher force-rate penalty. However, the extreme peak forces and the unloading of midstance force at some speeds **(D)** make this force-rate penalty unrealistic (see **Supplementary Video S1** for animations).

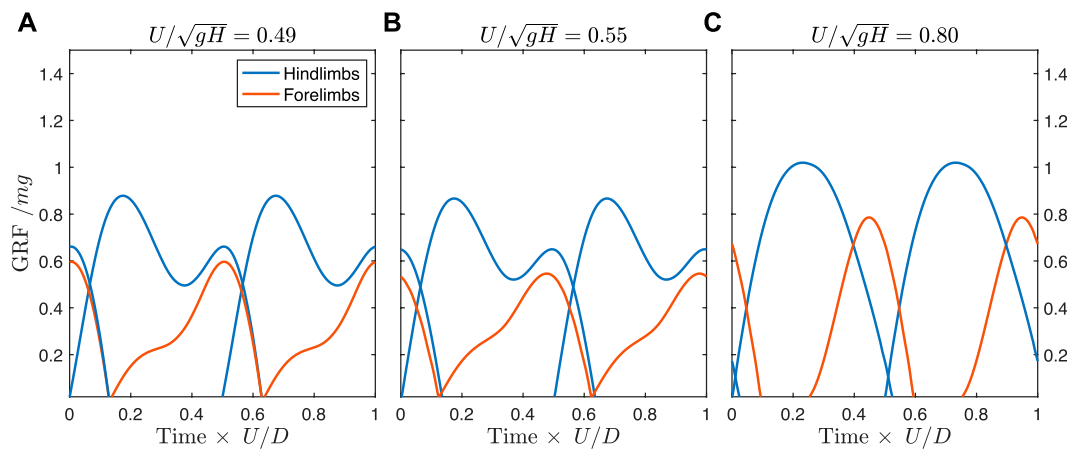

FIGURE 7 | Predicted ground reaction forces for the *Batrachotomus* model constrained to match the empirical track phase. **(A)** By a speed of 0.49, the optimal solution is to use skewed ground reaction forces in the forelimbs, with semi-vaulting forces in the hindlimbs. **(B)** This pattern is preserved at the transition point where the track phase remains constant with increasing speed. **(C)** By a speed of 0.80, the solution shifts to a running tölt, similar to the unconstrained case but differing in the timing of forelimb contact. The same solution is found at faster speeds in the constrained case, but with lower duty factor and higher peak forces (see **Supplementary Video S2** for animations).

the ground reaction force profiles of the slow-speed gait exhibit the double-humped shape characteristic of vaulting (**Figures 6A,D**), the faster gait is a hybrid, with vaulting hindlimbs and bouncing forelimbs (**Figures 6B,E**). This most closely matches the slow tölt of Icelandic horses (Biknevicius et al., 2004). Like Icelandic horses, the simulation switches to a "running tölt" at faster speeds: a four-beat symmetrical gait with single-humped ground reaction force profiles in all limbs (**Figure 6C**). The tölt is a rare gait in mammals (Vincelette, 2021), and unheard of in archosaurs, though it has been detected in fossil horse trackways (Renders, 1984; Vincelette, 2021).

At speeds above 0.4, however, the simulations differ markedly from fossil trackways in the track phase. Still, the trackways exhibit stark changes in the track phase, at around $U'_H = 0.6$ and

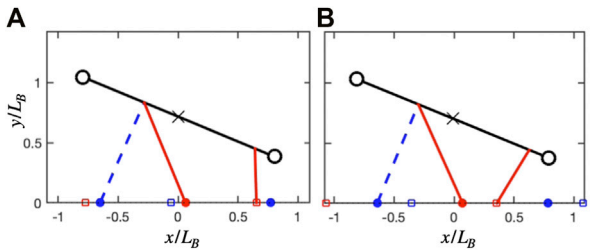

FIGURE 8 | Geometry at hindlimb step transition for the unconstrained and constrained track phase cases, both at $U_H^{'}$ = 0.49 and $c^{'}$ = 0.003. **(A)** In the unconstrained case, the forelimb is nearly vertical, allowing the hindlimbs to be effectively offloaded. The resulting ground reaction forces (GRF) are symmetrical, as shown in **Figure 6B**. **(B)** In the constrained track phase case, the shoulder is extended, so will provide a forward as well as vertical propulsive force. It can assist the hindlimbs pushoff in this position. GRF forces become asymmetrical, as shown in **Figure 7A**.

1.0, at similar times to when the simulations exhibit changes in gait. If the simulation is constrained to match the track phase of the fossil trackways, the solution remains qualitatively similar to the unconstrained case, inasmuch as exhibiting bouncing in the forelimbs, with vaulting in the hindlimbs at $U_H^{'}$ = 0.6 (**Figure 7**)—similar to a slow tölt—before transitioning to a bouncing mode in both limbs at $U_H^{'}$ = 1— similar to a fast tölt. The stark changes in the fossil track phase at $U_H^{'}$ = 0.6 and 1.0, its correspondence with a change in the limb phase according to analytical relations, combined with multiple simulations predicting gait transitions near these speeds, suggest that these fossil data demonstrate a gait transition in the pseudosuchian trackmakers.

Although the fossil trackways exhibit manus placed cranially to the ipsilateral pes in a couplet, qualitatively matching modern crocodylians in a walking trot (Kubo, 2008), the long trackway stride lengths imply gaits more similar to a dissociated trot or diagonal sequence. Modern crocodylians, the closest living relatives of *Batrachotomus*, do not normally transition to a four-beat gait at faster speeds, instead either continuing to trot or transitioning to asymmetrical gaits (Hutchinson et al., 2019). Although extant crocodylians do exhibit an increase in the limb phase as the speed increases for symmetrical gaits (**Supplementary Figure S3**), the change is much more gradual than observed here. Crocodylians do not always walk with the lateral sequence diagonal-couplet gait (**Supplementary Figure S3**; Hutchinson et al., 2019) held to be ancestral for quadrupedal gnathostomes (Wimberly et al., 2021). However, these results represent the first evidence that extinct pseudosuchians exhibited different gaits than their modern relatives, and the first evidence of a gait transition in an extinct pseudosuchian.

The use of a two-beat gait at slow speeds, and a four-beat gait at fast speeds, is consistent with an analysis by Polet (2021b). The large pitch moment of inertia of *Batrachotomus* relative to its glenoacetabular distance gives it a Murphy number of 3. Above a Murphy number of 1, a four-beat run is optimal because the energetic cost of pitching the body is lower than the energetic cost of moving the body up and down, and so it is not economical to reject pitching by using a trotting gait. However, in order to maintain vaulting in a typical four-beat walk, the body must pitch, which is energetically expensive for an animal with a large pitch moment of inertia. For this reason, a walking trot is favored at slow speeds.

Both the unconstrained and constrained cases exhibit similar solutions in ground reaction forces, but these are skewed in the latter case. In the unconstrained case, the forelimb is nearly vertical when the hindlimbs are in double support (**Figure 8A**). By having peak force at midstance, it can effectively offload the weight of the body during the costly step transition for the hindlimbs (Schroeder and Bertram, 2018). At the same time, the symmetrical, single-hump profile acts as a distributed pseudo-elastic "collision" (**Figure 6B**), which minimizes the cost of limb work while managing the force-rate penalty (Ruina et al., 2005; Rebula and Kuo, 2015).

In the constrained case, the shoulder is flexed during double support (**Figure 8A**), meaning that any pushing forces from the leg will generate both vertical and forward propulsion of the center of mass. This is less effective for offloading weight during transfer of support, but does contribute to the pre-transfer pushoff of the hindlimbs, which mitigates work-related energetic losses (Ruina et al., 2005; Rebula and Kuo, 2015; Schroeder and Bertram, 2018). Therefore, the force in the forelimbs can increase, while the second peak in the hindlimbs can decrease (**Figure 7A**). The asymmetry however results in a generative (plastic) distributed "collision," which typically requires more work than a symmetrical (pseudo-elastic) collision (Ruina et al., 2005).

The transition of trackways away from the analytical walking trot line occurs at around $U_H^{'}$ = 0.6 (**Figure 5**), well below the maximum speed for a pendular walk of $U_H^{'}$ = 1 (Usherwood, 2005), but matching the transition to a four-beat gait predicted by Polet (2021b) for a Murphy number of 3 in a perfectly symmetrical model (center of mass at midpoint of glenoacetabular distance, with all legs equal in length to glenoacetabular distance).

When the gait transition seems to occur in the trackway data, the ipsilateral manus and pes prints are nearly overstepping. Increasing the speed further without changing gait would result in overstepping, and would result in a collision of the ipsilateral manus and pes, unless the animal changed its limb orientations. Is it possible that the gait transition we infer here was forced due to this physical constraint, rather than any energetic consideration?

In modern crocodylians, foot collision appears to be avoided in the walking trot by changing yaw of the body so that the craniocaudal axis is not exactly aligned with the direction of motion. This results in manus prints being placed slightly to the left or right of pes prints (Kubo, 2008; see **Figures 2A,E** therein). This strategy is also employed by dogs when trotting, as can be seen in traces (Murie and Elbroch, 2005). There is no *a priori* reason to expect that "rauisuchians" such as *Batrachotomus* would have been unable to yaw their bodies in the same way in order to continue to employ a walking trot at higher speeds. Likewise, the planar model we use here is not constrained to avoid collisions of ipsilateral legs or feet. The transition, in this case, is driven completely by energetic considerations.

The earlier transition from a trot in the simulations (around $U_H^{'}$ = 0.40) seems to be driven by the relatively short forelimbs of *Batrachotomus* (61% of hindlimb length). A 10% increase in the

model's forelimb length increases the transition speed from 0.40 to 0.45, while a 50% increase changes it to 0.49 (**Supplementary Figures S4, 5**), simultaneously decreasing the track phase value at the transition speed. This may reflect a difference between the morphology of the real trackmakers and *Batrachotomus*. The reconstruction has a manus to pes length ratio of 0.58, compared to 0.35–0.38 in the trackways. This is also consistent with fossil footprint morphology, with the manus prints appearing digitigrade or semi-digitigrade in forelimbs (Diedrich, 2015; Klein and Lucas, 2021), roughly matching modern crocodylians (Hutson and Hutson, 2015), while *Batrachotomus* is interpreted as plantigrade. It is also possible that *Batrachotomus* in life exhibited a less flexed elbow than interpreted here, thereby increasing the effective forelimb lengths (**Figure 2**).

This is perhaps also reflected in the ratio between estimated horizontal glenoacetabular distance and pes length (L_{Bx}/L_P) in *Brachychirotherium* trackways (2.95–3.11), which match the *Batrachotomus* reconstruction more closely when absolute glenoacetabular distance is used (L_B/L_P = 3.08) rather than L_{Bx}/L_P (2.85). This may result from a more equal height of glenoid and acetabulum than previously assumed, but it could equally be due to morphological differences between *Batrachotomus* and *Brachychirotherium*, or uncertainties in the pedal reconstruction of *Batrachotomus* used in this study.

While the simulations provide evidence of a gait transition in the trackmakers, they do not predict the track phase well except at slow speeds. There may be several reasons for this discrepancy. First, the model may not accurately capture the energetics of gait alternatives in "rauisuchians." This may be due to neglecting important morphological features (e.g., legs with inertia), or physiological characteristics (e.g., muscles with force–velocity characteristics). Second, the trackmakers may not have followed the simple stride length to speed relationship proposed by Alexander (1976; based mainly on mammals). One reason may be due to a relatively reduced hip flexion and extension in some "rauisuchians" (Nesbitt et al., 2013), which was not considered in the present analysis. Third, the trackmaker may not resemble *Batrachotomus* in proportion, mass distribution, or other key areas. Finally, it is possible that energetics were not key determinants of locomotion for these trackmakers. The soft substrate where these tracks were formed, for example, could affect gait choice and phase relationships. Future developments in predictive simulation of pseudosuchian locomotion can address some of these issues by adding realism and evaluating the models within extant crocodylians.

CONCLUSION

We applied a planar, generalized quadrupedal model to the gait of *Batrachotomus kupferzellensis*, an extinct crocodile-line (pseudosuchian) archosaur. We compared our predictions to fossil trackways putatively left by close relatives of *Batrachotomus*. When optimized to minimize leg work and force rate squared, the model correctly predicted a sharp reduction in the track phase with speed, corresponding to a trot, at low speeds. Next, the model predicted a transition to a four-beat walk similar to a slow tölt, near the region where the fossil trackways deviated from the walking trot trajectory and appeared to transition to a diagonal sequence gait. Finally, when the fossil trackways exhibited another sharp transition in the track phase, the model predicted a transition to a four-beat gait similar to a fast tölt. This represents the first evidence of a gait transition in an extinct pseudosuchian, and the first evidence that "rauisuchians" like *Batrachotomus* may have exhibited some gaits different from modern crocodylians.

Because *Batrachotomus* is inferred to have had features of both modern crocodylians and mammals, trajectory optimization provides an opportunity to understand their gait where no direct analogue exists. According to the optimization results, the large pitch moment of inertia and erect limb posture of *Batrachotomus* made a tölt-like gait favorable, something not seen in any archosaurian group today and rare in mammals. This raises exciting questions, such as when this suite of gaits evolved in pseudosuchians or how often it did, and what the ancestral state was for Archosauria (birds, crocodiles, and all extinct descendants of their common ancestor, including Mesozoic dinosaurs). More sophisticated three-dimensional models incorporating lateral motions and more realistic morphology (e.g., Bishop et al., 2021) or analysis of neuromuscular control and stability may provide further insight.

DATA AVAILABILITY STATEMENT

The raw data supporting the conclusion of this article will be made available by the authors, without undue reservation.

AUTHOR CONTRIBUTIONS

The project was conceived by DP and JH, and both authors gathered data from the literature and wrote the manuscript. DP digitized trackways, analyzed data, and performed the simulations.

FUNDING

This work was supported by the European Research Council Advanced Investigator Award (Grant agreement ID: 695517) to JH.

ACKNOWLEDGMENTS

We thank Ashleigh Wiseman for her prior helpful discussions. We also thank Vivian Allen, Andrew Cuff and Peter Bishop for preparing the *Batrachotomus* model, as well as Eudald Mujal and Shinya Aoi for their thoughtful reviews, which greatly enhanced the manuscript.

SUPPLEMENTARY MATERIAL

The Supplementary Material for this article can be found online at: https://www.frontiersin.org/articles/10.3389/fbioe.2021.800311/full#supplementary-material

REFERENCES

Abramoff, M. D., Magalhães, P. J., and Ram, S. J. (2004). Image Processing with ImageJ. *Biophotonics Int.* 11, 36–42.

Alexander, R. M. (1976). Estimates of Speeds of Dinosaurs. *Nature* 261, 129–130. doi:10.1038/261129a0

Apesteguía, S., Riguetti, F., Citton, P., Veiga, G. D., Poiré, D. G., de Valais, S., et al. (2021). The Ruditayoj-Tunasniyoj Fossil Area (Chuquisaca, Bolivia): a Triassic Chirotheriid Megatracksite and Reinterpretation of Purported Thyreophoran Tracks. *Hist. Biol.* 33, 2883–2896. doi:10.1080/08912963.2020.1833328

Bertram, J. E. A., Lee, D. V., Case, H. N., and Todhunter, R. J. (2000). Comparison of the Trotting Gaits of Labrador Retrievers and Greyhounds. *Am. J. Vet. Res.* 61, 832–838. doi:10.2460/ajvr.2000.61.832

Biknevicius, A. R., Mullineaux, D. R., and Clayton, H. M. (2004). Ground Reaction Forces and Limb Function in Tölting Icelandic Horses. *Equine Vet. J.* 36, 743–747. doi:10.2746/0425164044848190

Bishop, P. J., Bates, K. T., Allen, V. R., Henderson, D. M., Randau, M., and Hutchinson, J. R. (2020). Relationships of Mass Properties and Body Proportions to Locomotor Habit in Terrestrial Archosauria. *Paleobiology* 46, 550–568. doi:10.1017/pab.2020.47

Bishop, P. J., Falisse, A., De Groote, F., and Hutchinson, J. R. (2021). Predictive Simulations of Running Gait Reveal a Critical Dynamic Role for the Tail in Bipedal Dinosaur Locomotion. *Sci. Adv.* 7, eabi7348. doi:10.1126/sciadv.abi7348

Bonaparte, J. F. (1984). Locomotion in Rauisuchid Thecodonts. *J. Vertebr. Paleontol.* 3, 210–218. doi:10.1080/02724634.1984.10011976

Clark, N. D. L., Aspen, P., and Corrance, H. (2002). *Chirotherium barthii* Kaup 1835 from the Triassic of the Isle of Arran, Scotland. *Scottish J. Geology.* 38, 83–92. doi:10.1144/sjg38020083

Clark, N. D. L., and Corrance, H. (2009). New Discoveries of *Isochirotherium herculis* (Egerton 1838) and a Reassessment of Chirotheriid Footprints from the Triassic of the Isle of Arran, Scotland. *Scottish J. Geology.* 45, 69–82. doi:10.1144/0036-9276/01-362

Diedrich, C. (2015). *Isochirotherium* Trackways, Their Possible Trackmakers (*? Arizonasaurus*): Intercontinental Giant Archosaur Migrations in the Middle Triassic Tsunami-Influenced Carbonate Intertidal Mud Flats of the European Germanic Basin. *Carbonates Evaporites* 30, 229–252. doi:10.1007/s13146-014-0228-z

Diedrich, C. (2012). Middle Triassic Chirotherid Trackways on Earthquake Influenced Intertidal Limulid Reproduction Flats of the European Germanic Basin Coasts. *Cent. Eur. J. Geo.* 4, 495–529. doi:10.2478/s13533-011-0080-9

Gill, P. E., Murray, W., and Saunders, M. A. (2005). SNOPT: An SQP Algorithm for Large-Scale Constrained Optimization. *SIAM Rev.* 47, 99–131. doi:10.1137/s0036144504446096

Gill, P. E., Murray, W., Saunders, M. A., and Wong, E. (2015). *User's Guide for SNOPT 7.5: Software for Large-Scale Nonlinear Programming*. La Jolla, CASan Diego: Department of Mathematics, University of California.

Gower, D. J., and Schoch, R. R. (2009). Postcranial Anatomy of the Rauisuchian archosaur *Batrachotomus kupferzellensis*. *J. Vertebr. Paleontol.* 29, 103–122. doi:10.1080/02724634.2009.10010365

Gower, D. (1999). The Cranial and Mandibular Osteology of a New Rauisuchian Archosaur from the Middle Triassic of Southern Germany. *Stuttgarter Beiträge Zur Naturkunde. Serie B (Geologie Paläontologie)* 280, 1–49.

Griffin, T. M., Main, R. P., and Farley, C. T. (2004). Biomechanics of Quadrupedal Walking: How Do Four-Legged Animals Achieve Inverted Pendulum-like Movements? *J. Exp. Biol.* 207 (2072), 3545–3558. doi:10.1242/jeb.01177

Henderson, D. M. (2003). Effects of Stomach Stones on the Buoyancy and Equilibrium of a Floating Crocodilian: a Computational Analysis. *Can. J. Zool.* 81, 1346–1357. doi:10.1139/z03-122

Hminna, A., Klein, H., Zouheir, T., Lagnaoui, A., Saber, H., Lallensack, J. N., et al. (2021). The Late Triassic Archosaur Ichnogenus *Brachychirotherium*: First Complete Step Cycles from Morocco, North Africa, with Implications for Trackmaker Identification and Ichnotaxonomy. *Hist. Biol.* 33, 723–736. doi:10.1080/08912963.2019.1658097

Hutchinson, J. R., Felkler, D., Houston, K., Chang, Y.-M., Brueggen, J., Kledzik, D., et al. (2019). Divergent Evolution of Terrestrial Locomotor Abilities in Extant Crocodylia. *Sci. Rep.* 9, 19302. doi:10.1038/s41598-019-55768-6

Hutson, J. D., and Hutson, K. N. (2015). Inferring the Prevalence and Function of finger Hyperextension in Archosauria from finger-joint Range of Motion in the American alligator. *J. Zool* 296, 189–199. doi:10.1111/jzo.12232

Jayes, A. S., and Alexander, R. M. (1978). Mechanics of Locomotion of Dogs (*Canis familiaris*) and Sheep (*Ovis aries*). *J. Zoolog.* 185, 289–308. doi:10.1111/j.1469-7998.1978.tb03334.x

Klein, H., Lucas, S. G., and Haubold, H. (2006). "Tetrapod Track Assemblage of the Redonda Formation (Upper Triassic, Chinle Group) in East-central New Mexico – Reevaluation of Ichnofaunal Diversity from Studies of New Material," in *The Triassic-Jurassic Terrestrial Transition*. Editors J. D. Harris, S. G. Lucas, J. A. Speilmann, M. G. Lockley, A. R. C. Milner, and J. I. Kirkland (Albuquerque, New Mexico: New Mexico Museum of Natural History and Science), 241–250.

Klein, H., and Lucas, S. G. (2021). *The Triassic Tetrapod Footprint Record*. Albuquerque, New Mexico: New Mexico Museum of Natural History and Science.

Kubo, T. (2008). In Quest of the *Pteraichnus* Trackmaker: Comparisons to Modern Crocodilians. *Acta Palaeontologica Pol.* 53, 405–412. doi:10.4202/app.2008.0304

Maes, L. D., Herbin, M., Hackert, R., Bels, V. L., and Abourachid, A. (2008). Steady Locomotion in Dogs: Temporal and Associated Spatial Coordination Patterns and the Effect of Speed. *J. Exp. Biol.* 211, 138–149. doi:10.1242/jeb.008243

Murie, O. J., and Elbroch, M. (2005). *A Field Guide to Animal Tracks*. New York, NY: Houghton Mifflin Harcourt.

Nesbitt, S. J., Brusatte, S. L., Desojo, J. B., Liparini, A., De França, M. A. G., Weinbaum, J. C., et al. (2013). Rauisuchia. *Geol. Soc. Lond. Spec. Publications* 379 (1), 241–274. doi:10.1144/SP379.1

Nyakatura, J. A., Melo, K., Horvat, T., Karakasiliotis, K., Allen, V. R., Andikfar, A., et al. (2019). Reverse-engineering the Locomotion of a Stem Amniote. *Nature* 565, 351–355. doi:10.1038/s41586-018-0851-2

Parrish, J. M. (1986). Locomotor Adaptations in the Hindlimb and Pelvis of the Thecodontia. *Hunteria* 1, 2–35.

Patterson, M. A., and Rao, A. V. (2014). GPOPS-II. *ACM Trans. Math. Softw.* 41, 1–37. doi:10.1145/2558904

Petti, F. M., Avanzini, M., Nicosia, U., Girardi, S., Bernardi, M., Ferretti, P., et al. (2009). Late Triassic (Early-middle Carnian) Chirotherian Tracks from the Val Sabbia Sandstone (Eastern Lombardy, Brescian Prealps, Northern Italy). *Riv. Ital. di Paleontol. e Stratigr.* 115, 277–290. doi:10.13130/2039-4942/6384

Polet, D. T., and Bertram, J. E. A. (2019). An Inelastic Quadrupedal Model Discovers Four-Beat Walking, Two-Beat Running, and Pseudo-elastic Actuation as Energetically Optimal. *PLOS Comput. Biol.* 15, e1007444. doi:10.1371/journal.pcbi.1007444

Polet, D. T. (2021a). Delyle/Optimize-Symmetrical-Quadruped: Optimize Symmetrical Quadruped. *Zenodo*. doi:10.5281/zenodo.5593594

Polet, D. T. (2021b). The Murphy Number: How Pitch Moment of Inertia Dictates Quadrupedal Walking and Running Energetics. *J. Exp. Biol.* 224, jeb228296. doi:10.1242/jeb.228296

Rebula, J. R., and Kuo, A. D. (2015). The Cost of Leg Forces in Bipedal Locomotion: A Simple Optimization Study. *PLOS ONE* 10, e0117384. doi:10.1371/journal.pone.0117384

Renders, E. (1984). The Gait of *Hipparion* Sp. From Fossil Footprints in Laetoli, Tanzania. *Nature* 308, 179–181. doi:10.1038/308179a0

Ruina, A., Bertram, J. E. A., and Srinivasan, M. (2005). A Collisional Model of the Energetic Cost of Support Work Qualitatively Explains Leg Sequencing in Walking and Galloping, Pseudo-elastic Leg Behavior in Running and the Walk-To-Run Transition. *J. Theor. Biol.* 237, 170–192. doi:10.1016/j.jtbi.2005.04.004

Schroeder, R. T., and Bertram, J. E. (2018). Minimally Actuated Walking: Identifying Core Challenges to Economical Legged Locomotion Reveals Novel Solutions. *Front. Robot. AI* 5, 58. doi:10.3389/frobt.2018.00058

Srinivasan, M. (2010). Fifteen Observations on the Structure of Energy-Minimizing Gaits in many Simple Biped Models. *J. R. Soc. Interf.* 8, 74–98. doi:10.1098/rsif.2009.0544

Stevens, K. A., Ernst, S., and Marty, D. (2016). "Uncertainty and Ambiguity in the Interpretation of Sauropod Trackways," in *Dinosaur Tracks: The Next Steps Life of the Past*. Editors P. L. Falkingham, D. Marty, and A. Richter (Bloomington, IN: Indiana University Press), 227–243.

Usherwood, J. R. (2020). An Extension to the Collisional Model of the Energetic Cost of Support Qualitatively Explains Trotting and the Trot-Canter Transition. *J. Exp. Zool.* 333, 9–19. doi:10.1002/jez.2268

Usherwood, J. R. (2005). Why Not Walk Faster? *Biol. Lett.* 1, 338–341. doi:10.1098/rsbl.2005.0312

Vincelette, A. (2021). Determining the Gait of Miocene, Pliocene, and Pleistocene Horses from Fossilized Trackways. *Foss. Rec.* 24, 151–169. doi:10.5194/fr-24-151-2021

Wikimedia Commons (2010). Diagram of *Brachychirotherium*. Available at: https://commons.wikimedia.org/wiki/File:Brachychirotherium.svg (Accessed September 9, 2021).

Willey, J. S., Biknevicius, A. R., Reilly, S. M., and Earls, K. D. (2004). The Tale of the Tail: Limb Function and Locomotor Mechanics in *Alligator mississippiensis*. *J. Exp. Biol.* 207, 553–563. doi:10.1242/jeb.00774

Wimberly, A. N., Slater, G. J., and Granatosky, M. C. (2021). Evolutionary History of Quadrupedal Walking Gaits Shows Mammalian Release from Locomotor Constraint. *Proc. R. Soc. B.* 288, 20210937. doi:10.1098/rspb.2021.0937

Xi, W., Yesilevskiy, Y., and Remy, C. D. (2016). Selecting Gaits for Economical Locomotion of Legged Robots. *Int. J. Robotics Res.* 35, 1140–1154. doi:10.1177/0278364915612572

Yesilevskiy, Y., Yang, W., and Remy, C. D. (2018). Spine Morphology and Energetics: How Principles from Nature Apply to Robotics. *Bioinspir. Biomim.* 13, 036002. doi:10.1088/1748-3190/aaaa9e

Conflict of Interest: The authors declare that the research was conducted in the absence of any commercial or financial relationships that could be construed as a potential conflict of interest.

frontiers in Bioengineering and Biotechnology

ORIGINAL RESEARCH
published: 04 February 2022
doi: 10.3389/fbioe.2021.769684

The Smooth Transition From Many-Legged to Bipedal Locomotion—Gradual Leg Force Reduction and its Impact on Total Ground Reaction Forces, Body Dynamics and Gait Transitions

Tom Weihmann *†

Department of Animal Physiology, Institute of Zoology, University of Cologne, Cologne, Germany

OPEN ACCESS

Edited by:
Marcus G Pandy,
The University of Melbourne, Australia

Reviewed by:
Christian Peham,
University of Veterinary Medicine Vienna, Austria
Simon Harrison,
CSIRO Data61, Australia

***Correspondence:**
Tom Weihmann
tom.weihmann@uni-koeln.de

†ORCID:
Tom Weihmann
orcid.org/0000-0002-6628-1816

Specialty section:
This article was submitted to Biomechanics, a section of the journal Frontiers in Bioengineering and Biotechnology

Received: *02 September 2021*
Accepted: *20 December 2021*
Published: *04 February 2022*

Citation:
Weihmann T (2022) The Smooth Transition From Many-Legged to Bipedal Locomotion—Gradual Leg Force Reduction and its Impact on Total Ground Reaction Forces, Body Dynamics and Gait Transitions. Front. Bioeng. Biotechnol. 9:769684. doi: 10.3389/fbioe.2021.769684

Most terrestrial animals move with a specific number of propulsive legs, which differs between clades. The reasons for these differences are often unknown and rarely queried, despite the underlying mechanisms being indispensable for understanding the evolution of multilegged locomotor systems in the animal kingdom and the development of swiftly moving robots. Moreover, when speeding up, a range of species change their number of propulsive legs. The reasons for this behaviour have proven equally elusive. In animals and robots, the number of propulsive legs also has a decisive impact on the movement dynamics of the centre of mass. Here, I use the leg force interference model to elucidate these issues by introducing gradually declining ground reaction forces in locomotor apparatuses with varying numbers of leg pairs in a first numeric approach dealing with these measures' impact on locomotion dynamics. The effects caused by the examined changes in ground reaction forces and timing thereof follow a continuum. However, the transition from quadrupedal to a bipedal locomotor system deviates from those between multilegged systems with different numbers of leg pairs. Only in quadrupeds do reduced ground reaction forces beneath one leg pair result in increased reliability of vertical body oscillations and therefore increased energy efficiency and dynamic stability of locomotion.

Keywords: ground reaction forces, duty factor, phase shift, body dynamics, leg force interference

INTRODUCTION

In legged terrestrial animals, as well as legged machines moving on level ground, body dynamics are characterised by the ground reaction forces (GRF) applied by the single legs and the temporal coordination between them (i.e., leg coordination patterns (Weihmann et al., 2016)). By and large, with low external friction body dynamics are directly equivalent to the sum of all forces applied to the ground, particularly at lower and cursorial speeds (Günther et al., 2021). By using a simple numerical approach to study the interaction of single leg ground forces in polypedal locomotor apparatuses, it has been shown previously that the number of walking legs involved significantly affects the impact of ipsilateral phase shifts onto overall ground force oscillations and body-dynamics accordingly (Weihmann, 2018).

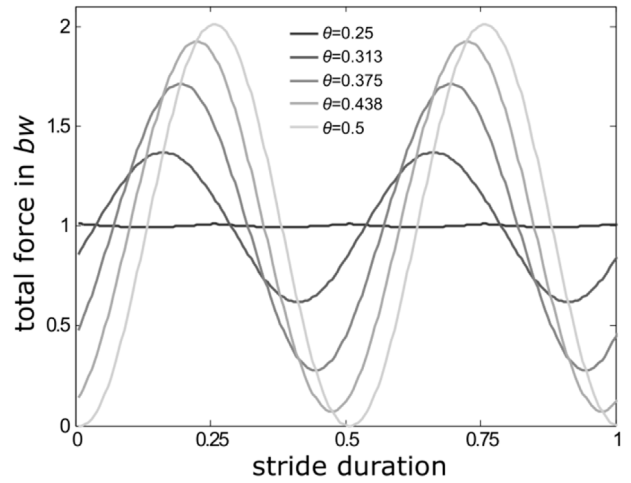

FIGURE 1 | Reduction of total force amplitudes with changing ipsilateral phase relations in a quadrupedal locomotor system moving with stance and swing durations of equal length, i.e. with a duty factor of 0.5. At $\theta = 0.5$ (light grey force trace), i.e. alternating sets of legs (trot), the consecutive sine-shaped GRF-traces coincide with the stance phases of the two successively active sets of legs. The more θ deviates from 0.5, single leg GRFs increasingly blend into each other and total force amplitudes decline to reach a minimum with only minor oscillations around body weight (*bw*) at $\theta = 0.25$ (dark grey line).

When accelerating from low to medium speeds, many few legged animals (i.e. those with less than or equal to four pairs of walking legs like vertebrates, insects and arachnids) shift ipsilateral phase relations (θ) from intermediate values towards values close to 0.5. Ipsilateral phase values describe the occurrence of a leg's stance phase within the cycle period of an adjacent leg on the same body side. With $\theta = 0.5$, and similar contralateral phase relations of a pair of pacemaker legs (which is typical for so-called symmetrical gaits like trot and its multilegged equivalents (Hildebrand, 1965)), two alternating sets of temporally synchronised sets of legs emerge. However, at medium and higher velocities, many vertebrates, and also a range of insect and arachnid species, shift ipsilateral phase relations significantly away from strict alternation ($\theta = 0.5$). Deviations from strictly alternating sets of legs result in reduced oscillations of the total vertical forces (**Figure 1**) and vertical oscillations of the animals' bodies accordingly. They are particularly advantageous when leg elasticities cannot be used owing to anatomical constraints or specific environmental conditions (Li et al., 2013; Gravish et al., 2014; Li et al., 2015; Weihmann, 2018).

Strict alternations of synchronised sets of legs are typical for medium-speed bouncing gaits, like trot or its polypedal equivalents. These gaits provide efficient storage and recovery of movement energy during stance (Blickhan and Full, 1993) and are currently widely employed for faster modes of locomotion in legged robots (e.g. Saranli et al., 2001; Birkmeyer et al., 2009).

In animals, neuronal networks with their enormous intrinsic variability can generate almost arbitrary leg coordination patterns. Evolution has brought forth similar rhythmic patterns of limb like appendages in a number of phylogenetically only loosely related groups, in which some have even evolved their legs independently of each other (e.g. Muybridge, 1887; Manton, 1950; Manton, 1952; Hildebrand, 1965; Lucifora and Vassallo, 2002; Nirody et al, 2021). Manmade machines and models mostly adopt coordination patterns that closely mimic those found in animals. Apparently, the interaction with the physical world and the constraints implied by physical laws, therefore, is more important than specifically how leg coordination is achieved (cp. Chiel and Beer, 1997).

Many polypedal animals reduce GRF gradually beneath some (mostly the anterior) of their walking legs, in particular at higher running speeds (Burrows and Hoyle, 1973; Full and Tu, 1991; Irschick and Jayne, 1999). In some lineages, differential leg use has led, via transitional forms, to varying numbers of propulsive leg pairs. Thus, in mammals (e.g. men, pangolin) and archosaurs, quadrupedal ancestors have repeatedly brought forth bipedal forms while some lineages of dinosaurs went the reverse direction and regained quadrupedalism (Maidment and Barrett, 2012). The evolution of arthropods also seems to be characterised by repeated and independent reductions in the number of propulsive legs. Particularly in small terrestrial forms, these reductions have probably extensive advantages regarding locomotion energetics and control effort, and therefore may have influenced major morphological changes in the course of these animals' transitions from marine to terrestrial habitats (Haeufle et al., 2014; Weihmann, 2020).

Among terrestrial arthropods, reductions in propulsive contributions of certain pairs of legs can be observed specifically in fast moving insects, crabs and arachnids. For the cockroach *Periplaneta americana*, concurrent increases in running speed and the body's angle to the substrate have been reported (Full and Tu, 1991). An increasingly upright body posture tends to successively reduce the ground contact of the relatively shorter anterior leg pairs, which results in decreasing duty factors (the quotient of stance phase duration and cycle duration of a leg) of these legs and, finally, can even lead to bipedal runs. In the mainly used running legs, lower duty factor values usually refer to higher running speeds and vice versa. Different species of ghost crabs have been observed to reduce the number of propulsive legs with increasing running speeds, which can also result in bipedal runs (Burrows and Hoyle, 1973; Blickhan and Full, 1987); although here the longest legs of the two sides of the body alternate with each other. In arachnids, a couple of lineages exist that typically use only three of their four pairs of legs for locomotion (Weihmann et al., 2016). Thus, harvestmen use their second legs for propulsion when climbing steep slopes (Smith et al., 2012), while these legs are solely of sensorial nature on shallower substrates (Sensenig and Shultz, 2006). However, also in spiders that usually run with all four pairs of their legs, stance durations and amplitudes of the legs' GRFs change with speed resulting in significantly reduced impulse contributions of the forelegs when running at high velocities (Weihmann, 2007). Moreover, carrying loads with anterior or posterior devices or uneven mass distribution in general (Zollikofer, 1994; Moll

et al., 2013), likely affects the loading conditions of the different pairs of legs that are distributed in anterior posterior directions along the body axis of animals or technical implementations accordingly.

Currently, it is largely unclear why animals change the number of propulsive legs when changing running speeds, however, since the behaviour has become established in a wide range of animals there seem to be some associated advantages. Energetically there are two different ways to optimise locomotion: 1) using vertical oscillations of the body's centre of mass (COM) for storage-recovery cycles of kinetic and potential energy (Alexander, 2003) or 2) keeping COM height as constant as possible in order to avoid losses (Weihmann, 2013). For attaining oscillation dynamics, the synchronisation of functional sets of legs is a requirement that enables efficient repulsion dynamics of the COM against gravity. When body dynamics follow that of an inverted pendulum, the COM reaches its highest position during mid-stance and movement energy is stored as potential energy, whereas the COM reaches its lowest position and movement energy is stored elastically at best, when body dynamics are similar to that of a spring mass system.

When animals move at constant speeds, vertical components of single leg GRFs are typically much larger than fore-aft and lateral forces, making them particularly suitable for use in energy storage and recovery cycles. This is true also in animals with sprawled legs such as reptiles or arthropods like insects and arachnids (Blickhan and Full, 1993; Biewener, 2003; Sensenig and Shultz, 2006; Weihmann et al., 2017). Accordingly and in absolute terms, overall vertical force amplitudes are particularly affected by phase shift induced ground force interferences, which makes them most decisive and characteristic for changes in COM dynamics and therefore gaits (Weihmann et al., 2016; Weihmann, 2020). In many biological and synthetic systems, vertical GRFs are approximately symmetrical around midstance (e.g. Blickhan and Full, 1987; Full et al., 1991; Blickhan and Full, 1993; Alexander, 2003; Biewener, 2003; Komsuoğlu et al., 2009; Lee, 2011; Weihmann et al., 2016) in particular when duty factors are not too high (but see the discussion section for the impact of deviations). Since ample time is available for the swing phases, in locomotor systems with many leg pairs, low duty factors can occur already at relatively low running speeds (Nirody, 2021), making symmetrical, one-humped single leg GRF traces the dominant pattern in a wide range of species.

The lower the number of propulsive legs synchronously in contact with the ground and the less sprawled leg positioning is, the larger are the vertical force components compared to lateral and fore-aft force components. However, animals with higher numbers of leg pairs like isopods, centipedes and millipedes, i.e. those who are likely to have a relatively high ratio of horizontal to vertical GRF, often have burrowing life styles and typically inhabit crevices and burrows. Most of them regularly have to deal with much higher counterforces, such as substrate friction (Manton, 1954; Manton, 1965; Jayaram and Full, 2016), than surface dwellers. Both, required propulsive force generation as well as bearing of body weight, here are distributed among many legs. In line with model predictions (Weihmann, 2018), coordinative changes in leg activity in these animals do not affect vertical, i.e. sagittal plane, body dynamics and regular vertical oscillations of the COM are largely missing.

The force interference model for integer numbers of walking legs (Weihmann, 2018) predicts decreasing total force amplitudes when ipsilateral leg coordination deviates from the strict alternating pattern. Shifting away from perfect alternation, results in symmetric minima of the total force amplitudes (cp. also **Figure 2**, left column). The position of these minima in the phase range are specific for the numbers of propulsive legs and closer to ipsilateral phase values of 0.5 the more legs an animal has. These minima are exploited by quadru-, hexa- and octopedal animals for energetic optimisation of their fast locomotion if storage-recovery cycles of kinetic and potential energy are not applicable (Weihmann et al., 2016; Weihmann et al., 2017; Weihmann, 2018).

The impact of the number of walking legs on body dynamics relies on general physical and physiological laws and principles. One of these principles shall be further explored in the present study. For this purpose, the leg force interference model (Weihmann, 2018) was adapted by implementing gradual reductions in the GRF of single leg pairs in relation to the remaining legs. This model extension allows scrutinising the effects of such reductions on overall body dynamics and examining the mechanisms that govern changes in the number of propulsive legs in the range from truly polypedal animals, like isopods, to quadrupeds that occasionally reduce the forces applied by their forefeet.

Animals that reduce the number of propulsive legs when speeding up can either keep the position of their body axis unaltered (e.g., lizards, Irschick and Jayne, 1999) or increase the body's angle of attack (e.g., cockroaches, Full and Tu, 1991). With alternating sets of legs, constant body orientation rather leads to mid-stance synchronisation whereas increasing body angles result in delayed foreleg touch-downs with synchronised take-offs. In other, mostly polypedal, species with uneven force distribution among the legs, rearward directed legs might also take-off prematurely.

Accordingly, four different regimes of force reduction were explored: i) where impulse reduction was achieved by reduction of the force amplitudes alone and ii to iv) where impulse reduction was achieved while maintaining the GRF's general shape, i.e. a cosine wave derived from previous experimental results and modeling approaches (Full et al., 1991; Blickhan and Full, 1993; Seipel et al., 2017 and see *Methods* and **Supplementary Figure S2**). Shape maintenance and simultaneous impulse reduction resulted in shorter contact durations. The timing of shorter contacts was aligned with either ii) touch down iii) mid stance or iv) take-off of an assumed unchanged step.

With synchronised sets of otherwise alternating sets of legs, the different reference points imply aligned touch-downs, mid-stances or take-offs of the complete set of legs. When ipsilateral phase relations were then changed, the alignment diminished accordingly; nevertheless, the initial alignment has consequences

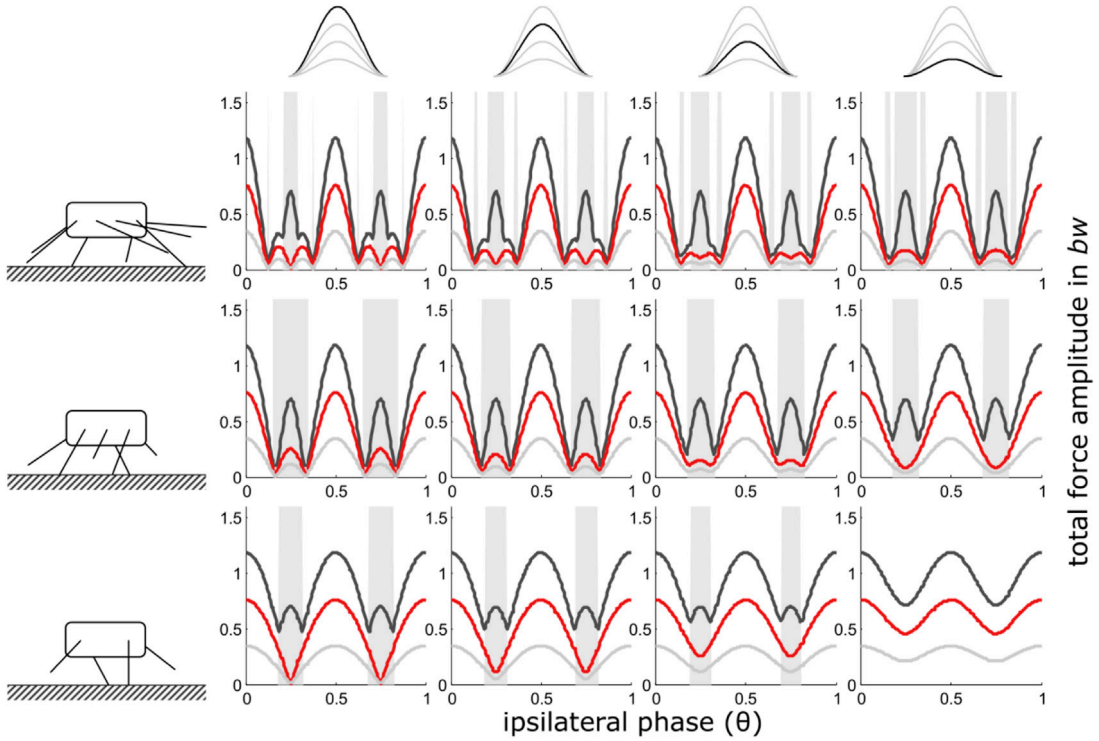

FIGURE 2 | Constant contact durations (i): Dependency of total vertical leg force amplitudes on the phase shift of ipsilateral adjacent legs and duty factor with gradually decreasing contributions of increasing numbers of leg pairs. Duty factors shown: 0.3 (dark grey), 0.5 (red) and 0.8 (light grey). The top row indicates the degree of reduction in the pair of legs with reduced GRF and the type of force alignment (here (i)). Accordingly, in the third column from the right, the impulse beneath one leg pair is reduced by ¼, in the 2nd column from the right by ½ and in the rightmost column by ¾. The pictograms to the left indicate the number of propulsive pairs of legs valid for the respective row of subplots, i.e. four in the upper row, three in the middle row and two in the bottom row. With low duty factors and intermediate phase shifts, the peak frequency of the force oscillations can deviate from two times the stride frequency; these intervals are shaded in grey.

on total force amplitudes for the whole range of leg coordination patterns.

RESULTS

When all legs generate the full amount of GRF, the results of the present approach cover those presented by Weihmann (2018); however, when the forces beneath one of the leg pairs diminish, the results can deviate significantly. With constant contact durations, the effects of gradual GRF reduction were largely restricted to quadrupeds. Reduced contact durations, as found when the GRF shape was maintained, resulted in more pronounced deviations from the patterns found when leg numbers changed by integers. Here, too, the deviations increase as the number of legs decreases.

i) Reduction of force amplitude and constant contact durations

The width of the central ranges of the phase graphs, with the maxima of the total force amplitudes at phase values of 0.5 (strict alternation of synchronised sets of legs), increases steadily from high numbers of pairs of walking legs towards lower numbers (**Figure 2**). However, during the transition from two to only one pair of propulsive legs the widening of the central range comes to an end and only the extent of the force amplitude minima decreases. Their positions in the phase range remain constant at $\theta = 0.25$ and $\theta = 0.75$. In quadrupedal locomotion (2 pairs of walking legs), every reduction of GRF in one pair of legs leads to diminishing minima of total force amplitude until, eventually, the force amplitude becomes constant when only 2 legs hit the ground alternatingly. With only one remaining pair of legs, naturally, ipsilateral phase shifts, and therefore the present model, are no longer applicable (see methods section). Here, other model approaches are better suited to investigate the dynamics of the COM (cp. Blickhan et al., 2007).

In contrast to the force reduction schemes with shape consistency (see below), the maxima of total force amplitudes for the different numbers of walking legs remained constant for a given duty factor when the contact durations of all leg pairs were constant.

As with integer numbers of pairs of legs (Weihmann, 2018), oscillation frequencies of more than twice the stride frequency occur predominantly at low duty factors (0.3) at intermediate ipsilateral phase relations (**Figure 2**). Affected phase values range between the amplitude minima of total forces that occur just adjacent to the force amplitude maxima at leg synchrony ($\theta = 0$ or 1) and leg alternation ($\theta = 0.5$). With less than four fully

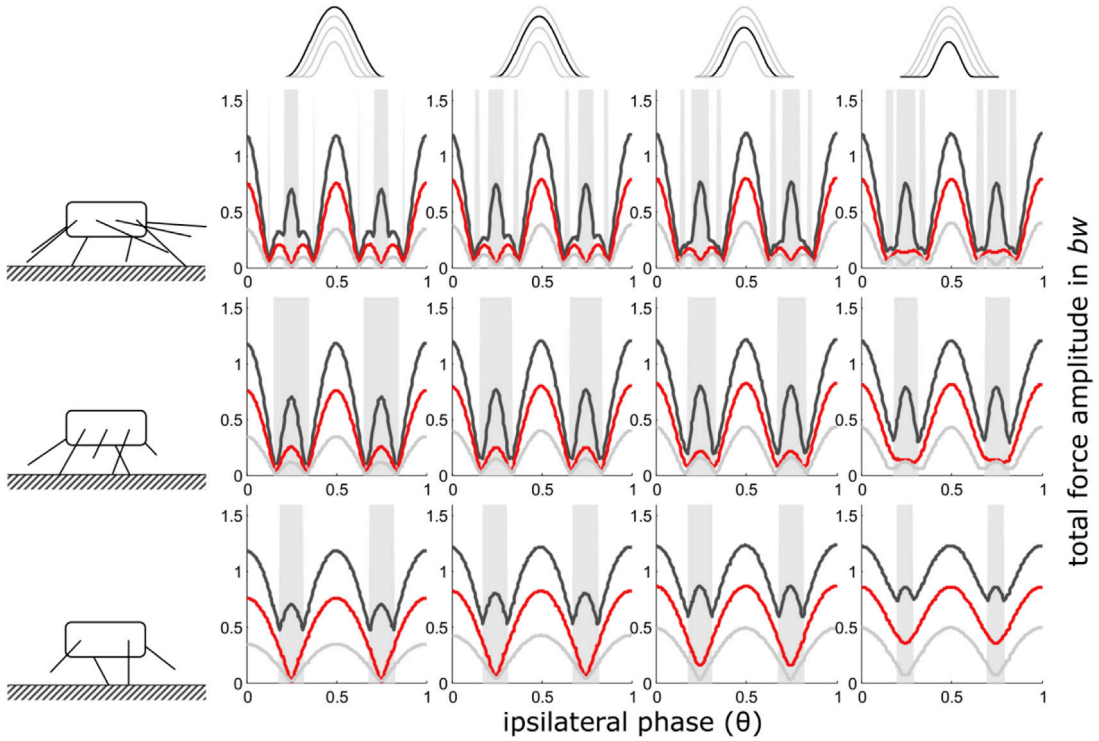

FIGURE 3 | Mid-stance as reference point (iii): Dependency of total vertical leg force amplitudes on the phase shift of ipsilateral adjacent legs and duty factor with gradually decreasing contributions of increasing numbers of leg pairs. GRF decreased while their shape (ratio of width to height) remained constant i.e. also contact durations decreased with the reduction of the impulses beneath leg pairs. Duty factors shown: 0.3 (dark grey), 0.5 (red) and 0.8 (light grey). The top row indicates the degree of reduction in the pair of legs with reduced GRF and the type of force alignment (mid-stance (iii)). Accordingly, in the third column from the right, the impulse beneath one leg pair is reduced by ¼, in the 2nd column from the right by ½ and in the rightmost column by ¾. The pictograms to the left indicate the number of propulsive pairs of legs valid for the respective row of subplots, i.e. four in the upper row, three in the middle row and two in the bottom row. With low duty factors and intermediate phase shifts, the peak frequency of the force oscillations assumed values higher than two times the stride frequency; these intervals are shaded in grey.

contributing legs, high oscillation frequencies diminished with decreasing force contributions of one leg pair.

iii) Shape consistent force reduction with mid-stance as reference point

In general, the results are similar to those where only force amplitude was reduced. Some differences occur with regard to the height of the total force amplitudes. While at low duty factors, maximum force amplitudes are still about the same for all numbers of pairs of legs, amplitude excesses occur when force contributions of one leg were reduced; particularly between 2 and 1 pair of walking legs and high duty factors, i.e. relatively low speeds (**Figure 3**). Due to these excesses, the slopes from intermediate phase values towards $\theta = 0.5$ of the total force amplitude increase.

iv) Shape consistent force reduction with take-off as reference point

As was generally the case with reduced contact durations, decreasing contact duration of one pair of legs led to excesses of the total force amplitudes, particularly at higher duty factors also when take-off or touch-down served as reference point for the timing of the legs with reduced GRF. However, in contrast to the previous condition, the occurrence of the total ground force maxima in the phase-range shifted away from $\theta = 0.5$ towards higher phase values when reduced GRFs were aligned with the take-off of regular force traces (**Figure 4**), and towards lower phase values when reduced GRFs were aligned with the touch-down (regime ii) of regular force traces (**Supplementary Figure S1**). This shift was particularly pronounced between two and one pair of legs and high duty factors. At high speeds and low duty factors, the shift was almost negligible.

DISCUSSION

Figuring out the advantages and disadvantages of using different numbers of legs and why in some clades the number of propulsive legs can vary is just as challenging as finding out ultimate reasons for speed dependent changes in the number of propulsive legs as found in a range of multilegged species (cp. Burrows and Hoyle, 1973; Full and Tu, 1991; Sensenig and Shultz, 2006; Clemente

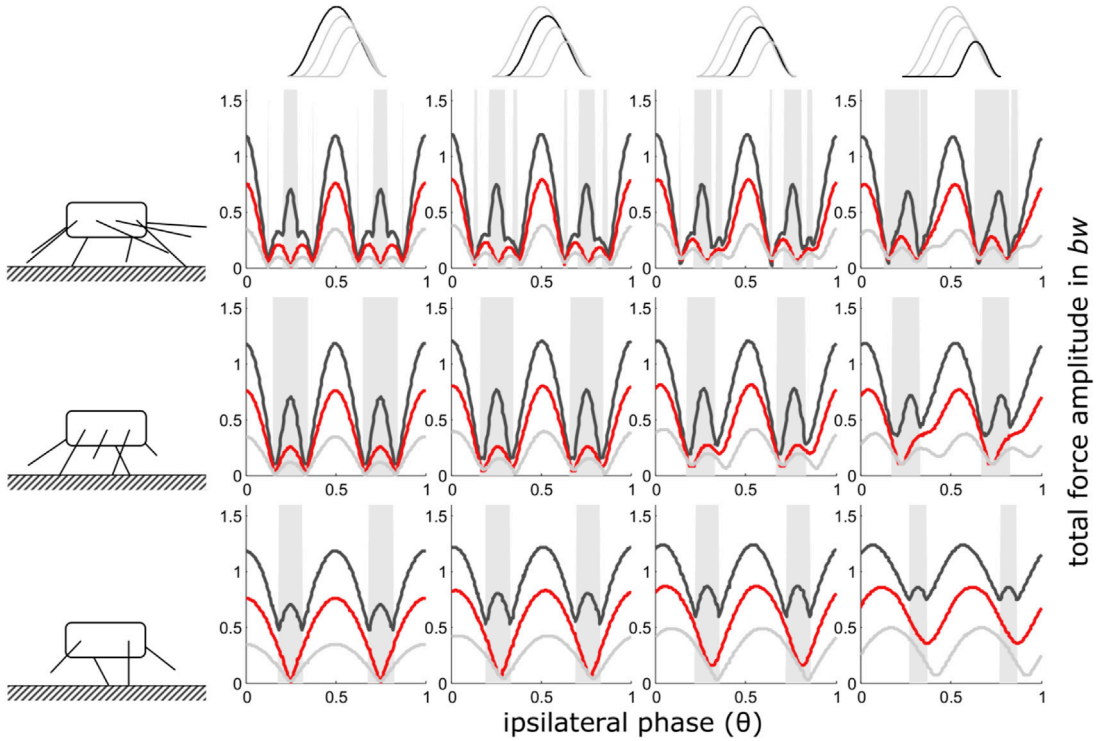

FIGURE 4 | Take-off as reference point (iv): Dependency of total vertical leg force amplitudes on the phase shift of ipsilateral adjacent legs and duty factor with gradually decreasing contributions of increasing numbers of leg pairs. GRF decreased while their shape (ratio of width to height) remained constant i.e. also contact durations decreased with the reduction of the impulses beneath leg pairs. Duty factors shown: 0.3 (dark grey), 0.5 (red) and 0.8 (light grey). The top row indicates the degree of reduction in the pair of legs with reduced GRF and the type of force alignment (take-off (iv)). Accordingly, in the third column from the right, the impulse beneath one leg pair is reduced by ¼, in the 2nd column from the right by ½ and in the rightmost column by ¾. The pictograms to the left indicate the number of propulsive pairs of legs valid for the respective row of subplots, i.e., four in the upper row, three in the middle row and two in the bottom row. With low duty factors and intermediate phase shifts, the peak frequency of the force oscillations assumed values higher than two times the stride frequency; these intervals are shaded in grey.

et al., 2008). In fact, the two questions seem to be intertwined. The present model helps to reveal some of the underlying mechanisms.

Though there are quite a few studies on the emergence of bipedalism (e.g. Harcourt-Smith and Aiello, 2004; Hirasaki et al., 2004; Crompton et al., 2008), particularly in view of our own preferred mode of locomotion, changes in the numbers of propulsive legs are much less studied with regard to multi-legged animals. Nevertheless, the underlying mechanisms have tremendous importance for both understanding the drivers of evolutionary processes affecting the locomotor system of multi-legged organisms, as well as the meaningful development of swiftly moving robots with polypedal designs.

The present study shows that, in principle, the mechanical effects of changes in leg numbers follow a continuum (**Figures 2–4**). Nevertheless, in quadrupedal locomotor systems, the reduction of GRF under some feet has decisively different consequences than similar reductions in systems with more than two pairs of legs. Therefore, the step from quadrupedal to bipedal locomotion seems to take place under somewhat different constraints.

Ancestral legged locomotor systems, just after a certain clade's colonisation of land, were rather slow and did not exploit energy cycling (Nyakatura et al., 2019; Weihmann, 2020). With such conditions, ipsilateral phase relations deviating from 0.5, i.e., metachronal wave coordination, were an effective way to avoid energetically costly vertical oscillations that might even disturb vision and position control (Zurek and Gilbert, 2014; Ardin et al., 2015; Druelle et al., 2019). In later developmental stages of terrestrial ecosystems, with established complex food-webs and accompanied coevolution towards efficient locomotion, synchronised sets of alternating legs became important means for energetic optimisation of locomotion and dynamic stabilisation in the sagittal plane (Blickhan and Full, 1993; Alexander, 2003; Blickhan et al., 2007).

With small numbers of legs, the alternating application of ground forces by sets of synchronised legs results in vertical oscillations of an animal's body of two times stride frequency (Weihmann et al., 2016). These oscillations can be used for temporal storage of movement energy during the sets' stance phases (see introduction). With temporally desynchronised sets of legs, vertical oscillations can be largely avoided (Weihmann, 2018). Accordingly, particularly in few-legged designs, synchronisation or desynchronisation of the legs in functional sets enables the choice between pronounced or small body oscillations, i.e. conditions that correspond best with the

constructional constraints and mechanical requirements of a locomotor apparatus as well as particular environmental requirements (Li et al., 2009; Weihmann and Blickhan, 2009; Jayaram and Full, 2016), both of which contribute to energetic optimisation.

Similar to the assumed evolutionary paths of legged animals, many extant species do not suddenly change their number of propulsive leg pairs, but instead do so gradually. Just as assumed, this gradual decline of the GRFs beneath some legs and the way in which it is achieved has some salient effects on the overall GRF and body dynamics.

It has been shown earlier, that the width of the central region in the phase graphs increases with decreasing numbers of leg pairs. This means that animals with a higher number of legs are less able to use vertical oscillations of the body for the energetic optimisation of their locomotion (Weihmann, 2018). However, in contrast to the general trend, at the transition from two to one propulsive leg pair, the position of the amplitude minimum in the phase space remains unchanged. Nonetheless, with gradually decreasing GRF under a pair of legs, the depth of the minima diminishes and the slope of the amplitude decrease continues to decline, particularly when contact durations of all legs were kept constant. Therefore, reducing GRF under one of the leg pairs increases the ability of quadrupeds to exploit vertical oscillations for energy recovery, even at phase relations where animals with more legs and even quadrupeds that equally distribute GRFs among their legs are affected by oscillation minima. However, this also means that oscillation minimisation can no longer be used as an energy optimisation tool.

Lizards and cockroaches can serve as excellent examples to illustrate the effects. The American cockroach (*P. americana*) gradually reduces the number of propulsive leg pairs from three to one when speeding up to their maximum running velocity of about 1.5 ms^{-1} (Full and Tu, 1991). At high running speeds, the legs reach cycle frequencies of up to 25 s^{-1} and faster runs are more likely affected by internal and external disturbances. Controlling such fast movements by reflex loops would require neuronal conduction speeds close to and beyond the physiological limits of the nervous system (Seyfarth and Pflüger, 1984; Schaefer et al., 1994; Sponberg and Full, 2008; More et al., 2010).

According to the predictions of the present model, the reduction of the GRFs under the forelegs and the gradual reduction of the number of leg pairs in contact with the substrate allows *P. americana* to increase the tolerance of its locomotor system against deviations from the ideal alternating leg coordination pattern, while still being able to effectively use vertical body dynamics for energy cycling. Interestingly, elasticities, allowing for efficient energy cycling, have been found precisely in the hips of the cockroaches' rear legs (Dudek and Full, 2006), i.e. the pair of legs that propel the animals at maximum running speeds.

Locomotor systems with fewer legs tend to have more pronounced vertical oscillations (Blickhan and Full, 1993). These oscillations, however, have been shown to be key for mechanically implemented stability mechanisms, i.e., self-stability (Schmitt and Holmes, 2000; Geyer et al., 2005). The locomotor system of hexapedally running cockroaches does not seem to be dynamically stabilised in the sagittal plane (Srinivasan and Holmes, 2008). However, the gradually declining GRF of some legs increases the stability of vertical COM oscillations and therefore also the cycling of kinetic and potential energies in the sagittal plane. Accordingly, gradual reduction of propulsive legs seems to be a suitable way to increase the animals' running stability against larger disturbances at high speeds. The same mechanisms seem to be at work in facultative bipedal lizards (cp. Druelle et al., 2019). In these fast sprinters, the range of ipsilateral phase relations in which leg elasticities can be effectively exploited and the robustness against coordinative deviations increases significantly when the GRF of the forelegs diminishes. In quadrupeds, when changing from two to only one propulsive leg pair, the increased robustness against disturbances could possibly be the main reason for bipedalism at high running speeds.

Long hindlegs, which are typical for bipedal species, allow for longer contact phases and therefore increased power generation and higher maximum running speeds (Günther et al., 2021). Long hindlegs and backward shift of the COM often have co-evolved and have mutually conditioned each other (Clemente et al., 2018). Correspondingly, tailless lizards cannot employ bipedal locomotion even if they would otherwise have been able to do so (Savvides et al., 2017). However, originally tailless species, like some monkeys, great apes or technical implementations like humanoid robots, can bring their COM over the hind limbs by raising the body. Like in cockroaches, this automatically reduces the GRFs generated by the forefeet and increases the stability of vertical body oscillations (see above). However, increasing bipedalism decreases the ability of a locomotor system, be it biological or mechanical, to employ asymmetrical gaits, i.e., gallop gaits and the employment of the lumbar spine for functional elongation of the legs (Günther et al., 2021). This functional lengthening gives the galloping gaits an advantage over symmetrical gaits when it comes to maximum speed performance. Accordingly, quadrupeds must choose between increased inherent stability of bipedal locomotion and higher maximum speed of quadrupedal gallop like locomotion.

Lizards and cockroaches are also good examples exhibiting two different ways of reducing the forces under their feet. Thus, most animals that facultatively reduce the number of propulsive legs, do so either with the body axis basically in parallel with the substrate or with a more erect body position. In both cases, a gradual increase of body height or of the position of the foreleg hips respectively results in gradual loss of ground contact in the relatively shorter anterior legs. The GRFs of these legs diminish as their contact phases reduce and load is transferred to other legs. With increasing speed, in American cockroaches, the body's angle of attack increases from about 0° to about 30° (Full and Tu, 1991). While no phase shifts of the forelegs' take-offs have been found (Delcomyn, 1971), this results in reduced contact phases by increasingly delayed touch-downs and finally complete omissions of the ground contacts.

A range of lizard species that become bipedal at higher running speeds (e.g. Irschick and Jayne, 1999; Clemente et al., 2008; Savvides et al., 2017), keep their body axis largely constant

in parallel with the substrate (Irschick and Jayne, 1999), which seems to be necessary in order to stabilise the vertical position of the head, supporting vision and vestibular perception (Druelle et al., 2019). When speeding up, they gradually increase the height of their body above the substrate and transfer body weight onto the longer hind limbs (Irschick and Jayne, 1999; Alexander, 2004)(https://www.youtube.com/watch?v=ExyMxKDxT9M). This results in diminishing contact durations of the forelegs, but in contrast to the cockroach, here, the timing of the force maxima does not necessarily shift. A similar pattern of force reduction can be assumed for likewise facultative quadrupedal dinosaurs of the hadrosaurid, iguanodontid or ceratopsid clades.

Since the model is principally insensitive against the position of the leg pair under which GRF is reduced, shortened stance phase durations due to early termination may find its equivalent in more rearward directed legs. Thus, in fast running spiders of the species *Ancylometes bogotensis* the contact durations of the forelegs (about 79%) as well as that of the rear legs (about 83%) are significantly shorter than that of the third and second legs (Weihmann, 2007).

However, exclusive amplitude reduction while contact durations are maintained might also be relevant in the locomotion of animals that do not necessarily reduce the number of propulsive leg pairs, particularly when anatomical characteristics cause an unbalanced weight distribution between rear and forelegs. Such imbalances are known for a number of ungulates, where typically the forelegs bear the greater weight (e.g. Biknevicius et al., 2004; Basu et al., 2019), but also for crocodiles, where the heavy tails cause higher load on the rear legs (Willey et al., 2004). Roughly equal contact durations for all propulsive legs, then, would facilitate a constant position of total force amplitude maxima at θ = 0.5 (**Figure 2**) and therefore predictable responses of total GRF and body dynamics to ipsilateral phase changes. The same applies to robots with uneven weight distribution either being caused by the mass distribution within their body or when carrying loads (see introduction).

Contrary to this, shorter contact phases of some legs result in more slender total force trajectories when the force maxima of all legs of a set coincide. This is particularly pronounced at the transition from two to one pair of legs, since with low numbers of leg pairs the characteristics of a single force trace have greater impact on the total GRF. Accordingly, emerging total force excesses are more pronounced in locomotor systems with fewer legs (**Supplementary Figure S3**). Moreover, additional phase shifts induced by shortening contact durations (θ_{add}, see methods) occupy larger proportions of a stride when duty factors are high, which results in pronounced total force excesses at medium to high duty factors. Since under these conditions the temporal overlap of the consecutive sets of legs is maximised and absolute COM oscillations are low, this should rarely impact running dynamics negatively.

With reference points other than the position of the force maximum (i.e., touch-down (ii) or take-off (iv)), decreasing contact durations of single leg pairs also led to shifts in the occurrence of total force amplitude maxima and minima. Also here applies, the lower the number of pairs of legs involved in the force interference and the higher the duty factor, the larger are the phase shifts of the amplitude maxima and minima. With more than two pairs of legs, this shift can also lead to asymmetries of the central region of the phase diagram were the force amplitude decline on one side is steeper than the other. These slope differences might be the reason for differences in the direction of phase deviations as observed in previous studies. Thus, when blaberid cockroaches change from alternating to high-speed metachronal leg coordination, they shift ipsilateral phases towards lower phase values (Weihmann et al., 2017), while mites shift towards higher values (Weihmann et al., 2016). When islandic horses use their notorious tölt gait, they also shift towards lower phase ratios (Hildebrand, 1965) with their forelegs bearing higher loads than their rear legs (Biknevicius et al., 2006). It seems conceivable that phase shifts are preferably adapted in the direction that enables smaller deviations from the alternating coordination pattern and thus reduces vertical oscillations more efficiently. Unfortunately, the lack of GRF measurements in blaberid cockroaches running at higher speeds with distinct metachronal leg coordination and even more so in mites, prevents further comparative inferences.

However, by reversing the reasoning, animals and legged machines aiming at smooth COM trajectories by using ipsilateral phase relations deviating from θ = 0.5 can experience sudden force and COM amplitude increases when the contact durations of some legs are accidentally delayed or terminated prematurely. Shortened contact durations can cause a sudden shift of the maximum total force amplitude away from the alternating coordination pattern, which has the potential to destabilise locomotion dynamics. Fortunately, pronounced phase shifts and therefore high relative changes in total force amplitudes are to be expected only at higher duty factors and lower speeds, where COM amplitudes are generally small. At higher speeds, the position of the total force amplitude maxima deviates only little from θ = 0.5. Interestingly, gradual reductions in the number of propulsive legs occur mainly when animals shift to higher running speeds (Burrows and Hoyle, 1973; Full and Tu, 1991; Clemente et al., 2008), i.e., when locomotor systems are less vulnerable against truncated contact phases.

Emerging force excesses (see **Supplementary Figures S3–S4**) are also a result of the way normalisation is implemented in the model. As the summed-up forces are divided by their mean value (see methods), an increased slenderness of the total force trajectory results in force amplitudes exceeding the values found for integer numbers of pairs of legs and unchanged contact durations. Nevertheless, in real animals and legged machines, total GRFs have to be strong enough to counteract gravitational forces, such that, under natural conditions, more slender total force traces would also lead to force maxima that exceed those of stouter ones.

At intermediate phase relations, i.e., when total force amplitudes are usually low, total forces and body dynamics accordingly are also affected by oscillation frequencies higher than the usual two times stride frequency (**Figures 2–4**). Particularly at low duty factors, these oscillations can have significant amplitudes. Unfortunately, their energy content cannot be recovered (Geyer et al., 2006). However, frequencies higher than twice the stride frequency are usually effectively

dissipated due to the damping properties of the leg muscles and other internal structures (Dudek and Full, 2006; Hooper et al., 2009; Schmitt and Günther, 2011; Weihmann, 2018; Weihmann, 2020), which is why these high frequencies are practically unobservable in animals. Nevertheless, in underdamped machines it can become a problem and should be taken into account.

Although the broad central regions of the amplitude-phase dependency in quadrupeds enables significant deviations from the ideal alternating coordination pattern without losing the ability to recover movement energy in the late stance phase (see above), the occurrence of harmonics, however, has the potential to hamper efficient locomotor dynamics. Nonetheless, particularly with strongly reduced GRF under one leg pair, the extent of high frequency oscillations decreases (**Figures 2–4**), making it tolerable to slip into the range were harmonics normally occur.

Facultatively bipedal species such as a range of lizard species (Clemente et al., 2018), monkeys (Ogihara et al., 2007), bipedal species like birds (Andrada et al., 2014; Daley and Birn-Jeffery, 2018) but also polypedal animals like ants (Reinhardt et al., 2009) or spiders (Weihmann, 2007) exhibit single leg GRFs deviating from the symmetrical cosine shapes used in the present approach. These deviations are required either to counteract posture induced pitch moments or they are caused, in polypedal species, by interacting horizontal leg force components as proposed by the lateral bracing hypothesis suggested for arthropods moving with alternating sets of synchronised legs (Weihmann, 2020). In particularly slow moving species like tortoises, skewed vertical ground forces can be caused also by the contraction properties of the driving muscles (Alexander, 2003). However, when single leg GRFs have tails to one side, either prior to or after the vertical force maximum, these tail forces are small if compared to the force maximum. Accordingly, they are probably of secondary importance for the force interference pattern, total body oscillation frequencies and amplitude but certainly deserve further examination since such deviating GRF shapes may affect the timing of the force maximum. Although timing effects are already mapped by the present approach (paradigms ii - iv), here only temporal deviations in the force-reduced legs are considered whereas temporal shifts of the force maximum in the remaining legs can result in additional changes in the phase dependency of the total force amplitudes. Otherwise deviating GRF shapes such as the two-humped patterns found in walking bi- and quadrupedal animals (Hodson et al., 2000; Geyer et al., 2006) might lead to higher than expected oscillation frequencies, i.e. they would appear as harmonics in the present approach. However, although central dips can, in principle, compromise the determination of the dominant vertical oscillation frequency, these dips are naturally smaller than the vertical forces of the single legs themselves, i.e. smaller than the main signal. Accordingly, deviations from the results of the present approach are likely to be small.

CONCLUSION

The reductionist approach and abstraction from the huge manifold of anatomical and control solutions of biological and technical legged locomotor apparatuses used here enables an overarching view. For arbitrary numbers of walking legs and all possible ipsilateral phase relations the model provides total force amplitudes and oscillation frequencies resulting from leg force interference. Real animals do usually use only small fractions of the generally possible combinations, which impedes the mapping of the entire solution space.

Despite its simplicity, the model provides insight in the effects of gradual ground force reduction. The results show that the transition from quadrupedal to bipedal designs differs from those between different polypedal designs. In quadrupeds only, the gradual force reduction in one pair of walking legs stabilises the vertical oscillations of total vertical GRF, which is a prerequisite for dynamic stabilisation of locomotion in the sagittal plane. Moreover, for certain conditions (paradigms ii and iv) the model shows, that total force maxima and minima can shift away from the positions they occupy with all legs exerting the full amount of GRF. Since these extremums' positions within the phase space appear to be causative for the occurrence of certain symmetrical gaits in a number of animals (Weihmann, 2018), the timing of legs with reduced GRF may provide a new perspective to help understand how and why specifically constructed animals adjust their leg coordination patterns.

METHODS

The present phenomenological model approach is based on vertical forces exerted by individual legs on the ground (cp. Weihmann, 2018), their interferences; and examines the amplitude of the total vertical force component and how it changes with changing ipsilateral phase relations (from 0 to 1). Here this examination is carried out for three different duty factors (0.3, 0.5 and 0.7). With decreasing duty factors total GRF amplitudes increase, except at such ipsilateral phases were leg force interference leads to diminishing force amplitudes (cp. **Figure 1**), which is due to shorter stance phases that require higher GRF to balance body weight.

By following Weihmann (2018), when calculating interferences of the single legs' vertical GRFs, all forces were summed up for an interval of 20 strides of the rear legs and divided by the mean of this sum, which resulted in total force oscillations normalised onto body weight. That is, the GRFs of all legs taken together just counterbalance the gravitational forces acting upon the animal's body. Afterwards, the resulting force oscillations were subjected to spectral analyses, which were accomplished by using a Fast Fourier Transformation algorithm. All analyses were performed using MatLab scripts (MATLAB 7.10.0; The MathWorks, Natick, MA, United States). Resulting amplitudes correspond to ½ of the peak to peak values of the total ground forces, i.e. the difference between the absolute maximum and minimum.

Initially, all GRFs have equal amplitudes for all walking legs and are applied for the same time intervals. Such patterns of force application and temporal distribution are supported by a wide range of experimental findings (Alexander, 2003) as well as model approaches focussed on spring mass dynamics (Blickhan et al.,

2017). According to these studies, force traces were assumed as symmetrical, i.e. leg loading and unloading required the same interval of time. In general, the forces applied during the legs' stance phases were modelled as $f_j = \frac{x}{2}(1 - \cos(2\pi t \cdot x))$ for the time interval t from 0 to take off, i.e., the start and the end of the stance phase (cp. **Figure 1**; **Supplementary Figure S2**); with x being 1 in regular steps and when impulse reduction was reached by reduction of force amplitude alone. The number of a pair of legs is indicated by the index j.

In contrast to previous work, here the GRFs of the respective anterior legs, i.e. those with the lowest index, were gradually reduced in defined steps of ¼ of the initial impulse, i.e., the area under the force trace. Hence, after four reduction steps, this resulted in a reduction of the number of leg pairs by one. Starting with four pairs of legs, the reduction continued until there was only one pair left. In real locomotor systems, the reduction would require a transfer of body weight to the remaining legs. Thus, force reduction in one pair of legs would result in increased GRFs in the remaining legs. However, with shape maintenance of the GRFs (see below) a force transfer leads to equivalent results if the differences between the impulses of the force-reduced and the remaining legs were kept constant at multiples of ¼ and the time axis is adjusted such that despite effectively increasing stride, contact and swing duration, the stride lengths were set to 1. The resulting geometrically similar single leg force traces interfere equivalently and due to the normalisation onto body weight, the resulting total force trajectories provide equivalent frequency spectrums and amplitude-phase dependencies.

With constant contact durations, the transfer of force towards the remaining legs results in increasingly steep single leg ground forces, i.e., an additional shape distortion of the GRFs affecting the interactions between the leg forces prior to normalisation onto body weight. This leads to strong total force excesses when the legs are synchronised. However, additional degrees of freedom like additional shape distortions should be avoided here which is why stride duration and force amplitude of unaffected legs was generally set to 1, which is equivalent to a previous approach with integer numbers of leg pairs (Weihmann, 2018). Concurrently, this approach facilitates comparability between locomotor apparatuses with different numbers of leg pairs and the comparison with experimentally obtained data.

Phase dependent changes in the total force amplitudes and resultant vertical body oscillations are unlikely to be useful with leg numbers above eight, i.e. four pairs of legs (Weihmann, 2018) and the model is not applicable if no ipsilateral phase relations can be applied, i.e. with only one pair of legs left. Therefore, **Figures 2–4**; **Supplementary Figure S3** show only the range from just above one active pair of legs to four pairs of legs. Nevertheless, the model applies to arbitrary numbers of leg pairs, as illustrated in **Supplementary Figure S4**.

When contact durations were kept constant and impulse reduction was achieved by reducing force amplitudes alone, x was unaltered and the force amplitudes beneath the forelegs reduced stepwise by ¼ of the initial value by multiplication with 0.75, 0.5, 0.25 or 0, respectively. When the general shape of the force trace (i.e. width to height ratio) was maintained, the values for x assumed the square root of these values, specifically 0.866; 0.7071 and 0.50, in the pair of legs with reduced GRF. This resulted in shape consistent reduced impulses of ¾, ½ and ¼ of a regular step (**Supplementary Figure S2**).

Strides are comprised of an initial stance and a subsequent swing phase where no forces are applied onto the ground. The quotient of contact duration and stride duration defines the duty factor β of a leg. Initially, stride duration, duty factors and ground forces were equal for all legs. In the present study, three different duty factors and their impact on total force and body dynamics are explored. The chosen values of 0.3, 0.5 and 0.7 are representative in a wide range of species for fast, medium and slow runs (Alexander, 2003). Keeping the shape of the GRF traces constant and reducing the impulse of some legs affects stance and swing durations as well as the duty factor of the respective legs, and also the timing of touch-down, take-off or the occurrence of the force maximum (see below).

The phase relations between legs were generally defined with regard to standard stride durations, which were set to 1. The ipsilateral phase shift θ was determined by the occurrence of one leg's touchdown within the stride period of an adjacent leg; and assumed values between 0 and 1. Owing to the circular nature of the distribution of phase relations, phase shifts of 0 and 1 are equivalent (Weihmann, 2013); each indicating the synchrony of the ipsilateral legs. However, due to static requirements and considerations, alternating sets of legs are more common in nature and technology.

In accordance with Weihmann (2018), contralateral phase relations between the rear legs, i.e. those legs with the highest index, were set to 0.5, i.e., they alternated strictly, which, in quadrupedal animals, is a characteristic of symmetrical gaits (Hildebrand, 1965). However, contralateral phase relations of about 0.5 are also often found in arthropods (Weihmann, 2020). In order to generate different leg coordination patterns, the θ of all ipsilateral legs were uniformly shifted from 0 to 1, which resulted in changing contralateral phase shifts in all leg pairs anterior to the rear legs. Whether the hind legs or the front legs served as pacemakers makes no difference. Although, in the model, force reduction was always started at leg pair 1 and proceeded to subsequent pairs of legs, the model is indifferent to the location of the force-reduced leg pair, since leg positions are not defined; therefore the model can consider reduced force in any leg. Ipsilateral phase, duty factor, number of leg pairs and x (i.e., the variable determining the impulse beneath the most anterior pair of legs), were the only changed parameters. Oscillations of total vertical forces, then, emerged from the interplay of these measures.

Reducing the impulse of legs while maintaining the shape of the force trace, resulted in shorter contact durations and sometimes led to additional temporal shifts. Since θ was defined according to touchdown and stride duration, kinematic phase was subject to additional phase shifts when shortened stance phases were aligned with mid-stance or take-off of the standard stance phases. Numerically, additional shifts were implemented prior to any regular ipsilateral phase shift as described above. If reduced stance durations were aligned with mid-stance, such that force maxima of the shortened and the standard stance phase concurred, the actual phase increased by an additional phase shift of $\theta_{add} = \frac{\beta-(\beta-x)}{2}$. With alignment at take-off, the additional phase shift was $\theta_{add} = \beta - (\beta - x)$.

DATA AVAILABILITY STATEMENT

All data presented are included in the article or **Supplementary Material**, further inquiries can be directed to the corresponding author.

AUTHOR CONTRIBUTIONS

The author confirms being the sole contributor of this work and has approved it for publication.

FUNDING

This research was funded by DFG (German Research Foundation) grant WE4664/5-1.

SUPPLEMENTARY MATERIAL

The Supplementary Material for this article can be found online at: https://www.frontiersin.org/articles/10.3389/fbioe.2021.769684/full#supplementary-material

REFERENCES

Alexander, R. M. (2004). Bipedal Animals, and Their Differences from Humans. *J. Anat.* 204, 321–330. doi:10.1111/j.0021-8782.2004.00289.x

Alexander, R. M. (2003). *Principles of Animal Locomotion*. Princeton, NJ: Princeton University Press.

Andrada, E., Rode, C., Sutedja, Y., Nyakatura, J. A., and Blickhan, R. (2014). Trunk Orientation Causes Asymmetries in Leg Function in Small Bird Terrestrial Locomotion. *Proc. R. Soc. B.* 281, 20141405. doi:10.1098/rspb.2014.1405

Ardin, P., Mangan, M., Wystrach, A., and Webb, B. (2015). How Variation in Head Pitch Could Affect Image Matching Algorithms for Ant Navigation. *J. Comp. Physiol. A.* 201, 585–597. doi:10.1007/s00359-015-1005-8

Basu, C., Wilson, A. M., and Hutchinson, J. R. (2019). The Locomotor Kinematics and Ground Reaction Forces of Walking Giraffes. *J. Exp. Biol.* 222, jeb159277. doi:10.1242/jeb.159277

Biewener, A. (2003). *Animal Locomotion (Oxford Animal Biology Series)*. Oxford: Oxford University Press.

Biknevicius, A. R., Mullineaux, D. R., and Clayton, H. M. (2004). Ground Reaction Forces and Limb Function in Tölting Icelandic Horses. *Equine Vet. J.* 36, 743–747. doi:10.2746/0425164044848190

Biknevicius, A. R., Mullineaux, D. R., and Clayton, H. M. (2006). Locomotor Mechanics of the Tölt in Icelandic Horses. *Am. J. Vet. Res.* 67, 1505–1510. doi:10.2460/ajvr.67.9.1505

Birkmeyer, P., Peterson, K., and Fearing, R. S. (2009). "Intelligent Robots and Systems," in IROS 2009 IEEE/RSJ International Conference on, St. Louis, MO, USA, 10-15 Oct. 2009 (IEEE), 2683–2689.

Blickhan, R., and Full, R. J. (1987). Locomotion Energetics of the Ghost Crab: II. Mechanics of the Centre of Mass during Walking and Running. *J. Exp. Biol.* 130, 155–174. doi:10.1242/jeb.130.1.155

Blickhan, R., and Full, R. J. (1993). Similarity in Multilegged Locomotion: Bouncing Like a Monopode. *J. Comp. Physiol. A.* 173, 509–517. doi:10.1007/bf00197760

Blickhan, R., Seyfarth, A., Geyer, H., Grimmer, S., Wagner, H., and Günther, M. (2007). Intelligence by Mechanics. *Phil. Trans. R. Soc. A.* 365, 199–220. doi:10.1098/rsta.2006.1911

Blickhan, R. (2017). "Terrestrial Locomotion," in *Animal Locomotion: Physical Principles and Adaptations*. Editors M. S. Gordon, R. Blickhan, J. O. Dabiri, and J. J. Videler (Boca Raton: CRC Press).

Burrows, M., and Hoyle, G. (1973). The Mechanism of Rapid Running in the Ghost Crab, Ocypode Ceratophthalma. *J. Exp. Biol.* 58, 327–349. doi:10.1242/jeb.58.2.327

Chiel, H. J., and Beer, R. D. (1997). The Brain Has a Body: Adaptive Behavior Emerges from Interactions of Nervous System, Body and Environment. *Trends Neurosciences* 20, 553–557. doi:10.1016/s0166-2236(97)01149-1

Clemente, C. J., Bishop, P. J., Newman, N., and Hocknull, S. A. (2018). Steady Bipedal Locomotion with a Forward Situated Whole-Body Centre of Mass: The Potential Importance of Temporally Asymmetric Ground Reaction Forces. *J. Zool* 304, 193–201. doi:10.1111/jzo.12521

Clemente, C. J., Withers, P. C., Thompson, G., and Lloyd, D. (2008). Why Go Bipedal? Locomotion and Morphology in Australian Agamid Lizards. *J. Exp. Biol.* 211, 2058–2065. doi:10.1242/jeb.018044

Crompton, R. H., Vereecke, E. E., and Thorpe, S. K. S. (2008). Locomotion and Posture from the Common Hominoid Ancestor to Fully Modern Hominins, with Special Reference to the Last Common Panin/Hominin Ancestor. *J. Anat.* 212, 501–543. doi:10.1111/j.1469-7580.2008.00870.x

Daley, M. A., and Birn-Jeffery, A. (2018). Scaling of Avian Bipedal Locomotion Reveals Independent Effects of Body Mass and Leg Posture on Gait. *J. Exp. Biol.* 221, jeb152538. doi:10.1242/jeb.152538

Delcomyn, F. (1971). The Effect of Limb Amputation on Locomotion in the Cockroach *Periplaneta Americana*. *J. Exp. Biol.* 54, 453–469. doi:10.1242/jeb.54.2.453

Druelle, F., Goyens, J., Vasilopoulou-Kampitsi, M., and Aerts, P. (2019). Compliant Legs Enable Lizards to Maintain High Running Speeds on Complex Terrains. *J. Exp. Biol.* 222, jeb195511. doi:10.1242/jeb.195511

Dudek, D. M., and Full, R. J. (2006). Passive Mechanical Properties of Legs from Running Insects. *J. Exp. Biol.* 209, 1502–1515. doi:10.1242/jeb.02146

Full, R. J., Blickhan, R., and Ting, L. H. (1991). Leg Design in Hexapedal Runners. *J. Exp. Biol.* 158, 369–390. doi:10.1242/jeb.158.1.369

Full, R. J., and Tu, M. S. (1991). Mechanics of a Rapid Running Insect: Two-, Four- and Six-Legged Locomotion. *J. Exp. Biol.* 156, 215–231. doi:10.1242/jeb.156.1.215

Geyer, H., Seyfarth, A., and Blickhan, R. (2006). Compliant Leg Behaviour Explains Basic Dynamics of Walking and Running. *Proc. R. Soc. B.* 273, 2861–2867. doi:10.1098/rspb.2006.3637

Geyer, H., Seyfarth, A., and Blickhan, R. (2005). Spring-mass Running: Simple Approximate Solution and Application to Gait Stability. *J. Theor. Biol.* 232, 315–328. doi:10.1016/j.jtbi.2004.08.015

Gravish, N., Umbanhowar, P. B., and Goldman, D. I. (2014). Force and Flow at the Onset of Drag in Plowed Granular Media. *Phys. Rev. E Stat. Nonlin Soft Matter Phys.* 89, 042202. doi:10.1103/PhysRevE.89.042202

Günther, M., Rockenfeller, R., Weihmann, W., and Haeufle, D. F. B. (2021). Rules of Nature's Formula Run: Muscle Mechanics during Late Stance Is the Key to Explaining Maximum Running Speed. *J. Theor. Biol.* 523, 110714.

Haeufle, D. F., Günther, M., Wunner, G., and Schmitt, S. (2014). Quantifying Control Effort of Biological and Technical Movements: An Information-Entropy-Based Approach. *Phys. Rev. E Stat. Nonlin. Soft Matter Phys.* 89, 012716. doi:10.1103/PhysRevE.89.012716

Harcourt-Smith, W. E. H., and Aiello, L. C. (2004). Fossils, Feet and the Evolution of Human Bipedal Locomotion. *J. Anat.* 204, 403–416. doi:10.1111/j.0021-8782.2004.00296.x

Hildebrand, M. (1965). Symmetrical Gaits of Horses. *Science* 150, 701–708. doi:10.1126/science.150.3697.701

Hirasaki, E., Ogihara, N., Hamada, Y., Kumakura, H., and Nakatsukasa, M. (2004). Do highly Trained Monkeys Walk like Humans? A Kinematic Study of Bipedal Locomotion in Bipedally Trained Japanese Macaques. *J. Hum. Evol.* 46, 739–750. doi:10.1016/j.jhevol.2004.04.004

Hodson, E., Clayton, H. M., and Lanovaz, J. L. (2000). The Forelimb in Walking Horses: 1. Kinematics and Ground Reaction Forces. *Equine Vet. J.* 32, 287–294. doi:10.2746/042516400777032237

Hooper, S. L., Guschlbauer, C., Blumel, M., Rosenbaum, P., Gruhn, M., Akay, T., et al. (2009). Neural Control of Unloaded Leg Posture and of Leg Swing in Stick Insect, Cockroach, and Mouse Differs from that in Larger Animals. *J. Neurosci.* 29, 4109–4119. doi:10.1523/jneurosci.5510-08.2009

Irschick, D. J., and Jayne, B. C. (1999). Comparative Three-Dimensional Kinematics of the Hindlimb for High-Speed Bipedal and Quadrupedal Locomotion of Lizards. *J. Exp. Biol.* 202, 1047–1065. doi:10.1242/jeb.202.9.1047

Jayaram, K., and Full, R. J. (2016). Cockroaches Traverse Crevices, Crawl Rapidly in Confined Spaces, and Inspire a Soft, Legged Robot. *Proc. Natl. Acad. Sci. USA* 113, E950–E957. doi:10.1073/pnas.1514591113

Komsuoğlu, H., Sohn, K., Full, R. J., and Koditschek, D. E. (2009). *Experimental Robotics*. University Park, PA: Springer, 303–317.
Lee, D. V. (2011). Effects of Grade and Mass Distribution on the Mechanics of Trotting in Dogs. *J. Exp. Biol.* 214 (3), 402–411. doi:10.1242/jeb.044487
Li, C., Pullin, A. O., Haldane, D. W., Lam, H. K., Fearing, R. S., and Full, R. J. (2015). Terradynamically Streamlined Shapes in Animals and Robots Enhance Traversability through Densely Cluttered Terrain. *Bioinspir. Biomim.* 10, 046003. doi:10.1088/1748-3190/10/4/046003
Li, C., Umbanhowar, P. B., Komsuoglu, H., Koditschek, D. E., and Goldman, D. I. (2009). Sensitive Dependence of the Motion of a Legged Robot on Granular Media. *Proc. Natl. Acad. Sci.* 106, 3029–3034. doi:10.1073/pnas.0809095106
Li, C., Zhang, T., and Goldman, D. I. (2013). A Terradynamics of Legged Locomotion on Granular Media. *Science* 339, 1408–1412. doi:10.1126/science.1229163
Lucifora, L. O., and Vassallo, A. I. (2002). Walking in Skates (Chondrichthyes, Rajidae): Anatomy, Behaviour and Analogies to Tetrapod Locomotion. *Biol. J. Linn. Soc.* 77, 35–41. doi:10.1046/j.1095-8312.2002.00085.x
Maidment, S. C. R., and Barrett, P. M. (2012). Does Morphological Convergence Imply Functional Similarity? A Test Using the Evolution of Quadrupedalism in Ornithischian Dinosaurs. *Proc. R. Soc. B.* 279, 3765–3771. doi:10.1098/rspb.2012.1040
Manton, S. M. (1952). The Evolution of Arthropodan Locomotory Mechanisms.- Part 2. General Introduction to the Locomotory Mechanisms of the Arthropoda. *J. Linn. Soc. Lond. Zoolog.* 42, 93–117. doi:10.1111/j.1096-3642.1952.tb01854.x
Manton, S. M. (1954). The Evolution of Arthropodan Locomotory Mechanisms.- Part 4. The Structure, Habits and Evolution of the Diplopoda. *J. Linn. Soc. Lond. Zoolog.* 42, 299–368. doi:10.1111/j.1096-3642.1954.tb02211.x
Manton, S. M. (1950). The Evolution of Arthropodan Locomotory Mechanisms.- Part I. The Locomotion of Peripatus. *J. Linn. Soc. Lond. Zoolog.* 41, 529–570. doi:10.1111/j.1096-3642.1950.tb01699.x
Manton, S. M. (1965). The Evolution of Arthropodan Locomotory Mechanisms. Part 8. Functional Requirements and Body Design in Chilopoda, Together with a Comparative Account of Their Skeleto-Muscular Systems and an Appendix on a Comparison between Burrowing Forces of Annelids an. *Zoolog. J. Linn. Soc.* 45, 251–484. doi:10.1111/j.1096-3642.1965.tb00500.x
Moll, K., Roces, F., and Federle, W. (2013). How Load-Carrying Ants Avoid Falling over: Mechanical Stability during Foraging in *Atta Vollenweideri* Grass-Cutting Ants. *PloS One* 8, e52816. doi:10.1371/journal.pone.0052816
More, H. L., Hutchinson, J. R., Collins, D. F., Weber, D. J., Aung, S. K. H., and Donelan, J. M. (2010). Scaling of Sensorimotor Control in Terrestrial Mammals. *Proc. R. Soc. B.* 277, 3563–3568. doi:10.1098/rspb.2010.0898
Muybridge, E. (1979). *Muybridge's Complete human and animal locomotion: all 781 plates from the Animal locomotion//by Eadweard Muybridge; introd. to the Dover edition by Anita Ventura Mozley*. New York: Dover Publications.
Nirody, J. A., Duran, L. A., Johnston, D., and Cohen, D. J. (2021). "Tardigrades Exhibit Robust Interlimb Coordination across Walking Speeds and Terrains," in Proceedings of the National Academy of Sciences, e2107289118.
Nirody, J. A. (2021). Universal Features in Panarthropod Inter-Limb Coordination during Forward Walking. *Integr. Comp. Biol.* 61, 710–722. doi:10.1093/icb/icab097
Nyakatura, J. A., Melo, K., Horvat, T., Karakasiliotis, K., Allen, V. R., Andikfar, A., et al. (2019). Reverse-Engineering the Locomotion of a Stem Amniote. *Nature* 565, 351–355. doi:10.1038/s41586-018-0851-2
Ogihara, N., Hirasaki, E., Kumakura, H., and Nakatsukasa, M. (2007). Ground-Reaction-Force Profiles of Bipedal Walking in Bipedally Trained Japanese Monkeys. *J. Hum. Evol.* 53, 302–308. doi:10.1016/j.jhevol.2007.04.004
Reinhardt, L., Weihmann, T., and Blickhan, R. (2009). Dynamics and Kinematics of Ant Locomotion: Do wood Ants Climb on Level Surfaces? *J. Exp. Biol.* 212, 2426–2435. doi:10.1242/jeb.026880
Saranli, U., Buehler, M., and Koditschek, D. E. (2001). RHex: A Simple and Highly Mobile Hexapod Robot. *Int. J. Robotics Res.* 20, 616–631. doi:10.1177/02783640122067570
Savvides, P., Stavrou, M., Pafilis, P., and Sfenthourakis, S. (2017). Tail Autotomy Affects Bipedalism but Not Sprint Performance in a Cursorial Mediterranean Lizard. *Sci. Nat.* 104, 3. doi:10.1007/s00114-016-1425-5
Schaefer, P. L., Kondagunta, G. V., and Ritzmann, R. E. (1994). Motion Analysis of Escape Movements Evoked by Tactile Stimulation in the Cockroach *Periplaneta Americana*. *J. Exp. Biol.* 190, 287–294. doi:10.1242/jeb.190.1.287
Schmitt, J., and Holmes, P. (2000). Mechanical Models for Insect Locomotion: Dynamics and Stability in the Horizontal Plane - II. Application. *Biol. Cybernetics* 83, 517–527. doi:10.1007/s004220000180
Schmitt, S., and Günther, M. (2011). Human Leg Impact: Energy Dissipation of Wobbling Masses. *Arch. Appl. Mech.* 81, 887–897. doi:10.1007/s00419-010-0458-z
Seipel, J., Kvalheim, M., Revzen, S., A. Sharbafi, M., and Seyfarth, A. (2017). "Conceptual Models of Legged Locomotion," in *Bioinspired Legged Locomotion*. Editors M. A. Sharbafi and A. Seyfarth (Oxford, UK: Butterworth-Heinemann), 55–131. doi:10.1016/b978-0-12-803766-9.00004-x
Sensenig, A. T., and Shultz, J. W. (2006). Mechanical Energy Oscillations during Locomotion in the Harvestman *Leiobunum Vittatum* (Opiliones). *J. Arachnology* 34, 627–633. doi:10.1636/0161-8202(2006)034[0627:meodli]2.0.co;2
Seyfarth, E.-A., and Pflüger, H.-J. (1984). Proprioceptor Distribution and Control of a Muscle Reflex in the Tibia of Spider Legs. *J. Neurobiol.* 15, 365–374. doi:10.1002/neu.480150506
Smith, A. T., Cook, D. R., Johnson, M. B., Townsend, V. R., and Proud, D. N. (2012). Comparative Study of Walking and Climbing Speeds Among Neotropical Harvestmen from Costa Rica. *J. Arachnology* 40, 304–308. doi:10.1636/hi10-103.1
Sponberg, S., and Full, R. J. (2008). Neuromechanical Response of Musculo-Skeletal Structures in Cockroaches during Rapid Running on Rough Terrain. *J. Exp. Biol.* 211, 433–446. doi:10.1242/jeb.012385
Srinivasan, M., and Holmes, P. (2008). How Well Can Spring-Mass-Like Telescoping Leg Models Fit Multi-Pedal Sagittal-Plane Locomotion Data? *J. Theor. Biol.* 255, 1–7. doi:10.1016/j.jtbi.2008.06.034
Weihmann, T. (2007). Biomechanische Analyse der ebenen Lokomotion von *Ancylometes bogotensis* (Keyserling, 1877) (Chelicerata, Arachnida, Lycosoidea). Biologisch-Pharmazeutische Fakultät, pp. 99. (Jena: Friedrich Schiller Universität Jena). Available at: http://www.db-thueringen.de/servlets/DerivateServlet/Derivate-14294/Dissertation.pdf.
Weihmann, T. (2018). Leg Force Interference in Polypedal Locomotion. *Sci. Adv.* 4, eaat3721. doi:10.1126/sciadv.aat3721
Weihmann, T., and Blickhan, R. (2009). Comparing Inclined Locomotion in a Ground-Living and a Climbing Ant Species: Sagittal Plane Kinematics. *J. Comp. Physiol. A.* 195, 1011–1020. doi:10.1007/s00359-009-0475-y
Weihmann, T., Brun, P.-G., and Pycroft, E. (2017). Speed Dependent Phase Shifts and Gait Changes in Cockroaches Running on Substrates of Different Slipperiness. *Front. Zool* 14, 54. doi:10.1186/s12983-017-0232-y
Weihmann, T. (2013). Crawling at High Speeds: Steady Level Locomotion in the Spider *Cupiennius salei* - Global Kinematics and Implications for Centre of Mass Dynamics. *PloS One* 8, e65788. doi:10.1371/journal.pone.0065788
Weihmann, T., Goetzke, H. H., and Günther, M. (2016). Requirements and Limits of Anatomy-Based Predictions of Locomotion in Terrestrial Arthropods with Emphasis on Arachnids. *J. Paleontol.* 89, 980–990. doi:10.1017/jpa.2016.33
Weihmann, T. (2020). Survey of Biomechanical Aspects of Arthropod Terrestrialisation - Substrate Bound Legged Locomotion. *Arthropod Struct. Develop.* 59, 100983. doi:10.1016/j.asd.2020.100983
Willey, J. S., Biknevicius, A. R., Reilly, S. M., and Earls, K. D. (2004). The Tale of the Tail: Limb Function and Locomotor Mechanics in Alligator Mississippiensis. *J. Exp. Biol.* 207, 553–563. doi:10.1242/jeb.00774
Zollikofer, C. (1994). Stepping Patterns in Ants - Influence of Load. *J. Exp. Biol.* 192, 119–127. doi:10.1242/jeb.192.1.119
Zurek, D. B., and Gilbert, C. (2014). Static Antennae Act as Locomotory Guides that Compensate for Visual Motion Blur in a Diurnal, Keen-Eyed Predator. *Proc. R. Soc. B.* 281, 20133072. doi:10.1098/rspb.2013.3072

Conflict of Interest: The author declares that the research was conducted in the absence of any commercial or financial relationships that could be construed as a potential conflict of interest.

frontiers in Bioengineering and Biotechnology

METHODS
published: 21 February 2022
doi: 10.3389/fbioe.2022.766748

A Coupled Biomechanical-Smoothed Particle Hydrodynamics Model for Horse Racing Tracks

Simon M. Harrison[1], R. Chris Whitton[2], Susan M. Stover[3], Jennifer E. Symons[4] and Paul W. Cleary[1]*

[1]Data61, CSIRO, Clayton, VIC, Australia, [2]Faculty of Veterinary and Agricultural Sciences, University of Melbourne, Melbourne, VIC, Australia, [3]School of Veterinary Medicine, University of California, Davis, Davis, CA, United States, [4]University of Portland, Portland, OR, United States

Distal limb injuries are common in racing horses and track surface properties have been associated with injury risk. To better understand how track surfaces may contribute to equine limb injury, we developed the first 3D computational model of the equine hoof interacting with a racetrack and simulated interactions with model representations of 1) a dirt surface and 2) an all-weather synthetic track. First, a computational track model using the Smoothed Particle Hydrodynamics (SPH) method with a Drucker-Prager (D-P) elastoplastic material model was developed. It was validated against analytical models and published data and then calibrated using results of a custom track testing device applied to the two racetrack types. Second, a sensitivity analysis was performed to determine which model parameters contribute most significantly to the mechanical response of the track under impact-type loading. Third, the SPH track model was coupled to a biomechanical model of the horse forelimb and applied to hoof-track impact for a horse galloping on each track surface. We found that 1) the SPH track model was well validated and it could be calibrated to accurately represent impact loading of racetrack surfaces at two angles of impact; 2) the amount of harrowing applied to the track had the largest effect on impact loading, followed by elastic modulus and cohesion; 3) the model is able to accurately simulate hoof-ground interaction and enables study of the relationship between track surface parameters and the loading on horses' distal forelimbs.

Keywords: elastoplastic, biomechanics, equine, gait, quadruped, large deformation

OPEN ACCESS

Edited by:
Gina Bertocci,
University of Louisville, United States

Reviewed by:
Natalya Kizilova,
Warsaw University of Technology, Poland
Peter Quesada,
University of Louisville, United States

****Correspondence:***
Simon M. Harrison
Simon.Harrison@csiro.au

Specialty section:
This article was submitted to Biomechanics, a section of the journal Frontiers in Bioengineering and Biotechnology

Received: *30 August 2021*
Accepted: *04 January 2022*
Published: *21 February 2022*

Citation:
Harrison SM, Whitton RC, Stover SM, Symons JE and Cleary PW (2022) A Coupled Biomechanical-Smoothed Particle Hydrodynamics Model for Horse Racing Tracks. Front. Bioeng. Biotechnol. 10:766748. doi: 10.3389/fbioe.2022.766748

INTRODUCTION

Forelimb injuries are common in racehorses often resulting in lameness and in severe cases death (Bailey et al., 1999; Parkin et al., 2006). The metacarpophalangeal (MCP) joint, or fetlock, is the site of most tendon, ligament, joint surface, and bone injuries (Bailey et al., 1999; Parkin et al., 2006). It is likely the MCP joint is prone to injury due to the large loads generated in this joint in galloping horses as a result of hyperextension during the stance phase of gait (Harrison et al., 2010, 2012, 2014).

Racetrack surface types have been associated with differences in musculoskeletal injury risk, with the likely reason being the effect of the surface on limb loading in the galloping horse. Typical track surfaces are dirt, sand, synthetic and turf. In North America turf and dirt tracks are associated with a higher risk of fatal and non-fatal fracture compared to synthetic tracks (Georgopoulos and Parkin

2017). In addition, track condition is associated with musculoskeletal injury rates with muddy dirt tracks and faster turf tracks having higher injury risk than fast dirt and slower turf tracks respectively (Hitchens et al., 2019).

Synthetic track material is typically a granular mix of sand, wax, and rubber particles. It has a different elastic and flow response to impact by the horse's hooves than do dirt and sand tracks. Dirt and synthetic tracks are prepared with a loose surface layer the depth of which affects peak loads in drop tests simulating hoof strike and fetlock extension in galloping horses (Mahaffey et al., 2013; Symons et al., 2014). However, it is still unknown how the horse limbs are loaded during contact with dirt and synthetic track surfaces and how rheological differences affect the risk of injury during racing. Measurement of hoof-ground forces during racing is not practical so computational simulation is required to provide insight into the force transmission through the distal limb.

Researchers at UCDavis have developed a track testing device (TTD) that measures the compressive and shear behaviour of a horse racetrack *in situ* (Setterbo et al., 2013). **Figure 1** shows (a-c) photos of the TTD performing impact experiments and (d-e) example force-displacement results from Setterbo et al. (2013). Symons et al. (2015) used this device to calibrate a one-dimensional spring model of the track response that was successfully combined with a musculoskeletal model (Symons et al., 2016). It is not clear how the nonlinear spring model developed can be related to objective measures of stiffness, plasticity, friction angle and porosity of the track material and so there is motivation for a more detailed track surface model. In addition, Symons et al. (2016) reported deviations of model results from expectations when the hoof was substantially angled to the horizontal plane, all of which suggests that a three-dimensional model of track surfaces may be required to represent all hoof-track interactions accurately.

Computational modelling studies of equine distal limb loading during locomotion have been used to understand tendon and bone loading but there remain limits on their scope and application. Limitations include:

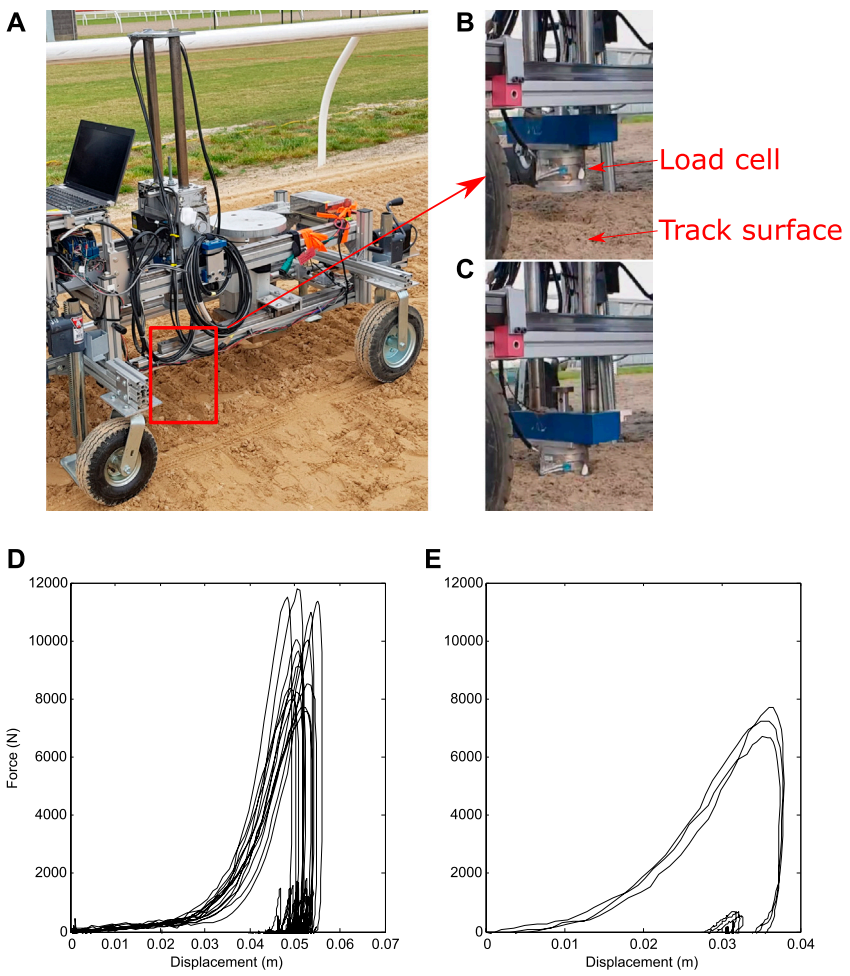

FIGURE 1 | (A–C) Photographs of the track testing device (TTD) and ensemble force-displacement results for the TTD experiments as reported in (Setterbo et al., 2013) for **(D)** the dirt track and **(E)** synthetic (all weather) track. In the TTD experiments, a cylindrical mass is dropped onto a track from a known height. External force and distance travelled are recorded with the purpose of characterising the impact properties of the track.

1. Use of gait speeds slower than those occurring during racing
2. The level of detail of the tendon, ligament, and muscle forces
3. The use of either very simple ground models or measured ground reaction data, or,
4. Focus on only the hoof and ignoring other body dynamics

Biewener (1998) developed the first comprehensive distal forelimb model, calculating some tendon forces that disagreed with experimental measures (Riemersma et al., 1996; Butcher et al., 2009) because distal joint torque constraints were ignored. Subsequent studies showed improved agreement with experimental measures by using distal joint torque constraints (Meershoek et al., 2001; Wilson et al., 2001; Swanstrom et al., 2005; Merritt et al., 2008), but contributions by separate elastic ligament structures were not predicted. Harrison et al. (2010) presented the most comprehensive and validated model to date, which included carpal muscle forces and more detailed representations of interactions between muscles, ligaments, and tendons. Only Reiser et al. (2000), Swanstrom et al. (2005) and Symons et al. (2016) have used forward dynamics to predict ground reaction force (GRF) and/or joint angles, but these models only considered 2D (sagittal plane) dynamics and used a simple spring model for the track that does not capture realistic elastic deformation and plastic flow behaviour.

Others have used models to predict the hoof-ground interaction without directly modelling the limb. Zhao et al. (2020) and Behnke (2017) used impact experiments and analytical (spring-dashpot) or 2D finite element (FE) models, respectively, to represent the hoof-ground interaction. They ignored the effects of joint movement during the hoof-ground contact, despite others showing the importance of these joint movements for moderating load (Wilson et al., 2001; McGuigan and Wilson, 2003). 3D models using Finite Element analysis (FEA) have been applied to hoof stresses in contact with different surfaces (treadmill, concrete, and sand) but the boundary conditions are typically generic or very simplistic and ignore the dynamics of the forelimb and torso (Newlyn et al., 1998; Hinterhofer et al., 2000; Hinterhofer et al., 2001; Thomason et al., 2002; Salo et al., 2010; Ramsey et al., 2013; Jansová et al., 2015; Akbari Shahkhosravi et al., 2021a; Akbari Shahkhosravi et al., 2021b). McCarty et al. (2016) presented the only study using FE to model both the response of the distal limb and the ground. They studied the dynamic impact of the hoof with the ground but did not consider muscle contractions or the full load cycle of the stance phase. A fully predictive model that incorporates all aspects of limb biomechanics and mechanical interactions with the track in three-dimensions is needed to better understand the relationship between gait movements, ground properties, internal body loading and injury.

Computer simulations of moving bodies interacting with flowing materials (such as water or soil in this study) require a mathematical method that can accurately represent large deformations and interactions with moving and deforming boundaries. A coupled biomechanical-Smoothed Particle Hydrodynamics (B-SPH) approach has been successfully used for human biomechanics in swimming (Cleary et al., 2013; Cohen et al., 2012, 2015, 2018), platform diving (Harrison et al., 2016b) and kayaking (Harrison et al., 2019). The B-SPH framework can be adjusted to include the flow of soil-like ground (Harrison and Cleary, 2013) and equine locomotion (Harrison et al., 2016a).

The purpose of this study is to develop a B-SPH model of equine locomotion to enable the study of the effects of changes to track material response on external body loading. We present coupled 3D dynamic models of the forelimb, the dirt and synthetic tracks, and the hoof-track interactions during galloping. The SPH track model is more realistic and general than that used in previous studies because it is based on a 3D elastic-plastic representation of material response under loading from the hoof. Others have used SPH to investigate and validate models of soil dynamics for application areas such as landslides (Bui et al., 2008; Wang et al., 2019; Zhan et al., 2020) or excavation (Li et al., 2018), but not biomechanics. The external and internal forces on the distal forelimb are calculated by combining the equine forelimb model given by Harrison et al. (2010) with a representation of the horse's centre of mass and interactions with the SPH track surface. The model track properties were calibrated using the data from Setterbo et al. (2013) and the forelimb model was driven using 2D motion capture data on the same surfaces (Symons et al., 2014). The resulting model is systematically evaluated for use in predicting vertical impact force at the hoof, shown to be critical for understanding joint stresses (Harrison et al., 2014), and for understanding how track surface properties affect the magnitudes of these loads.

NUMERICAL METHODS

The B-SPH model of hoof-track interaction is described in five stages:

1. A description of the SPH method and its application to impact/contact type scenarios
2. Verification of model resolution and validation of model outputs by comparison to analytical models and published simulation results
3. Calibration of track material parameters for the dirt and synthetic tracks described in Setterbo et al. (2013).
4. Sensitivity analysis of model outputs to changes in track material parameters
5. Demonstration of hoof-track interactions for cantering gait over the dirt and synthetic tracks

The Smoothed Particle Hydrodynamics Method for Elastic Solids

SPH is a numerical method for solving partial differential equations (PDEs). It is a meshless Lagrangian method in which the governing equations are solved on a moving set of particles that represent discretised volumes of material. See Monaghan (1994) and Cleary (1998) for detailed explanations of the method and reviews by (Monaghan, 2005; Gómez-Gesteira et al., 2010). It has been used extensively to simulate the dynamics of elastoplastic solids (Chen et al., 2001; Gray et al., 2001; Cleary,

2010) and elastic-brittle fracture (Cleary and Das, 2008; Das and Cleary, 2008, 2010, 2013; Harrison and Cleary, 2014).

SPH is suited to solid mechanics applications where large deformations and/or damage occurs. Unlike more traditional methods such as Finite Volume and Finite Element analysis that solve for material motion using grids or meshes, SPH particles represent specific volumes of material and move with the material velocity. These particles carry information about physical properties of the system such as pressure, density, velocity, stresses, history dependent properties such as plastic strain and damage which is advected without numerical diffusion. Forces between particles are determined using a smoothing kernel function and are dependent on the distance between the particles. The use of the kernel function allows the governing partial differential equations (PDEs) of the physical system to be converted into spatially discretised systems of ordinary differential equations (ODEs), which can then be integrated forward in time to predict the state of the system.

The SPH continuity equation for fluids given by Monaghan (1994) in a form suitable for predicting elastic dynamics is:

$$\frac{d\rho_a}{dt} = \sum_b m_b \boldsymbol{v}_{ab} \cdot \nabla_a \boldsymbol{W}_{ab} \tag{1}$$

where ρ_a is the density of particle a, t is time, m_b is the mass of particle b, where $\boldsymbol{v}_{ab} = \boldsymbol{v}_a - \boldsymbol{v}_b$ and $\mathbf{v}_\mathrm{a}$ and $\mathbf{v}_\mathrm{b}$ are the velocities of particles a and b. W is a cubic interpolation kernel function that is evaluated for the distance (magnitude of the vector $\mathbf{r}_\mathrm{ab}$) between particles a and b. The kernel function and its properties are described in Monaghan (2005).

Conservation of momentum for elastic solids results in the following acceleration equation (Libersky and Petschek, 1991):

$$\frac{d\boldsymbol{v}_a}{dt} = \sum_b m_b \left(\frac{\boldsymbol{\sigma}_a}{\rho_a^2} + \frac{\boldsymbol{\sigma}_b}{\rho_b^2} + \Pi_{ab}\boldsymbol{I} \right) \cdot \nabla_a \boldsymbol{W}_{ab} + \boldsymbol{g}_a \tag{2}$$

where $\boldsymbol{\sigma}_\mathrm{a}$ and $\boldsymbol{\sigma}_\mathrm{b}$ are the stress tensors of particles a and b, respectively, Π_{ab} is an artificial representation of viscosity terms that result in both shear and bulk viscosity and $\boldsymbol{I}$ is the identity tensor. $\boldsymbol{g}_a$ is the body force on particle a which in this case is gravity. The elastic stress tensor can be partitioned into a pressure part and a deviatoric stress component with deviatoric stress tensor, $\boldsymbol{S}$, and pressure P:

$$\boldsymbol{\sigma} = -P\boldsymbol{I} + \boldsymbol{S} \tag{3}$$

We use a linear model for the elastic stress versus strain relationship which gives a relationship between the pressure P and the density, ρ, typically referred to as an equation of state:

$$P = c^2 (\rho - \rho_0) \tag{4}$$

where ρ_0 is the reference density. The speed of sound c in the solid material is given by

$$c = \sqrt{\frac{K}{\rho_0}} \tag{5}$$

where K is the bulk modulus.

From Gray et al. (2001) the evolution of the deviatoric stress **S** is given in component form as:

$$\frac{dS^{ij}}{dt} = 2G\left(\dot{\varepsilon}^{ij} - \frac{1}{3}\delta^{ij}\dot{\varepsilon}^{kk} \right) + S^{ik}\Omega^{jk} + \Omega^{ik}S^{kj} \tag{6}$$

where $\dot{\varepsilon}$ is the strain tensor, δ^{ij} is the Kronecker delta, Ω^{jk} is the Jaumann rotation tensor, G is the shear modulus and indices i, j and k refer to three orthogonal directions in 3D space. The Einstein summation convention is used.

The strain rate tensor is calculated in an SPH form as

$$\dot{\varepsilon}_a = -\frac{1}{2}\sum_b \frac{m_b}{\rho_b}\left[(\boldsymbol{v}_{ab}\nabla_a \boldsymbol{W}_{ab})^T + \boldsymbol{v}_{ab}\nabla_a \boldsymbol{W}_{ab} \right] \tag{7}$$

and the Jaumann rotation tensor is expressed as:

$$\Omega_a = \frac{1}{2}\sum_b \frac{m_b}{\rho_b}\left[(\boldsymbol{v}_{ab}\nabla_a \boldsymbol{W}_{ab})^T - \boldsymbol{v}_{ab}\nabla_a \boldsymbol{W}_{ab} \right]. \tag{8}$$

The SPH method, particularly for elastic solids, can display tensile instabilities (Monaghan, 2000). The tensile instability correction proposed by Gray et al. (2001) is used here with a coefficient of 0.3 to inhibit these instabilities. This choice follows detailed evaluation of the tensile correction for SPH modelling of elastic solids in uniaxial compression tests (Das and Cleary, 2014).

Smoothed Particle Hydrodynamics for Elastoplastic Dynamics

The results of the track tester experiments by Setterbo et al. (2013) show that both track materials demonstrate elastoplastic behaviour (see **Figures 1D,E**). A Drucker-Prager (D-P) model (Bui et al., 2008) is suitable for representing the dynamics of such elastoplastic materials. Details of the D-P model are given in Lemiale et al. (2012). The D-P model assumes the material to be initially elastic with a correction made to the pressure and deviatoric stress if any plastic deformation is predicted.

The D-P criterion for yielding is:

$$\tau - \alpha P \begin{cases} < k \text{ if elastic} \\ \geq k \text{ if yielding} \end{cases}, \tag{9}$$

where τ is the shear yield stress and is given by:

$$\tau = \sqrt{\frac{1}{2}S^{ij}S^{ij}} \tag{10}$$

α is calculated from the friction angle, φ:

$$\alpha = \frac{6\sin\varphi}{\sqrt{3}(3 - \sin\varphi)} \tag{11}$$

and k is the yield strength which is calculated from α and the cohesion, c.

$$k = \frac{6c\cos\varphi}{\sqrt{3}(3 - \sin\varphi)} \tag{12}$$

The plastic deviatoric stress, $\boldsymbol{S^P}$, is related to the elastic deviatoric stress, $\boldsymbol{S}$:

$$\boldsymbol{S}^{\boldsymbol{P}} = -\frac{G\triangle\lambda}{\tau^{e}}\boldsymbol{S} \tag{13}$$

The total deviatoric stress, S^T, is a sum of elastic and plastic stresses

$$\boldsymbol{S}^{T} = \boldsymbol{S} + \boldsymbol{S}^{P} = \left(1 - \frac{G\triangle\lambda}{\tau}\right)\boldsymbol{S} \tag{14}$$

The plastic component of pressure, P^P is given by

$$P^{P} = K\beta\triangle\lambda, \tag{15}$$

where linear hardening is assumed and $\triangle\lambda$ is the increment of plastic strain,

$$\triangle\lambda = \frac{\tau - \alpha P - k}{G + \alpha\beta K + \eta} \quad , \tag{16}$$

β is calculated from α and the dilation angle ϕ

$$\beta = \frac{6\sin\phi}{\sqrt{3}\left(3 - \sin\varphi\right)}, \tag{17}$$

and η is calculated from the hardening modulus H

$$\eta = \frac{6H\cos\varphi}{\sqrt{3}\left(3 - \sin\varphi\right)} \tag{18}$$

The total pressure P^T is a sum of elastic and plastic components.

$$P^{T} = P + P^{P} \tag{19}$$

A second order predictor-corrector (explicit) integration scheme is used (see Monaghan, (2005) for details) with timestep, δt, chosen to be one-fifth of the Courant condition for stability of elastodynamic simulations:

$$\delta t = \frac{0.1h}{c} \tag{20}$$

where h is the SPH interpolation length.

Interactions Between Smoothed Particle Hydrodynamics Particles and Boundaries

Solid boundaries are represented by triangular surface meshes. The nodes of the boundary mesh are represented in the SPH method as boundary particles with a penalty force applied in the normal direction. The force is calculated using a Lennard-Jones style form based on the orthogonal distance of the moving SPH particles from the solid surface (Monaghan, 1994). The penalty force replaces the pressure force terms in the momentum equation (**Equation 2**) for elastic-boundary particle pairs. Non-slip boundary conditions in the directions tangential to the solid surfaces are implemented by including the elastic-boundary SPH particle pairs in the summations for the artificial viscosity in **Equation 2**. For moving bodies, the nodal positions and the normal vectors are updated at each time-step to reflect the current position of the surface. This is a flexible boundary implementation that allows very complex solid boundaries (Cleary et al., 2006a; 2006b), moving boundaries (Cleary et al., 2007) and deforming boundaries (Cohen et al., 2012; Harrison et al., 2016b) to be modelled.

Prior Validation of the Smoothed Particle Hydrodynamics Method for Solid Mechanics Applications

SPH has been shown to produce valid predictions for a large range of complicated behaviours of solid matter undergoing processes like those considered in the present work. Validation of the SPH method for these processes include comparison against exact solutions (Gray et al., 2001) and FEM solutions for uniaxial, biaxial, and loading of elastic solids (Das and Cleary, 2008, 2014; Pereira et al., 2017; Rausch et al., 2017), simple loading of beams and tensile failure under uniaxial loading (Ganzenmüller, 2015), and the deformation and failure of thin shelled materials (Maurel and Combescure, 2008). Other validations involve the comparison of simulation results with experimental data, for instance for fracturing of soft tissue (Rausch et al., 2017) and ice (Zhang et al., 2017), and machine cutting of metals (Limido et al., 2007; Xi et al., 2014).

Prior Validation of the Smoothed Particle Hydrodynamics Code

It is not sufficient to rely on general validation of the SPH method. Additionally, it is necessary to validate the specific code implementation used. The implementation used in this study has been validated for simulations of elastic/elasto-brittle solids. Das and Cleary compared stress wave attributes calculated by the SPH code to those calculated using a commercial finite element (FE) code for uniaxial, biaxial and triaxial compression of an elastic object (Das et al., 2007; Das and Cleary, 2008, Das and Cleary, 2014). The SPH solutions were found to agree very well with analytical and FEM model solutions. SPH was shown to be stable and robust for elastodynamic applications, predicting a smoother response than the FEM code in the early stages of loading.

SIMULATION CONFIGURATIONS

Smoothed Particle Hydrodynamics Track Structure Models

The dirt and synthetic racetracks used by Setterbo et al. (2013) differed in their material type and geometric structure. The tracks were of different depths and below each track were hard substrate such as rock. Each track was harrowed prior to the measurement which causes the top region of the track to be aerated and therefore have a lower resistance to deformation. The dirt track had a depth of 0.5 m and was harrowed to a depth of 8.6 cm. The synthetic track was 0.26 m deep and was harrowed to a depth of 5.0 cm.

The developed models of each track were designed to specifically represent the track geometry, material behaviour and harrowing depth. The hard under-surface was modelled as

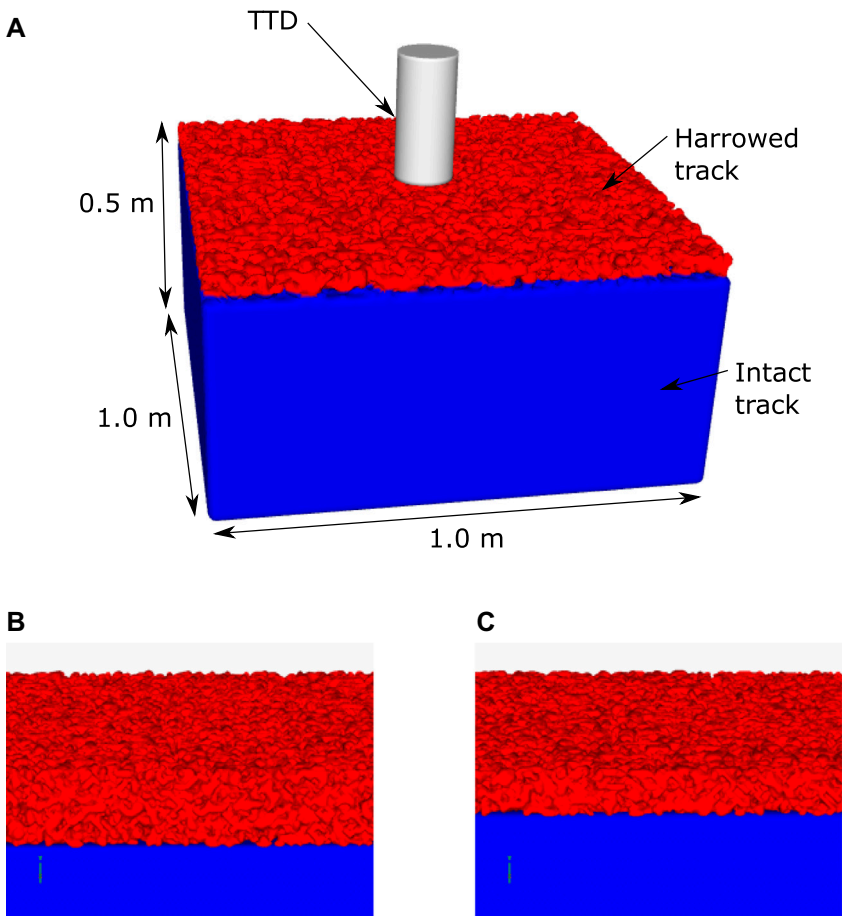

FIGURE 2 | Configuration of the simulation configuration for the track testing device. The configuration for the dirt track is shown in **(A)**. The top layer of the track has a large number of voids in the material to represent harrowing that is used to break up and soften the track surface. The track extends 0.5 m in depth, below which the ground is predominantly rock. The rock is modelled as a rigid boundary condition. The synthetic track has a depth of 0.26 m under which a rigid boundary condition is also used. Close-up views of the dirt track and synthetic track models are shown in **(B)** and **(C)** respectively, which show the non-smooth top surface created by harrowing. The track testing device (TTD) is dropped and the force and displacement are predicted by the simulation. These results are compared to the matching experimental measurements in order to calibrate the rheological component of the model for the deformation of each track surface.

a no-slip boundary. The aeration of the top section of the track by harrowing was modelled by randomly removing SPH particles from an initially densely packed array of particles to give a specific void space, which is the proportion of the volume that is air. The lower intact (non-harrowed) section remains solid, i.e. does not have any SPH particles removed. The geometric region modelled for the two track types are:

- For the dirt surface, a 0.5 m high x 1.0 m wide x 1.0 m long section of the track is discretised into 3.6 million SPH particles that are spaced at 5 mm. The harrowed region at the top is 8.6 cm deep.
- For the synthetic surface, a 0.26 m high x 1.0 m wide x 1.0 m long section of the track is discretised into 1.8 million SPH particles that are spaced at 5 mm. The harrowed region at the top is 5.0 cm deep.

Figure 2 shows the standard configuration of the calibration simulations for the two track types.

Rigid Body Model of the Track Testing Device

The TTD is a solid mass that is dropped onto the track surface during mechanical characterisation experiments (Setterbo et al., 2013). The device comprises a 27.8 kg, 12.7 cm diameter mass that, when dropped, travels down linear shafts until impact with the ground. It is represented in the model by a cylindrical mesh comprised of 1,700 nodes and 3,500 elements with average node spacing of 10 mm. The TTD is initially at rest with its lower surface at a height of 40.2 cm (Setterbo et al., 2013). The model TTD object is dynamically free to move in the vertical direction. External force on the TTD structure is calculated and the motion of the TTD in the vertical direction was predicted and recorded in each simulation.

Setup for the Horse Biomechanical Model

A model representation of one horse was developed using rigid body representations of the body limbs and a surface mesh representation of the hoof. Body kinematics were collected for the horse during a canter on the dirt and synthetic track surfaces

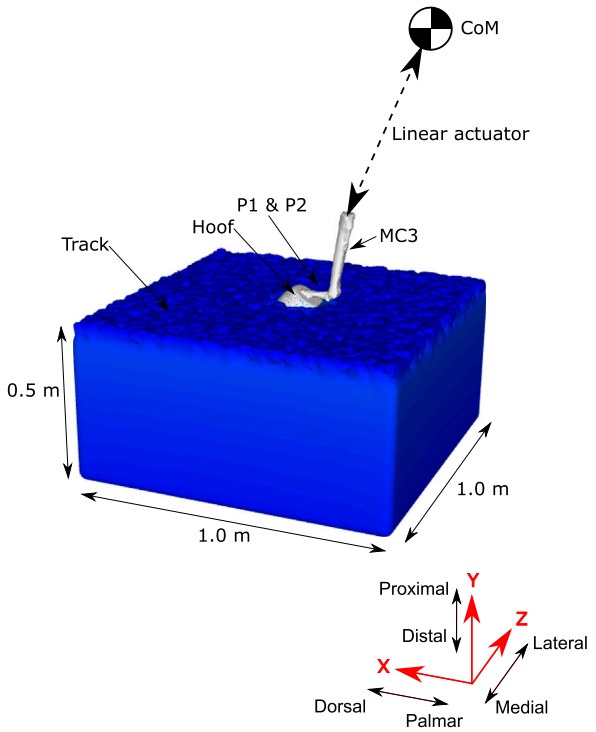

FIGURE 3 | Schematic of the forelimb skeletal model used to simulate hoof-track forces during locomotion. The SPH track model is the same as used for *Calibration of the Track Model Material Properties Using Data From the Track Testing Experiments* section. The forelimb is represented by surface meshes of the distal bones (for visualisation purposes) and the outside surface of the hoof. The position and orientation of the hoof is prescribed from motion capture data, but the vertical position of the hoof is predicted by the simulation.

(Symons et al., 2014). A generic geometric model of a hoof was developed from CT scans (850 node mesh and 1,700 triangular elements, average node spacing of 10 mm) (Harrison et al., 2014) and modified to include geometric representations of the shoes used during the experiments (Symons et al., 2014). Inertial effects from the limbs not in contact with the ground were assumed to be negligible and will be the subject of future investigations. A four-segment skeletal model was used to represent the dynamics of the body (see **Figure 3**). The vertical position of the centre of mass (CoM) was predicted by the simulation. The remaining translational and rotational degrees of freedom of the CoM and the rotation of the lower limb joints were prescribed from the kinematic data. The position and orientation of the hoof mesh was calculated at each time step from the skeletal model configuration.

EVALUATION OF THE ACCURACY OF SMOOTHED PARTICLE HYDRODYNAMICS FOR SOLID MECHANICS APPLICATIONS

Here we specifically validate the SPH track model by first determining the resolution of the SPH representation of the track required for accurate predictions and then by comparison of simulation results to:

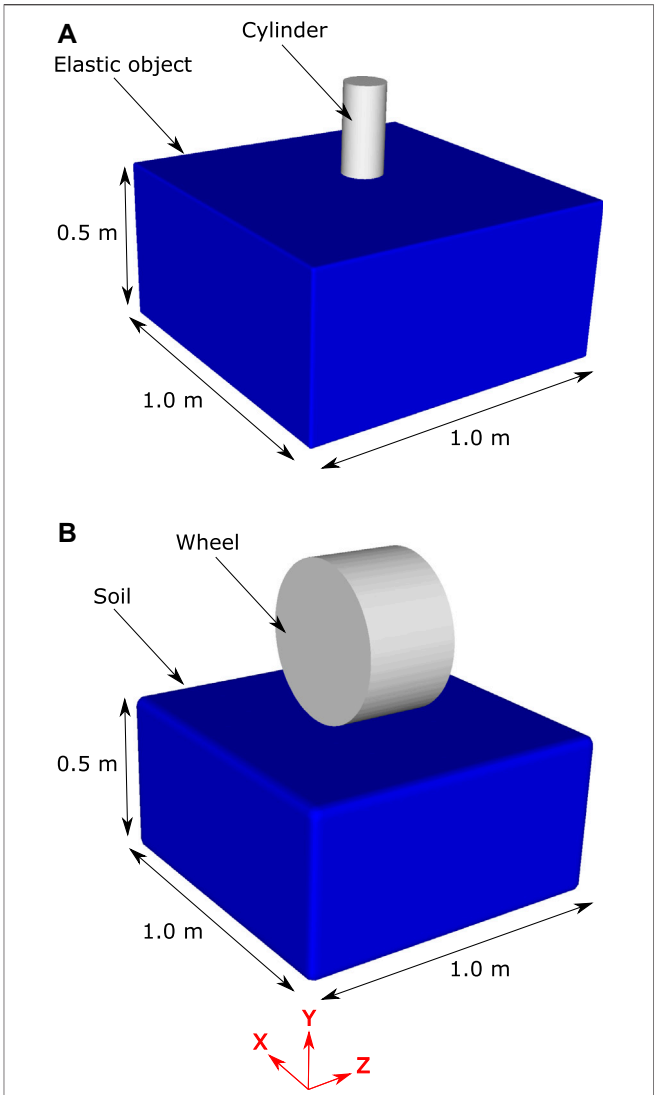

FIGURE 4 | The two simulation configurations used in the verification and validation analysis. Panel **(A)** shows the configuration for cylindrical indentation of an elastic solid "soil". Panel **(B)** shows the configuration for the indentation of an elastoplastic solid by a rigid wheel.

1. An analytical model for cylindrical indentation of an elastic object
2. An analytical model for indentation of a rigid wheel into a cohesive elastoplastic object with a negligible friction angle
3. A finite element (FE) model of indentation of a rigid wheel into an elastoplastic object with a large friction angle.

Cylindrical indentation of an Elastic Object

According to Sneddon (1965), assuming quasi-static loading (i.e. negligible inertial and gravity effects), the gradient of the force-displacement curve for small displacements (<5% of the cylinder diameter) is:

$$s = \frac{2GD}{(1-\upsilon)}, \tag{21}$$

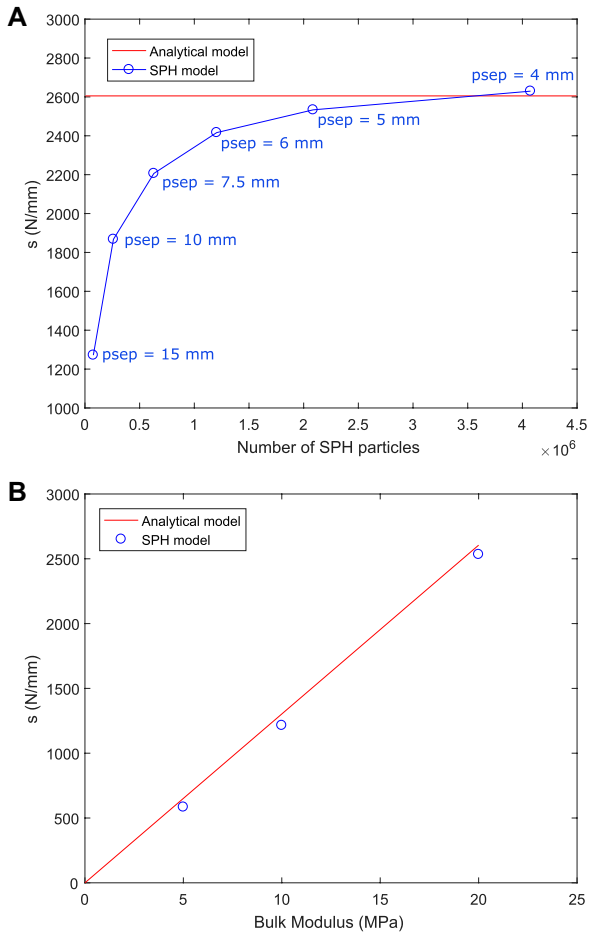

FIGURE 5 | (A) Predicted slope of the force-displacement curve for the cylindrical indentation simulation for different SPH resolutions, compared to the analytical model result. Particle separations (psep) of 4–15 mm were used in separate simulations of the indentation problem. The simulation results can be considered converged in respect to particle size and verified against the analytical model for a particle size of 5 mm or smaller. **(B)** Predicted slope of the force-displacement curve for the cylindrical indentation simulation for different values of bulk modulus, compared to the analytical model result for an SPH resolution of 5 mm.

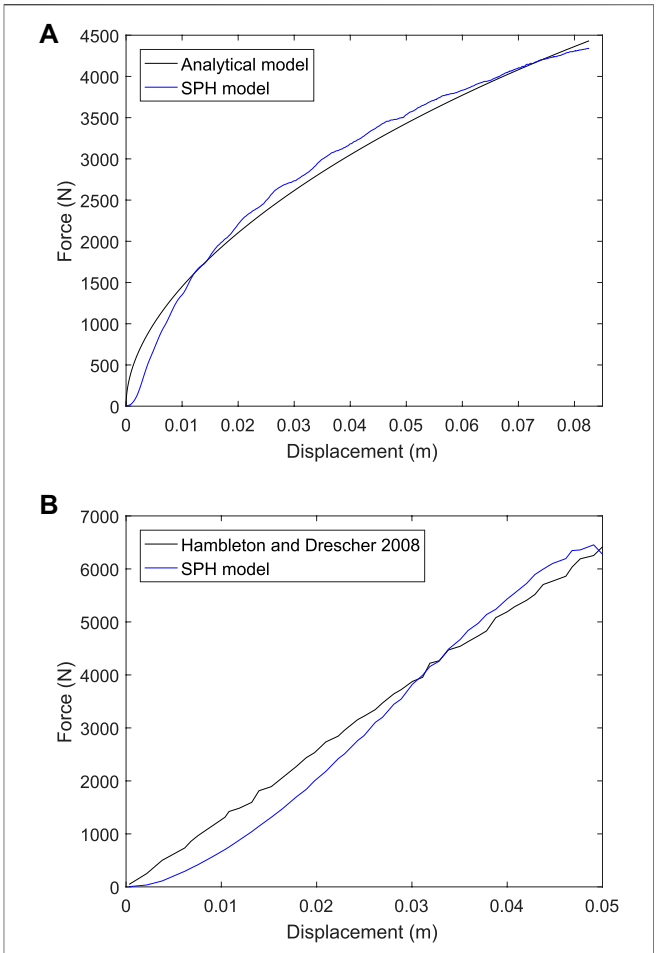

FIGURE 6 | Force-displacement results from simulations of wheel indentation into **(A)** a cohesive soil, and **(B)** a frictional soil from (Hambleton and Drescher, 2008) and for the current SPH model.

where s is the gradient of the force-displacement curve, D is the diameter of the cylinder, G is the shear modulus of the track surface, and v is the Poisson ratio of the track surface.

The simulation configuration is shown in **Figure 4A**. The elastic soil model is of dimensions 1.0 m × 0.26 m x 1.0 m and is represented by 1.8 million SPH particles that are spaced at 5 mm. All degrees of freedom of the SPH particles on all sides of the object except the top are fixed. The top surface of the elastic object is indented by a cylindrical shape in the form of a triangular mesh comprised of 1700 nodes and 3,500 elements. The indentor has a prescribed vertical velocity of 0.5 m/s and is initially positioned adjacent to the top surface of the elastic object. External force on the surface of the cylinder was recorded and the gradient of the simulated force-displacement results was compared to the analytical model for a range of SPH particle resolutions and three variations of elastic modulus.

Simulation predictions of force and displacement were used to calculate the slope, s, in **Eq. 21**. **Figure 5A** shows the simulation prediction of s for SPH resolutions from 15 mm down to 4 mm. There are substantial differences in the results with range from 15 to 6 mm, but the results between 6 and 4 mm cases are very similar. There is a demonstrable convergence of results as particle size is decreased with the differences between the 5 and 4 mm case being sufficiently small (<5%) to justify the use of the 5 mm case for the remainder of the simulations. The smaller SPH particle size results converge to the value expected from the analytical model which verifies predictive behaviour of the SPH method and software for this configuration. **Figure 5B** shows the value of s predicted by the SPH model and by analytical model for three cases of bulk modulus for the cylindrical indentation simulation. There is very good agreement between the SPH and analytical models, confirming that the model is accurate across a wide range of elastic moduli.

Indentation of a Rigid Wheel into Elastoplastic Soil

The SPH track model includes both elastic and plastic behaviour and the plastic model component must also be validated. Hambleton and Drescher (2008) presented an analytical model for a rigid wheel indenting soil with a negligible friction angle (which they termed a cohesive soil) and an FE model for a rigid wheel indenting soil with a large friction angle (which they termed a frictional soil).

Here we compare the results of the SPH track model to these two elastoplastic soil models. **Figure 4B** shows the SPH representation of the wheel indentation model published by (Hambleton and Dresher, 2008). A rigid wheel of diameter 0.5 m and thickness 0.3 m is positioned above a bed of SPH particles with dimensions: 0.5 m high x 1.0 m wide x 1.0 m long. The soil is represented by 150 thousand SPH particles that are spaced at 15 mm. The bulk and shear moduli of the soil are 4.1 and 1.9 MPa respectively. For the cohesive soil the cohesion is 6.1 kPa and the friction angle is 0°. For the frictional soil the cohesion is 61 Pa and the friction angle is 45°.

Comparisons of the force-displacement results from the SPH model with those of (Hambleton and Dresher, 2008) are shown in **Figure 6**. Results for a cohesive soil are shown in **Figure 6A**. Very good agreement is observed with a root mean squared error (RMSE) of only 132 N, which is 3% of the maximum force. Results for a frictional soil are given in **Figure 6B**. Good agreement is seen between these and the FE model results of (Hambleton and Dresher, 2008). The RMSE is 390 N, which is an acceptable 6% of the maximum force. These results confirm that the SPH D-P model can sufficiently accurately predict the response of plasticity in soils of the type used in horse racing.

CALIBRATION OF THE TRACK MODEL MATERIAL PROPERTIES USING DATA FROM THE TRACK TESTING EXPERIMENTS

Force-Displacement Data Measured by the Track Testing Device

Figures 1D,E shows the force-displacement results reported in Setterbo et al. (2013) for dirt and synthetic tracks. In each case the force trace rises slowly soon after contact and then rises sharply before peaking and dropping to zero quickly. The substantially different loading and unloading force traces indicate an elastoplastic response for both tracks. The force for the dirt track is less than for the synthetic track for small displacements but increases more sharply at large displacements resulting in a higher peak force. Despite the controlled nature of the impact there is a large amount of variability in data from repeats of the experiment, which suggests that the material is significantly inhomogeneous. During gait, the path and velocity of the hoof may vary significantly between strides and these effects combined suggest that stride-to-stride loading on the hoof could vary substantially.

Calibration Method

SPH models of the dirt and synthetic tracks, as characterised by Setterbo et al. (2013), were constructed and calibrated. First, the geometry of each track was represented by specific simulation configurations (see *Smoothed Particle Hydrodynamics Track Structure Models*). Second, the elastic material properties of the track models were estimated from the TTD experiment results using an analytical model for cylindrical indentation (described in *Cylindrical indentation of an Elastic Object*). Third, the friction angle D-P material parameter was estimated using a characterisation of similar track materials from another study (Peterson et al., 2016). Fourth, TTD impact simulations were performed for each track surface for a vertical and 20° from vertical impact. Force-displacement results from the simulations were then compared to the measurements of Setterbo et al. (2013). The material parameters were iteratively adjusted to find an acceptable fit between model and experimental results.

Deformation Behaviour

The TTD model material parameters were calibrated using the data from Setterbo et al. (2013) (**Figures 1D,E**). These material properties are listed in **Table 1**. **Figure 7** shows deformation behaviour for the calibrated dirt track model in the virtual TTD test for a vertical impact (left columns) and an impact at 20° off-vertical alignment. For the vertical impact, the TTD contacted the track after 22 ms and a small vertical force is transmitted from the track surface into the TTD. Stresses in the harrowed section of the track directly below the TTD are substantial (>1 MPa) and the TTD compressed approximately half of the harrowed thickness of track. At 30 ms, the TTD has compressed the harrowed section of the track and as a result substantial stresses are induced in the non-harrowed section of the track below. At 40 ms, the TTD rebounds upwards and the stresses in the track and the force transmitted to the TTD decline.

For the 20° off-vertical impact on the dirt track (**Figure 7**, right column), the stress under the TTD is higher under its lead side due to its greater penetration of the track (**Figure 7D**). The force is lower for the 20° angle impact (**Figure 7D**) than for the vertical impact (**Figure 7C**) at an equivalent of track penetration. This results in a smaller deceleration of the TTD for the angled impact compared to the vertical impact and therefore a later peak in force. The peak force occurs at 38 ms for the angled impact and the force is directed approximately through the centreline of the TTD. Between 38 and 50 ms, the TTD rebounds and stresses decay to zero.

Figure 8 shows deformation behaviour for the simulated TTD experiment for the calibrated synthetic track model. At 14 ms, the TTD contacted the track and a moderate vertical force is transmitted from the track onto the TTD. Stresses are less than 500 kPa and the deformation of the track is small. At 24 ms, the TTD has penetrated the track and substantial stresses have been induced in the track spreading radially from the TTD-ground contact surface. The peak force occurs at 24 ms, which is 6 ms earlier than for the dirt track. The stresses in the track are smaller than for the dirt track at maximum displacement. From 24 to 34 ms, the TTD rebounds upwards and

TABLE 1 | Calibrated elastic and D-P material parameters for the SPH model of each track material.

Material property	Dirt (harrowed)	Dirt (intact)	Synthetic (harrowed)	Synthetic (intact)
Depth of material (cm)	8.6	41.4	5	21
SPH resolution (mm)	5.0	5.0	5.0	5.0
Bulk modulus, K (MPa)	80	80	30	30
Shear modulus, G (MPa)	27	27	10	10
Cohesion, c (Pa)	2,500	2,500	250	250
Friction angle, φ (degrees)	45	45	45	45
Dilation angle, ϕ (degrees)	5	5	5	5
Harrowing (percentage material removed)	70%	0%	65%	0%

the stresses in the track and the force imparted to the TTD decline. Similar to the dirt simulations, the angled impact produces higher stresses under the lead side of the TTD (**Figures 8D,F,H**). Peak force occurs 4 ms later than for the vertical impact due to the smaller contact area causing lower decelerating forces.

The complexity of the transient stress fields and the non-linear behaviour of the TTD motion highlight the strong need to include realistic predictions of the ground deformation and force response as opposed to using highly simplified spring-based interaction models.

Calibrated Material Properties

Figure 9 shows the calibration curve for each track type for both the vertical and 20° from vertical impact experiments. Model predictions agreed well with the experimental results for both cases, especially for the initial loading response of the synthetic track and the peak force. This good agreement across different loading scenarios shows that a three-dimensional model can successfully represent the effects of different material properties, effects of harrowing (and the resulting void space in the upper region of track) and types of impacts without any changes to the underlying model. The unloading phase is moderately less well predicted by the model, suggesting that there is opportunity for further improvements such as taking account of the granular nature of some of the material and the rheological accuracy of the viscoelastic and/or plastic components of the model. Since peak loads are likely substantial contributors to injury, this level of accuracy is more than sufficient for the current purpose.

Table 1 lists the calibrated material parameters for the harrowed and non-harrowed (intact) sections for the SPH track models. The peak force transmitted to the TTD is higher for the dirt track than the synthetic track because it has a larger bulk modulus and cohesion. The softer initial response of the dirt track compared to the synthetic track occurs due to the higher void space of the harrowed track (70% void volume for the dirt track as compared to 65% for the synthetic track) and the larger depth of harrowing (8.6 cm for the dirt track as compared to 5 cm for the synthetic track). The dilation angle was found to have little effect on results and so the same values were used for both track surfaces.

SENSITIVITY OF TRACK IMPACT RESPONSE TO TRACK POROSITY AND ELASTOPLASTIC MATERIAL PARAMETERS

A first step towards using the track surface model for reducing racehorse injury is to understand the relationship between model results and variations in each model parameter. The D-P model has been used for simulating the mechanical response of soil during impact and landslides (Bui et al., 2008; Lemiale et al., 2012; López et al., 2012), but it has not previously been used to investigate loading on a body during exercise. Therefore, a sensitivity analysis was performed to determine the relative effect of each parameter on model results. The investigated material parameters included bulk modulus (K), cohesion (c), friction angle (φ), and the degree of porosity created by harrowing. **Table 2** shows the ranges of the parameters investigated for each track type. In each simulation case the simulation parameter values were as described in **Table 1**, except for the one parameter being evaluated which was changed to the value indicated in **Table 2**. The outputs of each sensitivity analysis include the maximum displacement of the TTD, the gradient of the force-displacement curve during loading and the peak force.

Figure 10A and **Figure 10B** show the effect of changes to bulk modulus on the dynamic response of the two D-P track models. Increased bulk modulus increases the slope of the force trace for both the loading and unloading phases of the impact. The maximum displacement of the TTD is decreased for larger bulk modulus because force per unit displacement is increased leading to larger decelerating forces being imparted to the TTD. The peak force increases monotonically with increased bulk stiffness for the synthetic track, but not for the dirt track because the nonlinear effects of plastic flow (especially for the harrowed component) cause different force-displacement responses.

Figure 10C and **Figure 10D** show the effect of changes to cohesion parameter on the dynamic response of the D-P track models. An increase to cohesion substantially increases the force at initial impact and increases the peak load. The regions of track material below the TTD with stresses above the cohesion limit plastically flow away from the TTD, reducing the resistance to compression and therefore the load transmitted onto the TTD. Thus, maximum displacement is decreased when cohesion is increased. Increasing the load on the TTD leads to decreases in the duration of impact and the maximum displacement.

Force-displacement results are found to be sensitive to the friction angle (**Figure 11A,B**). **Equations (9–12)** show that friction angle controls the yield criteria and therefore affects whether the track responds to force with an elastic or plastic response. Increased friction angle increases the stress at which yielding occurs and as a result the track behaves elastically for longer and allows higher forces before yielding. The slope of the

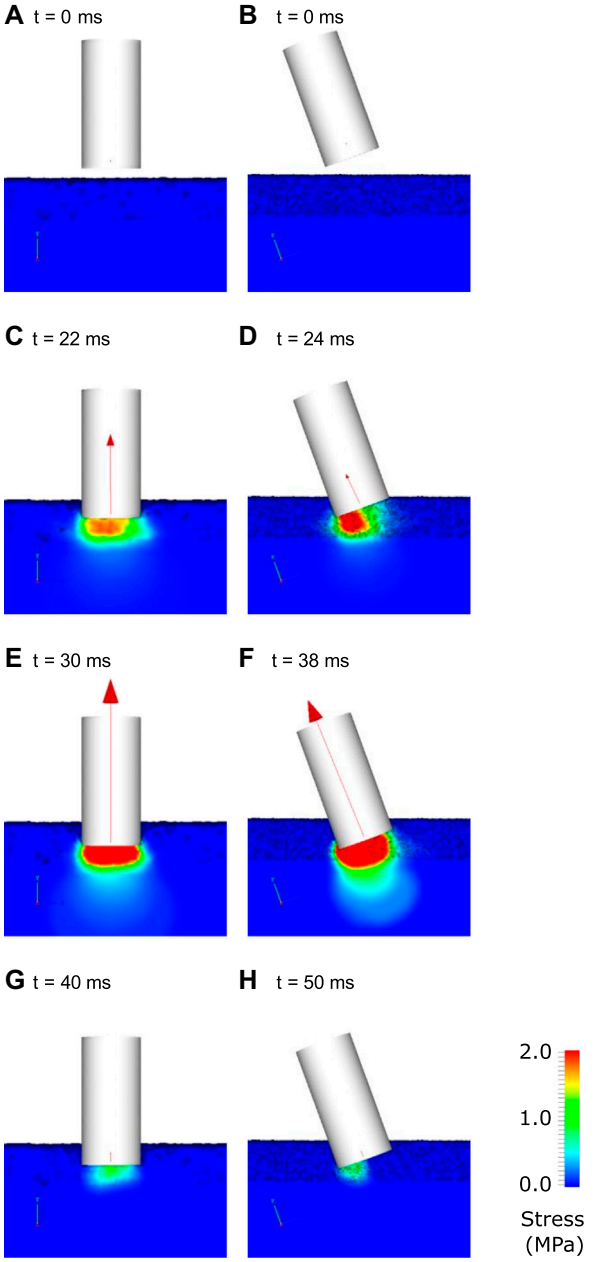

FIGURE 7 | Visualisation of the interaction of the track testing device with ground for the case a dirt track. The left columns show the results for a vertical impact and the right column shows results for an angled impact. The track is coloured by von Mises stress at various times indicated by labels **(A–H)**. The net force on the TTD is shown as a red vector.

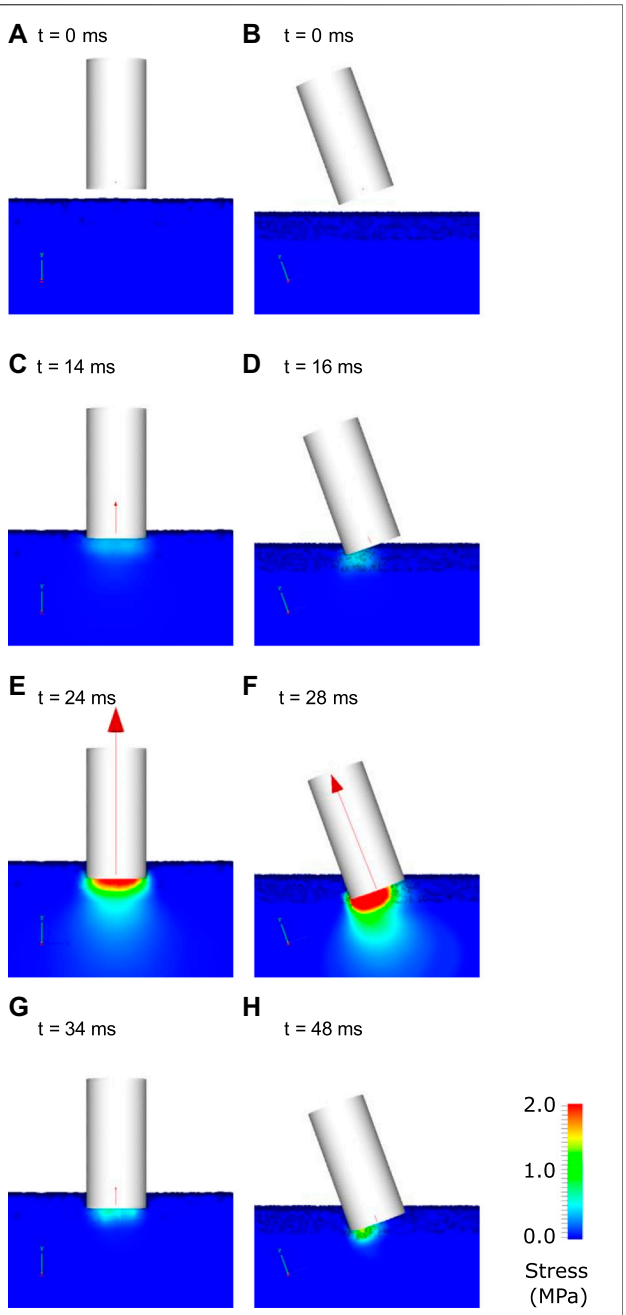

FIGURE 8 | Visualisation of the interaction of the track testing device with ground for the case a synthetic track. The left columns show the results for a vertical impact and the right column shows results for an angled impact. The track is coloured by von Mises stress at various times indicated by labels **(A–H)**. The net force on the TTD is shown as a red vector.

force-displacement curve (which is the effective stiffness of the track) is higher during loading with the peak displacement decreasing and peak force increasing (as should be expected).

The porosity of the top surface of the track following harrowing has the largest effect on the force-displacement results during impact (**Figure 11C,D**). Symons et al. (2016) also showed that harrowing has the highest influence on predicted force results using a 2D musculoskeletal model coupled to a 1D ground model. Porosity is quantified by a measure called void space, which is the proportion of the volume that is air. Increased void space in the top layer decreases the effective stiffness of the material and increases its ability to flow under load. As a result, an increase to the amount of modelled harrowing (and therefore void space) has a similar effect, simultaneously reducing both the bulk modulus

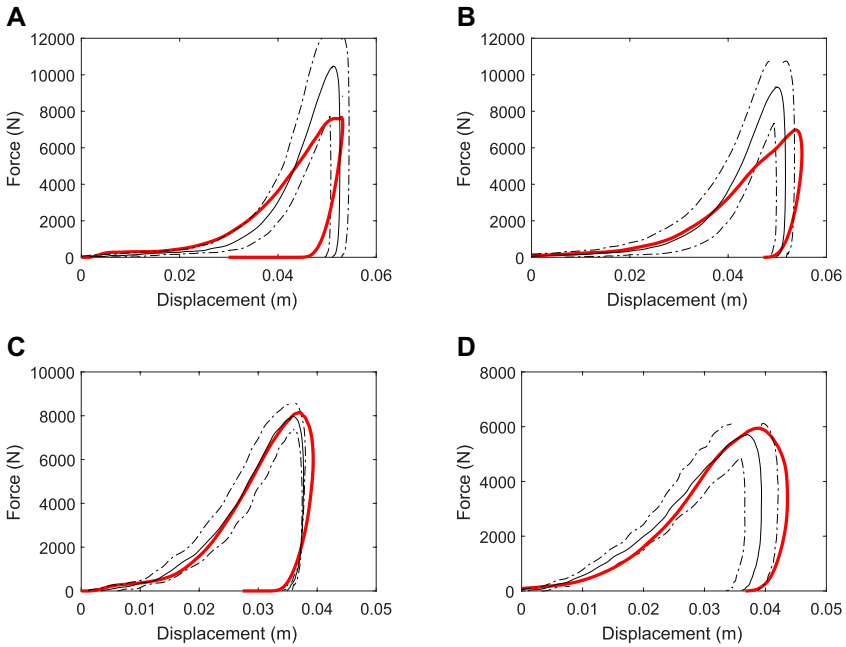

FIGURE 9 | Variation of force-time results for simulations using the calibrated material parameters of the **(A,B)** dirt, and **(C,D)** synthetic tracks. Results for the vertical impact are shown in the left column (A, C) and for the 20° from vertical impact are shown in the right column (B, D). The experimental data is shown as mean (solid black line) ± standard deviation (dashed black lines) and the simulation data is shown as a red solid line.

TABLE 2 | Variations in material parameters considered in sensitivity study.

	Dirt track			Synthetic track		
Parameter	Low	Baseline	High	Low	Baseline	High
Bulk modulus, K (MPa)	50	80	100	20	30	40
Cohesion, c (kPa)	0.25	2.5	25	0.025	0.25	2.5
Friction angle, φ (degrees)	25	45	65	35	45	55
Harrowing (percentage material removed)	60	70	80	60	65	70

and cohesion. Specifically, this substantially reduces the initial impact force and increases the maximum displacement and duration of impact. The penetration distance observed in experiment cannot be matched by the model if the void space is less than 70% for the dirt track (**Figure 11C**) and 60% for the synthetic track (**Figure 11D**). The void space of these harrowed tracks has not been measured, so it is not currently possible to evaluate these estimations of porosity.

APPLICATION OF THE BIOMECHANICS-SMOOTHED PARTICLE HYDRODYNAMICS TRACK SURFACE MODEL TO EQUINE LOCOMOTION

The motivation of the current work is to be able to simulate equine locomotion on racetrack surfaces to better understand the relationship between racetrack mechanical properties and loading at common injury sites in the distal forelimb. So as a final step we use the calibrated track surface model interacting with the horse limb biomechanical model to calculate loading on the fore-hoof for three cases of horses cantering on the same dirt and synthetic surfaces.

Simulations were run using openMP parallelisation over 36 cores and took 12 and 5.5 h for the dirt and synthetic surfaces, respectively. The difference in time taken for each simulation is directly attributable to the difference in bulk modulus between the two tracks models (**Table 1**), which determines the required timestep (**Equation 20**). The dirt material has a higher bulk modulus, therefore a smaller timestep, and thus more timesteps (and more computational time) to complete the full simulation.

Visualisations of typical results for the coupled B-SPH track surface model results are shown in **Figure 12**. They are for one phase of the horse stance (the period in which one forelimb hoof is in contact with the ground). Initially, the hoof is above the ground and moving downwards. Stresses in the track are

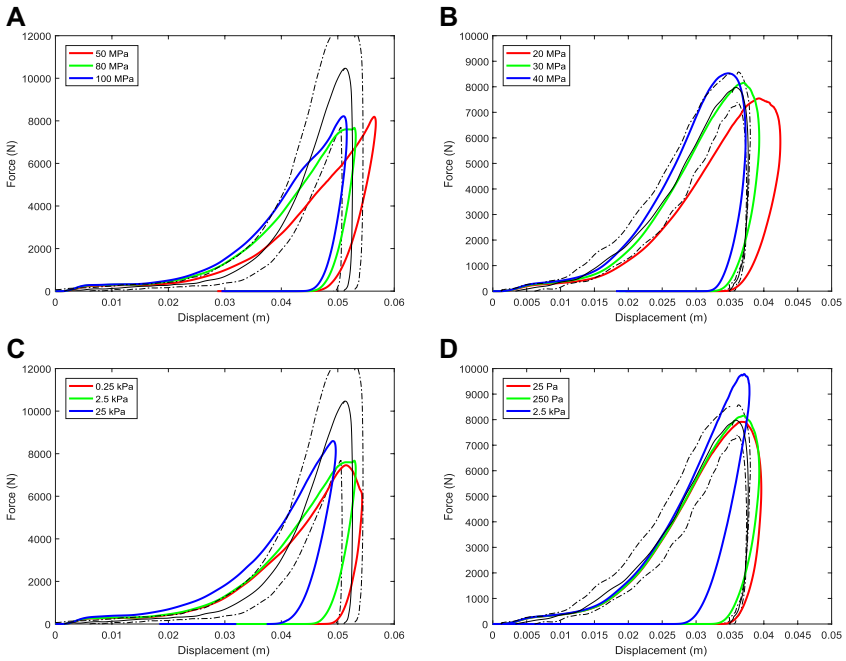

FIGURE 10 | Variation of force-displacement results for the simulated track testing device with changes to **(A,B)** bulk modulus and **(C,D)** cohesion parameters of the track. Results for the dirt track are shown in the left column (a, c) for the synthetic track are shown in the right column (b, d).

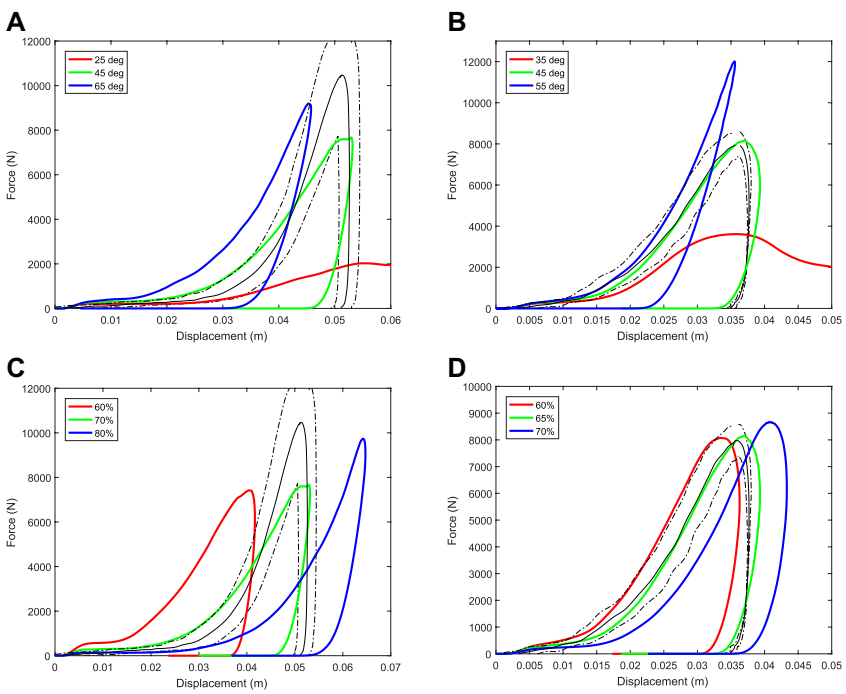

FIGURE 11 | Variation of force-displacement results for the simulated track testing device with changes to **(A,B)** the friction angle parameter and **(C,D)** variations to the void space (or the volume proportion of air) in the harrowed upper section of track of the track. Results for the dirt track are shown in the left column (a, c) for the synthetic track are shown in the right column (b, d).

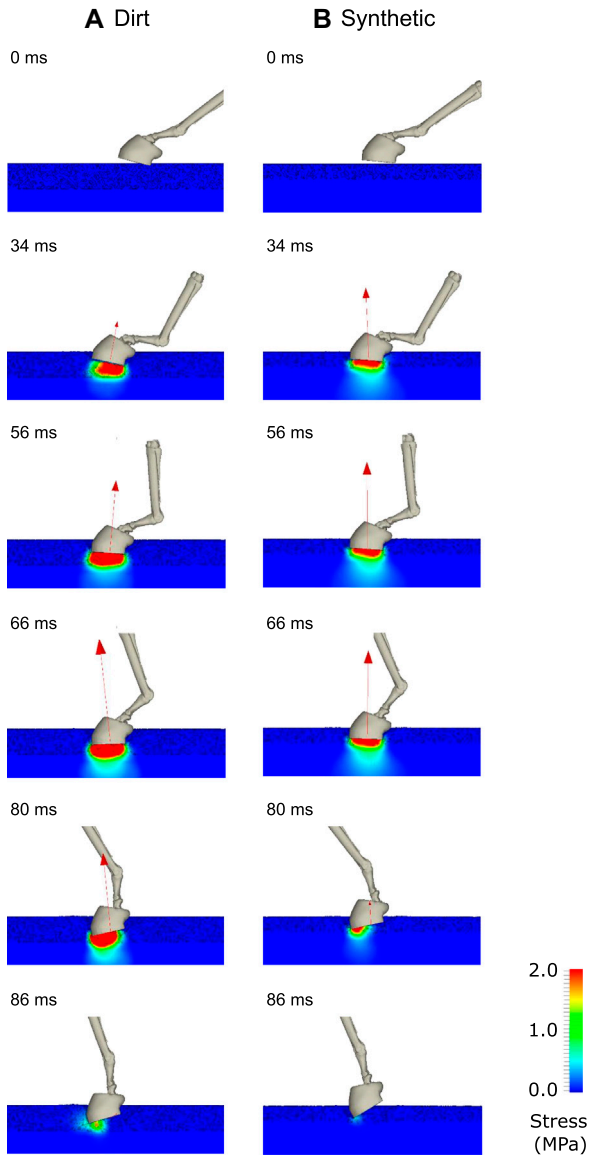

FIGURE 12 | Visualisation of the gait simulations using the coupled B-SPH model for **(A)** the dirt track and **(B)** the synthetic track. The bones of the distal limb and the outside surface of the hoof are shown in each instant. The ground reaction force is shown as a red vector. The track surface is coloured by von Mises stress.

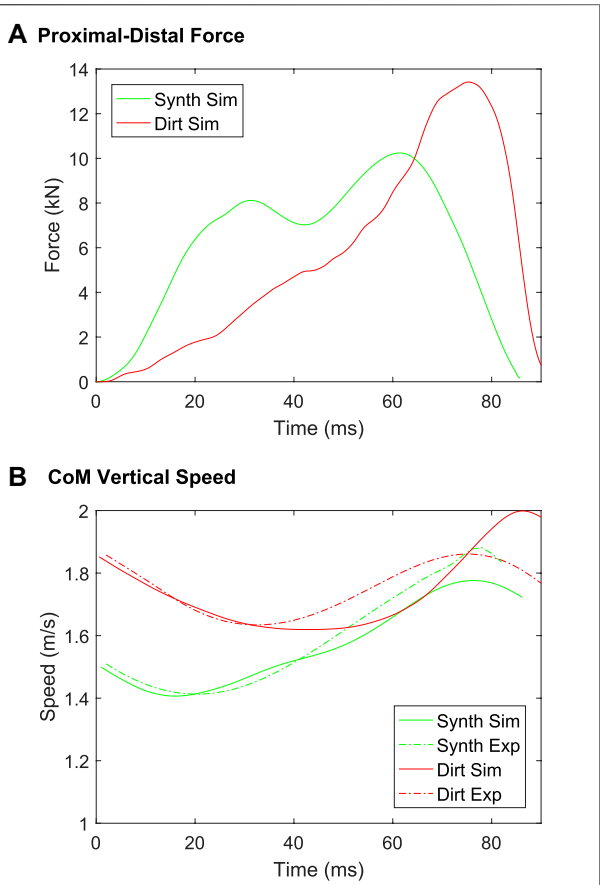

FIGURE 13 | B-SPH model predictions of **(A)** ground reaction force and **(B)** centre of mass (CoM) speed in the proximal-distal (vertical) direction, for the synthetic and dirt track surfaces.

approximately zero (shown by the blue colour) since it is unloaded and in hydrostatic equilibrium.

At 34 ms, the downward moving hoof has made contact with the track surface. The harrowed track material (with visible voids) below the hoof experiences medium stress levels (light blue and green colours) as it compresses. The synthetic track (right) has a smaller harrowed depth (**Table 1**) and therefore (for a similar compressive displacement) has higher compressive stresses. The ground reaction force (GRF) vector is larger for the synthetic track than for the dirt track because of the higher stresses at this time in the stance phase. Yielding of the harrowed material occurs and the resulting plastic flow creates a footprint in the track. Negligible stress is transmitted to the non-harrowed material below the hoof because of the plastic flow of the intervening harrowed material. Between 56 and 80 ms, the stresses in the harrowed material increase in magnitude and the depth of the footprint increases. As the harrowed material below the hoof compresses, voids collapse leading to greater stress transmission, which allows stress to be transmitted through the non-harrowed basal material. The GRF increases substantially in magnitude once the harrowed material is largely compressed.

Since the dirt track has a larger depth of harrowing than the synthetic track, the increase in GRF occurs at a slower rate. Between 80 and 90 ms, the stance phase is completed and the hoof is lifted off the ground. This occurs earlier for the synthetic track than the dirt track because forces were imparted earlier (due to the lower amount of harrowing). As with the results of the previous section, the amount of harrowing appears to be the most significant factor contributing to the mechanical response of the hoof-track interaction.

The model predictions of vertical ground reaction force and centre of mass speed are shown in **Figure 13**. The force for the synthetic track rises more quickly than for the dirt track, but

peaks at a smaller force level than occurs for the dirt track (**Figure 13A**). The apparent softness of the dirt track early in the stance phase arises predominantly from the porosity of the structure and once compressed the material is less forgiving (from a stress transmission and peak force perspective for the horse). After the harrowed layer is sufficiently compressed and stresses are fully transmitted to the non-harrowed material, the force in the dirt track is higher than for the synthetic track. This occurs because the bulk and shear moduli are higher for the dirt track than for the synthetic track (**Table 1**). The large vertical forces predicted by the model will create very large flexion-extension torques about the distal joints, especially the fetlock joint, which are implicated in high joint stresses and elevated injury risk (Harrison et al., 2014). These model results show how hoof impact loading can be moderated by effective track surface design. Specifically, they show that changes in track elastic modulus and harrowing depth can affect both the loading rate and the peak amount of force imparted onto the hoof and therefore into the horse's forelimbs. It is unclear however what type of track response is most suitable for reducing risk of musculoskeletal injury in the racehorse and this will be the focus of future applications of the musculoskeletal model.

Figure 13B shows a comparison of the vertical speed of the centre of mass as measured (from Symons et al., 2014) and as predicted by the B-SPH model. For both the dirt and synthetic tracks the measured and predicted speed during decelerating phase matches well (0–40 ms for the dirt track, 0–25 ms for the synthetic track). The agreement is moderately good for the synthetic track throughout the stance phase. The model predicts the upward movement of the centre of mass (40–80 ms) with lesser agreement for the dirt track. The results of Setterbo et al. (2013) show that there are large variations in force magnitude for the dirt track, especially for high levels of penetration depth. Considering the variation in the experimental results, we consider our predictions of ground reaction force and centre of mass speed to be sufficiently accurate for purpose.

Many aspects of these simulations can be compared to the work by others. Behnke (2018) used a 2D FE model to simulate the response of hoof-ground contact on asphalt and sand which was then used to calibrate a simple spring-dashpot model of the interaction. Limb dynamics (joint angle changes) were ignored. Their predictions for peak vertical forces were almost identical for the different surfaces. Symons et al. (2016) used a sequence of spring-dashpots and a dynamic limb model to evaluate the MCP joint angle on dirt and synthetic tracks. They predicted higher MCP joint angles, indicating high ground reaction forces (McGuigan and Wilson, 2003), for the dirt track than for the synthetic track. Our model predictions better agree with Symons et al. (2016) than the simpler model of Behnke, specifically that the peak vertical force is different for different surfaces (**Figure 13A**). Others have shown that SPH is effective for replicating soil behaviour due to its ability to deal with complex moving and deforming boundaries and the plastic flow of solid materials (Bui et al., 2008; Li et al., 2018; Wang et al., 2019).

FUTURE MODEL EXTENSIONS

Many aspects of the model will be extended for greater utility in understanding distal limb injury. Currently the model does not include the dynamics of all four limbs and this may contribute small amounts of error to both the predictions of ground reaction force and body dynamics. The model will be extended to include all body joints and their effects on body dynamics. Joint angles are prescribed from 2D kinematic measurements for specific track surfaces in the present study which precludes the model's use for novel surface conditions. Joint angles will be predicted in future work from the load transmission between muscles, tendons, ligaments, and external forces. Stresses in the bones, cartilage, muscles, tendons, and ligaments can be predicted simultaneously by representing these structures using an SPH or FE approach, extending the ability for the modelling framework to investigate the cause of injury or disease in specific regions of the distal limb.

CONCLUSION

A coupled B-SPH model of horse interaction with track surfaces is presented, which combines three-dimensional representations of the track (included the effects of harrowing), elastic and plastic deformation, the dynamics of the horse's body, and the interactions between the track and the hoof. Being fully predictive, the model can be used to investigate the relationship between track surface properties and limb loading and may provide insight into the cause of common distal limb injuries.

The SPH track deformation model is validated by comparison to analytical models and finite element model results from the published literature. A particle resolution convergence analysis verifies that an SPH particle size of 5 mm is sufficient for accurate predictions of elastic and plastic dynamics. Validation analyses show that both the predicted elastic and plastic response of the track are sufficiently accurate.

The track model is calibrated for use with two different track surface types: dirt and synthetic (all weather). Previous experiments are reproduced *in silico* including the geometric structure of each track and the testing device. Elastic and plastic material parameters are determined by iteratively modifying them to produce an acceptable match between simulation predictions and experimental measures of force and displacement. The calibrated values of bulk and shear modulus are found to be higher for the dirt track than for the synthetic track. This difference in elastic properties is then identified as the cause of higher impact forces observed for the dirt track.

A sensitivity analysis is presented to demonstrate how such a predictive model can provide new insight into the way in which track modifications might reduce loading and presumably therefore injury risk. The analysis shows that the amount of track harrowing has a larger effect on loading during impact testing than any other factor. This result has been suggested by others with a different modelling framework (Symons et al., 2016). Variations in elastic modulus, cohesion and friction angle have a smaller, but still considerable, effect on model

results and changes to dilation angle has a negligible effect on results.

Finally, the coupled B-SPH model is applied to equine locomotion over two track surfaces to demonstrate its use for investigating limb loading during racing-type gait. The rate of loading of the hoof during initial impact is higher for the synthetic track than for the dirt track, due to its lower porosity (or lesser harrowing). The peak force on the hoof is higher for the dirt track because the harrowed tracks are fully compressed by the hoof at the timing of each peak (thus eliminating the differences in harrowing between the tracks), and the elastic moduli and cohesion are both higher for the dirt track. Model predictions of vertical centre of mass speed are reasonable considering the variance of track material response. In future work, the model will be used to calculate tendon forces and joint stresses, and to predict gait responses to changes in track material properties so as to elucidate the relationship between track surface properties and injury risk.

DATA AVAILABILITY STATEMENT

The datasets presented in this article are not readily available because of the very large size of simulation results files and the proprietary data format used. Requests to access the datasets should be directed to SH.

ETHICS STATEMENT

The animal study was reviewed and approved by UC Davis Institutional Animal Care and Use Committee. Written informed consent was obtained from the owners for the participation of their animals in this study.

AUTHOR CONTRIBUTIONS

All authors contributed to the design of the study and the writing of the manuscript. SH performed the simulations and generated the figures.

FUNDING

This study received funding from Racing Victoria Limited and the Victorian Racing Industry Fund of the Victorian State Government. The funder was not involved in the study design, collection, analysis, interpretation of data, the writing of this article or the decision to submit it for publication. Funding was also received from the University of Melbourne and the Commonwealth Scientific and Industrial Research Organisation (CSIRO).

REFERENCES

Akbari Shahkhosravi, N., C. R. Bellenzani, M., M. S. Davies, H., and Komeili, A. (2021a). The Influence of Equine Limb Conformation on the Biomechanical Responses of the Hoof: An *In Vivo* and Finite Element Study. *J. Biomech.* 128, 110715. doi:10.1016/j.jbiomech.2021.110715

Akbari Shahkhosravi, N., Gohari, S., Komeili, A., Burvill, C., and Davies, H. (2021b). Linear Elastic and Hyperelastic Studies of Equine Hoof Mechanical Response at Different Hydration Levels. *J. Mech. Behav. Biomed. Mater.* 121, 104622. doi:10.1016/j.jmbbm.2021.104622

Bailey, C. J., Reid, S. W. J., Hodgson, D. R., and Rose, R. J. (1999). Impact of Injuries and Disease on a Cohort of Two- and Three-Year-Old Thoroughbreds in Training. *Vet. Rec.* 145, 487–493. doi:10.1136/vr.145.17.487

Behnke, R. (2018). Numerical Time-Domain Modelling of Hoof-Ground Interaction during the Stance Phase. *Equine Vet. J.* 50, 519–524. doi:10.1111/evj.12782

Biewener, A. A. (1998). Muscle-tendon Stresses and Elastic Energy Storage during Locomotion in the Horse. *Comp. Biochem. Physiol. B: Biochem. Mol. Biol.* 120, 73–87. doi:10.1016/s0305-0491(98)00024-8

Bui, H. H., Fukagawa, R., Sako, K., and Ohno, S. (2008). Lagrangian Meshfree Particles Method (SPH) for Large Deformation and Failure Flows of Geomaterial Using Elastic-Plastic Soil Constitutive Model. *Int. J. Numer. Anal. Meth. Geomech.* 32, 1537–1570. doi:10.1002/nag.688

Butcher, M. T., Hermanson, J. W., Ducharme, N. G., Mitchell, L. M., Soderholm, L. V., and Bertram, J. E. A. (2009). Contractile Behavior of the Forelimb Digital Flexors during Steady-State Locomotion in Horses (*Equus caballus*): an Initial Test of Muscle Architectural Hypotheses about *In Vivo* Function. *Comp. Biochem. Physiol. A: Mol. Integr. Physiol.* 152, 100–114. doi:10.1016/j.cbpa.2008.09.007

Chen, J. K., Beraun, J. E., and Jih, C. J. (2001). A Corrective Smoothed Particle Method for Transient Elastoplastic Dynamics. *Comput. Mech.* 27, 177–187. doi:10.1007/s004660100236

Cleary, P. W., Cohen, R. C. Z., Harrison, S. M., Sinnott, M. D., Prakash, M., and Mead, S. (2013). Prediction of Industrial, Biophysical and Extreme Geophysical Flows Using Particle Methods. *Eng. Computations* 30, 157–196. doi:10.1108/02644401311304845

Cleary, P. W., and Das, R. (2008). "The Potential for SPH Modelling of Solid Deformation and Fracture," in *IUTAM Symposium on Theoretical, Computational and Modelling Aspects of Inelastic Media* (Springer), 287–296.

Cleary, P. W. (2010). Elastoplastic Deformation during Projectile-wall Collision. *Appl. Math. Model.* 34, 266–283. doi:10.1016/j.apm.2009.04.004

Cleary, P. W., Ha, J., Prakash, M., and Nguyen, T. (2006a). 3D SPH flow predictions and validation for high pressure die casting of automotive components. *Appl. Math. Model.* 30, 1406–1427. doi:10.1016/j.apm.2006.03.012

Cleary, P. W. (1998). Modelling Confined Multi-Material Heat and Mass Flows Using SPH. *Appl. Math. Model.* 22, 981–993. doi:10.1016/s0307-904x(98)10031-8

Cleary, P. W., Prakash, M., and Ha, J. (2006b). Novel Applications of Smoothed Particle Hydrodynamics (SPH) in Metal Forming. *J. Mater. Process. Techn.* 177, 41–48. doi:10.1016/j.jmatprotec.2006.03.237

Cleary, P. W., Prakash, M., Ha, J., Stokes, N., and Scott, C. (2007). Smooth Particle Hydrodynamics: Status and Future Potential. *Pcfd* 7, 70–90. doi:10.1504/pcfd.2007.013000

Cohen, R. C. Z., Cleary, P. W., Mason, B. R., and Pease, D. L. (2018). Forces during Front Crawl Swimming at Different Stroke Rates. *Sports Eng.* 21, 63–73. doi:10.1007/s12283-017-0246-x

Cohen, R. C. Z., Cleary, P. W., Mason, B. R., and Pease, D. L. (2015). The Role of the Hand during Freestyle Swimming. *J. Biomech. Eng.* 137, 111007. doi:10.1115/1.4031586

Cohen, R. C. Z., Cleary, P. W., and Mason, B. R. (2012). Simulations of Dolphin Kick Swimming Using Smoothed Particle Hydrodynamics. *Hum. Mov. Sci.* 31, 604–619. doi:10.1016/j.humov.2011.06.008

Das, R., and Cleary, P. W. (2013). A Mesh-free Approach for Fracture Modelling of Gravity Dams under Earthquake. *Int. J. Fract.* 179, 9–33. doi:10.1007/s10704-012-9766-3

Das, R., and Cleary, P. W. (2010). Effect of Rock Shapes on Brittle Fracture Using Smoothed Particle Hydrodynamics. *Theor. Appl. Fracture Mech.* 53, 47–60. doi:10.1016/j.tafmec.2009.12.004

Das, R., and Cleary, P. W. (2014). Evaluation of Accuracy and Stability of the Classical SPH Method under Uniaxial Compression. *J. Sci. Comput.* 64(3): 858–897.doi:10.1007/s10915-014-9948-4

Das, R., and Cleary, P. W. (2008). Modelling Stress Wave Propagation under Biaxial Loading Using SPH. in" Presented at the XXII International Congress of Theoretical and Applied Mechanics

Das, R., Cleary, P. W., and others (2007). "Modelling Stress Wave Propagation and Triaxial Compression Test Using Smoothed Particle Hydrodynamics," in *Proceedings of the 5th Australasian Congress on Applied Mechanics* (Brisbane, Australia: Engineers Australia), 659.

Ganzenmüller, G. C. (2015). An Hourglass Control Algorithm for Lagrangian Smooth Particle Hydrodynamics. *Comput. Methods Appl. Mech. Eng.* 286, 87–106.

Gomez-Gesteira, M., Rogers, B. D., Dalrymple, R. A., and Crespo, A. J. C. (2010). State-of-the-art of Classical SPH for Free-Surface Flows. *J. Hydraulic Res.* 48, 6–27. doi:10.1080/00221686.2010.9641242

Gray, J. P., Monaghan, J. J., and Swift, R. P. (2001). SPH Elastic Dynamics. *Comput. Methods Appl. Mech. Eng.* 190, 6641–6662. doi:10.1016/s0045-7825(01)00254-7

Hambleton, J. P., and Drescher, A. (2008). Modeling Wheel-Induced Rutting in Soils: Indentation. *J. Terramechanics* 45, 201–211. doi:10.1016/j.jterra.2008.11.001

Harrison, S. M., Chris Whitton, R., Kawcak, C. E., Stover, S. M., and Pandy, M. G. (2014). Evaluation of a Subject-specific Finite-Element Model of the Equine Metacarpophalangeal Joint under Physiological Load. *J. Biomech.* 47, 65–73. doi:10.1016/j.jbiomech.2013.10.001

Harrison, S. M., and Cleary, P. (2013). Dynamic Prediction of Body Dynamics during Walking on Soft Surfaces. in" Presented at the 19th Annual Scientific Meeting of the Australian & New Zealand Orthopaedic Research Society

Harrison, S. M., Cleary, P. W., and Cohen, R. C. Z. (2019). Dynamic Simulation of Flat Water Kayaking Using a Coupled Biomechanical-Smoothed Particle Hydrodynamics Model. *Hum. Mov. Sci.* 64, 252–273. doi:10.1016/j.humov.2019.02.003

Harrison, S. M., Cleary, P. W., Symons, J., Stover, S., and Pandy, M. (2016a). A Computational Model of Hoof-Ground Dynamic Interaction for Evaluating Muscle and Joint Reaction Forces during Equine Locomotion. *Equine Vet. J.* 48, 20.

Harrison, S. M., and Cleary, P. W. (2014). Towards Modelling of Fluid Flow and Food Breakage by the Teeth in the Oral Cavity Using Smoothed Particle Hydrodynamics (SPH). *Eur. Food Res. Technol.* 238, 185–215. doi:10.1007/s00217-013-2077-8

Harrison, S. M., Cohen, R. C. Z., Cleary, P. W., Barris, S., and Rose, G. (2016b). A Coupled Biomechanical-Smoothed Particle Hydrodynamics Model for Predicting the Loading on the Body during Elite Platform Diving. *Appl. Math. Model.* 40, 3812–3831. doi:10.1016/j.apm.2015.11.009

Harrison, S. M., Whitton, R. C., Kawcak, C. E., Stover, S. M., and Pandy, M. G. (2010). Relationship between Muscle Forces, Joint Loading and Utilization of Elastic Strain Energy in Equine Locomotion. *J. Exp. Biol.* 213, 3998–4009. doi:10.1242/jeb.044545

Harrison, S. M., Whitton, R. C., King, M., Haussler, K. K., Kawcak, C. E., Stover, S. M., et al. (2012). Forelimb Muscle Activity during Equine Locomotion. *J. Exp. Biol.* 215, 2980–2991. doi:10.1242/jeb.065441

Hinterhofer, C., Stanek, C., and Haider, H. (2001). Finite Element Analysis (FEA) as a Model to Predict Effects of Farriery on the Equine Hoof. *Equine Vet. J.* 33, 58–62. doi:10.1111/j.2042-3306.2001.tb05360.x

Hinterhofer, C., Stanek, C., and Haider, H. (2000). The Effect of Flat Horseshoes, Raised Heels and Lowered Heels on the Biomechanics of the Equine Hoof Assessed by Finite Element Analysis (FEA). *J. Vet. Med. Ser. A* 47, 73–82. doi:10.1046/j.1439-0442.2000.00263.x

Hitchens, P. L., Morrice-West, A. V., Stevenson, M. A., and Whitton, R. C. (2019). Meta-analysis of Risk Factors for Racehorse Catastrophic Musculoskeletal Injury in Flat Racing. *Vet. J.* 245, 29–40. doi:10.1016/j.tvjl.2018.11.014

Jansová, M., Ondoková, L., Vychytil, J., Kochová, P., Witter, K., and Tonar, Z. (2015). A Finite Element Model of an Equine Hoof. *J. Equine Vet. Sci.* 35, 60–69.

Lemiale, V., Mead, S., and Cleary, P. (2012). Numerical Modelling of Landslide Events Using a Combination of Continuum and Discrete Methods. in" Ninth International Conference on Computational Fluid Dynamics in the Minerals and Process Industries. Melbourne, Australia.

Li, S., Chen, X., Chen, W., Zhu, S., Li, Y., Yang, L., et al. (2018). Soil-cutting Simulation and Parameter Optimization of Handheld Tiller's Rotary Blade by Smoothed Particle Hydrodynamics Modelling and Taguchi Method. *J. Clean. Prod.* 179, 55–62. doi:10.1016/j.jclepro.2017.12.228

Libersky, L. D., and Petschek, A. G. (1991). "Smooth Particle Hydrodynamics with Strength of Materials," in *Advances in the Free-Lagrange Method Including Contributions on Adaptive Gridding and the Smooth Particle Hydrodynamics Method* (Springer), 248–257.

Limido, J., Espinosa, C., Salaün, M., and Lacome, J. L. (2007). SPH Method Applied to High Speed Cutting Modelling. *Int. J. Mech. Sci.* 49, 898–908. doi:10.1016/j.ijmecsci.2006.11.005

López, Y. R., Roose, D., and Morfa, C. R. (2012). Dynamic Particle Refinement in SPH: Application to Free Surface Flow and Non-cohesive Soil Simulations. *Comput. Mech.* 51, 731–741.

Mahaffey, C. A., Peterson, M. L., and Roepstorff, L. (2013). The Effects of Varying Cushion Depth on Dynamic Loading in Shallow Sand Thoroughbred Horse Dirt Racetracks. *Biosyst. Eng.* 114, 178–186. doi:10.1016/j.biosystemseng.2012.12.004

Maurel, B., and Combescure, A. (2008). An SPH Shell Formulation for Plasticity and Fracture Analysis in Explicit Dynamics. *Int. J. Numer. Meth. Engng* 76, 949–971. doi:10.1002/nme.2316

McCarty, C. A., Thomason, J. J., Gordon, K. D., Burkhart, T. A., Milner, J. S., and Holdsworth, D. W. (2016). Finite-Element Analysis of Bone Stresses on Primary Impact in a Large-Animal Model: The Distal End of the Equine Third Metacarpal. *PLOS ONE* 11, e0159541. doi:10.1371/journal.pone.0159541

McGuigan, M. P., and Wilson, A. M. (2003). The Effect of Gait and Digital Flexor Muscle Activation on Limb Compliance in the Forelimb of the horseEquus Caballus. *J. Exp. Biol.* 206, 1325–1336. doi:10.1242/jeb.00254

Meershoek, L. S., Bogert, A. J. v. d., and Schamhardt, H. C. (2001). Model Formulation and Determination of *In Vitro* Parameters of a Noninvasive Method to Calculate Flexor Tendon Forces in the Equine Forelimb. *Am. J. Vet. Res.* 62, 1585–1593. doi:10.2460/ajvr.2001.62.1585

Merritt, J. S., Davies, H., Burvill, C., and Pandy, M. G. (2008). Influence of Muscle-Tendon Wrapping on Calculations of Joint Reaction Forces in the Equine Distal Forelimb. *Biomed. Res. Int.* 2008, 1–9. doi:10.1155/2008/165730

Monaghan, J. J. (1994). Simulating Free Surface Flows with SPH. *J. Comput. Phys.* 110, 399–406. doi:10.1006/jcph.1994.1034

Monaghan, J. J. (2005). Smoothed Particle Hydrodynamics. *Rep. Prog. Phys.* 68, 1703–1759. doi:10.1088/0034-4885/68/8/r01

Monaghan, J. J. (2000). SPH without a Tensile Instability. *J. Comput. Phys.* 159, 290–311. doi:10.1006/jcph.2000.6439

Newlyn, H. A., Collins, S. N., Cope, B. C., Hopegood, L., Latham, R. J., and Reilly, J. D. (1998). Finite Element Analysis of Static Loading in Donkey Hoof wall. *Equine Vet. J. Suppl.* 30, 103–110. doi:10.1111/j.2042-3306.1998.tb05128.x

Parkin, T. D. H., Clegg, P. D., French, N. P., Proudman, C. J., Riggs, C. M., Singer, E. R., et al. (2006). Catastrophic Fracture of the Lateral Condyle of the Third Metacarpus/metatarsus in UK Racehorses - Fracture Descriptions and Pre-existing Pathology. *Vet. J.* 171, 157–165. doi:10.1016/j.tvjl.2004.10.009

Pereira, G. G., Cleary, P. W., and Lemiale, V. (2017). SPH Method Applied to Compression of Solid Materials for a Variety of Loading Conditions. *Appl. Math. Model.* 44, 72–90. doi:10.1016/j.apm.2016.12.009

Peterson, M., Vel, S., and Jin, Z. (2016). Constitutive Modelling of Equestrian Surface Materials. *Equine Vet. J.* 48, 12.

Ramsey, G. D., Hunter, P. J., and Nash, M. P. (2013). The Influence of Loading Conditions on Equine Hoof Capsule Deflections and Stored Energy Assessed by Finite Element Analysis. *Biosyst. Eng.* 115, 283–290. doi:10.1016/j.biosystemseng.2013.04.002

Rausch, M. K., Karniadakis, G. E., and Humphrey, J. D. (2017). Modeling Soft Tissue Damage and Failure Using a Combined Particle/Continuum Approach. *Biomech. Model. Mechanobiol.* 16, 249–261. doi:10.1007/s10237-016-0814-1

Riemersma, D. J., Bogert, A. J., Jansen, M. O., and Schamhardt, H. C. (1996). Tendon Strain in the Forelimbs as a Function of Gait and Ground Characteristics and *In Vitro* Limb Loading in Ponies. *Equine Vet. J.* 28, 133–138. doi:10.1111/j.2042-3306.1996.tb01605.x

Salo, Z., Thomason, J. J., and Runciman, R. J. (2010). Analysis of Strain and Stress in the Equine Hoof Using Finite Element Analysis: Comparison with Minimum Principal Strains Recorded *In Vivo*. *Biosyst. Eng.* 107, 262–270. doi:10.1016/j.biosystemseng.2010.08.010

Setterbo, J. J., Fyhrie, P. B., Hubbard, M., Upadhyaya, S. K., and Stover, S. M. (2013). Dynamic Properties of a Dirt and a Synthetic Equine Racetrack Surface Measured by a Track-Testing Device. *Equine Vet. J.* 45, 25–30. doi:10.1111/j.2042-3306.2012.00582.x

Sneddon, I. N. (1965). The Relation between Load and Penetration in the Axisymmetric Boussinesq Problem for a Punch of Arbitrary Profile. *Int. J. Eng. Sci.* 3, 47–57. doi:10.1016/0020-7225(65)90019-4

Swanstrom, M. D., Zarucco, L., Hubbard, M., Stover, S. M., and Hawkins, D. A. (2005). Musculoskeletal Modeling and Dynamic Simulation of the Thoroughbred Equine Forelimb during Stance Phase of the Gallop. *J. Biomech. Eng.* 127, 318–328. doi:10.1115/1.1865196

Symons, J. E., Fyhrie, D. P., Hawkins, D. A., Upadhyaya, S. K., and Stover, S. M. (2015). Modeling Equine Race Surface Vertical Mechanical Behaviors in a Musculoskeletal Modeling Environment. *J. Biomech.* 48 (4), 566–572. doi:10.1016/j.jbiomech.2015.01.006

Symons, J. E., Garcia, T. C., and Stover, S. M. (2014). Distal Hindlimb Kinematics of Galloping Thoroughbred Racehorses on Dirt and Synthetic Racetrack Surfaces. *Equine Vet. J.* 46, 227–232. doi:10.1111/evj.12113

Symons, J. E., Hawkins, D. A., Fyhrie, D. P., Upadhyaya, S. K., and Stover, S. M. (2016). Hitting the Ground Running: Evaluating an Integrated Racehorse Limb and Race Surface Computational Model. *J. Biomech.* 49, 1711–1717. doi:10.1016/j.jbiomech.2016.03.057

Thomason, J. J., McClinchey, H. L., and Jofriet, J. C. (2002). Analysis of Strain and Stress in the Equine Hoof Capsule Using Finite Element Methods: Comparison with Principal Strains Recorded *In Vivo*. *Equine Vet. J.* 34, 719–725. doi:10.2746/042516402776250388

Wang, Y., Qin, Z., Liu, X., and Li, L. (2019). Probabilistic Analysis of post-failure Behavior of Soil Slopes Using Random Smoothed Particle Hydrodynamics. *Eng. Geology.* 261, 105266. doi:10.1016/j.enggeo.2019.105266

Wilson, A. M., McGuigan, M. P., Su, A., and van den Bogert, A. J. (2001). Horses Damp the spring in Their Step. *Nature* 414, 895–899. doi:10.1038/414895a

Xi, Y., Bermingham, M., Wang, G., and Dargusch, M. (2014). SPH/FE Modeling of Cutting Force and Chip Formation during Thermally Assisted Machining of Ti6Al4V alloy. *Comput. Mater. Sci.* 84, 188–197. doi:10.1016/j.commatsci.2013.12.018

Zhan, L., Peng, C., Zhang, B., and Wu, W. (2020). A SPH Framework for Dynamic Interaction between Soil and Rigid Body System with Hybrid Contact Method. *Int. J. Numer. Anal. Methods Geomech* 44, 1446–1471. doi:10.1002/nag.3070

Zhang, N., Zheng, X., and Ma, Q. (2017). Updated Smoothed Particle Hydrodynamics for Simulating Bending and Compression Failure Progress of Ice. *Water* 9, 882. doi:10.3390/w9110882

Conflict of Interest: The authors declare that the research was conducted in the absence of any commercial or financial relationships that could be construed as a potential conflict of interest.

Publisher's Note: All claims expressed in this article are solely those of the authors and do not necessarily represent those of their affiliated organizations, or those of the publisher, the editors, and the reviewers. Any product that may be evaluated in this article, or claim that may be made by its manufacturer, is not guaranteed or endorsed by the publisher.

frontiers in Bioengineering and Biotechnology

ORIGINAL RESEARCH
published: 28 February 2022
doi: 10.3389/fbioe.2022.825157

Center of Mass Offset Enhances the Selection of Transverse Gallop in High-Speed Running by Horses: A Modeling Study

Takumi Yamada[1], Shinya Aoi[2], Mau Adachi[1], Tomoya Kamimura[3], Yasuo Higurashi[4], Naomi Wada[4], Kazuo Tsuchiya[2] and Fumitoshi Matsuno[1]*

[1]Department of Mechanical Engineering and Science, Graduate School of Engineering, Kyoto University, Kyoto, Japan, [2]Department of Aeronautics and Astronautics, Graduate School of Engineering, Kyoto University, Kyoto, Japan, [3]Department of Electrical and Mechanical Engineering, Nagoya Institute of Technology, Nagoya, Japan, [4]Laboratory of System Physiology, Joint Faculty of Veterinary Medicine, Yamaguchi University, Yamaguchi, Japan

Horses use the transverse gallop in high-speed running. However, different animals use different gaits, and the gait preference of horses remains largely unclear. Horses have fore-aft asymmetry in their body structure and their center of mass (CoM) is anteriorly located far from the center of the body. Since such a CoM offset affects the running dynamics, we hypothesize that the CoM offset of horses is important in gait selection. In order to verify our hypothesis and clarify the gait selection mechanisms by horses from a dynamic viewpoint, we developed a simple model with CoM offset and investigated its effects on running. Specifically, we numerically obtained periodic solutions and classified these solutions into six types of gaits, including the transverse gallop, based on the footfall pattern. Our results show that the transverse gallop is optimal when the CoM offset is located at the position estimated in horses. Our findings provide useful insight into the gait selection mechanisms in high-speed running of horses.

Keywords: horse, transverse gallop, center of mass offset, gait selection, model

OPEN ACCESS

Edited by:
John R. Hutchinson, Royal Veterinary College (RVC), United Kingdom

Reviewed by:
John E. A. Bertram, University of Calgary, Canada
Michael Peterson, University of Kentucky, United States

****Correspondence:***
Shinya Aoi
shinya_aoi@kuaero.kyoto-u.ac.jp

Specialty section:
This article was submitted to Biomechanics, a section of the journal Frontiers in Bioengineering and Biotechnology

Received: *30 November 2021*
Accepted: *11 January 2022*
Published: *28 February 2022*

Citation:
Yamada T, Aoi S, Adachi M, Kamimura T, Higurashi Y, Wada N, Tsuchiya K and Matsuno F (2022) Center of Mass Offset Enhances the Selection of Transverse Gallop in High-Speed Running by Horses: A Modeling Study. Front. Bioeng. Biotechnol. 10:825157. doi: 10.3389/fbioe.2022.825157

1 INTRODUCTION

Horses use the transverse gallop in high-speed locomotion. This gait has one flight phase in one gait cycle. Specifically, the hind legs first touch the ground, and then the fore legs touch the ground. After that, a flight phase appears. This gait is different from the rotary gallop in cheetahs, which has two flight phases, each of which appears after the touchdowns of the fore legs and those of the hind legs (Bertram and Gutmann, 2008; Biancardi and Minetti, 2012). The gaits of quadrupeds when running at their fastest speeds vary between species, and it remains unclear why horses use the transverse gallop.

Horses have fore-aft asymmetry in their body structure. In particular, they have a long neck, and their center of mass (CoM) is anteriorly located and far from the center of the body (Buchner et al., 1997; Self Davies et al., 2019). Such a CoM offset affects the dynamics of the running motion. For example, when the fore-aft CoM location of dogs was changed by carrying a weight during trotting, which is characterized by the simultaneous touchdown of the diagonal fore and hind legs, the footfall pattern changed (Lee et al., 2004). Specifically, the fore and hind legs came to touch the ground first when the load was applied to the anterior and posterior sides, respectively. In other words, the CoM

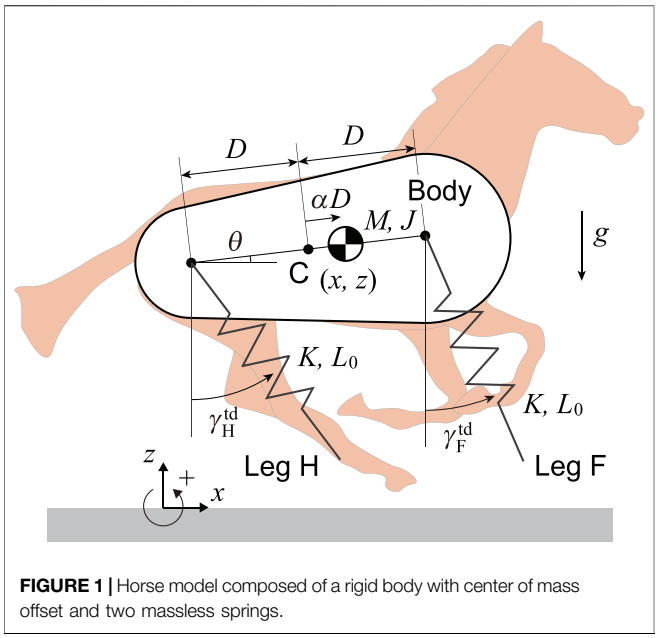

FIGURE 1 | Horse model composed of a rigid body with center of mass offset and two massless springs.

offset changed the gait. Therefore, we hypothesize that the CoM offset of horses plays an important role in their gait selection.

Since animal locomotion is a complex phenomenon generated through dynamical interactions between the body mechanical system, the nervous system, and the environment, it is difficult to fully understand the mechanisms for gait selection in animals only from observation. Therefore, simple models, which extract essential elements for the running dynamics, have been used to clarify the mechanisms (Tanase et al., 2015; Gan et al., 2016; Chen et al., 2019; Kamimura et al., 2021). Poulakakis et al. (2006) used a simple quadrupedal model and showed the relationship between the pitch angular velocity and the number of flight phases in one gait cycle during bounding gait. In addition, Zou and Schmiedeler (2006) used a model focusing on the vertical and pitch movements and derived a stability condition depending on the CoM offset. However, the model did not incorporate horizontal movement, and the mechanism for the gait selection remains unclear.

In the present study, we investigated the effects of the CoM offset on quadrupedal running in order to verify our hypothesis from a dynamic viewpoint. Specifically, we constructed a bounding model with CoM offset and searched periodic solutions by numerical simulations. We then classified the obtained solutions into six types of gaits depending on the footfall pattern and examined which gait is optimal based on performance criteria. Our findings provide useful insight into the mechanisms for high-speed running in horses.

2 METHODS

2.1 Model

We used a horse model composed of a rigid body and two massless springs on the sagittal plane (**Figure 1**). The springs represent the fore and hind legs (Legs F and H) and are connected to the body by smoothly rotating joints. Here, M and J are the mass and moment of inertia around the CoM of the body, respectively. The distance between the leg joints is $2D$. The CoM is located at a distance of αD ($-1 \le \alpha \le 1$) from the center C between the leg joints, where $\alpha = 0$ corresponds to C, and $\alpha = 1$ and -1 correspond to the joints of the fore and hind legs, respectively. Moreover, x and z are the horizontal and vertical positions of the CoM, respectively, and θ is the pitch angle relative to the horizontal line. The spring constant and neutral length of both the fore and hind legs are K and L_0, respectively. When Leg i (i = F, H) is in the air, its length remains L_0 and its angle also maintains the touchdown angle γ_i^{td}. The positive direction of these angles is counterclockwise. When the tip of the leg reaches the ground, it is constrained to the ground and behaves as a frictionless pin joint. When the leg length returns to L_0 after the compression, the tip leaves the ground. Since the touchdown and liftoff occur at the neutral length and our model has no dissipative component, such as friction or a damper, our model is energy conservative.

The equations of motion of the model are given by

$$M\ddot{x} = \sum_{i=\mathrm{F,H}} -F_i \sin\gamma_i \tag{1a}$$

$$M\ddot{z} = \sum_{i=\mathrm{F,H}} F_i \cos\gamma_i - Mg \tag{1b}$$

$$J\ddot{\theta} = F_{\mathrm{F}}(1-\alpha)D\cos(\gamma_{\mathrm{F}}-\theta) - F_{\mathrm{H}}(1+\alpha)D\cos(\gamma_{\mathrm{H}}-\theta), \tag{1c}$$

where

$$F_i = \begin{cases} 0 & \text{swing phase} \\ K(L_0 - L_i) & \text{stance phase} \end{cases} \quad i = \mathrm{F,H} \tag{2}$$

and L_i and γ_i (i = F, H) are the length and angle, respectively, of Leg i relative to the vertical line. Moreover, γ_i is determined by the joint and touchdown positions of Leg i. The touchdown condition $r_i^{\mathrm{td}} = 0$ and liftoff condition $r_i^{\mathrm{lo}} = 0$ of Leg i are given by

$$\begin{aligned} r_i^{\mathrm{td}} &= z + (\varepsilon_i - \alpha)D\sin\theta - L_0\cos\gamma_i^{\mathrm{td}} = 0 \\ r_i^{\mathrm{lo}} &= L_0 - L_i = 0, \end{aligned} \quad i = \mathrm{F,H} \tag{3}$$

where $\varepsilon_{\mathrm{F}} = 1$ and $\varepsilon_{\mathrm{H}} = -1$.

The physical parameters of the model were determined based on the estimated values of Thoroughbreds (*Equus ferus caballus*). In particular, we used M = 490 kg and J = 167 kgm^2 based on Swanstrom et al. (2005). We used D = 0.48 m from the distance between the shoulder and hip joints and L_0 = 1.33 m from the average value of the distances between the shoulder joint and the toe of the fore limb and between the hip joint and the toe of the hind limb based on Grossi and Canals, (2010). We used K = 45.4 kN/m based on Farley et al. (1993).

2.2 Gait

The gait is generally determined based on the order of touchdown and liftoff of the legs. We defined the following four phases: flight (FL), fore leg stance (FS), hind leg stance (HS), and double stance (DS). In FL, both legs are in the air. In FS, only the fore leg is in contact with the ground. In HS, only the hind leg is in contact with the ground. In DS, both legs are in contact with the ground.

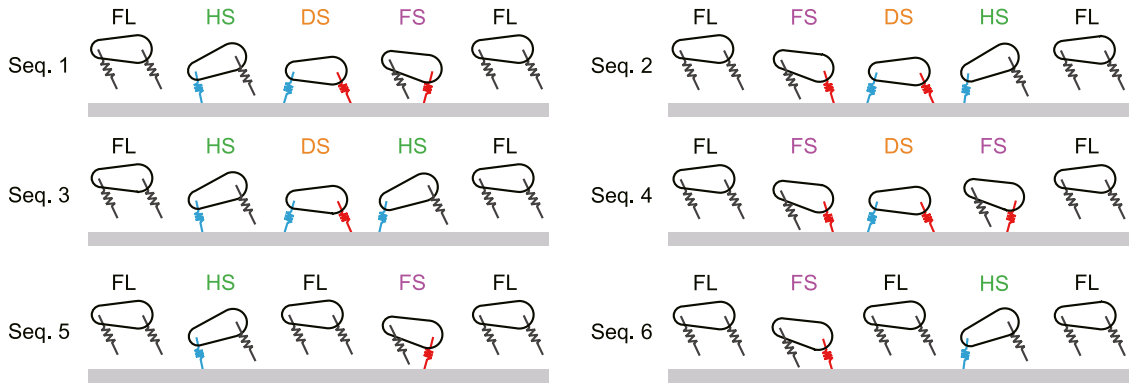

FIGURE 2 | Six possible phase transitions (Sequences 1 . . . 6) from one apex to the next apex. FL, FS, HS, and DS stand for flight, fore leg stance, hind leg stance, and double stance, respectively.

We investigated motions (periodic solutions) starting from an apex (i.e., $\dot{z} = 0$ in FL) and returning to the next apex after each leg touches the ground once. The periodic solutions are obtained by the transitions between these phases. The phase transitions of the periodic solutions are classified into six sequences (Sequences 1 ... 6), as shown in **Figure 2**. In Sequence 1, the hind leg first touches the ground (HS), and then the fore leg touches the ground so that two legs are in contact with the ground (DS). After that, the hind leg first leaves the ground (FS), and then the fore leg leaves the ground to return to FL. This gait has one flight phase and one double stance phase and corresponds to the transverse gallop in horses (Hildebrand, 1977; Biancardi and Minetti, 2012). Sequence 2 is obtained by swapping the behaviors of the fore and hind legs in Sequence 1. In Sequence 3, the hind leg first touches the ground (HS), and then the fore leg touches the ground, so that two legs are in contact with the ground (DS). After that, the fore leg first leaves the ground (HS), and then the hind leg leaves the ground to return to FL. This gait also has one flight phase and one double stance phase. Sequence 4 is obtained by swapping the behaviors of the fore and hind legs in Sequence 3. In Sequence 5, the hind leg touches the ground (HS) and then leaves the ground to return to FL. After that, the fore leg touches the ground (FS), and then leaves the ground to once again return to FL. This gait has two flight phases but no double stance phase. Sequence 6 is obtained by swapping the behaviors of the fore and hind legs in Sequence 5. Sequences 5 and 6 are identical when the time profile of one sequence is shifted by half a gait cycle.

2.3 Search of Solutions

In order to find periodic solutions, we defined the Poincaré section at the apex of the CoM ($\dot{z} = 0$). Since x monotonically increases during locomotion and is not periodic, we used $q = [z\ \theta\ \dot{x}\ \dot{\theta}]^\top$ as the state on the Poincaré section. We used the touchdown angles as the parameter set $u = [\gamma_H^{td}\ \gamma_F^{td}]^\top$. The Poincaré map P is then defined as

$$q_{n+1} = P(q_n, u_n) \tag{4}$$

where q_n is the state at the nth intersection with the Poincaré section, and u_n is the nth parameter set. A periodic solution satisfies

$$q^* = P(q^*, u^*) \tag{5}$$

where q^* is the fixed point on the Poincaré section. We numerically searched fixed points for periodic solutions using the Newton-Raphson method.

2.4 Performance Criteria

In order to evaluate the obtained solutions, we used the gait stability as a performance criterion (Poulakakis et al., 2006; Tanase et al., 2015; Kamimura et al., 2021). In order to analyze the gait stability, we investigated the eigenvalues of the linearized Poincaré map around the fixed points on the Poincaré section. Since our model is energy conservative, the solution is asymptotically stable, when all of the eigenvalues, except for one eigenvalue of 1, are located inside the unit circle on the complex plane. Otherwise, the solution is unstable.

Horses stabilize their gaze during running by preventing the pitch movement of the body from disturbing the head (Dunbar et al., 2008). Therefore, we also used the fluctuation of the pitch movement of the body as another performance criterion, which is obtained from the difference between the maximum and minimum values of θ for one gait cycle.

3 RESULTS

3.1 Effect of Center of Mass Offset on Gait Pattern

First, we set the total energy of our model as $E = 20.3$ kJ (gravitational potential energy is 0 at the ground level) and the forward speed at the apex as $\dot{x}^* = 7.5$ m/s (horizontal kinetic energy $T^* = M(\dot{x}^*)^2/2 = 13.8$ kJ) based on the measured data in horses (Minetti et al., 1999). We then searched periodic solutions in the range of $-0.5 \le \alpha \le 0.5$ and $-1.5 \le \dot{\theta}^* \le 1.5$. As a result, we found a unique solution for each set of $(\alpha, \dot{\theta}^*)$ in this range, the

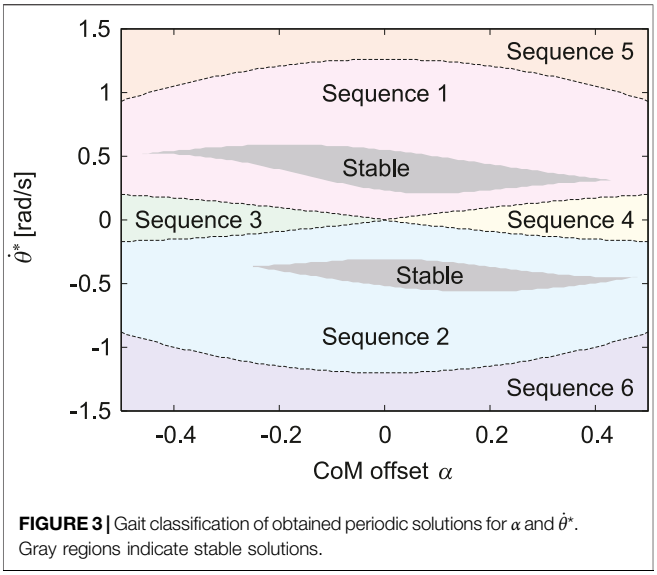

FIGURE 3 | Gait classification of obtained periodic solutions for α and $\dot{\theta}^*$. Gray regions indicate stable solutions.

gait of which is classified into Sequences 1 through 6, as shown in **Figure 3**. The gait boundaries are symmetric with respect to $\alpha = 0$ and $\dot{\theta}^* = 0$, and four boundaries of Sequences 1, 2, 3, and 4 meet at $\alpha = 0$ and $\dot{\theta}^* = 0$. When $\alpha = 0$, the solutions have four types of gait, labeled as Sequences 1, 2, 5, and 6. For the solutions with $\dot{\theta}^* > 0$, the hind leg first touches the ground. Specifically, Sequence 1 appears when $\dot{\theta}^*$ is small, and Sequence 5 appears when $\dot{\theta}^*$ is large. In contrast, for the solutions with $\dot{\theta}^* < 0$, the fore leg first touches the ground. Specifically, Sequence 2 appears when $|\dot{\theta}^*|$ is small, and Sequence 6 appears when $|\dot{\theta}^*|$ is large. In addition to the four gaits, Sequences 3 and 4 appear around $\dot{\theta}^* = 0$ when $\alpha < 0$ and when $\alpha > 0$, respectively. As $|\alpha|$ increases, the range of $\dot{\theta}^*$ of Sequences 1 and 2 decreases and that of Sequences 3, 4, 5, and 6 increases. Stable solutions exist only in Sequences 1 and 2 at $-0.46 < \alpha < 0.48$. Specifically, only Sequence 1 is stable when the CoM is located posteriorly at $-0.46 < \alpha < -0.25$, and only Sequence 2 is stable when the CoM is located anteriorly at $0.44 < \alpha < 0.48$.

Next, we investigate the time profiles of the periodic solutions in order to clarify the characteristition with α. First, **Figure 4A** shows the tixme profile of z, θ, and $\dot{x}$ of the solution for $\alpha = 0$ and $\dot{\theta}^* = 0$, at which the four boundaries of Sequences 1, 2, 3, and 4 meet (**Figure 3**). In this case, the fore and hind legs touch and leave the ground simultaneously. The trajectories of z and $\dot{x}$ are symmetric with respect to 50% of the gait cycle, and θ is always zero. Next, **Figure 4B** shows the time profiles of typical solutions of each gait for $\alpha = 0$, ±0.2, and ±0.4, where $\dot{\theta}^* = 0.5, -0.5, 0, 0, 1.5$, and -1.5 rad/s are used for Sequences 1, 2, 3, 4, 5, and 6, respectively. As a common feature of all gaits, when $\alpha = 0$, the timings of touchdown and liftoff are shifted depending on $\dot{\theta}^*$ and are no longer simultaneous between the fore and hind legs. However, the trajectories of z and $\dot{x}$ remain symmetric with respect to 50% of the gait cycle, regardless of $\dot{\theta}^*$. Although θ^* remains 0, specific waveforms appear in θ depending on $\dot{\theta}^*$. The trajectory of θ is symmetric with respect to the intersection of $\theta = 0$ and 50% of the gait cycle. As α increases, the stance phase duration increases and decreases for the fore and hind legs, respectively, and the trajectories and phases become asymmetric.

Sequences 1 and 2 have solutions for all $\alpha = 0$, ±0.2, and ±0.4, the trajectories and phases of which are symmetric with respect to 50% of the gait cycle. As α increases, the onset and end of the DS phase are advanced in Sequence 1 and delayed in Sequence 2, whereas those of the FL phase remains almost unchanged. Here, z has a one-peak shape and remains almost unchanged. Although the waveform of θ remains almost unchanged, the mean value decreases. The timing at which $\dot{x}$ takes the minimum value is delayed in Sequence 1 and advanced in Sequence 2. However, the minimum value decreases as $|\alpha|$ increases.

Sequence 3 has solutions only for $\alpha = -0.2$ and -0.4, and Sequence 4 has solutions only for $\alpha = 0.2$ and 0.4. These trajectories are identical for the same $|\alpha|$. In addition, these phases are also identical when the timings of touchdown and liftoff are swapped between the fore and hind legs. Unlike Sequences 1 and 2, the trajectories and the timings of touchdown and liftoff are symmetric with respect to 50% of the gait cycle regardless of α. Here, z has a one-peak shape and remains almost unchanged as α increases. The waveform of θ remains almost unchanged, whereas the mean value decreases. The minimum value of $\dot{x}$ decreases as $|\alpha|$ increases.

Sequences 5 and 6 have solutions for all $\alpha = 0$, ±0.2, and ±0.4, the trajectories and phases of which are symmetric with respect to 50% of the gait cycle. When $\alpha = 0$, z has a two-peak shape. As $|\alpha|$ increases, one of the two peaks decreases and the two-peak shape changes into a one-peak shape. As α increases, the FS and HS phases are advanced in Sequence 5 and delayed in Sequence 6. Whereas the mean value of θ remain almost unchanged, the peak timings change in accordance with changes in the FS and HS phases. Since Sequences 5 and 6 have two FL phases, $\dot{x}$ has two minimum values in the FS and HS phases. Regardless of α, our model is accelerated in the HS phase and decelerated in the FS phase in Sequence 5, and vice versa in Sequence 6. As α increases, the minimum value of $\dot{x}$ in the HS phase increases and that in the FS phase decreases in both Sequences 5 and 6.

3.2 Effect of Speed on Gait Performance

Although the previous section investigated the effects of the CoM offset α on the gait pattern using the average speed, horses have a wide range of speed for galloping (Hoyt and Taylor, 1981; Minetti et al., 1999). In this section, we investigate the effects of speed on the gait characteristics using the estimated value of α in horses ($\alpha = 0.2$) (Self Davies et al., 2019) compared with those using $\alpha = 0$.

The total energy E of our model is explained by the horizontal translational kinetic energy $T^* = M(\dot{x}^*)^2/2$, gravitational potential energy $U^* = Mgz^*$, and rotational kinetic energy $R^* = J(\dot{\theta}^*)^2/2$ at the apex ($E = T^* + U^* + R^*$). We searched for periodic solutions by changing T^* and $U^* + R^*$ from the previous results of $\alpha = 0.2$ and 0. **Figures 5A,B** compare the region for T^* and $U^* + R^*$ where periodic solutions are found and that where stable periodic solutions are found for $\alpha = 0.2$ and 0, respectively. In both figures, although solutions, including unstable solutions, are widely distributed for T^* and $U^* + R^*$ (no solution is found below 5.9 kJ of $U^* + R^*$), stable solutions exist only in a limited range for $U^* + R^*$. In other words, when the forward speed increases, only

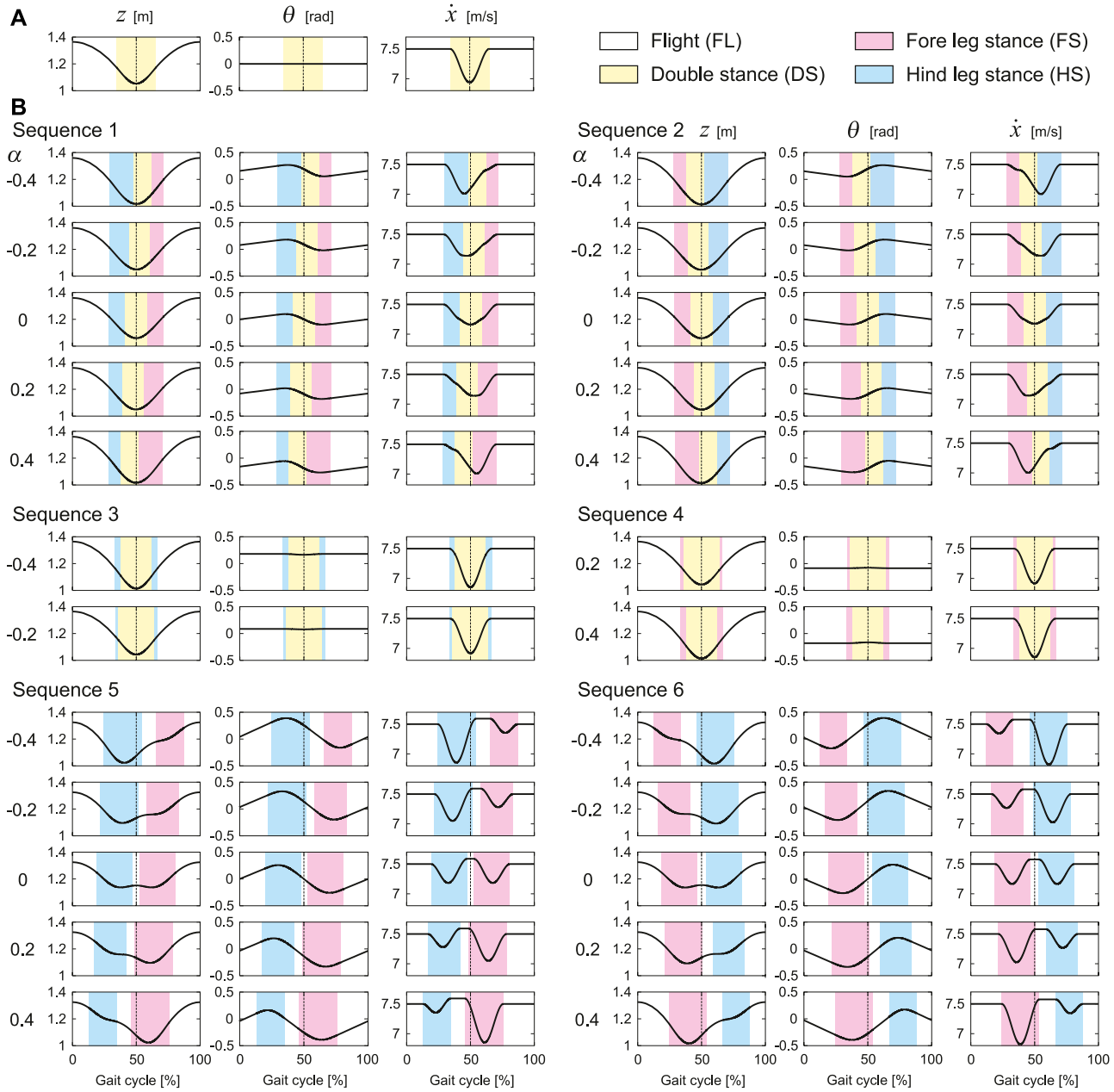

FIGURE 4 | Characteristics of time profiles of z, θ, and $\dot{x}$ and phases of periodic solutions depending on α and gait. **(A)** Solution for $\alpha = 0$ and $\dot{\theta}^* = 0$. **(B)** Typical solutions of each gait for $\alpha = 0$, ±0.2, and ±0.4, where $\dot{\theta}^* = 0.5, -0.5, 0, 0, 1.5$, and −1.5 rad/s are used for Sequences 1, 2, 3, 4, 5, and 6, respectively (see **Supplementary Video S1**).

the horizontal translational kinetic energy increases, whereas the other energies are almost unchanged in the stable solutions.

Next, we searched for periodic solutions by using $U^* + R^* = 6.6$ kJ, which corresponds to the value obtained from $E = 20.3$ kJ and $T^* = 13.8$ kJ used in **Figure 3**, and by changing $\dot{x}^*$ in 5–10 m/s of the speed range ($T^* = 6.1$–24.5 kJ) of the horse galloping (Hoyt and Taylor, 1981; Minetti et al., 1999). **Figures 6A,B** show the fluctuation of the pitch movement of the body for $\dot{x}^*$ of the obtained stable solutions for $\alpha = 0.2$ and 0, respectively. In both figures, only Sequences 1 and 2 have stable solutions in the same way as **Figure 3**. When $\alpha = 0.2$, the stable solutions of Sequence 1 exist in a wider range of $\dot{x}^*$ and have smaller pitch fluctuations than those of Sequence 2. In contrast, when $\alpha = 0$, the range of $\dot{x}^*$ of the stable solutions is almost identical and the pitch fluctuations also are not much different between Sequences 1 and 2.

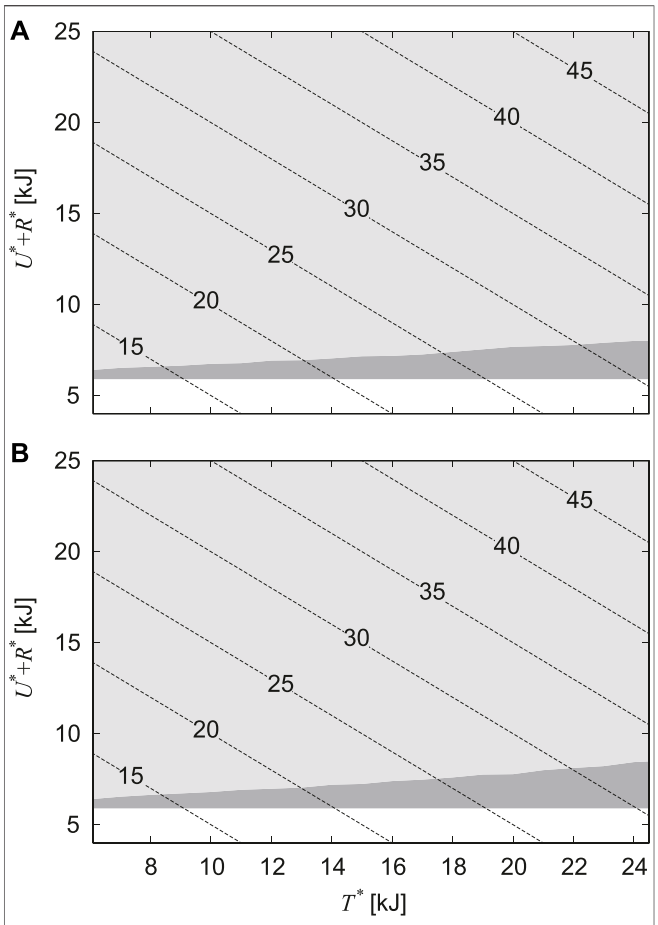

FIGURE 5 | Regions in which periodic solutions are found for horizontal translational kinetic energy T^* and the sum of gravitational potential energy and rotational kinetic energy $U^* + R^*$. **(A)** $\alpha = 0.2$ and **(B)** $\alpha = 0$. The light and dark gray regions indicate that the solutions are unstable and stable, respectively. The dotted lines indicate the contour of total energy E.

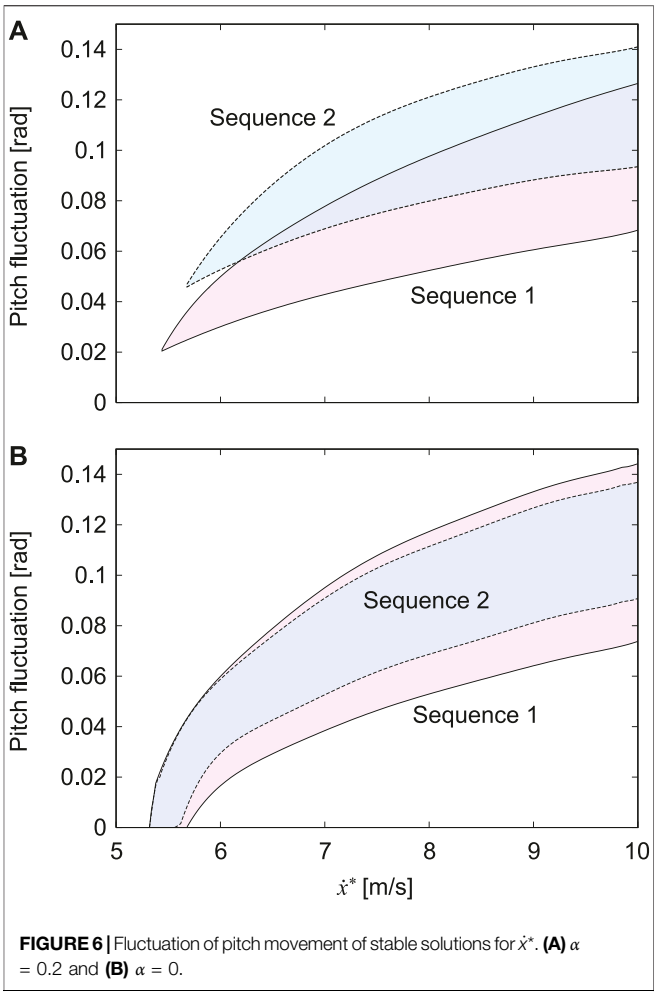

FIGURE 6 | Fluctuation of pitch movement of stable solutions for $\dot{x}^*$. **(A)** $\alpha = 0.2$ and **(B)** $\alpha = 0$.

4 DISCUSSION

4.1 Effect of Center of Mass Offset on Gait

The proposed model has six types of gaits, labeled Sequences 1 through 6 (**Figure 2**). In Sequences 1, 2, 5, and 6, when a leg first touches the ground, this leg leaves the ground earlier than the other leg. As a result of the search of periodic solutions, we found only these four sequences when the CoM is located at the center ($\alpha = 0$), as shown in **Figure 3**. In Sequences 3 and 4, when a leg first touches the ground, this leg leaves the ground later than the other leg (**Figure 2**). Sequences 3 and 4 appeared only when the CoM is located posteriorly ($\alpha < 0$) and anteriorly ($\alpha > 0$), respectively (**Figure 3**). In other words, the introduction of the CoM offset α to the model allowed Sequences 3 and 4 to appear.

Whereas the trajectories and phases of the periodic solutions were symmetric for $\alpha = 0$, the solutions became asymmetric as $|\alpha|$ increased (**Figure 4**). However, the asymmetric tendency depended on the gait. Specifically, as $|\alpha|$ increased, the trajectories and phases showed higher asymmetry in order of Sequences 3 and 4, Sequences 1 and 2, Sequences 5 and 6 (**Figure 4**). These reasons can be explained from the viewpoint of the dynamics of the body rotation. Specifically, the body rotation is created by the moment of force by the ground reaction forces from the fore and hind legs. Therefore, the periodic solutions require the moment of impulse generated for one gait cycle to be balanced between the fore and hind legs. When $\alpha > 0$, the distances from the CoM to the joints of the fore and hind legs are short and long, respectively. Therefore, the moment of impulse is balanced by increasing the magnitude of the ground reaction force and stance phase duration of the fore leg and by decreasing those of the hind leg, and vice versa when $\alpha < 0$. In the DS phase, the net moment applied to the body is reduced by the positive moment from the fore leg and negative moment from the hind leg, which decreases the asymmetry of the body rotation. Since the DS phase duration decreased in order of Sequences 3 and 4, Sequences 1 and 2, Sequences 5 and 6, the asymmetry of the trajectories and phases increased in this order.

This can also explain why Sequences 3 and 4 appear in $\alpha < 0$ and $\alpha > 0$, respectively. Specifically, in Sequences 3 and 4, when a leg first touches the ground, this leg leaves the ground later than the other leg (**Figure 2**). Based on the solution for $\alpha = 0$ and $\dot{\theta}^* = 0$, where both legs touch and leave the ground simultaneously (**Figure 4A**). Since the stance phase duration

of the hind leg became longer than that of the fore leg for $\alpha < 0$, Sequence 3 appeared, and vice versa for $\alpha > 0$ and Sequence 4 (**Figure 4B**).

4.2 Gait Selection by Horses

Sequence 1 has one flight phase, after which the hind leg first touches the ground (**Figure 2**), and thus corresponds to the transverse gallop used by horses and gnus (Muybridge, 1957; Pennycuick, 1975; Hildebrand, 1977; Hildebrand, 1989). Sequence 2 has one flight phase, after which the fore leg first touches the ground (**Figure 2**), and thus corresponds to the transverse gallop used by deer and antelopes (Bigalike, 1972; FitzGibbon and Fanshawe, 1988; Hildebrand, 1989). Sequences 3 and 4 also have one flight phase (**Figure 2**). When touchdown and liftoff occur almost simultaneously between the fore and hind legs and the pitch fluctuation is small, as obtained in **Figure 4B**, these gaits correspond to the pronk used by springboks and Thomson's gazelles (Bigalike, 1972; FitzGibbon and Fanshawe, 1988; Hildebrand, 1989). In contrast, Sequences 5 and 6 have two flight phases and thus correspond to the rotary gallop used by cheetahs and greyhounds (Muybridge, 1957; Hildebrand, 1977; Hildebrand, 1989; Bertram and Gutmann, 2008; Biancardi and Minetti, 2012; Hudson et al., 2012).

When we used the physical parameters estimated in horses, including the CoM offset $\alpha = 0.2$, only Sequences 1 and 2 had stable solutions (**Figures 3**, **6**). Sequence 1 had a wider speed range (5.5–10 m/s) than Sequence 2 (5.8–10 m/s) (**Figure 6**) and the speed range of Sequence 1 was closer to that of a galloping horse (5–10 m/s) (Hoyt and Taylor, 1981; Minetti et al., 1999). Furthermore, Sequence 1 had smaller pitch fluctuations (2.2–7.2 deg) than Sequence 2 (3.2–7.9 deg) (**Figure 6A**), and the amount of the fluctuations of Sequence 1 was closer to that of a galloping horse (2–8 deg) (Dunbar et al., 2008). However, when we used $\alpha = 0$ instead of $\alpha = 0.2$ estimated in horses, although Sequences 1 and 2 also had stable solutions, the speed range and pitch fluctuation were not much different between Sequence 1 and 2 (**Figure 6B**). Our results suggest that Sequence 1, which corresponds to the transverse gallop actually used by horses, is a suitable gait for horses from a dynamical viewpoint.

4.3 Vertical and Pitch Movements

Although stable periodic solutions existed for a large range of the horizontal translational kinetic energy T^*, these solutions existed for a limited range of the sum of the gravitational and rotational kinetic energies $U^* + R^*$ (**Figure 5**). This means that the stability of bounding mainly depends on the vertical and pitch movements of the body. Thus far, simple models focusing on the vertical and pitching movements have been used to investigate the gait stability (Berkemeier, 1998; Zou and Schmiedeler, 2006; De and Koditschek, 2018; Kamimura et al., 2021). In particular, Berkemeier (1998) investigated the stability of bounding (which corresponds to Sequences 5 and 6) using a symmetrical model, which is identical to our model with $\alpha = 0$, and derived the stability condition as $\mu < 1$, where $\mu = J/(MD^2)$. Zou and Schmiedeler (2006) improved his model by introducing the CoM offset α, as in the present study, and derived the stability condition for $\alpha > 0$ as $\mu < 1 - \alpha^2$. For the physical parameter $\mu = 1.48$ estimated in horses (Swanstrom et al., 2005), our results showed that all solutions of Sequences 5 and 6 were unstable, regardless of α (**Figure 3**), which is consistent with their results.

While dogs have a larger CoM offset ($\alpha = 0.28$) (Ben-Amotz et al., 2020) than horses ($\alpha = 0.2$) (Self Davies et al., 2019), they use both transverse and rotary gallop depending on the speed (Biancardi and Minetti, 2012). Polet (2021) showed that the pitch moment of inertia plays an important role for the gait determination using a simple model. In addition to the CoM offset, we would like to investigate the contribution of the pitch moment of inertia to the gait selection in the future.

4.4 Limitations and Future Research

Ground reaction forces of animals during fast running show sinusoidal patterns (Alexander et al., 1986; Full and Tu, 1991; Farley et al., 1993). Blickhan (1989) and McMahon and Cheng (1990) introduced a simple spring-mass model to achieve these patterns for the ground reaction forces. This representation of the leg by a linear spring successfully described and predicted animal locomotion (Blickhan and Full, 1993; Farley et al., 1993; Deng et al., 2012; Tanase et al., 2015; Gan et al., 2016). For example, Gan et al. (2016) reproduced three different gaits (walk, trot, and tölt) of horses by using a quadrupedal spring-mass model and suggested that different quadrupedal gaits are interpreted as different elastic oscillations. Moreover, passively stable running allows the controller and sensing to be simple, even when there are disturbances (Poulakakis et al., 2006). Therefore, such a simple passive model is useful to investigate the gait selection mechanisms by animals (Tanase et al., 2015; Kamimura et al., 2021). However, actual animals lose kinetic energy by collisions of their legs with the ground and by dissipation via friction and compensate for this loss by their muscles. Energy efficiency is an important factor for animal gait (Ruina et al., 2005; Chatzakos and Papadopoulos, 2009; Cao and Poulakakis, 2015; Polet and Bertram, 2019; Polet, 2021). We would like to introduce the elements for energy dissipation and generation in order to obtain a deeper understanding of the running mechanism in animals in the future.

In addition to the CoM offset and pitch moment of inertia, different characteristics between the fore and hind legs could also influence the running dynamics. For example, the muscle mass of the hind legs is greater than that of the fore legs in horses, and it has been suggested that the main role of the fore legs is to support the body weight, whereas that of the hind legs is to generate driving forces (Payne et al., 2005; Crook et al., 2008). Therefore, future investigations of the effects of different characteristics of the legs would be useful for a better understanding of the relationship between the body structure and running in animals.

In the present study, we used the physical parameters estimated in horses to discuss the gait selection by horses. Physical parameters, such as body weight, moment of inertia, and leg length, vary between species. Different parameters could influence the gait preference. We would like to investigate gait selection by animals other than horses in order to clarify the mechanisms for difference gaits between species in future studies.

DATA AVAILABILITY STATEMENT

The raw data supporting the conclusion of this article will be made available by the authors, without undue reservation.

AUTHOR CONTRIBUTIONS

SA and FM contributed to the design of this study. TY conducted the numerical simulation and analysis in consultation with SA, MA, TK, YH, NW, KT, and FM. TY and SA wrote the manuscript, and all of the authors reviewed and approved the manuscript.

FUNDING

This study was supported in part by JSPS KAKENHI Grant Number JP20H00229 and JST FOREST Program Grant Number JPMJFR2021.

SUPPLEMENTARY MATERIAL

The Supplementary Material for this article can be found online at: https://www.frontiersin.org/articles/10.3389/fbioe.2022.825157/full#supplementary-material

REFERENCES

Alexander, R. M., Bennett, M. B., and Ker, R. F. (1986). Mechanical Properties and Function of the Paw Pads of Some Mammals. *J. Zoolog.* 209 (3), 405–419. doi:10.1111/j.1469-7998.1986.tb03601.x

Ben-Amotz, R., Dycus, D., Levine, D., Arruda, A. G., Fagan, N., and Marcellin-Little, D. (2020). Stance and Weight Distribution after Tibial Plateau Leveling Osteotomy in Forelimb and Hind Limb Amputee Dogs. *BMC Vet. Res.* 16, 188. doi:10.1186/s12917-020-02402-7

Berkemeier, M. D. (1998). Modeling the Dynamics of Quadrupedal Running. *Int. J. Robotics Res.* 17 (9), 971–985. doi:10.1177/027836499801700905

Bertram, J. E. A., and Gutmann, A. (2008). Motions of the Running Horse and Cheetah Revisited: Fundamental Mechanics of the Transverse and Rotary Gallop. *J. R. Soc. Interf.* 6 (35), 549–559. doi:10.1098/rsif.2008.0328

Biancardi, C. M., and Minetti, A. E. (2012). Biomechanical Determinants of Transverse and Rotary Gallop in Cursorial Mammals. *J. Exp. Biol.* 215 (23), 4144–4156. doi:10.1242/jeb.073031

Bigalike, R. (1972). Observations on the Behaviour and Feeding Habits of the Springbok, *Antidorcas marsupialis*. *Afr. Zool.* 7 (1), 333–359.

Blickhan, R. (1989). The spring-mass Model for Running and Hopping. *J. Biomech.* 22 (11-12), 1217–1227. doi:10.1016/0021-9290(89)90224-8

Blickhan, R., and Full, R. (1993). Similarity in Multilegged Locomotion: Bouncing like a Monopode. *J. Comp. Physiol. A.* 173 (5), 509–517. doi:10.1007/bf00197760

Buchner, H. H. F., Savelberg, H. H. C. M., Schamhardt, H. C., and Barneveld, A. (1997). Inertial Properties of Dutch Warmblood Horses. *J. Biomech.* 30 (6), 653–658. doi:10.1016/s0021-9290(97)00005-5

Cao, Q., and Poulakakis, I. (2015). On the Energetics of Quadrupedal Running: Predicting the Metabolic Cost of Transport via a Flexible-Torso Model. *Bioinspir. Biomim.* 10 (5), 056008. doi:10.1088/1748-3190/10/5/056008

Chatzakos, P., and Papadopoulos, E. (2009). Bio-inspired Design of Electrically-Driven Bounding Quadrupeds via Parametric Analysis. *Mechanism Machine Theor.* 44, 559–579. doi:10.1016/j.mechmachtheory.2008.08.007

Chen, D., Gong, C., Xing, F., Zhou, C., Qi, M., and Wang, L. (2019). The Effect of Head Movement on the Bounding Gait of a Quadruped Robot with an Active Spine. *Adv. Mech. Eng.* 11 (9), 1–13. doi:10.1177/1687814019876184

Crook, T. C., Cruickshank, S. E., McGowan, C. M., Stubbs, N., Wakeling, J. M., Wilson, A. M., et al. (2008). Comparative Anatomy and Muscle Architecture of Selected Hind Limb Muscles in the Quarter Horse and Arab. *J. Anat.* 212 (2), 144–152. doi:10.1111/j.1469-7580.2007.00848.x

De, A., and Koditschek, D. E. (2018). Vertical Hopper Compositions for Preflexive and Feedback-Stabilized Quadrupedal Bounding, Pacing, Pronking, and Trotting. *Int. J. Robotics Res.* 37 (7), 743–778. doi:10.1177/0278364918779874

Deng, Q., Wang, S., Xu, W., Mo, J., and Liang, Q. (2012). Quasi Passive Bounding of a Quadruped Model with Articulated Spine. *Mechanism Machine Theor.* 52, 232–242. doi:10.1016/j.mechmachtheory.2012.02.003

Dunbar, D. C., Macpherson, J. M., Simmons, R. W., and Zarcades, A. (2008). Stabilization and Mobility of the Head, Neck and Trunk in Horses during Overground Locomotion: Comparisons with Humans and Other Primates. *J. Exp. Biol.* 211 (24), 3889–3907. doi:10.1242/jeb.020578

Farley, C. T., Glasheen, J., and McMahon, T. A. (1993). Running Springs: Speed and Animal Size. *J. Exp. Biol.* 185, 71–86. doi:10.1242/jeb.185.1.71

FitzGibbon, C. D., and Fanshawe, J. H. (1988). Stotting in Thomson's Gazelles: an Honest Signal of Condition. *Behav. Ecol. Sociobiol.* 23 (2), 69–74. doi:10.1007/bf00299889

Full, R. J., and Tu, M. S. (1991). Mechanics of a Rapid Running Insect: Two-, Four- and Six-Legged Locomotion. *J. Exp. Biol.* 156 (1), 215–231. doi:10.1242/jeb.156.1.215

Gan, Z., Wiestner, T., Weishaupt, M. A., Waldern, N. M., and David Remy, C. (2016). Passive Dynamics Explain Quadrupedal Walking, Trotting, and Tölting. *J. Comput. Nonlinear Dyn.* 11 (2), 0210081–2100812. doi:10.1115/1.4030622

Grossi, B., and Canals, M. (2010). Comparison of the Morphology of the Limbs of Juvenile and Adult Horses (*Equus Caballus*) and Their Implications on the Locomotor Biomechanics. *J. Exp. Zool A. Ecol. Genet. Physiol.* 313 (5), 292–300. doi:10.1002/jez.598

Hildebrand, M. (1977). Analysis of Asymmetrical Gaits. *J. Mammalogy* 58 (2), 131–156. doi:10.2307/1379571

Hildebrand, M. (1989). The Quadrupedal Gaits of Vertebrates. *BioScience* 39 (11), 766–775. doi:10.2307/1311182

Hoyt, D. F., and Taylor, C. R. (1981). Gait and the Energetics of Locomotion in Horses. *Nature* 292 (5820), 239–240. doi:10.1038/292239a0

Hudson, P. E., Corr, S. A., and Wilson, A. M. (2012). High Speed Galloping in the Cheetah (*Acinonyx* Jubatus) and the Racing Greyhound (*Canis* familiaris): Spatio-Temporal and Kinetic Characteristics. *J. Exp. Biol.* 215 (14), 2425–2434. doi:10.1242/jeb.066720

Kamimura, T., Aoi, S., Higurashi, Y., Wada, N., Tsuchiya, K., and Matsuno, F. (2021). Dynamical Determinants Enabling Two Different Types of Flight in Cheetah Gallop to Enhance Speed through Spine Movement. *Sci. Rep.* 11 (1), 9631. doi:10.1038/s41598-021-88879-0

Lee, D. V., Stakebake, E. F., Walter, R. M., and Carrier, D. R. (2004). Effects of Mass Distribution on the Mechanics of Level Trotting in Dogs. *J. Exp. Biol.* 207 (10), 1715–1728. doi:10.1242/jeb.00947

McMahon, T. A., and Cheng, G. C. (1990). The Mechanics of Running: How Does Stiffness Couple with Speed? *J. Biomech.* 23 (1), 65–78. doi:10.1016/0021-9290(90)90042-2

Minetti, A. E., Ardigò, L. P., Reinach, E., and Saibene, F. (1999). The Relationship between Mechanical Work and Energy Expenditure of Locomotion in Horses. *J. Exp. Biol.* 202 (17), 2329–2338. doi:10.1242/jeb.202.17.2329

Muybridge, E. (1957). *Animals in Motion*. New York: Dover Publications.

Payne, R. C., Veenman, P., and Wilson, A. M. (2005). The Role of the Extrinsic Thoracic Limb Muscles in Equine Locomotion. *J. Anat.* 206 (2), 193–204. doi:10.1111/j.1469-7580.2005.00353.x

Pennycuick, C. J. (1975). On the Running of the Gnu (*Connochaetes Taurinus*) and Other Animals. *J. Exp. Biol.* 63, 775–799. doi:10.1242/jeb.63.3.775

Polet, D. T. (2021). The Murphy Number: How Pitch Moment of Inertia Dictates Quadrupedal Walking and Running Energetics. *J. Exp. Biol.* 224, jeb228296. doi:10.1242/jeb.228296

Polet, D. T., and Bertram, J. E. A. (2019). An Inelastic Quadrupedal Model Discovers Four-Beat Walking, Two-Beat Running, and Pseudo-elastic

Actuation as Energetically Optimal. *Plos Comput. Biol.* 15 (11), e1007444. doi:10.1371/journal.pcbi.1007444

Poulakakis, I., Papadopoulos, E., and Buehler, M. (2006). On the Stability of the Passive Dynamics of Quadrupedal Running with a Bounding Gait. *Int. J. Robotics Res.* 25 (7), 669–687. doi:10.1177/0278364906066768

Ruina, A., Bertram, J. E. A., and Srinivasan, M. (2005). A Collisional Model of the Energetic Cost of Support Work Qualitatively Explains Leg Sequencing in Walking and Galloping, Pseudo-elastic Leg Behavior in Running and the Walk-To-Run Transition. *J. Theor. Biol.* 237 (2), 170–192. doi:10.1016/j.jtbi.2005.04.004

Self Davies, Z. T., Spence, A. J., and Wilson, A. M. (2019). Ground Reaction Forces of Overground Galloping in Ridden Thoroughbred Racehorses. *J. Exp. Biol.* 222 (16), jeb204107. doi:10.1242/jeb.204107

Swanstrom, M. D., Zarucco, L., Hubbard, M., Stover, S. M., and Hawkins, D. A. (2005). Musculoskeletal Modeling and Dynamic Simulation of the Thoroughbred Equine Forelimb during Stance Phase of the Gallop. *J. Biomech. Eng.* 127 (2), 318–328. doi:10.1115/1.1865196

Tanase, M., Ambe, Y., Aoi, S., and Matsuno, F. (2015). A Galloping Quadruped Model Using Left-Right Asymmetry in Touchdown Angles. *J. Biomech.* 48 (12), 3383–3389. doi:10.1016/j.jbiomech.2015.06.003

Zou, H., and Schmiedeler, J. P. (2006). The Effect of Asymmetrical Body-Mass Distribution on the Stability and Dynamics of Quadruped Bounding. *IEEE Trans. Robot.* 22 (4), 711–723. doi:10.1109/tro.2006.875477

Conflict of Interest: The authors declare that the research was conducted in the absence of any commercial or financial relationships that could be construed as a potential conflict of interest.

frontiers in Bioengineering and Biotechnology

ORIGINAL RESEARCH
published: 01 March 2022
doi: 10.3389/fbioe.2022.767914

Kinematic Modeling at the Ant Scale: Propagation of Model Parameter Uncertainties

Santiago Arroyave-Tobon[1†]*, *Jordan Drapin*[2†], *Anton Kaniewski*[1], *Jean-Marc Linares*[1] and *Pierre Moretto*[2]

[1]Institut Des Sciences Du Mouvement, Faculté Des Sciences Du Sport, Aix-Marseille Université, CNRS, Marseille, France, [2]Centre de Recherches sur la Cognition Animale (CRCA), Centre de Biologie Intégrative (CBI), Université de Toulouse, CNRS, UPS, Toulouse, France

Quadrupeds and hexapods are known by their ability to adapt their locomotive patterns to their functions in the environment. Computational modeling of animal movement can help to better understand the emergence of locomotive patterns and their body dynamics. Although considerable progress has been made in this subject in recent years, the strengths and limitations of kinematic simulations at the scale of small moving animals are not well understood. In response to this, this work evaluated the effects of modeling uncertainties on kinematic simulations at small scale. In order to do so, a multibody model of a *Messor barbarus* ant was developed. The model was built from 3D scans coming from X-ray micro-computed tomography. Joint geometrical parameters were estimated from the articular surfaces of the exoskeleton. Kinematic data of a free walking ant was acquired using high-speed synchronized video cameras. Spatial coordinates of 49 virtual markers were used to run inverse kinematics simulations using the OpenSim software. The sensitivity of the model's predictions to joint geometrical parameters and marker position uncertainties was evaluated by means of two Monte Carlo simulations. The developed model was four times more sensitive to perturbations on marker position than those of the joint geometrical parameters. These results are of interest for locomotion studies of small quadrupeds, octopods, and other multi-legged animals.

Keywords: multibody, inverse kinematics, ant, motion capture, uncertainty

OPEN ACCESS

Edited by:
John R. Hutchinson, Royal Veterinary College, United Kingdom

Reviewed by:
Tom Weihmann, Universität zu Köln, Germany
Toni Wöhrl, Friedrich Schiller University Jena, Germany

***Correspondence:**
Santiago Arroyave-Tobon
santiago.arroyave-tobon@univ-amu.fr

[†]These authors have contributed equally to this work and share first authorship

Specialty section:
This article was submitted to Biomechanics, a section of the journal Frontiers in Bioengineering and Biotechnology

Received: *31 August 2021*
Accepted: *20 January 2022*
Published: *01 March 2022*

Citation:
Arroyave-Tobon S, Drapin J, Kaniewski A, Linares J-M and Moretto P (2022) Kinematic Modeling at the Ant Scale: Propagation of Model Parameter Uncertainties. Front. Bioeng. Biotechnol. 10:767914. doi: 10.3389/fbioe.2022.767914

1 INTRODUCTION

Legged locomotion is the most common form of terrestrial animal movement (Christensen et al., 2021). Even if quadrupedal and hexapodal forms of locomotion have evolved independently (Blickhan and Full, 1987), they present similarities. Both quadrupeds and hexapods can adapt their locomotive patterns according to their objective (Hoyt and Taylor, 1981; Nirody, 2021). Like quadrupeds, hexapods exhibit a wide variety of locomotor strategies (Nirody, 2021), e.g., walking, running, and jumping (Musthak Ali et al., 1992) or even swimming (Schultheiss and Guénard, 2021) and gliding hovering (Yanoviak et al., 2005). As some quadrupeds do, insects change smoothly the inter-leg coordination patterns based on their locomotion speed (Ambe et al., 2018). In the metachronous gait (or direct wave gait), hexapods propagate swinging movements from the hind legs to the forelegs, similarly as quadrupeds do in the walking gait (Ambe et al., 2018). In tripod gait, hexapods move their diagonal legs in phases, as quadrupeds do in the trotting gait (Ambe

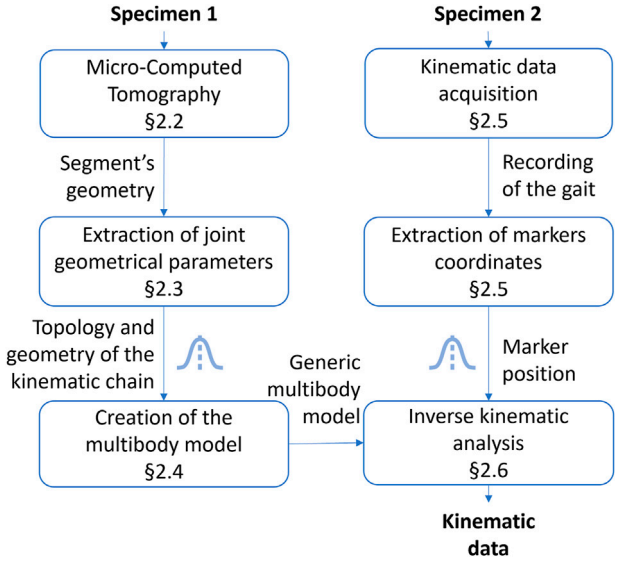

FIGURE 1 | Followed research methodology. The Gaussian distribution icon indicates model parameters subjected to uncertainty.

et al., 2018). These equivalences in the locomotion mechanics generate similar ground reaction force patterns in quadrupeds and hexapods, as demonstrated experimentally by Full et al. (1991). In that study, the authors demonstrated that at constant average speed, cockroaches function as a spring–mass system in which three legs add up to function as one leg of a biped or two legs of a quadruped.

As opposed to bipedal and quadrupedal locomotion, hexapodal locomotion is characterized by its plasticity. For instance, hexapods can adopt quadrupedal or bipedal gaits to increase speed, as has been shown in cockroaches (Full et al., 1991). The bipedal posture adopted when the insect stands up allows for a longer stride length while maintaining the same stride frequency, thus raising the speed. In stick insects, the coordination of the middle legs and hind legs is similar to the typical regular gait of quadrupeds (Grabowska et al., 2012). The emergence of quadrupedal gaits on hexapod robots has also been demonstrated when a sudden fault event occurs to one leg (Yang and Kim, 1998). However, these adaptations deserve further analysis to better understand the plasticity and dynamics of multi-legged gait.

The hexapodal gait has been first described as an alternative tripod gait that ensures high static stability (Hughes, 1952) regardless of the support. Yet studies estimating ground reaction forces demonstrate different functions of the rear, median, and front legs (sustain, propel, push, or drag) (Cruse, 1976; Full et al., 1991; Grabowska et al., 2012; Reinhardt and Blickhan, 2014; Wöhrl et al., 2017). Other studies, dedicated to the effects of the ground substrates or load carried, demonstrated the plasticity of the tripod gait in response to mechanical constraints (Bernadou et al., 2011; Pfeffer et al., 2019; Merienne et al., 2020). These studies suggest that hexapodal gait is more complex than a mere alternating tripod one. Furthermore, the small scale and lack of a precise description of the architecture of the musculoskeletal system could explain why the hexapodal gait is less documented than the quadrupedal or bipedal gaits.

Learning how insects adapt their locomotion strategies to their environment (motor and neural control), how each body segment moves for a given locomotion strategy (kinematics), and how forces are generated (muscle actuation) and transmitted (joint dynamics) could help answer biological questions and develop engineering applications. For instance, kinematic, dynamic, and motor control data regarding animal locomotion proved indispensable for bio-inspired robotics development. Particularly, some examples of applications include bio-inspired robot architecture (Lu et al., 2018), bio-inspired control strategies for legged robots (Dupeyroux et al., 2019; Ouyang et al., 2021), and bio-inspired actuation systems (Ahn et al., 2019), among others.

Computational modeling of animal movement can help us better understand the emergence of locomotive patterns and their mechanics by means of musculoskeletal models. A musculoskeletal model is composed of a kinematic model coupled to a dynamic model. The kinematic model, which represents the skeletal system, is a set of body segments connected by joints (i.e., a multibody system). A dynamic model, which represents the muscular system, is a set of actuators attached to the skeletal system.

The proper development of the kinematic model is essential for predicting later muscle and joint forces (Dunne et al., 2021). In kinematic modeling, constrained inverse kinematics, as opposed to with unconstrained inverse kinematics, leads to a more realistic prediction of joint kinematics. Conversely, unconstrained inverse kinematics, which permits a fast exploitation of experimental data using stick models, can generate unrealistic behaviors, such as a model's body segment changing length (Dunne et al., 2021). This kind of behavior is unsuitable for musculoskeletal simulations. In constrained kinematic modeling, which is conducted using multibody models, the position and orientation of each segment of the kinematic chain are derived from the trajectories of experimental markers. This is done by optimizing procedures that minimize the weighted least-squares distance between experimental markers and the corresponding markers placed on the kinematic model (Lu and O'Connor, 1999). The position and orientation of each segment of the kinematic chain, together with their first-order derivatives, can be used for further muscle and joint force estimation.

In the case of vertebrates, the development and use of musculoskeletal models are mainly motivated by medical applications (REFS). In the case of insects, motivations are mostly related to biology, ecology, and evolution. Ramdya et al. (2017) developed a multibody model of *Drosophila* to study fast locomotor gaits. Guo et al. (2018) proposed a neuromusculoskeletal model for insects to study control strategies in gait patterns. David et al. (2016) and Blanke et al. (2017) developed musculoskeletal models of the dragonfly's mandible to study bite forces. A kinematic model of stick insects was developed by Theunissen and Dürr (2013). In the case of ants, locomotion studies mostly focus on experimental

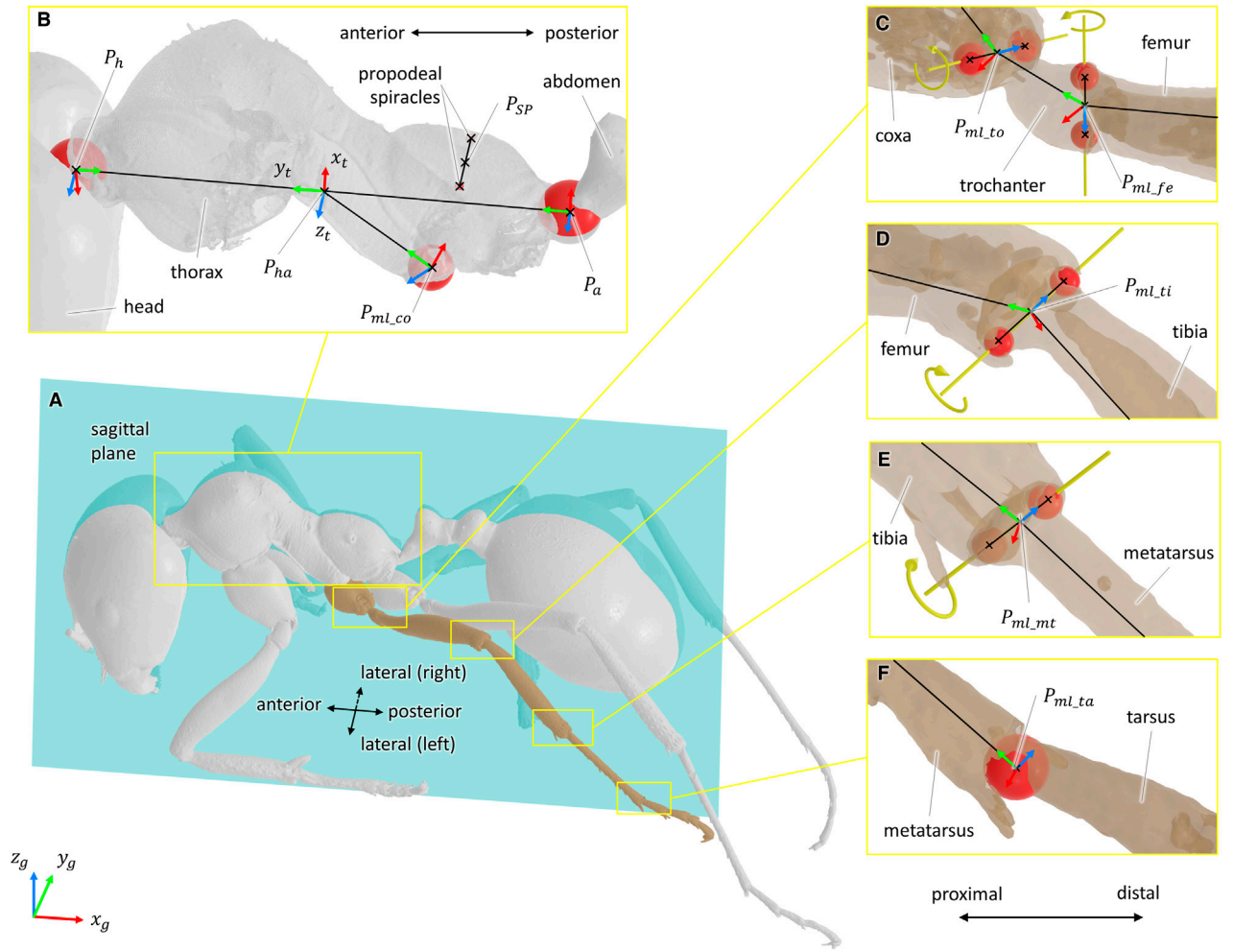

FIGURE 2 | Definition of the joint geometrical parameters and coordinate systems. For all coordinate systems, the *x*-axis is represented in red, the *y*-axis in green, and the *z*-axis in blue. For ball-and-socket joints, a sphere fitted to the articular surface was considered as the center of the rotation of the joint. For hinge joints, the rotation axis was defined as the line passing through the center of two spheres fitted to the condyles of the joint. Fitted spheres are represented in red, and rotation axes are represented in yellow. **(A)** Representation of the sagittal plane. **(B)** Geometrical elements used to define the sagittal plane, the coordinate system of the thorax (x_t, y_t, z_t), and the coordinate system of the middle left coxa. The point P_{SP} was defined as the mid-point of the line segment passing through the center of the two propodeal spiracles. The points P_h and P_a correspond to the center of the spheres fitted to the thorax/head and thorax/abdomen joints, respectively. The point P_{ml_co} corresponds to the center of the sphere fitted to the articular surface of the middle left thorax/coxa joint. **(C–E)** Geometrical elements used to define the rotation axes and the coordinate systems of the coxa/trochanter, trochanter/femur, femur/tibia, and tibia/metatarsus joints. In respective order, the points P_{ml_to}, P_{ml_fe}, P_{fe_ti}, and P_{ti_mt} were defined as the mid-points of the line segments representing the rotation axis of the joints. **(F)** Geometrical elements used the rotation center and the coordinate systems of the metatarsus/tarsus joint. The point P_{ml_ta} corresponds to the center of the sphere fitted to the articular surface of the metatarsus/tarsus joint.

procedures. Examples are video-based kinematic analysis (Weihmann and Blickhan, 2009; Moll et al., 2010; Pfeffer et al., 2019), stepping pattern analysis (Zollikofer, 1994), center of mass tracking (Reinhardt and Blickhan, 2014; Merienne et al., 2020; Merienne et al., 2021), quantification of ground reaction forces (Reinhardt et al., 2009; Wöhrl et al., 2017), and mandible forces (Zhang et al., 2020), among others.

Despite the aforementioned examples, the use of musculoskeletal models at the insect scale is not yet widespread, probably due to the technological barriers to acquire experimental data (kinematic, dynamic, and morphometric data). When we compare the relative resolution of motion capture systems *vs*. the subject size, it can be argued that motion capture at the human scale is far more accurate than at the insect scale. In human motion analysis using reflective markers, the measuring uncertainty can reach 0.33 mm in a volume of $5.5 \times 1.2 \times 2.0\ m^3$ (Eichelberger et al., 2016) (0.0275% in the smallest dimension). Motion analysis by means of physical markers is not easy in small insects. A pattern-matching procedure based on video films is a feasible solution for the moment. With the use of this technique at the small scale, our setup reached, on average, 3% resolution in each dimension of the calibrated volume (including tracking errors and pattern recognition errors). The difficulty with small scales lies in keeping the depth of field of the camera at a reasonable size when zooming in to get a clear whole-body image. This problem

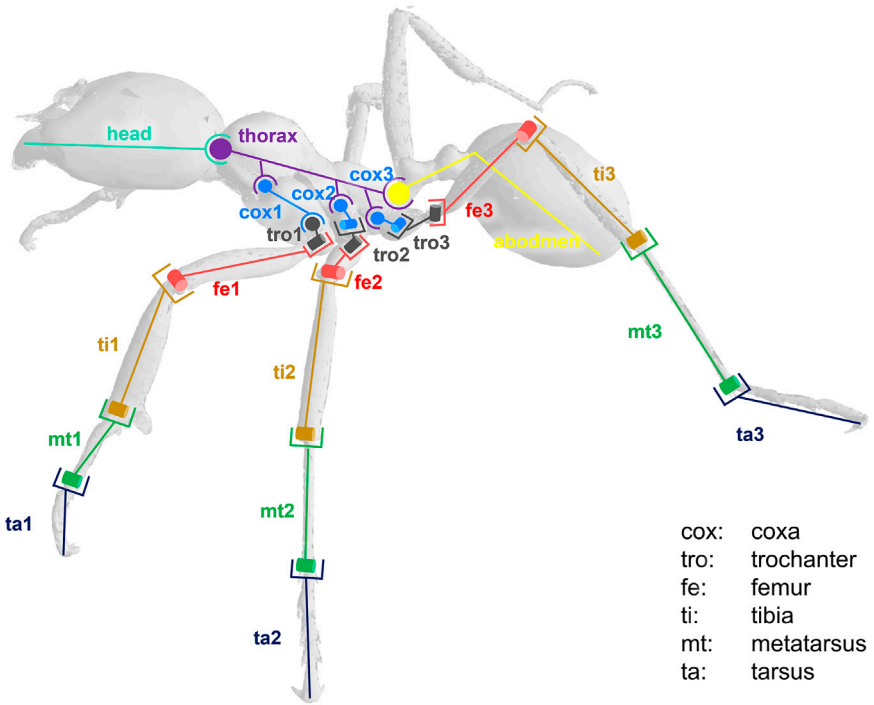

FIGURE 3 | Kinematic chain representing half of the ant locomotor system. Anatomy: th (thorax), pet (petiole), abd (abdomen), cox (coxa), tro (trochanter), fe (femur), ti (tibia), mt (metatarsus), ta (tarsus). Type of joint: hinge (example: mt/ta) or ball and socket (example: head/thorax).

is not encountered in larger subjects because the lenses are far from the objective. Similar difficulties are faced in morphometric data acquisition in small insects, which is required for the definition of joint locations in musculoskeletal modeling. This implies that the effect of uncertainties in musculoskeletal modeling at the insect scale must be considered and evaluated to understand the limits of this tool in locomotion analysis. Estimation of uncertainties in kinematic modeling has been widely addressed at the human scale (see, for example, Groen et al., 2012; El Habachi et al., 2015; Martelli et al., 2015). At the insect scale, however, it is unclear how modeling assumptions affect predicted results in kinematic modeling.

The present work therefore evaluated the effects of modeling assumptions in kinematic analysis at the small insect scale, particularly on a *Messor barbarus* ant. To achieve this objective, (1) a whole-body kinematic model of the *Messor barbarus* ant was developed (**Section 2.1**), (2) an inverse kinematics simulation of the ant gait was reproduced using the developed model and experimental kinematic data (**Section 2.6**), and (3) the sensitivity of the predicted results regarding model parameter uncertainties was evaluated (**Section 2.7**).

2 METHODS

The global research methodology followed in this work is illustrated in **Figure 1**. Specimens 1 and 2 belong to the medium-sized caste of the *Messor barbarus* species (more details in **Section 2.1**). Specimen 1 was used to build a 3D model from micro-computed tomography (**Section 2.2**). 3D models of body segments were used to extract joint geometrical parameters and to create a multibody model (**Section 2.3** and **Section 2.4**). Specimen 2 was used to acquire experimental kinematic data and to extract marker trajectories (**Section 2.5**). Experimental kinematic data were used to scale the multibody model and to run an inverse kinematics simulation (**Section 2.6**). To evaluate the impact of the propagation of model parameter uncertainties on joint angles, two Monte Carlo (MC) simulations were conducted (**Section 2.7**). Model parameters subjected to uncertainty are represented by a Gaussian distribution icon in **Figure 1**.

2.1 Experimental Model

We used workers from a colony of *Messor barbarus* collected in April 2018 in Saint-Hippolyte (42°78 north; 2°97 east, Pyrénées-Orientales, France). *Messor barbarus* is a seed-collecting ant whose mature colonies can harbor tens of thousands of individuals (Hölldobler and Wilson, 1990). The body mass of the scanned subject was 8.92 mg.

The main colony was kept in a box (L: 50 cm × W: 30 cm × H: 15 cm) with walls coated with Fluon® to prevent ants from escaping. The ants could shelter inside nests formed with test tubes (length: 20 cm; diameter: 2.5 cm) covered with opaque paper. They had access to water and a mixture of bird seeds. The experimental room was maintained at a constant

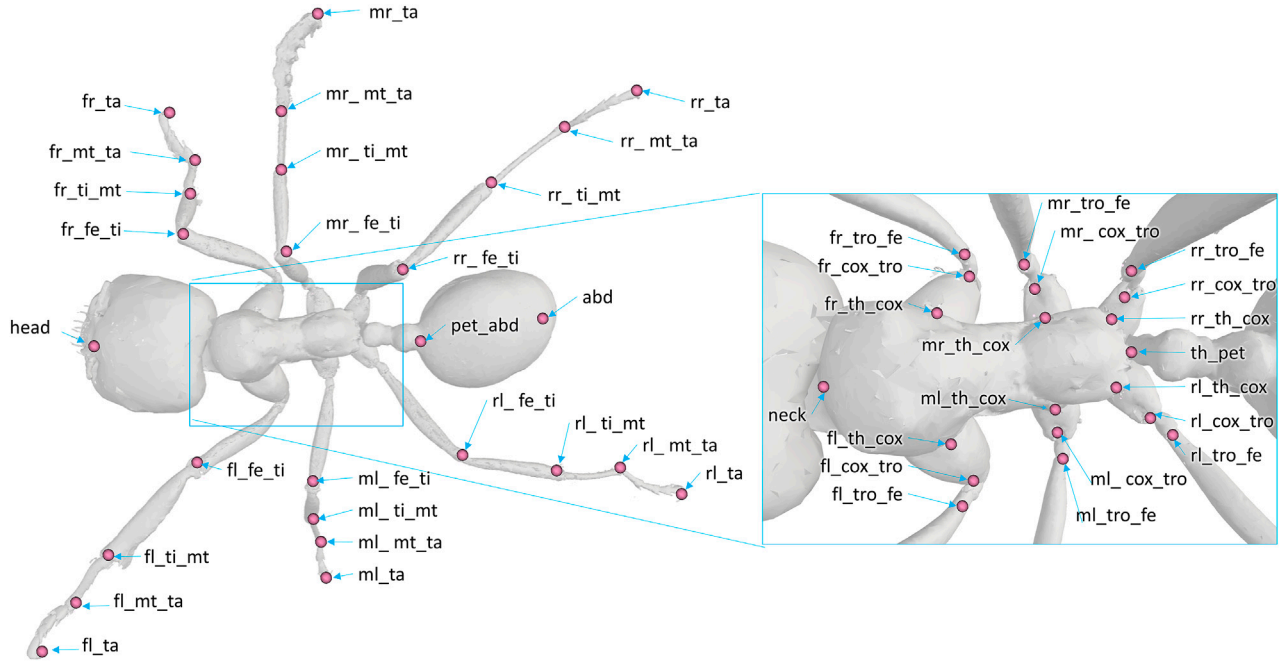

FIGURE 4 | Position and denomination of the markers on the model. The following abbreviations are used for the denomination of the markers. Prefix: f (front), m (middle), or r (rear); position: l (left), r (right). Anatomy and articulation: th (thorax), pet (petiole), abd (abdomen), cox (coxa), tro (trochanter), fe (femur), ti (tibia), mt (metatarsus), ta (tarsus).

TABLE 1 | Maximum range of motion allowable for each degree of freedom of trunk joints. Values are presented per leg: front, middle, and rear. The same values were used for left and right legs. These values were determined in OpenSim by articulating each degree of freedom of the model until some structures of the joint segments touch each other.

degree of freedom	Maximum allowable range of motion (deg)
thorax/head adduction	75
thorax/head internal rotation	40
thorax/head flexion	120
thorax/abdomen adduction	25
thorax/abdomen internal rotation	60
thorax/abdomen flexion	100

TABLE 2 | Maximum range of motion allowable for each degree of freedom of the leg joints. Values are presented per leg: front, middle, and rear. The same values were used for left and right legs. These values were determined in OpenSim by articulating each degree of freedom of the model until some structures of the joint segment touch. Non-allocated values (NA) correspond to blocked degrees of freedom.

degree of freedom	Front legs (deg)	Middle legs (deg)	Rear legs (deg)
thorax/cox abduction	70	80	110
thorax/cox internal	40	55	105
thorax/cox flexion	80	100	105
cox/tro abduction	120	NA	NA
cox/tro internal	165	NA	NA
cox/tro flexion	180	120	130
tro/fe flexion	130	180	120
fe/ti flexion	160	165	190
ti/mt flexion	190	200	175
mt/ta flexion	200	200	240

temperature of 26°C (thermometer: TFA Dostmann/Wertheim) and under an artificial photoperiod regime 12 h:12 h (light:dark).

2.2 Micro-Computed Tomography

Following the procedure used by Peeters et al. (2020), specimen 1 was stored in 90% ethanol, then stained in a 2 M iodine solution for a minimum of 24 h, and transferred into micro-tubes filled with 99% ethanol. It was then transferred to the Okinawa Institute of Science and Technology Graduate University (OIST, Japan) to be scanned using micro-computed tomography (μ-CT). This was performed using a Zeiss Xradia 510 Versa 3D X-ray microscope operated by the Zeiss Scout-and-Scan Control System software (version 11.1). A vertical stitching enabled a three-times scanning along a head–trunk–gaster axis, each with a resolution of 933 × 1,013 × 988 pixels (providing a voxel of 5.7 μm). These scans were compiled to increase the resolution of the whole ant body to 3,159 × 1,013 × 988 pixels. The DICOM images of the μ-CT scan were used to build the 3D models of the body segments. A segmentation was done using ITK-SNAP (version 3.6.0) (Yushkevich et al., 2006) to differentiate the body segments as follows: head, thorax, abdomen, coxa, trochanter, femur, tibia, metatarsus, and tarsus. The four tarsal segments were lumped all into a unique rigid segment called tarsus in this work.

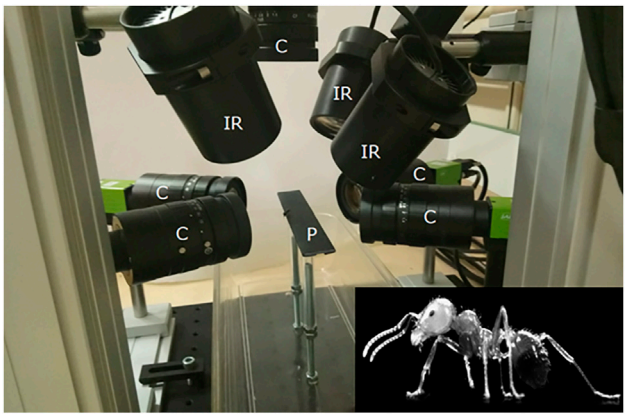

FIGURE 5 | Video acquisition system. The experimental setup was composed of a wide walkway where the ant walked through and was captured by five cameras. C: cameras, IR: infrared spots, P: 250 × 20 mm wide walkway.

2.3 Extraction of Joint Geometrical Parameters

Defining the types of joints was done from both literature and morphometric data (Liu et al., 2019). From the 3D models of the body segments, joint geometrical parameters were estimated from the articular surfaces of the exoskeleton using a CAD software (3D EXPERIENCE, Dassault Systèmes, France). For ball-and-socket joints, the center of a sphere fitted to the articular surface was considered as the center of rotation of the joint (see **Figures 2B,F**). For hinge joints, the rotation axis was defined as the line passing through the center of two spheres fitted to the condyles of the joint (see **Figures 2C–E**). The procedure to determine joint geometrical parameter was also used in insect biomechanical modeling by Blanke et al. (2017). Because of low perceived motion and to facilitate the convergence of the inverse kinematics algorithm, the internal rotation of the metatarsus of each leg was not considered [it was assumed as a blocked degree of freedom (DOF)].

2.4 Creation of the Multibody Model

A multibody model was created, representing the whole-body locomotor system of the *Messor barbarus*.

According to the recommendations of the ISB (Wu et al., 2002, 2005), a coordinate system was defined for each body segment and for the ground. All coordinate systems were defined as right-handed and orthogonal, as follows (see **Figure 2**):

- Definition of the sagittal plane: plane perpendicular to the line passing through the center of two spheres fitted to the propodeal spiracles and containing the point P_{SP}. Point P_{SP} was defined as the mid-point of the line segment defined by the two propodeal spiracles, see **Figure 2B**.
- Global coordinate system (x_g, y_g, z_g): The z_g-axis points upward, parallel to the field of gravity. The x_g-axis points in the direction opposite the direction of travel. The y_g-axis was defined as the common axis perpendicular to x_g- and z_g-axes.
- Thorax coordinate system (x_t, y_t, z_t): the origin of this coordinate system was defined as the mid-point of the line segment passing through the center of the spheres fitted to the thorax/neck joint and thorax/abdomen joints, points P_h and P_a in **Figure 2B**, respectively. The y_t-axis was defined parallel to the line segment P_hP_a and pointing anteriorly. The x_t-axis was defined as the common axis perpendicular to the normal vector of the sagittal plane and to y_t. The z_t-axis was defined as the common axis perpendicular to x_t- and y_t-axes.
- For hinge joints, the origin of the coordinate system was chosen as the mid-point of the line segment representing the rotation axis (for example, points P_{ml_to} and P_{ml_fe} in **Figure 2C**, P_{ml_ti} in **Figure 2D**, and P_{ml_mt} in **Figure 2E**). The z-axis was defined parallel to the rotation axis and pointing medially. The y-axis was defined perpendicular to the z-axis and pointing to the origin of the coordinate system of the previous segment. The x-axis was defined as the common axis perpendicular to y- and z-axes.
- For ball-and-socket joints, the origin of the coordinate system was chosen as the center of the sphere fitted to the articular surface (for example, points P_{ml_co} and P_{ml_ta} in **Figures 2B,F**, respectively). The y-axis was defined parallel to the line passing through the origin of the coordinate system and the origin of the coordinate system of the previous segment and pointing proximally. The x-axis was defined as the common axis perpendicular to the normal vector of the sagittal plane and to y. The z-axis was defined as the common axis perpendicular to x- and y-axes.

According to the previous definitions of the coordinate systems, the following convention for rotations was adopted: abduction, positive rotation about the x-axis; adduction, negative rotation about the x-axis; internal rotation, positive rotation about the y-axis; external rotation, negative rotation about the y-axis; flexion, negative rotation about the z-axis; and extension, positive rotation about the z-axis.

The model was composed of 39 segments and 65 DOFs. Segments were considered as rigid bodies, and joints were considered without clearance. Half of the kinematic chain of this model is presented in **Figure 3**. Forty-seven virtual markers were placed on the model according to the tracked anatomical landmarks (see **Figure 4**). The model was created using the software tool NSM Builder (version 2.1) (Valente et al., 2017) and finally exported in an OpenSim format. The range of motion of the joints was constrained to feasible values to aid the convergence of the inverse kinematics algorithm. These values were determined in OpenSim by articulating each DOF of the model until some structures of the joint segments touch each other. Obtained values are presented in **Tables 1** and **2**.

2.5 Kinematic Data Acquisition and Treatment

Kinematic data of a free walking ant (mean speed over the length of the calibrated walkway: 3.4 mm s^{-1}) were acquired using high-speed synchronized video cameras (AI GO-5000M-

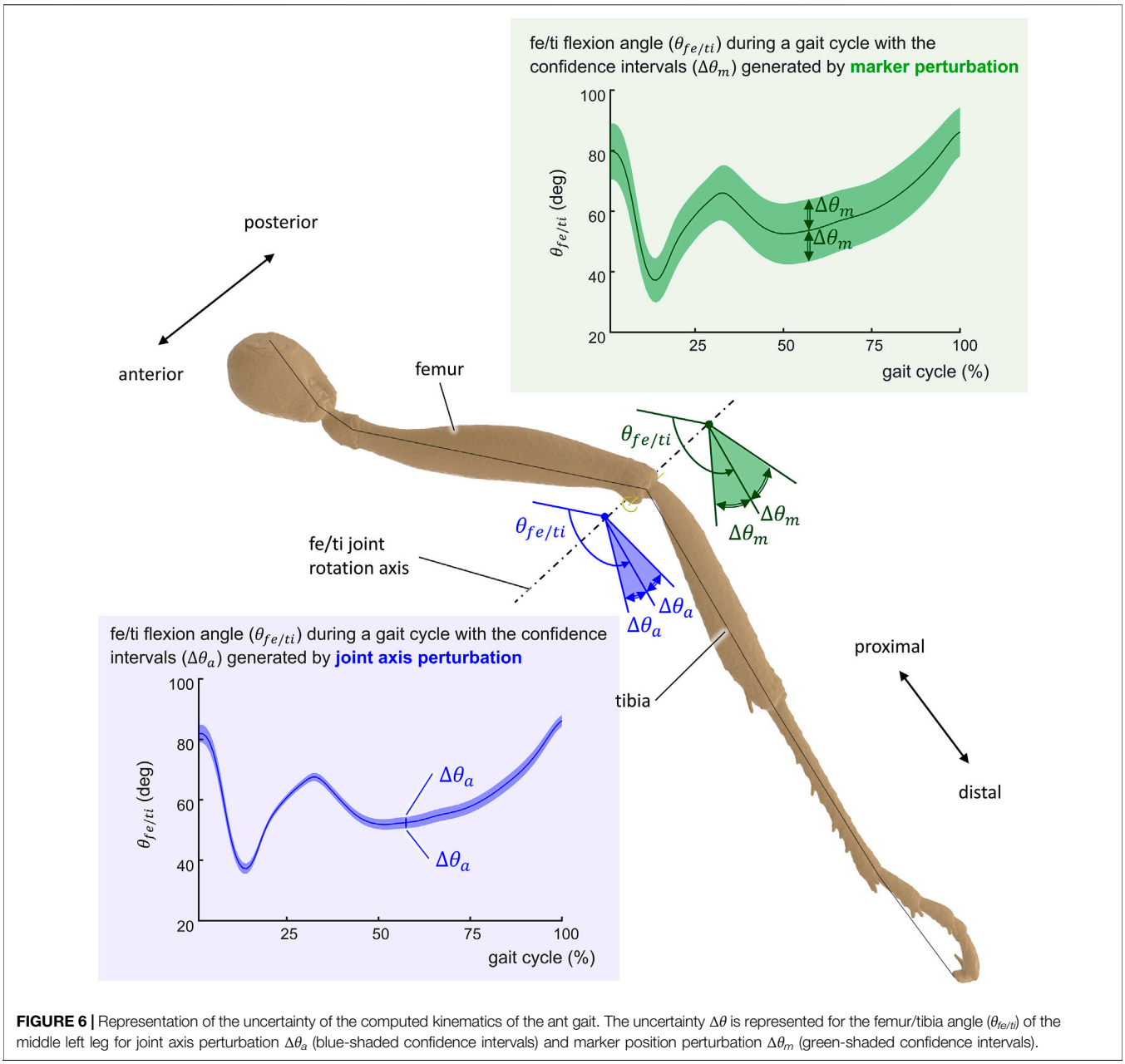

FIGURE 6 | Representation of the uncertainty of the computed kinematics of the ant gait. The uncertainty $\Delta\theta$ is represented for the femur/tibia angle ($\theta_{fe/ti}$) of the middle left leg for joint axis perturbation $\Delta\theta_a$ (blue-shaded confidence intervals) and marker position perturbation $\Delta\theta_m$ (green-shaded confidence intervals).

TABLE 3 | Results of the inverse kinematic simulation for the trunk joints. Reported values represent the range of motion in degrees of the joint angles.

degree of freedom	Range of motion (deg)
thorax/head abduction	19.5
thorax/head internal rotation	9.0
thorax/head flexion	13.3
thorax/abdomen abduction	11.9
thorax/abdomen internal rotation	14.2
thorax/abdomen flexion	13.8

PMCL). The experimental setup was composed of a wide walkway where the ant walked through, with five cameras (one on the top and two for each side or the walkway) and three infrared spots (see **Figure 5**). The shutter time was 1/3,333 s, and the acquisition time was set to 10 s with a sampling frequency of 300 Hz. The infrared spots were added to compensate this short shutter time. The resolution of the camera sensor was 2,560 × 2,048 pixels. Using the Hiris software of R&D Vision (version 5.2.0), the active sensor window was adjusted to the ant size in a 2,000 × 418 pixel rectangular area. The average field of vision of the cameras was

TABLE 4 | Results of the inverse kinematic simulation for the leg joints. Reported values represent the range of motion in degrees of the joint angles. Non-allocated values (NA) correspond to blocked degrees of freedom.

degree of freedom	Front right leg (deg)	Middle right leg (deg)	Rear right leg (deg)	Front left leg (deg)	Middle left leg (deg)	Rear left leg (deg)
thorax/cox abduction	40.7	32.0	16.5	19.1	23.4	27.2
thorax/cox internal rotation	29.3	54.0	35.7	28.1	26.0	16.3
thorax/cox flexion	26.5	25.9	90.6	22.1	39.4	14.9
cox/tro abduction	78.2	NA	NA	74.6	NA	NA
cox/tro internal rotation	76.3	NA	NA	47.3	NA	NA
cox/tro flexion	90.0	30.6	30.2	43.9	48.3	42.4
tro/fe flexion	120.7	53.1	103.9	78.6	27.2	15.6
fe/ti flexion	61.6	73.6	66.7	39.3	38.2	60.2
ti/mt flexion	53.8	41.0	29.0	63.4	17.7	17.2
mt/ta flexion	56.9	36.2	43.5	57.7	NA	23.4

TABLE 5 | Results of the sensitivity analysis. These results represent the average signal-to-noise ratio per joint obtained from marker perturbation (first column) and axis perturbation (second column). In the case of cox/tro, tro/fe, fe/ti, ti/mt, and mt/ta joints, averages were calculated from the signal-to-noise ratio of the six legs.

Joint	Signal-to-noise ratio from marker perturbation	Signal-to-noise ratio from axis perturbation
all joints	2.20	8.10
right-hand side joints	2.29	7.96
left-hand side joints	2.27	8.92
front legs joints	1.54	9.13
middle legs joints	2.82	8.05
rear legs joints	2.69	7.97
thorax/head	1.71	5.08
thorax/abdomen	1.38	4.97
thorax/cox	1.58	4.65
cox/tro	2.73	7.25
tro/fe	1.57	5.52
fe/ti	6.87	27.63
ti/mt	1.70	8.62
mt/ta	1.19	7.14

$15.8 \times 4.9 \times 7.8$ mm that gives a spatial resolution of 0.0096 mm/pixel. Obtained raw videos are available from the project repository.

Following a similar protocol as Merienne et al. (2020), the filming procedure was as follows. (1) The ant was randomly collected from the colony and left in a box for 15 min in order to reduce the stress of the capture. (2) The ant was located at the beginning of the walkway and the recording started when it entered in the calibrated volume. The temperature of the room was $26 \pm 0.2^{\circ}$ during the filming procedure. Only one gait cycle was studied to avoid the variability of the motor control during different gait cycles (change of the walking speed, balance management, and change of movement direction).

Video recordings were processed afterwards with the Vicon Peakmotus (version 10) software tool. Segment extremities were tracked semi-automatically during a gait cycle using a pattern-matching technique. The gait cycle was defined when the left middle leg leaves the ground and lifts, and it ends when that same leg leaves the ground again. Kinematic data were filtered with fourth-order Butterworth low-pass filters with a cutoff frequency of 5 Hz. It was then resampled from 300 to 100 Hz to decrease computation time. Spatial coordinates of the anatomical landmarks (those represented in **Figure 4**) were exported on a c3d format file. This file is available from the project repository.

2.6 Model Scaling and Inverse Kinematics Analysis

Spatial coordinates of the anatomical landmarks were used to scale the multibody model and to run inverse kinematics simulations. A scaling procedure was carried out to fit the model (originally created from the morphology of specimen 1) to the morphology of specimen 2. This was performed using the open-source software tool OpenSim (version 4.0) (Seth et al., 2018). Using the scaled model, inverse kinematics simulations were also performed in OpenSim. Joint angles as well as root mean square errors (RMSEs) were obtained from these simulations.

2.7 Propagation of Model Parameter Uncertainties

In order to evaluate the sensitivity of the calculated kinematic data to model parameter uncertainties, two MC simulations were conducted. A similar procedure was used by Martelli et al. (2015) and Myers et al. (2015).

In the first MC simulation, the position of model markers was randomly perturbed according to their uncertainty. Random values were assumed to have a uniform distribution (i.e., all outcomes were considered as equally likely). Variations were assumed to be

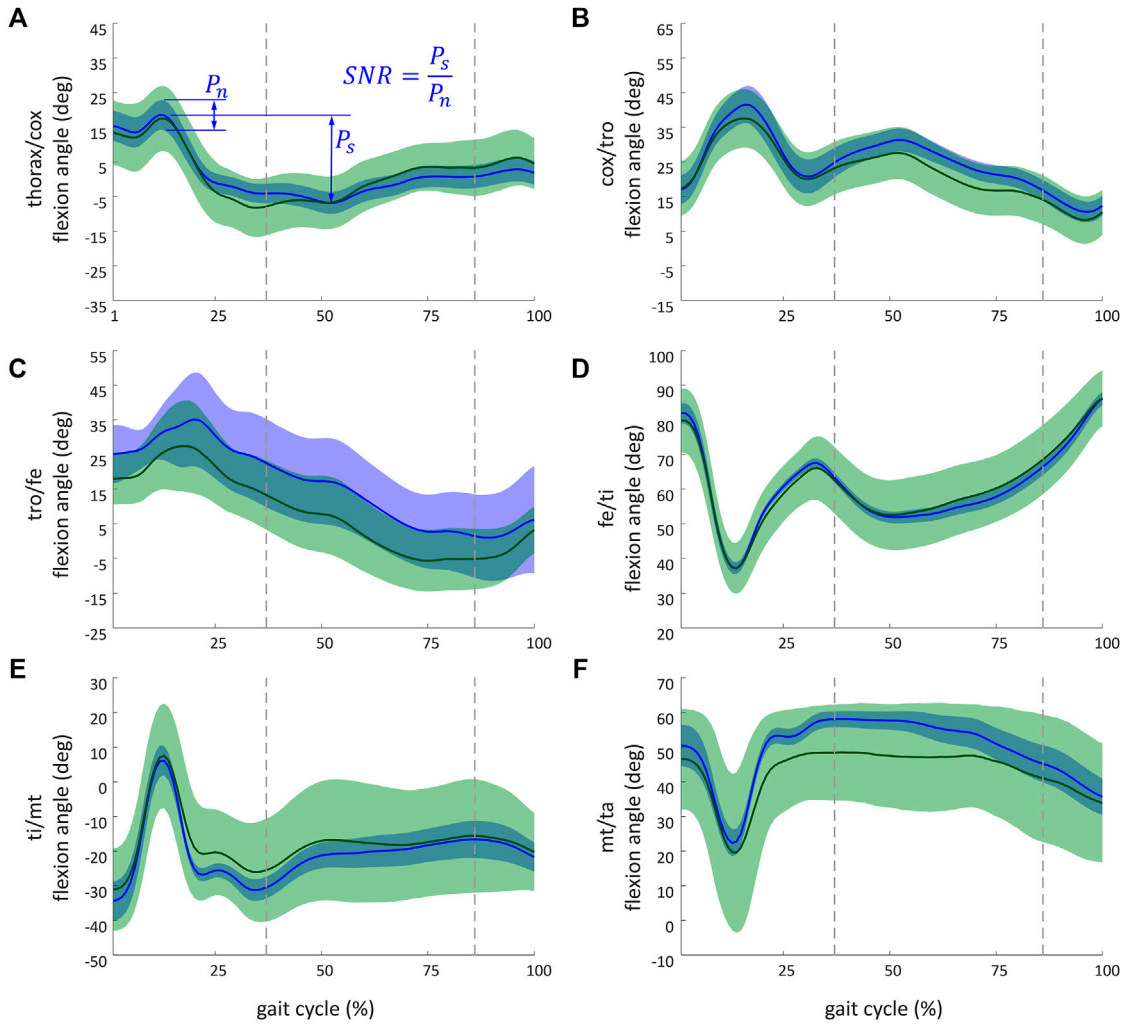

FIGURE 7 | Kinematic results obtained from the simulation of the ant model and the experimental kinematic data for flexion angle of the middle right leg of **(A)** thorax/cox; **(B)** cox/tro; **(C)** tro/fe; **(D)** fe/ti; **(E)** ti/mt, and **(F)** mt/ta. The recorded and simulated gait cycles lasted 1.39 s. These results are a sample of the whole set of results available from the project repository. Solid lines indicate the mean values from the Monte Carlo simulations from the marker perturbation (green) and from the axis perturbation (blue). For marker and axis perturbations, respectively, the green- and blue-shaded regions represent the confidence interval (calculated as twice the standard deviation). The dashed vertical lines (37% and 87%) indicate when legs of both tripods were on the ground. The SNR of the thorax/cox flexion angle obtained from the axis perturbation simulation is illustrated in **(A)**. P_s (standing for power of the signal) corresponds to the peak-to-peak amplitude of the signal. P_n (standing for power of the noise) corresponds to the maximal coverage interval of the joint angle during the gait.

the same in all directions of the measurement volume. Therefore, the uncertainty zone for the model markers was assumed to be spherical. The radius of these spherical uncertainty zones was chosen as a common residual value for the camera calibration process for the used experimental setup: 0.4 mm.

In the second MC simulation, joint geometrical parameters (location and orientation) were randomly disturbed. The uncertainty in location and orientation of joints is mainly related with operator-dependent variability of the treatment and identification of the articular surfaces. In order to define perturbation magnitude (translation and rotation) introduced to the joint geometrical parameters, several procedures of identification of articular surfaces were carried out. Cylindrical uncertainty zones were assumed for hinge joints, while spherical uncertainty zones were assumed for ball-and-socket joints. The radius of the cylindrical and spherical uncertainty zones was considered to be the same for all the joints and equal to 0.2 mm.

These MC simulations were implemented and run by means of the OpenSim API. One thousand iterations were carried out for each MC simulation, which were enough to guarantee a stabilization of average values. Average values of joint angles at each time step were calculated from the obtained results. Coverage intervals were defined as twice the standard deviation. A graphical representation of these results is presented in **Figure 6**. The sensitivity of the kinematic results regarding model parameter uncertainties was defined as the signal-to-noise ratio (SNR) of the joint angles during the gait. The SNR was calculated as the maximum amplitude of the signal (also called power of the signal, P_s) divided by the maximum coverage interval (also

TABLE 6 | Summary of studies investigating ant kinematics.

Study	Analyzed angle	Specie	Methods	Range of motion (deg)	Corresponding range of motion from this study (deg)
Weihmann and Blickhan (2009)	thorax/head flexion	*Cataglyphis fortis*	video-based analysis (250 Hz, 480 × 480 pixels of camera resolution)	5	13
Weihmann and Blickhan (2009)	thorax/head flexion	*Formica pratensis*	video-based analysis (250 Hz, 480 × 480 pixels of camera resolution)	5	13
Reinhardt and Blickhan (2014)	thorax/head flexion	*Formica polyctena*	video-based analysis (500 Hz, 768 × 512 pixels of camera resolution)	10	13
Weihmann and Blickhan (2009)	thorax/abdomen flexion	*Cataglyphis fortis*	video-based analysis (250 Hz, 480 × 480 pixels of camera resolution)	10	14
Weihmann and Blickhan (2009)	thorax/abdomen flexion	*Formica pratensis*	video-based analysis (250 Hz, 480 × 480 pixels of camera resolution)	14	14
Reinhardt and Blickhan (2014)	thorax/abdomen flexion	*Formica polyctena*	video-based analysis (500 Hz, 768 × 512 pixels of camera resolution)	10	14
Guo et al. (2018)	thorax/cx flexion angle on middle left leg	*Cataglyphis fortis*	video-based analysis (500 Hz, 480 × 480 pixels of camera resolution)	63	39
Guo et al. (2018)	cx/fe flexion angle on middle left leg	*Cataglyphis fortis*	video-based analysis (500 Hz, 480 × 480 pixels of camera resolution)	37	27
Guo et al. (2018)	fe/tb flexion angle on middle left leg	*Cataglyphis fortis*	video-based analysis (500 Hz, 480 × 480 pixels of camera resolution)	83	38

called power of the noise, P_n) of the joint angle during the gait. Therefore, an SNR value was obtained per degree of freedom for the analyzed gait cycle.

3 RESULTS

In order to determine how modeling assumptions affect inverse kinematic results at the ant scale, a multibody model of the *Messor barbarus* was developed together with a simulation framework to evaluate its sensitivity. Both the model and the simulation framework are freely available on the SimTK repository: https://simtk.org/projects/barbarus. From the experimental kinematic data, an inverse kinematic simulation was conducted. The results of this simulation, representing a gait cycle of free locomotion of the *Messor barbarus*, are summarized in **Tables 3** and **4**. A video of the simulated kinematics is available from the project repository.

These results correspond to the range of motion of the joint angles. The whole set of results is available from the project repository and can also be reproduced from the model and the experimental kinematic data. It can be noticed that the trochanter/femur (tr/fe) joint is the one with the wider range of motion, while the thorax/coxa joints exhibit the smallest one. The average RMSE of the inverse kinematic simulation was 0.21 mm, which corresponds to 3.2% of the specimen size.

The sensitivity of the kinematic results regarding model parameter uncertainties was evaluated by means of the SNR. These results are summarized per set of joints, from marker perturbation as well as from axis perturbation, in **Table 5**. High SNR values indicate that the power of the signal (computed joint angle) is representative with respect to the power of the noise (confidence intervals). SNR values near or lower than 1 indicate that the dynamics of the signal of interest might be hidden by noise. It can be noticed that the computed kinematics is more sensitive to marker perturbation compared to joint axis perturbation (**Table 5**). The perturbation applied to the markers generated an SNR of 2.2 in average for all the joints. This means that the dynamics of the studied signal (computed joint angles) can be observed despite possible variations during the motion analysis process. The SNR from axis perturbation was almost four times higher than that from marker perturbation. No significant differences in sensitivity were found between the joints of the legs on the right side of the body with respect to those on the left side. No tendency can be inferred from the sensitivity of the joints with respect to their anterior–posterior position: front, middle, and rear. The joint that showed the highest SNR values (consequently a lower sensitivity) was the fe/ti joint, and this was the case for both marker and axis perturbations.

Figure 7 illustrates kinematic results obtained from the simulation of the ant model and the experimental kinematic data for joints of the middle right leg [(**Figure 7A**) thorax/cox, (**Figure 7B**) cox/tro, (**Figure 7C**) tro/fe, (**Figure 7D**) fe/ti, (**Figure 7E**) ti/mt, and (**Figure 7F**) mt/ta flexion angles]. Mean values (in solid lines) from both MC simulations (marker and axis perturbations) are shown with their corresponding confidence intervals (shaded regions). The green line and shaded region represent the results from the marker perturbation, and the blue line and shaded region represent the results from the axis perturbation. The SNR of the thorax/cox flexion angle obtained from the axis perturbation simulation is illustrated in **Figure 7A**. From these results, it can be noticed that the confidence intervals of the joint angles when disturbing the axis location and orientation were smaller than the confidence intervals obtained from the marker position perturbation.

4 DISCUSSION AND CONCLUSIONS

In this paper, the propagation of parameter uncertainties in kinematic modelling has been evaluated at the small scale. This work

demonstrates the feasibility of using biomechanical models to study locomotion in relatively small animals. Because of their scale, motion analysis techniques for hexapods are less developed compared to those for quadrupeds and bipeds. In relatively big animals, the use of several reflective markers per segment allows a good precision of the kinematic data. However, the use of physical markers is not easy in motion analysis in small insects. This implies that the capabilities of the small-scale biomechanical modeling techniques must be well evaluated.

To do so, a multibody model of a *Messor barbarus* ant was developed. It is available in open source from the project repository and can be used and enhanced by the scientific community. Besides, the model could allow biologists to study function/structure relationships of *Messor barbarus*. The whole set of experimental and simulated kinematic data is also available from the project repository.

In spite of the differences in morphology of the studied species, the obtained joint angles were in the same order of magnitude as those reported in the literature about ant kinematics (see **Table 6**). The difference between angle range of left and right legs comes from the fact that the ant did not walk perfectly straight. Obtained kinematic data are valuable for roboticians to implement bio-inspired gaits in robots (see Ouyang et al. (2021) for example).

A possible error source in the conducted kinematic simulation could be linked to the use of two different specimens for acquiring experimental data (one for the geometrical 3D model and one for the experimental kinematic data). When using two subjects to perform a constrained kinematics simulation, a scaling procedure is required, which is naturally an additional source of errors. This might be one of the main reasons for the obtained RMSE values. In comparison to human locomotion simulations, the obtained normalized RMSE values for ant locomotion simulation were greater. In human simulations, it is recommended not to exceed 0.6% relative RMSE regarding body size (in contrast to a normalized RMSE of 3.2% obtained in this work). This difference can also be related to the fact that the ant body is composed of more segments than the human one.

Thanks to the developed model, the impact of the propagation of model parameter uncertainties in inverse kinematic simulations at the insect scale was evaluated. Obtained SNR values indicate that the geometric and kinematic measurement techniques used are feasible for the development of multibody models at the ant scale. The fact that the model is more sensitive to marker perturbations indicates that efforts in kinematic modeling at the ant scale must be centered around the kinematic acquisition (marker definition, placement, tracking, etc.) rather than geometric acquisition (μ-CT, segmentation, joint parameter definition, etc.). The fact of experiencing lower sensitivity at the fe/ti joint can be explained by the large range of motion of this joint and, also, because it is composed of the two longest segments of the limb. Long segments are easier to track, plus the perturbation of the measurement process has a lower impact than in the case of short segments. The fact of having no significant differences in sensitivity between the joints of the legs on the right side of the body compared to those on the left side can be associated to the symmetry of the video acquisition system regarding the walkway.

This study presents several limitations, however. From an experimental point of view, the following aspects can be improved. Each body segment was tracked by only two markers. The number of tracked markers per segments could be increased to improve the quality of the simulation. Additionally, emerging automatic tracking techniques (i.e., deep-learning-powered motion tracking) must be explored as an alternative to reduce tracking time and to increase the number of tracked points per segment. Finally, the four tarsal segments were all lumped into a unique rigid segment. This was due to the configuration and the capacity of the experimental setup (camera resolution, number of cameras, camera position, etc.), which did not provide enough resolution to track the tarsal segments individually. On the other hand, from a modeling point of view, the segments of the ant were considered as rigid bodies because of the complexity of taking body deformation into consideration. This assumption merits a profound analysis in order to determine the effects of segment compliance in insect locomotion, which seems to play an important role (Blickhan et al., 2021).

Finally, future work is required to develop a dynamic model of the ant gait. This requires determining muscle parameters (geometrical and force-generating parameters), segment mass and inertia properties, and ground reaction forces. This study contributes to the construction of a musculoskeletal model of ants which can be useful in the study of evolution, neural control, and biomimetic applications.

DATA AVAILABILITY STATEMENT

The datasets presented in this study can be found in online repositories. The names of the repository/repositories and accession number(s) can be found in the article/Supplementary Material.

AUTHOR CONTRIBUTIONS

SA-T made significant contributions to the conception, design, execution, and interpretation of the findings being published and drafting and revising of the manuscript. JD made significant contributions to the biological studies, extractions of data, interpretations of the findings being published, and drafting and revising the manuscript. AK made significant contributions to the execution and interpretation of the findings being published. PM and J-ML made significant and substantial contributions to the conception, design, and interpretation of the findings being published as well as revising the manuscript.

FUNDING

This work was partially subsidized by the CNRS AO MITI Biomim funding. Work by JD was supported by a scholarship from the *Collectivité Territoriale de Martinique*.

ACKNOWLEDGMENTS

The authors would like to thank Pr. Evan Okonomo and Francisco Hita Garcia (Biodiversity and Biocomplexity

Unit, Okinawa Institute of Science and Technology, Japan) who performed the scans that enabled determination of the segment and joint geometries. They would also like to acknowledge Moran Le Gleau's contribution to the treatment of the μ-CT under the supervision of Adam Khalife and Tanguy Puluhen for his help during the development of the multibody model. Thanks also to the CNRS GDR 2088 Biomim who encouraged this work.

REFERENCES

Ahn, C., Liang, X., and Cai, S. (2019). Bioinspired Design of Light-Powered Crawling, Squeezing, and Jumping Untethered Soft Robot. *Adv. Mater. Technol.* 4, 1900185. doi:10.1002/admt.201900185

Ambe, Y., Aoi, S., Nachstedt, T., Manoonpong, P., Wörgötter, F., and Matsuno, F. (2018). Simple Analytical Model Reveals the Functional Role of Embodied Sensorimotor Interaction in Hexapod Gaits. *PLOS ONE* 13, e0192469. doi:10.1371/journal.pone.0192469

Bernadou, A., Espadaler, X., Dos-Reis, V., and Fourcassié, V. (2011). Effect of Substrate Roughness on Load Selection in the Seed-Harvester Ant Messor Barbarus L. (Hymenoptera, Formicidae). *Behav. Ecol. Sociobiol.* 65, 1763–1771. doi:10.1007/s00265-011-1184-4

Blanke, A., Watson, P. J., Holbrey, R., and Fagan, M. J. (2017). Computational Biomechanics Changes Our View on Insect Head Evolution. *Proc. R. Soc. B.* 284, 20162412. doi:10.1098/rspb.2016.2412

Blickhan, R., and Full, R. J. (1987). Locomotion Energetics of the Ghost Crab: II. Mechanics of the Centre of Mass during Walking and Running. *J. Exp. Biol.* 130, 155–174. doi:10.1242/jeb.130.1.155

Blickhan, R., Weihmann, T., and Barth, F. G. (2021). Measuring Strain in the Exoskeleton of Spiders-Virtues and Caveats. *J. Comp. Physiol. A.* 207, 191–204. doi:10.1007/s00359-020-01458-y

Christensen, K. B., Günther, M., Schmitt, S., and Siebert, T. (2021). Cross-bridge Mechanics Estimated from Skeletal Muscles' Work-Loop Responses to Impacts in Legged Locomotion. *Sci. Rep.* 11, 23638. doi:10.1038/s41598-021-02819-6

Cruse, H. (1976). The Function of the Legs in the Free Walking Stick insect,Carausius Morosus. *J. Comp. Physiol.* 112, 235–262. doi:10.1007/BF00606541

David, S., Funken, J., Potthast, W., and Blanke, A. (2016). Musculoskeletal Modelling under an Evolutionary Perspective: Deciphering the Role of Single Muscle Regions in Closely Related Insects. *J. R. Soc. Interf.* 13, 20160675. doi:10.1098/rsif.2016.0675

Dunne, J. J., Uchida, T. K., Besier, T. F., Delp, S. L., and Seth, A. (2021). A Marker Registration Method to Improve Joint Angles Computed by Constrained Inverse Kinematics. *PLOS ONE* 16, e0252425–11. doi:10.1371/journal.pone.0252425

Dupeyroux, J., Serres, J. R., and Viollet, S. (2019). Antbot: A Six-Legged Walking Robot Able to home like Desert Ants in Outdoor Environments. *Sci. Robot* 4, 307. doi:10.1126/scirobotics.aau0307

Eichelberger, P., Ferraro, M., Minder, U., Denton, T., Blasimann, A., Krause, F., et al. (2016). Analysis of Accuracy in Optical Motion Capture - A Protocol for Laboratory Setup Evaluation. *J. Biomech.* 49, 2085–2088. doi:10.1016/j.jbiomech.2016.05.007

El Habachi, A., Moissenet, F., Duprey, S., Cheze, L., and Dumas, R. (2015). Global Sensitivity Analysis of the Joint Kinematics during Gait to the Parameters of a Lower Limb Multi-Body Model. *Med. Biol. Eng. Comput.* 53, 655–667. doi:10.1007/s11517-015-1269-8

Full, R. J., Blickhan, R., and Ting, L. H. (1991). Leg Design in Hexapedal Runners. *J. Exp. Biol.* 158, 369–390. doi:10.1242/jeb.158.1.369

Grabowska, M., Godlewska, E., Schmidt, J., and Daun-Gruhn, S. (2012). Quadrupedal Gaits in Hexapod Animals - Inter-leg Coordination in Free-Walking Adult Stick Insects. *J. Exp. Biol.* 215, 4255–4266. doi:10.1242/jeb.073643

Groen, B. E., Geurts, M., Nienhuis, B., and Duysens, J. (2012). Sensitivity of the Olga and Vcm Models to Erroneous Marker Placement: Effects on 3d-Gait Kinematics. *Gait & Posture* 35, 517–521. doi:10.1016/j.gaitpost.2011.11.019

Guo, S., Lin, J., Wöhrl, T., and Liao, M. (2018). A Neuro-Musculo-Skeletal Model for Insects with Data-Driven Optimization. *Sci. Rep.* 8, 2129. doi:10.1038/s41598-018-20093-x

Hölldobler, B., and Wilson, E. O. (1990). *The Ants*. Cambridge: Harvard University Press. doi:10.2307/1419398

Hoyt, D. F., and Taylor, C. R. (1981). Gait and the Energetics of Locomotion in Horses. *Nature* 292, 239–240. doi:10.1038/292239a0

Hughes, G. M. (1952). The Co-ordination of Insect Movements. *J. Exp. Biol.* 29, 267–285. doi:10.1242/jeb.29.2.267

Jung-Min Yang, J.-M., and Jong-Hwan Kim, J.-H. (1998). Fault-tolerant Locomotion of the Hexapod Robot. *IEEE Trans. Syst. Man. Cybern. B* 28, 109–116. doi:10.1109/3477.658585

Liu, S.-P., Richter, A., Stoessel, A., and Beutel, R. G. (2019). The Mesosomal Anatomy of Myrmecia Nigrocincta Workers and Evolutionary Transformations in Formicidae (Hymenoptera). *Arthropod Syst. Phylogeny* 77, 1–19. doi:10.26049/ASP77-1-2019-01

Lu, H., Zhang, M., Yang, Y., Huang, Q., Fukuda, T., Wang, Z., et al. (2018). A Bioinspired Multilegged Soft Millirobot that Functions in Both Dry and Wet Conditions. *Nat. Commun.* 9, 3944. doi:10.1038/s41467-018-06491-9

Lu, T.-W., and O'Connor, J. J. (1999). Bone Position Estimation from Skin Marker Co-ordinates Using Global Optimisation with Joint Constraints. *J. Biomech.* 32, 129–134. doi:10.1016/S0021-9290(98)00158-4

Martelli, S., Valente, G., Viceconti, M., and Taddei, F. (2015). Sensitivity of a Subject-specific Musculoskeletal Model to the Uncertainties on the Joint Axes Location. *Comput. Methods Biomech. Biomed. Eng.* 18, 1555–1563. doi:10.1080/10255842.2014.930134

Merienne, H., Latil, G., Moretto, P., and Fourcassié, V. (2021). Dynamics of Locomotion in the Seed Harvesting Ant Messor Barbarus: Effect of Individual Body Mass and Transported Load Mass. *PeerJ* 9, e10664. doi:10.7717/PEERJ.10664

Merienne, H., Latil, G., Moretto, P., and Fourcassié, V. (2020). Walking Kinematics in the Polymorphic Seed Harvester Ant Messor Barbarus: Influence of Body Size and Load Carriage. *J. Exp. Biol.* 223, 205690. doi:10.1242/JEB.205690

Moll, K., Roces, F., and Federle, W. (2010). Foraging Grass-Cutting Ants (Atta Vollenweideri) Maintain Stability by Balancing Their Loads with Controlled Head Movements. *J. Comp. Physiol. A.* 196, 471–480. doi:10.1007/s00359-010-0535-3

Musthak Ali, T. M., Baroni Urbani, C., and Billen, J. (1992). Multiple Jumping Behaviors in the antHarpegnathos Saltator. *Naturwissenschaften* 79, 374–376. doi:10.1007/BF01140185

Myers, C. A., Laz, P. J., Shelburne, K. B., and Davidson, B. S. (2015). A Probabilistic Approach to Quantify the Impact of Uncertainty Propagation in Musculoskeletal Simulations. *Ann. Biomed. Eng.* 43, 1098–1111. doi:10.1007/s10439-014-1181-7

Nirody, J. A. (2021). Universal Features in Panarthropod Inter-limb Coordination during Forward Walking. *Integr. Comp. Biol.* 61, 710–722. doi:10.1093/ICB/ICAB097

Ouyang, W., Chi, H., Pang, J., Liang, W., and Ren, Q. (2021). Adaptive Locomotion Control of a Hexapod Robot via Bio-Inspired Learning. *Front. Neurorobot.* 15, 1. doi:10.3389/fnbot.2021.627157

Peeters, C., Keller, R. A., Khalife, A., Fischer, G., Katzke, J., Blanke, A., et al. (2020). The Loss of Flight in Ant Workers Enabled an Evolutionary Redesign of the Thorax for Ground Labour. *Front. Zool* 17, 33. doi:10.1186/s12983-020-00375-9

Pfeffer, S. E., Wahl, V. L., Wittlinger, M., and Wolf, H. (2019). High-speed Locomotion in the Saharan Silver Ant, Cataglyphis Bombycina. *J. Exp. Biol.* 222, 198705. doi:10.1242/jeb.198705

Ramdya, P., Thandiackal, R., Cherney, R., Asselborn, T., Benton, R., Ijspeert, A. J., et al. (2017). Climbing Favours the Tripod Gait over Alternative Faster Insect Gaits. *Nat. Commun.* 8, 14494. doi:10.1038/ncomms14494

Reinhardt, L., and Blickhan, R. (2014). Level Locomotion in wood Ants: Evidence for Grounded Running. *J. Exp. Biol.* 217, 2358–2370. doi:10.1242/jeb.098426

Reinhardt, L., Weihmann, T., and Blickhan, R. (2009). Dynamics and Kinematics of Ant Locomotion: Do wood Ants Climb on Level Surfaces? *J. Exp. Biol.* 212, 2426–2435. doi:10.1242/jeb.026880

Schultheiss, P., and Guénard, B. (2021). Kinematic Study of Six Mangrove Ant Species (Hymenoptera: Formicidae) Reveals Different Swimming Styles and Abilities. *Myrmecological News* 31, 217–224. doi:10.25849/MYRMECOL.NEWS\\text{_}031:217

Seth, A., Hicks, J. L., Uchida, T. K., Habib, A., Dembia, C. L., Dunne, J. J., et al. (2018). OpenSim: Simulating Musculoskeletal Dynamics and Neuromuscular Control to Study Human and Animal Movement. *Plos Comput. Biol.* 14, e1006223. doi:10.1371/journal.pcbi.1006223

Theunissen, L. M., and Dürr, V. (2013). Insects Use Two Distinct Classes of Steps during Unrestrained Locomotion. *PLoS ONE* 8, e85321. doi:10.1371/journal.pone.0085321

Valente, G., Crimi, G., Vanella, N., Schileo, E., and Taddei, F. (2017). nmsBuilder : Freeware to Create Subject-specific Musculoskeletal Models for OpenSim. *Comput. Methods Programs Biomed.* 152, 85–92. doi:10.1016/j.cmpb.2017.09.012

Weihmann, T., and Blickhan, R. (2009). Comparing Inclined Locomotion in a Ground-Living and a Climbing Ant Species: Sagittal Plane Kinematics. *J. Comp. Physiol. A.* 195, 1011–1020. doi:10.1007/s00359-009-0475-y

Wöhrl, T., Reinhardt, L., and Blickhan, R. (2017). Propulsion in Hexapod Locomotion: How Do Desert Ants Traverse Slopes? *J. Exp. Biol.* 220, 1618. doi:10.1242/jeb.137505

Wu, G., Siegler, S., Allard, P., Kirtley, C., Leardini, A., Rosenbaum, D., et al. (2002). ISB Recommendation on Definitions of Joint Coordinate System of Various Joints for the Reporting of Human Joint Motion-Part I: Ankle, Hip, and Spine. *J. Biomech.* 35, 543–548. doi:10.1016/S0021-9290(01)00222-6

Wu, G., van der Helm, F. C. T., Veeger, H. E. J., Makhsous, M., Van Roy, P., Anglin, C., et al. (2005). ISB Recommendation on Definitions of Joint Coordinate Systems of Various Joints for the Reporting of Human Joint Motion-Part II: Shoulder, Elbow, Wrist and Hand. *J. Biomech.* 38, 981–992. doi:10.1016/j.jbiomech.2004.05.042

Yanoviak, S. P., Dudley, R., and Kaspari, M. (2005). Directed Aerial Descent in Canopy Ants. *Nature* 433, 624–626. doi:10.1038/nature03254

Yushkevich, P. A., Piven, J., Hazlett, H. C., Smith, R. G., Ho, S., Gee, J. C., et al. (2006). User-guided 3d Active Contour Segmentation of Anatomical Structures: Significantly Improved Efficiency and Reliability. *NeuroImage* 31, 1116–1128. doi:10.1016/j.neuroimage.2006.01.015

Zhang, W., Li, M., Zheng, G., Guan, Z., Wu, J., and Wu, Z. (2020). Multifunctional Mandibles of Ants: Variation in Gripping Behavior Facilitated by Specific Microstructures and Kinematics. *J. Insect Physiol.* 120, 103993. doi:10.1016/j.jinsphys.2019.103993

Zollikofer, C. (1994). Stepping Patterns in Ants - Influence of Body Morphology. *J. Exp. Biol.* 192, 107–118. doi:10.1242/jeb.192.1.107

Conflict of Interest: The authors declare that the research was conducted in the absence of any commercial or financial relationships that could be construed as a potential conflict of interest.

Publisher's Note: All claims expressed in this article are solely those of the authors and do not necessarily represent those of their affiliated organizations, or those of the publisher, the editors, and the reviewers. Any product that may be evaluated in this article, or claim that may be made by its manufacturer, is not guaranteed or endorsed by the publisher.

frontiers | Frontiers in Bioengineering and Biotechnology

ORIGINAL RESEARCH
published: 01 April 2022
doi: 10.3389/fbioe.2022.806174

Functional Analysis of Anuran Pelvic and Thigh Anatomy Using Musculoskeletal Modelling of *Phlyctimantis maculatus*

A. J. Collings[1,2]*, *E. A. Eberhard*[2,3], *C. Basu*[2,4] and *C. T. Richards*[2]

[1]School of Health and Life Sciences, Teesside University, Middlesbrough, United Kingdom, [2]Structure and Motion Laboratory, Royal Veterinary College, Hatfield, United Kingdom, [3]Swiss Federal Institute of Technology Lausanne, Lausanne, Switzerland, [4]School of Veterinary Medicine, University of Surrey, Guildford, United Kingdom

Using their abundant musculature, frogs are able to exhibit outstanding behavioural versatility. However, understanding the dynamic motion of their 30 + hindlimb muscles, with multi-joint action, and curved pathways, is challenging. This is particularly true in walking, a relatively understudied, but complex frog gait. Building on prior musculoskeletal modelling work we construct and analyse a 3D musculoskeletal model of the spine, pelvis, and hindlimb of *Phlyctimantis maculatus* (previously known as *Kassina maculata*) to simulate the natural motion of muscle pathways as joints rotate during locomotion. Combining experimental kinematics and DICE-CT scan data we use several simulations conducted in MuJoCo to decouple femur and pelvic motions, generating new insights into the functional mechanics of walking in frogs. Outputs demonstrate pelvic lateral rotation about the iliosacral joint influences moment arm magnitude in the majority of hindlimb muscles. The extent of pelvic influence depends on femoral angle which changes muscle function in some instances. The workflow presented here can be used to help experimentalists predict which muscles to probe with *in vivo* techniques towards a better understanding of how anuran musculoskeletal mechanics enable multiple behaviours.

Keywords: Anuran, Pelvis, Musculoskeletal modelling, Moment arm, Walking locomotion, Pelvic lateral rotation, MuJoCo

OPEN ACCESS

Edited by:
Gina Bertocci,
University of Louisville, United States

Reviewed by:
Shinya Aoi,
Kyoto University, Japan
Crystal Reynaga,
Bryn Mawr College, United States

***Correspondence:**
A. J. Collings
a.collings@tees.ac.uk

Specialty section:
This article was submitted to Biomechanics, a section of the journal Frontiers in Bioengineering and Biotechnology

Received: *31 October 2021*
Accepted: *08 March 2022*
Published: *01 April 2022*

Citation:
Collings AJ, Eberhard EA, Basu C and Richards CT (2022) Functional Analysis of Anuran Pelvic and Thigh Anatomy Using Musculoskeletal Modelling of Phlyctimantis maculatus. Front. Bioeng. Biotechnol. 10:806174. doi: 10.3389/fbioe.2022.806174

INTRODUCTION

Frogs use their abundant musculature to exhibit astonishing behavioural versatility (Kargo and Giszter, 2000; Kargo et al., 2002). To coordinate these numerous muscles, frogs (and other vertebrates) activate groups of muscles ("synergies") to elegantly control motion (d'Avella and Lacquaniti, 2013). Yet, over a century ago, Lombard and Abbott proposed that motor signals do not fully explain limb motion, stating " [limb movements] *have the appearance of being the result of finely adjusted nervous coordinations, are really due to the mechanical conditions under which the muscles act on the bones.*" (Lombard and Abbott, 1907). Hence, elucidating not only the neurological, but also the biomechanical properties is crucial for understanding limb function.

Unfortunately, understanding frog hindlimbs is challenging; they have 30 + muscles, several crossing multiple joints, and following curved pathways around bones or other muscles (Dunlap, 1960; Duellman and Trueb, 1986; Kargo et al., 2002; Přikryl et al., 2009; Collings and Richards, 2019). Additionally, unlike limbs that move in simple planar motion (e.g. mice; Mendes et al., 2015) frog

hindlimbs move simultaneously in three planes (Astley & Roberts, 2014; Richards et al., 2017; Collings et al., 2019), possibly causing time-varying shifts in muscle action (Lombard & Abbott, 1907). For example, the mouse semimembranosus is a simple hip extensor/knee flexor (Charles et al., 2016), whereas the frog semimembranosus shifts from knee flexor to extensor, likely due to the out-of-plane movements of the shank (Lombard & Abbott, 1907). Hence, we are unlikely to determine limb mechanical function simply by studying muscle attachments.

In situ experimentation directly measures muscle actions about joints *via* electrical stimulation (e.g. Přikryl et al., 2009) or by moment arm measurements (e.g. Lieber and Boakes, 1988). However, such approaches are limited because they rarely consider simultaneous action from multiple muscles (although see Lombard & Abbott, 1907). Furthermore, moment arm distances can vary with joint angle meaning that postural changes can alter a muscle's contribution to joint torque (e.g., Lieber and Shoemaker, 1992). In these cases where parameters are too numerous to cover in an experimental context, modelling approaches are useful.

In the spirit of prior musculoskeletal modelling work (e.g. OpenSim; Delp et al., 2007; Kargo et al., 2002; Kargo and Rome, 2002) we construct and analyse a 3D musculoskeletal model of the spine, pelvis, and hindlimb of *Phlyctimantis maculatus* (previously known as *Kassina maculata;* common name the red legged running frog) to simulate the natural motion of muscle pathways as joints rotate during frog walking. *P. maculatus* ideal because it is a habitual walker (Ahn et al., 2004; Reynaga et al., 2018; Collings et al., 2019). In this species, stride length is mainly driven by horizontal motion of the femur during walking (Collings et al., 2019) which is powered by intricate musculature linking the pelvis to the leg (Lombard & Abbott, 1907; Kargo and Rome, 2002; Přikryl et al., 2009; Collings and Richards, 2019). Horizontal motion of the femur is coupled with lateral rotation of the pelvis (Emerson and De Jongh, 1980; Collings et al., 2019). Originally thought to increase stride length, pelvic lateral rotation has been shown recently to have a relatively unsubstantial effect on stride length during walking (Collings et al., 2019). However, before this lateral rotation was discovered, Lombard and Abbott observed that the actions of femoral muscles change drastically depending on the angle between the pelvis and femur (Lombard and Abbott, 1907). Given the importance of femoral motion in walking, we therefore hypothesise that pelvic lateral rotation increases muscle moment arms of femoral muscles during the walking stride cycle.

Using experimental kinematics (Collings et al., 2019) and a DICE CT model (Collings and Richards, 2019) we produced 1) a range of hypothetical simulations decoupling femur and pelvic rotations and 2) kinematics-driven simulations based on a typical walking trial. We found that muscles crossing the hips are most effective in flexion/extension or long-axis rotation (as opposed to abduction/adduction). Furthermore, their moment arm magnitudes were impacted by both femoral angle and pelvic lateral rotation during walking. Additionally, the axial muscle mechanics were influenced by lateral and dorsoventral rotation at the iliosacral (IS) joints. Our study thus demonstrates how computational kinematic reconstruction can non-invasively estimate time-varying muscle moment arms in vertebrate limbs. We propose that our workflow can be used to generate detailed predictions to help experimentalists determine which muscles to probe with *in vivo* techniques. To our knowledge, this is the first study to quantify moment arms in a walking frog and, hence, opens an important opportunity to better understand how their musculoskeletal mechanics enable multiple behaviours.

MATERIALS AND METHODS

We built a musculoskeletal model of the pelvis and hindlimb based on a *Phlyctimantis maculata* (formerly *Kassina maculata*) specimen (Collings and Richards, 2019). The model consists of 6 separate skeletal components, 16 muscles, and 5 joints (**Table 1**). To animate the model, we used a forward kinematics approach where joint angle data drive the motions of the joints and musculature. The methods applied to building the model required several steps, presented as a workflow diagram (**Figure 1**). To generate our simulation three main data inputs are required: 1) skeletal morphology, 2) joint kinematics data (experimental or hypothetical) and 3) a document specifying both the model topology (i.e., specific connections of muscles and joints to bones) as well as the dimensions and proportions of all elements. The morphology information includes 3D surface geometry of the specimen skeleton. Joint kinematics data is in the form of joint angles (specifically Euler angles or quaternions). Finally, the anatomical information required to assemble all musculoskeletal elements is specified in an XML template file. Further anatomical information such as the joint centres of rotation and specific muscle attachment sites are input into this template to generate an XML model. Together, the 3D surface geometry and the XML model generate a model 'puppet' containing only information defining the geometry of the musculoskeletal system, but no information regarding posture of joint orientations. Kinematics data, either experimental or hypothetical, is then input along with the 3D skeletal geometry and the XML model to generate a simulation using the physics engine MuJoCo (Todorov et al., 2012). Although MuJoCo is conventionally used to solve forward/inverse dynamics problems, it can also be used for kinematics computations. In the present study, we apply MuJoCo's forward kinematics function (part of its larger dynamics pipeline) to compute the positions of the bone segments and corresponding muscle moment arms. We note that the XML template presented in this study can be used as a generalised template for any frog specimen from spine to tarsometatarsus (TMT) and any kinematics data set can be input into this workflow providing it appears in the same format, therefore allowing investigation of any frog species (extinct or extant), not only *P. maculatus*. Specific anatomy obtained through traditional dissection and DICE μCT techniques (Collings and Richards, 2019) were used to generate the model puppet which was then animated using representative experimental kinematics from a prior study (Collings et al., 2019). Here we used an example trial closest representing the average joint kinematics of the walking trials in Collings et al. (2019).

TABLE 1 | A summary table listing the bones, muscles, and joints modelled. Note the predicted functions of the muscles are based on published data from Přikryl et al. (2009).

Model Components	MTU	Abbreviation	Further Information
Bones	Spine and Sacrum	N/A	Mesh consisted of the five vertebral elements modelled as one unit
	Urostyle		Single bone continuous with sacrum forming sacrourostylic joint
	Pelvis		Single bone forming paired iliosacral joints
	Femur		Single bone forming hip joint. Left femur aminated with kinematics. Right femur mirrored
	Tibiofibula		Fused paired bones forming knee joint. Left tibiofibular animated with kinematics. Right is mirrored
	Tarsals		Paired bones forming ankle joint. Left tarsals animated with kinematics. Right are mirrored
Muscles	Coccygeoiliacus (right)	CI (right)	MTUs: 3; proximal middle, distal
	Coccygeoiliacus (left)	CI (left)	MTU colour: Dark green
			Attachment sites: Iliac shaft and urostyle shaft
			Via sites: None
			Multiarticular: No
			Predicted function: Pelvic lateral and dorsoventral rotation
	Iliolumbaris (right)	IL (right)	MTUs: 4
	Iliolumbaris (left)	IL (left)	MTU colour: Golden yellow
			Attachment sites: Pre-sacral vertebrae and proximal ilia tips
			Via sites: None
			Multiarticular: No
			Predicted function: Pelvic lateral rotation, anterior-posterior sliding of ilia, spinal bending
	Iliacus externus	IE	MTUs: 1
			MTU colour: Red
			Attachment sites: Proxima iliac shaft and proximal femur
			Via sites: One at distal ilium
			Multiarticular: No
			Predicted function: Hip flexion
	Semimembranosus	SM	MTUs: 1
			MTU colour: Yellow
			Attachment sites: Ischial/iliac rim and lateral tibiofibula
			Via sites: None
			Multiarticular: Yes
			Predicted function: Hip extension
	Iliofibularis	IFB	MTUs: 1
			MTU colour: Light blue
			Attachment sites: Distal ilium and lateral tibiofibula
			Via sites: None
			Multiarticular: Yes
			Predicted function: Hip extension
	Obturator externus	OE	MTUs: 1
			MTU colour: Dark blue
			Attachment sites: Ischium (ventral border) and femur (mid-shaft)
			Via sites: None
			Multiarticular: No
			Predicted function: Hip extension
	Sartorius	SA	MTUs: 1
			MTU colour: Deep red-purple
			Attachment sites: Ischium (ventral border) and medial tibiofibula
			Via sites: None
			Multiarticular: Yes
			Predicted function: Hip flexion and adduction
	Adductor longus	AL	MTUs: 1
			MTU colour: Teal
			Attachment sites: Ischium (ventral border) and medial tibiofibula
			Via sites: None
			Multiarticular: Yes
			Predicted function: Hip flexion and adduction
	Adductor magnus	AM	MTUs: 2?
			MTU colour: Light mint green
			Attachment sites: Ischium (ventral border) and distal femur
			Via sites: None
			Multiarticular: No
			Predicted function: Hip flexion and adduction
	Gracilis major	GR	MTUs: 1

(Continued on following page)

TABLE 1 | (*Continued*) A summary table listing the bones, muscles, and joints modelled. Note the predicted functions of the muscles are based on published data from Přikryl et al. (2009).

Model Components	MTU	Abbreviation	Further Information
			MTU colour: Grey Attachment sites: Ischium and medial tibiofibula *Via* sites: None Multiarticular: Yes Predicted function: Hip extension and adduction
	Iliofemoralis	IFM	MTUs: 1 MTU colour: Dark blue Attachment sites: Ilium (ventral border) and femur (mid-shaft) *Via* sites: None Multiarticular: No Predicted function: Hip extension and adduction
	Iliacus internus	II	MTUs: 2 MTU colour: Light orange Attachment sites: Distal ilium (dorsal surface) and proximal femur *Via* sites: Distal ilium (ventral surface) Multiarticular: No Predicted function: Hip flexion and abduction
	Pyriformis	PY	MTUs: 1 MTU colour: Light red Attachment sites: Distal urostyle and proximal femur *Via* sites: No Multiarticular: No Predicted function: Hip abduction
	Cruralis and Gluteus maximus	CR/GL	MTUs: 1 MTU colour: Pink and Purple Attachment sites: Ilium and anterior tibiofibula *Via* sites: No Multiarticular: Yes Predicted function: Knee extension and hip flexion
Joints	Sacrourostylic	SU	Modelled joint type: Hinge Degrees of freedom: 2 Motion permitted: Lateral and dorsoventral rotation
	Sacroiliac (right) Sacroiliac (left)	IS (right) IS (left)	Modelled joint type: Double hinge Degrees of freedom: 2 Motion permitted: Lateral and dorsoventral rotation
	Hip	N/A	Modelled joint type: Ball Degrees of freedom: 3 Motion permitted: Flexion/extension, adduction/abduction, long axis rotation
	Knee		Modelled joint type: Rolling Degrees of freedom: 2 motion permitted: Flexion/extension, fore-aft translation
	Ankle		Modelled joint type: Ball Degrees of freedom: 3 Motion permitted: Flexion/extension, adduction/abduction, long axis rotation

Compiling Model Object Information

3D meshes of all bones (excluding all bones distal to the TMT joint), and muscles of the spine, pelvis, and left femur [excluding tensor fascia latae (TFL), pectineus (PEC), quadratus femoris (QF), gemellus (GE), and obturator internus (OI) muscles] were exported as STL files and subsequently loaded into Rhinoceros 3D (Version 5 SR14, Robert McNeel and Associates, Barcelona, Spain). Bones of the digits were excluded due to their complexity and the fact that foot-ground interactions were not the focus of the present study. Only muscles acting about the hip joint were included. The small hip muscles and those encasing the femoral head (TFL, GE, OI, QF) were excluded due to their very small size. Each STL mesh was scaled around the origin according to the scan resolution (17.64 μm). The following information was then compiled; approximate joint centre of rotation, segment local reference frames, muscle attachment and *via* sites, and wrapping geometries and side sites, each of these steps and terminologies are explained below.

Joint Centres of Rotation

Approximate joint centres of rotation for the sarco-urostylic (SU), sacroiliac (SI), hip, knee, and ankle joints were assigned using the point tool in Rhinoceros 3D as follows. The SU joint centre was placed at the midline position where the urostyle articulated with the sacrum. Since the IS X and Y joints are bilaterally symmetrical paired joints, a single centre of rotation

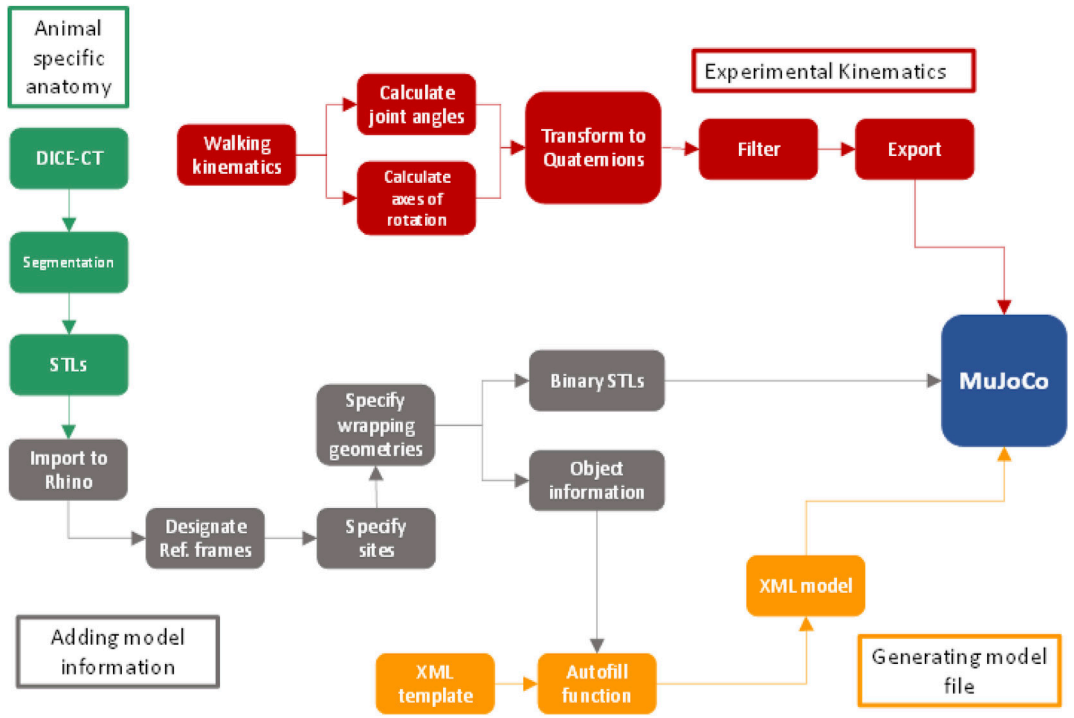

FIGURE 1 | Workflow diagram depicting the required steps for data collection from animal to model.

was defined for both joints as the point equidistant between them. The hip joint centre of rotation was calculated by manually fitting a sphere to the head of the femur (using the STL mesh as an anatomical guide), representing the femoral head, and assigning joint centre of rotation as the centre of the sphere. After Kargo and Rome (Kargo and Rome, 2002), the knee joint centre was calculated as a "rolling joint" allowing the tibia-fibula to slide along the rounded articular surface of the femur. The parameters specifying the rolling action were taken from previously published anatomical data (Kargo and Rome, 2002). The joint centre of rotation for the ankle joint was calculated by drawing a line through the long axis of each limb segment and assigning joint centre of rotation as the intersection of the two long axis lines.

Segment Local Reference Frames

To inform model output data (kinematics and moment arms) definitions, it was necessary to first define local reference frames. In order to define a local reference frame, three points were required; a local origin, an axis vector, and a corresponding point; together these three points were used to define a plane. A local origin for each skeletal segment was created corresponding to repeatable landmarks. For example, the hip, knee, and urostyle local origins were assigned to coincide with the joint centres of rotation for the hip joint, knee joint and SU joint, respectively. The local origin of the pelvis was assigned as the distal most point along the midline, and for the tarsals the local origin was assigned as the centre-most point at the proximal end of the bones, where they fuse. A second point, the axis vector point, was then placed in line with the local origin to generate an axis vector. To ensure the axis vector lined up with meaningful anatomical rotations (i.e., flexion/extension, abduction/adduction, and cranial/caudal long axis rotation), the axis vector point was placed such that the resulting vector fell in line with the long axis of the bone, or created an orthogonal line with the long axis of the bone. A third arbitrary corresponding point was then placed to generate a plane between the local origin point, and the axis vector point. Using those three points, a custom MATLAB function (R2016b, The MathWorks, Inc., Natick, Massachusetts, United States) automatically generated the set of orthogonal frame axes. Through the positioning of the points, local reference frames for all segments were assigned such that positive Z was aligned along the long axis of the segment. For the urostyle, spine, and pelvis positive *Y* axis was aligned straight up with respect to the local origin, and positive *X* axis to the right of the segment origin. For the hindlimb segments, *X* and *Y* axes were based on surface features on the articular surfaces of the bone; X across the adduction/abduction plane of the segment, and Y across the flexion/extension plane. All local origins, local axes, and approximate joint centres of rotation are shown in **Figure 2**.

Muscle Attachment and *Via* Sites

Muscle attachment sites were assigned with the use of the 3D meshes of the individual muscles by placing landmark points, using the point tool in Rhinoceros 3D, at their origination and insertion sites. For some muscles, it was sufficient to use a single point each to represent the muscle origin and insertion, whereas those muscles with large attachment areas required multiple

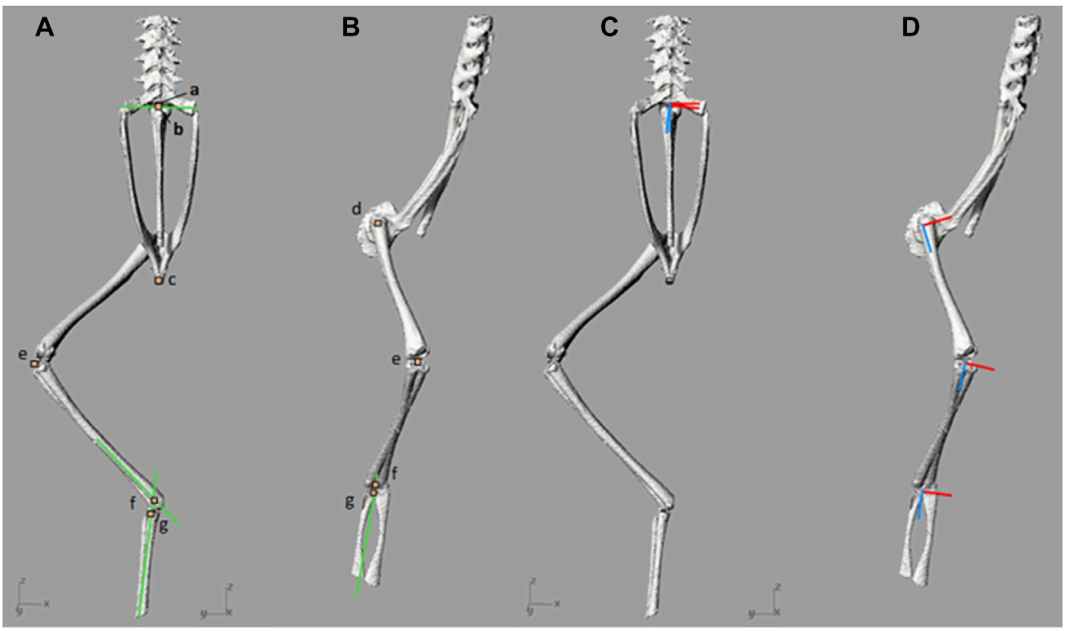

FIGURE 2 | (A,B)—Local origins and approximate joint centres of rotation, and **(C,D)**—joint local axes. Joint origins and approximate centres of rotation are denoted by orange squares which have been enlarged for visualisation. Marker a) includes the local origin for the spine and the urostyle, as well as the sacro-urostylic joint centre of rotation. Marker b) represents the sacroiliac joint centre of rotation. Marker c) represents the pelvic local origin. Marker d) includes the femur local origin and the hip joint centre of rotation. Marker e) includes the tibiofibula local origin and the knee joint centre of rotation. Marker f) represents the ankle joint centre of rotation and marker g) represents the tarsal segment local origin. The green lines present in **(A)** and **(B)** are the reference lines used to find SI and ankle joint centres of rotation. In **(C)** and **(D)**, the *X* axes are red and *Z* axes are blue.

points to define origination and insertion. In some instances, muscles insert into other muscle bellies [gluteus (GL) into cruralis (CR)] or into shared aponeuroses (CR). In those cases, both muscles shared the insertion point of the larger muscle or the aponeurosis (Hutchinson, personal communications).

For those muscles that exhibited particularly complex geometries [e.g., iliacus externus (IE)], additional *via* sites were used. A *via* site is an additional point placed along the muscle pathway that the MuJoCo muscle tendon unit (MTU) must run through. Note that the term muscle tendon unit in this circumstance is uniform in properties, therefore the entire path is assumed to be muscle as opposed to both muscle and tendon. Since the MTU in MuJoCo represents the shortest distance between the two attachment sites, *via* sites can be used to constrain the muscle pathway. The IE muscle, for example, runs the length of the lateral surface of the ilium and attaches to the proximal femur. For this muscle, attachment sites were placed at the origin (anterior ilium) and at the insertion point on the proximal femur, a *via* site was then also placed on the posterior ilium such that the MTU would run from the origin, along the lateral surface of the ilium, through the *via* site, and to the origin. Without the use of the *via* sites, the MTU would not be constrained to the lateral surface of the ilium.

Finally, since the contrast enhancing agent used was unable to resolve tendinous tissue, the muscle meshes of those muscles with tendinous insertions did not make contact with the bone meshes. Consequently, placing insertion points for these muscles required estimation based on the muscle belly pathway and anatomical knowledge gained from the traditional dissection of other animals of the same species (Collings and Richards, 2019). In particularly challenging cases, where the tendon was relatively long, the line tool in Rhinoceros 3D was used to draw a line through the muscle belly midline to best represent muscle line of action, where this line intersected the bone mesh the muscle was estimated to insert. All muscle attachment site points were placed on to the skeletal meshes in the global reference frame. The point coordinates would later be automatically transformed from the global reference frame to the local reference frame of the segment they were situated on when loaded into the MATLAB autofill function (described below).

Wrapping Geometries and Side Sites

In MuJoCo MTUs are modelled as the straight line between attachment sites. However, even with the use of *via* sites, modelling a MTU as a straight line often resulted in cases where the MTU would 'clip' through the bone meshes or other MTUs. Therefore, to avoid such collisions and more accurately represent the natural smooth curved muscle pathways, wrapping geometries were implemented. MuJoCo permits each MTU to wrap around a single wrapping geometry between any two sites, ignoring all other geometries. When wrapping over geometries between sites the MTU length is then the shortest arc length over the wrapping geometry. The muscle 3D surface STL meshes were used to inform size, position, and orientation of the wrapping geometries, which were either spheres or cylinders of infinite length, created using the Sphere

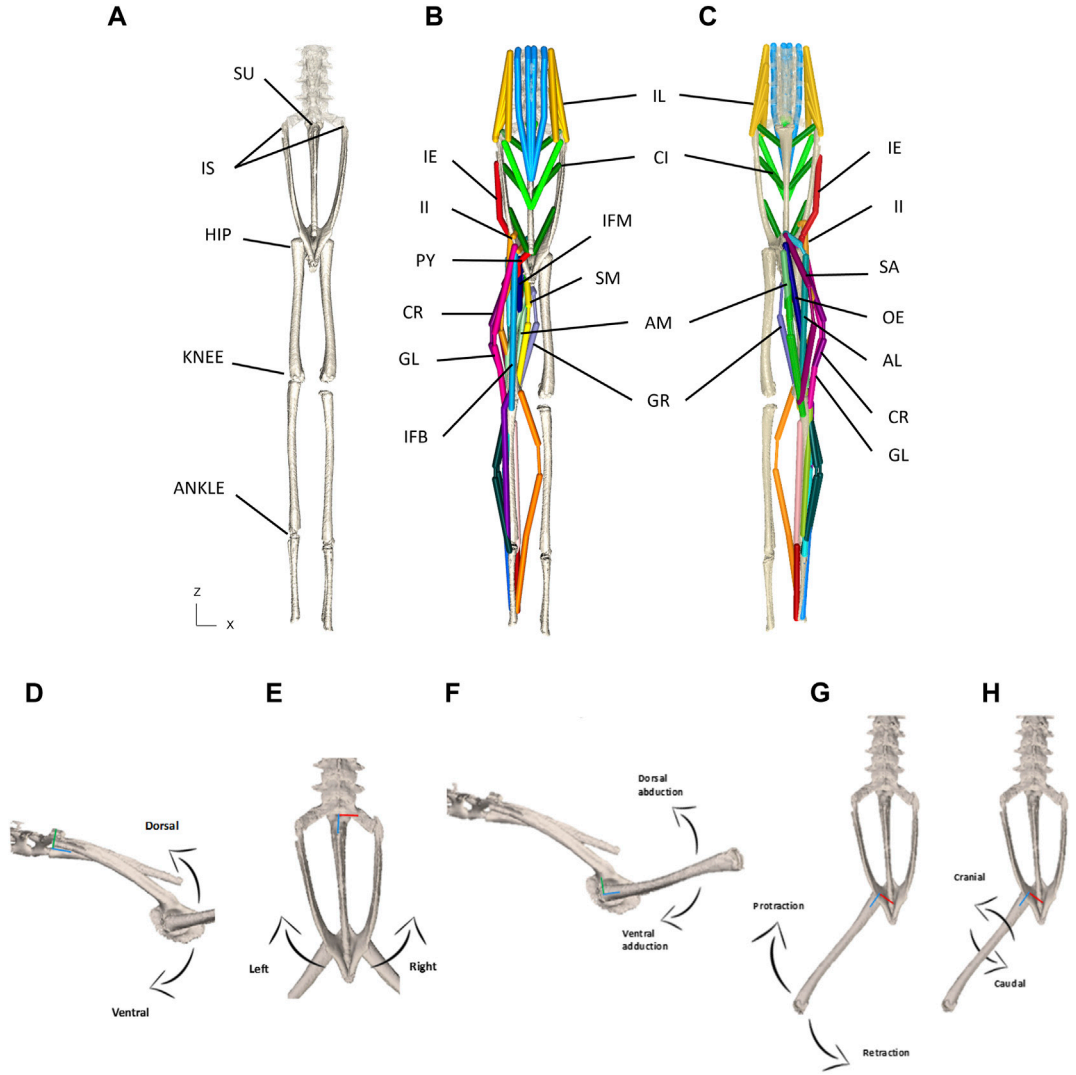

FIGURE 3 | (A–C) Model puppet shown in 'zero' pose from dorsal **(A,B)** and ventral **(C)** view. Skeletal elements only shown in **(A)** and all MTUs shown in **(B,C)**. Note that shank muscles are included but not reported on in this paper. Please See **Table 1** for muscle abbreviations. **(D–H)** Schematic for the visualisation of permitted rotational degrees of freedom for the pelvis at the SI joint **(D,E)** and the femur at the hip joint **(F–H)**. **(D)**—lateral view depicting dorso-ventral rotation about the *X* axis. **(E)**—Dorsal view depicting lateral rotation about the *Y* axis. **(F)**—lateral view depicting dorso-vetral abduction/adduction about the *X* axis. **(G)**—Dorsal view depicting protraction/retraction about the *Y* axis. **(H)**—Dorsal view depicting cranial/caudal long axis rotation about the *Z* axis. The *X* axes are red, *Y* axes are green, and *Z* axes are blue.

and Cylinder tools in Rhinoceros 3D, respectively. Specific side sites for each wrapping geometry were also placed. These side sides were required to specify the hemisphere or semicircle of the wrapping geometry that the MTU was permitted to wrap over. In other words, the side sites acted to constrain the MTU pathway to one cross sectional plane of the wrapping geometries throughout a simulation. Without side sites, the MTUs are free to wrap over whichever surface of the wrapping geometry allows the shortest path length.

MuJoCo Model File Generation

All model information was exported from Rhinoceros 3D. The object information (point coordinates and wrapping geometry data) was exported as a text file, whereas the skeletal segment meshes were exported as binary STL files. To minimise computation time, any mesh that contained more than 200,000 polygons first required a reduction in mesh size which was conducted using the ReduceMesh tool.

Since MuJoCo requires model information in XML format, an XML template was created and subsequently populated with all model object information from the Rhinoceros 3D object information text file (e.g., coordinates of origin/insertion/*via* sites as well as of joint centres). This was achieved using a custom autofill function written in MATLAB. Additional information was input directly into the XML file, including joint type. The hip and ankle joints were defined as a ball joint, the left and right IS joints, and the

SU joint were defined as hinge joints, and the knee joint was defined as a rolling joint (a hinge joint with some fore-aft translation, see above). The ball joint degrees of freedom allowed adduction/abduction about the *X* axis, flexion/extension about the *Y* axis, and long axis rotation about the *Z* axis. The IS hinge joint was modelled with two degrees of freedom by placing two hinge joints at the same centre of rotation. One hinge joint permitted dorsal/ventral rotation about X, and the second overlying hinge joint allowed lateral rotation about Y. The same approach was taken for modelling the SU hinge joint, a bicondylar joint modelled with a single centre of rotation between the two condyles. This approach permitted the joints to be modelled as hinges operating in both the sagittal plane and the frontal plane.

Once populated the XML file acted essentially as the model 'puppet' (**Figures 3A–C**). In order to animate the model, an input file containing joint kinematic information was required. The XML files and other supporting files as well as code will be shared in Github repository upon acceptance.

Export of Limb Segment Angles From Experimental Kinematics

Joint angle data was calculated from previously recorded skin marker-based experimental kinematics coordinate data for walking (Collings et al., 2019) using a custom MATLAB script. Limb segment orientations relative to the body were calculated and expressed as quaternions.

As described above, we used ball joints to characterise various joints. Although a ball joint is characterised by three rotational degrees of freedom, our calculations directly account for only two rotations (flexion/extension and abduction/adduction); the third rotation, cranial/caudal long axis rotation is only inferred by a set of post-hoc calculations, as explained below.

A body plane was defined using the paired shoulder girdle and ilia markers, all hindlimb and pelvic marker motion were then calculated with respect to that plane. Joint segments were expressed as vectors and joint angles were calculated as the Arc Cosine of the dot product of the normalised vectors defining the joint (**Eq. 1**). The joint axis of rotation was then calculated as the cross product of the normalised joint segment vectors (**Eq. 2**).

$$\text{JointAngle} = \text{Arccosine}\left(\text{Normalised vector1} \cdot \text{Normalised vector2}\right) \quad (1)$$

$$\text{JointAxis} = \text{Normalised vector1} * \text{Normalised vector2} \quad (2)$$

Where **vector1** is the proximal segment defining a joint and **vector2** is the distal segment. The joint angles were transformed into quaternions using the following formula (**Eq. 3**):

$$\text{Quaternion} = \text{Cos}(\theta/2), \text{XSin}(\theta/2), \text{YSin}(\theta/2), \text{ZSin}(\theta/2) \quad (3)$$

Where θ is Joint Angle and *X, Y, Z* are the X, Y, Z coordinates of the normalised axis of rotation.

Quaternions offer an alternative method of describing the orientation of an object in space. They are formatted as four numbers, one scalar unit along with a three-dimensional vector, as shown in **Eq. 3**. Quaternions were used in this instance to express the orientation of the joint segments throughout the stride cycle, a computationally quicker and easier method than combining rotation matrices for X, Y, Z coordinates. The joint quaternions were filtered using a Reverse Butterworth filter with a cut off frequency of 30 Hz. To animate the joint motion of the right hindlimb during walking, the left hindlimb kinematics were played 180° out of phase.

Note that segment movements can occur in any plane. For example, if two limb segments are in the horizontal plane, the resulting rotation axis points vertically. Conversely, if the two segments are in the vertical plane, the resulting rotation axis is horizontal. In reality, during walking, frogs move their limb segments simultaneously in the horizontal and vertical planes (Collings et al., 2019), thus the rotation axes point diagonally to reflect a mixture of flexion/extension and abduction/adduction (Richards, 2019). Hence, **Eqs 1–3** allow us to capture two degrees of rotational freedom (flexion/extension; abduction/adduction). However, due to our non-invasive approach, kinematic data were collected using external marker points placed on approximate joint centres of rotation; each limb segment position was defined only by proximal and distal joints. Therefore, long axis rotation of limb segments could not be resolved from our experimental setup. To estimate long axis rotation, we applied some assumptions and performed a series of post-hoc calculations as follows.

Since kinematic data were collected using external marker points placed on approximate joint centres of rotation, each limb segment position was defined by two marker points (the proximal and distal joints). Long axis rotation of limb segments therefore could not be resolved from our experimental setup. However, using some underlying assumptions, it was possible to estimate long axis rotation. We assumed that the femur, tibiofibula, and tarsal segments would be aligned such that deviation from the flexion/extension axis is minimised. Given that each local *Y* axis corresponds to the flexion/extension plane of the limb segment, it was possible to implement a series of rotations to align limb segment *Y* axes. Firstly, the femur was rotated about its local *Z* axis, such that the *Y* axis of the femur aligned with the cross product between the *Z* axis of the femur and the *Z* axis of the tibiofibula. Secondly, the tarsal segment was rotated about its *Z* axes such that the *Y* axis of the tarsals aligned with the cross product between the *Z* axis of the tarsals and the *Z* axis of the tibiofibula. Finally, the tibiofibula was rotated about its *Z* axis so that the *Y* axis of the tibiofibula was aligned halfway between the *Y* axes of both the femur and tarsals. In other words, the angle between the *Y* axes of the tibiofibula and the femur was equal to the angle between the *Y* axes of the tibiofibula and the tarsals.

Model Simulations in MuJoCo

Simulations were run in MuJoCo using the XML model and joint angle inputs. Two sets of simulations were run to elucidate 1) the impact of femoral and pelvic dorsoventral angle, and 2) the impact of pelvic lateral rotation on hindlimb moment arms during walking; these are referred to as the hypothetical and the walking sequence simulations, respectively.

TABLE 2 | List of simulation parameters, input data, and output data for all hypothetical and walking sequence simulations run in this study. MTU (muscle tendon unit), IS (Iliosacral joint).

Simulation Name	Simulation Type (SI Movie Number)	Simulation Parameters pelvis	Simulation Parameters femur	Inputs	Outputs
HYP_01	Hypothetical (1 and 2)	Pelvis laterally rotating IS joint fully extended	Left femur held at 10°	Pelvic lateral rotation angle as Sin wave fluctuating+/-8° about midline	Moment arm for all hindlimb and axial MTUs
HYP_02	Hypothetical (3 and 4)	Pelvis laterally rotating IS joint fully extended	Left femur held at 45°		
HYP_03	Hypothetical (5 and 6)	Pelvis laterally rotating IS joint fully extended	Left femur held at 90°		
HYP_04	Hypothetical (7 and 8)	Pelvis laterally rotating IS joint fully extended	Left femur held at 135°		
HYP_05	Hypothetical (9 and 10)	Pelvis laterally rotating IS joint flexed ventrally to 22°	Left femur held at 10°		
HYP_06	Hypothetical (11 and 12)	Pelvis laterally rotating IS joint flexed ventrally to 45°	Left femur held at 10°		
RUN_ROT	Walking sequence (13 and 14)	No modification	No modification	Experimental kinematics from exemplar trial for full stride cycle	
RUN_FIX	Walking sequence (15 and 16)	Pelvic lateral rotation fixed	No modification		

The hypothetical simulations are a highly simplified set of "numerical experiments" intended to systematically explore how pelvis and femur ranges of motion influence muscle moment arms. They were run using a set of hypothetical joint input angles. The pelvis was set to rotate laterally +/−8° (Collings et al., 2019) across the midline about the *Y* axis, starting from the right rotating past midline to the left and back to the right in a sine wave pattern. This was classed as one lateral pelvic rotation sequence. The femur was then positioned at 4 different static protraction angles in the horizontal plane (10, 45, 90, and 135°) to mimic key positions in a walking stride from full retraction to full protraction. One full pelvic rotation sequence was recorded per femur angle. For example, for the 10-degree condition, the femur is fixed at 10° (nearly fully protracted) whilst the pelvis rotates laterally from right to left then back. During these simulations the pelvis was held in dorsoventral flexion of 45° and the femur was held static at each respective angle such that the only time-varying rotation was lateral rotation of the pelvis about the IS joints. This set of simulations was then repeated while the pelvis was held in dorsoventral flexion of 0, 22 and 45° (**Table 2**; see SI for movies).

The walking sequence simulations were run using joint angle inputs from a representative walking trial collected experimentally (Collings et al., 2019). The walking simulations ran from stance phase-stance phase through one full stride cycle. This simulation was repeated twice, firstly with no modification to the experimental kinematics and secondly where pelvic lateral rotation at the IS joints was fixed (as per Collings et al., 2019; see SI for movies).

Each simulation output the moment arm of each relevant MTU in each frame of locomotion.

Table 2 provides a list of the simulation inputs, parameters, and outputs. Animations of all conditions can be found in the Supplementary Information with movie names corresponding to the simulation names.

Muscle Moment Arm Output Data

MuJoCo resolved the moment arms of each individual MTU into the different components depending on the joint degrees of freedom. In this instance, moment arms represent the ratio of input force to output torque about each axis. The torque output of a given muscle is therefore proportional to the input force and the moment arm. A large moment arm permits the muscle to generate a proportionally larger torque per given input force, whereas a small moment arm would require the given muscle to input a proportionally larger force to maintain a given output torque.

Moment arms can also be thought of as distances, whereby the output torque is equal to the input force multiplied by the perpendicular distance from the pivot. Moment arm distance (*r*) in 3D can be calculated from the moment arm outputs of MuJoCo using the following equation (**Eq. 4**).

$$r = \sqrt{X^2 + Y^2 + Z^2} \tag{4}$$

Where *r* is the perpendicular distance between the joint centre of rotation and muscle line of action, X, Y, and Z are the muscle force to joint torque ratios about the X, Y, and *Z* axes, respectively.

Since the IS joint was modelled using two hinge joints sharing the same centre of rotation, the pelvis was free to move dorsoventrally (about X) and laterally (about Y) (**Figures 3D,E**), and thus each MTU acting upon this joint had a moment arm about X and a moment arm about Y. For the remaining hindlimb joints, each MTU acting on those joints had three moment arm values calculated: X, Y, and Z corresponding to adduction/abduction (Add/Abd), protraction/retraction (or flexion/extension, Flex/Ex), and long axis rotation (LAR), respectively, (**Figures 3F–H**). Moment arm analysis was not conducted about the SU joint in this study since there is little evidence to suggest motion at this joint is significant (Emerson, 1979; Emerson and De Jongh 1980).

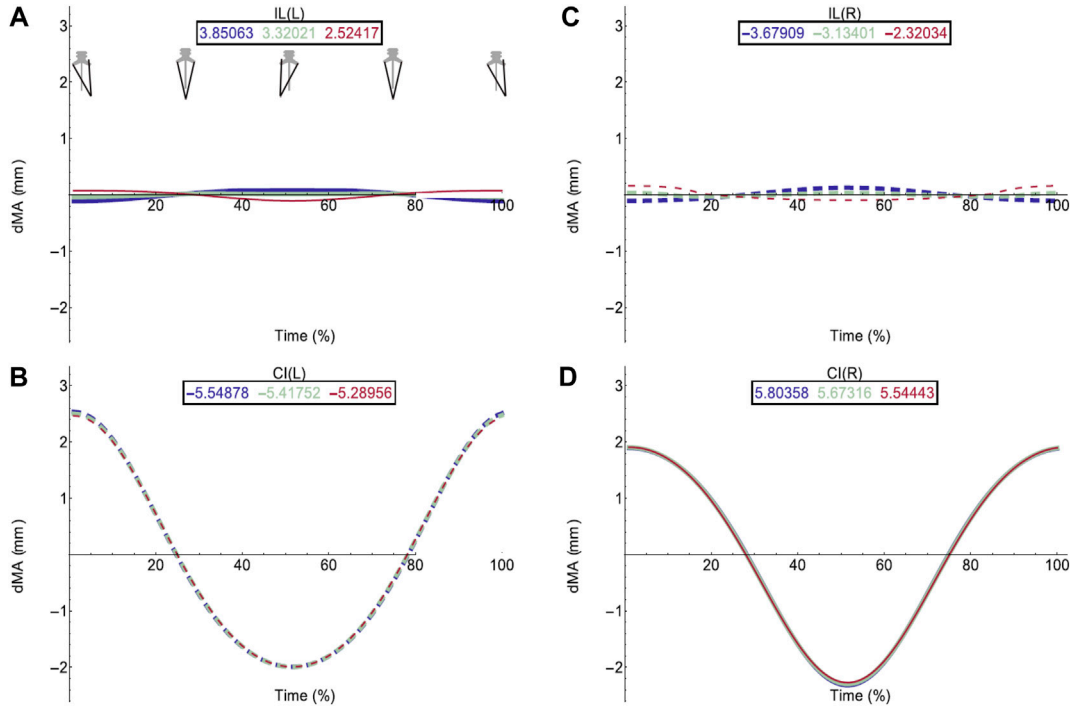

FIGURE 4 | Effect of pelvic rotation on axial muscle moment arms. Changes in moment arm (dMA) versus time are shown for **(A)** the left Iliolumbaris, IL (L), **(B)** left coccygeoiliacus, CI (L), **(C)** right Iliolumbaris, IL (R), **(D)** right coccygeoiliacus, CI (R). Schematic icons indicate the position of the pelvis moving sinusoidally from right (time 0%) to centre (25%) to left (50%) to centre (75%) to right (100%). For each muscle, three hypothetical conditions were run: dorso-ventral iliosacral joint in the extended position (blue), half-flexed (light green) and fully flexed (red). For all conditions, the femur is held at 10° whilst all other joints are held at zero degrees. Traces are shown as changes relative to the mean moment arm (see Methods) such that positive versus negative values indicate deflection above versus below the mean. Boxed values show the mean moment arm value for each condition with colours corresponding to the respective ΔMA plots. Solid versus dashed lines represent positive moment arms (flexion—lateral rotation to the left) versus negative (extension—lateral rotation to the right) such that a change from solid to dashed indicates a change in muscle function. Moment arms for abduction/adduction and long-axis rotation are in SI.

Since the hip joint was modelled as a ball joint, the hindlimb MTUs spanning this joint have moment arm values about three axes corresponding to protraction/retraction (rotation about Y), abduction/adduction (rotation about X), and cranial/caudal long axis rotation (rotation about Z). In the protraction/retraction plane, MTUs with positive moment arm values generate hip flexion (i.e., femur protraction) whereas those with negative moment arm values are associated with hip extension (i.e., femur retraction). In the abduction/adduction plane, MTUs with positive moment arm values generate hip abduction (i.e., raise the femur dorsally) whereas those with negative moment arm values are associated with hip adduction (i.e., lower the femur ventrally). Finally, for long axis rotation, MTUs with positive moment arm values generate caudal rotation (i.e., roll the femur clockwise caudally) whereas those with negative moment arm values are associated with cranial rotation (i.e., roll the femur anti-clockwise cranially).

A list of muscles including *via* sites are shown in **Table 1** and the specific *via* site information is documented in the model XML file. For all muscles, including those with one or more *via* sites, MuJoCo's kinematics pipeline computes the minimum length path between origin and insertion (while also passing through *via* sites). Moment arms are subsequently calculated by computing the following (**Eq. 5**):

$$\text{Moment arm vector} = \text{gradient}\left[L(q)\right] \tag{5}$$

Where L (q) is the vector of muscle lengths as a function of joint angle. Hence, the correspondence between muscle length changes and joint angle changes is used to solve for muscle moment arms (see MuJoCo documentation; MuJoCo.org).

Data Analysis

All data from simulations were exported into Mathematica (Wolfram, Hanborough, United Kingdom) for further analysis. Although the current *P. maculatus* model contains 48 MTU's, we analysed the functions of sixteen muscles that act primarily on the spine, pelvis and upper limb.

RESULTS

Hypothetical Simulations: Axial Muscles

Moment arm plots for all muscles are shown in **Figures 4**–**6**. **Tables 3**, **4** describe the qualitative influence of all tested factors for each MTU moment arm for the axial and hindlimb muscles, respectively.

The hypothetical simulations demonstrated that the left IL and right CI had positive moment arms (left lateral rotation) and the

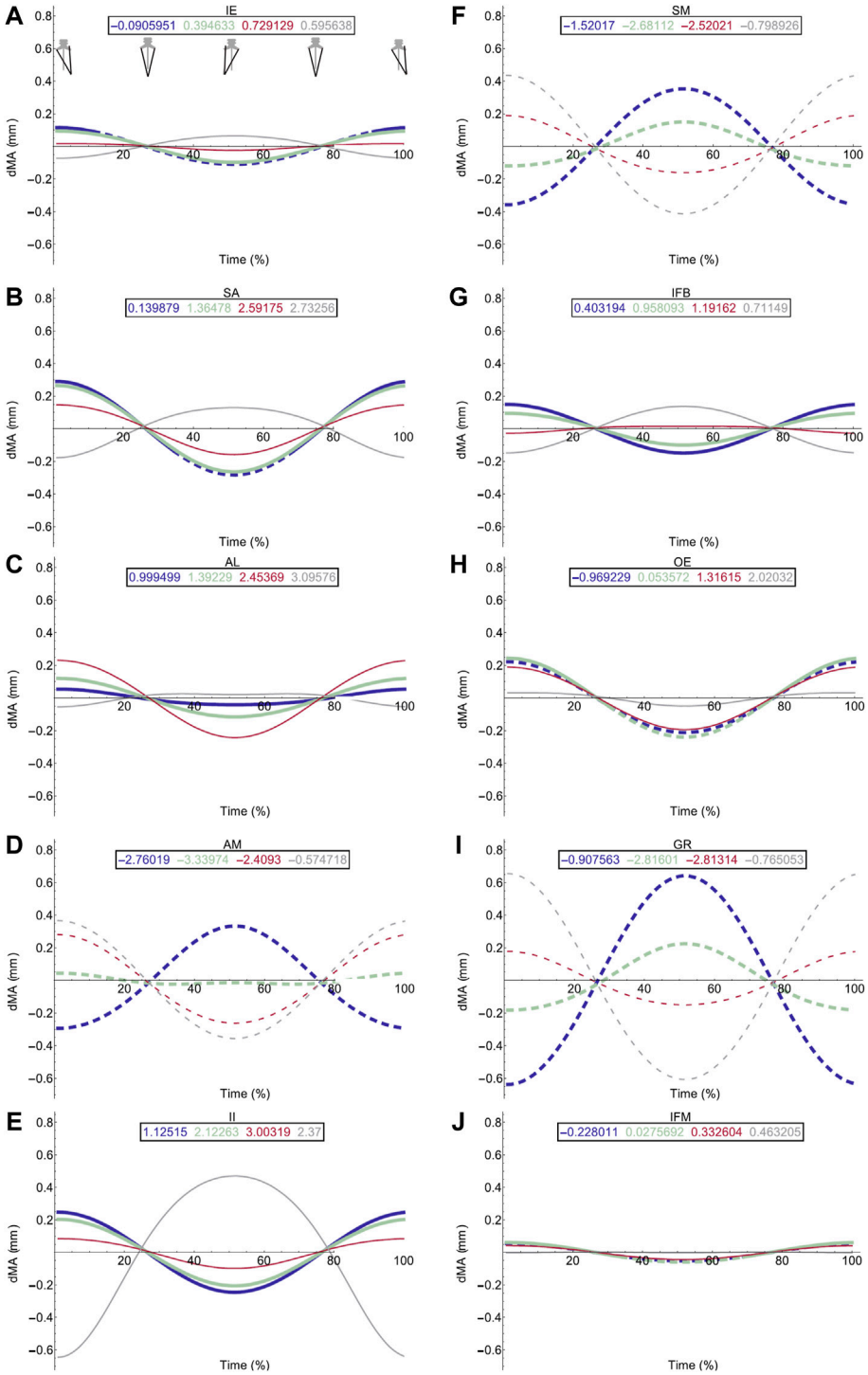

FIGURE 5 | Effect of pelvic rotation on femoral protractor and retractor muscle moment arms. Changes in flexion/extension moment arm (dMA) versus time are shown for protractor muscles **(A–E)**; Iliacus externus, IE, **(A)**, sartorius, SA **(B)**, adductor longus, AL, **(C)**, adductor magnus, AM, **(D)**, Iliacus internus, Il **(E)** and retractors **(F–J)**; semimembranosus, SM **(F)**, iliofibularis, IFB **(G)**, obturator externus, OE **(H)**, gracilis minor and major, GR **(I)**, iliofemoralis, IFM **(J)**. For each muscle, four hypothetical conditions were run: femur held at 10° (blue), 45° (light green), 90° (red) and 135° (grey). Note that for these hypothetical conditions, 0° is defined as fully retracted as seen in the null pose (**Figure 2 (E,F)** such that 10° is near full femur retraction and 135 is near fully protracted. Solid versus dashed lines represent positive moment arms (flexion—femur protraction) versus negative (extension—femur retraction) such that a change from solid to dashed indicates a change in muscle function.

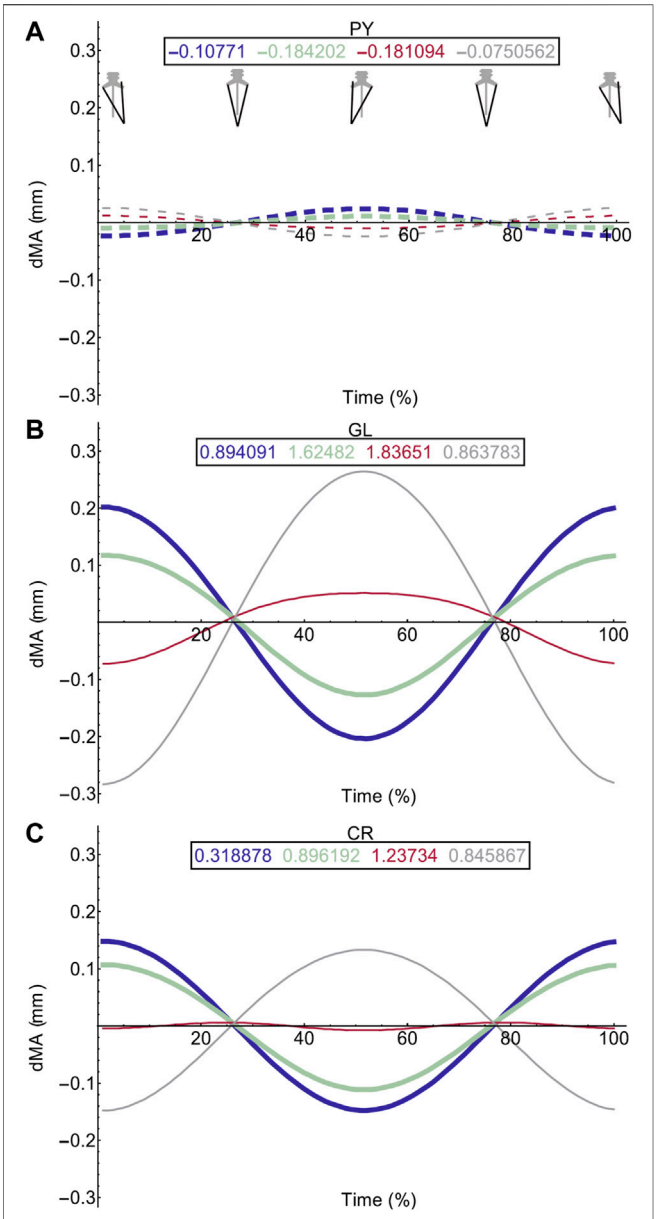

FIGURE 6 | Effect of pelvic rotation on miscellaneous muscle moment arms. Changes in flexion/extension moment arm (dMA) versus time are shown for pyriformis, PY **(A)**, gluteus maximus, GL **(B)**, cruralis, CR **(C)**. See **Figure 7** caption for further details. Solid versus dashed lines represent positive moment arms (flexion—femur protraction) versus negative (extension—femur retraction) such that a change from solid to dashed indicates a change in muscle function.

right IL and left CI had negative moment arms (right lateral rotation) throughout pelvic rotation. Both axial muscle moment arms were impacted by pelvic lateral and dorsoventral rotation to differing extents. While the function of the CI muscles remained the same throughout the pelvic rotation cycle, the moment arm outputs fluctuated in a sinusoidal wave approximately+/−2 mm about the mean indicating pelvic lateral rotation impacted moment arm magnitudes (**Figures 4B,D**). This impact on the CI moment arm remained the same despite dorsoventral rotation. The mean moment arms however were approximately 0.3 mm higher when the pelvis was extended versus flexed.

Similar to the CI, function of the IL muscles remained the same throughout the pelvic lateral rotation cycle. While there was a very slight fluctuation about the mean, this change in magnitude with lateral rotation was barely measurable, indicating that pelvic lateral rotation had a far smaller impact on IL muscles compared with CI muscles. However, the IL muscles showed more variation in average moment arm in response to dorsoventral rotation ranging from 3.85 mm (extended)—2.5 mm (full flexed) and the shallow wave form was inverted in the fully flexed simulation (**Figures 4A,C**).

Hypothetical Simulations: Femoral Muscles

Pelvic lateral rotation influenced moment arm magnitudes for muscles crossing the hip (**Table 4**). Generally, the impact of pelvic lateral rotation (i.e., peak-to-peak amplitude of the waveform) was more pronounced in the protractor muscles (IE, SA, AL, AM, II; **Figure 5**). The retractor group muscles presented shallower wave forms and magnitude changes were most dramatic in flexion/extension (Flex/Ex) components. In all muscles, the adduction/abduction (Add/Abd) moments were less dependent on lateral rotation than Flex/Ex and long axis rotation (LAR). Hence, only the Flex/Ex moments will be discussed here, and LAR and Add/Abd outputs are shown in SI. The IE and SA were the only MTUs where a change in sign (or 'function') of the moment was observed in response to pelvic lateral rotation; this was only seen when the femur was fully extended (10°). Sometimes, the strength of the impact of lateral rotation on the moment arm magnitudes depended also on the femur angle, for example in OE (**Figure 4H**), where pelvic lateral rotation only influenced moment arm magnitudes when the femur was positioned at 0, 45, and 90° (**Figure 4H**). In other instances, the position of the femur determined whether the waveform flipped (i.e., whether it increased as the pelvis rotated to the left or decreased as it rotated). A clear example of this "flipping" can be seen in the II MTU (**Figure 4E**) where lateral rotation creates a sine wave output at 0, 45, and 90°, but a cosine wave at 135°. In functional terms, for the II when the femur is fully flexed (135°), pelvic lateral

TABLE 3 | Results of hypothetical simulations HYP_01, HYP_05, and HYP_06 describing the influence of pelvic lateral rotation and pelvic dorsoventral rotation on the lateral rotation moment arms of the axial muscles.

Predicted Functional Group	MTU	Influence of pelvic Lateral Rotation	Influence of pelvic dorsoventral Rotation
Axial muscles	CI	Change in moment magnitude, left and right inverted	Change in moment magnitude
	IL	Change in moment magnitude but pattern dependent on dorsoventral angle of pelvis	Change in moment magnitude and varying influence on pelvic lateral rotation

TABLE 4 | Results of hypothetical simulations HYP_01-HYP_06 describing the influence of pelvic lateral rotation and femur angle in the flexion/extension plane on the flexion/extension (FE), long axis rotation (LAR), and abduction/adduction (AA) moment arms of the hindlimb muscles.

Predicted Functional Group	MTU	Impact of pelvic Lateral Rotation	Impact of femur Angle (Flexion/extension)
Protractors	IE	Change in moment magnitude (increase or decrease dependent femur angle)	Change in moment magnitude and function in FE and LAR
Retractors	SM	Shallow change in FE magnitude only	Change in FE and LAR magnitudes. Influence of pelvic lateral rotation dampened in mid femoral angles
	IFB	Slight impact in FE magnitude only (increase or decrease dependent femur angle)	Change in FE magnitude
	OE	Shallow change in FE magnitude only	Decrease in FE moment magnitude and switch of function from protractor to retractor in full extension
Protraction and adduction	SA	Shallow impact on FE moment magnitudes and AA moment (only when femur is fully retracted)	Influences the magnitude of all moment arms. Changes in sign/function seen in the AA moment when femur at full retraction angle
	AL	Only shallow magnitude changes in flexion/extension moment arms when femur is at 90°	Change in FE and LAR magnitudes with more retracted femoral angle
	AM	Change in FE moment magnitude	Small change in FE and LAR moment magnitude and change in FE function
Retraction and adduction	GR	Change in FE and LAR moment magnitudes	Small change in LAR moment magnitudes when femur in retracted position Variable FE moments dependant on femur angle. Very little impact of AA moments
	IFM	Very shallow change in FE moment magnitude only	Small change in FE magnitude and change in FE sign/function from positive to negative at full femoral retraction angle
Protraction and abduction	II	Change in moment magnitudes but dependant on femur angle	Change in all magnitudes and change in FE sign/function. Some impact on long axis rotation and abduction/adduction moment arm magnitudes. Larger influence on flexion/extension moment arm magnitudes
Abduction	PY	None	Very small changes in FE and LAR magnitude
Knee extensor	CR/GL	Impact on FE moment magnitudes (except when femur at 90°)	Small influence on magnitude in LAR and AA. Larger influence on FE, strongest at 90° and weakest at full retraction

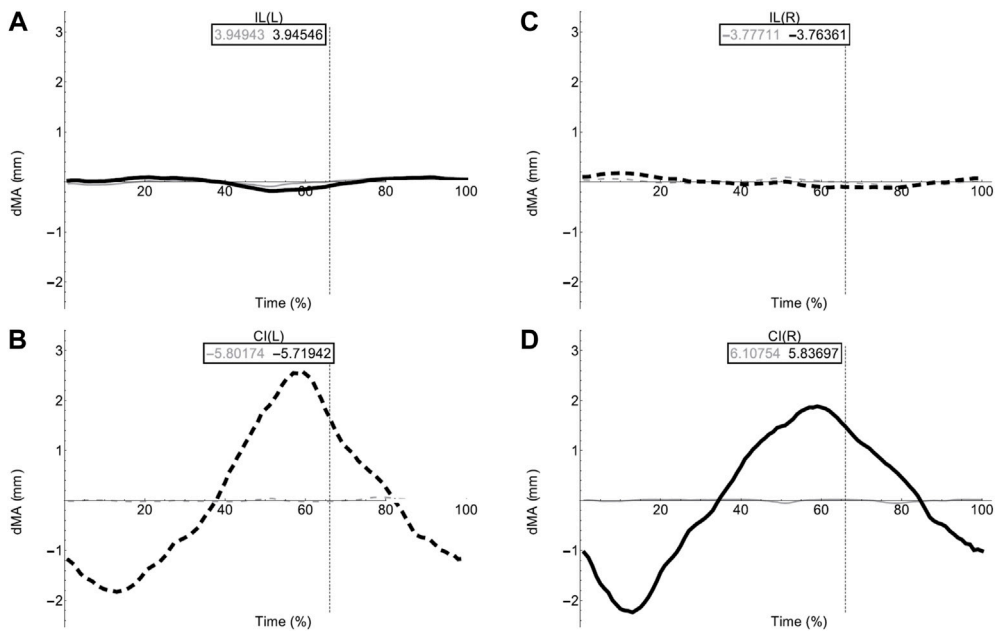

FIGURE 7 | Axial muscle moment arms during walking. Changes in moment arm (dMA) versus time are shown for **(A)** the left Iliolumbaris, IL (L), **(B)** left coccygeoiliacus, CI (L), **(C)** right Iliolumbaris, IL (R), **(D)** right coccygeoiliacus, CI (R) for simulations with a mobile pelvis (natural condition; black) versus a fixed pelvis (simulated condition; grey). See **Figure 3** caption for further details. Solid versus dashed lines represent positive moment arms (flexion—femur protraction) versus negative (extension—femur retraction) such that a change from solid to dashed indicates a change in muscle function.

TABLE 5 | Results of walking sequence simulations RUN_ROT and RUN_FIX describing the impact of fixing pelvic lateral rotation on the lateral rotation moment arms of the axial muscles during walking.

Predicted Functional Group	MTU	Moment arm	Impact of Fixed pelvic Rotation	Summary of Function
Axial muscles	CI (right and left)	Time varying moments creating a triangular shape waveform through the stride cycle	Elimination of moment arm magnitude fluctuation	Left and right antagonistic pairs generating left and right lateral rotation of pelvis about SI joint
		Both left and right MTU moments arm magnitudes peak at the onset of swing phase but have opposite moments	Comparably weaker moments when each respective muscle is likely to be active	Right CI produces left rotation and Left CI produces right rotation of the pelvis
	IL (right and left)	Time varying moments creating the inverted waveform with respect to the CI	Reduction in moment arm magnitude fluctuation	Left and right antagonistic pairs generating left and right lateral rotation of pelvis about SI joint
		Both left and right MTU moments magnitudes peak during stance phase but have opposite moments	Comparably weaker moments when each respective muscle is likely to be active	Left IL produces left rotation and Right IL produces right rotation of the pelvis

rotation increases II flexion moment arm as the pelvis rotates to the left, whereas when passed 90° pelvic lateral rotation decreases II flexion moment arm as the pelvis rotates to the left.

Femur angle had a pronounced impact on MTU moment arms, influencing both magnitude (all MTUs except IFM) and moment arm sign ('function') (IFM and OE). For some MTUs (mostly protractors) moment arm magnitudes became progressively stronger as the femur flexed, for example AL (**Figure 4C**) where the mean flexion moment arm increased from approximately 1 mm at 0°, to 3.1 mm at 135°. In others (mostly retractors), the moment arms became weaker with femur flexion, for example AM (**Figure 4D**) where the mean extension moment arm decreased from −3.4 mm at 45° to −0.6 mm at 135°. In some cases, the moment arms were strongest at the mid angles (45 and 90°), but weakest at the extremes, as is true for GR (**Figure 4I**) and GL (**Figure 6B**).

Walking Sequence Simulations: Axial Muscles

Table 5 provides a summary of function and describes the impact of fixing pelvic lateral rotation during a walking sequence on the axial muscles. Simulation outputs for the axial muscles can be seen in **Figure 7**.

Fixing pelvic lateral rotation had little impact on the mean moment arm values for either the left or right CI and IL muscles. However, the fluctuation in magnitude of the CI moment arm with pelvic lateral rotation was impacted. In **Figures 7B,D**, the moment arm output for the fixed simulation is a flat line that does not fluctuate about zero whereas the unaltered walking simulation output is a triangular wave form fluctuating approximately+/−2 mm about zero.

Walking Sequence Simulations: Femoral Muscles

Table 6 provides functional interpretations and descriptions of pelvic lateral rotation impact in the Flex/Ex plane of motion and summarises function for each MTU during walking. Data for the LAR and Add/Abd planes are excluded from this comparative table since moment arm magnitudes were comparatively low and/or were minimally impacted by pelvic lateral rotation (see SI).

Flexion/Extension Moment Arms During Walking Locomotion

Flex/Ex moment arm plots for all muscles are shown in **Figures 8**, **9**. For those muscles represented by multiple MTUs, the MTU with the strongest moment arm value is presented.

In contrast to the pelvic MTU moment arms in walking (**Figure 7**), the hindlimb moment arms did not exhibit the same triangular wave patterns, but instead showed smoother sinusoidal fluctuations in values (**Figures 8**, **9**). The SM, AM, and GR MTUs maintained negative Flex/Ex moment arm values throughout the walking stride suggesting that, at all limb positions, these muscles function as hip extensors (i.e., would retract the femur). Whereas the IE, SA, AL, II, OE, CR/GL maintained positive Flex/Ex moments throughout the stride cycle suggesting these muscles function as hip flexors (i.e., would protract the femur). As the limb unfolded during the stance phase the protractor moment arm of these muscles became progressively weaker until the hip was flexed in the swing phase. As the femur was protracted progressively further the moment arms became progressively stronger, suggesting these muscles are most effective at producing hip flexion once the femur has already begun to protract. The IFB, IFM, and PY muscles fluctuated from positive moments to negative moments throughout the stride cycle, starting as flexors, switching to extensors during stance phase and negative during swing, flipping back to positive as the limb realigns itself for the onset of the next stance phase.

Fixing pelvic lateral rotation impacted the protractor and retractor muscles differently. In terms of mean moment arm value, those MTUs with flexor moment arms (i.e., protractors; including IFB) as well as GR, SM, and PY (which have extensor moments) were ~0–10% weaker when the pelvis was fixed. However, for the remaining MTUs, AM and IFM, the mean moment arms were ~3–20% stronger when the pelvis was fixed. There were also differences in the level of fluctuation about the mean value in many of the muscles, where the fixed pelvic outputs

TABLE 6 | Results of walking sequence simulations RUN_ROT and RUN_FIX describing the impact of fixing pelvic lateral rotation on the flexion/extension (FE) moment arms of the hindlimb muscles.

Predicted Functional Group	MTU	FE Plane	Fixed Pelvis	Summary of Function
Protraction	IE	Dist—weak flexor moment becomes extensor moment during limb retraction Prox—flexor moment that weakens throughout stance phase as limb retracts	Dist - Slight strengthening of extensor moment Prox—Flexor moment weakened during stance phase	Hip flexor
Protraction and adduction	SA	Flexor moment but gets weaker during limb retraction	Weakened flexor moment during stance phase	Hip flexor
	AL	Flexor moment weakens as limb retracts and strengthens through protraction peaking as limb is brought into protracted position ready for stance onset	No significant change	Hip flexor
	AM (crv)	Extensor moment strengthens as limb retracts Str—starts weak protractor, towards zero with retraction	Similar pattern and magnitude however moment is slightly weaker during limb retraction and slightly stringer during swing phase AM str—weakens flexor moment and strengthens the extensor moment	Hip extensor and cranial rotator
Protraction and abduction	II	Lat and Med—Flexor moment which weakens during stance phase	Lat—weakened flexor moment causing a flip to very weak extensor moment as the limb approaches full retraction Med—weakened flexor moment	Hip flexor and caudal rotator
Retraction	SM	Extensor moment that is weakens as limb protracts in swing phase	Extensor moment is weakened during stance phase	Hip extensor
	IFB	Flexor moment which flips to weak extensor moment as hindlimb approach maximum retraction during stance	Slight strengthening of extensor moment during stance phase	Caudal rotator, weak Hip extensor during stance and Hip flexor during swing
	OE	Flexor moment which weakens throughout stance phase	Weakened flexor moment causing a flip to very weak extensor moment as the limb approaches full retraction	
Cranial rotator and Hip flexor				
Retraction and adduction	GR	Extensor moment gets weaker as hindlimb retracts in stance phase	Extensor moment weakened significantly during stance phase	Hip extensor
	IFM	Flexor moment which flips to extensor moment as hindlimb approach maximum retraction during stance	Very slight strengthening of extensor moment during stance phase	Caudal rotator, Hip extensor during stance and Hip flexor during swing
Abduction	PY	Extensor moment gets stronger with retraction	No significant change	Hip extensor and caudal rotator
Knee extensor	CR/GL	Flexor moment gets weaker with limb retraction	Weakened flexor moment throughout limb retraction	Hip flexor

showed more exaggerated peaks and troughs compared with the unaltered pelvic simulation outputs. For example, the mean moment arm in the SA MTU in the fixed simulation is lower than is was in the rotating simulation (1.76 versus 2.02 mm; **Figure 8B**), yet the fixed simulation showed a wider fluctuation about the mean with higher peaks at time 0 and 100% (~0.8 mm compared with 0.6 mm) as well as lower troughs at time 55% (approaching −1.5 mm compared with just under −1 mm).

Long Axis Rotation and Abduction/Adduction of the Femur

Most MTUs had lower moment values in LAR compared with values in Flex/Ex (see SI). The II, IFM, IFB, and PY had the strongest caudal rotator moments, whereas the AM, SA, and OE had the strongest cranial rotator moments. Generally, regardless of moment sign, LAR rotators were strongest mid-stride cycle as the limb makes the transition from stance to swing. Fixing pelvic lateral rotation had little effect on moment arm magnitudes in any of the hindlimb muscles (see SI for remaining moment arm components).

DISCUSSION

The present study combined anatomical data with experimental kinematics to build and animate a 3D musculoskeletal model of the frog *P. maculatus*. Two sets of simulations were used to elucidate the mechanical impacts of pelvic lateral rotation during walking locomotion. The first allowed exploration of the entire integrated system during walking whereas the hypothetical simulation with the

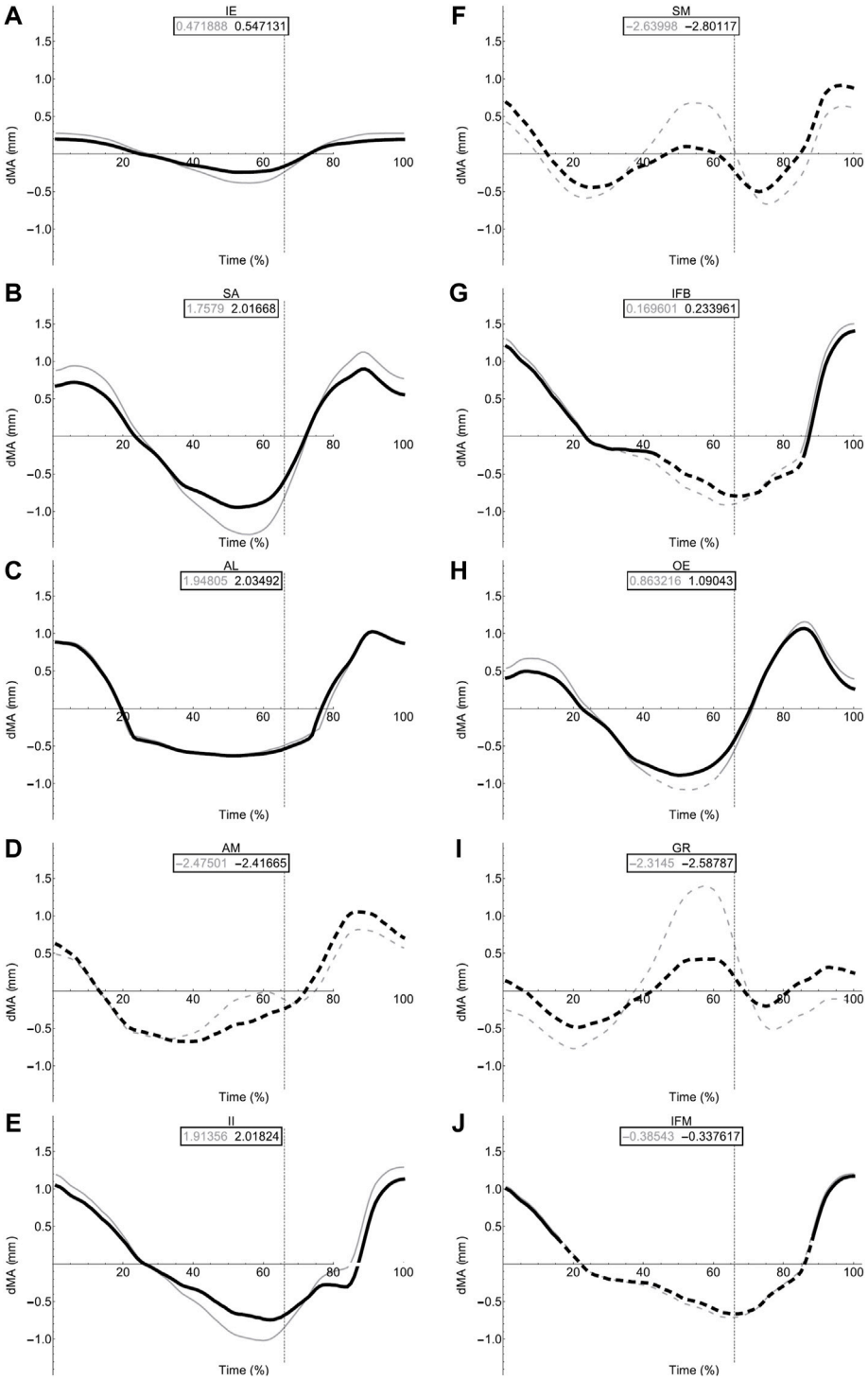

FIGURE 8 | Femoral muscle moment arms during walking. Changes in moment arm (dMA) versus time are shown for protractor muscles **(A–E)**; Iliacus externus, IE, **(A)**, sartorius, SA **(B)**, adductor longus, AL, **(C)**, adductor magnus, AM, **(D)**, Iliacus internus, Il **(E)** and retractors **(F–J)**; semimembranosus, SM **(F)**, iliofibularis, IFB **(G)**, obturator externus, OE **(H)**, gracilis minor and major, GR **(I)**, iliofemoralis, IFM **(J)** for simulations with a mobile pelvis (natural condition; black) versus a fixed pelvis (simulated condition; grey). See **Figure 7** caption for further details. Solid versus dashed lines represent positive moment arms (flexion—femur protraction) versus negative (extension—femur retraction) such that a change from solid to dashed indicates a change in muscle function.

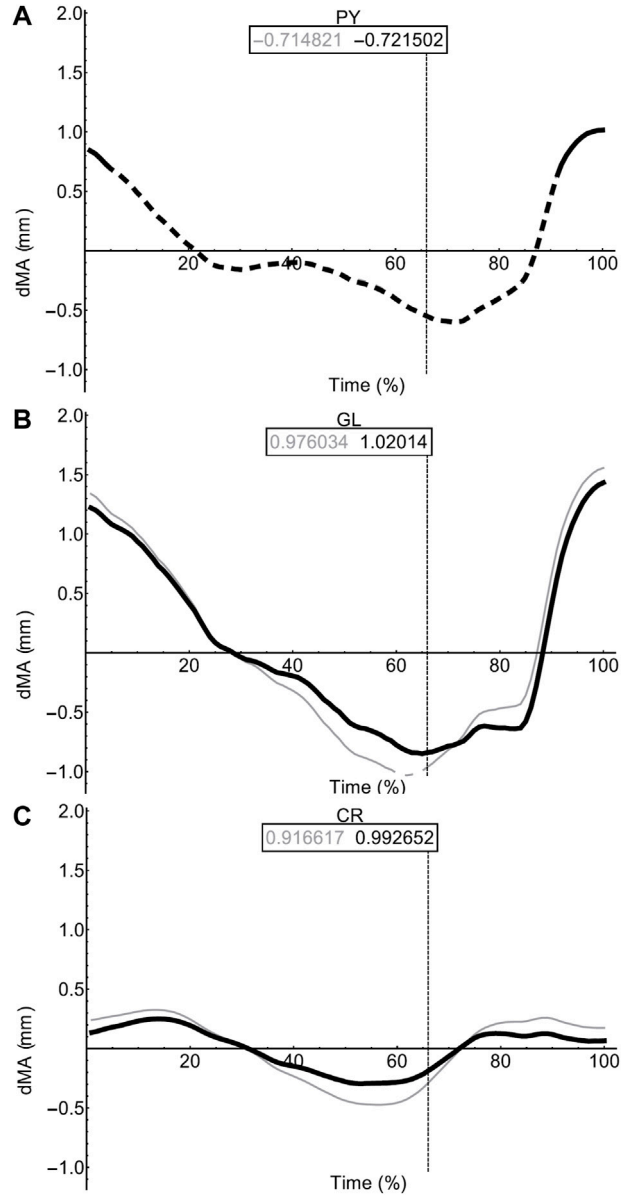

FIGURE 9 | Miscellaneous muscle moment arms during walking. Changes in moment arm (dMA) versus time are shown for pyriformis, PY **(A)**, gluteus maximus, GL **(B)**, cruralis, CR **(C)**. for simulations with a mobile pelvis (natural condition; black) versus a fixed pelvis (simulated condition; grey). See **Figure 7** caption for further details. Solid versus dashed lines represent positive moment arms (flexion - —femur protraction) versus negative (extension—femur retraction) such that a change from solid to dashed indicates a change in muscle function.

fixed pelvis allowed us to isolate the impact of lateral rotation by the pelvis without confounding effects from the other joint motions.

Axial Muscles Have Greater Leverage in the Walking Configuration

The mechanical function of the pelvis and the axial muscles is not obvious. The 3D geometry and model motion combined with previously published EMG data (Emerson and De Jongh, 1980) indicates that the CI and IL form contralateral pairs where the left CI is active simultaneously with the right IL, and vice versa. Consequently, the *left* CI and *right* IL work together rotating the pelvis to the *right* (the opposite then being true for left lateral rotation). EMG data, however, is unable to resolve how effective those muscles are during their activation cycles and how those actions change with pelvis and limb motion.

Through our simulations, we measured the action of the pelvic muscles during various pelvic rotations (dorsoventral and lateral) and built our understanding of how pelvic motion influences the leverage of the pelvic muscles. In both the hypothetical simulation and the walking sequence simulations the moment arm magnitudes of the axial muscles were time variable in accordance with the hypothetical limb positions and lateral rotation of the pelvis. At full protraction of the left limb (maximum rotation of the pelvis to the left), the right IL and the left CI reached their maximum moment magnitudes. This means that when the right CI and left IL are contracted, they have their weakest moment arm magnitude; and the opposite muscle bellies for both muscles have their largest moment arms while relaxed. Consequently, as the relaxed muscle bellies are activated, they are able to generate a proportionally large amount of torque to swing the pelvis rapidly back in the other direction at the same time as the antagonistic muscle bellies relax and passively lengthen. This allows the pelvis to contribute to limb protraction and retraction during walking while minimising any potential counter-torque effects if contralateral axial muscle activations overlap.

Dorsoventral rotation of the pelvis additionally impacted moment arm magnitudes in the axial muscles, in agreement with Lombard and Abbott's (1907) excitation study. The impact of increased dorsoventral rotation at the IS joint, however, acted to weaken the lateral rotation moment arm magnitudes for all axial muscles on both sides, except the proximal belly of the CI muscles. When interpreted along with the EMG data (Emerson and De Jongh, 1980) for walking and jumping this weakening is functionally logical. While the pelvis is in a more extended dorsoventral angle (spine and pelvis are more in-line) as is the case in walking, the axial muscles have greater mechanical advantage for generating the left and right lateral rotation seen during walking locomotion. Whereas when adopting a crouched position, with a dorsoventrally flexed pelvis, as observed during jump preparation, the mean moment arm magnitudes for lateral rotation are ~5% (CI) and ~35% (IL) lower. Additionally, during walking the muscles are activated reciprocally in contralateral pairs, whereas in jumping both the left and right axial muscles are activated simultaneously. Along with previously recorded activation patterns, our simulations support the idea that when in a walking configuration the pelvis can contribute to hindlimb range of motion effectively *via* lateral rotation, whereas when in a jumping configuration the pelvis is able to take on a stabilisation role. Again, this relationship suggests the effects of counter-torque in the pelvis can be minimised in walking but also in jumping if muscle activations aren't exactly simultaneous on both sides.

Hindlimb Muscle Function Cannot Be Fully Inferred From Static Anatomy

For the most part, moment arm outputs for the hindlimb muscles during locomotion are in agreement with the predicted muscle functions published in the literature (Lombard and Abbott, 1907; Kargo and Rome, 2002; Přikryl et al., 2009). There are however a few exceptions. The CR/GL muscles were categorised in the knee extensor functional group based on excitation data from Přikryl et al. (2009), and since they cross both the hip and knee joint, we would expect them to exhibit joint moments about the hip and the knee. Given their biarticular nature, it is unsurprising that these muscles exhibited flexor moments about the hip in the current study. The AM was predicted to be a protractor and adductor of the femur, yet moment arm outputs during walking simulations suggest this muscle is better suited to femur cranial rotation and retraction during walking. The OE was predicted to be a femur retractor however moment arm outputs suggest this muscle is more likely to function as a protractor and cranial long axis rotator. Additionally, IFB and IFM both exhibited variable moments flipping between protractors and retractor moments through the course of the stride cycle despite being predicted retractors.

We propose two alternative reasons for the differences in function between our model and prior literature: 1) geometric variation between species, and 2) moment arm variation due to posture. It is reasonable to expect then, that a more apparent variation in muscle insertion position across different species may have the power to impact muscle moment arm sufficiently to result in a switching of predicted major function. There are also fundamental differences in methodological approach to interpreting muscle function between the data from Přikryl et al. (2009) and the functional data collected from our musculoskeletal model. Since the model presents moment arm data throughout a stride cycle, the major function of the muscle in question is interpreted based on the limb configuration in which the muscle is most likely to be active (i.e., when the MTU was shortening). Kinematics data (Collings et al., 2019) demonstrates the wide range of motion in the hindlimb during walking. Further, the present study highlights the impact that femoral angle can have on moment arm magnitude of thigh muscles. Kargo and Rome (2002) note also that muscle function changed due to hindlimb configuration, Engelkes et al. (2020) also show that humerus position impacts muscle moment arms in the pectoral girdle. It is unlikely that the full range of limb configurations was explored during the excitation study. Thus, differences in reported major functions may be due to differences in limb position throughout the stride cycle.

The proportion of muscles with flexor moments (femur protractors) versus those with extensor moments (femur retractors) was greater than expected. Of the muscles included in our model, eight had flexor moments where only four had extensor moments. This was unexpected given the assumption that limb retraction propels forward motion not only in walking but also jumping. However, while there are twice as many muscle bellies, the split of muscle mass between protractors and retractors is more equal. The AM, SM, and GR are large muscles forming nearly the entire extensor compartment of the hindlimb, whereas the protractors tended to be thin strap muscles or smaller cylindrical muscles (Collings and Richards, 2019). The total mass of the retractors is approximately 0.67 g while the mass of the protractors is only slightly higher at 0.89 g (Collings, unpublished data). These observations suggest that protraction and limb position require more precision to place the hindlimb in the correct configuration to be ready for a more powerful retraction to drive forward motion in the desired direction.

Both Pelvic Lateral Rotation and Hindlimb Angle Impact Muscle Moments

Given that limb configuration has previously been shown to impact moment arms and subsequent muscle functions (Kargo and Rome, 2002; Engelkes et al., 2020), and dorsoventral rotation of the pelvis impacted muscle functions during Lombard and Abbott's (1907) excitation study, we predicted that pelvic lateral rotation would alter the moment arm relationships of the muscles spanning the hip joint. We investigated this by generating and comparing the outputs of a range of hypothetical trials and an experimental walking simulation. The range of hypothetical trials demonstrated that pelvic lateral rotation and hindlimb position influences the magnitude of many of the MTU moment arms (especially Flex/Ex). The position of the femur also in some instances changed the sinusoidal moment arm pattern, such as in the AM where the moment arm magnitudes got stronger as the pelvis rotated to the left when the femur was held at 90° or 135° but got weaker while rotating to the left when held at 10°. Since walking entails a synchronised combination of both pelvic lateral rotation and femur protraction/retraction, the timing of these two motions not only impacts the ability of the pelvis to contribute to limb retraction in terms of stride length (Collings et al., 2019), but also in terms of muscle mechanics.

Pelvic lateral rotation had a differential impact on the flexor and extensor hindlimb muscle moment arms, depending on their function. Those muscles with protractor moments and some of the muscles with retractor moments (SM and GR) benefitted from pelvic lateral rotation with increased moments. The fluctuation in moment arm magnitude was also increased in the fixed pelvic simulations suggesting that pelvic lateral rotation dampens the effect of femur angle throughout the stride cycle, therefore allowing the moments to stay as strong as they could be at each point during the stride cycle (or given femur position).

Of course, the current interpretations come with the caveat of being true given that all else remains equal. In reality, the animals would likely compensate for the reduced moment if their pelvis were to be fixed anatomically. The present walking simulations combined with previous kinematic studies investigating the impact on stride length (Collings et al., 2019) suggest that pelvic lateral rotation is not required for walking but that it does contribute by making it slightly mechanically easier. With a fixed pelvis, the muscles would need to work slightly harder to generate equal torque.

The Results of Our Computational Approach Become Hypotheses for Future Experiments

In addition to the caveat above, the present study has several limitations due to its computational approach which can be

placed into four categories: MTU morphology, Muscle force, Muscle activation, Bone kinematics.

MTU Morphology: Wrapping Surfaces Don't Capture the Morphology Exactly

The inclusion of wrapping surfaces into the construction of the model puppet did allow for muscle pathways to be mimicked however it is not possible to capture all details of the muscle and tendon architecture in our model. For example, the MTUs in MuJoCo assume the muscle and tendon components function in unison to generate net length change. Resolving the independent change in muscle fascicle length versus tendon stretch. Thus, MTU function in this paper is an assumption based on muscle leverage. To resolve, the model output could be compared with tendon travel experiments and sonomicrometry as in Konow et al. (2012).

Muscle Force: We Do Not Know Muscle Forces

While we can calculate muscle moment arm, we do not have the data output from this model to resolve muscle force output. With further work using an inverse dynamics approach to calculate predicted muscle force from the joint kinematics and MTU geometry, force outputs can be predicted.

Muscle Activation: We Cannot Verify Muscle Activation

This means that although we assume that when an MTU is shortening the muscle would be actively contracting we cannot verify muscle activation patterns for eccentric muscle activations. Where possible we have verified MTU length changes with previously published EMG data however, unlike the pelvic muscles, there are currently no published muscle activation data for any of the hindlimb muscles during walking. However, the present model allows muscles of interest to be identified for the informed planning of future *in vivo* studies. With EMG and sonomicrometry data, for example, activation timings and length changes for the muscles can resolve whether muscles are concentrically or eccentrically contracting. It is suggested that EMG data is collected for the major muscles of the hindlimb and compared with the moment arm data collected here to allow further resolution of hindlimb muscle function during walking.

Bone Kinematics: Joint Kinematics Were Estimated From Surface Markers Only

This paper took a non-invasive approach to collecting kinematic data, but this does mean that one notable assumption that we cannot verify is the long axis rotations of the femur, tibiofibula and tarsal segments. Since our experimental set-up did not resolve these empirically, we worked with the assumption that these segments would be rotated about their long axis in a manner which consistently aligned their flexion/extension axes. Experimental observation of the skeletal kinematics [using xray reconstruction of moving morphology (XROMM)] during walking is required to confirm or challenge this assumption, and to assess to what degree MTU and moment arm changes are sensitive to long axis rotations. Our anatomical model coupled with the kinematic motion can highlight bones of interest and assist in identifying potential implant sites and surgery strategies for the bone markers required for XROMM.

Despite the limitations, our approach is extremely valuable because it allows precise hypotheses to be generated that can then be directly addressed with further experimental work and computational work (e.g., inverse dynamics etc.).

CONCLUSION

The following conclusions were drawn from the data presented in this paper:

1. Pelvic dorsoventral rotation and pelvic lateral rotation angle have the power to impact moment arms of the axial and hindlimb muscles crossing the hip joint.
2. In walking postures, axial muscle moment arms are at their strongest in the lateral rotation plane and hindlimb muscles are strongest in Flex/Ex plane.
3. Pelvic lateral rotation contributes to limb motion by strengthening flexor (and some extensor) moment arms in the hindlimb muscles.

P. maculatus thus appear to have a musculoskeletal anatomy that enables them to modulate pelvic and hindlimb motion with alternative activation patterns and postural changes, respectively, ultimately permitting multifunctionality.

DATA AVAILABILITY STATEMENT

All XML files, supporting files, and custom code are available in the follwing GitHub repository https://github.com/frogtronics/mujoco150_KM.

ETHICS STATEMENT

All experimental and anatomical data used in the model presented here were collected in previous studies (Collings et al., 2019; Collings and Richards, 2019) using procedures conducted under the Home Office License 70/8242.

AUTHOR CONTRIBUTIONS

Experimental design: AC and CR. Data collection: AC and EE. Data analysis: AC, EE, and CB. Data interpretation: AC. Wrote Mathematica and MATLAB code: AC, EE, CR, and CB. Drafted the manuscript: AC, CR, and CB. Read, commented on or approved the final manuscript: EE, CR, and CB.

FUNDING

Funding for this work was provided by a European Research Council Starting Grant (PIPA338271) awarded to CR.

ACKNOWLEDGMENTS

We thank John Hutchinson and James Charles for their valuable insights and advice regarding musculoskeletal modelling. Futhermore, we would like to thank both reviewers for their thorough and constructive reviews that were instrumental in strengthening this paper.

SUPPLEMENTARY MATERIAL

The Supplementary Material for this article can be found online at: https://www.frontiersin.org/articles/10.3389/fbioe.2022.806174/full#supplementary-material

REFERENCES

Ahn, A. N., Furrow, E., and Biewener, A. A. (2004). Walking and Running in the Red-Legged Running Frog,Kassina Maculata. *J. Exp. Biol.* 207, 399–410. doi:10.1242/jeb.00761

Astley, H. C., and Roberts, T. J. (2014). The Mechanics of Elastic Loading and Recoil in Anuran Jumping. *J. Exp. Biol.* 217, 4372–4378. doi:10.1242/jeb.110296

Charles, J. P., Cappellari, O., Spence, A. J., Wells, D. J., and Hutchinson, J. R. (2016). Muscle Moment Arms and Sensitivity Analysis of A Mouse Hindlimb Musculoskeletal Model. *J. Anat.* 229, 514–535. doi:10.1111/joa.12461

Collings, A. J., and Richards, C. T. (2019). Digital Dissection of the Pelvis and Hindlimb of the Red-Legged Running Frog, Phlyctimantis Maculatus, Using Diffusible Iodine Contrast Enhanced Computed Microtomography (DICE μCT). *PeerJ* 7, e7003. doi:10.7717/peerj.7003

Collings, A. J., Porro, L. B., Hill, C., and Richards, C. T. (2019). The Impact of Pelvic Lateral Rotation on Hindlimb Kinematics and Stride Length in the Red-Legged Running Frog, Kassina Maculata. *R. Soc. Open Sci.* 6, 190060. doi:10.1098/rsos.190060

d'Avella, A., and Lacquaniti, F. (2013). Control of Reaching Movements by Muscle Synergy Combinations. *Front. Comput. Neurosci.* 7, 42. doi:10.3389/fncom.2013.00042

Delp, S. L., Anderson, F. C., Arnold, A. S., Loan, P., Habib, A., John, C. T., et al. (2007). OpenSim: Open-Source Software to Create and Analyze Dynamic Simulations of Movement. *IEEE Trans. Biomed. Eng.* 54, 1940–1950. doi:10.1109/tbme.2007.901024

Duellman, W. E., and Trueb, L. (1986). *Biology of Amphibians*. USA: McGraw-Hill.

Dunlap, D. G. (1960). The Comparative Myology of the Pelvic Appendage in the Salientia. *J. Morphol.* 106, 1–76. doi:10.1002/jmor.1051060102

Emerson, S. B., and De Jongh, H. J. (1980). Muscle Activity at the Ilio-Sacral Articulation of Frogs. *J. Morphol.* 166, 129–144. doi:10.1002/jmor.1051660202

Emerson, S. B. (1979). The Ilio-Sacral Articulation in Frogs: Form and Function. *Biol. J. Linn. Soc.* 11, 153–168. doi:10.1111/j.1095-8312.1979.tb00032.x

Engelkes, K., Kath, L., Kleinteich, T., Hammel, J. U., Beerlink, A., and Haas, A. (2020). Ecomorphology of the Pectoral Girdle in Anurans (Amphibia, Anura): Shape Diversity and Biomechanical Considerations. *Ecol. Evol.* 10, 11467–11487. doi:10.1002/ece3.6784

Kargo, W. J., and Giszter, S. F. (2000). Rapid Correction of Aimed Movements by Summation of Force-Field Primitives. *J. Neurosci.* 20, 409–426. doi:10.1523/jneurosci.20-01-00409.2000

Kargo, W. J., Nelson, F., and Rome, L. C. (2002). Jumping in Frogs: Assessing the Design of the Skeletal System by Anatomically Realistic Modeling and Forward Dynamic Simulation. *J. Exp. Biol.* 205, 1683–1702. doi:10.1242/jeb.205.12.1683

Kargo, W. J., and Rome, L. C. (2002). Functional Morphology of Proximal Hindlimb Muscles in the Frog *Rana pipiens*. *J. Exp. Biol.* 205, 1987–2004. doi:10.1242/jeb.205.14.1987

Konow, N., Azizi, E., and Roberts, T. J. (2012). Muscle Power Attenuation by Tendon during Energy Dissipation. *Proc. R. Soc. B.* 279, 1108–1113. doi:10.1098/rspb.2011.1435

Lieber, R. L., and Boakes, J. L. (1988). Sarcomere Length and Joint Kinematics during Torque Production in Frog Hindlimb. *Am. J. Physiology-Cell Physiol.* 254, C759–C768. doi:10.1152/ajpcell.1988.254.6.c759

Lieber, R. L., and Shoemaker, S. D. (1992). Muscle, Joint, and Tendon Contributions to the Torque Profile of Frog Hip Joint. *Am. J. Physiology-Regulatory, Integr. Comp. Physiol.* 263, R586–R590. doi:10.1152/ajpregu.1992.263.3.r586

Lombard, W. P., and Abbott, F. M. (1907). The Mechanical Effects Produced by the Contraction of Individual Muscles of the Thigh of the Frog. *Am. J. Physiology-Legacy Content* 20, 1–60. doi:10.1152/ajplegacy.1907.20.1.1

Mendes, C. S., Bartos, I., Márka, Z., Akay, T., Márka, S., and Mann, R. S. (2015). Quantification of Gait Parameters in Freely Walking Rodents. *BMC Biol.* 13, 50. doi:10.1186/s12915-015-0154-0

Přikryl, T., Aerts, P., Havelková, P., Herrel, A., and Roček, Z. (2009). Pelvic and Thigh Musculature in Frogs (Anura) and Origin of Anuran Jumping Locomotion. *J. Anat.* 214, 100–139. doi:10.1111/j.1469-7580.2008.01006.x

Reynaga, C. M., Astley, H. C., and Azizi, E. (2018). Morphological and Kinematic Specializations of Walking Frogs. *J. Exp. Zool.* 329, 87–98. doi:10.1002/jez.2182

Richards, C. T., Porro, L. B., and Collings, A. J. (2017). Kinematic Control of Extreme Jump Angles in the Red-Legged Running Frog, Kassina Maculata. *J. Exp. Biol.* 220, 1894–1904. doi:10.1242/jeb.144279

Richards, C. T. (2019). Energy Flow in Multibody Limb Models: a Case Study in Frogs. *Integr. Comp. Biol.* 59 (6), 1559–1572. doi:10.1093/icb/icz142

Todorov, E., Erez, T., and Tassa, Y. (2012). "MuJoCo: A Physics Engine for Model-Based Control," in 2012 IEEE/RSJ Int. Conf. on Intel. Rob. Syst, Vilamoura-Algarve, Portugal, 7-12 Oct. 2012 (IEEE). doi:10.1109/iros.2012.6386109

Conflict of Interest: The authors declare that the research was conducted in the absence of any commercial or financial relationships that could be construed as a potential conflict of interest.

Publisher's Note: All claims expressed in this article are solely those of the authors and do not necessarily represent those of their affiliated organizations, or those of the publisher, the editors and the reviewers. Any product that may be evaluated in this article, or claim that may be made by its manufacturer, is not guaranteed or endorsed by the publisher.

frontiers | Frontiers in Bioengineering and Biotechnology

ORIGINAL RESEARCH
published: 08 April 2022
doi: 10.3389/fbioe.2022.825149

Contribution of Afferent Feedback to Adaptive Hindlimb Walking in Cats: A Neuromusculoskeletal Modeling Study

Yongi Kim[1], Shinya Aoi[1], Soichiro Fujiki[2], Simon M. Danner[3], Sergey N. Markin[3], Jessica Ausborn[3], Ilya A. Rybak[3], Dai Yanagihara[4], Kei Senda[1] and Kazuo Tsuchiya[1]*

[1]Department of Aeronautics and Astronautics, Graduate School of Engineering, Kyoto University, Kyoto Daigaku-Katsura, Kyoto, Japan, [2]Department of Physiology, School of Medicine, Dokkyo Medical University, Tochigi, Japan, [3]Department of Neurobiology and Anatomy, Drexel University College of Medicine, Philadelphia, PA, United States, [4]Department of Life Sciences, Graduate School of Arts and Sciences, The University of Tokyo, Tokyo, Japan

Mammalian locomotion is generated by central pattern generators (CPGs) in the spinal cord, which produce alternating flexor and extensor activities controlling the locomotor movements of each limb. Afferent feedback signals from the limbs are integrated by the CPGs to provide adaptive control of locomotion. Responses of CPG-generated neural activity to afferent feedback stimulation have been previously studied during fictive locomotion in immobilized cats. Yet, locomotion in awake, behaving animals involves dynamic interactions between central neuronal circuits, afferent feedback, musculoskeletal system, and environment. To study these complex interactions, we developed a model simulating interactions between a half-center CPG and the musculoskeletal system of a cat hindlimb. Then, we analyzed the role of afferent feedback in the locomotor adaptation from a dynamic viewpoint using the methods of dynamical systems theory and nullcline analysis. Our model reproduced limb movements during regular cat walking as well as adaptive changes of these movements when the foot steps into a hole. The model generates important insights into the mechanism for adaptive locomotion resulting from dynamic interactions between the CPG-based neural circuits, the musculoskeletal system, and the environment.

Keywords: walking, cat, neuromusculoskeletal model, central pattern generator, afferent feedback

OPEN ACCESS

Edited by:
Denis J. Marcellin-Little, University of California, Davis, United States

Reviewed by:
Epaminondas Rosa, Illinois State University, United States
Michael Georg Metzen, McGill University, Canada

****Correspondence:***
Shinya Aoi
shinya_aoi@kuaero.kyoto-u.ac.jp

Specialty section:
This article was submitted to Biomechanics, a section of the journal Frontiers in Bioengineering and Biotechnology

Received: *30 November 2021*
Accepted: *04 February 2022*
Published: *08 April 2022*

Citation:
Kim Y, Aoi S, Fujiki S, Danner SM, Markin SN, Ausborn J, Rybak IA, Yanagihara D, Senda K and Tsuchiya K (2022) Contribution of Afferent Feedback to Adaptive Hindlimb Walking in Cats: A Neuromusculoskeletal Modeling Study. Front. Bioeng. Biotechnol. 10:825149. doi: 10.3389/fbioe.2022.825149

1 INTRODUCTION

Mammalian locomotion is generated by the central pattern generators (CPGs) located in the spinal cord, which control the movements of each limb (Grillner, 1981; Rossignol, 1996; Orlovsky et al., 1999; Rossignol et al., 2006). CPGs produce the basic locomotor rhythm and create alternating flexor and extensor motoneuron (Mn) activities. Furthermore, they integrate afferent feedback signals to achieve adaptive locomotion.

CPGs can operate without afferent feedback and continuous electrical stimulation of the midbrain locomotor region in immobilized decerebrate cats produces "fictive locomotion" consisting of rhythmic alternating activation of flexor and extensor Mns similar to that occurring during normal locomotion in intact animals (Rossignol, 1996). Such fictive locomotor preparations have been used to investigate the mechanism for the adaptive regulation of locomotor patterns by somatosensory

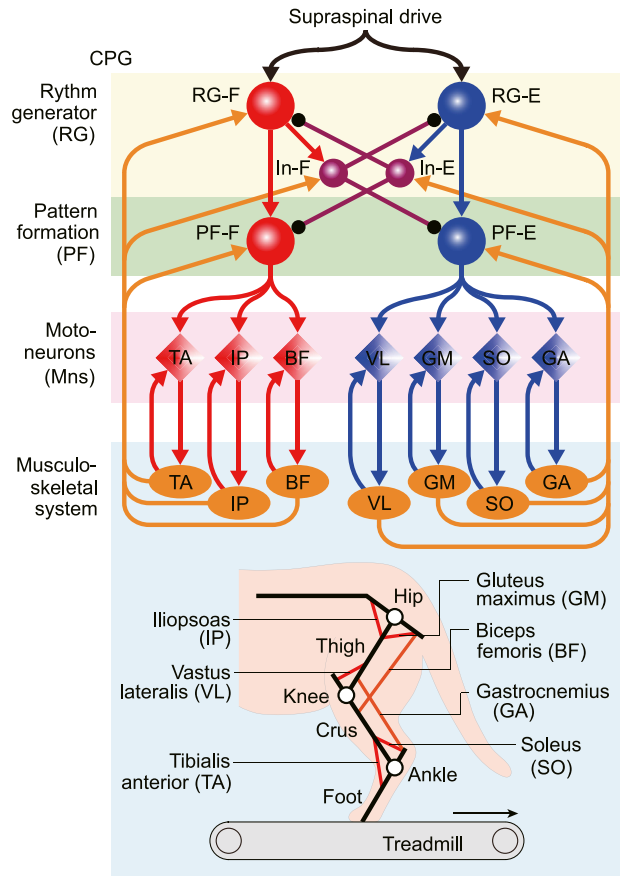

FIGURE 1 | Neuromusculoskeletal model of a cat hindlimb composed of a neural network and a musculoskeletal model. The neural network model consists of a two-level central pattern generator (CPG) with rhythm generating (RG) and pattern formation (PF) circuits and motoneurons (Mns). This network generates motor commands through Mns and receives afferent feedback signals from the musculoskeletal model (orange arrows). The musculoskeletal model, which consists of three rigid links (black lines) and seven muscles (red and orange lines), walks on a treadmill.

afferent feedback. These studies have shown that stimulation of flexor and extensor sensory afferents can delay or advance flexion-to-extension or extension-to-flexion transitions depending on the timing of the afferent stimulation (Guertin et al., 1995; Perreault et al., 1995; McCrea, 2001; Stecina et al., 2005). In our previous modeling work (Fujiki et al., 2019), we used a half-center type CPG model and analyzed its responses to afferent stimulation using dynamic systems theory based on nullclines. This previous study was limited to the consideration of only neural responses without interaction between the neural and musculoskeletal systems.

However, the mammalian locomotion is a complex phenomenon involving dynamic interactions between the neural circuits, the musculoskeletal system, and the environment. To investigate these interactions and the roles of afferent feedback in adaptive locomotion, investigators studied locomotion in both intact and decerebrate or spinal animals walking on a treadmill by applying various disturbances or introducing holes and obstacles on the treadmill to disturb normal locomotion (Hiebert et al., 1994; Lam and Pearson, 2001; Drew et al., 2002). Although these studies have revealed adaptive responses to such disturbances, the adaptation mechanisms based on the interactions between the neural system, musculoskeletal system, and environment remain poorly understood.

Here, we extended our previous models (Markin et al., 2010, 2016), which integrated a two-level half-center CPG and a musculoskeletal model of the cat hindlimbs and simulated steady walking, to investigate the mechanism of locomotor adaptation in response to perturbations from a dynamical viewpoint. We determined the necessary model parameters through optimization that allows the model to reproduce regular walking movements on a treadmill. We considered locomotion with the presence of holes in the walking surface, which evoked locomotor disturbances that allowed us to analyze the roles of afferent feedback from flexor and extensor muscles to stabilize locomotion. Particularly, the model realistically reproduced adaptive changes in locomotor characteristics observed when the paw of a cat hindlimb stepped into a hole (Hiebert et al., 1994). The model suggests an afferent feedback-based mechanism for locomotor adaptation, which we analyzed based on dynamical systems theory methods using nullclines (Fujiki et al., 2019). Our simulation and analysis provide important insights into the mechanisms for adaptive locomotion based on dynamic interactions between the neural system, the musculoskeletal system, and the environment.

2 MODEL

Figure 1 shows our neuromusculoskeletal model, which consists of a musculoskeletal model of a cat hindlimb and a spinal CPG model to drive the musculoskeletal model.

2.1 Musculoskeletal Model

The skeletal model is two-dimensional and consists of three rigid links representing the thigh, crus, and foot. These links are connected by the knee and ankle joints, and the hip joint is fixed above a treadmill. The model walks on the treadmill with a belt speed of 0.4 m/s based on Prilutsky et al. (2016). When the thigh, crus, and foot are in a straight line and parallel to the vertical line, the hip angle is 135° and the knee and ankle angles are both 180°. The joint angles increase as the joints are extending. The contact between the limb tip and treadmill were modeled using viscoelastic elements. We derived the equations of motion for the skeletal model using Lagrangian equations, where we used the same physical parameters for the skeletal model as those in Ekeberg and Pearson (2005), and solved the equations numerically using the fourth-order Runge-Kutta method with a time step of 0.04 ms.

The skeletal model is driven by seven Hill-type muscles including five uni-articular muscles which are: hip flexor (iliopsoas, IP), hip extensor (gluteus maximus, GM), knee extensor (vastus lateralis, VL), ankle flexor (tibialis anterior, TA), ankle extensor (soleus, SO), and two bi-articular muscles

including hip extensor/knee flexor (biceps femoris, BF) and knee flexor/ankle extensor (gastrocnemius, GA). We assumed that the moment arms of all muscles are constant. Each muscle generates the muscle tension through contractile and passive elements. The muscle model consisting of contractile and passive elements is based on the same description and parameters in Ekeberg and Pearson (2005). Specifically, the muscle force $F_m\,(m \in \{\mathrm{M}\} = \{\mathrm{IP, GM, VL, TA, SO, BF, GA}\})$ is given by

$$F_m = F_m^{\max}\left(a_m F_m^{\mathrm{l}} F_m^{\mathrm{v}} + F_m^{\mathrm{p}}\right) \tag{1}$$

where $F_m^{\max}$ is the maximum isometric force, a_m is the muscle activation $(0 \le a_m \le 1)$, F_m^{l} is the force-length relationship, F_m^{v} is the force-velocity relationship, and F_m^{p} is the passive component. The muscle lengths were normalized by $l_m^{\max}$, which was set so that all uni-articular muscles had a length of 85% of $l_m^{\max}$ and all bi-articular muscles were at 75% at a neutral posture with the hip at 65°, the knee at 90°, and the ankle at 100°. In addition, 2° of joint motion corresponded to 1% of muscle length change, except for the GA muscle, where 1.5° at the ankle or 4.5° at the knee was required. The muscle contractile velocities were normalized by $l_m^{\max}$ as well.

The muscle activation a_m $(m \in \{\mathrm{M}\})$ determines the muscle tension generated by the contractile element and the dynamics of a_m is given by a low-pass filter (Yakovenko et al., 2004) as follows:

$$\dot{a}_m + \frac{1}{\tau_{\mathrm{act}}}\left(\frac{\tau_{\mathrm{act}}}{\tau_{\mathrm{dact}}} + \left[1 - \frac{\tau_{\mathrm{act}}}{\tau_{\mathrm{dact}}}\right]u_m\right)a_m = \frac{1}{\tau_{\mathrm{act}}}u_m \tag{2}$$

where τ_{act} and τ_{dact} are activation and deactivation time constants (20 and 32 ms, respectively), and u_m is the motor command determined from the activities of the corresponding Mn of the CPG model.

2.2 CPG Model

The locomotor CPG has been suggested to consist of hierarchical networks, which include rhythm generator (RG) and pattern formation (PF) networks (Rybak et al., 2006a,b). The RG network generates the rhythmic activities while the PF network generates the spatiotemporal patterns of motor commands. For the RG model, we used two neuron populations of flexor and extensor centers (RG-F and RG-E), which receive a supraspinal drive, and two populations of inhibitory interneurons (In-F and In-E), which provide mutual inhibition between the RG-F and RG-E centers. The PF was modeled using two neuron populations of flexor and extensor centers (PF-F and PF-E). The PF-F and PF-E neuron populations receive the excitatory input from the RG-F and RG-E neuron populations, and inhibitory input from the In-E and In-F neuron populations, respectively. Seven Mn populations provide activation for each muscle in the musculoskeletal model (Mn-m, $m \in \{\mathrm{M}\}$). The Mns of flexor muscles Mn-IP, Mn-TA, and Mn-BF receive excitatory input from the PF-F neuron populations, while those of extensor muscles Mn-GM, Mn-VL, Mn-SO, and Mn-GA receive the excitatory input from the PF-E neuron populations. Synaptic interactions between all neuron populations are shown in **Figure 1**.

Each population is described as an activity-based (non-spiking) neuron model (Ermentrout, 1994; Markin et al., 2010; Molkov et al., 2015; Danner et al., 2016, 2017). The state of each neuron is characterized by the membrane potential V_i for $i \in \{\mathrm{RG}\}$, $\{\mathrm{In}\}$, $\{\mathrm{PF}\}$, and $\{\mathrm{Mn}\}$, where $\{\mathrm{RG}\} = \{\mathrm{RG\text{-}F, RG\text{-}E}\}$, $\{\mathrm{In}\} = \{\mathrm{In\text{-}F, In\text{-}E}\}$, $\{\mathrm{PF}\} = \{\mathrm{PF\text{-}F, PF\text{-}E}\}$, and $\{\mathrm{Mn}\} = \{\mathrm{Mn}\text{-}m \mid m \in \{\mathrm{M}\}\}$. The RG, PF, and Mn neurons incorporate a persistent (slowly-inactivating) sodium current that defines the intrinsic rhythmogenic properties of these neurons. The intrinsic oscillations in the RG, PF, and Mn neurons depend on the variable h_i $(i \in \{\mathrm{RG}\}, \{\mathrm{PF}\}, \{\mathrm{Mn}\})$ that defines the slow inactivation of the persistent sodium channel. The RG-F and RG-E neurons can produce rhythmic activities. However, if uncoupled, the RG-E neuron is in the tonic regime due to the supraspinal drive and produces sustained activity. Rhythmic oscillations of the RG neurons are defined by the RG-F neuron, which provides rhythmic inhibition of the RG-E neuron through the In-F neuron. The supraspinal drive to the RG-F neuron determines the oscillation frequency. When the PF and Mn neurons are uncoupled, they do not produce rhythmic activities due to the relatively low maximum conductance of the sodium current. Instead, these neurons produce rhythmic activities through the excitatory inputs from the correspondent RG neurons.

For the state variable for this model, we used $\boldsymbol{V} = [V_{\{\mathrm{RG}\}}, V_{\{\mathrm{In}\}}, V_{\{\mathrm{PF}\}}, V_{\{\mathrm{Mn}\}}]^{\mathrm{T}}$ and $\boldsymbol{h} = [h_{\{\mathrm{RG}\}}, h_{\{\mathrm{PF}\}}, h_{\{\mathrm{Mn}\}}]^{\mathrm{T}}$. The dynamics of the membrane potential V_i is described as

$$C\dot{V}_i = \begin{cases} -I_{\mathrm{NaP}}(V_i, h_i) - I_{\mathrm{Leak}}(V_i) - I^i_{\mathrm{SynE}}(\boldsymbol{V}) - I^i_{\mathrm{SynI}}(\boldsymbol{V}) \\ \qquad\qquad i \in \{\mathrm{RG}\}, \{\mathrm{PF}\}, \{\mathrm{Mn}\}, \\ -I_{\mathrm{Leak}}(V_i) - I^i_{\mathrm{SynE}}(\boldsymbol{V}) - I^i_{\mathrm{SynI}}(\boldsymbol{V}) \quad i \in \{\mathrm{In}\}, \end{cases} \tag{3}$$

where C is the membrane capacitance, I_{NaP} is the persistent sodium current, I_{Leak} is the leakage current, and I^i_{SynE} and I^i_{SynI} are the respective currents in excitatory synapses and inhibitory synapses. The ionic current I_{NaP} and leakage current I_{Leak} are described as

$$\begin{aligned} I_{\mathrm{NaP}}(V_i, h_i) &= \hat{g}^i_{\mathrm{NaP}} m_{\mathrm{NaP}}(V_i) h_i \{V_i - E_{\mathrm{Na}}\} \quad i \in \{\mathrm{RG}\}, \{\mathrm{PF}\}, \{\mathrm{Mn}\}, \\ I_{\mathrm{Leak}}(V_i) &= \hat{g}^i_{\mathrm{Leak}} \{V_i - E^i_{\mathrm{Leak}}\} \quad i \in \{\mathrm{RG}\}, \{\mathrm{In}\}, \{\mathrm{PF}\}, \{\mathrm{Mn}\}, \end{aligned} \tag{4}$$

where $\hat{g}^i_{\mathrm{NaP}}$ and $\hat{g}^i_{\mathrm{Leak}}$ are the maximum conductances of the corresponding currents, and E_{Na} and E^i_{Leak} the reversal potentials. In addition, m_{NaP} is the activation of the sodium channel of the RG, PF, and Mn neurons and is described as

$$m_{\mathrm{NaP}}(V_i) = \frac{1}{1 + \exp\left(-\frac{V_i + 40.0}{6.0}\right)} \quad i \in \{\mathrm{RG}\}, \{\mathrm{PF}\}, \{\mathrm{Mn}\}. \tag{5}$$

The dynamics of the inactivation of the sodium channel h_i of the RG, PF, and Mn neurons is given by

$$\tau(V_i)\dot{h}_i = h_\infty(V_i) - h_i \quad i \in \{\mathrm{RG}\}, \{\mathrm{PF}\}, \{\mathrm{Mn}\}, \tag{6}$$

where

$$h_\infty(V_i) = \frac{1}{1+\exp\left(\frac{V_i+45.0}{4.0}\right)}, \tag{7}$$
$$\tau(V_i) = 320 + \frac{320}{\cosh\left(\frac{V_i+35.0}{15.0}\right)}\ \text{ms} \quad i \in \{\text{RG}\},\{\text{PF}\},\{\text{Mn}\}$$

The currents generated by the synapses I^i_{SynE} and I^i_{SynI} are given by

$$I^i_{\text{SynE}} = \hat{g}_{\text{SynE}}\left\{V_i - E_{\text{SynE}}\right\}\left\{\sum_{j\in\{\text{RG}\},\{\text{In}\},\{\text{PF}\}} \alpha_{ij} f\left(V_j\right) + \gamma_i d + s_i\right\},$$
$$I^i_{\text{SynI}} = \hat{g}_{\text{SynI}}\left\{V_i - E^i_{\text{SynI}}\right\}\left\{\sum_{j\in\{\text{RG}\},\{\text{In}\},\{\text{PF}\}} \beta_{ij} f\left(V_j\right)\right\}$$
$$i \in \{\text{RG}\},\{\text{In}\},\{\text{PF}\},\{\text{Mn}\}, \tag{8}$$

where $\hat{g}_{\text{SynE}}$ and $\hat{g}_{\text{SynI}}$ are the maximum conductances of the corresponding currents; E_{SynE} and E^i_{SynI} are the reversal potentials of the corresponding currents; d is the tonic drive from the supraspinal region; s_i is the afferent feedback from the musculoskeletal model (as determined in **Section 4.1**); and α_{ij}, β_{ij}, and γ_i are the weight coefficients, where $\beta_{ij} = 0$ for $i \in \{\text{Mn}\}$ and $\gamma_i = 0$ for $i \in \{\text{PF}\}$ and $\{\text{Mn}\}$. Moreover, the output function f translates V into the integrated population activity and is given by

$$f(V_i) = \begin{cases} 0 & V_i < V_{\text{th}}, \\ (V_i - V_{\text{th}})/(V_{\max} - V_{\text{th}}) & V_{\text{th}} < V_i < V_{\max}, \\ 1 & V_{\max} < V_i, \end{cases} \tag{9}$$

where V_{th} and $V_{\max}$ are the lower and upper threshold potentials, respectively. The motor command u_m ($m \in \{\text{M}\}$) is given by $u_m = f(V_{\text{Mn}\text{-}m})$. Based on Fujiki et al. (2019) and Markin et al. (2010), we determined the parameters for the CPG model (see **Appendix A**) except for α_{ij}, β_{ij}, and γ_i for $i \in \{\text{Mn}\}$, which we determined through optimization, as described in **Section 4.2**.

2.3 Calculation of Nullcline

The nullcline is a set of points at which the derivative of a differential equation is equal to zero. It reflects the structure of the solution of the differential equation. After the CPG model was integrated with the musculoskeletal model to achieve steady walking, we used a nullcline-based method, as in our previous work (Fujiki et al., 2019), to investigate the mechanism of the response of the CPG model to a disturbance during steady walking. Specifically, the state of the CPG model is given by $(\boldsymbol{V}, \boldsymbol{h})$, and the nullclines for the RG neurons are given by

$$\begin{cases} N^{\text{V}}_i = \left\{(\boldsymbol{V},\boldsymbol{h}) \middle| \dot{V}_i = 0\right\}, \\ N^{\text{h}}_i = \left\{(\boldsymbol{V},\boldsymbol{h}) \middle| \dot{h}_i = 0\right\}, \end{cases} \quad i \in \{\text{RG}\}. \tag{10}$$

To clarify the dynamics of each RG neuron, we focused on the V_i-h_i space ($i \in \{\text{RG}\}$) for the nullclines by assuming that the other variables V_j ($j \in \{\text{RG}\},\{\text{In}\},\{\text{PF}\},\{\text{Mn}\}, j \neq i$) and h_k ($k \in \{\text{RG}\},\{\text{PF}\},\{\text{Mn}\}, k \neq i$) are stably oscillating during steady walking. Therefore, we modify N^{V}_i and N^{h}_i in **Eq. 10** as

$$\begin{cases} \hat{N}^{\text{V}}_i = \left\{(V_i,h_i) \middle| \dot{V}_i = 0, V_j = V^*_j, h_k = h^*_k\right\}, \\ \hat{N}^{\text{h}}_i = \left\{(V_i,h_i) \middle| \dot{h}_i = 0, V_j = V^*_j, h_k = h^*_k\right\}, \end{cases}$$
$$i \in \{\text{RG}\}, j \in \{\text{RG}\},\{\text{In}\},\{\text{PF}\},\{\text{Mn}\}, j \neq i, k \in \{\text{RG}\},\{\text{PF}\},\{\text{Mn}\}, k \neq i, \tag{11}$$

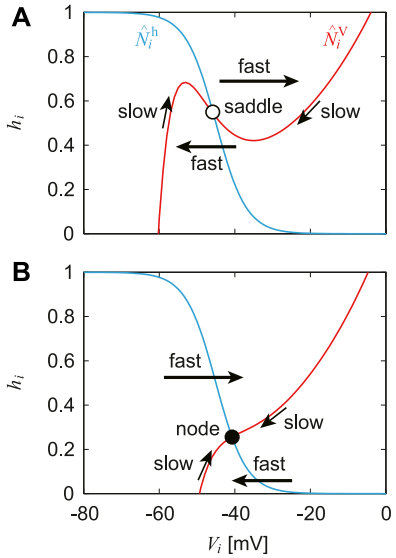

FIGURE 2 | Nullclines $\hat{N}^{\text{V}}_i$ and $\hat{N}^{\text{h}}_i$ for $i \in \{\text{RG}\}$ of RG neurons in the phase plane and fast and slow dynamics that the state (V_i, h_i) for $i \in \{\text{RG}\}$ follows. **(A)** $\hat{N}^{\text{V}}_i$ has two different inflection points and intersection with $\hat{N}^{\text{h}}_i$ is saddle equilibrium point. **(B)** $\hat{N}^{\text{V}}_i$ changes monotonically and intersection with $\hat{N}^{\text{h}}_i$ is stable node equilibrium point. Bold and thin arrows represent fast and slow dynamics, respectively.

where x^* indicates x for the stable oscillation during steady walking.

While $\hat{N}^{\text{h}}_i$ ($i \in \{\text{RG}\}$) has a sigmoid shape and does not change with time, $\hat{N}^{\text{V}}_i$ ($i \in \{\text{RG}\}$) has a cubic curve shape and changes by afferent feedback and input from other neurons. Specifically, $\hat{N}^{\text{V}}_i$ mainly has the two different situations shown in **Figures 2A,B**, one with two different inflection points at which the sign of the slope changes, and one with a monotonic variation. In the former case (**Figure 2A**), the intersection of $\hat{N}^{\text{V}}_i$ and $\hat{N}^{\text{h}}_i$ is a saddle equilibrium point. Because the time constant for the dynamics of V_i ($i \in \{\text{RG}\}$) is smaller than that for h_i ($i \in \{\text{RG}\}$), the following two features are present (Fujiki et al., 2019; Molkov et al., 2015; Spardy et al., 2011): 1. near where $\hat{N}^{\text{V}}_i$ has positive slope, the state (V_i, h_i) is slowly attracted to the inflection point along $\hat{N}^{\text{V}}_i$ (slow dynamics) and 2. near the inflection points, the state (V_i, h_i) jumps to the opposite part of $\hat{N}^{\text{V}}_i$ with a positive slope (fast dynamics). In the latter case (**Figure 2B**), the intersection of $\hat{N}^{\text{V}}_i$ and $\hat{N}^{\text{h}}_i$ is a stable node equilibrium point having the following two features (Spardy et al., 2011; Fujiki et al., 2019): 1. when the state (V_i, h_i) is away from $\hat{N}^{\text{V}}_i$, it is quickly attracted to $\hat{N}^{\text{V}}_i$ (fast dynamics), and 2. near $\hat{N}^{\text{V}}_i$, the state (V_i, h_i) is slowly attracted to the stable node along $\hat{N}^{\text{V}}_i$ (slow dynamics). As described above, the switch between fast and slow dynamics depends on the relationship between the state and the nullcline, and adaptive responses are achieved through the changes in $\hat{N}^{\text{V}}_i$ by afferent feedback.

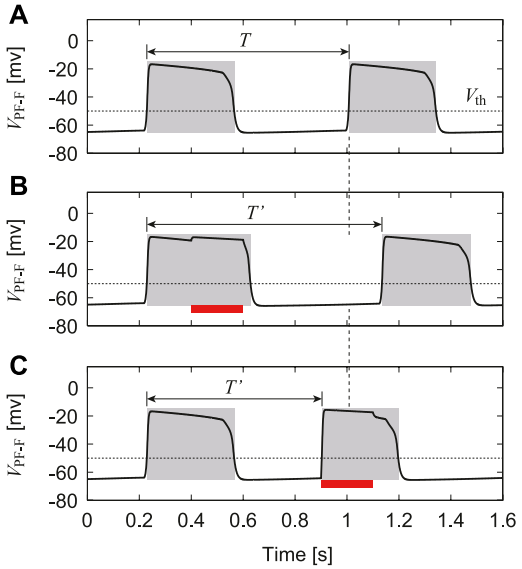

FIGURE 3 | Change in membrane potential of PF-F neuron by stimulation: **(A)** No stimulation. **(B)** Stimulation to the flexor side during the active phase, which increases the duration of the current active phase and cycle ($T' > T$). **(C)** Stimulation to the flexor side during the silent phase, which initiates the active phase and decreases the cycle duration ($T' < T$). Red bars indicate the application of stimulation. Gray regions indicate active phases.

3 VERIFYING THE CPG MODEL BY PHASE-DEPENDENT RESPONSE IN FICTIVE LOCOMOTION

Even when our CPG model is separated from the musculoskeletal model (or receives no feedback signals), it produces rhythmic activities and exhibits stable oscillations, as shown in **Figure 3**. Based on these oscillations, we define the active phase for each neuron as the time interval during which the neuron's potential is higher than V_{th}, and the silent phase as the time interval when the potential is lower than V_{th}. We also define the cycle period T as the time interval between two consecutive onsets of the active phase of the PF-F neuron and the phase of the oscillation as $\phi = 2\pi t/T \in [0, 2\pi)$.

To verify our CPG model, we investigated the phase-dependent response of the CPG activities based on previous studies (Demir et al., 1997; Fujiki et al., 2019) and compared the results with those obtained by experiments with fictive locomotion in cats (Duysens, 1977; Schomburg et al., 1998). Specifically, we used only the CPG model (RG, In, and PF neurons) separated from the musculoskeletal model. After the oscillation of the CPG model stabilized, we applied a 200-ms stimulus to the flexor (RG-F, In-F, and PF-F) or extensor (RG-E, In-E, and PF-E) neurons, where the intensity of the stimulation was set as follows: $s_{RG\text{-}F} = s_{In\text{-}F} = s_{PF\text{-}F} = 0.2$ and $s_{RG\text{-}E} = s_{In\text{-}E} = s_{PF\text{-}E} = 0$ for the stimulation to the flexor side and $s_{RG\text{-}F} = s_{In\text{-}F} = s_{PF\text{-}F} = 0.0$ and $s_{RG\text{-}E} = s_{In\text{-}E} = s_{PF\text{-}E} = 0.2$ for the stimulation to the extensor side in **Eq. 8**. Suppose that the neuron activity is perturbed by stimulation with a phase $\phi_s \in [0, 2\pi)$ and the period of the PF-F neuron changes from T to $T'(\phi_s)$, as shown in **Figure 3**. To explain the phase shift of the neuron activity in response to the stimulation, we define

$$\Delta(\phi_s) = 2\pi \frac{T'(\phi_s) - T}{T} \tag{12}$$

Figure 4A shows the phase shift Δ of the PF-F neuron activity after the stimulation of sensory inputs on the flexor side at ϕ_s. When the stimulation was applied during the silent phase of the PF-F neuron ($2.70 \le \phi_s \le 2\pi$), it caused an earlier transition to the active phase, and this advanced start decreased with ϕ_s. In contrast, almost no phase shift occurred when the stimulation was applied at the beginning of the active phase of the PF-F neuron ($0 \le \phi_s \le 0.44$). However, the neuron activity was delayed by the stimulation during the middle and end of the active phase ($0.44 \le \phi_s \le 2.70$). These trends were similar to those observed during fictive locomotion in spinal cats (Schomburg et al., 1998; Frigon et al., 2010), as shown in **Figure 4A**.

Figure 4B shows Δ after stimulation of the extensor side. The active and silent phase of the PF-F neuron corresponds to the silent and active phase, respectively, of the PF-E neuron. The neuron activity was advanced at the middle of the silent phase of the PF-E neuron ($0.63 \le \phi_s \le 2.64$) and was delayed at the end of the active phase of the PF-E neuron ($4.27 \le \phi_s \le 6.16$). The response of the stimulation of the extensor side was qualitatively similar to that for the flexor side. Moreover, the trends were consistent with those observed during fictive locomotion in decerebrate cats (Duysens, 1977; Schomburg et al., 1998; Frigon et al., 2010), as shown in **Figure 4B**. These results verify the validity of our CPG model.

4 DETERMINING THE MOTOR CONTROL MODEL BY OPTIMIZATION TO REPRODUCE NORMAL WALKING

We integrated the CPG and musculoskeletal models to determine the remaining parameters for the CPG model through an optimization to produce normal walking on the treadmill.

4.1 Afferent Feedback From the Musculoskeletal Model

We determined the afferent feedback s_i in **Eq. 8** based on Markin et al. (2010) as follows:

$$s_i = \sum_{m \in \{M\}} \left(k_{im}^{v} \left(v_m^{norm} \right)^{0.6} + k_{im}^{d} d_m^{norm} + k_{im}^{f} F_m^{norm} \right) \quad i \in \{RG\}, \{In\}, \{PF\}, \tag{13}$$

where

$$v_m^{norm} = \begin{cases} v_m / l_m^{max} & v_m > 0, \\ 0 & \text{otherwise;} \end{cases} \tag{14}$$

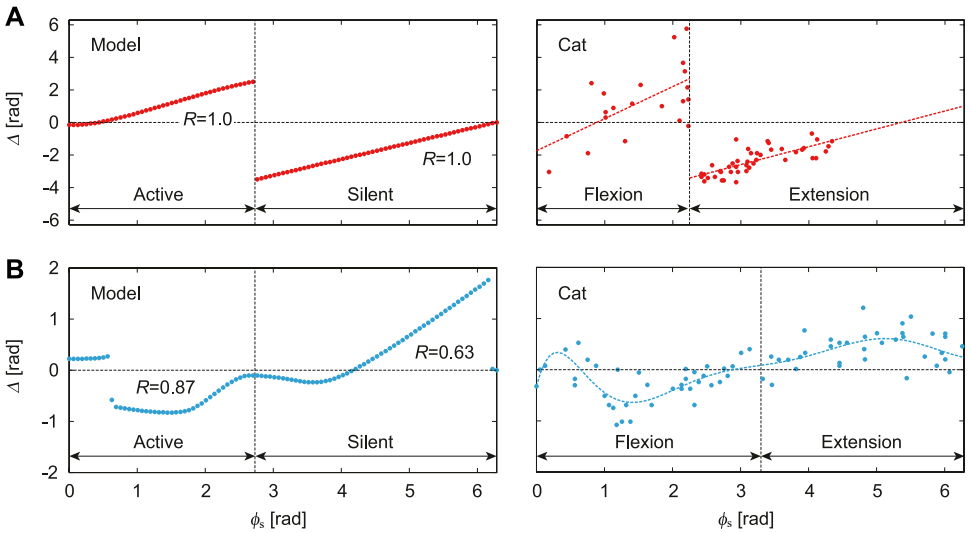

FIGURE 4 | Phase-dependent response of CPG model to a stimulation. **(A)** Response of PF-F neuron in our model to stimulation of the flexor side compared with the response against flexor muscle stimulation during fictive locomotion in spinal cats [adapted from Schomburg et al. (1998)], where the dotted lines are approximate functions using a first order polynomial for each flexion and extension phase. **(B)** Response of PF-F neuron of our model to stimulation of the extensor side compared with the response against extensor muscle stimulation during fictive locomotion in decerebrate cats [adapted from Duysens (1977)], where the dotted line is an approximate function using an eighth order polynomial. *R* is the correlation coefficient between the active/silent phase of the simulation results and flexion/extension phase of the approximate function.

$$a_m^{\text{norm}} = \begin{cases} (l_m - l_{\text{th}})/l_m^{\max} & l_m > l_{\text{th}}, \\ 0 & \text{otherwise}; \end{cases} \tag{15}$$

$$F_m^{\text{norm}} = \begin{cases} F_m/F_m^{\max} & F_m > 0, \\ 0 & \text{otherwise}; \end{cases} \tag{16}$$

$$l_{\text{th}} = 0.9 l_m^{\max}; \tag{17}$$

v_m, l_m, and F_m are the velocity, length, and force of muscle m, respectively, and k_{im}^{v}, k_{im}^{d}, and k_{im}^{f} are the corresponding weight coefficients. The three terms on the right-hand side of **Eq. 13** represent the velocity, length, and force feedback from muscle m. The coefficients k_{im}^{v}, k_{im}^{d}, and k_{im}^{f} are given as follows: for the flexor side (i = RG-F, In-F, PF-F),

$$\left(k_{im}^{\text{v}}, k_{im}^{\text{d}}, k_{im}^{\text{f}}\right) = \begin{cases} \left(k_{\text{F}}^{\text{v}}, k_{\text{F}}^{\text{d}}, k_{\text{F}}^{\text{f}}\right) & m = \text{IP, TA, BF}, \\ (0,0,0) & \text{otherwise}; \end{cases} \tag{18}$$

for the extensor side (i = RG-E, In-E, PF-E),

$$\left(k_{im}^{\text{v}}, k_{im}^{\text{d}}, k_{im}^{\text{f}}\right) = \begin{cases} \left(k_{\text{E}}^{\text{v}}, k_{\text{E}}^{\text{d}}, k_{\text{E}}^{\text{f}}\right) & m = \text{GM, VL, SO, GA}, \\ (0,0,0) & \text{otherwise}; \end{cases} \tag{19}$$

and for the Mns ($i \in \{\text{Mn}\}$),

$$\left(k_{im}^{\text{v}}, k_{im}^{\text{d}}, k_{im}^{\text{f}}\right) = \begin{cases} \left(\eta k_{\text{F}}^{\text{v}}, \eta k_{\text{F}}^{\text{d}}, \eta k_{\text{F}}^{\text{f}}\right) & i = \text{Mn-}m\,(m = \text{IP, TA, BF}), \\ \left(\eta k_{\text{E}}^{\text{v}}, \eta k_{\text{E}}^{\text{d}}, \eta k_{\text{E}}^{\text{f}}\right) & i = \text{Mn-}m\,(m = \text{GM, VL, SO, GA}), \\ (0,0,0) & \text{otherwise}. \end{cases} \tag{20}$$

We determined $k_{\text{F}}^{\text{v}}, k_{\text{F}}^{\text{d}}, k_{\text{F}}^{\text{f}}, k_{\text{E}}^{\text{v}}, k_{\text{E}}^{\text{d}}, k_{\text{E}}^{\text{f}}$, and η through the optimization technique described in the next section.

4.2 Optimization to Determine Motor Control Parameters

We integrated the CPG and musculoskeletal models and determined the motor control parameters through an optimization to produce normal walking on the treadmill based on the measured kinematic data for cats (Prilutsky et al., 2016). Specifically, we determined the following 14 parameters; $\alpha_{\text{Mn-IP,PF-F}}$, $\alpha_{\text{Mn-GM,PF-E}}$, $\alpha_{\text{Mn-VL,PF-E}}$, $\alpha_{\text{Mn-TA,PF-F}}$, $\alpha_{\text{Mn-SO,PF-E}}$, $\alpha_{\text{Mn-BF,PF-F}}$, and $\alpha_{\text{Mn-GA,PF-E}}$ in **Eq. 8** (the other a_{ij}'s for $i \in \{\text{Mn}\}$ are 0) and $k_{\text{F}}^{\text{v}}, k_{\text{F}}^{\text{d}}, k_{\text{F}}^{\text{f}}, k_{\text{E}}^{\text{v}}, k_{\text{E}}^{\text{d}}, k_{\text{E}}^{\text{f}}$, and η in **Eqs. 18–20**. We used the covariance matrix adaptation evolution strategy (CMA-ES) (Hansen et al., 2003) as the optimization method to minimize the following loss function:

$$\varepsilon = \int_{t_1}^{t_2} \sum_{i \in \{\text{J}\}} \left(\theta_i - \hat{\theta}_i\right)^2 dt \tag{21}$$

where $\{\text{J}\} = \{\text{Hip, Knee, Ankle}\}$, θ_i and $\hat{\theta}_i$ are the simulated and measured joint angles, and t_1 and t_2 were determined to evaluate the error for two gait cycles after steady walking was achieved.

Figure 5 shows the results obtained by the optimization. The model parameters determined by the optimization are shown in **Appendix B**. **Figure 5A** shows the membrane potentials of the RG, PF, and Mn neurons and the velocity, length, and force feedback of the flexor and extensor muscles. The rhythmic activities of the RG-F and RG-E neurons were transmitted to the Mn neurons through the PF neurons and the afferent feedback was used in normal walking. **Figures 5B,C** show the joint angles and muscle activations, respectively, compared with the data measured for cats (Prilutsky

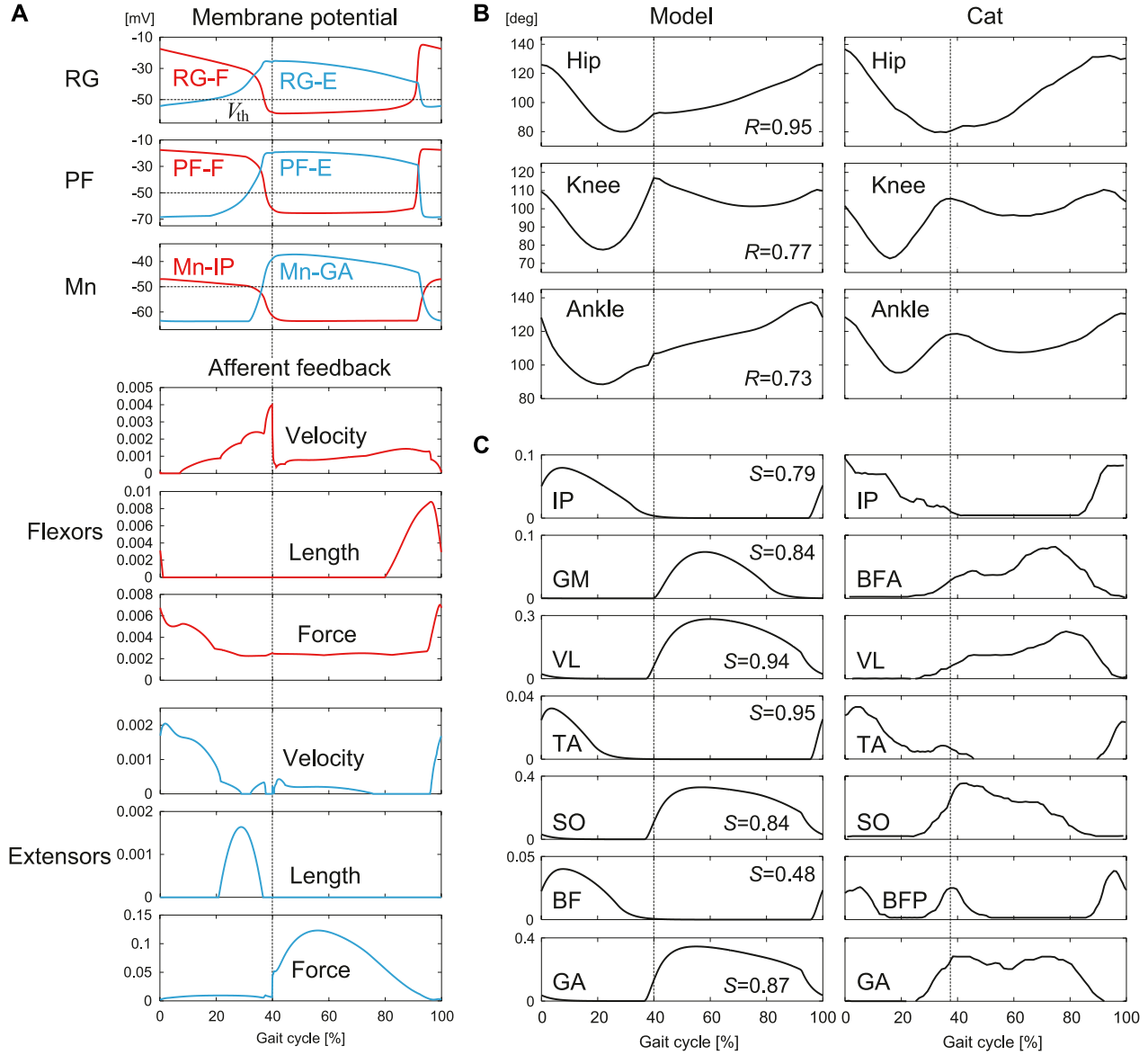

FIGURE 5 | Simulation results for normal walking obtained by the optimization: **(A)** Membrane potentials of CPG neurons and afferent feedback from flexor and extensor muscles. **(B)** Joint angles and **(C)** muscle activations compared with measured data in cat [adapted from Prilutsky et al. (2016)]. *R* is the correlation coefficient and *S* is the cosine similarity. Liftoffs are represented by 0 and 100% in the gait cycle. Vertical lines indicate touchdowns.

et al., 2016). The simulated joint angles and muscle activities have patterns similar to those for the measured data. These results verify that our model reproduced regular cat walking on a treadmill through the interactions between the neural system, the musculoskeletal system, and the environment by the optimization.

5 ADAPTIVE RESPONSE TO STEPPING INTO A HOLE DURING TREADMILL WALKING

To investigate the role of afferent feedback in adaptive locomotion, we applied a disturbance to our model and compared the responses with those measured for cats. Moreover, we clarified the adaptation mechanism based on dynamic systems theory methods.

5.1 Comparison of Simulation Results and Measured Data

Afferent feedback plays important roles in adaptive walking. To clarify these roles, a treadmill with a hole has been used in experiments with cats (Gorassini et al., 1994; Hiebert et al., 1994), where the cat body and forelimbs are supported and the cat walks on the treadmill only with the hindlimbs. When the foot of a hindlimb steps into the hole, it loses ground contact,

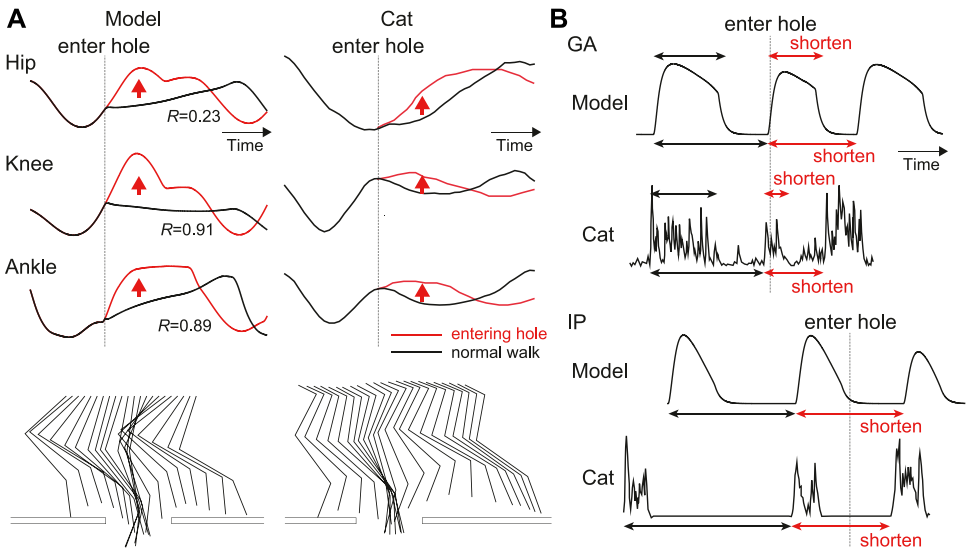

FIGURE 6 | Simulation results when on paw enters a hole compared with those during normal walking: **(A)** Joint angles and stick diagrams compared with measured data [adapted from Hiebert et al. (1994) for entering a hole and from Prilutsky et al. (2016) for normal walking]. These data are shown from the liftoff before entering a hole to the touchdown after entering the hole. *R* is the correlation coefficient of the results after entering the hole. The stick diagrams are shifted to the left by according to the distance traveled by the treadmill belt. **(B)** Activities of IP and GA muscles compared with measured data in spinal cat [adapted from Hiebert et al. (1994)]. Upper arrows indicate the activity duration, and lower ones indicate the intervals between the onsets of current and subsequent activities.

and an appropriate response based on afferent feedback is required to continue walking. The investigation of the response to stepping into a hole highlights the roles of afferent feedback from the flexor and extensor muscles in generating adaptive walking. Hiebert et al. (1994) showed that when the foot of a hindlimb of a spinal cat entered a hole, the activities of the extensor muscles were shortened and the next onsets of the activities of the flexor and extensor muscles were advanced, which quickly lifted the foot out of the hole. We conducted a simulation of our model in the same situation as Hiebert et al. (1994) using the model parameters determined in the previous section to generate normal walking and compared the results with the measured data from animal experiments. In the simulation, after our model achieved steady walking on a treadmill, we emulated a hole by setting the ground reaction force to zero when the foot touched the treadmill belt until the foot went below the belt and returned back above it.

Figure 6 compares the simulation results when the foot entered a hole with those during normal walking. Specifically, **Figure 6A** shows the joint angles and stick diagrams. When the foot stepped into the hole, the hip, knee, and ankle joints were first extended. After that, these joints were flexed to lift the foot above the treadmill belt and then the foot landed on the belt. This behavior was consistent with that observed in the animal experiment. **Figure 6B** shows the activation of the IP and GA muscles representing the flexor and extensor muscles, respectively. The activation of the GA muscle was shortened and the onset of the next activation was advanced compared with those in normal walking. The onset of the next activation of the IP muscle was also advanced. These responses were consistent with those in the animal experiment. These results verify that our model reproduced adaptive responses in cats when a foot steps into a hole during walking, even without changing the model parameters, which were determined to reproduce normal walking.

5.2 Investigating the Adaptation Mechanism

We investigated the adaptation mechanism *via* afferent feedback when the foot stepped into a hole based on the nullclines of the RG neurons in the phase plane. **Figure 7** compares the stimulation results for the RG neurons between entering a hole and normal walking. Specifically, **Figure 7A** shows the time profiles of the membrane potentials of the RG-F and RG-E neurons and the velocity, length, and force feedback from the flexor and extensor muscles. **Figures 7B,C** show the trajectories of the state $(V_{\text{RG-F}}, h_{\text{RG-F}})$ of the RG-F neuron and the state $(V_{\text{RG-E}}, h_{\text{RG-E}})$ of the RG-E neuron, and the changes in the nullclines $\hat{N}^{\text{V}}_{\text{RG-F}}$ of the RG-F neuron and $\hat{N}^{\text{V}}_{\text{RG-E}}$ of the RG-E neuron (because $\hat{N}^{\text{h}}_{\text{RG-F}}$ and $\hat{N}^{\text{h}}_{\text{RG-E}}$ do not change, they are not shown), respectively, in their phase planes. Although a stable limit cycle appeared during normal walking, the trajectories diverged after the foot entered the hole. Therefore, just before the foot entered the hole, which corresponds to the touchdown in normal walking ("a" in **Figure 7**), the trajectories and nullclines were identical between entering a hole and normal walking.

In the RG-F neuron, the local maximum of the nullcline decreased 0.1 s after entering the hole ("b" in **Figure 7**) due to the increased velocity and length feedback from the flexor muscles. The trajectory was attracted to the nullcline while following the slow dynamics. As a result, $V_{\text{RG-F}}$ increased slightly. In the RG-E neuron, the nullcline remained almost

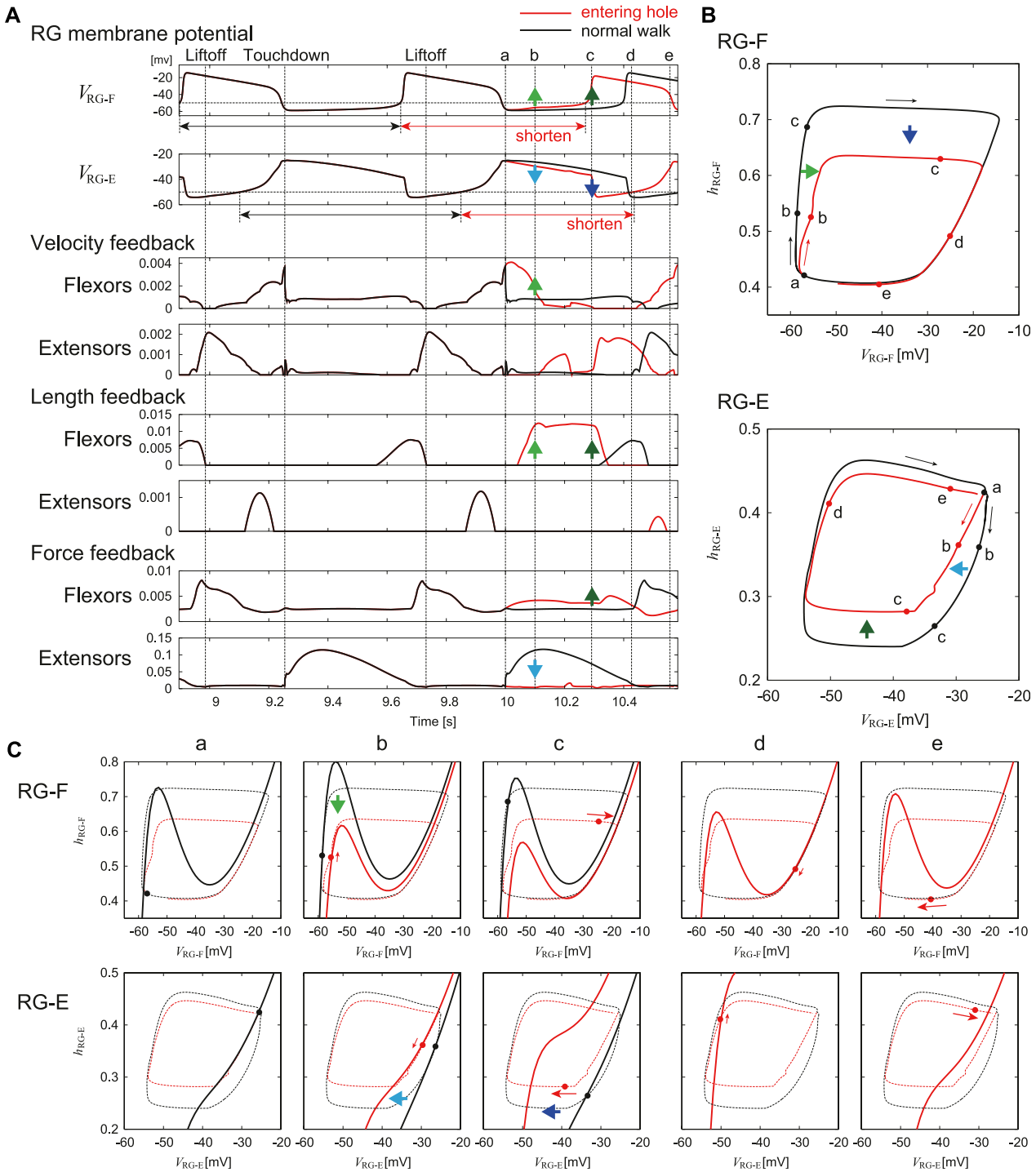

FIGURE 7 | Comparison of the response of RG neurons to a foot entering a hole with steady oscillation during normal walking. **(A)** Time profiles of membrane potentials and afferent feedback from flexor and extensor muscles. "a" indicates the time at which the foot enters the hole (touchdown in normal walking). "b"–"e" indicate the lapsed times of 0.1, 0.29, 0.43, and 0.56 s, respectively, after "a". **(B)** Trajectories of $(V_{RG\text{-}F}, h_{RG\text{-}F})$ and $(V_{RG\text{-}E}, h_{RG\text{-}E})$ in phase planes. **(C)** Changes of nullclines $\hat{N}^{V}_{RG\text{-}F}$ and $N^{V}_{RG\text{-}E}$.

unchanged from that in "a" due to the loss of the force feedback from the extensor muscles. In other words, the nullcline moved to the left compared to that in normal walking. The trajectory was attracted to the nullcline while following the slow dynamics. As a result, $V_{RG\text{-}E}$ decreased slightly.

In the RG-F neuron, the local maximum of the nullcline further decreased 0.29 s after the foot entered the hole ("c" in **Figure 7**) due to the increase in the length and force feedback from the flexor muscles. The state entered the fast dynamics by passing over the local maximum. As a result, $V_{\text{RG-F}}$ rapidly underwent a large increase to initiate the next activity. In the RG-E neuron, the nullcline moved significantly to the left due to the increased inhibition from the RG-F neuron, which made the state enter the fast dynamics. As a result, $V_{\text{RG-E}}$ decreased strongly and the activity was rapidly terminated.

As a result of these changes, the onset of the next activity of the RG-F neuron was advanced and the current activity of the RG-E neuron was shortened. The state $(V_{\text{RG-F}}, h_{\text{RG-F}})$ of the RG-F neuron and the state $(V_{\text{RG-E}}, h_{\text{RG-E}})$ of the RG-E neuron followed the slow dynamics in "d" in **Figure 7** and the trajectories and nullclines in "e" in **Figure 7** almost returned to those of "a" in **Figure 7** through the fast dynamics to continue normal walking. These results clarify the mechanims how our model produced adaptive responses during stepping into a hole through the interactions between the neural system, the musculoskeletal system, and the environment using dynamic systems theory based on nullclines.

6 DISCUSSION

6.1 Adaptive Responses to Entering a Hole

To continue walking after one of its feet steps into a hole, the cat must quickly pull the foot out of the hole and step onto the treadmill belt again. To provide this behavior the CPG should modify the motor commands based on afferent feedback. Similar to normal walking, the extensor muscles start their activity before touchdown to support the body weight. However, when a foot enters a hole without touchdown, the muscle activity excessively extends the hip, knee, and ankle joints. Therefore, for stable walking it is necessary to quickly terminate extension and start flexion. It has been suggested that unloading of ankle extensor muscles and activation of the Ia and II sensory afferents from flexor muscles play an important role in the transition from stance to swing during normal walking in cats (Duysens and Pearson, 1980; Pearson et al., 1992; Hiebert et al., 1996). Studies of locomotion in spinal cats when holes were present showed that the unloading of the extensor muscle due to the lack of touchdown caused early termination of the extensor activity (Hiebert et al., 1994). In our model, this phase transition was provided by the velocity and length dependent (Ia, II) as well as the force dependent (Ib) feedback. Our simulations have shown that the early termination of extensor activity and early initiation of flexor activity can result from unloading of the extensor muscles ("b" in **Figure 7C**) and increasing the activity of Ia and II afferent feedback from the flexor muscles of knee and ankle ("c" in **Figure 7C**) when the foot entering into a hole, which is consistent with the animal experiments. It is important to mention that, although the parameters for afferent feedback were determined during optimization performed to reproduce the normal walking, the afferent feedback incorporated in the model allowed the model to reproduce adaptive changes of locomotor characteristics during stepping into a hole. Furthermore, the mechanism responsible for this adaptive response was explained by the transition from the slow to fast dynamics in the RG neurons induced by the changes in the nullclines due to afferent feedback (**Figure 7**).

The adaptive locomotor behavior during stepping into a hole can be also interpreted based on the phase-dependent response of the CPG activity. Stimulation of extensor afferents during the active phase in fictive locomotion of decerebrate cats was shown to increase and prolong the extensor activity (Duysens, 1977), and our isolated CPG model was able to reproduce the phase-dependent response (**Figure 4B**). In the model, during in normal walking, Ib feedback from extensors increased during the stance phase due to the ground reaction force, which increased and prolonged the activities of the extensor half center of the CPG (**Figure 5B**). However, when the foot entered the hole, the force feedback from the extensor muscles was reduced due to the lack of the ground reaction force and the activity of the extensor half center was reduced (**Figures 6B**, **7A**). Similarly, stimulation of flexors afferents during the silent phase in fictive locomotion in decerebrate cats inhibited the extensor activity and initiated transition to flexion (Schomburg et al., 1998), and our isolated CPG model also reproduced these phase-dependent responses (**Figure 4A**). The flexor muscles in our model were stretched when the foot entered into a hole and afferent feedback from the flexor side increased (**Figure 6B**), which inhibited the activities of extensor muscles and shortened the stance phase leading to an advanced onset of the swing phase. As a result, the extension of the joints stopped and they were strongly flexed to pull the foot out of the hole.

6.2 Limitations and Future Works

In this study, we focused only on simulation of walking with a single hole as a source of locomotor disturbance. This allowed us to investigate the roles of afferent feedback from both flexor and extensor muscles because stepping into a hole caused unloading of extensor muscles and stretching of flexor muscles. We have not considered other walking disturbances tested experimentally, such as the presence of obstacles, cutaneous stimulation, and mechanical blockage of limb flexion (Forssberg et al., 1977; Lam and Pearson, 2001; Drew et al., 2002). In particular, while we focused on a hole without a bottom, a foot can have touchdown in a hole with a bottom depending on the depth, which changes the afferent feedback and phase transition. In the future, we would like to simulate walking with these other disturbances to provide mechanistic understanding of adaptation observed during locomotion. In addition, our model would be useful to investigate the responses when afferent feedback does not work well due to the paralysis and provides wrong information.

Because our present model used only one pair of the PF neurons (a PF-F neuron for the flexor side and a PF-E neuron for the extensor side), the motor commands activated the flexor and extensor muscles in strict alternation. However, in the biological system, some muscles show activity in both swing and stance phases and some muscles are active during only part of one phase (Prilutsky et al., 2016). In addition,

muscle synergy analysis suggested that muscle activities during animal walking can be explained by the combination of a few basic patterns (Dominici et al., 2011). Several previous CPG models have been proposed to produce such multiple patterns by increasing the complexity of the PF network (Markin et al., 2016). It has been also suggested that some afferent feedback is projected to the contralateral side of the CPG (McCrea, 2001). We will include these components in a more elaborated model in the future.

Also in this work, we only modeled one hindlimb, which did not allow us to consider interlimb coordination. The latter is also known to play an important role in adaptive walking (Forssberg et al., 1980). Particularly, when a foot of one limb enters a hole, the activity of the extensor muscle of the contralateral limb has been shown to increase to compensate for the weight support (Hiebert et al., 1994). In addition, animals change their gait patterns, such as walking, trotting, and galloping, depending on locomotor speed by controlling the interlimb coordination. A neural model simulating coordination between RG circuits controlling each limb has been proposed (Danner et al., 2016, 2017). These interactions will be included in the future extended model simulating locomotion with two forelimbs and two hindlimbs.

DATA AVAILABILITY STATEMENT

The raw data supporting the conclusion of this article will be made available by the authors, without undue reservation.

AUTHOR CONTRIBUTIONS

SA developed the study design in consultation with the other co-authors. YK performed simulation experiments and analyzed the data in consultation with SA, SF, SD, SM, JA, and IR. YK and SA wrote the manuscript and SD, SM, JA, and IR revised it. All the authors reviewed and approved it.

FUNDING

This study was supported in part by JSPS KAKENHI Grant Numbers JP19KK0377, JP20H00229, and JP20KK0226; JST FOREST Program Grant Number JPMJFR2021; NIH grants R01NS100928, R01NS110550, R01NS112304, and R01NS115900; and NSF grant 2113069.

REFERENCES

Danner, S. M., Wilshin, S. D., Shevtsova, N. A., and Rybak, I. A. (2016). Central Control of Interlimb Coordination and Speed-dependent Gait Expression in Quadrupeds. *J. Physiol.* 594 (23), 6947–6967. doi:10.1113/jp272787

Danner, S. M., Shevtsova, N. A., Frigon, A., and Rybak, I. A. (2017). Computational Modeling of Spinal Circuits Controlling Limb Coordination and Gaits in Quadrupeds. *Elife* 6, 1–25. doi:10.7554/eLife.31050

Demir, S. S., Butera, R. J., DeFranceschi, A. A., Clark, J. W., and Byrne, J. H. (1997). Phase Sensitivity and Entrainment in a Modeled Bursting Neuron. *Biophysical J.* 72 (2), 579–594. doi:10.1016/s0006-3495(97)78697-1

Dominici, N., Ivanenko, Y. P., Cappellini, G., d'Avella, A., Mondì, V., Cicchese, M., et al. (2011). Locomotor Primitives in Newborn Babies and Their Development. *Science* 334 (6058), 997–999. doi:10.1126/science.1210617

Drew, T., Jiang, W., and Widajewicz, W. (2002). Contributions of the Motor Cortex to the Control of the Hindlimbs during Locomotion in the Cat. *Brain Res. Brain Res. Rev.* 40 (1-3), 178–191. doi:10.1016/s0165-0173(02)00200-x

Duysens, J., and Pearson, K. G. (1980). Inhibition of Flexor Burst Generation by Loading Ankle Extensor Muscles in Walking Cats. *Brain Res.* 187 (2), 321–332. doi:10.1016/0006-8993(80)90206-1

Duysens, J. (1977). Reflex Control of Locomotion as Revealed by Stimulation of Cutaneous Afferents in Spontaneously Walking Premammillary Cats. *J. Neurophysiol.* 40 (4), 737–751. doi:10.1152/jn.1977.40.4.737

Ekeberg, Ö., and Pearson, K. (2005). Computer Simulation of Stepping in the Hind Legs of the Cat: An Examination of Mechanisms Regulating the Stance-To-Swing Transition. *J. Neurophysiol.* 94 (6), 4256–4268. doi:10.1152/jn.00065.2005

Ermentrout, B. (1994). Reduction of Conductance-Based Models with Slow Synapses to Neural Nets. *Neural Comput.* 6 (4), 679–695. doi:10.1162/neco.1994.6.4.679

Forssberg, H., Grillner, S., and Rossignol, S. (1977). Phasic Gain Control of Reflexes from the Dorsum of the Paw during Spinal Locomotion. *Brain Res.* 132 (1), 121–139. doi:10.1016/0006-8993(77)90710-7

Forssberg, H., Grillner, S., Halbertsma, J., and Rossignol, S. (1980). The Locomotion of the Low Spinal Cat. Ii. Interlimb Coordination. *Acta Physiol. Scand.* 108 (3), 283–295. doi:10.1111/j.1748-1716.1980.tb06534.x

Frigon, A., Sirois, J., and Gossard, J.-P. (2010). Effects of Ankle and Hip Muscle Afferent Inputs on Rhythm Generation during Fictive Locomotion. *J. Neurophysiol.* 103 (3), 1591–1605. doi:10.1152/jn.01028.2009

Fujiki, S., Aoi, S., Tsuchiya, K., Danner, S. M., Rybak, I. A., and Yanagihara, D. (2019). Phase-dependent Response to Afferent Stimulation during Fictive Locomotion: A Computational Modeling Study. *Front. Neurosci.* 13, 1288. doi:10.3389/fnins.2019.01288

Gorassini, M. A., Prochazka, A., Hiebert, G. W., and Gauthier, M. J. (1994). Corrective Responses to Loss of Ground Support during Walking. I. Intact Cats. *J. Neurophysiol.* 71 (2), 603–610. doi:10.1152/jn.1994.71.2.603

Grillner, S. (1981). "Control of Locomotion in Bipeds, Tetrapods, and Fish," in *Handbook of Physiology, Sect. 1. The Nervous System: Motor Control*. Editor V. B. Brooks (Bethesda, MD: American Physiological Society), Vol. II, Pt. 2, 1179–1236. doi:10.1002/cphy.cp010226

Guertin, P., Angel, M. J., Perreault, M. C., and McCrea, D. A. (1995). Ankle Extensor Group I Afferents Excite Extensors throughout the Hindlimb during Fictive Locomotion in the Cat. *J. Physiol.* 487, 197–209. doi:10.1113/jphysiol.1995.sp020871

Hansen, N., Müller, S. D., and Koumoutsakos, P. (2003). Reducing the Time Complexity of the Derandomized Evolution Strategy with Covariance Matrix Adaptation (CMA-ES). *Evol. Comput.* 11 (1), 1–18. doi:10.1162/106365603321828970

Hiebert, G. W., Gorassini, M. A., Jiang, W., Prochazka, A., and Pearson, K. G. (1994). Corrective Responses to Loss of Ground Support during Walking. ii. Comparison of Intact and Chronic Spinal Cats. *J. Neurophysiol.* 71 (2), 611–622. doi:10.1152/jn.1994.71.2.611

Hiebert, G. W., Whelan, P. J., Prochazka, A., and Pearson, K. G. (1996). Contribution of Hind Limb Flexor Muscle Afferents to the Timing of Phase Transitions in the Cat Step Cycle. *J. Neurophysiol.* 75 (3), 1126–1137. doi:10.1152/jn.1996.75.3.1126

Lam, T., and Pearson, K. G. (2001). Proprioceptive Modulation of Hip Flexor Activity during the Swing Phase of Locomotion in Decerebrate Cats. *J. Neurophysiol.* 86 (3), 1321–1332. doi:10.1152/jn.2001.86.3.1321

Markin, S. N., Klishko, A. N., Shevtsova, N. A., Lemay, M. A., Prilutsky, B. I., and Rybak, I. A. (2010). Afferent Control of Locomotor Cpg: Insights from a Simple Neuromechanical Model. *Ann. N. Y. Acad. Sci.* 1198, 21–34. doi:10.1111/j.1749-6632.2010.05435.x

Markin, S. N., Klishko, A. N., Shevtsova, N. A., Lemay, M. A., Prilutsky, B. I., and Rybak, I. A. (2016). "A Neuromechanical Model of Spinal Control of Locomotion," in *Neuromechanical Modeling of Posture and Locomotion*. Editors B. I. Prilutsky and D. H. Edwards (New York: Springer Science), 21–65. doi:10.1007/978-1-4939-3267-2_2

McCrea, D. A. (2001). Spinal Circuitry of Sensorimotor Control of Locomotion. *J. Physiol.* 533 (1), 41–50. doi:10.1111/j.1469-7793.2001.0041b.x

Molkov, Y. I., Bacak, B. J., Talpalar, A. E., and Rybak, I. A. (2015). Mechanisms of Left-Right Coordination in Mammalian Locomotor Pattern Generation

Circuits: A Mathematical Modeling View. *Plos Comput. Biol.* 11 (5), e1004270–40. doi:10.1371/journal.pcbi.1004270

Orlovsky, G., Deliagina, T. G., and Grillner, S. (1999). *Neuronal Control of Locomotion: From Mollusc to Man*. Oxford, United Kingdom: Oxford University Press.

Pearson, K. G., Ramirez, J. M., and Jiang, W. (1992). Entrainment of the Locomotor Rhythm by Group Ib Afferents from Ankle Extensor Muscles in Spinal Cats. *Exp. Brain Res.* 90 (3), 557–566. doi:10.1007/BF00230939

Perreault, M. C., Angel, M. J., Guertin, P., and McCrea, D. A. (1995). Effects of Stimulation of Hindlimb Flexor Group Ii Afferents during Fictive Locomotion in the Cat. *J. Physiol.* 487, 211–220. doi:10.1113/jphysiol.1995.sp020872

Prilutsky, B. I., Klishko, A. N., Weber, D. J., and Lemay, M. A. (2016). "Computing Motion Dependent Afferent Activity during Cat Locomotion Using a Forward Dynamics Musculoskeletal Model," in *Neuromechanical Modeling of Posture and Locomotion*. Editors B. I. Prilutsky and D. H. Edwards (New York: Springer Science), 273–307. doi:10.1007/978-1-4939-3267-2_10

Rossignol, S., Dubuc, R., and Gossard, J.-P. (2006). Dynamic Sensorimotor Interactions in Locomotion. *Physiol. Rev.* 86 (1), 89–154. doi:10.1152/physrev.00028.2005

Rossignol, S. (1996). "Neural Control of Stereotypic Limb Movements," in *Handbook of Physiology, Sect. 12. Exercise: Regulation and Integration of Multiple Systems*. Editors L. B. Rowell and J. T. Sheperd (Oxford: American Physiological Society), 173–216. doi:10.1002/cphy.cp120105

Rybak, I. A., Shevtsova, N. A., Lafreniere-Roula, M., and McCrea, D. A. (2006a). Modelling Spinal Circuitry Involved in Locomotor Pattern Generation: Insights from Deletions during Fictive Locomotion. *J. Physiol.* 577 (2), 617–639. doi:10.1113/jphysiol.2006.118703

Rybak, I. A., Stecina, K., Shevtsova, N. A., and McCrea, D. A. (2006b). Modelling Spinal Circuitry Involved in Locomotor Pattern Generation: Insights from the Effects of Afferent Stimulation. *J. Physiol.* 577 (2), 641–658. doi:10.1113/jphysiol.2006.118711

Schomburg, E. D., Petersen, N., Barajon, I., and Hultborn, H. (1998). Flexor Reflex Afferents Reset the Step Cycle during Fictive Locomotion in the Cat. *Exp. Brain Res.* 122 (3), 339–350. doi:10.1007/s002210050522

Spardy, L. E., Markin, S. N., Shevtsova, N. A., Prilutsky, B. I., Rybak, I. A., and Rubin, J. E. (2011). A Dynamical Systems Analysis of Afferent Control in a Neuromechanical Model of Locomotion: I. Rhythm Generation. *J. Neural Eng.* 8 (6), 065003–065031. doi:10.1088/1741-2560/8/6/065003

Stecina, K., Quevedo, J., and McCrea, D. A. (2005). Parallel Reflex Pathways from Flexor Muscle Afferents Evoking Resetting and Flexion Enhancement during Fictive Locomotion and Scratch in the Cat. *J. Physiol.* 569, 275–290. doi:10.1113/jphysiol.2005.095505

Yakovenko, S., Gritsenko, V., and Prochazka, A. (2004). Contribution of Stretch Reflexes to Locomotor Control: A Modeling Study. *Biol. Cybernetics* 90 (2), 146–155. doi:10.1007/s00422-003-0449-z

Conflict of Interest: The authors declare that the research was conducted in the absence of any commercial or financial relationships that could be construed as a potential conflict of interest.

APPENDIX

A Parameters for CPG Model

Based on Molkov et al. (2015), Danner et al. (2016), Danner et al. (2017), Markin et al. (2010), and Fujiki et al. (2019), we determined the parameters for the synaptic connections α_{ij}, β_{ij}, and γ_i ($i \in \{\text{RG}\}, \{\text{In}\}, \{\text{PF}\}$, $j \in \{\text{RG}\}, \{\text{In}\}$) and those for the currents $\hat{g}^i_{\text{Leak}}$, $\hat{g}^i_{\text{NaP}}$, E^i_{SynI}, and E^i_{Leak} ($i \in \{\text{RG}\}, \{\text{In}\}, \{\text{PF}\}, \{\text{Mn}\}$) as shown in **Tables 1**, **2**, respectively. We used the following parameter values: $\hat{g}_{\text{SynE}} = 10\,\text{nS}$, $\hat{g}_{\text{SynI}} = 10\,\text{nS}$, $E_{\text{SynE}} = -10\,\text{mV}$, $E_{\text{Na}} = 55\,\text{mV}$, $C = 20\,\text{pF}$, $V_{\text{th}} = -50\,\text{mV}$, $V_{\max} = 0\,\text{mV}$, and $d = 1.0$.

B Parameters Determined by Optimization to Generate Normal Walking

Through the optimization needed to generate normal walking, the parameters for the synaptic connections α_{ij} ($i \in \{\text{Mn}\}$, $j \in \{\text{PF}\}$) were determined as shown in **Table 3** and the weight coefficients for afferent feedback were determined as follows: $k^{\text{v}}_{\text{F}} = 0.001$, $k^{\text{d}}_{\text{F}} = 0.15$, $k^{\text{f}}_{\text{F}} = 0.077$, $k^{\text{v}}_{\text{E}} = 0.000\,39$, $k^{\text{d}}_{\text{E}} = 0.058$, $k^{\text{f}}_{\text{E}} = 0.2$, and $\eta = 0.27$.

TABLE 1 | Parameters for synaptic connections.

Source *j*	Target neuron *i*					
	RG-F	**RG-E**	**In-F**	**In-E**	**PF-F**	**PF-E**
Excitatory connections α_{ij}						
RG-F	0	0	0.4	0	0.7	0
RG-E	0	0	0	0.4	0	0.7
Inhibitory connections β_{ij}						
In-F	0	0.7	0	0	0	2.1
In-E	0.1	0	0	0	0.3	0
Connections from supraspinal drive γ_i	0.02	0.15	0	0	0	0

TABLE 2 | Parameters for currents.

	Target neuron *i*			
	$i \in \{\text{RG}\}$	$i \in \{\text{In}\}$	$i \in \{\text{PF}\}$	$i \in \{\text{Mn}\}$
$\hat{g}^i_{\text{Leak}}$	4.5	2.8	1.6	1.6
$\hat{g}^i_{\text{NaP}}$	4.5	—	0.5	0.3
E^i_{SynI}	−75	−75	−70	−70
E^i_{Leak}	−62.5	−60	−64	−64

TABLE 3 | Optimized parameters for synaptic connections.

Source *j*	Target motoneuron *i*						
	Mn-IP	**Mn-GM**	**Mn-VL**	**Mn-TA**	**Mn-SO**	**Mn-BF**	**Mn-GA**
Excitatory connections α_{ij}							
PF-F	0.084	0	0	0.074	0	0.077	0
PF-E	0	0.82	0.13	0	0.16	0	0.18

frontiers | Frontiers in Bioengineering and Biotechnology

ORIGINAL RESEARCH
published: 14 April 2022
doi: 10.3389/fbioe.2022.825638

Three Characteristics of Cheetah Galloping Improve Running Performance Through Spinal Movement: A Modeling Study

Tomoya Kamimura[1], Kaho Sato[1], Shinya Aoi[2]*, Yasuo Higurashi[3], Naomi Wada[3], Kazuo Tsuchiya[2], Akihito Sano[1] and Fumitoshi Matsuno[4]*

[1]Department of Electrical and Mechanical Engineering, Nagoya Institute of Technology, Aichi, Japan, [2]Department of Aeronautics and Astronautics, Graduate School of Engineering, Kyoto University, Kyoto, Japan, [3]Laboratory of System Physiology, Joint Faculty of Veterinary Medicine, Yamaguchi University, Yamaguchi, Japan, [4]Department of Mechanical Engineering and Science, Graduate School of Engineering, Kyoto University, Kyoto, Japan

OPEN ACCESS

Edited by:
Marcus G. Pandy,
The University of Melbourne, Australia

Reviewed by:
Michael Granatosky,
New York Institute of Technology, United States
Shunsuke Shigaki,
Osaka University, Japan
David V. Lee,
University of Nevada, United States

***Correspondence:**
Tomoya Kamimura
kamimura.tomoya@nitech.ac.jp
Shinya Aoi
shinya_aoi@kuaero.kyoto-u.ac.jp

Specialty section:
This article was submitted to Biomechanics, a section of the journal Frontiers in Bioengineering and Biotechnology

Received: *30 November 2021*
Accepted: *18 March 2022*
Published: *14 April 2022*

Citation:
Kamimura T, Sato K, Aoi S, Higurashi Y, Wada N, Tsuchiya K, Sano A and Matsuno F (2022) Three Characteristics of Cheetah Galloping Improve Running Performance Through Spinal Movement: A Modeling Study. Front. Bioeng. Biotechnol. 10:825638. doi: 10.3389/fbioe.2022.825638

Cheetahs are the fastest land animal. Their galloping shows three characteristics: small vertical movement of their center of mass, small whole-body pitching movement, and large spine bending movement. We hypothesize that these characteristics lead to enhanced gait performance in cheetahs, including higher gait speed. In this study, we used a simple model with a spine joint and torsional spring, which emulate the body flexibility, to verify our hypothesis from a dynamic perspective. Specifically, we numerically searched periodic solutions and evaluated what extent each solution shows the three characteristics. We then evaluated the gait performance and found that the solutions with the characteristics achieve high performances. This result supports our hypothesis. Furthermore, we revealed the mechanism for the high performances through the dynamics of the spine movement. These findings extend the current understanding of the dynamic mechanisms underlying high-speed locomotion in cheetahs.

Keywords: quadruped, cheetah, galloping, spine bending, simple model

1 INTRODUCTION

Cheetahs are the fastest land animal. They use galloping when moving at their highest speeds, which involves remarkable spine bending movement (Hildebrand, 1959; Bertram and Gutmann, 2009) and stable head height during running. The spine movement allows cheetahs' gallop to involve two types of flight phase, extended and gathered, as shown in **Figure 1** (Hildebrand, 1959, Hildebrand, 1961; English, 1980; Walter and Carrier, 2007; Kamimura et al., 2021). The stable height of the head allows cheetahs to maintain visual contact with their prey, which is achieved not only through a well-designed controller (Grohé et al., 2018), but also through small vertical movements of their center of mass (COM) and small pitching movements of their whole body (Wada, 2011; Ichikawa et al., 2018). The characteristics of cheetah galloping can be summarized as follows: small vertical COM movement, small whole-body pitching movement, and large spine bending movement. We hypothesize that these characteristics provide cheetahs enhanced gait performance, including higher gait speed. However, animal running is a complex phenomenon generated through dynamic interactions between the body's mechanical systems, nervous system, and the environment; it is difficult to fully understand the mechanisms underlying cheetah galloping only through observational studies.

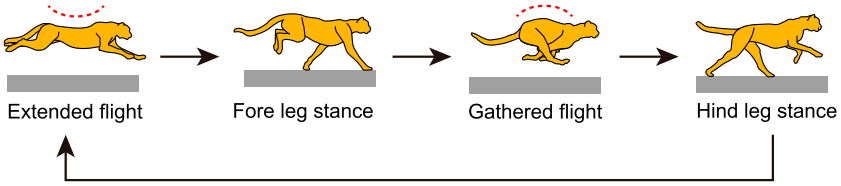

FIGURE 1 | Cheetah galloping involves two types of flight, extended and gathered, which are achieved through spinal movement. Extended and gathered flight occur after liftoff of hindlegs and forelegs, respectively.

To overcome the limitations of the observational approach, modeling research approaches have recently attracted attention (Alexander, 1988; Swanstrom et al., 2005; Bertram and Gutmann, 2009; Aoi et al., 2017; Ambe et al., 2018; Fujiki et al., 2018; Aoi et al., 2019; Toeda et al., 2019). Because the legs can be represented by springs, quadruped models with spring legs were developed to investigate the common and unique principles of animal gaits from a dynamic perspective (Full and Koditschek, 1999; Blickhan and Full, 1993; Farley et al., 1993; Tanase et al., 2015; Gan et al., 2016, Gan et al., 2018; Yamada et al., 2022). Recently, such models have been further improved to investigate the dynamic role of spine bending movements in quadruped running (Cao and Poulakakis, 2013; Pouya et al., 2017; Wang et al., 2017; Kamimura et al., 2015, Kamimura et al., 2018; Yesilevskiy et al., 2018; Adachi et al., 2020). Moreover, quadruped robots equipped with a spine bending mechanism have been developed to investigate the effect of spinal movement on running (Pouya et al., 2017; Chen et al., 2019; Fukuhara et al., 2020, Fukuhara et al., 2021). Furthermore, some researchers focused on the impulse from the ground reaction force to reveal the mechanisms underlying various quadruped gaits (Ruina et al., 2005; Usherwood and Davies, 2017; Usherwood, 2020; Polet, 2021; Kamimura et al., 2021). However, because few researchers have focused on the three characteristics of cheetah galloping, the dynamic effects of the characteristics on running and their mechanisms remain largely unclear.

In our previous studies (Kamimura et al., 2015, Kamimura et al., 2018, Kamimura et al., 2021), we used simple models to reveal the mechanisms under which cheetahs utilize their spinal movements to involve the two types of flight phase to achieve high-speed galloping. However, we focused only on spinal movement and did not incorporate the two other characteristics of cheetah galloping: small vertical COM movement and small whole-body pitching movement. In this paper, we extended our previous models to verify our hypothesis that the three characteristics of cheetah galloping enhance gait performance, including gait speed, and clarify their mechanisms. Specifically, we numerically searched for periodic solutions, and evaluated what extent each solution shows the three gait characteristics. In addition, we compared the three characteristics of the solutions with the measured data of actual cheetahs. We then evaluated gait performance to reveal the relationship between the gait characteristics and performance. Furthermore, we compared the solutions with and without the gait characteristics to reveal the mechanisms by which the three characteristics allow cheetahs to achieve high performance when galloping.

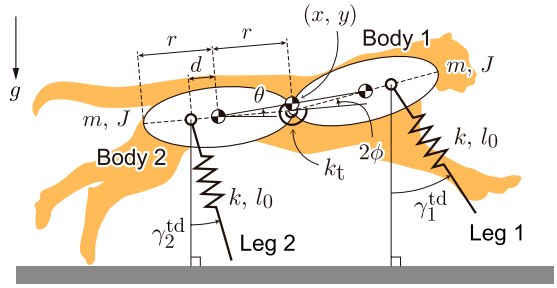

FIGURE 2 | Our model consists of two rigid bodies connected by a joint with torsional spring and two massless spring legs.

2 METHODS

2.1 Model

To investigate the bounding gait of the model with spine flexibility as in previous studies (Cao and Poulakakis, 2013; Kamimura et al., 2015, Kamimura et al., 2018), we used a two-dimensional model (**Figure 2**) composed of two rigid bodies (Bodies 1 and 2) and two massless spring legs (Legs 1 and 2). The bodies were connected by a joint, which was modeled to emulate the bending movement of the spine and has a torsional spring with a spring constant of k_t. x and y represent the horizontal and vertical positions, respectively, of the COM of the whole body. θ represents the pitch angle of the line connecting the two COMs of the rigid bodies relative to the horizontal line, that is the pitch angle of the whole body. The spine joint angle is represented by 2ϕ. We assumed that the fore and hind parts of the model had the same physical parameters. The mass and moment of inertia around the COM of each body are represented by m and J, respectively. The length of each body is $2r$. The distance between the COM and leg joint is d, which is positive when the leg joint is outside the COM relative to the spine joint. The torsional spring is at equilibrium position when the fore and hind bodies are in a straight line ($\phi = 0$). The gravitational acceleration is g. The spring constant and nominal length of leg springs are k and l_0, respectively. When Leg i ($i = 1, 2$) is in the air, its length remains l_0 and its angle keeps the touchdown angle, γ_i^{td}.

When the tip of the leg reaches the ground, it is constrained on the ground and behaves as a frictionless pin joint. When the stance leg returns to its nominal length after compression, the tip leaves the ground, and the leg angle immediately returns to the touchdown angle γ_i^{td}. The model conserves energy because the

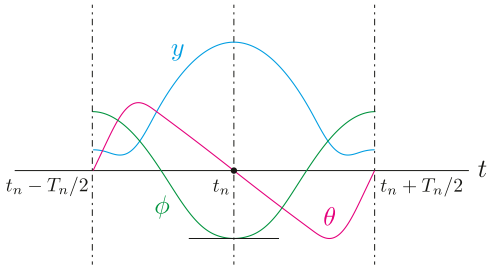

FIGURE 3 | Additional constraints $\theta(t_n) = 0$ and $\dot{\phi}(t_n) = 0$ to achieve symmetrical periodic solutions. y, θ, and ϕ are COM height, whole-body pitch angle, and relative angle between Bodies 1 and 2, respectively.

touchdown and liftoff occur at the nominal length and the model has no dissipative structure, such as friction or a damper.

The equations of motion of the model are given by

$$M(q)\ddot{q} + h(q,\dot{q}) + v(q) = 0 \tag{1}$$

where $q = [x\ y\ \theta\ \phi]^\top$,

$$M(q) = \begin{bmatrix} 2m & 0 & 0 & 0 \\ 0 & 2m & 0 & 0 \\ 0 & 0 & 2J + 2mr^2\cos^2\phi & 0 \\ 0 & 0 & 0 & 2J + 2mr^2\sin^2\phi \end{bmatrix},$$

$$h(q,\dot{q}) = \begin{bmatrix} 0 \\ 0 \\ -4mr^2\dot{\theta}\dot{\phi}\cos\phi\sin\phi \\ 2mr^2\left(\dot{\theta}^2 + \dot{\phi}^2\right) \end{bmatrix},$$

$$v(q) = \begin{bmatrix} 0 \\ 2mg \\ 0 \\ 4k_t\phi \end{bmatrix} + k(l_1 - l_0)\begin{bmatrix} \partial l_1/\partial x \\ \partial l_1/\partial y \\ \partial l_1/\partial\theta \\ \partial l_1/\partial\phi \end{bmatrix} + k(l_2 - l_0)\begin{bmatrix} \partial l_2/\partial x \\ \partial l_2/\partial y \\ \partial l_2/\partial\theta \\ \partial l_2/\partial\phi \end{bmatrix},$$

$$l_i = \begin{cases} l_0, & \text{when Leg } i \text{ is in the air} \\ \left[\left\{x + (-1)^i(r+d)\cos\theta\cos\phi - x_i^{\text{toe}}\right\}^2\right. & \\ \left. + \left\{y + (-1)^i(r+d)\sin\theta\cos\phi\right\}^2\right]^{\frac{1}{2}}, & i = 1,2 \\ & \text{when Leg } i \text{ is in the stance phase} \end{cases}$$

and x_i^{toe} is the contact position of Leg i.

From the measured cheetah data (Kamimura et al., 2021), we determined the physical parameters as follows: m = 19 kg, J = 0.53 kgm^2, r = 0.29 m, l_0 = 0.69 m, and d = 0.06 m. We used k_t = 100 Nm/rad and k = 15000 N/m to reproduce a similar locomotor behavior to that of cheetahs from the perspective of body bending and gait cycle.

2.2 Search for Periodic Solutions

To find periodic solutions of the model, we defined the Poincaré section at the apex height of the COM of the whole body ($\dot{y} = 0$). We set $t = t_n$ at the nth apex height. We assumed that both legs have to experience the stance phase once before the next intersection with the Poincaré section. We neglected the horizontal position to determine periodic solutions because it monotonically increases during locomotion and is not periodic. We assumed the following two constraints to movement based on Raibert (1986):

$$\theta(t_n) = 0, \tag{2a}$$

$$\dot{\phi}(t_n) = 0, \tag{2b}$$

so that the whole-body posture is symmetrical about a vertical axis through the spine joint and that the body spring is fully bent at the apex height, as shown in **Figure 3**. This allows symmetrical periodic solutions to be achieved that satisfy

$$y(t_n + \tau) = y(t_n - \tau), \tag{3a}$$

$$\phi(t_n + \tau) = \phi(t_n - \tau), \tag{3b}$$

$$\theta(t_n + \tau) = -\theta(t_n - \tau), \tag{3c}$$

where $t_n - T_n/2 \le \tau \le t_n + T_n/2$ and $T_n = t_{n+1} - t_n$.

We used the Poincaré map P denoted by

$$z_{n+1} = P(z_n, u_n), \tag{4}$$

where $z_n = [y(t_n)\ \phi(t_n)\ \dot{\theta}(t_n)]$ was the state variable at the nth intersection with the Poincaré section and $u_n = [y_{1n}^{\text{td}}\ y_{2n}^{\text{td}}]$ was the parameter set. To find the solutions, we fixed the total energy E, and $\dot{x}(t_n)$ was determined using other variables. For a periodic solution, $z^\star = P(z^\star, u^\star)$ is satisfied, where $z^\star$ is a fixed point on the Poincaré section. We numerically searched for fixed points for periodic solutions using the Newton–Raphson method.

2.3 Classification of Solutions

In the obtained periodic solutions, some solutions only had one flight phase and one double stance phase. Other solutions had two flight phases but no double stance phase. In addition, the flight

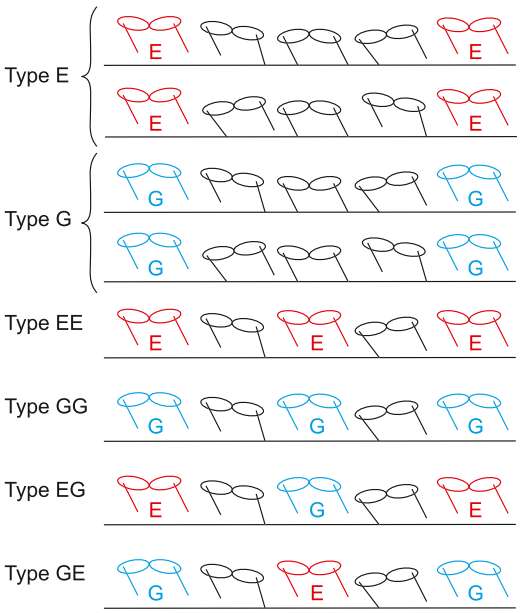

FIGURE 4 | Six types of periodic solution.

phases are classified into two types based on the spine joint movement: extended and gathered. In extended flight, the spine joint is extended ($\phi > 0$) at the mid-flight phase. In gathered flight, the spine joint is flexed ($\phi < 0$) at the mid-flight phase. As a result, periodic solutions are classified into six types as shown in **Figure 4**:

1 Type E: Single extended flight with double stance
2 Type G: Single gathered flight with double stance
3 Type EE: Two extended flights without double stance
4 Type GG: Two gathered flights without double stance
5 Type EG: Two different flights (first: extended, second: gathered) without double stance
6 Type GE: Two different flights (first: gathered, second: extended) without double stance

where we assumed that the foreleg (Leg 1) is the first to touch down in solutions with two flights (Types EE, GG, EG, and GE).

2.4 Gait Characteristics of Cheetahs

Cheetah galloping shows three characteristics: small vertical COM movement, small whole-body pitching movement, and large spine bending movement. To evaluate to what extent the obtained periodic solutions showed these characteristics, we investigated the fluctuations of the COM height δ_y, whole-body pitch angle δ_θ, and spine joint angle δ_ϕ, by examining the difference between the maximum and minimum values of $y(t)$, $\theta(t)$, and $\phi(t)$, respectively, in one gait cycle as follows:

$$\delta_y = \max_{t_n \le t \le t_n+T_n} y(t) - \min_{t_n \le t \le t_n+T_n} y(t), \tag{5}$$

$$\delta_\theta = \max_{t_n \le t \le t_n+T_n} \theta(t) - \min_{t_n \le t \le t_n+T_n} \theta(t), \tag{6}$$

$$\delta_\phi = \max_{t_n \le t \le t_n+T_n} \phi(t) - \min_{t_n \le t \le t_n+T_n} \phi(t). \tag{7}$$

We compared these three characteristics with measured cheetah data in Kamimura et al. (2021), where four adult male cheetahs (40–50 kg) ran at a speed of 15–18 m/s. We analyzed eight strides (five from one cheetah and three from the others) and determined δ_y by the fluctuation of the height of the middle point between the shoulder joint and the greater trochanter of the femur, δ_θ by the fluctuation of the pitch angle of the line connecting the roots of the head and the tail, and δ_ϕ by the fluctuation of the relative angle between the lines connecting the root of neck and 12th thoracic vertebra (T12), and T12 and root of the tail.

2.5 Performance Criteria

To evaluate the gait performance of the obtained solutions, we used the following three criteria: average horizontal velocity, impulse from the ground reaction force, and stability. The average horizontal velocity for one gait cycle of the periodic solution was calculated as

$$\bar{v} = \frac{1}{T_n}\int_{t_n}^{t_n+T_n} \dot{x}(t)\mathrm{d}t = \frac{x(t_n+T_n) - x(t_n)}{T_n}. \tag{8}$$

We evaluated the following aspects of the impulse from the ground reaction force: net, positive horizontal, negative horizontal, and vertical impulse. The net impulse for one gait cycle from the foreleg was identical to that from the hind-leg due to the symmetry of the motion and was obtained by

$$p = -\int_{t_n}^{t_n+T_n} k(l_0 - l_i(t))\mathrm{d}t \quad i = 1, 2 \tag{9}$$

In the stance phase of Leg i (i = 1, 2), when $\gamma_i > 0$, the horizontal ground reaction force reduces the horizontal velocity of the COM. In contrast, it increases when $\gamma_i < 0$. Because $\gamma_i^{\mathrm{td}} > 0$ is satisfied for all obtained periodic solutions, we assumed that γ_i monotonically decreases and liftoff occurs with $\gamma_i < 0$. The negative horizontal impulse p_i^{x-} and positive horizontal impulse p_i^{x-} were then obtained by

$$p_i^{x-} = -\int_{t_n}^{t_n+T_{ni}} k(l_0 - l_i(t))\sin\gamma_i(t)\mathrm{d}t, \quad i = 1, 2 \tag{10}$$

$$p_i^{x+} = -\int_{t_n+T_{ni}}^{t_n+T_n} k(l_0 - l_i(t))\sin\gamma_i(t)\mathrm{d}t, \quad i = 1, 2 \tag{11}$$

where $t_n + T_{ni}$ is the moment when $\gamma_i = 0$ is achieved. Note that the amount of acceleration by the foreleg and deceleration by the hind-leg are identical, and the acceleration by the hind-leg and deceleration by the foreleg are identical. In other words, $p_i^{x-} = -p_j^{x+}$ is satisfied for (i, j) = (1, 2) and (2, 1). The vertical impulse from the foreleg is identical to that from the hind-leg and was obtained by

$$p^y = \int_{t_n}^{t_n+T_n} k(l_0 - l_i(t))\cos\gamma_i(t)\mathrm{d}t \quad i = 1, 2 \tag{12}$$

The stability was determined by the eigenvalues of the linearized Poincaré map around the fixed point on the Poincaré section. Because our model was energy conservative, the solution was asymptotically stable when all of the eigenvalues, except for one eigenvalue of 1, were inside the unit cycle in the complex plane (these magnitudes are less than 1).

3 RESULTS

3.1 Periodic Solutions

We numerically searched for periodic solutions using E_0 = 4500 J to achieve a gait speed similar to that of cheetah galloping. **Figure 5A** shows the obtained solutions for $\dot{\theta}^\star = -1.5, -0.5, 0.5,$ and 1.5 rad/s. Although five types of solutions (Types E, G, EE, EG, and GE) were found, Type GG was not. Regardless of the value of $\dot{\theta}^\star$, the solutions could be divided into two parts: Branch 1 (upper) and Branch 2 (lower). While Branch 1 was obtained over a wide range of $y^\star$, Branch 2 was obtained for a smaller range and folded. In other words, Branch 2 had two solutions for each $y^\star$ in the specific range. **Figure 5B** shows the obtained solutions in the $y^\star$-$\dot{\theta}^\star$-$\phi^\star$ space, where the left and right figures show Branches 1 and 2, respectively. When $\dot{\theta}^\star$ was small, the solutions involved only one flight phase (Types E and G). When $\dot{\theta}^\star$ was large, the solutions had two different flight phases (Types EG, GE, and EE). Type EE existed only in Branch 1, where $|\dot{\theta}^\star|$ is large and $y^\star$ is small.

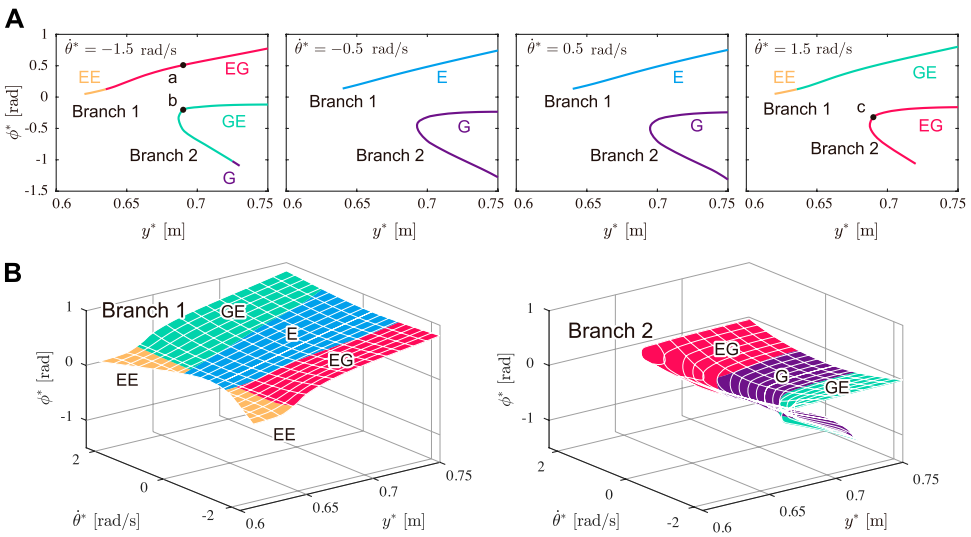

FIGURE 5 | Obtained solutions (Type E: blue, Type G: purple, Type EE: yellow, Type EG: red, and Type GE: green). **(A)** Solutions for $\dot{\theta}^* = -1.5, -0.5, 0.5$, and 1.5 rad/s. Black dots (a, b, and c) indicate the solutions used in **Figure 6**. **(B)** Solutions plotted in y^*-$\dot{\theta}^*$-ϕ^* space. Left and right figures show Branches 1 and 2, respectively.

Figure 6 shows the time profiles and snapshots of typical solutions for $y^* = 0.69$ m. **Figures 6A,B** show the solution in Branch 1 (Type EG, a in **Figure 5A**) and one of the solutions in Branch 2 with smaller $|\phi^*|$ (Type GE, b in **Figure 5A**), respectively, for $\dot{\theta}^* = -1.5$ rad/s. **Figure 6C** shows one of the solutions in Branch 2 with smaller $|\phi^*|$ (Type EG, c in **Figure 5A**) for $\dot{\theta}^* = 1.5$ rad/s.

When we compare the time profiles of the state variables between **Figures 6A,B**, there is no qualitative difference in x, y, θ, $\dot{y}$, and $\dot{\theta}$. In contrast, the signs of ϕ and $\dot{\phi}$ are different, which results in different solution types (Types EG and GE). In addition, the time profiles of $\dot{x}$ are partially different. Specifically, while $\dot{x}$ during the flight phase before touchdown of the foreleg is larger than that after the touchdown of the hind-leg in **Figure 6A**, it is smaller in **Figure 6B**. Furthermore, while $\dot{\phi}$ has only one peak in **Figure 6A**, it has three peaks in **Figure 6B**. When we compare the time profiles of the state variables between **Figures 6A,C**, the durations of two flights are different despite the same solution type (Type EG). Specifically, while the duration of the gathered flight (second flight) is shorter than that of extended flight (first flight) in **Figure 6A**, it is longer in **Figure 6C**. Furthermore, the time profiles of ϕ and $\dot{\phi}$ are also different. Specifically, in the stance phases in **Figure 6A**, $\phi < 0$, in **Figure 6C**, $\phi > 0$. In addition, while $\dot{\phi}$ has only one peak in **Figure 6A**, it has three peaks in **Figure 6C**.

To understand the mechanism underlying the differences between Branches 1 and 2, we compared the torque on the spine joint ϕ in the stance phases. While the joint torque τ_t on ϕ from the body spring (first term in the fourth row of $v(q)$ in **Eq. 1**) is positive to extend the spine joint in the stance phases in **Figure 6A**, it is negative to bend the spine joint in **Figures 6B,C**. The moments τ_1 and τ_2 on ϕ from the ground reaction forces of Legs 1 and 2, respectively (second and third terms, respectively, in the fourth row of $v(q)$ in **Eq. 1**), are both positive to extend the spine joint.

3.2 Gait Characteristics of Solutions

We quantitatively evaluated what extent each obtained solution shows the characteristics of cheetah galloping. **Figures 7A–C** show the fluctuations in the COM height δ_y, whole-body pitch angle δ_θ, and spine joint angle δ_ϕ, respectively, for y^* of the obtained solutions with $\dot{\theta}^* = \pm 1.5$ rad/s. δ_y and δ_θ of Branch 1 were smaller than those of Branch 2 for each y^*, regardless of $\dot{\theta}^*$. In contrast, Branch 2 involved a larger δ_ϕ and smaller δ_ϕ than that of Branch 1 for each y^*. When we compare the solutions indicated by a (Branch 1) and b (Branch 2) in **Figure 5A**, solution a has a larger δ_ϕ.

From the measured cheetah data, we obtained $\delta_y = 0.057 \pm 0.012$ (S.E.) m, $\delta_\theta = 0.20 \pm 0.016$ rad, and $\delta_\phi = 0.47 \pm 0.029$ rad, as shown in **Figure 7**, where black lines and grey areas show the average values and standard errors, respectively, of eight strides of the measured cheetah data. The solutions of Branch 1 showed closer values for δ_y, δ_θ, and δ_ϕ to those of the measured data than the solutions of Branch 2.

3.3 Gait Performance of Solutions

We evaluated the gait performance of the obtained solutions by focusing on the difference between the two branches. **Figure 8A** shows the average horizontal velocity $\bar{v}$ of the solutions found for $\dot{\theta}^* = \pm 1.5$ rad/s. It shows 14.5–15 m/s, which is consistent with the velocity range of cheetah galloping (Hudson et al., 2012). It monotonically increases as y^* decreases in Branch 1. Branch 2 involves a larger $\bar{v}$ and smaller $\bar{v}$ than those of Branch 1 for each y^*. However, Branch 1 has a larger range of y^* than Branch 2 and the maximum $\bar{v}$ of Branch 1 is slightly larger than that of Branch 2.

Figures 8B–D show the net impulse p, horizontal impulses p_1^{x+} and p_1^{x-}, and vertical impulse p^y, respectively, for $\dot{\theta}^* = \pm 1.5$ rad/s. The horizontal impulses p_2^{x+} and p_2^{x-} are not shown because $p_2^{x+} = -p_1^{x-}$ and $p_2^{x-} = -p_1^{x+}$ are satisfied. For all

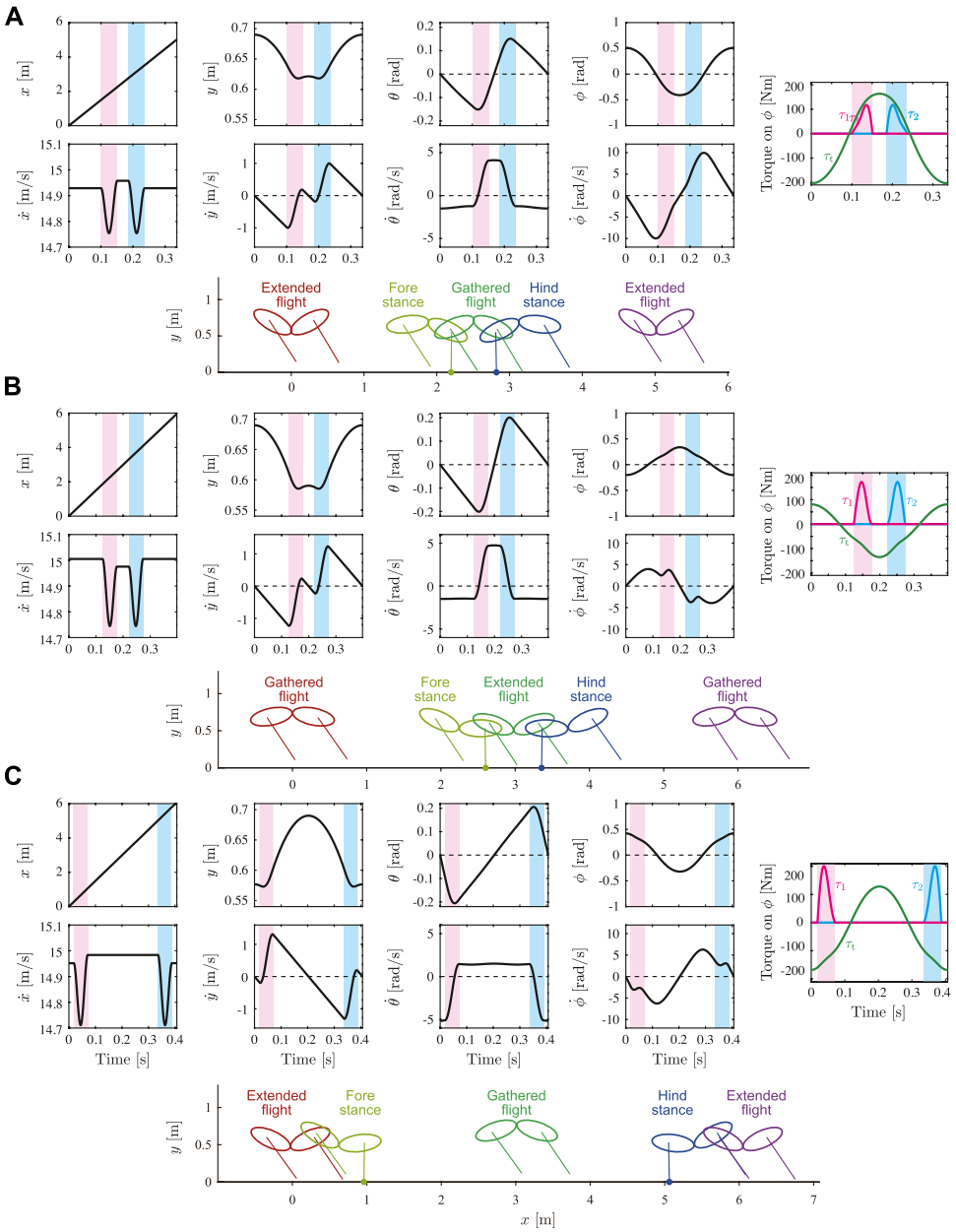

FIGURE 6 | Time profiles and snapshots of typical solutions for y^* = 0.69 m. Snapshots illustrate state at mid-stance or mid-flight in each phase (see **Supplementary Movie**). **(A)** Solution in Branch 1 (Type EG, a in **Figure 5**) and **(B)** solution in Branch 2 (Type GE, b in **Figure 5**) for $\dot{\theta}^*$ = −1.5 rad/s. **(C)** Solution in Branch 2 (Type EG, c in **Figure 5**) for $\dot{\theta}^*$ = 1.5 rad/s. Red and blue shaded areas indicate stance phase of foreleg and hind-leg, respectively.

impulses, Branch 1 involves smaller absolute values than those of Branch 2.

Branch 2 has no stable solution and stable solutions were found only in Branch 1. **Figure 8E** shows the contour of the maximum eigenvalue of the linearized Poincaré map around the fixed point on the Poincaré section of Branch 1 projected onto the y^*-$\dot{\theta}^*$ plane. Only Types E, EG, and GE have stable solutions. No solutions were found in the white area. In addition, $\dot{\theta}^* < 0$ has a larger area where the maximum eigenvalue is smaller than 0.9 than $\dot{\theta}^* > 0$.

4 DISCUSSION

Cheetahs are the fastest land animals. Their galloping shows three characteristics: small fluctuations in the COM height and whole-body pitch angle, and notable spinal bending. In this study, to clarify the dynamic mechanisms underlying these characteristics, we constructed a simple model and numerically obtained periodic solutions. The obtained solutions were classified into six types with respect to their flight phase and the spine joint movement. Solutions of Types E and G involve single flight with double

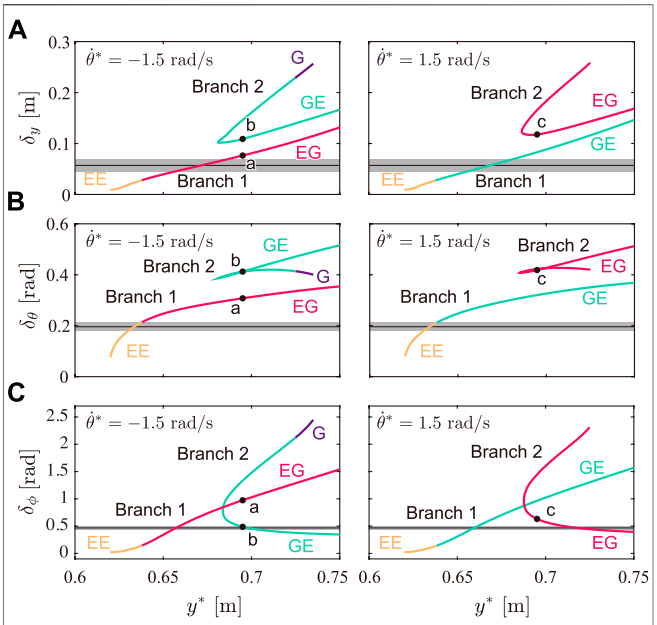

FIGURE 7 | Gait characteristics of solutions. Fluctuations of **(A)** COM height δ_y, **(B)** whole-body pitch angle δ_θ, and **(C)** spine joint angle δ_ϕ for y^* for solutions with $\dot{\theta}^* = \pm 1.5$ rad/s. Black dots (a, b, and c) indicate the solutions in **Figure 5A**. Black lines and grey areas show average values and standard errors, respectively, of eight strides of measured cheetah data.

stance, whose flight is extended and gathered, respectively. Solutions of Types EE and GG involve two flights without double stance, whose flights are both extended and both gathered, respectively. Solutions of Types EG and GE involve two flights without double stance, whose flights are extended and gathered like cheetahs. While the first and second flights are extended and gathered, respectively, for solutions of Type EG, they are gathered and extended for solutions of Type GE.

4.1 Comparison of Gait Characteristics and Performance Between Branches 1 and 2

The obtained periodic solutions were classified into two branches: Branch 1 and Branch 2 (Branch 2 has two solutions for each y^*, as shown in **Figure 5A**). We compared the three characteristics in cheetah galloping between the solutions of Branches 1 and 2. The solutions of Branch 1 involved smaller fluctuations of the COM height δ_y and whole-body pitch angle δ_θ than those of both solutions of Branch 2 for each y^*, as shown in **Figures 7A,B**, respectively. Moreover, the solutions of Branch 1 were obtained over a wider range of apex COM height y^* than the solutions of Branch 2, as shown in **Figure 5A**. Therefore, the solutions of Branch 1 showed smaller vertical movement of the COM and whole-body pitching movement than the solutions of Branch 2, which is consistent with cheetah galloping. Furthermore, the two solutions of Branch 2 for each y^* involve larger and smaller fluctuations of the spine joint angle δ_ϕ than that of the solution of Branch 1 (**Figure 7C**). However, the solutions of Branch 2 with larger δ_ϕ involve larger δ_y (**Figure 7A**), smaller average horizontal velocity $\bar{v}$ (**Figure 8A**), and larger net impulse p (**Figure 8B**) than those of the other solutions, which indicates that although the solutions involve notable spinal bending, they do not show the characteristics of cheetah galloping (this mechanism is discussed in the next section). The solutions of Branch 1 have sufficiently larger δ_ϕ than the solutions of

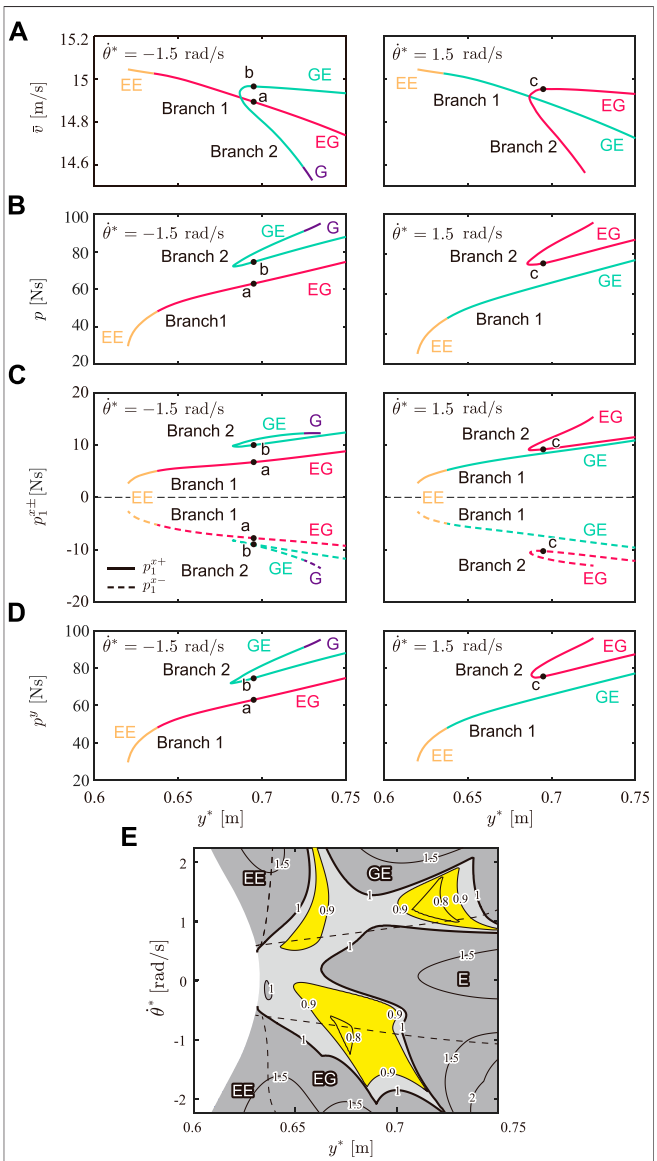

FIGURE 8 | Gait performance of solutions. **(A)** Averaged horizontal velocity $\bar{v}$, **(B)** net impulse p, **(C)** horizontal impulses p_1^{x+} and p_1^{x-}, and **(D)** vertical impulse p^y for y^* of solutions with $\dot{\theta}^* = \pm 1.5$ rad/s. Black dots (a, b, and c) indicate the solutions in **Figure 5A**. **(E)** Contour of maximum eigenvalue of solutions in Branch 1. Dotted lines indicate boundaries of solution types. No solution was found in white area. When maximum eigenvalue is less than 1, solution is stable (light grey and yellow areas). Dark grey areas indicate unstable solutions, which have maximum eigenvalues greater than 1. Yellow areas indicate stable solutions with maximum eigenvalue less than 0.9.

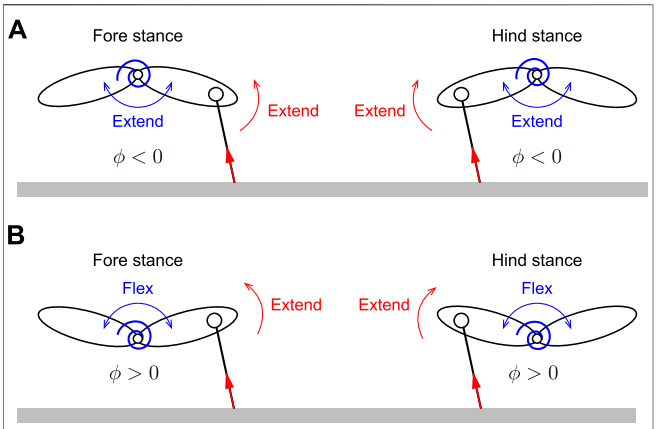

FIGURE 9 | Contribution of body spring and ground reaction force to spine joint dynamics. **(A)** Both body spring and ground reaction force extend spine joint in solutions of Branch 1. **(B)** While body spring flexes spine joint, ground reaction force extends spine joint in solutions of Branch 2.

Branch 2 with smaller δ_ϕ, which implies that the solutions of Branch 1 also show the third characteristic (large spine bending movement) well. Therefore, the solutions of Branch 1 clearly show the characteristics of cheetah galloping than the solutions of Branch 2.

We next compared the three gait performances between the solutions of Branches 1 and 2. Although the solution of Type EE in Branch 1 involves the maximum average horizontal velocity $\bar{v}$ (**Figure 8A**), the solutions of Branch 1 have larger $\bar{v}$ than the solutions of Branch 2, even when we focus on the solutions of Types EG and GE, which involve two types of flight phase in one gait cycle, similar to cheetah galloping. Furthermore, the solutions of Branch 1 have smaller net impulse p from the ground reaction force than the solutions of Branch 2 (**Figure 8B**). Moreover, while Branch 1 involves stable solutions (**Figure 8E**), Branch 2 does not. These results show that the solutions in Branch 1, which show the characteristics of cheetah galloping well, lead to better gait performance than those of Branch 2.

4.2 Mechanisms for Different Characteristics and Performance Between Branches 1 and 2

An important difference between the solutions of Branches 1 and 2 appears in the directions of the joint torque τ_t on the spine joint ϕ by the body spring, and the moments τ_1 and τ_2 on ϕ from the ground reaction forces of Legs 1 and 2, respectively. τ_1 and τ_2 extend the spine joint regardless of Branch (**Figures 6**, **9**). In contrast, the direction of τ_t depends on the Branch. Specifically, while τ_t extends the spine joint in the stance phase of both the foreleg and hind-leg in the solutions of Branch 1 because $\phi < 0$ (**Figure 6A**), it bends in the solutions of Branch 2 because $\phi > 0$ (**Figures 6B,C**). Therefore, while the directions of τ_t and τ_i ($i = 1, 2$) are the same in the solutions of Branch 1, they are opposite in the solutions of Branch 2. This difference explains that the ground reaction forces enhance spinal movement in the solutions of Branch 1 whereas they prevent in the solutions of Branch 2. In addition, the opposite direction induced three peaks in $\dot{\phi}$ in the solutions of Branch 2 (**Figures 6B,C**).

Because of the different directions of the torque on the spine joint described above, while the body spring pushes the legs down in the solutions of Branch 2, it pulls the legs up in the solutions of Branch 1, which made the net impulse p of the solutions of Branch 2 larger than that of the solutions of Branch 1 (**Figure 8B**). Furthermore, the horizontal impulses $|p_1^{x-}|$ and p_1^{x+} of the solutions of Branch 2 are also larger than those of the solutions of Branch 1 (**Figure 8C**). The COM is decelerated by p_i^{x-} in the first half of the stance phase of Leg i ($i = 1, 2$) ($\gamma_i > 0$) and accelerated by p_i^{x+} in the second half of the stance phase ($\gamma_i < 0$). Because the solutions of Branch 2 have larger values of $|p_i^{x-}|$ and p_i^{x+} than the solutions of Branch 1, the COM of the solutions of Branch 2 undergoes greater deceleration and acceleration than that of the solutions of Branch 1. Therefore, even if the solutions of Branches 1 and 2 have the same horizontal velocity in the flight phases, the solutions of Branch 1 have a higher average horizontal velocity $\bar{v}$ than the solutions of Branch 2. Furthermore, the solutions of Branch 1 had a wider range of y^* than the solutions of Branch 2 (**Figure 5A**). When the total energy is identical, the decrease in potential energy leads to an increase in kinetic energy. When $\dot{\theta}^*$ is also identical, which results in the same rotational kinetic energy in the solutions of Branches 1 and 2, the solutions of Branch 1 can have more translational kinetic energy than the solutions of Branch 2, which results in higher $\bar{v}$. These explain why the solutions of Branch 1 involve higher average horizontal velocities than the solutions of Branch 2, although the solutions of Branch 1 involve smaller impulses from the ground reaction forces than the solutions of Branch 2. It has been also suggested that spinal movement enhances gait speed because it allows cheetahs to swing their limbs further and increase their stride length (Hildebrand, 1959, Hildebrand, 1961; English, 1980; Schilling and Hackert, 2006; Walter and Carrier, 2007).

The mechanism under which the solutions of Branch 1 showed the characteristics of cheetah galloping can be explained by the difference in the impulses between the solutions of Branches 1 and 2. When the model receives a large vertical impulse p^y, the model lifts off the ground with a large momentum in the y direction, which results in a large change in the COM height δ_y. Because the solutions of Branch 1 had a smaller vertical impulse p^y than the solutions of Branch 2 (**Figure 8D**), the solutions of Branch 1 involved a smaller δ_y than that of the solutions of Branch 2 (**Figure 7A**). Furthermore, in the solutions without a double stance phase (Types EE, EG, and GE), when the model receives a small impulse, the model lifts off the ground with a small angular momentum in the θ direction, which results in a small fluctuation of the whole-body pitch angle δ_θ. Therefore, because the solutions of Branch 1 had smaller impulses than the solutions of Branch 2, the solutions of Branch 1 involved smaller δ_θ than the solutions of Branch 2 (**Figure 7B**). When we focus on solutions with a double stance phase (Type G), δ_θ is smaller than that of the solution of Type GE of Branch 2 (**Figure 7B**), even when the solutions of Type G have larger impulse p than the solutions of Type GE of Branch 2 (**Figure 8B**). This is because the direction of moments from the

ground reaction forces on the forelegs and hindlegs are in opposite directions and these effects are canceled in the double stance phase. However, the δ_θ of the solutions of Branch 2 is still larger than that of the solutions of Branch 1 (**Figure 7B**) because p of the solutions of Branch 1 is smaller than that of the solutions of Branch 2 (**Figure 8B**).

Moreover, since both the body spring and ground reaction force generate moments to extend the spine joint in the solutions of Branch 1 (**Figure 9A**), spinal movement is enhanced and results in larger fluctuations of the spine joint angle δ_ϕ than those in the solutions of Branch 2 with smaller δ_ϕ (**Figure 7C**), where the moment from the ground reaction force prevents spinal movement (**Figure 9B**). Although spinal movement in the solutions of Branch 2 with a larger δ_ϕ is also prevented, they have larger δ_ϕ than the solutions of Branch 1. This is because while the spine bending in the solutions of Branch 2 with small δ_ϕ mainly appears in the stance phase, which is prevented by the ground reaction forces, the spine bending in the solutions of Branch 2 with large δ_ϕ appears in the flight phase, which is not prevented by ground reaction forces. However, the impulse of the solutions of Branch 2 with larger δ_ϕ is larger than that of the solutions of Branch 1 because the directions of torque from the body spring and ground reaction force are opposite, similar to the solutions of Branch 2 with smaller δ_ϕ.

From the discussion above, we revealed the mechanism of why the solutions of Branch 1, which showed the characteristics of cheetah galloping well, achieved better gait performances than those of the solutions of Branch 2. Specifically, the ground reaction forces of the solutions of Branch 1 were reduced through the spine bending movement, which results in high-speed and stable locomotion, even they involved small impulses on the legs.

4.3 Why Cheetahs Use Type EG

The cheetah gallop is also characterized by involving two types of flights: extended and gathered (Hildebrand, 1989). In their galloping, the forelegs touch the ground after extended flight, and the gathered flight follows the liftoff of the forelegs. The hindlegs touch the ground after gathered flight, and extended flight follows the liftoff of the hindlegs (**Figure 1**). Therefore, the solutions of Type EG correspond to the cheetah galloping, as shown in **Figure 4**.

We obtained not only the solutions of Type EG but also the solutions of Type GE for both Branches 1 and 2, which also have two different flights, but in which the foreleg touches the ground after the gathered flight and the foreleg touches the ground after the extended flight (**Figure 4**). Although the solutions of Types E, G, EE were also found, no solution of only Type GG was found. This is consistent with Kamimura et al. (2021), where a simple model did not have any solutions of Type GG when $d > 0$, where d is the distance between the COM of the body and leg joint (**Figure 2**). When we compare the solutions of Types EG and GE of Branch 1, although there is no significant difference in the maximum values of the horizontal velocity $\bar{v}$ (**Figure 8A**), the net impulse p of the solutions of Type EG was slightly smaller than that of the solutions of Type GE (**Figure 8B**). When we focus on the gait stability, although the solutions of Type GE have a larger stable area for $y^\star$ and $\dot{\theta}^\star$ than that of the solutions of Type EG, the solutions of Type EG have a larger area, where the maximum eigenvalue is less than 0.9, and are more stable than the solutions of Type GE (**Figure 8E**). These results suggest a reason why cheetahs prefer a gait corresponding to the solutions of Type EG over a gait corresponding to the solutions of Type GE.

4.4 Limitations and Future Works

As shown in the solutions of Branch 1 (**Figure 6**), while $\dot{x}$ is larger after the liftoff of the foreleg than that before the touchdown of the foreleg, it is smaller after the liftoff of the hind-leg than that before the touchdown of the hind-leg. This indicates that the forelegs and hindlegs contribute to acceleration and deceleration, respectively. In contrast, it is reported that the forelegs and hindlegs contribute to deceleration and acceleration, respectively, in actual cheetah galloping (Bertram and Gutmann, 2009). Since $\dot{x}$ is smaller after the liftoff of the foreleg than that before the touchdown of the foreleg and it is larger after the liftoff of the hind-leg than that before the touchdown of the hind-leg, the solutions of Branch 2 are rather consistent with cheetah galloping from the viewpoint of the roles of acceleration and deceleration of the forelegs and hindlegs. This discrepancy is possibly because our model neglected the mass of the legs and the asymmetry of the fore and hind parts of the body. We would like to consider these effects in future research.

Furthermore, the solutions of Branch 1, which show three characteristics of cheetah galloping, have the same magnitude of flexion and extension of the spine (**Figure 6**). In contrast, the spinal hyperextension caused by the hind leg extension is inhibited by the epaxial muscles, which prevents the loss of propulsive forces by the hind legs in cheetahs (English, 1980; Wada et al., 2010). In addition, the hyperextension of the spinal column is prevented by the spinous processes. This discrepancy is mainly because our model has the same stiffness for the flexion and extension in the body spring, which does not prevent the hyperextension of the spine unlike the epaxial muscles and spinal processes of actual cheetahs. Moreover, although we assumed that the body spring is at the equilibrium position when the fore and hind bodies are in a straight line, the spine of actual cheetahs is supposed to be at the neutral position when the spine is slightly flexed. In future research, we would like to investigate the effects of such asymmetry properties.

Although galloping is characterized by different foot-contact timings between four legs, our model focused only on different foot-contact timings between the fore and hind legs. Different foot-contact timings between the left and right legs influence the gait stability and performances. In future research, we would like to improve our model to investigate the dynamical effects of different foot-contact timings between four legs on quadrupedal galloping.

Furthermore, although our model does not have any actuator or dissipation, actual cheetahs lose energy through collisions and inject energy via muscles. Moreover, trunk muscles work

effectively during acceleration. In future research, we also would like to incorporate these effects to our model to improve the understanding of the mechanism of cheetah galloping.

DATA AVAILABILITY STATEMENT

The raw data supporting the conclusion of this article will be made available by the authors, without undue reservation.

AUTHOR CONTRIBUTIONS

TK, SA, and FM contributed to the design of this study. TK and KS conducted the numerical simulation and analysis in consultation with SA, YH, NW, KT, AS, and FM. TK and SA wrote the manuscript and all the authors reviewed and approved it.

FUNDING

This study was supported in part by JSPS KAKENHI Grant Numbers JP20K22392, JP21K14104, and JP20H00229; and JST FOREST Program Grant Number JPMJFR2021.

SUPPLEMENTARY MATERIAL

The Supplementary Material for this article can be found online at: https://www.frontiersin.org/articles/10.3389/fbioe.2022.825638/full#supplementary-material

REFERENCES

Adachi, M., Aoi, S., Kamimura, T., Tsuchiya, K., and Matsuno, F. (2020). Body Torsional Flexibility Effects on Stability during Trotting and Pacing Based on a Simple Analytical Model. *Bioinspir. Biomim.* 15, 055001. doi:10.1088/1748-3190/ab968d

Alexander, R. M. (1988). Why Mammals Gallop. *Am. Zool* 28, 237–245. doi:10.1093/icb/28.1.237

Ambe, Y., Aoi, S., Nachstedt, T., Manoonpong, P., Wörgötter, F., and Matsuno, F. (2018). Simple Analytical Model Reveals the Functional Role of Embodied Sensorimotor Interaction in Hexapod Gaits. *PLOS ONE* 13, e0192469. doi:10.1371/journal.pone.0192469

Aoi, S., Manoonpong, P., Ambe, Y., Matsuno, F., and Wörgötter, F. (2017). Adaptive Control Strategies for Interlimb Coordination in Legged Robots: A Review. *Front. Neurorobot.* 11, 39. doi:10.3389/fnbot.2017.00039

Aoi, S., Ohashi, T., Bamba, R., Fujiki, S., Tamura, D., Funato, T., et al. (2019). Neuromusculoskeletal Model that Walks and Runs across a Speed Range with a Few Motor Control Parameter Changes Based on the Muscle Synergy Hypothesis. *Sci. Rep.* 9, 369. doi:10.1038/s41598-018-37460-3

Bertram, J. E. A., and Gutmann, A. (2009). Motions of the Running Horse and Cheetah Revisited: Fundamental Mechanics of the Transverse and Rotary Gallop. *J. R. Soc. Interf.* 6, 549–559. doi:10.1098/rsif.2008.0328

Blickhan, R., and Full, R. (1993). Similarity in Multilegged Locomotion: Bouncing like a Monopode. *J. Comp. Physiol. A.* 173, 509–517. doi:10.1007/bf00197760

Cao, Q., and Poulakakis, I. (2013). Quadrupedal Bounding with a Segmented Flexible Torso: Passive Stability and Feedback Control. *Bioinspir. Biomim.* 8, 046007. doi:10.1088/1748-3182/8/4/046007

Chen, J., San, H., Wu, X., Zhou, C., Qi, M., and Wang, L. (2019). Gait Regulation of a Bionic Quadruped Robot with Antiparallelogram Leg Based on CPG Oscillator. *Complexity* 2019, 1–11. doi:10.1155/2019/5491298

English, A. W. (1980). The Functions of the Lumbar Spine during Stepping in the Cat. *J. Morphol.* 165, 55–66. doi:10.1002/jmor.1051650106

Farley, C. T., Glasheen, J., and McMahon, T. A. (1993). Running Springs: Speed and Animal Size. *J. Exp. Biol.* 185, 71–86. doi:10.1242/jeb.185.1.71

Fujiki, S., Aoi, S., Funato, T., Sato, Y., Tsuchiya, K., and Yanagihara, D. (2018). Adaptive Hindlimb Split-belt Treadmill Walking in Rats by Controlling Basic Muscle Activation Patterns via Phase Resetting. *Sci. Rep.* 8, 17341. doi:10.1038/s41598-018-35714-8

Fukuhara, A., Koizumi, Y., Baba, T., Suzuki, S., Kano, T., and Ishiguro, A. (2021). Simple Decentralized Control Mechanism that Enables Limb Adjustment for Adaptive Quadruped Running. *Proc. R. Soc. B Biol. Sci.* 288, 20211622. doi:10.1098/rspb.2021.1622

Fukuhara, A., Koizumi, Y., Suzuki, S., Kano, T., and Ishiguro, A. (2020). Decentralized Control Mechanism for Body-Limb Coordination in Quadruped Running. *Adaptive Behav.* 28, 151–164. doi:10.1177/1059712319865180

Full, R. J., and Koditschek, D. E. (1999). Templates and Anchors: Neuromechanical Hypotheses of Legged Locomotion on Land. *J. Exp. Biol.* 202, 3325–3332. doi:10.1242/jeb.202.23.3325

Gan, Z., Wiestner, T., Weishaupt, M. A., Waldern, N. M., and David Remy, C. (2016). Passive Dynamics Explain Quadrupedal Walking, Trotting, and Tölting. *J. Comput. Nonlinear. Dyn.* 11, 0210081–2100812. doi:10.1115/1.4030622

Gan, Z., Jiao, Z., and Remy, C. D. (2018). On the Dynamic Similarity between Bipeds and Quadrupeds: a Case Study on Bounding. *IEEE Robot. Autom. Lett.* 3, 3614–3621. doi:10.1109/lra.2018.2854923

Grohé, C., Lee, B., and Flynn, J. J. (2018). Recent Inner Ear Specialization for High-Speed Hunting in Cheetahs. *Sci. Rep.* 8, 2301. doi:10.1038/s41598-018-20198-3

Hildebrand, M. (1961). Further Studies on Locomotion of the Cheetah. *J. Mammalogy* 42, 84–91. doi:10.2307/1377246

Hildebrand, M. (1959). Motions of the Running Cheetah and Horse. *J. Mammalogy* 40, 481–495. doi:10.2307/1376265

Hildebrand, M. (1989). The Quadrupedal Gaits of Vertebrates. *Bioscience* 39, 766–775. doi:10.2307/1311182

Hudson, P. E., Corr, S. A., and Wilson, A. M. (2012). High Speed Galloping in the Cheetah (*Acinonyx Jubatus*) and the Racing Greyhound (*Canis familiaris*): Spatio-Temporal and Kinetic Characteristics. *J. Exp. Biol.* 215, 2425–2434. doi:10.1242/jeb.066720

Ichikawa, H., Matsuo, T., Haiya, M., Higurashi, Y., and Wada, N. (2018). Gait Characteristics of Cheetahs (*Acinonyx Jubatus*) and Greyhounds (*Canis lupus Familiaris*) Running on Curves. *Mammal Study* 43, 199–206. doi:10.3106/ms2017-0089

Kamimura, T., Ambe, Y., Aoi, S., and Matsuno, F. (2015). Body Flexibility Effects on Foot Loading Based on Quadruped Bounding Models. *Artif. Life Robotics* 20, 270–275. doi:10.1007/s10015-015-0223-z

Kamimura, T., Aoi, S., Higurashi, Y., Wada, N., Tsuchiya, K., and Matsuno, F. (2021). Dynamical Determinants Enabling Two Different Types of Flight in Cheetah Gallop to Enhance Speed through Spine Movement. *Sci. Rep.* 11, 9631. doi:10.1038/s41598-021-88879-0

Kamimura, T., Aoi, S., Tsuchiya, K., and Matsuno, F. (2018). Body Flexibility Effects on Foot Loading in Quadruped Bounding Based on a Simple Analytical Model. *IEEE Robot. Autom. Lett.* 3, 2830–2837. doi:10.1109/lra.2018.2842925

Polet, D. T. (2021). The murphy Number: How Pitch Moment of Inertia Dictates Quadrupedal Walking and Running Energetics. *J. Exp. Biol.* 224, jeb228296. doi:10.1242/jeb.228296

Pouya, S., Khodabakhsh, M., Spröwitz, A., and Ijspeert, A. (2017). Spinal Joint Compliance and Actuation in a Simulated Bounding Quadruped Robot. *Auton. Robot* 41, 437–452. doi:10.1007/s10514-015-9540-2

Raibert, M. (1986). *Legged Robots that Balance*. Cambridge: MIT Press.

Ruina, A., Bertram, J. E. A., and Srinivasan, M. (2005). A Collisional Model of the Energetic Cost of Support Work Qualitatively Explains Leg Sequencing in Walking and Galloping, Pseudo-elastic Leg Behavior in Running and the Walk-To-Run Transition. *J. Theor. Biol.* 237, 170–192. doi:10.1016/j.jtbi.2005.04.004

Schilling, N., and Hackert, R. (2006). Sagittal Spine Movements of Small Therian Mammals during Asymmetrical Gaits. *J. Exp. Biol.* 209, 3925–3939. doi:10.1242/jeb.02400

Swanstrom, M. D., Zarucco, L., Hubbard, M., Stover, S. M., and Hawkins, D. A. (2005). Musculoskeletal Modeling and Dynamic Simulation of the Thoroughbred Equine Forelimb during Stance Phase of the Gallop. *J. Biomech. Eng.* 127, 318–328. doi:10.1115/1.1865196

Tanase, M., Ambe, Y., Aoi, S., and Matsuno, F. (2015). A Galloping Quadruped Model Using Left-Right Asymmetry in Touchdown Angles. *J. Biomech.* 48, 3383–3389. doi:10.1016/j.jbiomech.2015.06.003

Toeda, M., Aoi, S., Fujiki, S., Funato, T., Tsuchiya, K., and Yanagihara, D. (2019). Gait Generation and its Energy Efficiency Based on Rat Neuromusculoskeletal Model. *Front. Neurosci.* 13, 1337. doi:10.3389/fnins.2019.01337

Usherwood, J. R., and Self Davies, Z. T. (2017). Work Minimization Accounts for Footfall Phasing in Slow Quadrupedal Gaits. *eLife* 6, e29495. doi:10.7554/eLife.29495

Usherwood, J. R. (2020). An Extension to the Collisional Model of the Energetic Cost of Support Qualitatively Explains Trotting and the Trot-Canter Transition. *J. Exp. Zool.* 333, 9–19. doi:10.1002/jez.2268

Wada, N. (2011). The Mechanism of the Cheetah's Run. *Annu. Meet. Mammalogical Soc. Jpn. [In Japanese]* 2011, 95–101.

Wada, Y., Goto, M., Sano, Y., Hosoido, T., and Wada, N. (2010). The Polysynaptic Pathways from the Low Threshold Cutaneous Afferents of the Trunk to Motoneurons Innervating Hindlimb Muscles in the Spinal Cat. *J. Vet. Med. Sci.* 72, 73–76. doi:10.1292/jvms.09-0233

Walter, R. M., and Carrier, D. R. (2007). Ground Forces Applied by Galloping Dogs. *J. Exp. Biol.* 210, 208–216. doi:10.1242/jeb.02645

Wang, C., Zhang, T., Wei, X., Long, Y., and Wang, S. (2017). Dynamic Characteristics and Stability Criterion of Rotary Galloping Gait with an Articulated Passive Spine Joint. *Adv. Robotics* 31, 168–183. doi:10.1080/01691864.2016.1256230

Yamada, T., Aoi, S., Adachi, M., Kamimura, T., Higurashi, Y., Wada, N., et al. (2022). Center of Mass Offset Enhances the Selection of Transverse Gallop in High-Speed Running by Horses: A Modeling Study. *Front. Bioeng. Biotechnol.* 10, 825157. doi:10.3389/fbioe.2022.825157

Yesilevskiy, Y., Yang, W., and Remy, C. D. (2018). Spine Morphology and Energetics: How Principles from Nature Apply to Robotics. *Bioinspir. Biomim.* 13, 036002. doi:10.1088/1748-3190/aaaa9e

Conflict of Interest: The authors declare that the research was conducted in the absence of any commercial or financial relationships that could be construed as a potential conflict of interest.

Publisher's Note: All claims expressed in this article are solely those of the authors and do not necessarily represent those of their affiliated organizations, or those of the publisher, the editors and the reviewers. Any product that may be evaluated in this article, or claim that may be made by its manufacturer, is not guaranteed or endorsed by the publisher.

frontiers | Frontiers in Veterinary Science

ORIGINAL RESEARCH
published: 21 April 2022
doi: 10.3389/fvets.2022.836043

New Insights for the Design of Bionic Robots: Adaptive Motion Adjustment Strategies During Feline Landings

*Datao Xu[1], Huiyu Zhou[1,2], Xinyan Jiang[1], Shudong Li[1], Qiaolin Zhang[1], Julien S. Baker[3] and Yaodong Gu[1]**

[1] Faculty of Sports Science, Ningbo University, Ningbo, China, [2] School of Health and Life Sciences, University of the West of Scotland, Paisley, United Kingdom, [3] Department of Sport and Physical Education, Hong Kong Baptist University, Kowloon, Hong Kong SAR, China

Felines have significant advantages in terms of sports energy efficiency and flexibility compared with other animals, especially in terms of jumping and landing. The biomechanical characteristics of a feline (cat) landing from different heights can provide new insights into bionic robot design based on research results and the needs of bionic engineering. The purpose of this work was to investigate the adaptive motion adjustment strategy of the cat landing using a machine learning algorithm and finite element analysis (FEA). In a bionic robot, there are considerations in the design of the mechanical legs. (1) The coordination mechanism of each joint should be adjusted intelligently according to the force at the bottom of each mechanical leg. Specifically, with the increase in force at the bottom of the mechanical leg, the main joint bearing the impact load gradually shifts from the distal joint to the proximal joint; (2) the hardness of the materials located around the center of each joint of the bionic mechanical leg should be strengthened to increase service life; (3) the center of gravity of the robot should be lowered and the robot posture should be kept forward as far as possible to reduce machine wear and improve robot operational accuracy.

Keywords: feline landing, bionic robots, deep learning method, finite element analysis, bionic engineering

OPEN ACCESS

Edited by:
John R. Hutchinson, Royal Veterinary College (RVC), United Kingdom

Reviewed by:
Dusan Radivoje Mitic, University of Belgrade, Serbia
Shinya Aoi, Kyoto University, Japan

***Correspondence:**
Yaodong Gu
guyaodong@nbu.edu.cn

Specialty section:
This article was submitted to Veterinary Neurology and Neurosurgery, a section of the journal Frontiers in Veterinary Science

Received: *15 December 2021*
Accepted: *09 March 2022*
Published: *21 April 2022*

Citation:
Xu D, Zhou H, Jiang X, Li S, Zhang Q, Baker JS and Gu Y (2022) New Insights for the Design of Bionic Robots: Adaptive Motion Adjustment Strategies During Feline Landings. Front. Vet. Sci. 9:836043. doi: 10.3389/fvets.2022.836043

INTRODUCTION

Animal species have inspired and helped to develop much of contemporary human technology. Without the inspiration obtained through animal models, the world's naturalistic progress would be impossible. Bionic robots are products that have developed and combined the characteristics of animals and human technology. Bionic robots' mobility mechanisms are often built on the bionics principle, replicating animal motion sections of the body or motion models while walking or running (1). Bionic robot design has gained momentum in recent years because robots have the potential to play a major role in replacing humans in difficult working environments, engage in rescue missions, space exploration, and so forth (2–5). Although wheeled and tracked robots move effectively on flat ground, the majority of bionic robots are capable of working in complicated and crowded terrain. Therefore, robots with legs can replicate humans and animals and are more adaptable for use in most situations. Previous studies have illustrated that the present legged

robots include: a lizard bionic robot (6), a hexapod bionic robot (7), and an eight-legged bionic robot (8). It is worth mentioning that a leopard bionic robot devised by the Massachusetts Institute of Technology has a running speed that can reach 22 km/h (9). The previous studies used bionic mechanisms in the design of their robots, but their attention still focused on movement over flat ground. The benefits of bionic robots are that they are adapted to a variety of challenging terrains, such as debris rescue, geological exploration, and military reconnaissance. A robot incorporating jumping ability can jump to a level several times higher than its height (10); this function provides this jumping robot with excellent ability to move in complicated surroundings and compares well with the flea robot (11) and a miniature jumping robot (12).

The statement that it is easier to climb up the mountain than go down applies to this scenario. The design of the jumping robot did consider the ability for moving on complicated terrain but neglected to consider how the jumping robot returned to the initial jumping position. Quadrupeds have evolved a variety of distinct biological structures during the last million years, allowing them to adapt to a variety of habitats and terrains (13). As a typical quadruped, felines are well-known for their innate athletic abilities, particularly during jumping and landing (14, 15). Cats, because of their landing buffering mechanisms, may land safely from high locations without injuring themselves. When we consider the animal's capacity to land safely from great heights, the phrase "cats have nine lives" seems appropriate. Several examples have been documented in which the fatality rate of cats recorded when falling from great heights is $<10\%$ (16). Vnuk further went on to discover that when a feline fell from a great height, there was a 96.5% chance of survival. This intriguing phenomenon has initiated much scholarly curiosity. The cat can deal with the impact load of the ground easily. This can reduce joint injury and joint driving burden because of the cat's unique landing mechanism. The cats' forelimbs as the initial contact point for cats when performing a landing is one of the most important parts of the feline body during the landing phase. Previous studies have indicated that the forelimbs are important when performing a landing phase, as they absorb more weight, help with maneuvering, and are active during deceleration (17). Therefore, exploring the landing mechanism of each joint when a cat lands from different heights, provides new insights for the design of bionic robots.

Cats often jump from high levels, and their joints absorb several times their body weight in impact forces. Conventional biomechanical experiments (such as animal experiments, *in vitro* cadaveric specimens, etc.) often cannot fully reflect the real biomechanical changes of internal bones, but three-dimensional finite element analysis (FEA) can simulate the complex mechanical environment in a mathematical form and provide internal mechanical information (18, 19). FEA facilitates the measurement of external forces and the analysis of internal stresses during the experimental investigation and provides a better understanding of the cat's special landing mechanism. This knowledge has implications for the design of bionic robots, particularly during jumping and landing. In addition, a limiting factor in the construction of biomechanical models is the inability to analyze waveform data effectively, especially when different load factors affect the derived kinetic variables. Principal component analysis (PCA) is more sensitive than traditional parameter-based analysis techniques in detecting differences in kinematic and kinetic waveforms (20, 21). More and more studies are using PCA in time series datasets such as motion posture, gait, and ground reaction force (GRF), because PCA allows the detection of time-varying coordinated correlation patterns (22–25). Therefore, PCA can be used to extract the main characteristics of the GRF and motion posture of cats during landing, which can not only determine the potential relationship between variables but also reveal the main findings within the data set.

Recently, machine learning methods focusing on time series data analysis have been gradually applied in the field of motion analysis (such as support vector machine, artificial neural network, multivariable statistical analysis) (26–30). At the same time, the progress of motion capture technology, mechanical sensing technology, and signal processing technology makes biomechanical data acquisition diversified and refined, which provides the prerequisite for the application of big data-driven machine learning methods in the field of biomechanics (22, 28, 31). For example, artificial neural networks have been applied to gait pattern recognition and feature classification and realized personalized recognition and judgment of human gait patterns (27, 30, 32). Machine learning approaches have shown the potential to solve motion-related biomechanical problems and provide new insights into complex modeling systems. However, they all have the same problem of being a black box that does not provide any information about what makes the decisions (33, 34). The main reason is that all kinds of mappings in these models have non-linear characteristics, which leads to the lack of interpretability of classification prediction results (35). In the view of applications related to pattern recognition, the simple answers of "yes" or "no" sometimes have little or limited value because this does not validate classification decisions. Therefore, layer-wise relevance propagation (LRP) technology was proposed to solve the problem of lack of interpretability (35). LRP is a technology used to identify important relevance through backward propagation in neural networks, which measures the contribution of each input variable to the overall predicted outcomes. LRP has been successfully applied to many classification and recognition tasks in different scenarios, such as text, image, and pattern recognition (32, 36, 37). Therefore, the application of LRP in cat landing pattern recognition can improve the overall transparency of the classifier and make the classification results interpretable, thus providing reliable applied biomechanical diagnostic results.

Therefore, the purpose of this study was to investigate the biomechanical characteristics of a cat landing from different heights and provide new insights into bionic robot design based on the research findings and the needs of bionic engineering. According to previous studies, the segment parameters of the rigid body where the joints in the claw are far smaller than those of the rigid body where the wrist, elbow, and shoulder joints are (38), so this study only investigated the wrist, elbow, and shoulder joints in the inverse kinetics model. Specifically, this work was

performed to investigate the adaptive motion adjustment strategy of the cat forelimb at each joint (wrist, elbow, and shoulder) during the landing phase using a machine learning algorithm and FEA. The first objective was to recognize and classify the kinematic and kinetic patterns of a cat's forelimbs when landing from different heights using the deep neural network (DNN) classification model and then to perform interpretability analysis of the classification results using LRP technology calculating the relevance score. The second objective was to reconstruct the waveform data (GRF and sagittal joint angle) during landing based on PCA, then extract the force and angle at the end of the landing phase (maximum elbow flexion) into the finite element model to analyze the stress distribution of the cat right forelimb bone. Finally, the aim of exploring the adaptive motion adjustment strategies of each joint during landing from different heights was achieved by combining the above results.

MATERIALS AND METHODS

Since the FEA can only investigate the stress distribution of the cat forelimb bone during the landing, and cannot discuss the biomechanical characteristics of the cat during the whole landing phase, this study combined the inverse kinetics model and the deep learning method to achieve the purpose of exploring the biomechanical characteristics of the whole landing phase of the cat, as well as the coordination strategy of each joint of the cat's forelimb when landing at different heights. Therefore, to more comprehensively explore the biomechanical characteristics of cat landing, the current study was mainly carried out from two aspects: (1) PCA and FEA; (2) inverse kinetics and deep learning method (DNN and LRP). Firstly, the GRF and joint kinematics (sagittal joint angle of wrist elbow shoulder) were collected when the cat landed from four different heights (60, 80, 100, and 120 cm). The landing phase was determined as the initial contact point to maximum elbow flexion. Then, the next steps are mainly divided into two steps. Step 1: Using PCA to reconstruct the data waveform of the three-direction GRF (anterior/posterior, medial/lateral, and vertical) and sagittal joint angle (wrist, elbow, and shoulder), the reconstructed waveform was the data waveform of the whole landing phase. Then, the GRF and joint angle data values of each landing height at the time point of the end of the landing phase (maximum elbow flexion) are extracted from the reconstructed waveform and substituted into the finite element model to investigate the stress distribution of the cat's right forelimb bone. Step 2: Three directions GRF (anterior/posterior, medial/lateral, and vertical) and sagittal joint angle (wrist, elbow, and shoulder) during the whole landing phase were taken as the imported data and then, the inverse kinetics to calculate the joint moment was used. After that, the data sets of each joint angle and moment during the whole landing phase were imported into the deep learning model to explore the landing strategies when cats land from different heights.

Animals

A total of 60 healthy adult Chinese domesticated cats (aged 2.85 $\pm$ 0.49 years, body mass 4.32 $\pm$ 0.53 kg) were recruited *via* written consent from a local breeder for voluntary participation in this study. Prior to data collection, a full clinical examination was performed to ensure that there were no health issues that could impact the result of this study. Finally, a total of 56 subject cats were included in the experiment. A cat of moderate size, aged 3 years and weighing 4 kg, was selected from 56 cats. The cat was photographed by CT. The CT scan was obtained and performed by a qualified veterinarian in a pet hospital. Before obtaining the CT data, the cat was examined by a veterinarian to make sure there were no health problems or foot injuries. This study was approved by the Animal Care and Use Ethics Committee of Ningbo University (NBUAEC20200621).

Experimental Protocol and Procedures

All tests were performed in the biomechanics laboratory at Ningbo University Research Academy of Grand Health. A force platform (Kistler, Switzerland) was set at a 1,000 Hz sampling frequency for GRF data collection when performing the landing task. Two high-speed cameras (Fastcam SA3, Photron, Japan) were set at 1,000 Hz and used for kinematic data collection during each landing task.

Before data collection, all cats were fully familiarized with the environment (test room), using toys and food to divert their attention. Before the formal start of the experiment, to ensure the smooth progress of the experiment, the cat was brought to the laboratory by its owner to tempt the cat with food or toys to complete the experimental process. This process lasted for 1 h each time, three times a week until the cat could be enticed by food and toys and could accurately jump to the designated area. The height of 0.6, 0.8, 1, and 1.2 m was taken as the heights selected for this experiment. Each cat was asked to jump from four heights, and 10 groups of data were collected for each height. A total of 40 groups of data were obtained from each one of the cats. To avoid cat fatigue, only one height was selected for 10 groups of data collection every test day.

The cat owner encouraged the cat to sit in a squat position on the jumping platform while the height of the table was adjusted to the specific required height. There was a 5-min break between each landing task to avoid inaccurate data collection caused by fatigue. There was no apparent tilt of the body, and the cat's head and body were facing forward when the cat landed. The experiment was considered successful when the cat's forelimb landed in the designated area and the cat continued to move away from the designated area, with no injuries or adverse reactions after the experiment.

Figure 1A shows that two high-speed cameras were placed at the diagonal level of the force plate at a distance of 5 m from the landing target area, forming an $\sim$45° angle between the principal optical axis of the two cameras. To build the space coordinate, three-dimensional (3-D) coordinates were placed on the center of the force platform. **Figure 1B** illustrates the cat landing from a ready position to initiate contact in the landing target area. **Figure 1D** shows the placement of a red marker point. The red marker point was used to ensure each one of the skeleton and joint positions for further data processing.

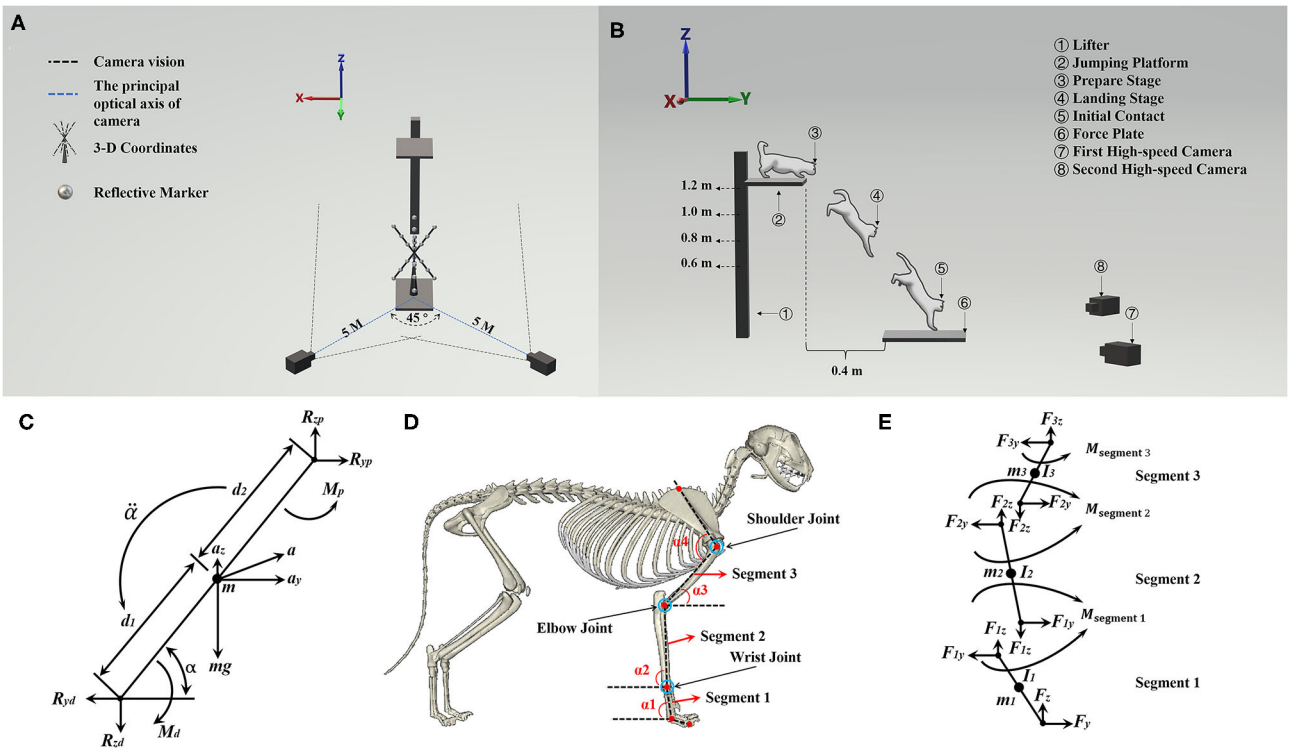

FIGURE 1 | (A) Illustration of the position of two high-speed cameras and 3-D coordinates. **(B)** Illustration of cat landing procedure from the ready position to initial forelimbs contacting the ground; it also shows the position between the jumping platform and the force plate. **(C)** The complete free-body diagram of a single forelimb segment, shows reaction and gravitational forces, net moments of force, and all linear and angular accelerations. **(D)** Illustration of the position of red marker points on the forelimbs of cats (α_1, α_2, and α_3 were used to calculate the joint moment, α_4 is the shoulder joint angle), and the red marker point with a blue circle shows the bone marking the position of the wrist, elbow, and shoulder joint. **(E)** Freebody diagrams of the three rigid links, which include the joint reaction forces acting on each joint and the segment moment.

Data Collection and Processing

The vertical GRF > 10 N was used to define the force plate's initial contact point (39). From the first contact point until the second peak vertical GRF time point, the landing phase was determined as the initial contact point (0% landing phase) to maximum elbow flexion (100% landing phase). Butterworth low-pass filters were used to filter the GRF data (filter order: fourth-order zero-phase lag, cut-off frequency: 50 Hz) (40). SIMI°-Motion 7.50 (Simi Reality Motion Systems GmbH, Munich, Germany) 3-D motion analysis system was used to analyze the landing phase of cats. **Figure 1D** shows the location of each trajectory marker point in red which was used for analysis. Then, the wrist, elbow, and shoulder sagittal plane joint angles were taken as an output from SIMI°-Motion, and the Butterworth fourth-order low-pass filter with a cutoff frequency of 6 Hz was used to digitally filter the original joint angle data. Each landing height (60, 80, 100, and 120 cm) of each joint (wrist, elbow, shoulder) of sagittal plane joint angle data and each landing height (60, 80, 100, and 120 cm) of each direction (X-axis: lateral and medial GRF; Y-axis: anterior and posterior GRF; Z-axis: vertical GRF) of GRF data were expanded into 100 data point's curve by a self-written MATLAB script. Finally, the dataset of GRF and joint angle were input to MATLAB to run the Inverse Kinetics Algorithm and PCA.

Inverse Kinetics Algorithm

In this study, we investigated only the sagittal motion of cat landing, as the main motion of a cat on landing is in the sagittal plane (41, 42). Therefore, the GRF and joint angle of the wrist, elbow, and shoulder during the landing phase were taken as the imported data, and then the inverse kinetics algorithm to calculate the joint moment of the wrist, elbow, and shoulder was used. The Y-axis was defined as the anterior/posterior direction, and the Z-axis was defined as the vertical direction. The right forelimb of the cat was analyzed by splitting into three rigid links and considered as a rigid body model of planar link segment (arm: segment 1; forearm: segment 2; carpals: segment 3). At the same time, the segment parameters (segment mass, moment of inertia) were obtained based on the previous study (38), which combined the joint kinematics and GRF to calculate the joint moment based on the inverse kinetics (43). Each forelimb segment was assumed to act separately under a combination of gravity, joint reaction forces, and muscle moments. As shown

in **Figure 1C**, *Eq*. 1, *Eq*. 2, and *Eq*. 3 can be obtained based on **Figure 1C** (43):

$$\sum F_y = ma_y = R_{yp} - R_{yd} \tag{1}$$

$$\sum F_z = ma_z = R_{zp} - R_{zd} - mg \tag{2}$$

$$\sum M = M_p - M_d = I_0\ddot{\alpha} \tag{3}$$

where the F_y is the reaction forces in the Y-axis direction and the F_z is the reaction forces in the Z-axis direction; the m is the mass of segment; the a_y and a_z are the Y-axis and Z-axis components of acceleration of the center of mass (COM), respectively; M is the joint moment of the current segment; M_d and M_p are the distal and proximal joint moment of the segment, respectively; I_0 is the moment of inertia in the plane of movement; α is the angle of the segment in the plane of movement; $\ddot{\alpha}$ is the angular acceleration of the segment, and the arrow below the $\ddot{\alpha}$ is the direction of the $\ddot{\alpha}$. In **Figure 1C**, the R_{yp} and R_{zp} are the Y-axis and Z-axis direction proximal joint reaction force, and the R_{yd} and R_{zd} are the Y-axis and Z-axis direction distal joint reaction force.

The right forelimb of the cat was analyzed by splitting the forelimb into three rigid links (as shown in **Figures 1D,E**). The COM was set at the midpoint of each segment. Then, Eq. 4, Eq. 5, and Eq. 6 can be derived from Eq. 1, Eq. 2, and Eq. 3. Therefore, the joint moment in segment 2 (Eq. 7, Eq. 8, and Eq. 9) of the right forelimb can be calculated according to segment 1 (Eq. 4, Eq. 5, and Eq. 6), and segment 3 (Eq. 10, Eq. 11, and Eq. 12) of the right forelimb can be calculated according to segment 2 (Eq. 7, Eq. 8, and Eq.9̃).
For segment 1:

$$F_{1y} - F_y = m_1\left(-\frac{L_1}{2}\dot{\alpha}_1^2\cos\alpha_1 - \frac{L_1}{2}\ddot{\alpha}_1\sin\alpha_1\right) \tag{4}$$

$$F_{1z} - F_z - m_1g = m_1\left(-\frac{L_1}{2}\dot{\alpha}_1^2\sin\alpha_1 + \frac{L_1}{2}\ddot{\alpha}_1\cos\alpha_1\right) \tag{5}$$

$$M_{\text{segment 1}} + F_{1y}\frac{L_1}{2}\sin\alpha_1 - F_{1z}\frac{L_1}{2}\cos\alpha_1 + F_y\frac{L_1}{2}\sin\alpha_1 - F_z\frac{L_1}{2}\cos\alpha_1 = -I_1\ddot{\alpha}_1 \tag{6}$$

For segment 2:

$$F_{2y} - F_{1y} = m_2\left[-L_1\left(\dot{\alpha}_1^2\cos\alpha_1 + \ddot{\alpha}_1\sin\alpha_1\right) - \frac{L_2}{2}\left(\dot{\alpha}_2^2\cos\alpha_2 + \ddot{\alpha}_2\sin\alpha_2\right)\right] \tag{7}$$

$$F_{2z} - F_{1z} - m_2g = m_2\left[L_1\left(-\dot{\alpha}_1^2\sin\alpha_1 + \ddot{\alpha}_1\cos\alpha_1\right) + \frac{L_2}{2}\left(-\dot{\alpha}_2^2\sin\alpha_2 + \ddot{\alpha}_2\cos\alpha_2\right)\right] \tag{8}$$

$$M_{\text{segment 2}} - M_{\text{segment 1}} + F_{2y}\frac{L_2}{2}\sin\alpha_2 - F_{2z}\frac{L_2}{2}\cos\alpha_2 + F_{1y}\frac{L_2}{2}\sin\alpha_2 - F_{1z}\frac{L_2}{2}\cos\alpha_2 = -I_2\ddot{\alpha}_2 \tag{9}$$

For segment 3:

$$F_{3y} - F_{2y} = m_3\left[-L_1\left(\dot{\alpha}_1^2\cos\alpha_1 + \ddot{\alpha}_1\sin\alpha_1\right) - L_2\left(\dot{\alpha}_2^2\cos\alpha_2 + \ddot{\alpha}_2\sin\alpha_2\right) + \frac{L_3}{2}\left(\dot{\alpha}_3^2\cos\alpha_3 + \ddot{\alpha}_3\sin\alpha_3\right)\right] \tag{10}$$

$$F_{3z} - F_{2z} - m_3g = m_3\left[L_1\left(-\dot{\alpha}_1^2\sin\alpha_1 + \ddot{\alpha}_1\cos\alpha_1\right) + L_2\left(-\dot{\alpha}_2^2\sin\alpha_2 + \ddot{\alpha}_2\cos\alpha_2\right) + \frac{L_3}{2}\left(-\dot{\alpha}_3^2\sin\alpha_3 + \ddot{\alpha}_3\cos\alpha_3\right)\right] \tag{11}$$

$$M_{\text{segment 3}} - M_{\text{segment 2}} + F_{3y}\frac{L_3}{2}\sin\alpha_3 - F_{3z}\frac{L_3}{2}\cos\alpha_3 + F_{2y}\frac{L_3}{2}\sin\alpha_3 - F_{2z}\frac{L_3}{2}\cos\alpha_3 = I_3\ddot{\alpha}_3 \tag{12}$$

where the F_{1y}, F_{2y}, and F_{3y} are the Y-axis direction proximal joint reaction force of segment 1, segment 2, and segment 3, respectively; the α_1, α_2, and α_3 are the angles of segment 1, segment 2, and segment 3 with the horizontal plane, respectively; the α_4 is the shoulder joint angle; the F_{1z}, F_{2z}, and F_{3z} are the Z-axis direction proximal joint reaction force of segment 1, segment 2, and segment 3, respectively; m_1, m_2, and m_3 are the mass of segment 1, segment 2, and segment 3, respectively; the L_1, L_2, and L_3 are the length of segment 1, segment 2, and segment 3, respectively; the $M_{\text{segment 1}}$, $M_{\text{segment 2}}$, and $M_{\text{segment 3}}$ are the proximal joint moment of segment 1, segment 2, and segment 3, respectively; the I_1, I_2, and I_3 are the moment of inertia of segment 1, segment 2, and segment 3, respectively. α_1, α_2, α_3, and α_4 were the angle defined by this study, which was collected by the high-speed camera and mainly used to calculate the joint moment. According to a previous study (44), the mass of the arm, forearm, and carpals is 2.37, 1.30, and 0.30% of the body mass, respectively. The moment of inertia at COM of the arm, forearm, and carpals are 391.81, 233.34, 7.51, respectively (unit: g*cm^2).

The whole inverse kinetics algorithm was realized by a self-written MATLAB (MATLAB R2019a, MathWorks, United States) script. Then, the joint moment of the wrist, elbow, and shoulder was obtained by inverse kinetics. Each landing height (60, 80, 100, and 120 cm) of each joint (wrist, elbow, and shoulder) of sagittal plane joint kinematics (joint angle) and joint kinetics (joint moment) data were expanded into 100 data point's curve by a self-written MATLAB script too. Finally, four matrices were obtained (representing four datasets from different landing heights): $M_{60\text{ cm}}$, $M_{80\text{ cm}}$, $M_{100\text{ cm}}$, $M_{120\text{ cm}}$. Where the $M_{60\text{ cm}}$, $M_{80\text{ cm}}$, $M_{100\text{ cm}}$, and $M_{120\text{ cm}}$ are the data matrices

(including the data sets of joint angle and joint moment) of 60 cm, 80 cm, 100 cm, and 120 cm landing height, respectively. The dimensions of these four matrices are all $560^{*}_{\text{row}}600_{\text{column}}$, 560 represents 560 successful trails (a total of 56 subject cats and 10 successful data were collected for each cat), and 600 represents 600 time-series data points (3 sets of kinematic data and 3 sets of kinetic data, each of which contains 100 data points). The M_1 ($M_1 = M_{60\text{ cm}} + M_{80\text{ cm}}$), M_2 ($M_2 = M_{80\text{ cm}} + M_{100\text{ cm}}$), and M_3 ($M_3 = M_{100\text{ cm}} + M_{120\text{ cm}}$) are the data matrices that combined the $M_{60\text{ cm}}$ and $M_{80\text{ cm}}$, $M_{80\text{ cm}}$ and $M_{100\text{ cm}}$, $M_{100\text{ cm}}$ and $M_{120\text{ cm}}$, respectively. Finally, a total of three times DNN and LRP analyses were performed, which included input matrices M_1, M_2, and M_3 independently.

Data Analysis

Principal Component Analysis

The PCA is a multivariate statistical analysis method that converts multiple indexes into several comprehensive indexes by orthogonal rotation transformation with the idea of dimensionality reduction and the premise of losing little information. The comprehensive index generated by transformation is usually called the principal component (PC), in which each PC is a linear combination of the original variable, and each PC is unrelated to the other. It is also an unbiased method for extracting relevant information from high-dimensional data, considering the major components that account for a large portion of the total data set. In this way, it is possible to consider only a few principal components without losing too much information when studying complex problems. Therefore, it is easier to grasp the main contradiction, reveal the regularity between the internal variables of things, and simplify the problem to improve the efficiency of analysis (45–47). The primary function of PCA is to obtain a set of non-redundant variables to describe a certain phenomenon or process compactly (data dimension reduction). In other words, the reconstruction of waveform data using PCA can extract the main features of the waveform and determine the underlying relationships between variables. Therefore, the waveform data reconstructed by PCA can represent the most important part of the whole data set, rather than the simple average value. From a numerical point of view, some of the waveform data of landing at different heights vary greatly, while others vary little. This goes back to the nature of the data features, and what represents the nature of the current data set is the data that has changed a lot or a little after reconstruction. Therefore, PCA was used to reconstruct the data waveform in this study.

In this work, the dataset of GRF and joint angle were conducted by PCA, the waveform data of each variable was then reconstructed. For the dataset of GRF, separate PCA was conducted for each height (0.6, 0.8, 1, 1.2 m) in each direction (X-axis: lateral and medial GRF; Y-axis: anterior and posterior GRF; Z-axis: vertical GRF) resulting in twelve analyses direction. For the dataset of joint angle, separate PCA was conducted for each height (0.6, 0.8, 1, 1.2 m) in each joint (wrist joint, elbow joint, shoulder joint) resulting in twelve analyses direction. For each PCA, a total of 560 sets of data were designed, and each set corresponded to 100 data points, combined into a 100 × 560 $(n \times p)$ matrix. The 560-dimensional vector constituted by these 560 groups of data is the original variable X_1

$$X_1 = \begin{bmatrix} x_{11} & x_{12} & \cdots & x_{1p} \\ x_{n1} & x_{22} & \cdots & x_{2p} \\ \vdots & \ddots & \ddots & \vdots \\ x_{n1} & x_{n2} & \cdots & x_{np} \end{bmatrix} = \left(x_1, x_2, \ldots, x_p\right)$$

where n represents 100 data points after interpolation and using $t\,(i)$ $(i = 1, 2, \ldots, n)$ to denote the specific time point in the landing phase. At each specific time point, the cat had a specific landing posture and corresponded to a specific vector in the GRF and joint angle. The matrix X_1 was normalized by the "zscore" function of MATLAB, and this function was based on the mean and standard deviation of the original data for data normalization. After that, the covariance matrix $Cov\,(X_1)$ was calculated based on the normalized matrix. The eigenvalues λ_i were extracted from the covariance matrix $Cov\,(X_1)$, as well as orthogonalized unit eigenvectors β_i were calculated from the covariance matrix $Cov\,(X_1)$. The eigenvalues λ_i following ranking $\lambda_1 \geq \lambda_2 \geq \ldots \geq \lambda_p \geq 0$ with $\sum_{i=1}^{p} \lambda_i = 1$. The orthogonalized unit eigenvectors β_i is the coefficient of PC scores PC_i concerning the original variable X_1. The PC scores PC_i represent important landing waveform characteristics, which include overall magnitude, timing differences, and shape (the differences in the amplitude during different time points or phases). The principal component(PC_1, PC_2, …, PC_m) to be selected is determined by the accumulative contribution rate of variance information $G\,(m)$, and it was calculated as

$$G\,(m) = \frac{\sum_{i=1}^{m} \lambda_i}{\sum_{k=1}^{p} \lambda_k} \tag{13}$$

According to the values of the accumulative contribution rate of variance information $G\,(m)$, the number of PC scores PC_i were determined. Finally, the waveform data were reconstructed based on the PC scores, that is also called the principal GRF and principal joint angle. Specifically, the selected PC scores were multiplied by the transpose of the PC coefficient matrix. Then, each sample was multiplied by the sample's standard deviation vector with the addition of the mean vector to reconstruct waveforms (30). The GRF (anterior/posterior, medial/lateral, vertical) value and sagittal joint angle (wrist, elbow, shoulder) value at the time point of maximum elbow flexion during the landing phase were extracted from the reconstructed waveform (principal GRF and principal joint angle) then imported into Mimics to FEA, respectively.

Finite Element Analysis

The whole-body CT images of cats were collected at 0.5 mm intervals, and only the right forelimb was analyzed. Previous studies have shown that the maximum elbow flexion point during landing is a turning point that best represents the characteristics of cat landing patterns (42, 48). Therefore, this study established a finite element model based on the position of each bone joint during maximum elbow flexion. MIMICS16.0 (Materialise, Leuven, Belgium) segmented 25

bones (one scapula, one humerus, one radius, one ulna, seven carpal bones, five metacarpals, and nine phalanges) and their inclusions. The output of each bone was placed in STL format and imported into Geomagic (Geomagic, Inc., Research Triangle Park, NC, United States) for smoothing. Finally, the IGES file format for each bone was exported. The model in SolidWorks (SolidWorks Corporation, MA, United States, 2017) was assembled, according to the corresponding angles of different falling heights, establishing a three-dimensional solid model and a verification model of cat forelimbs under four different heights (the joint angle of each joint of each landing height are shown in **Figure 2B**), and generating ligaments according to anatomical characteristics (49). The final model is shown in **Figures 2A,B**.

The cat's lower limbs and related parts have similar structures, so all tissues are idealized as linear elastic isotropic materials. According to the published literature (50–52). The material properties of each part are shown in **Table 1**. The soft tissue and bone in the finite element model are modeled based on CT images, and the cartilage is modeled in Solidworks based on the anatomical structure of the cat's forelimb. All of the above are solid parts. Ligaments are simulated in the Workbench (ANSYS, Inc., Canonsburg, United States) using line elements that only stretch. The modeling of the above elements is strictly based on the anatomical structure of the cat's forelimb.

The purpose of FEA was to investigate the stress distribution of the cat's right forelimb bone when the cat is hit by an external force. In this study, the PCA was used to optimize the measured GRF, and the reconstructed GRF waveform data is the external force borne by the cat when it lands from the height plate, so the external force was used as the input of the finite element model. The right forelimb model under static conditions is considered. Load and boundary conditions are applied to the right forelimb of the cat. The boundary condition is fixed on the inside of the scapula, and the load is applied to the lower surface of the ground to simulate the external force when falling. The medial edge of the scapula was fixed. The interaction between the foot and the ground is simulated as a foot system, which is a commonly used method in biomechanical modeling of the human foot (**Figure 2C**). The plate is endowed with elastic properties to simulate concrete ground support. The vertical external force is applied under the plate, and the external force of different heights is shown in **Figure 2D**. This study adopts two kinds of contact relations: (1) binding, there is no relative sliding displacement between the two parts of the binding under force; (2) friction, the contact condition between soft tissue and bone is set as binding, and the claw produces friction contact ($\mu = 0.8$). At the same time, due to the presence of synovial fluid, the friction coefficient between bone and cartilage at the joint was determined to be $0.01(\mu = 0.01)$.

The verification of the model refers to the human foot numerical model, and the finite element foot model is verified by the plantar pressure distribution (53–55). Therefore, the paw contact pressure and contact area distribution of cats are also extracted from the pressure platform measurements (Munich novelty, Germany). The experimental pressure data are collected under static standing conditions, and the cat is placed quietly on the force platform with a GRF of 1/4 of body weight for comparison with simulation results (52) (**Figure 2D**).

DNN Model and Layer-Wise Relevance Propagation Analysis

Neural networks are extensive parallel networks composed of adaptive simple units whose organization can simulate the interactions of biological nervous systems to real-world objects (56). Neural networks with more than two hidden layers are defined as DNNs. It is generally believed that the DNN can improve the accuracy of the whole model (57). In this study, the application of the DNN model was mainly biased to improve the accuracy of the model (57). In other applications of neural networks, the reason they don't use DNN is that DNN is less efficient (time-consuming), which in many cases is not allowed. However, the current study does not consider the operation efficiency, so a DNN model with 10 hidden layers was designed under the condition of repeated model training and adjustment according to the actual data. The matrices M_1, M_2, and M_3 were conducted using LRP analysis respectively. For the input matrices M_1, the data of the $M_{60\ cm}$ was set at positive class, and the data of the $M_{80\ cm}$ was set at negative class. For the input matrices M_2, the data of the $M_{80\ cm}$ was set at positive class, and the data of the $M_{100\ cm}$ was set at negative class. For the input matrices M_3, the data of the $M_{100\ cm}$ was set at positive class, and the data of the $M_{120\ cm}$ was set at negative class. Before the data training, 1,120 sample data sets were randomly distributed through the functions, and then 80% of the data sets (896 sample data sets) were extracted as training sets, and the remaining 20% (224 sample data sets) as test sets.

First, a DNN was established that included one input layer, 10 hidden layers, and one output layer, and the per-layer nodes were determined by the input data shape (27). Therefore, the nodes of the input layer, hidden layers, and output layer were 600, 1,200, and 2. The layers of the neural network are fully connected, which means the neuron of the n-th layers must be connected to the neuron of the $(n + 1)$-th layer. A linear relation function and an activation function were used to calculate the new values between layers. The linear relationship function z of the model constructed in this study is:

$$z = \sum_{i=1}^{n+1-th} w_i u_i + b \tag{14}$$

where w_i is the connection weight of the i-th neuron, the u_i is the input from the i-th neuro, the b is the constant of the function, and the $m - th$ is the $m - th$ layers neural network. The activation function $A\ (c)$ of the hidden layer used the hyperbolic tangent function:

$$A\ (c) = \frac{e^c - e^{-c}}{e^c + e^{-c}} \tag{15}$$

where the c is the input scalar of the hyperbolic tangent function. The hyperbolic tangent function expands the mapped range of the Sigmoid function from [0, 1] to [-1, 1], which produces

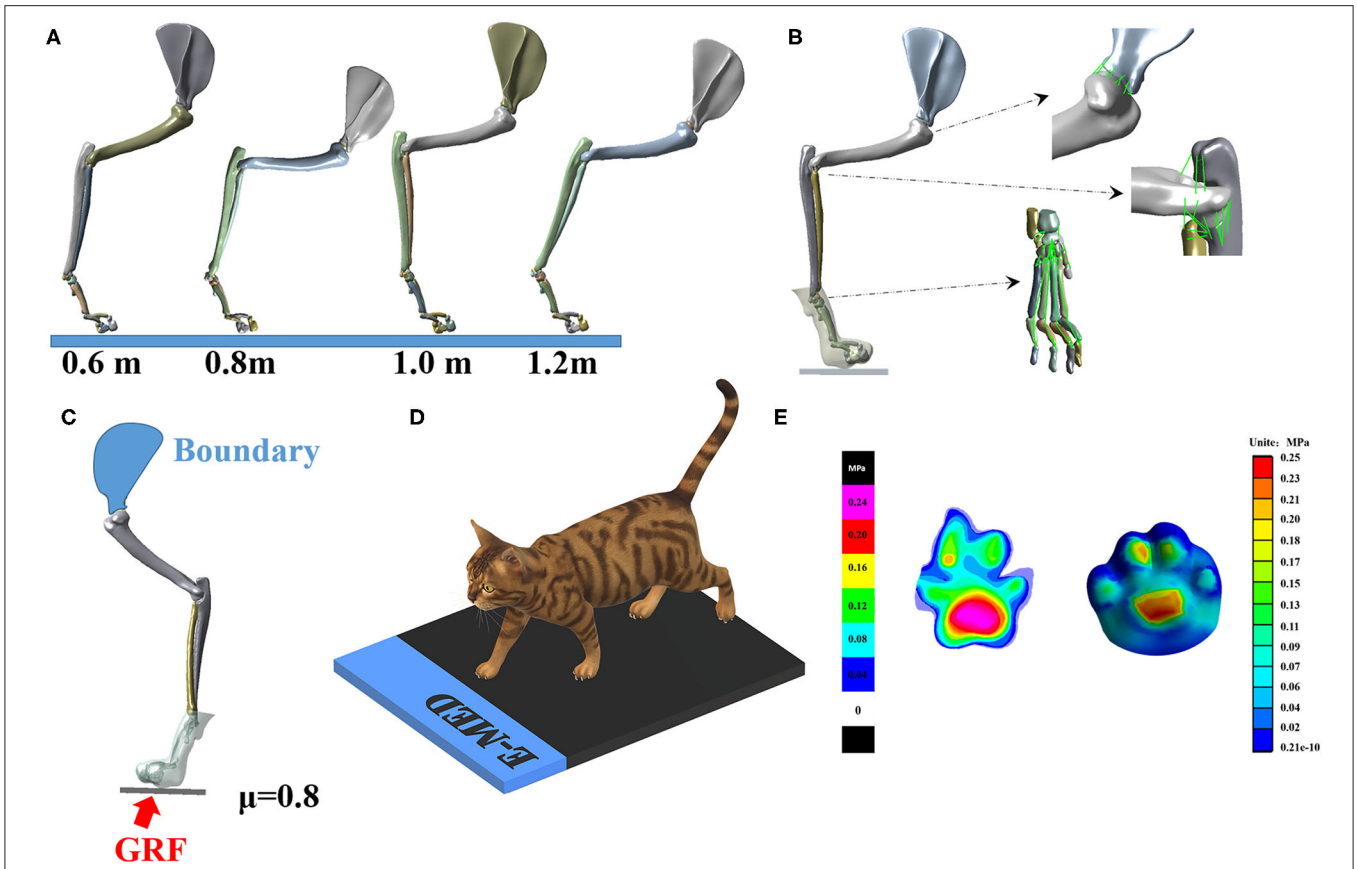

FIGURE 2 | (A) Finite element 3D model of right forelimb at four landing heights. **(B)** Illustration of ligament and soft tissue of model. **(C)** Illustration of loading and boundary conditions. **(D)** Experimental verification of plantar pressure of cat right forelimbs. **(E)** Experimental verification results (left) and finite element simulation results (right). The scales on the left and right diagrams are different; please refer to their scales.

better training performance. The batch size was set at 25, and the epoch limit was set at 3,000. Following DNN training, the relevance score was calculated by the LRP, and the performance of the classifier was evaluated by the accuracy achieved and other parameters.

Layer-wise relevance propagation is a technology used to identify important relevance through backward propagation in neural networks. Backward propagation is a conservative relevance redistribution process in which the neurons that contribute the most to the upper layer receive the most relevance from the upper layer. In general, LRP aims to narrow the gap between the classification and interpretability of multi-layer neural networks on non-linear cores (35, 58, 59).

The overall idea is to understand the contribution of a single feature of dataset x to the prediction $f(x)$ made by the classifier f in pattern recognition and classification tasks. That is, the positive or negative contribution of each feature to the classification result for dataset x can be calculated, and the degree of such contribution can be accurately measured to a certain extent (The contribution of each input feature $x(d)$ to a particular prediction $f(x)$; the d is the input data of $x(d)$ function). In the setting of the classifier is a mapping f: $J^v \rightarrow J^1$ (J is a generic symbol for mapping; v is the v-th layers), $f(x) > 0$ indicates the existence of a learning structure. The constraint of classification is to find the differential contribution relative to the most uncertain state of the classification, which is then represented by the root point $f(x_0) = 0$. By factoring the prediction $f(x)$ into the sum of the individual input feature $x(d)$:

$$f(x) = \sum_{d=1}^{v} R_d \tag{16}$$

where R_d is the relevance score of the d-th layers. In the classifier, whether for non-linear support vector machines or

TABLE 1 | Material properties of the cat's right forelimbs model components.

Component	Young's modulus E (MPa)	Poisson's ratio ν
Paw	0.15	0.45
Bone	15,000	0.3
Cartilage	1	0.4
Ligaments	260	0.4
Plate	17,000	0.4

neural networks, the first layer is the input features, and the last layer is the predicted output of the classifier. Meanwhile, each layer is part of the features extracted from dataset x after running the classification algorithm. The l-th layer is modeled as a vector $z = \left(z_d^l\right)_{d=1}^{V(l)}$ with dimensionality $V(l)$. LRP has a relevance score $R_d^{(l+1)}$ for each dimension $z_d^{(l+1)}$ of vector z at layer $l+1$. A relevance score $R_d^{(l)}$ is found in each dimension z_d^l of vector z near the next layer l of the input layer, as shown in the following formula:

$$f(x) = \ldots = \sum_{d\in l+1} R_d^{(l+1)} = \sum_{d\in l} R_d^{(l)} = \ldots = \sum_d R_d^{(1)} \quad (17)$$

The inter-hierarchical relevance is represented by the message $R_{i\leftarrow j}^{(l,\,l+1)}$ between neuron i and j, and these messages can be sent along with each connection. The output $f(x)$ is then passed from one neuron to the next by backward propagation. The relevance of neurons is defined as the sum of incoming messages; then the sum runs over the sinks at layer $l+1$ for a fixed neuron i at layer l.

$$R_j^{(l)} = \sum_{k:\ i \text{ is input for neuron } j} R_{i\leftarrow j}^{(l,\,l+1)} \quad (18)$$

The input of the next neuron in the direction is defined during classification; then the sum runs over the sources at layer l for a fixed neuron k at layer $l+1$. In general, this can be expressed as:

$$R_k^{(l+1)} = \sum_{i:\ i \textit{ is input for neuron } k} R_{i\leftarrow k}^{(l,\ l+1)} \quad (19)$$

The relevance of each layer is calculated by backward propagation: the relevance $R_i^{(l)}$ is expressed as a function of the upper relevance $R_j^{(l+1)}$, and the back propagates the relevance until the input feature is reached. By the relevance of the neuron $R_j^{(l+1)}$to the classification decision $f(x)$, the relevance is then decomposed according to the message $R_{i\leftarrow j}$ sent to the upper layer of neurons. Holding the conservation property:

$$\sum_i R_{i\leftarrow j}^{(l,\,l+1)} = R_j^{(l+1)} \quad (20)$$

For the linear network $f(x) = \sum_i z_{ij}$, the relevance is $R_j = f(x)$, and the decomposition is directly by $R_{i\leftarrow j} = z_{ij}$. Through hyperbolic tangent function and rectification function two monotone increasing functions, the pre-activation function z_{ij} provides a reasonable way to measure the relative contribution of x_i to R_j for each neuron. Based on the proportion of local pre-activation and global pre-activation, the selection of association decomposition is obtained:

$$R_{i\leftarrow j}^{(l,\,l+1)} = \frac{z_{ij}}{z_j} * R_j^{(l+1)} \quad (21)$$

where z_j is the weight connecting the neuron x_j. The relevance $R_{i\leftarrow j}$ are shown in

$$\sum_i R_{i\leftarrow j}^{(l,\,l+1)} = R_j^{(l+1)*}\left(1-\frac{b_j}{z_j}\right) \quad (22)$$

where b_j is the bias term of the j -layer neuron. Multiplier accounts represent the relevance absorbed by the bias term, and the residual bias correlations can be reassigned to each neuron x_i. According to the determined rule (*Eq*. 21), through adding up the correlations of all neurons in the upper layer i (combined *Eq*. 18 and *Eq*. 19), the overall relevance of all neurons in the next layer j can be obtained:

$$R_i^{(l)} = \sum_j R_{i\leftarrow j}^{(l,\,l+1)} \quad (23)$$

The relevance propagates from one layer to another until it reaches the input feature $x(d)$, where the relevance $R_d^{(1)}$ provides the hierarchical eigen-decomposition required for the decision $f(x)$. More details can be found by referring to Sebastian's study (58). All algorithms were run in MATLAB R2019a, by self-written scripts according to the LRP toolbox (60).

The relevance of correctly classified cat landing patterns was extracted by defining logical variables, and then a relevance score was assigned to each input variable. LRP determines the correlation between each variable and the predicted results of the model and normalizes the LRP-derived association patterns to their respective maximum values for comparison. Since the input variables are collected in the time domain, and the adjacent values are interdependent, the fluctuation of the relevance score can be reduced by smoothing. Therefore, the average of the correlation patterns was corrected and smoothed; then the smoothed correlation pattern was rescaled from 0 (no correlation) to 1 (the highest correlation). The whole smoothing process was repeated three times, with the preceding and following points of each point weighted by 25%. The sum of weights equal to 1, which was accomplished by simulating the Gaussian filter. To explore the influence of different variables on the accuracy of model classification, all variables were sorted according to the correlation between variables, and then the top 100 variables with the highest relevance scores were selected to explain and analyze the cat landing pattern.

Evaluate the Performance of the Classifier

Combine the results of the classification model into a 2*2 table called confusion matrix $m = \begin{pmatrix} TP & FN \\ FP & TN \end{pmatrix}$, which fully describes the results of the classification task (61). True Positives (TP): Actual positives that are correctly predicted positives; False Negatives (FN): Actual positives that are wrongly predicted negatives; True Negatives (TN): Actual negatives that are correctly predicted; False Positives (FP): Actual negatives that are wrongly predicted positives.

Then, considering the possibility of unbalanced class distribution, the following indicators were calculated to evaluate the performance of the classifier.

1. The accuracy of a classifier on a given set of tests is the percentage of tuples that are correctly classified by the classifier:

$$\text{accuracy}= \frac{TP + TN}{TP + FN + FP + TN} \tag{24}$$

2. The sensitivity (also called recall) is the true positive cases recognition rate, which means the percentage of positive tuples correctly identified:

$$\text{sensitivity/recall}= \frac{TP}{TP + FN} \tag{25}$$

3. The specificity is the true positive cases recognition rate, which means the percentage of negative tuples correctly identified:

$$\text{specificity}= \frac{TN}{FP + TN} \tag{26}$$

4. The precision is a measure of accuracy, which means the percentage of tuples marked as positive that are positive:

$$\text{precision}= \frac{TP}{TP + FP} \tag{27}$$

5. $F_1 - score$ is the harmonic average of accuracy and recall rate, which means the recall rate is weighted once as much as the precision:

$$F_1 - \text{score} = \frac{2^{*}rmprecision^{*}\text{recall}}{\text{precision} + \text{recall}} \tag{28}$$

6. Receiver operating characteristic (ROC) curves is a useful visual tool for comparing classifier models, which can provide objective and neutral advice regardless of cost/benefit when making decisions. The ROC curve shows the tradeoff between the true positive rate (TPR) and the false positive rate (FPR) for the classifier model. The increase in TPR comes at the expense of the increase in FPR:

$$TPR= \frac{TP}{TP + FN} \tag{29}$$

$$FPR= \frac{FP}{FP + TN} \tag{30}$$

The Y-axis of the ROC curve represents TPR and the X-axis represents FPR, and the area under the ROC curve (*AUC*) is a measure of model accuracy:

$$AUC= \frac{(TPR - FPR + 1)}{2} \tag{31}$$

7. Matthew's correlation coefficient (MCC) is a contingency matrix method (61). MCC can be used to calculate the Pearson product-moment correlation coefficient (62) between the actual value and the predicted value:

$$MCC= \frac{TP^{*}TN - FP^{*}FN}{\sqrt{(TP + FP) * (TP + FN) * (TN + FP) *(TN + FN)}} \tag{32}$$

RESULTS

Results of GRF, Joint Kinematics, and Joint Kinetics

Figure 3A clearly shows the GRF dataset in three directions (anterior and posterior, medial and lateral, and vertical) during the cat landing phase from different heights (60, 80, 100, and 120 cm). **Figure 3B** clearly shows the joint kinematics (sagittal joint angle) dataset on three joint angles (wrist, elbow, and shoulder) during the cat landing phase from different heights (60, 80, 100, and 120 cm). **Figure 3C** clearly shows the joint kinetics (sagittal joint moment) dataset on three joint angles (wrist, elbow, and shoulder) during the cat landing phase from different heights (60, 80, 100, and 120 cm).

Results of PCA

The contribution rate of the first PC score for most variables was more than 90%, so the first PC was determined to reconstruct the waveform. The first PC score for each landing height and each joint flexion angle are shown in **Figure 4A**, the reconstructed waveform (principal joint angle) based on the first PC score are shown in **Figure 4A**. According to the principal joint angle, the joint angle value for each landing height for the maximum elbow flexion was extracted (the detailed values are shown in **Figure 4B**). The first PC score for each landing height and each direction GRF are shown in **Figure 4C**, the reconstructed waveform (principal GRF) based on the first PC score are shown in **Figure 4C**. According to the principal GRF, the GRF value for each landing height of the maximum elbow flexion was extracted (the detailed values are shown in **Figure 4D**). Finally, the joint angle (**Figure 4B**) and GRF (**Figure 4D**) data values of each landing height at the time point of the end of the landing phase (maximum elbow flexion) are extracted from the reconstructed waveform and substituted into the finite element model to investigate the stress distribution of the cat right forelimb bone.

Results of FEA

Validity Verification of the Finite Element Model

For the validation of the cat's paw finite element model, the numerically predicted, and the experimentally obtained paw pressure distributions were compared. The paw pressure concentrated mainly on the metaphorical pad concerning the finite element or the experimental results. The numerically predicted contact area was ∼57 cm^2 in comparison to the experimentally obtained 54 cm^2, which showed 5.6% higher over-prediction. The maximal pressure in the finite element model was located at the metaphorical pad in the measurement. The finite element model predicted a peak pressure of 0.25 MPa, while the experimental result, measured using a pressure platform, was 0.27 MPa, a difference of 8%. The results show that the numerically determined pressure distribution in the fore-left paw was in good agreement with experimental data, as shown in **Figure 2E**.

Stress Distribution of the Forelimb

The stress distribution of the forelimb as a result of falling from different heights is shown in **Figure 5**. From the stress

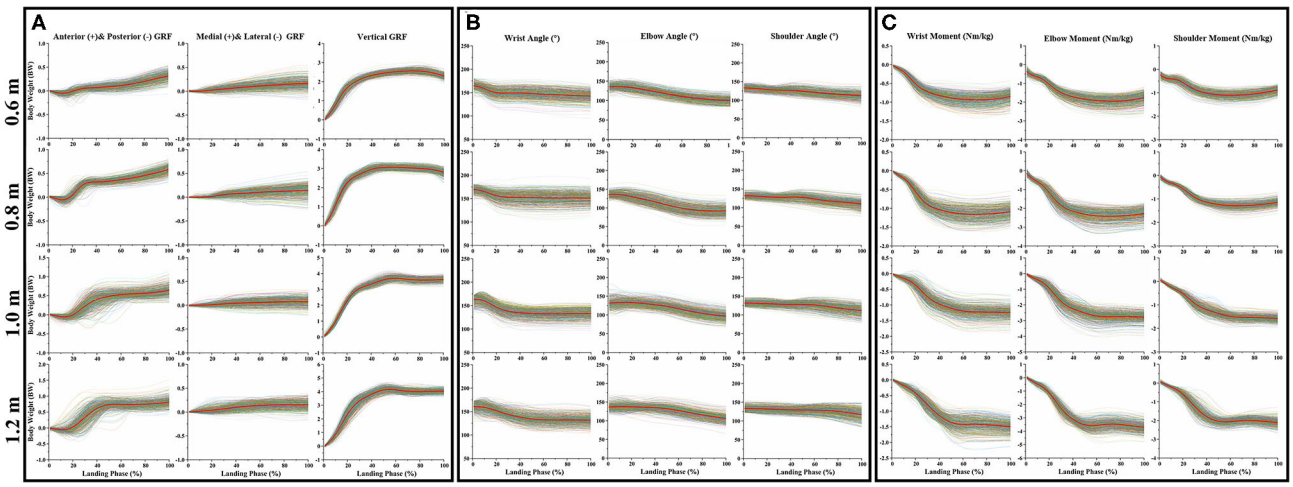

FIGURE 3 | The data waveform curves of GRF, joint angle, and joint moment. **(A)** Illustrates the changes in GRF in three directions (anterior and posterior, medial and lateral, and vertical) during the cat landing phase from different heights. **(B)** Illustrates the changes of three joint angles (wrist, elbow, and shoulder) during the cat landing phase from different heights. **(C)** Illustrates the changes of three joint moments (wrist, elbow, and shoulder) during the cat landing phase from different heights. The colored data of each image represented 560 data sets recorded during the cat landing phase from different heights. The red line data of each image represents the average value of 560 data sets during the cat landing phase from different heights. On the left of each image, the scale displays the change of GRF/angle/moment values. Zero to one hundred below each image presents a landing phase.

distribution in the figure, it can be seen that the maximum stress of the forelimb is mainly concentrated in each joint when landing, indicating that the risk of joint injury is higher when the cat falls. However, the maximum stress of each joint does not simply increase with the increase of height, because the angle of each joint is also different when falling from different heights, so the stress change trend of each joint is also different. The maximum stress value of each joint is shown in **Figure 5E**. From the maximum stress value in the figure, we can see that when the cat hits the ground, the maximum stress value of the shoulder joint is the largest, followed by the elbow joint and the wrist joint, indicating that the shoulder joint is the most important buffer joint, followed by the elbow joint and wrist joint. This study found that the maximum stress of the elbow joint and wrist joint decreased compared with 0.6 m at 0.8 m height, while the angle of the elbow joint and shoulder joint was the smallest at 0.8 m height, and the angle of the wrist joint was the largest at 0.8 m height. In the case of increased height, the cat's forelimbs are bent to achieve a damping effect, but not all the joint bending damping effect is efficient, the wrist joint stress also has a downward trend, but its angle is the largest. Investigating the metacarpals of cats, it can be seen that in all metacarpals, stress is mainly concentrated in the second and third metacarpals.

Performance of DNN Classification Models

For the matrices M_1, there were 111 positive classes and 113 negative classes in the 224 test set samples extracted by a random function. Among them, 102 TP, 9 FN, 100 TN, and 13 FP were obtained by the DNN classifier. For the matrices M_2, there were 114 positive classes and 110 negative classes in the 224 test set samples extracted by a random function. Among them, 108 TP, 6 FN, 107 TN, and 3 FP were obtained by the DNN classifier. For the matrices M_3, there were 116 positive classes and 108 negative classes in the 224 test set samples extracted by a random function. Among them, 113 TP, 3 FN, 103 TN, and 5 FP were obtained by the DNN classifier.

All classification performance parameters are presented in **Figure 6**. For the classifier of the DNN models based on the matrices M_1, the model shows a lower accurate rate (accuracy rate: 90.18%) than the matrices M_2 (accuracy rate: 95.98%) and matrices M_3 (accuracy rate: 96.43%). At the same time, the classifier of the DNN models based on the matrices M_1 also show the lower $F_1-score$ (0.9027) and MCC (0.8041) than the matrices M_2 ($F_1-score$: 0.96, MCC: 0.92) and the matrices M_3 ($F_1-score$: 0.9658, MCC: 0.8757).

The ROC curves are shown in **Figure 6**, the ROC curves of the classifier of the DNN models based on the matrices M_2 (**Figure 6B**) and the matrices M_3 (**Figure 6C**) presented a good classification performance over the entire area. However, the ROC curves based on the matrices M_1 (**Figure 6A**) show the worse classification performance during the about $(0_{FPR}-0.8_{FPR})^*(0.88_{TPR}-1_{TPR})$ area. The classifier of the DNN models based on the matrices M_1 show the lower AUC (0.9019) than the matrices M_2 (AUC: 0.96) and matrices M_3 (AUC: 0.9639). Overall, the classifier of the DNN models based on the matrices M_1 has a bad performance from the perspective of overall indicators.

Results of LRP

For the results based on matrices M_1, which compared the landing patterns between the cat landing from 60 cm platform and landing from 80 cm platform. For the LRP results based on matrices M_2, which compared the landing patterns between the cat landing from 80 cm platform and landing from 100 cm

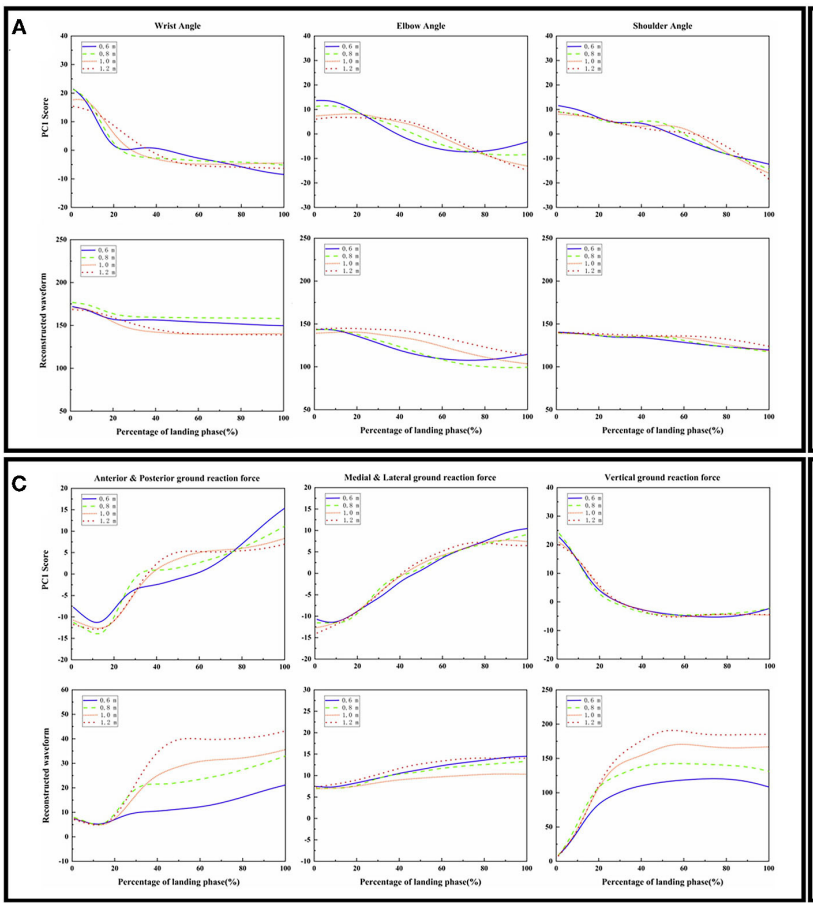

FIGURE 4 | (A) The first PC scores PC_1 for each landing height and each joint sagittal angle (wrist joint, elbow joint, and shoulder joint), the reconstructed waveform (principal joint angle) based on the first PC scores PC_1. **(B)** The value of the principal joint angle of the maximum wrist flexion data point in each joint during landing from different heights. **(C)** The first PC scores PC_1 for each landing height and each direction GRF (anterior and posterior, medial and lateral, and vertical), the reconstructed waveform (principal GRF) based on the first PC scores PC_1. **(D)** The value of principal GRF of the maximum wrist flexion data point in each direction during landing from different heights.

platform. The LRP results based on matrices M_3 compared the landing patterns between the cat landing from the 100 cm platform and the 120 cm platform.

For the results based on matrices M_1, M_2, and M_3, the relative contribution of variables during the overall cat landing phase are shown in **Figures 7A,D,G**, respectively. The variables recorded at every 1% of the landing phase interval are related to successfully matching the landing pattern. The detailed distribution of relevance score during each joint (wrist, elbow, and shoulder) of kinematics (joint angle) and kinetics (joint moment) are shown in **Figures 7B,E,H** (M_1), (M_2), and (M_3). There were revealing findings contributing to the distribution of the variables on time points between the cat landing from different height platforms during the overall landing movement patterns. The summed contribution of the relevance score of each joint (wrist, elbow, and shoulder) of kinematics (joint angle) and kinetics (joint moment) trajectories are shown in **Figures 7C,F,I** (M_1), (M_2), (M_3). For **Figure 7C**, the summed contribution of the relevance score of the wrist flexion angle, elbow flexion angle, shoulder flexion angle, wrist flexion moment, elbow flexion moment, shoulder flexion moment was 19.98, 16.81, 11.06, 21.25, 17.07, and 13.84%, respectively. For **Figure 7F**, the summed contribution of the relevance score of the wrist flexion angle, elbow flexion angle, shoulder flexion angle, wrist flexion moment, elbow flexion moment, shoulder flexion moment was 17.45, 16.78, 14.17, 16.88, 17.08, and 17.64%, respectively. For **Figure 7I**, the summed contribution of the relevance score of the wrist flexion angle, elbow flexion angle, shoulder flexion angle, wrist flexion moment, elbow flexion moment, shoulder flexion moment was 11.10, 19.18, 20.13, 14.63, 15.13, and 19.83% respectively.

There are 600 relevant variables in this study, including 6 trajectory variables, and each trajectory variable include 100 relevant variables (1%–100% landing phase). Notable highly relevant variables (the top 100 relevant variables with the highest correlation relevance) during the landing phase are shown in **Figure 6**. **Figure 6D** represents the results based on matrices M_1: (1) For the wrist kinematics, there was a high relevance score in

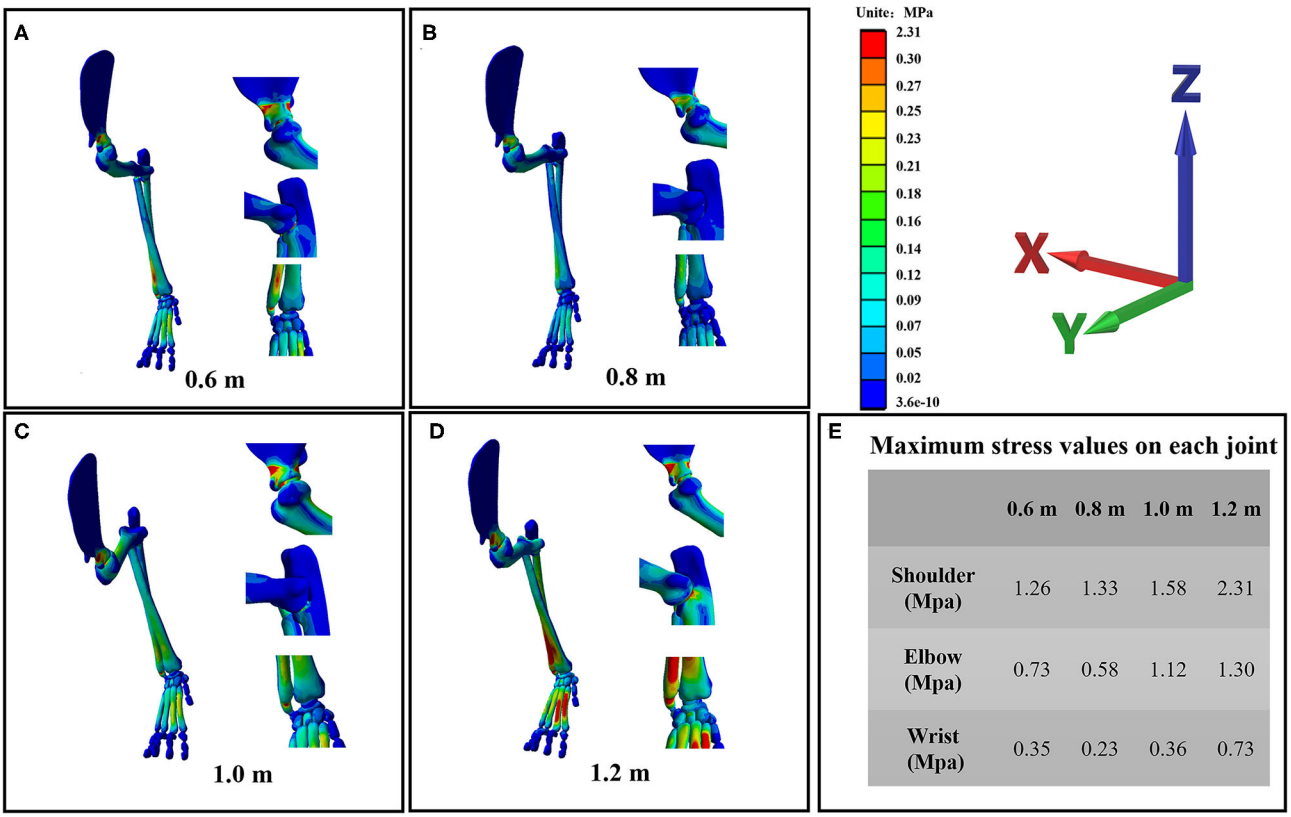

	0.6 m	0.8 m	1.0 m	1.2 m
Shoulder (Mpa)	1.26	1.33	1.58	2.31
Elbow (Mpa)	0.73	0.58	1.12	1.30
Wrist (Mpa)	0.35	0.23	0.36	0.73

FIGURE 5 | (A–D) are the stress distribution details of the wrist joint, elbow joint, and shoulder joint of the cat's right forelimb landing from four heights of 0.6, 0.8, 1, and 1.2 m, respectively. **(E)** The maximum stress value of each joint at each landing height.

flexion angle during the 9–11, 67–68, and 75–98% landing phase; (2) For the elbow kinematics, there are high relevance scores in flexion angles during the 65–71, 78, 82–85, and 91–97% landing phase; (3) For the shoulder kinematics, there was a high relevance score in flexion angle during the 31–32, and 47–53% landing phase; (4) For the wrist kinetics, there was a high relevance score in flexion moment during the 2–6, 10–15, 25–28, and 41–47% landing phase; (5) For the elbow kinematics, there was a high relevance score in flexion moment during the 9–12, 30–32, and 42–47% landing phase; (6) For the shoulder kinematics, there were high relevance scores in flexion moment during the 3–7 and 98–100% landing phase. **Figure 6E** represents the result based on matrices M_2: (1). For the wrist kinematics, there were high relevance scores in flexion angle during the 3–5, 9–11, and 77–80% landing phase; (2) For the elbow kinematics, there were high relevance scores in flexion angle during the 87–93 and 98–99% landing phase; (3) For the shoulder kinematics, there were high relevance scores in flexion angle during the 10–17, 30–32, 62, 66–69, and 83–86% landing phase; (4) For the wrist kinetics, there were high relevance scores in flexion moment during the 13–15, 18–19, 31–33, and 84–91% landing phase; (5) For the elbow kinematics, there were high relevance scores in flexion moment during the 12–17 and 74–79% landing phase; (6) For the shoulder kinematics, there was a high relevance score in flexion moment during the 1–2, 7–15, 49–52, 59–62, and 65–78% landing phase.

Figure 6F represents the result based on matrices M_3: (1) For the wrist kinematics, there were high relevance scores in flexion angle during the 33% landing phase; (2) For the elbow kinematics, there were high relevance scores in flexion angle during the 7, 40–47, 51–58, 64–66, and 90–91% landing phase; (3) For the shoulder kinematics, there was a high relevance score in flexion angle during the 9–15, 23–30, 61–62, 69–75, 86–92, and 96–100% landing phase; (4) For the wrist kinetics, there were high relevance scores in flexion moment during the 82–89% landing phase; (5) For the elbow kinematics, there were high relevance scores in flexion moment during the 56–63% landing phase; (6) For the shoulder kinematics, there were high relevance scores in flexion moment during the 42–64 and 73–74% landing phase.

DISCUSSION

This study was designed to investigate the biomechanical characteristics of a cat landing from different heights and provide new insights into bionic robot design based on the research results and the needs of bionic engineering. Specifically, the present work was to investigate the adaptive motion adjustment strategy of the cat's forelimb for each joint (wrist, elbow, and shoulder) during the landing phase using a machine learning algorithm and FEA. The present results suggest that as the cats'

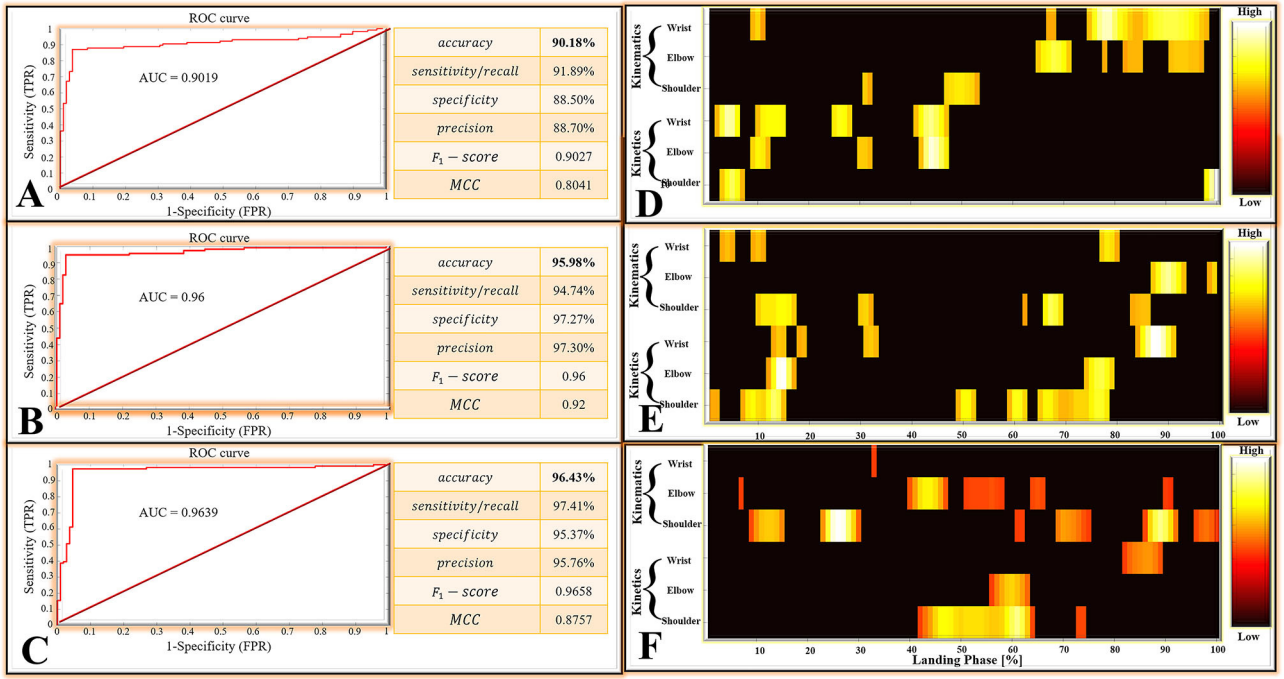

FIGURE 6 | (A) The classifier performance results of the DNN models based on the matrices M_1. **(B)** The classifier performance results of the DNN models are based on the matrices M_2. **(C)** The classifier performance results of the DNN models are based on the matrices M_3. ROC, Receiver Operating Characteristic; AUC, Area Under the ROC Curve; MCC, Matthews Correlation Coefficient; TPR, True Positive Rate; FPR, False Positive Rate. **(D–F)** Notable highly relevant variable during each joint (wrist, elbow, and shoulder) of kinematics (joint angle) and kinetics (joint moment). The top 100 variables with the highest correlation relevance. **(D–F)** are the result based on matrices M_1, M_2, and M_3, respectively.

landing height gradually increases, the cat exhibits an adaptive movement adjustment strategy that gradually shifts from the distal joints (wrist joint) of the forelimbs to the proximal joints (shoulder joint) when responding to ground impact loads. Previous studies have shown that it is primarily the muscles of the limbs that act as dampers when cats land, dissipating impact and reducing damage (42, 63). Few studies have considered the role of joint coordination when cats land from a high place. The current results seem to provide new information and understanding of why when cats land from the high place they perform an excellent method of dissipating the impact of landing, thus protecting themselves from injury. The application of this intrinsic landing mechanism in the design of bionic robots is worth considering by related field researchers.

With the rapid development of bionic technology, bionic mobile robots have been widely used in military, scientific research, medical, aerospace, and many other fields. Among them, research into leg bionic mechanisms is very important to improve the movement ability of bionic robots (1). It is well-known that cats have significant advantages in terms of sports energy efficiency and sports flexibility compared with other animals. The cat's forelimbs play a leading role in free movement, while their hind limbs play a driving role (64). To compare a cat with a car, a cat's forelimbs may represent "the steering wheel" of the car and its hind limbs the "engine." For landing motion, however, the cat's forelimbs play a crucial role in landing because they absorb most of the impact load (41, 42). In the current study, we investigated the biomechanical differences in cats landing from four different heights. The DNN classification model and LRP were used for pattern recognition and interpretability analysis of landing patterns at different heights. During the identification of landing modes with landing heights of 60 and 80 cm, we found that the contribution rates to the relevance score of the wrist joint were the greatest, reaching 41.23%, surpassing the elbow (33.88%) and shoulder (24.9%). During the identification of landing modes with landing heights of 80 and 100 cm, the contribution rates of the wrist (34.33%), elbow (33.86%), and shoulder joint (31.81%) were the same. When the landing heights were 100 and 120 cm, the contribution rates to the relevance score of the shoulder joint were the greatest, reaching 39.96%, surpassing the elbow (34.31%) and wrist (25.73%). With the increase in landing height (from 60 to 120 cm), the joint that contributed most to the landing pattern recognition gradually shifted from the distal joint (wrist joint) to the proximal joint (shoulder joint). This seems to be the adaptive movement adjustment that the cat demonstrates during the landing process. By autonomously adjusting the biomechanical mechanism of each joint landing at different heights, the cat can maximize the landing performance and reduce landing damage.

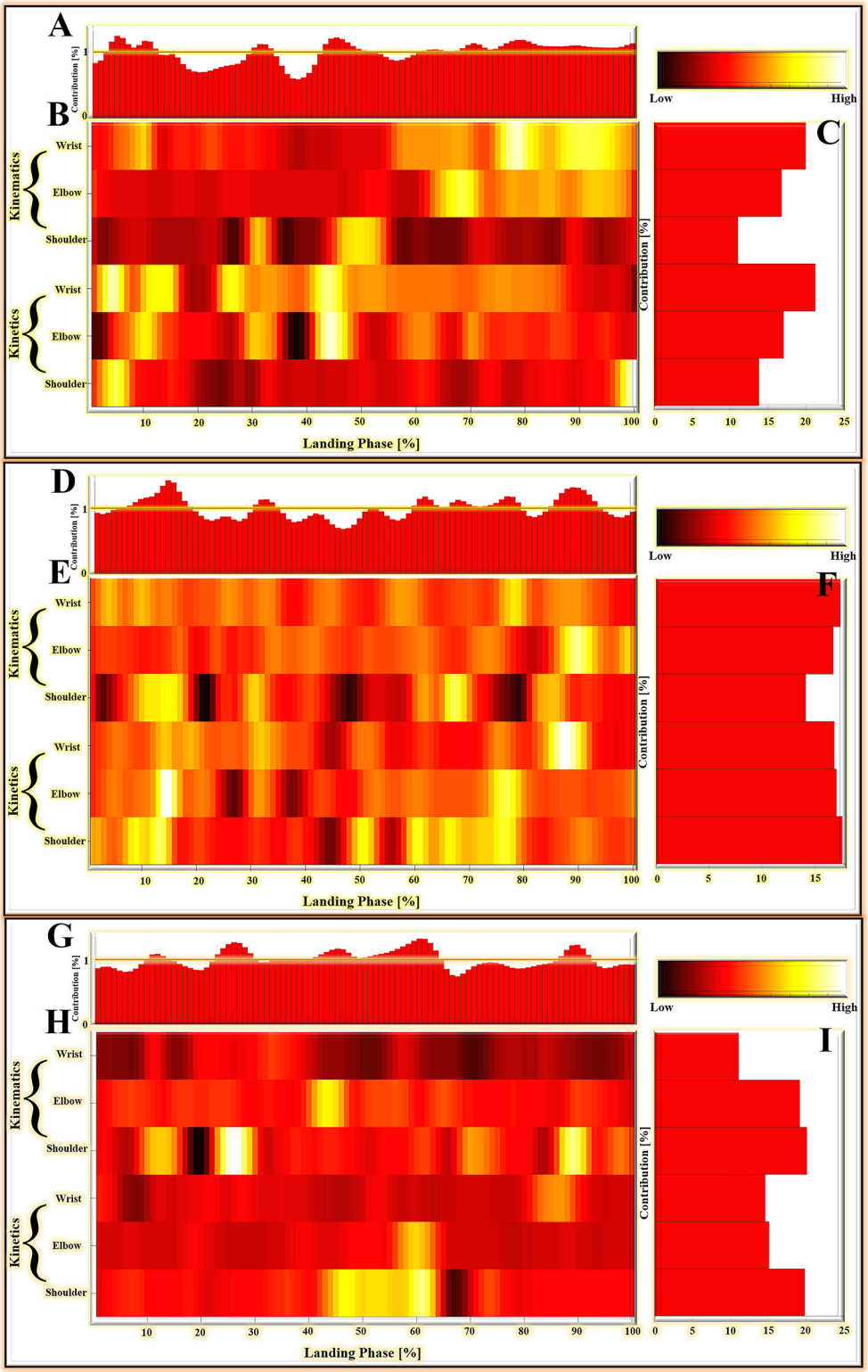

FIGURE 7 | (A–C) The LPR results in the average absolute relevance score of every variable in the landing pattern based on matrices M_1. **(D–F)** The LPR results in the average absolute relevance score of every variable in the landing pattern based on matrices M_2. **(G–I)** The LPR results in the average absolute relevance score of every variable in the landing pattern based on matrices M_3. **(A,D,G)** The relative contribution of variables during the overall landing phase (1–100%). **(B,E,H)** The detailed distribution of relevance score during each joint (wrist, elbow, and shoulder) of kinematics (joint angle) and kinetics (joint moment). The lighter colors mean

(Continued)

FIGURE 7 | high relevance variables; the darker colors mean low relevance variables. The model relied more on lighter-colored variables; the darker-colored variables had less relevance with correctly classified gait patterns. **(C,F,I)** The summed contribution of the relevance score of each joint (wrist, elbow, and shoulder) of kinematics (joint angle) and kinetics (joint moment) trajectories.

From a biomechanical standpoint, the paw pads, limb bones, and coordinated joints can operate as a multi-level (foot-level, limb-level, and joint-level) cushioning system when landing, effectively dissipating the shock (48). At the same time, the cat's limb muscles play a crucial role in the landing process (63). Previous studies have shown that the amplitude and duration of muscle activity during landing are autonomously modulated by the cat depending on the height of the landing (42, 63, 65). Therefore, the adaptive movement adjustment strategy exhibited by cats during landing may be the result of muscle mobilization and control. Why, with the gradual increase in landing height, does the main joint that bears the impact load gradually from the wrist joint move to the elbow joint, and up to the shoulder, but not toward the wrist joint? It could be the cat's unique landing mechanism, or maybe it is more "economical" with the cat's landing mechanism. Of course, these speculations need to be further confirmed, and the specific causes also need to be further investigated.

When a bionic robot lands, it needs to face many problems such as contact collision and friction with the ground. Contact impact with the ground is a complex phenomenon, as factors such as material properties and contact surfaces need to be considered (44, 66). The impact of the contact between the mechanical leg and the ground will cause the vibration of the bionic robot, thus affecting its stability, service life, and control accuracy (67–69). From the view of FEA results, when the cat landed at different heights, the maximum stress of each joint appeared in the styloid process of the ulna, the coronal process of the ulna, and the neck of the scapula. The wrist and elbow joints are similar to the easily fractured parts of humans, but the easily fractured parts of shoulder joints are different from those of humans. The most prone parts of the human shoulder joint are the acromion and the acromial end of the clavicle, followed by the neck of the scapula. This is mainly due to structural differences (70). There is a great difference in the function of the cat's forelimb and the human upper limb. The cat's forelimb acts as a buffer when landing. With the evolution of biology, the cat's acromion and collarbone shorten, and this structure does not have direct comparisons with humans. As a result, the risk of fracture of the acromion is greatly reduced. The position of the maximum stress distribution is mainly distributed in the narrower parts at the two ends of the bone. In the design of bionic robots, the hardness of the joint should be strengthened to reduce machine wear and tear, thus affecting the control accuracy and reducing service life.

In addition to the material properties of the machine and the coordination mechanism of each joint, the posture of the bionic robot during landing is also the key to a good cushioning mechanism (71). At the same time, the bionic robot can control body posture to achieve a stable motion state in the air attitude adjustment stage, which can also provide a basis for a good landing (72). With the increase of height, the GRF increases, but the maximum stress of each joint does not increase, which was related to the angle of the cat's forelimbs. It can be seen from the results that the cat has the largest angle of the wrist and the smallest angle of shoulder and elbow when landing at a height of 0.8 m, and the body shows a posture of leaning forward and a low center of gravity. When landing at this height, the stress of the elbow joint and wrist joint is lower than that of other joints, which is caused by low height and small GRF and the low center of gravity and forward posture of the body. The relationship between the specific posture and the stress of each joint needs to be further explored. Falling with this kind of posture will reduce the stress of the lower limb joints to a certain extent, which has some implications for the falling posture of the bionic robots.

Over time, tetrapods have evolved many unique biological structures that help them adapt to a variety of environments and terrains. The design of bionic robots based on these animals with excellent locomotion ability needs to consider various factors. From the results of the present study, when cats land from lower heights (60 and 80 cm), the adaptive movement adjustment strategy makes the wrist joint the main joint that bears the impact load. With the gradual increase in landing height (100 and 120 cm), the main joint that bears the impact load gradually moves to the elbow joint, and up to the shoulder. Further research is needed to understand exactly why cats exhibit this landing mechanism. However, there is no doubt that this adaptive movement adjustment strategy allows the cat to cushion the impact load when landing, improve landing stability, and reduce landing damage. Therefore, when designing bionic robots, we suggest that the coordination mechanism of each joint should be adjusted intelligently according to the force at the bottom of the mechanical leg so that the robot can better buffer the impact load during the landing process. Specifically, with the increase of the force at the bottom of the mechanical leg, the main joint bearing the impact load gradually shifts from the distal joint to the proximal joint. We also found that the position of the maximum stress distribution is mainly distributed in the narrower parts of the two ends of the bone. Therefore, it is necessary to strengthen the hardness of materials around the center of each joint of the bionic robot leg. Finally, lowering the center of gravity of the robot during the landing process and keeping the posture forward as much as possible are also important mechanisms to reduce machine wear and improve the accuracy of robot operation. In conclusion, this study can directly provide a biomechanical theoretical basis and technical support for the innovative design and development of bionic robots with high energy efficiency motion characteristics and has important scientific significance.

There are some limitations in the present study. (1) The results of this study could be influenced by different varieties, genders, ages, and weights of the cats. In our ongoing study, we will expand our test sample to validate the results of this study. (2) We only built one FEA model to analyze the data, and the model won't be representative of all the features of the cat. We will engage more FEA models of cats during the next study to avoid results that might be affected by individual differences. (3) The finite element model in this study is only a simplified model, which simplifies the material properties of bones and ligaments to linear materials, and does not involve the internal and external forces of forepaw muscles and tendons. The ligaments were modeled by a straight node-to-node link element, and the specific variation in ligament positioning in the standing phase was not considered. Specific changes in the position of the ligament in the falling stage were not taken into consideration, so the model needs further optimization. (4) In this study, the FEA only explored the stress distribution at the maximum elbow flexion, and subsequent studies should also investigate other time points of the landing phase.

DATA AVAILABILITY STATEMENT

The raw data supporting the conclusions of this article will be made available by the authors, without undue reservation.

ETHICS STATEMENT

The animal study was reviewed and approved by Animal Care and Use Ethics Committee of Ningbo University. Written informed consent was obtained from the owners for the participation of their animals in this study.

AUTHOR CONTRIBUTIONS

All authors have made substantial contributions to the manuscript. DX, HZ, and YG were responsible for the conception and design of the study. DX, XJ, QZ, SL, JB, and YG were responsible for data acquisition and data processing. HZ, XJ, QZ, and JB were responsible for data analysis and interpretation and drafting the article. DX and YG revised the manuscript critically. All authors read, provided feedback, and approved the submitted version.

FUNDING

This study was sponsored by the National Natural Science Foundation of China (No. 81772423), the Key Project of the National Social Science Foundation of China (19ZDA352), Key R&D Program of Zhejiang Province China (2021C03130), and K. C. Wong Magna Fund in Ningbo University.

REFERENCES

1. Song M, Xu Z, Wang X, Li X, Fang Y. Research on kinematics and biomechanics of the bionic mechanism. *IOP Conf Ser Earth Environ Sci.* (2018) 170:042060. doi: 10.1088/1755-1315/170/4/042060
2. Li Y, Li M, Zhu H, Hu E, Tang C, Li P, et al. Development and applications of rescue robots for explosion accidents in coal mines. *J Field Robot.* (2020) 37:466–89. doi: 10.1002/rob.21920
3. Moosavian SA, Rastegari R, Papadopoulos E. Multiple impedance control for space free-flying robots. *J Guid Control Dynam.* (2005) 28:939–47. doi: 10.2514/1.10252
4. Biswal P, Mohanty PK. Development of quadruped walking robots: a review. *Ain Shams Eng J.* (2020) 12:2017–31. doi: 10.1016/j.asej.2020.11.005
5. Ito K, Ishigaki Y. Semiautonomous centipede-like robot for rubble-development of an actual scale robot for rescue operation. *Int J Adv Robot Syst.* (2015) 6:75–83. doi: 10.1504/IJAMECHS.2015.070709
6. Nam W, Seo T, Kim B, Jeon D, Cho KJ, Kim J. Kinematic analysis and experimental verification on the locomotion of gecko. *J Boinic Eng.* (2009) 6:246–54. doi: 10.1016/S1672-6529(08)60121-3
7. Roy SS, Pratihar DK. Effects of turning gait parameters on energy consumption and stability of a six-legged walking. *robot Robot Auton Syst.* (2012) 60:72–82. doi: 10.1016/j.robot.2011.08.013
8. Vidoni R, Gasparetto A. Efficient force distribution and leg posture for a bio-inspired spider robot. *robot Robot Auton.* (2011) 59:142–50. doi: 10.1016/j.robot.2010.10.001
9. Hyun DJ, Seok S, Lee J, Kim S. High speed trot-running: implementation of a hierarchical controller using proprioceptive impedance control on the MIT Cheetah. *Int J Adv Robot Res.* (2014) 33:1417–45. doi: 10.1177/0278364914532150
10. Chen D, Chen K, Zhang Z, Zhang B. Mechanism of locust air posture adjustment. *J Bionc Eng.* (2015) 12:418–31. doi: 10.1016/S1672-6529(14)60133-5
11. Noh M, Kim SW, An S, Koh JS, Cho KJ. Flea-inspired catapult mechanism for miniature jumping robots. *IEEE T Robot.* (2012) 28:1007–18. doi: 10.1109/TRO.2012.2198510
12. Kovac M, Fuchs M, Guignard A, Zufferey JC, Floreano DA. A miniature 7g jumping robot. In: *IEEE International Conference on Robotics and Automation*. Piscataway, NJ: IEEE. (2008). doi: 10.1109/ROBOT.2008.4543236
13. Woodward MA, Sitti M. Morphological intelligence counters foot slipping in the desert locust and dynamic robots. *P Natl A Sci India B.* (2018) 115:E8358–67. doi: 10.1073/pnas.1804239115
14. Hildebrand M. Motions of the running cheetah and horse. *J Mammal.* (1959) 40:481–95. doi: 10.2307/1376265
15. Koob T, Long JJ. The vertebrate body axis: evolution and mechanical function. *Am Zool.* (2000) 40:1–018. doi: 10.1093/icb/40.1.1
16. Vnuk D, Pirkić B, Matičić D, Radišić B, Stejskal M, Babić T, et al. Feline high-rise syndrome: 119 cases (1998–2001). *J Feline Med Surg.* (2004) 6:305–12. doi: 10.1016/j.jfms.2003.07.001
17. Souza A, Pinto A, Marvulle V, Matera J. Evaluation of vertical forces in the pads of German Shepherd dogs. *Vet Comp Orthopaed.* (2013) 26:06–11. doi: 10.3415/VCOT-11-07-0100
18. Zhang Q, Chon T, Zhang Y, Baker JS, Gu Y. Finite element analysis of the lumbar spine in adolescent idiopathic scoliosis subjected to different loads. *Comput Biol Med.* (2021) 136:104745. doi: 10.1016/j.compbiomed.2021.104745
19. Zhang Y, Awrejcewicz J, Baker JS, Gu Y. Cartilage stiffness effect on foot biomechanics of Chinese bound foot: a finite element analysis. *Front Physiol.* (2018) 9:1434. doi: 10.3389/fphys.2018.01434
20. Wrigley AT, Albert WJ, Deluzio KJ, Stevenson JM. Differentiating lifting technique between those who develop low back pain and those who do not. *Clin Biomech.* (2005) 20:254–63. doi: 10.1016/j.clinbiomech.2004.11.008
21. Wrigley AT, Albert WJ, Deluzio KJ, Stevenson JM. Principal component analysis of lifting waveforms. *Clin Biomech.* (2006) 21:567–78. doi: 10.1016/j.clinbiomech.2006.01.004
22. Figueiredo J, Santos CP, Moreno JC. Automatic recognition of gait patterns in human motor disorders using machine learning: a review. *Med Eng Phys.* (2018) 53:1–12. doi: 10.1016/j.medengphy.2017.12.006

23. Nigg BM, Baltich J, Maurer C, Federolf P. Shoe midsole hardness, sex and age effects on lower extremity kinematics during running. *J Biomech*. (2012) 45:1692–7. doi: 10.1016/j.jbiomech.2012.03.027
24. Robbins SM, Renaud PJ, Pearsall DJ. Principal component analysis identifies differences in ice hockey skating stride between high-and low-calibre players. *Sport Biomech.* (2021) 20:131–49. doi: 10.1080/14763141.2018.1524510
25. Yu L, Mei Q, Xiang L, Liu W, Mohamad NI, István B, et al. Principal component analysis of the running ground reaction forces with different speeds. *Front Bioeng Biotech.* (2021) 9:629809. doi: 10.3389/fbioe.2021.629809
26. Chau T. A review of analytical techniques for gait data. Part 2: neural network and wavelet methods. *Gait Posture.* (2001) 13:102–20. doi: 10.1016/S0966-6362(00)00095-3
27. Hoitz F, Von Tscharner V, Baltich J, Nigg BM. Individuality decoded by running patterns: movement characteristics that determine the uniqueness of human running. *PLoS ONE.* (2021) 16:e0249657. doi: 10.1371/journal.pone.0249657
28. Schöllhorn WI. Applications of artificial neural nets in clinical biomechanics. *Clin Biomech*. (2004) 19:876–98. doi: 10.1016/j.clinbiomech
29. Shi Z, Sun D. Conflict between weightlifting and health? The importance of injury prevention and technology assistance. *Phys Act Health.* (2022) 6:1–4. doi: 10.5334/paah.158
30. Clermont CA, Phinyomark A, Osis ST, Ferber R. Classification of higher-and lower-mileage runners based on running kinematics. *J Sport Health*. (2019) 8:249–57. doi: 10.1016/j.jshs.2017.08.003
31. Phinyomark A, Petri G, Ibáñez-Marcelo E, Osis ST, Ferber R. Analysis of big data in gait biomechanics: current trends and future directions. *J Med Biol Eng.* (2018) 38:244–60. doi: 10.1007/s40846-017-0297-2
32. Horst F, Lapuschkin S, Samek W, Müller KR, Schöllhorn WI. Explaining the unique nature of individual gait patterns with deep learning. *Sci Rep.* (2019) 9:1–13. doi: 10.1038/s41598-019-38748-8
33. Baehrens D, Schroeter T, Harmeling S, Kawanabe M, Hansen K, Müller KR. How to explain individual classification decisions. *J Mach Learn Res.* (2010) 11:1803–31. doi: 10.48550/arXiv.0912.1128
34. Montavon G, Samek W, Müller KR. Methods for interpreting and understanding deep neural networks. *Digit Signal Process*. (2018) 73:1–15. doi: 10.1016/j.dsp.2017.10.011
35. Bach S, Binder A, Montavon G, Klauschen F, Müller KR, Samek W. On pixel-wise explanations for non-linear classifier decisions by layer-wise relevance propagation. *PLoS ONE.* (2015) 10:e0130140. doi: 10.1371/journal.pone.0130140
36. Xu D, Quan W, Zhou H, Sun D, Baker JS, Gu Y. Explaining the differences of gait patterns between high and low-mileage runners with machine learning. *Sci Rep.* (2022) 12:2981. doi: 10.1038/s41598-022-07054-1
37. Samek W, Binder A, Montavon G, Lapuschkin S, Müller KR. Evaluating the visualization of what a deep neural network has learned. *IEEE Trans Neural Netw Learn Syst.* (2016) 28:2660–73. doi: 10.1109/TNNLS.2016.2599820
38. Hoy MG, Zernicke RF. Modulation of limb dynamics in the swing phase of locomotion. *J Biomech.* (1985) 18:49–60. doi: 10.1016/0021-9290(85)90044-2
39. Xu D, Zhou H, Baker JS, István B, Gu Y. An investigation of differences in lower extremity biomechanics during single-leg landing from height using bionic shoes and normal shoes. *Front Bioeng Biotech.* (2021) 9:679123. doi: 10.3389/fbioe.2021.679123
40. Xu D, Jiang X, Cen X, Baker JS, Gu Y. Single-leg landings following a volleyball spike may increase the risk of anterior cruciate ligament injury more than landing on both-legs. *Appl Sci.* (2021) 11:130. doi: 10.3390/app11010130
41. Wu X, Pei B, Pei Y, Wu N, Zhou K, Hao Y, et al. Contributions of limb joints to energy absorption during landing in cats. *Appl Bionics Biomech.* (2019) 2019:3815612. doi: 10.1155/2019/3815612
42. Zhang Z, Yu H, Yang J, Wang L, Yang L. How cat lands: insights into contribution of the forelimbs and hindlimbs to attenuating impact force. *Chin Sci Bull.* (2014) 59:3325–32. doi: 10.1007/s11434-014-0328-0
43. Winter DA. *Biomechanics and Motor Control of Human Movement*. Hoboken, NJ: John Wiley & Sons. (2009). doi: 10.1002/9780470549148
44. Flores P, Lankarani HM. *Contact Force Models for Multibody Dynamics*. Berlin: Springer (2016). p. 226. doi: 10.1007/978-3-319-30897-5
45. Daffertshofer A, Lamoth CJ, Meijer OG, Beek PJ. PCA in studying coordination and variability: a tutorial. *Clin Biomech*. (2004) 19:415–28. doi: 10.1016/j.clinbiomech.2004.01.005
46. Quan W, Zhou H, Xu D, Li S, Baker JS, Gu Y. Competitive and recreational running kinematics examined using principal components analysis. *Healthcare.* (2021) 9:1321. doi: 10.3390/healthcare9101321
47. Wold S, Geladi P, Esbensen K, Öhman J. Multi-way principal components-and PLS-analysis. *J Chemometr.* (1987) 1:41–56. doi: 10.1002/cem.1180010107
48. Wu X, Pei B, Pei Y, Wang W, Hao Y, Zhou K. How do cats resist landing injury: insights into the multi-level buffering mechanism. *J Bionic Eng.* (2020) 17:600–10. doi: 10.1007/s42235-020-0048-x
49. Longo M, Modina SC, Bellotti A, Di Giancamillo M. Advances in the anatomic study of the interscapular region of the cat. *BMC Vet Res.* (2015) 11:1–9. doi: 10.1186/s12917-015-0562-y
50. Pena E, Calvo B, Martinez M, Doblare M. A three-dimensional finite element analysis of the combined behavior of ligaments and menisci in the healthy human knee joint. *J Biomech*. (2006) 39:1686–701. doi: 10.1016/j.jbiomech.2005.04.030
51. Shahar R, Banks-Sills L, Eliasy R. Stress and strain distribution in the intact canine femur: finite element analysis. *Med Eng Phys.* (2003) 25:387–95. doi: 10.1016/S1350-4533(03)00002-X
52. Wang M, Song Y, Baker JS, Fekete G, Ugbolue UC, Li S, et al. The biomechanical characteristics of a feline distal forelimb: a finite element analysis study. *Comput Biol Med*. (2021) 129:104174. doi: 10.1016/j.compbiomed.2020.104174
53. Behforootan S, Chatzistergos P, Naemi R, Chockalingam N. Finite element modelling of the foot for clinical application: a systematic review. *Med Eng Phys*. (2017) 39:1–11. doi: 10.1016/j.medengphy.2016.10.011
54. Chen WP, Tang FT, Ju CW. Stress distribution of the foot during mid-stance to push-off in barefoot gait: a 3-D finite element analysis. *Clin Biomech.* (2001) 16:614–20. doi: 10.1016/S0268-0033(01)00047-X
55. Cheung JTM, Zhang M, Leung AK, Fan YB. Three-dimensional finite element analysis of the foot during standing—a material sensitivity study. *J Biomech*. (2005) 38:1045–54. doi: 10.1016/j.jbiomech.2004.05.035
56. Kohonen T. An introduction to neural computing. *Neural Netw*. (1988) 1:3–16. doi: 10.1016/0893-6080(88)90020-2
57. Liu W, Wang Z, Liu X, Zeng N, Liu Y, Alsaadi FE. A survey of deep neural network architectures and their applications. *Neurocomputing*. (2017) 234:11–26. doi: 10.1016/j.neucom.2016.12.038
58. Montavon G, Binder A, Lapuschkin S, Samek W, Müller KR. Layer-wise relevance propagation: an overview. Explainable AI: interpreting, explaining and visualizing deep learning. Springer Nature Ltd, Berlin, Germany. (2019). doi: 10.1007/978-3-030-28954-6_10
59. Binder A, Bach S, Montavon G, Müller KR, Samek W. Layer-wise relevance propagation for deep neural network architectures. In: *Information Science and Applications (ICISA). Lecture Notes in Electrical Engineering, vol. 376*. Singapore: Springer (2016). p. 913–22. doi: 10.1007/978-981-10-0557-2_87
60. Lapuschkin S, Binder A, Montavon G, Müller KR, Samek W. The LRP toolbox for artificial neural networks. *J Mach Learn Res.* (2016) 17:3938–42. Available online at: http://jmlr.org/papers/v17/15-618.html
61. Chicco D, Jurman G. The advantages of the Matthews correlation coefficient (MCC) over F1 score and accuracy in binary classification evaluation. *BMC Genom.* (2020) 21:1–13. doi: 10.1186/s12864-019-6413-7
62. Powers DM. Evaluation: from precision, recall and F-measure to ROC, informedness, markedness and correlation. *Int J Mach Learn Tech.* (2020) 2:37–63. doi: 10.48550/arXiv.2010.16061
63. Prilutsky BI, Herzog W, Leonard TR, Allinger TL. Role of the muscle belly and tendon of soleus, gastrocnemius, and plantaris in mechanical energy absorption and generation during cat locomotion. *J Biomech.* (1996) 29:417–34. doi: 10.1016/0021-9290(95)00085-2
64. Liu C, Wang G, Zhou H, Mei Y, Asafo-Duho BM. Adaptability of kinetic parameters to a narrow speed range in healthy free-moving cats. *Math Probl Eng.* (2020) 24:1–9. doi: 10.1155/2020/2954329
65. Prochazka A, Schofield P, Westerman RA, Ziccone SP. Reflexes in cat ankle muscles after landing from falls. *J Physiol.* (1977) 272:705–19. doi: 10.1113/jphysiol.1977.sp012068
66. Corral E, Moreno RG, García MG, Castejón C. Nonlinear phenomena of contact in multibody systems dynamics: a review. *Nonlinear Dyn.* (2021) 104:1269–95. doi: 10.1007/s11071-021-06344-z

67. Ma F, Ni L, Wei L, Nie J, Wu L, Jia W. *Posture Control of All Terrain Mobile Robot With Vibration Isolation System*. Berlin: Springer (2019) 1794–807. doi: 10.1007/978-3-030-38077-9_205
68. Yin J. Design of foot cam vibration damping system for forest walking robot. In: *International Conference on Big Data Analytics for Cyber-Physical-Systems*. Berlin: Springer (2020) 1303:45–51. doi: 10.1007/978-981-33-4572-0_7
69. Song H, Kong K. Analysis of vibrations transmitted to the quadruped robot body during trotting with different stiffness of feet. In: *2018 18th International Conference on Control, Automation and Systems (ICCAS 2018)*. PyeongChang, South Korea: Institute of Control, Robotics and Systems (2018).
70. Von Falck C, Hawi N. Frakturdiagnostik: obere Extremität. *Radiologe.* (2020) 60:541–8. doi: 10.1007/s00117-020-00682-6
71. Cong Q, Shi X, Wang J, Xiong Y, Su B, Jiang L, et al. Design of bionic buffering and vibration reduction foot for legged robots. *Appl Bionics Biomech.* (2021) 2021:1–9. doi: 10.1155/2021/5510993
72. Chen K, Chen D, Zhang Z, Zhang B. Analysis of wings effects on locust-like robot air posture. *J Beijing University Aeronau Astronau.* (2016) 42:165. doi: 10.13700/j.bh.1001-5965.2015.0098

Conflict of Interest: The authors declare that the research was conducted in the absence of any commercial or financial relationships that could be construed as a potential conflict of interest.

frontiers | Frontiers in Bioengineering and Biotechnology

ORIGINAL RESEARCH
published: 27 April 2022
doi: 10.3389/fbioe.2022.804826

A Template Model Explains Jerboa Gait Transitions Across a Broad Range of Speeds

*Jiayu Ding [1], Talia Y. Moore [2] and Zhenyu Gan [1]**

[1]*Dynamic Locomotion and Robotics Laboratory, Department of Mechanical and Aerospace Engineering, Syracuse University, Syracuse, NY, United States,* [2]*Evolution and Motion of Biology and Robotics Laboratory, Department of Mechanical Engineering, Robotics Institute, Ecology and Evolutionary Biology, and Museum of Zoology, University of MI, Ann Arbor, MI, United States*

For cursorial animals that maintain high speeds for extended durations of locomotion, transitions between footfall patterns (gaits) predictably occur at distinct speed ranges. How do transitions among gaits occur for non-cursorial animals? Jerboas (*Jaculus*) are bipedal hopping rodents that frequently transition between gaits throughout their entire speed range. It has been hypothesized that these non-cursorial bipedal gait transitions are likely to enhance their maneuverability and predator evasion ability. However, it is difficult to use the underlying dynamics of these locomotion patterns to predict gait transitions due to the large number of degrees of freedom expressed by the animals. To this end, we used empirical jerboa kinematics and dynamics to develop a unified spring Loaded Inverted Pendulum model with defined passive swing leg motions. To find periodic solutions of this model, we formulated the gait search as a boundary value problem and described an asymmetrical running gait exhibited by the jerboas that emerged from the numerical search. To understand how jerboas change from one gait to another, we employed an optimization approach and used the proposed model to reproduce observed patterns of jerboa gait transitions. We then ran a detailed numerical study of the structure of gait patterns using a continuation approach in which transitions are represented by bifurcations. We found two primary mechanisms to increase the range of speeds at which gait transitions can occur. Coupled changes in the neutral leg swing angle alter leg dynamics. This mechanism generates changes in gait features (e.g., touchdown leg angle and timings of gait events) that have previously been shown to induce gait transitions. This mechanism slightly alters the speeds at which existing gait transitions occur. The model can also uncouple the left and right neutral leg swing angle, which generates asymmetries between left and right leg dynamics. New gait transitions emerge from uncoupled models across a broad range of speeds. In both the experimental observations and in the model, the majority of the gait transitions involve the skipping and asymmetrical running gaits generated by the uncoupled neutral leg swing angle mechanism. This simulated jerboa model is capable of systematically reproducing all biologically relevant gait transitions at a broad range of speeds.

Keywords: legged robots, dynamics, bipedal locomotion, non-cursorial locomotion, gait transitions

OPEN ACCESS

Edited by:
John R Hutchinson, Royal Veterinary College (RVC), United Kingdom

Reviewed by:
Steve Heim, Massachusetts Institute of Technology, United States
David V Lee, University of Nevada, Las Vegas, United States
Christian Hubicki, Florida Agricultural and Mechanical University, United States

****Correspondence:***
Zhenyu Gan
zgan02@syr.edu

Specialty section:
This article was submitted to Biomechanics, a section of the journal Frontiers in Bioengineering and Biotechnology

Received: *29 October 2021*
Accepted: *14 March 2022*
Published: *27 April 2022*

Citation:
Ding J, Moore TY and Gan Z (2022) A Template Model Explains Jerboa Gait Transitions Across a Broad Range of Speeds. Front. Bioeng. Biotechnol. 10:804826. doi: 10.3389/fbioe.2022.804826

1 INTRODUCTION

Despite vast differences in morphology, the locomotion patterns of many legged animals are strikingly similar (Alexander, 2002). Typically, these gait patterns can be characterized by repeated footfall sequences (Alexander, 1984; Hildebrand, 1989), the ground reaction force profile (Alexander, 2009) or by how gravitational, potential and kinetic energies are exchanged over the course of a stride (Cavagna et al., 1977). As the speed of locomotion increases, quadrupedal cursorial animals, such as horses or gazelles, switch from using a walking gait at low speeds to a trotting or pacing gait at intermediate speeds, and then a galloping gait at their highest speeds. Previous studies suggest that each gait minimizes oxygen consumption (Hoyt and Taylor, 1981; Minetti et al., 1999) and minimizes the loading impact on the musculoskeletal system (Farley and Taylor, 1991; Lee et al., 2011) at a distinct speed range. Therefore, transitioning between gaits as speed increases helps cursorial animals minimize the cost of sustained steady-state locomotion, thereby enhancing endurance at high speeds. Based on these fundamental principles, the speeds at which cursorial gaits occur can be predicted by the ratio of centripetal to gravitational force (as an animal moves over its supporting limb), or the Froude number (Alexander and Jayes, 2009).

On the other hand, rapid and energetically costly changes in acceleration and direction of movement are important for small animals evading predators (Biewener and Blickhan, 1988; Chance and Russell, 2009; Domenici et al., 2011). Some quadrupedal and hexapedal prey animals temporarily rear up on hindlimbs and use bipedal locomotion to enhance acceleration during escape (Full and Tu, 1991; Clemente, 2014). Notably, jerboas (Dipodidae) are desert rodents that evolved obligately bipedal locomotion from quadrupedal ancestors. Although pentapedal (quadrupedal with additional support from the tail) locomotion occurs during in postnatal development (Eilam and Shefer, 1997), and quadrupedal locomotion is used infrequently at slower speeds (Happold, 1967), jerboas are the only hopping rodent to use multiple bipedal gaits as their primary mode of locomotion as adults (Moore et al., 2017). The hopping, skipping, and running gaits are used throughout the entire jerboa speed ranges, with frequent ($\approx 50\%$ of all recorded trials) transitions between gaits that are not predicted by the Froude equation (Moore et al., 2017). Because each gait is associated with a distinct range of acceleration, rather than speed, frequent gait transitions likely enhance the potential maneuverability and predator evasion ability of a jerboa (Moore et al., 2017). Thus, building models to characterize non-cursorial locomotion can help us understand more agile and maneuverable locomotion.

The center of mass dynamics and kinematics for a wide variety of cursorial animals can be modeled using a simplified "template" approach with minimal degrees of freedom (Full and Koditschek, 1999). McGeer (1990) demonstrated that an Inverted Pendulum model (IP) with two rigid legs is capable of walking on a sloped ramp without the help of any additional controllers or actuators. A Spring-Loaded Inverted Pendulum (SLIP) model explains the kinetic and potential energy exchanges in running gaits (Blickhan, 1989; Farley et al., 1993). These models have been shown to explain the locomotion of cursorial animals that differ greatly in size, leg number, or posture. The simplicity and broad applicability of these template models have made them invaluable for designing controllers for legged robots (Hereid et al., 2014; DSCC, 2015).

Although these simplified models have been useful for generating single-gait controllers, efficient and reliable transitioning between gaits has been a consistent challenge for legged robotics. Many robots use a heuristic controller that initiates a gait transition by either stopping locomotion entirely and then performing a sequence of procedures to guide the system into another gait pattern or adding energy into the system by providing a thrust during the stance phases. These existing controllers usually generate abrupt changes in center of mass trajectories or leg speeds (Hyun et al., 2014; Hyun et al., 2016). Most recently, reinforced learning controllers (Hwangbo et al., 2019; Siekmann et al., 2020) have been proposed to enable smooth and stable gait changes. However, this approach not only requires a large amount of data gathered from a particular application, but very limited knowledge can be learned about why and how this type of controller might outperform its conventional counterparts. Empirical data from animals has informed theoretical models to explain how gait transitions can be initiated across a broad range of speeds, potentially reveal new methodologies for synthesizing switching controllers.

For quadrupedal locomotion, gaits can be modeled as dynamical systems for which gaits with inter-limb coordination are stable attractors (Schöner et al., 1990). In these models, gait transitions associated with lack of coordination can be identified as bifurcations along gait system paths in parameter space. Genetic knockouts in pattern-generating neural pathways confirm that changes in synchronization between fore-hind and left-right leg pairs can induce a gait transition as speed increases (Danner et al., 2016). Breaking coordination between limbs has been successfully used as a mechanism to transition a quadrupedal robot from walking to trotting (Shinya et al., 2013). Previous studies have described how changes in gait features (i.e., leg contact angle, timing of gait events) result in gait transitions, it is difficult to translate these findings into robotic controllers but without understanding how model dynamics result in such changes in gait features. For bipedal locomotion, Geyer et al. (2006) found that a unified SLIP model can explain both bipedal walking and running gaits, which suggests that these two gaits are different oscillation modes of the same mechanical system with different energy levels. This insight has been useful for predicting gait transitions in cursorial bipeds (Gan et al., 2018b).

Here, we built upon previous template models (Geyer et al., 2006; O'Connor, 2009; Shen and Seipel, 2012) to provide the first insights into the factors determining the gait transitions of non-cursorial bipeds, such as jerboas. First, we experimentally measured Lesser Egyptian jerboa (*Jaculus*) kinematics and dynamics for each gait across a broad range of speeds. We used numerical optimization to match an extended SLIP model (Gan et al., 2018b) to the jerboa data. The resulting walking and running gaits were similar to the ones found in

(Geyer et al., 2006). However, while the previous model required directly changing the angle of attack, the passive dynamics of the proposed model determine swing leg motion to generate different gaits. As a result, many other gaits, including those that require two different leg contact angles (e.g., asymmetrical bipedal skipping) emerge from the proposed model as a natural continuation from the gait search. We formally defined asymmetrical running, a jerboa gait that emerged from the numerical search. Using a detailed parameter scan, we identified two distinct mechanisms to induce a transition between these four gaits (walking, running, skipping and asymmetrical running). The proposed bipedal model that couples the neutral angle of both legs during the swing phase can change this angle to induce a gait transition. Alternatively, the model can uncouple the offset between the neutral angle of each leg during the swing phase to induce a gait transition. With these two mechanisms, the extended SLIP model is capable of matching the jerboa pattern of transitioning between gaits across a broad range of speeds. We also found that on the Poincaré section, the fixed points of the skipping gait are in close proximity to solutions found for all other gaits, which explains why jerboas transition to and from skipping gaits most frequently (Moore et al., 2017). Thus, this extended SLIP model matches empirical jerboa kinematics and dynamics, predicts gait transitions throughout a broad range of speeds, and provides a mechanism for initiating these gait transitions.

2 METHODS

2.1 Animal Experiments

Details of the data collection procedure were reported in a previous publication in which the speeds and acceleration ranges associated with each gait were determined (Moore et al., 2017). Trials were collected from five captive male jerboas traveling along a narrow track ($2 \times 0.15 \times 0.4$ m^3) over a two-axis force platform (0.06×0.12 m^2) and past a high-speed video camera recording at 500 fps. We visually categorized the gait of each stride by footfall pattern. Both feet striking and lifting off simultaneously were considered hopping. Overlapping but non-simultaneous foot strikes were considered skipping, according to previous work (Moore et al., 2017). If the same leg maintained the leading foot position, this gait would be equivalent to a bipedal gallop, as defined in previous gait research (Schropfer et al., 1985; Gan et al., 2018b). An aerial phase between each foot strike was considered running if each aerial phase was approximately the same duration.

To extract the kinematic data (i.e., center of mass (COM) locations and leg angles over one stride) from the video recordings, we used **DeepLabCut**, a markerless pose estimation framework leveraging a deep neural network (DNN) (Mathis et al., 2018). In this study, 35 videos that contained a whole stride of a single gait pattern were used to train the DNN. All three common jerboa gaits reported in (Moore et al., 2017) (i.e., hopping, skipping, running) were included in this study. Roughly 1/3 of the total frames of each video were selected as the training data set. In these frames, we manually labelled the location of the eye, the tail-base, and the two feet, as shown in **Figure 1** A. We estimated the COM location as the midpoint between the eye and the tail-base. Then the leg angles were calculated as the orientation of the line segments connecting the COM to the feet.

2.2 Model Description

The proposed model used in this study consists of a point mass as the main body, with mass m, and two massless legs, as illustrated in **Figure 1B**. The vertical and horizontal positions of the main body were defined by the variables $x(t)$ and $y(t)$, respectively. Left and right legs (with index $i \in [l, r]$) were modeled as massless linear springs with resting leg length l_o and total spring stiffness k. Both legs were connected to the main body through frictionless rotational joints, with the joint angle $\alpha_i(t)$ measured from the vertical axis (positive in the counterclockwise direction). Comparing with the convectional SLIP model, which ignores swing leg motions by setting the leg to predefined angles of attack immediately after lifting off, we added a torsional passive spring to control the leg swing motion during the flight phase of each leg. This is similar to the monopedal SLIP model with hip torque and leg damping proposed by (Shen and Seipel, 2012), in which active constant hip torques and leg dampings during the stance phase improved the stability and robustness of locomotion. In contrast, the torsional springs in our model provide passive torques enable the rotational motions of the swing legs to facilitate gait transitions. The torsional spring directly connected the leg to the main body at angle, φ_i (hereafter referred to as the neutral swing leg angle (NSLA), measured with respect to the vertical direction (**Figure 1B**). By fixing the oscillation frequency ω, this torsional spring dictates the swing leg rotational speed and amplitude and determines the desired contact angle at the moment of touchdown. Because we can assume that the torsional spring stiffness and the foot mass have infinitesimal values, they do not affect stance leg kinematics or dynamics (Gan et al., 2018b).

In our work, we ran optimizations to fit the trajectories of leg angles (**Figure 2**) to determine the oscillation frequency ω. The full set of parameters of the proposed model is denoted as $\vec{p} := [m, l_o, g, k, \omega, \varphi_l, \varphi_r]$.

The total stride time was defined as T and its value was not known before finding a gait pattern of the proposed model. Without loss of generality, we chose the apex transition ($\dot{y}_o = \dot{y}(T) = 0\ \sqrt{l_o g}$) as the Poincaré section. This means that the beginning of each gait cycle was defined as the peak of the aerial phase, when the COM was highest off of the ground. To reproduce all observed bipedal gait patterns of jerboas and analyze their transitions, we did not prescribe a specific footfall pattern. Instead, we introduced four timing variables t_i^j (with index $i \in [l, r]$, $j \in [td, lo]$), for the touchdown and liftoff events that are confined within the time interval of one stride $[0, T)$. Their values were determined and sorted through the gait finding process, as detailed in Section 2.4. The full set of timing variables of the proposed model is encapsulated in a vector $\vec{t}^T := [t_l^{td}, t_l^{lo}, t_r^{td}, t_r^{lo}, T]$.

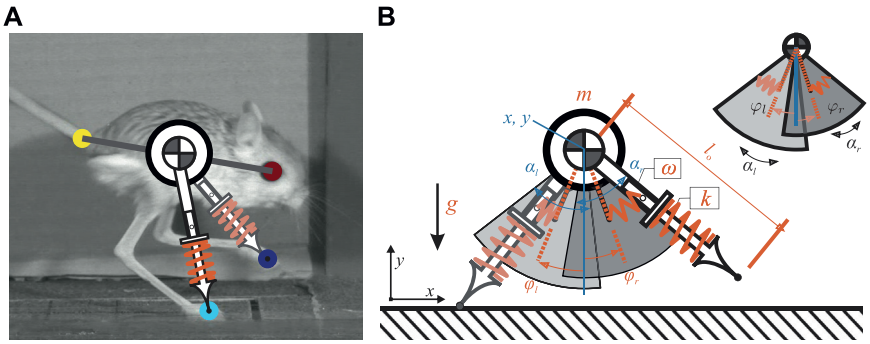

FIGURE 1 | (A) shows how the proposed model relates to a jerboa. The COM location is approximated as the midpoint between the eye and the tail-base. The leg angles are estimated by the orientation of the line segments connecting the COM to the feet **(B)** illustrates the proposed SLIP model with passive swing leg motion. There are four continuous states (shown in blue) including the position of the torso (x, y) as well as the leg angles $(\alpha_{l_0}, \alpha_{r_0})$. Model parameters are highlighted in red, including total body mass, m, uncompressed leg length, l_o, gravity, g, and leg stiffness, k. Adding a torsional spring to a SLIP model enables motion of passive swing leg. The rotational speeds of both swing legs are determined by ω and the neutral leg angle are φ_l and φ_r respectfully. Note that the neutral leg swing angle for the right leg, φ_r, is different from that of the left leg, demonstrating an uncoupled model. A simplified version of the model showing the range of the swing leg motion is also shown in the top-right corner.

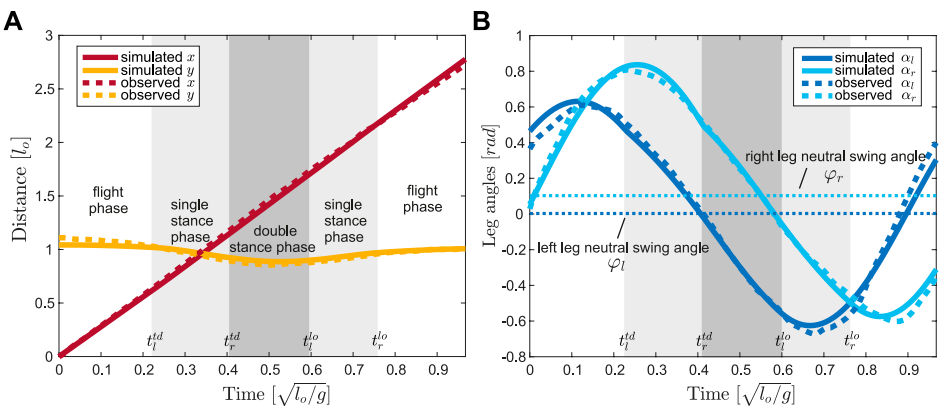

FIGURE 2 | Trajectory optimization results, in solid lines, for **(A)** the COM position $[x, y]$ and **(B)** the leg angles $[\alpha_{l_0}, \alpha_{r_0}]$ of trial 1802–*j*30 closely match the empirical data, in dashed lines. The fitting result shows whole stride, starting from the apex transition, when $t \in [0, T]$ in the flight phase (white background). The single stance phases are indicated by the lighter gray background and the double stance phases are indicated by the darker gray background. Compared to the rotational motion of the left leg (dark blue), the right leg rotations are translated anteriorly (light blue), which is reflected in our model by setting the neutral leg swing angles to φ_l =0.032 rad and φ_r =0.137 rad, marked by horizontal dotted lines in **(B)**. The difference between φ_l and φ_r is the offset in uncoupled leg models.

2.3 Equations of Motion

Using the position and velocity vectors $\vec{q}^T := [x, y, \alpha_l, \alpha_r]$, $\dot{\vec{q}}^T := [\dot{x}, \dot{y}, \dot{\alpha}_l, \dot{\alpha}_r]$ to describe the state of the system, we expressed the dynamics as a set of second-order time-varying differential equations $\ddot{\vec{q}} = f(\vec{q}, \dot{\vec{q}}, \vec{t}, \vec{p})$ that is parameterized by $\vec{p}$. The equations of motion (EOM) were defined for the main body as:

$$\ddot{x} = F_x/m, \quad \ddot{y} = F_y/m - g, \tag{1}$$

where F_x and F_y represent the net forces and torques generated by the leg pairs. The dynamics of the leg pairs depended on whether the legs were in contact with the ground. During the swing phase, the leg was set to its uncompressed original length l_o and the leg angular accelerations were defined by:

$$\ddot{\alpha}_{\text{swing},i} = 1/l_o\left(\ddot{x}\cos\alpha_i + (g + \ddot{y})\sin\alpha_i\right) + \omega^2 m(\alpha_i - \varphi_i), \tag{2}$$

During stance, we assumed that the ground has infinite friction so that the stance foot did not slide on the ground. A holonomic constraint was introduced to make sure the horizontal position of the contact foot $(x_{c,i})$ was stationary.

$$x_{c,i} - x - y\tan\alpha_i = 0, \tag{3}$$

Whenever a leg entered stance phase, the angular acceleration of that leg was determined by the accelerations of the main body, which was directly computed from the above ground constraint by taking the time derivative twice:

$$\ddot{\alpha}_{\text{stance},i} = -2\dot{\alpha}_i^2\tan(\alpha_i) - \frac{2\dot{\alpha}_i\dot{y}}{y} - \frac{\ddot{x} + \ddot{y}\tan(\alpha_i)}{y\sec^2(\alpha_i)}. \tag{4}$$

In addition, at the moments of touch-down t_i^{td}, the leg velocities were reset according to the holonomic constraint **Equation (3)**, resulting in additional discrete dynamics to ensure zero stance foot velocity when integrating **Equation (4)**. t_i^{td+} and t_i^{td-} were

used to indicate the moments right after and before the touchdown event of a leg, respectively.

$$\dot{\vec{q}}\left(t_i^{td+}\right) = h\left(\vec{q}\left(t_i^{td-}\right), \dot{\vec{q}}\left(t_i^{td-}\right)\right). \tag{5}$$

Posterior neutral leg swing angles usually induced a premature touchdown event during anterior swing leg motion, causing the leg to immediately rotate posteriorly and inducing a large angular velocity reset (**Eq. (5)**). Because this behavior is rarely seen in jerboa locomotion, we terminated the numerical search when this phenomenon was detected.

2.4 Gait Finding and Continuation

Due to the nonlinearity and the hybrid nature of the EOM presented in Section 2.3, it was not possible to find explicit periodic solutions of the proposed model. Therefore, in this work we identified gait patterns as numerical solutions dictated by the initial condition of the continuous states $\vec{q}_o$, $\dot{\vec{q}}_o$ and system parameters $\vec{p}^T$. Because a gait of the system is a periodic motion, finding a bipedal gait in this model was equivalent to solving a root of the following set of constraint equations:

$$\begin{aligned} &\text{find} \quad \vec{q}_o, \dot{\vec{q}}_o, \vec{t} \\ &\text{such that :} \\ &\begin{cases} \vec{q}(T) - \vec{q}_o = 0, \\ \dot{\vec{q}}(T) - \dot{\vec{q}}_o = 0, \\ y\left(t_i^j\right) - l_o \cos\left(\alpha_i\left(t_i^j\right)\right) = 0 \quad \text{for every} \quad i \in [l, r], j \in [td, lo]. \end{cases} \end{aligned} \tag{6}$$

This is a passive model with no additional controllers or actuators. When the parameters of the proposed model were fixed, there were 13 variables ($\vec{q}_o$, $\dot{\vec{q}}_o$, $\vec{t}$) and 12 constraints (equalities listed in **Eq. (6)**). For such a conservative model, the total energy stored in the system can be calculated as $E = \frac{1}{2}m\dot{x}_o^2 + \frac{1}{2}m\dot{y}_o^2 + mgy_o$, so varying the initial conditions is equivalent to changing the total energy. As a result, periodic solutions formed one-dimensional manifolds (hereafter referred to as **branches**) as the total energy stored in the system varied. We integrated the system over a complete stride using the Runge-Kutta-Fehlberg Method (RKF) (Fehlberg, 1969) and solved for roots of the above equalities using the fsolve function of Matlab. Finding the first periodic motion (gait) of the proposed model requires a good estimation of the initial states. It is the easiest to start with a solution of zero forward speed in which the horizontal position of COM, the leg angles, and leg angular velocities remain at zeros during the whole stride. Once one periodic motion was found, we ran numerical continuations using the predictor and corrector method (Gan et al., 2018a) to quickly explore the adjacent periodic solutions and their transitions to other gait patterns. Because most of the gait transitions appeared from the numerical search as a **bifurcation point**, at which one of the Floquet multipliers of the system is equal to +1, the corresponding eigenvector was approximately directed towards the solution with the new gait pattern (Gan et al., 2018b).

In nature, jerboas move with step-to-step changes in stride length, direction, gait, and speed and rarely demonstrate exact periodic gait patterns. In this work, we assume they are utilizing a stabilizing controller for a desired limit cycle, which is changed discretely each step. We also assume that the state of the jerboa is always within the region of attraction of the controller and the desired limit cycles. Additionally, we only explored gaits with a left-leg phase advance because the motions of the left-advanced gaits and right-advanced gaits were identical when the leg parameters were the same and the two legs were switched. Thus, although they occurred in the animals, we did not mathematically explore gait transitions between left-advanced and right-advanced skipping gaits.

2.5 Parameter Identification

To reduce the number of free parameters and identify their values in the proposed model, we normalized all values in the model in terms of the total mass of the system, m, the uncompressed leg length, l_o, and the gravity on Earth, g (Hof, 1996). The estimation of leg stiffness was based on the assumptions that legs were massless and that they behaved as simple linear springs. The period of the oscillation around the leg was therefore dictated by the spring stiffness, according to $\sqrt{k/m}$. To estimate the swing leg oscillation frequency ω, and to determine how well the proposed model can explain the empirical motions of jerboas, we proposed the following optimization framework.

By solving **Equation (6)**, the simulated model trajectories of positions and velocities of a periodic solution can be represented by a 3-tuple $\vec{X} := (\vec{q}^{\bigstar}, \dot{\vec{q}}^{\bigstar}, \vec{t}^{\bigstar})$. For the nth experimental trial, the residual function $C_n(\vec{X}, \vec{p})$ quantifies how well the model with a specific parameter set $\vec{p}$ predicted the kinematics of the locomotion pattern in jerboas. The empirical positions and velocities of jerboas from the nth experimental trial were denoted by $\vec{q}_n^e$ and $\dot{\vec{q}}_n^e$, respectively. The value of this cost function was minimized as a nonlinear optimization problem with an optimal set of parameters, $\vec{p}$:

$$C_{opt} = \min_{X,\, p} \left\{ C_n \colon = \int_0^{T^{\bigstar}} \left\| \vec{q}^{\bigstar}(t, p) - \vec{q}_n^e(t) \right\|^2 + \left\| \dot{\vec{q}}^{\bigstar}(t, p) - \dot{\vec{q}}_n^e(t) \right\|^2 dt \right\}. \tag{7}$$

This algorithm was implemented in Matlab using sequential quadratic programming (SQP). Each optimization problem can be solved on a regular desktop computer with an Intel Core i7 3.4 GHz processor in a few minutes.

3 RESULTS

In this study we created a high-fidelity template model that can accurately reproduce jerboa gait transitions. First we demonstrate a simulated skipping gait pattern from the template model using the proposed optimization algorithm. Next, Section 3.2 formally defines the symmetric and asymmetric jerboa gaits, including the first description of the asymmetrical running gait. Then, we analyze the effects of varying NLSA in two different scenarios. In Section 3.3, the NLSA of both legs are varied together and thereafter referred as the coupled leg model. In Section 3.4, we allow offset, or differences, in the right and left NLSA and call it the uncoupled leg model. In the last section, we validate our

TABLE 1 | Optimized initial states and system parameters of the proposed model associated with all 12 empirical trials of jerboa skipping locomotion are listed in this table. The optimized trajectory of trial 1802-j30 corresponds to **Figure 2**. All states and parameters are normalized with respect to the total mass of the system, m, the uncompressed leg length, l_o, and the gravity on Earth, g.

Jerboa	**j30**				**j38**				**j44**			**j61**
Recording	**1802**	**1826**	**1827**	**1828**	**2007**	**2018**	**2029**	**2035**	**1138**	**1317**	**1320**	**1940**
States	**sim exp**	**sim exp**	**sim exp**	**sim exp**	**sim exp**	**sim exp**	**sim exp**	**sim exp**	**sim exp**	**sim exp**	**sim exp**	**sim exp**
$\dot{x}_o\ \sqrt{g/l_o}$	2.86 2.22	4.27 4.05	5.01 5.47	4.07 3.61	3.88 4.73	3.83 4.06	4.64 5.09	3.64 3.52	1.79 1.53	1.82 1.99	2.08 2.30	2.15 2.13
$y_o\ l_o$	1.04 1.11	0.96 1.01	0.90 0.96	0.86 0.88	1.15 1.26	1.16 1.22	0.98 1.09	1.08 1.11	1.33 1.36	1.19 1.34	1.07 1.17	1.10 1.15
$\dot{y}_o\ \sqrt{g/l_o}$	0.01 0.15	0.01–0.21	0.00–0.04	0.00–0.26	-0.12–0.16	0.00 0.03	-0.07–0.91	-0.09 0.07	-0.18 0.12	-0.02–0.33	0.00–0.10	0.00–0.82
$\alpha_{l_0}\ rad$	0.35 0.36	0.27 0.30	0.55 0.55	0.15 0.06	0.36 0.47	-0.17–0.64	0.17 0.08	0.19 0.13	-0.32–0.38	0.01–0.06	-0.15–0.36	0.23 0.24
$\dot{\alpha}_{l_0}\ \sqrt{g/l_o}$	3.18 3.90	5.18 7.72	4.07 4.33	5.14 7.41	3.61 2.28	3.21 4.39	5.16 8.12	4.47 4.72	2.52 2.87	1.84 2.20	1.79 2.89	2.33 1.27
$\alpha_{r_0}\ rad$	0.12 0.03	0.66 0.76	0.68 0.69	0.45 0.33	0.36 0.32	-0.24–0.32	-0.08–0.29	-0.21–0.45	0.56 0.29	0.41 0.44	0.49 0.41	-0.30–0.33
$\dot{\alpha}_{r_0}\ \sqrt{g/l_o}$	4.15 7.09	3.59 1.92	2.21 1.33	4.49 7.79	2.83 2.80	4.61 5.52	5.66 6.89	4.33 5.52	-0.21 1.56	0.91 0.89	1.67 3.11	3.33 2.28
Timing	**sim exp**	**sim exp**	**sim exp**	**sim exp**	**sim exp**	**sim exp**	**sim exp**	**sim exp**	**sim exp**	**sim exp**	**sim exp**	**sim exp**
$t_l^{td}\ \sqrt{l_o/g}$	0.45 0.32	0.44 0.50	0.53 0.49	0.49 0.54	0.47 0.43	0.38 0.36	0.30 0.28	0.48 0.47	0.43 0.51	0.45 0.50	0.52 0.52	0.27 0.31
$t_l^{lo}\ \sqrt{l_o/g}$	0.60 0.56	0.63 0.68	0.68 0.67	0.61 0.74	0.59 0.60	0.52 0.56	0.47 0.44	0.64 0.66	0.68 0.78	0.65 0.71	0.65 0.74	0.68 0.66
$t_r^{td}\ \sqrt{l_o/g}$	0.45 0.45	0.29 0.36	0.29 0.33	0.46 0.43	0.64 0.60	0.48 0.47	0.43 0.48	0.61 0.61	0.44 0.31	0.26 0.29	0.37 0.30	0.60 0.49
$t_r^{lo}\ \sqrt{l_o/g}$	0.81 0.68	0.49 0.57	0.56 0.51	0.62 0.61	0.72 0.78	0.60 0.65	0.62 0.69	0.85 0.79	0.57 0.50	0.47 0.46	0.51 0.52	0.85 0.77
Duty Factor	0.26 0.24	0.19 0.20	0.21 0.18	0.14 0.19	0.12 0.17	0.13 0.19	0.18 0.19	0.20 0.18	0.19 0.23	0.21 0.19	0.14 0.22	0.33 0.31
Stride Time $\sqrt{l_o/g}$	0.93 0.97	0.91 0.79	0.68 0.69	0.84 0.81	0.91 0.90	1.27 1.24	0.90 0.88	0.90 0.92	1.77 1.70	1.66 1.60	1.51 1.44	0.83 0.87
Stride Length l_o	2.69 2.73	3.89 3.30	3.38 3.34	3.37 3.13	3.52 3.38	5.01 4.84	4.17 4.11	3.28 3.40	3.05 2.97	3.13 2.93	3.18 2.88	1.91 2.01
Average Speed $\sqrt{g/l_o}$	2.88 2.81	4.26 4.13	4.99 4.85	4.00 3.83	3.86 3.76	3.99 3.88	4.64 4.70	3.64 3.71	1.73 1.75	1.91 1.83	2.12 1.99	2.32 2.44
R-squared												
X	0.99	0.99	0.99	0.99	0.99	0.99	0.99	0.99	0.99	0.99	0.98	0.99
Y	0.88	0.97	0.90	0.94	0.83	0.92	0.84	0.93	0.95	0.89	0.88	0.95
α_l	0.99	0.98	0.99	0.99	0.99	0.90	0.99	0.99	0.99	0.97	0.86	0.97
α_r	0.99	0.99	0.99	0.99	0.99	0.99	0.98	0.98	0.97	0.99	0.97	0.98
Parameters												
$\omega\ \sqrt{g/l_o}$	6.49	6.87	6.99	6.75	5.86	4.84	6.37	5.94	3.27	3.63	4.08	7.17
$\varphi_l\ rad$	0.02	0.23	0.32	0.28	0.03	-0.17	-0.45	-0.12	-0.15	0.18	0.26	-0.10
$\varphi_r\ rad$	0.17	0.03	0.00	0.22	0.40	-0.01	-0.09	0.07	0.16	-0.10	-0.04	-0.05

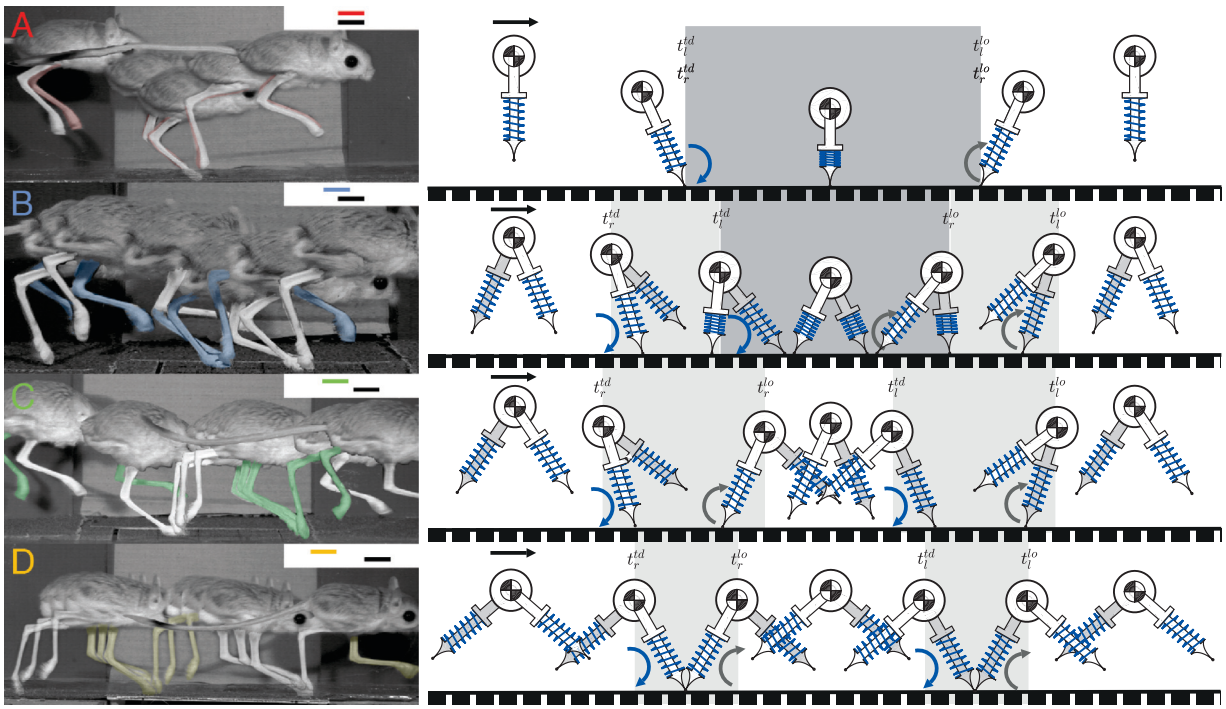

FIGURE 3 | The apex transitions, touchdowns, and liftoffs for one stride of four different gait patterns are demonstrated by jerboas on the left, with inset gait diagrams showing footfall patterns, the corresponding simulated gait patterns using our model are shown on the right. The right leg of jerboa is shown in white and the left leg is in the same color as the corresponding gait branches shown in the inset gait diagram and in **Figure 4**. The left leg of the model is shown in grey and the right leg is in white **(A)** shows hopping in which both feet strike and lift off simultaneously **(B)** shows skipping with overlapping but non-simultaneous foot strikes (**C**) shows asymmetrical running with two different aerial phases **(D)** shows symmetrical running which contains two aerial phases with approximately the same duration. Blue curved arrows indicate leg touchdown (t_i^{td}) and the gray curved arrows denote liftoff events (t_i^{lo}).

model by comparing our predictions to empirical gait transition data from jerboas. The framework we created and a video showing the jerboa gait transitions have been included in the **Supplementary Material**.

3.1 Optimized Model Parameters Recreate Empirical Observations

As mentioned in the previous sections, the full set of parameters of the proposed model was denoted as $\vec{p}_T := [m, l_o, g, k, \omega, \varphi_l, \varphi_r]$. All values were normalized and m, the uncompressed leg length, l_o, and the gravity on Earth, g which were all set to a value of one. Based on the methods in Section 2.5, the mean value and the standard deviation of the leg spring stiffness was estimated at $k = 19.24 \pm 2.43\ mg/l_o$. Swing leg oscillation frequency ω varied minimally across trials for each jerboa (e.g., $6.77 \pm 0.18\ \sqrt{g/l_o}$ for j30, $5.75 \pm 0.65\ \sqrt{g/l_o}$ for j38). Because the deviations of both leg stiffness and swing leg oscillation frequency were relatively small in our entire data set, we assumed they were not the major contributors to the gait transitions in jerboas. Thus, we set leg stiffness to $20\ mg/l_o$ for the subsequent simulations and used $6.5\ \sqrt{g/l_o}$. For a given set of parameters, we exhaustively searched for solutions, which resulted in a maximum forward speed of $29\sqrt{gl_o}$. Although these branches included unrealistic speeds, all gait transitions emerged below $8\sqrt{gl_o}$. The optimized parameters (**Table 1**) produced trajectories that closely match the empirical jerboa COM location and both leg angles (coefficient of determination $0.83 <$ R-squared < 0.99, **Figure 2**).

3.2 Symmetrical and Asymmetrical Gaits Lie on Two Distinct Continua

Based on the numerical search described in Section 2.4, we found periodic solutions for five different gait patterns: walking, hopping, skipping, symmetrical running, and asymmetrical running (**Figure 3**). The definitions of the first four gait patterns follow the conventions described in Section 2.1 and in previous research (Happold, 1967; Eilam and Shefer, 1997; Moore et al., 2017), while asymmetrical running is a novel gait presented this study (Section 3.2.2).

3.2.1 The Nominal Model has Neutral Leg Swing Angles of Zero

All the identified locomotion patterns form one-dimensional branches connected to one another through bifurcation points on the Poincaré section (**Figure 4**). These solution branches are hereafter referred to as the **gait structure**. Just as in our previous SLIP model (Gan et al., 2018a), setting both the neutral leg swing angles to zero results in a nominal gait structure symmetric about the plane $\alpha_{l_0} = 0$ rad.

Symmetrical gaits, walking and running, form one continuum (purple and yellow in **Figure 4**). For symmetrical gaits, identical

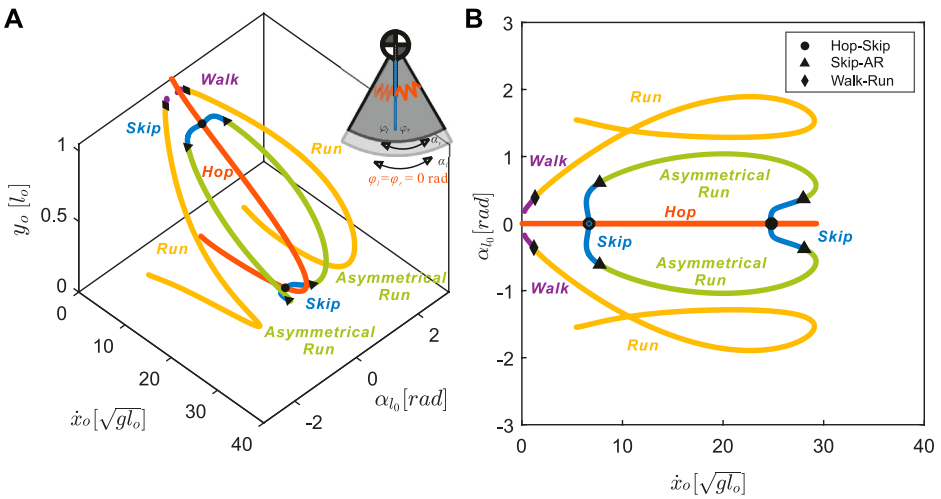

FIGURE 4 | The nominal model with neutral swing leg angles of zero, $\varphi_l = \varphi_r = 0[rad]$, results in symmetrical gait structures (all other parameters were fixed as described in Section 3.1). Each point on the branches represents a distinct periodic motion, or a stationary point on **(A)** a 3D projection and **(B)** a 2D projection of the Poincaré section ($\dot{y} = 0$) with respect to the apex height y_o, forward speed $\dot{x}_o$, and left leg angle α_{l_0}. Hopping to skipping, skipping to asymmetrical running, and walking to symmetrical running transition are represented by circles, triangles, and diamonds respectively. For gait solutions with a negative leg angle, the opposite leg has a phase advance.

leg movements are out of phase by half a stride ($|t_l^j - t_r^j| = T/2$) (Hildebrand, 1967). Walking (purple in **Figure 4**) appears only at low speeds and is characterized by a lack of aerial phase (i.e., $0 < t_r^{td} < t_l^{lo} < t_l^{td} < t_r^{lo} < T$). When the forward speed reaches $\dot{x}_o = 1.21\sqrt{gl_o}$ (diamonds in **Figure 4**), one leg strikes the ground at the exact moment when the other leg leaves the ground, i.e. $t_i^{td} = t_{\bar{i}}^{lo}$ where $i \in [l, r]$ and $\bar{i}$ denotes the index of the opposite leg. As speed further increases, liftoff of one foot occurs before touchdown of the other foot and walking smoothly transitions to running with aerial phases between each footfall, i.e. $0 < t_r^{td} < t_r^{lo} < t_l^{td} < t_l^{lo} < T$ (**Figure 3D**, yellow in **Figure 4**).

A distinct continuum connects the three **asymmetrical gaits**: hopping, skipping, and asymmetrical running (red, blue, and green lines in **Figure 4**), for which the phase shift between legs is not equal to half a stride ($|t_l^j - t_r^j| \neq T/2$) (Hildebrand, 1977). Along the hopping branch (**Figure 3A**, red in **Figure 4**), leg motions are synchronized, i.e. $0 < t_r^{td} = t_l^{td} < t_r^{lo} = t_l^{lo} < T$. This synchronization is broken, via hopf bifurcations (Hassard et al., 1981, Chapter 1), at two different speeds (circles in **Figure 4B**), both leading to skipping (**Figure 3B**, blue in **Figure 4B**) with overlapping footfall patterns (i.e. $0 < t_r^{td} < t_l^{td} < t_r^{lo} < t_l^{lo} < T$).

3.2.2 Definition of Asymmetrical Running

At skipping speeds $\dot{x}_o = 7.72\sqrt{gl_o}$ or $28.06\sqrt{gl_o}$ (triangles in **Figure 4**), previously overlapping touchdown and liftoff events occur simultaneously (e.g., $t_l^{td} = t_r^{lo}$). At intermediate speeds, a short aerial phase emerges in the middle of the stride. As opposed to symmetrical running, gaits in which two aerial phases are unequal in duration (**Figure 3C**) are **asymmetrical running**, with distinct contact angles for each leg and footfall pattern $0 < t_r^{td} < t_r^{lo} < t_l^{td} < t_l^{lo} < T$. In the following sections we will show that the asymmetrical running gait plays an important role in gait transitions and appears ubiquitously in the gait structure as we sweep the parameter space spanned by neutral leg swing angles.

3.3 Coupled Changes in Neutral Leg Swing Angle Shift the Speeds of Existing Gait Transitions

3.3.1 Anterior Shifts in Coupled Neutral Leg Swing Angle Preserve Symmetrical Gait Structure

As we increased the values of $\varphi_l = \varphi_r$, the legs immediately rotated anteriorly at liftoff (see the inset at the top right corner of **Figure 5A**). After reaching the maximum anterior position, the legs would rotate posteriorly prior to ground contact, i.e. swing leg retraction (Seyfarth et al., 2003). Despite this change in kinematics, the transitions to walking (diamonds in **Figure 6**) remained approximately at the same speed, $1.2\sqrt{gl_o}$.

On the other hand, negative neutral leg swing angles (posteriorly shifted) induced changes in the shape of the gait branches. As shown in **Figure 5B**, at low speeds, there were no viable solutions for walking or running because the swing legs failed to maintain a positive leg angle at the moment of touch-down, which is required to keep moving in the positive horizontal direction.

At higher speeds, the curved regions of the branches, corresponding to solutions that include swing leg retraction, disappeared. Instead, higher speed running solutions involved swing legs rotating forward at the moment of touch-down, which induced an angular velocity reset and large plastic collision losses. When we further decreased the value of neutral leg swing angles, the entire running branch shrank towards the mid-speed region, eventually vanishing at approximately $\varphi_i = -0.8$ rad.

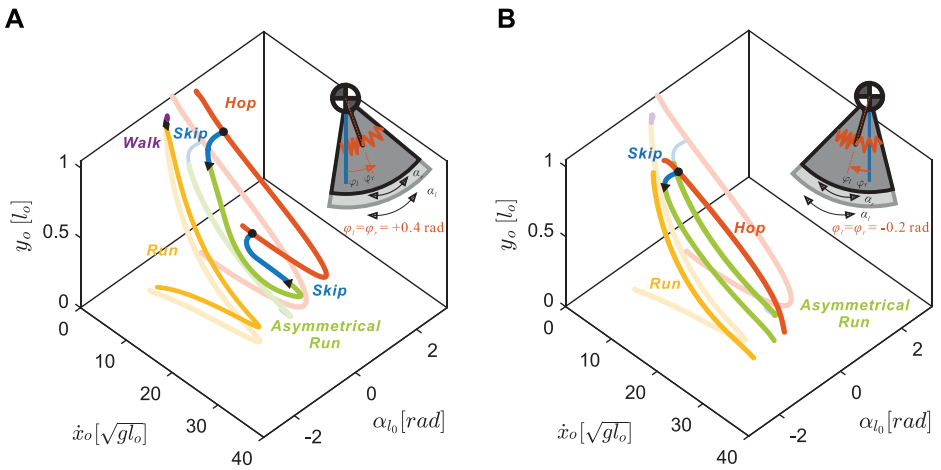

FIGURE 5 | Coupled changes in the neutral leg swing angles affect the gait structure of the nominal model (transparent lines) on the Poincaré section with respect to the apex height, y_o, forward speed, $\dot{x}_o$, and left leg angle, α_{l_0} **(A)** A positive neutral leg swing angle, $\varphi_l = \varphi_r$ =0.4 rad, preserves and translates gait structure **(B)** A negative neutral leg swing angle, $\varphi_l = \varphi_r$ =–0.2 rad, alters gait structure. All other parameters including leg stiffness, k, and swing leg oscillation frequency, ω, were fixed as described in Section 3.1. In both plots, only gaits with left-leg-advanced are shown because symmetry is preserved. The inset model diagrams show the range of leg rotational motions (dark grey sector for α_{r_0}, light grey sector for α_{l_0}) and the neutral leg angles.

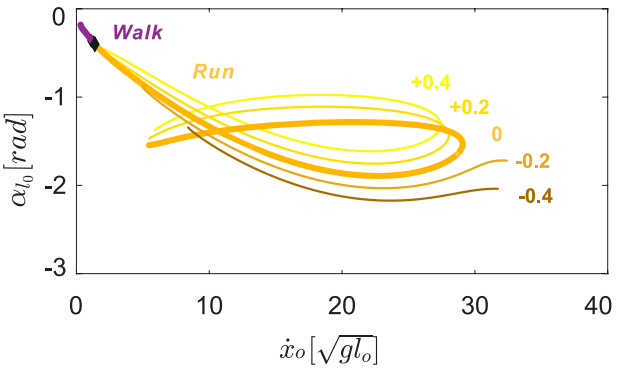

FIGURE 6 | Symmetrical gait structures for $\varphi_l = \varphi_r \in [-0.4, -0.2, 0, +0.2, +0.4]$ rad. Positive neutral leg swing angles retain the running branch shape and transition speed. Negative neutral leg swing angles shrink the running gait structure towards the mid-speed region, eliminating walking.

3.3.2 As Coupled NLSA Varies, the Speed of Higher Speed Transitions Changes More Than Lower Speed Transitions

Hopping solutions were found in the range of $-0.8 < \varphi_i < 1.5$ rad (**Figure 7A**). Minor changes in the shape of hopping branches were observed as we varied φ_i in the positive direction. However, as we gradually decreased the values of the NLSA, periodic hopping gaits were only identified at mid-speed ranges with reduced landing impact. As in running gaits, hopping with emergent swing leg retractions were identified only at moderate speeds.

For all hopping branches with different NLSA values (red curves in **Figure 7A**), there was always at least one hop - skip transition point (circles in **Figure 7A,B**) and no transitions to asymmetrical running. As the hopping branch crosses a bifurcation point, the symmetry in the leg motions is broken, desynchronizing motions of the leg pair to generate skipping gaits with a staggered timings of touchdown events (see **Figure 3A,B**). One hop - skip transition usually occurred at lower speeds and another at higher speeds, near the turning points. The location of the low speed hop - skip transition point varied minimally as the NLSA were altered. In contrast, the higher speed hop - skip transition point showed more variation in speed with changes in NLSA than the lower speed transition point (**Figure 7A**). For negative φ_i, the swing leg angular velocity reset occurred before the high speed transition points could be found.

Starting from the hop - skip transitions points (circles), skipping gaits bifurcated from the hopping branches and emerged at discontinuous locations on the Poincaré section (**Figure 7B**). The lower speed branch was shorter than the higher speed branches for positive neutral leg swing angles. The branches with higher average forward speeds disappeared very quickly because of the impractical swing leg behavior with a maximal forward speed around $29\sqrt{gl_o}$. The asymmetrical running gait provided a smooth transition branch that bridged the two isolated skipping branches for the same neutral leg swing angle (**Figure 7C**).

Skipping solutions were found in the range of $-0.7 < \varphi_i < 1.0$ rad. However, when the NLSA were larger than +0.4 rad, the maximum value during swing motion of the legs exceeded a value of 1.7 rad ($\pi/2$), which would be biologically unrealistic. Therefore, only results from $\varphi_l = \varphi_r \in [-0.4, +0.4]$ are shown. The skip - asymmetrical run transitions showed a similar pattern to the hop - skip transitions. The lower speed skip - asymmetrical run transitions always occurred when the forward speed reached approximately $8\sqrt{gl_o}$. For the higher speed transitions, the locations varied more with positive changes in neutral leg swing angle. As soon as the neutral leg swing angles became negative, higher speed transitions between skipping and asymmetrical running were no longer viable.

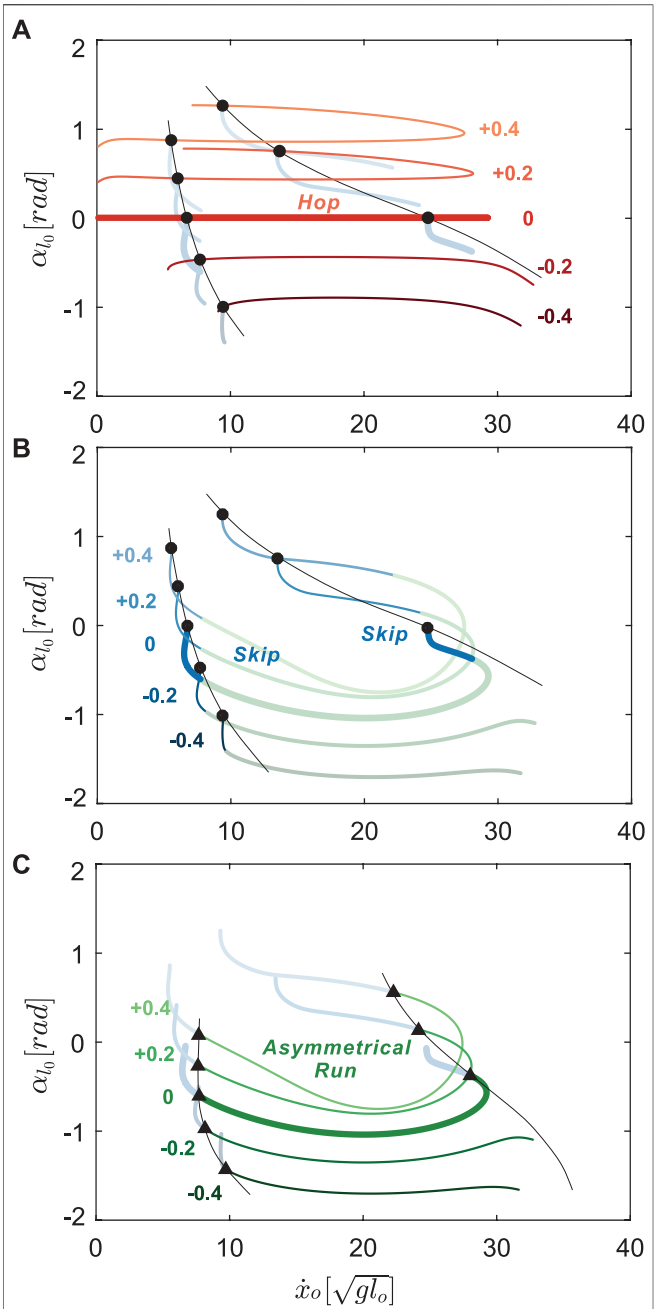

FIGURE 7 | Hopping (A), skipping **(B)**, and asymmetrical running gait branches (C) with $\varphi_l = \varphi_r \in [-0.4, -0.2, 0, +0.2, +0.4]$ rad. Thicker colored lines represent the nominal gait structure (**Figure 4**). Hop-skip transitions are circles in **(A)** and **(B)**, skip-running transitions are triangles in **(C)**. Thin black lines trace gait transitions across varying neutral leg swing angles. The higher speed hop - skip transition point showed more variation in speed with changes in NLSA than the lower speed transition point.

3.4 Uncoupled Changes in Neutral Leg Swing Angle Introduce New Transitions

Uncoupling the neutral swing angles for each leg, i.e. $\varphi_l \neq \varphi_r$, resulted in drastic changes in both gait structure and the locations of gait transitions (**Figure 8**). Without symmetry, skipping and asymmetrical running became the only two feasible gait patterns. Furthermore, the model symmetry between left-leg-advanced and right-leg-advanced solutions were no longer preserved for more offset values, $|\varphi_l - \varphi_r| > 0$, of the uncoupled model because simply switching the leg angles would not result in identical COM motion. For clarity, only the left-leg-advanced solutions for small offset values were included in the analysis.

With uncoupled neutral leg swing angles, more skipping and asymmetrical running gait solutions became possible by slightly disrupting the symmetry of the symmetrical running and hopping gaits. With positive offset in the left neutral leg swing angle ($\varphi_l - \varphi_r > 0$), the asymmetrical running branch elongated by closely matching the symmetrical running gait (see **Figure 8A**). In contrast to the skipping branch of the coupled leg model, which connected directly to the hopping branch (opaque blue curve in **Figure 8A**), the uncoupled skipping branch continued to the lower speed regions in which the flight phases became shorter and shorter until they were replaced by a double stance phase.

On the other hand, with negative offset, the skipping branch (blue curve in **Figure 8B**) higher speed regions closely resemble the symmetrical hopping gait (red curve). When speeds were too fast or too slow, these skipping gaits joined with the asymmetrical running branch and formed the 1-dimensional manifold as a closed loop. The size of this loop decreased with the value of the left neutral leg angle. No solutions were found past $\varphi_l = -0.14$ rad, where the solution branch became a single dot.

Combining positive and negative variations in neutral leg angle offset shows that asymmetrical gaits spanned the gaps between symmetrical running branches (**Figure 9**). Thus, changing the offset between left and right neutral leg angles effectively enables transitions between symmetrical and asymmetrical gaits. Even within the asymmetrical gait structure, skipping-asymmetrical running transition points (triangles in **Figure 9**) spanned nearly the entire range of speed in response to small variations in neutral leg swing angles. Specifically, the forward speed of transition points varied from 1.30 to $29.26\sqrt{gl_o}$, while the left leg neutral leg swing angle only varied from −0.06 to 0.14 rad (**Figure 9B**). In comparison to the large gaps between gait transitions in the coupled model (Section 3.3), the uncoupled model finds abundant solutions for gait transitions throughout the full range of speeds (**Figure 10**).

3.5 Validation

To validate our model, we compared our predictions to empirical gait transition data from jerboas. We found that jerboas swing each leg with a different, non-zero neutral leg swing angle. Specifically, jerboas tend to fix the neutral swing leg angle of one leg while varying the neutral swing leg angle of the other leg. For instance, for j38 (column 5–8 in **Table 1**) the neutral swing leg angle φ_r for its right leg was −0.08 ± 0.31 rad while φ_l was 0.00 ± 0.06 rad. As shown in **Figure 4**, with the same set of parameters, $\vec{p}^T = [m, l_o, g, k, \omega, \varphi_l, \varphi_r]$, our model can reproduce five bipedal gaits simply by regulating the initial states and altering the total energy. From our experimental data set, there were four gait transitions between skipping and asymmetrical running (T1 to T4 in **Figure 11**) and four

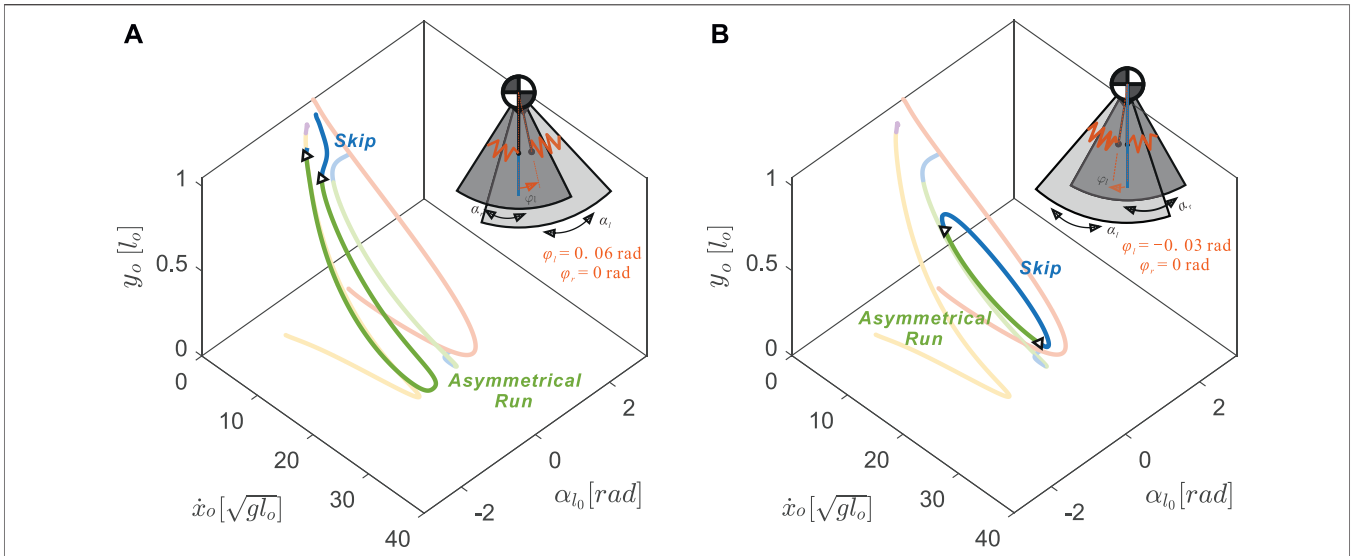

FIGURE 8 | Uncoupling the neutral leg swing angles ($\varphi_l \neq \varphi_r$) resulted in drastic changes in 3D gait branch shape with respect to the nominal model (transparent curves from **Figure 4**) **(A)** An anterior shift, φ_l =+0.06 rad, caused the asymmetrical running branch to subsume portions of the previously symmetrical running branch (yellow) **(B)** A posterior shift, φ_l =−0.03 rad, caused the skipping branch to subsume portions of the previously symmetrical hopping gait (red) to form a closed loop. The inset model diagrams show the range of leg rotational motions (dark grey sector for α_{r_0}, light grey sector for α_{l_0}) and the neutral leg angles.

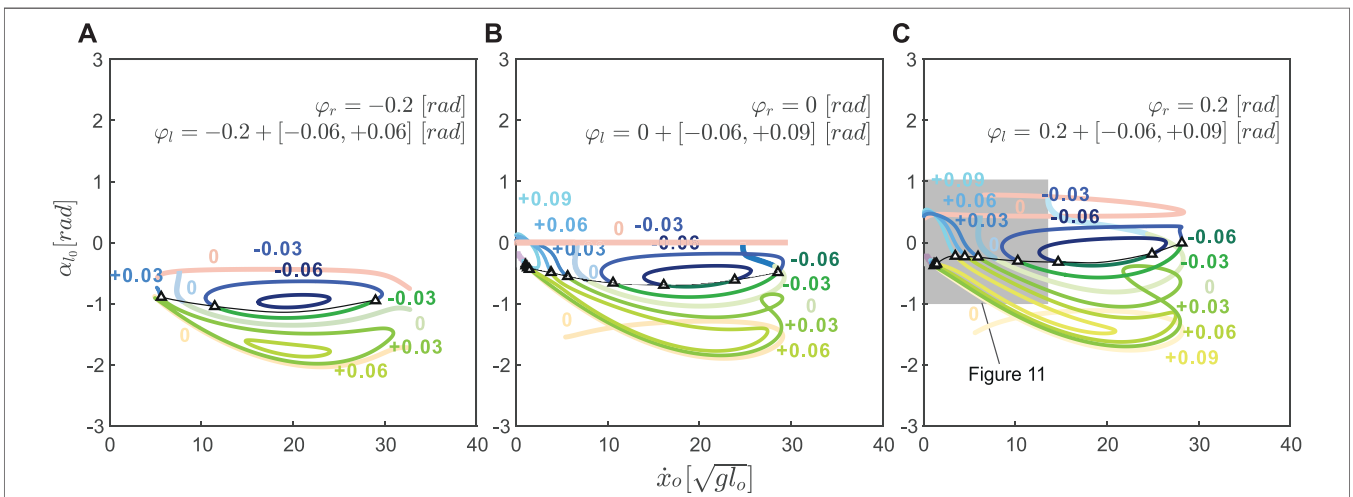

FIGURE 9 | The fixed neutral leg swing angle, φ_r, and the varying neutral leg swing angle, φ_l, interact to affect asymmetrical gait structure in uncoupled models. In all plots, the coupled $\varphi_l = \varphi_r \in [-0.2, 0, +0.2]$ rad gait structures are shown as transparent curves. In all cases, skipping and asymmetrical running spanned the gap between the hopping and symmetrical running branches. The gait transitions points (triangles) spanned almost the entire speed range. Comparing **(A)**, **(B)**, and **(C)**, demonstrates that gait structure varies greatly with neutral leg swing angle offset. The shadowed region in **Figure 9C** is shown in **Figure 11** as a comparison between simulation solutions and experimental data.

transitions from hopping to other gaits (T5 to T8 in **Figure 11**). These transitions occurred when the NLSA (φ_r) were close to 0.2 rad and were thus compared to model predictions with similar NLSA values (shaded region in **Figure 9C**). In both T1 and T3, neither the uncoupled nor the coupled model accurately predicts the behavior of the transition (i.e., the empirical transition line from cross to circle does not cross the model transition line). A closer examination of the video data revealed that these trials involved a jerboa decelerating to a stop, which could be a multiple - step process and is a behavior that has not been investigated by our model. The other two transitions from skipping to asymmetrical running (T2 and T4), however, clearly fell into the regions predicted by our uncoupled model and crossed the uncoupled transition line as expected. Four transitions from hopping to other gaits (T5 to T8) were observed through the range of speeds from 4.19 to $5.47\sqrt{gl_o}$. Because of the short recording window and the large stride lengths of the jerboas at higher speeds, the apex transitions of the stride after hopping are not visible, but the kinematic data suggest that these are transitions either to skipping or asymmetrical running. All of

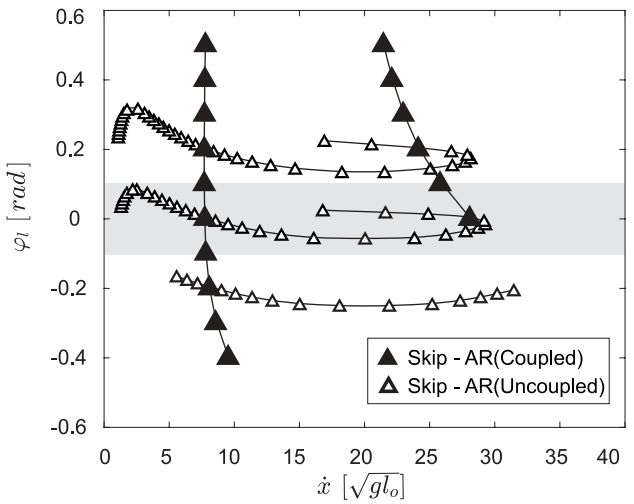

FIGURE 10 | The skip - asymmetrical run (AR) transitions for the coupled model, $\varphi_r = \varphi_l \in [-0.5, 0.5]$, vary slightly with speed and occur in two narrow ranges of speed. The uncoupled model, φ_r =[−0.2,0,0.2], finds far more solutions for the same type of gait transition throughout a broader speed range.

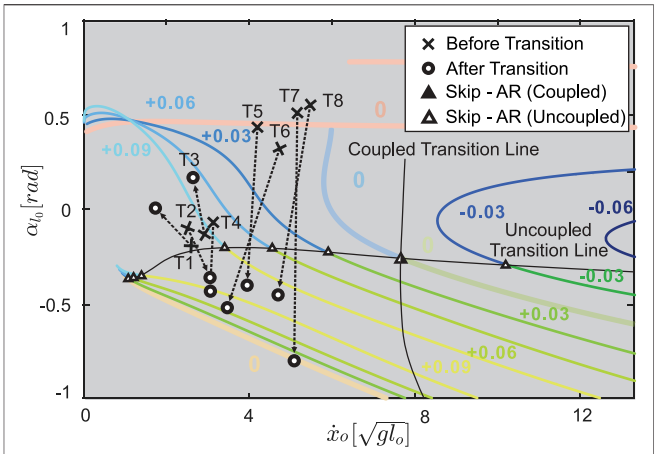

FIGURE 11 | Transitions observed from the jerboa experiments (crosses to circles) in comparison to the predicted gait structure in uncoupled models (colored branches and triangles from **Figure 9C**) and the predicted transition lines (solid triangles represent coupled transitions and hollow triangles represent uncoupled transitions, the intersection of coupled and uncoupled transition is shown in half-solid and half-hollow). The crosses indicate the apex states before the transition, the hollowed circles are the apex state after transition, and the arrows show the transition directions on the Poincaré section. T1 to T4 show skip - asymmetrical run (AR) transitions, while T5 to T8 show transitions from hopping. The arrows pass through, or near, hollow triangles, showing that the model with the uncoupled, rather than the coupled, NLSA mechanism accurately predicts gait transitions that are observed in empirical data.

these trials passed the gait transition line suggested by our uncoupled leg model within one stride (the black line connected through hollow triangles) rather than the coupled leg model (black line connected through the solid triangles), matching our observation that jerboas tend to uncouple leg NLSA during locomotion. These results suggest that for non - stopping behaviors, our proposed model dynamics generate biologically relevant predictions of gait transitions.

4 DISCUSSION

We present the first computational model to reproduce the locomotion patterns and gait transitions of the non-cursorial jerboa. By adding a torsional spring to a unified SLIP-like model, we varied the model swing leg dynamics to match jerboa locomotion patterns. This model accurately reproduced previously described hopping, symmetrical running, and skipping gaits and enabled the formal characterization of walking and asymmetrical running gaits for the first time. The discovery of the asymmetrical running gait describes previously unused data recorded of jerboa locomotion that did not fit into the pre-existing gait categories. Furthermore, the results of this study suggest there exist two distinct mechanisms (i.e., coupled leg motions in Section 3.3 and uncoupled leg motions in Section 3.4) for gait transitions. This modeling approach can be used to shed light on the underlying dynamics of other non-cursorial or previously uncharacterized locomotion and can inform the design of robotic controllers capable of smoothly transitioning between gaits.

In the coupled leg model, the number of gait transitions and the unique pairs of gaits between which transitions can occur remain invariant to changes in neutral leg angle. Because they lie on distinct continua, symmetrical and asymmetrical gaits can only transition to gaits of the same type, rather than across types. The existing high-speed transition between asymmetrical gaits occurs at a slightly broader range of speeds when the coupled neutral leg swing angle changes. For asymmetrical gaits, all transitions involve the skipping gait; there are no smooth transitions directly between hopping and asymmetrical running.

Our model suggests that by uncoupling the motions of a leg pair, jerboas can greatly vary the range of speeds at which gait transitions can occur and introduce novel transitions between asymmetrical and symmetrical gaits. As shown in **Figure 10** C, by varying the φ_l by merely +0.08 rad (4.6°), the speed at which the skip - asymmetrical run transition occurs increases from 0 to 7.5 $\sqrt{gl_o}$. This demonstrates how at any speed, a jerboa can change its swing leg behavior and instantaneously transition to another gait pattern within one step. Moreover, changing the neutral leg angle anteriorly causing a shift of the whole gait branch to low speed regions and vice versa. This uncoupled swing leg strategy provides a mechanistic explanation for the observation that jerboas use gait transitions to quickly accelerate, decelerate, or regularize its forward speed (Moore et al., 2017). Another key observation of this study is that the skipping gait and asymmetrical running gait played critical roles in bridging the symmetrical gaits and asymmetrical gaits. For example, in **Figure 8A**, when the left neutral leg angle shifted anteriorly, the asymmetrical running (green curve) approached the vicinity of the running branch (opaque yellow curve). With posterior shifts in neutral leg swing angle, as shown in **Figure 8B**, the skipping gait (blue curves) approached the bipedal hopping gait (red transparent curve) across a broad range of speeds. Throughout this process, skipping and asymmetrical running remained on the same continuum with each other.

The results from our model reflect two mathematical definitions of gait asymmetry (Ian and Golubitsky, 1993, Chapter 8) — temporal asymmetry creates phase desynchronization between the legs (which can occur either with coupled or uncoupled changes in NLSA), while model asymmetry (e.g., uncoupled changes in NLSA) generates distinct leg behaviors. The model behaviors that arise from this mathematical distinction provide a useful framework to identify the mechanisms by which genes control motion coordination (Andersson et al., 2012).

Although previous work with conventional SLIP models succeeded in eliciting gait transitions (Geyer et al., 2006), a gait identified by providing a pre-defined leg contact angle provides no intuitive explanation for the system dynamics that generate the necessary changes in contact angle. In our proposed model, we add a torsional spring so that changes in leg contact angles become governed by the passive dynamics of the system. Thus, gait structure emerges as a result of model parameters, which provide a mechanistic explanation for the resulting gait transitions. This distinction can further enhance our understanding of animal gaits and lay the foundation for better legged robot controller design.

For example, as shown in **Figure 11**, in some cases (**Figure 11**, T4 & T7) jerboas may transition from one fixed point to another fixed point on the same gait structure. This would mean that the jerboa kept using the same set of parameters (including the same NLSAs) and only altered the total energy in a single step. In other cases (**Figure 11**, T3 & T5), transitions between branches would indicate that both the total energy and the NLSAs have been altered to facilitate these transitions.

Our work can also inform controller design because it suggests that we can use virtual constraints (Westervelt et al., 2018, Chapter 1) that control leg swing behavior by modeling it as a pendulum with a torsional spring. Then we can modulate the total energy in the system to accelerate, decelerate, or switch gaits, while compensating for energy losses through joint friction or collisions. One can also use our solution branches as "a lookup table" in the design of locomotion controllers as proposed in our previous work (Cnops et al., 2015). To dynamically and efficiently change locomotion pattern at any desired gait or speed, if the current states of the application are known, the controller can search for an optimal trajectory to plan either a one - step or multiple - step process without performing any expensive calculation.

Many of the solutions found in the proposed bipedal model can be directly applied to quadrupedal locomotion. According to the idea of dynamic similarity (Alexander and Jayes, 1983), when quadrupedal animals synchronize their leg motions in pairs (i.e., trotting, pacing, and bounding), the leg pair behaves as a unified leg with a greater stiffness. As discussed in our previous work (Gan et al., 2018a), the running and hopping branches in the gait structure of the bipeds are functionally identical to the trotting and pronking gaits of quadrupeds. Similarly, the shapes of skipping and asymmetrical running branches in the bipedal model will closely resemble bounding and galloping in the quadrupedal model. However, in the quadrupedal model, because legs pairs are connected to the torso at different locations, the asymmetrical gaits with different sequences of leg touchdowns will create unbalanced moments about the COM of the main body and cause the torso to rotate. As a result, the actual bounding and galloping branches of the quadrupedal model will also depend on the inertial properties of the torso. In general, when the quadrupedal model shares similar parameter values to those of the proposed bipedal model, we expect similar transitions will happen among these quadrupedal gaits, based on the gait structure shown in Section 3.2.

In our future work, we plan to extend our model by adding another pair of legs to find transitions between quadrupedal and bipedal locomotion, as observed in the escape behaviors of lizards, rodents, cockroaches, and during the locomotor development of jerboas (Marlow, 1969; Full and Tu, 1991; Eilam and Shefer, 1997; Clemente, 2014). A combined quadrupedal and bipedal model can provide novel insights into the neurological changes that likely facilitate the evolution of ephemeral and obligate bipedal locomotion.

DATA AVAILABILITY STATEMENT

The model and results for this study can be found in the UM Deep Blue Data repository https://doi.org/10.7302/ewaa-qm16.

ETHICS STATEMENT

Ethical review and approval was not required for the animal study because The animal data were previously published in an ethically reviewed study.

AUTHOR CONTRIBUTIONS

ZG and TM conceived of the idea for this study. TM collected and interpreted the empirical jerboa data. JD and ZG constructed and analyzed the numerical model. All authors interpreted the results and contributed to writing the manuscript.

FUNDING

This work was supported by a Harvard Chapman Memorial Fellowship to TM.

ACKNOWLEDGMENTS

We would like to thank Andy Biewener, Kim Cooper, and Pedro Ramirez for assistance collecting the jerboa data.

SUPPLEMENTARY MATERIAL

The Supplementary Material for this article can be found online at: https://www.frontiersin.org/articles/10.3389/fbioe.2022.804826/full#supplementary-material

REFERENCES

Alexander, R. M., and Jayes, A. S. (1983). A Dynamic Similarity Hypothesis for the Gaits of Quadrupedal Mammals. *J. Zoolog.* 201, 135–152. doi:10.1111/j.1469-7998.1983.tb04266.x

Alexander, R. M., and Jayes, A. S. (2009). A Dynamic Similarity Hypothesis for the Gaits of Quadrupedal Mammals. *J. Zoolog.* 201, 135–152. doi:10.1111/j.1469-7998.1983.tb04266.x

Alexander, R. M. (2009). Optimum Walking Techniques for Quadrupeds and Bipeds. *J. Zoolog.* 192, 97–117. doi:10.1111/j.1469-7998.1980.tb04222.x

Alexander, R. M. (2002). *Principles of Animal Locomotion*. Princeton, NJ: Princeton University Press. doi:10.1515/9781400849512

Alexander, R. M. (1984). The Gaits of Bipedal and Quadrupedal Animals. *Int. J. Robotics Res.* 3, 49–59. doi:10.1177/027836498400300205

Andersson, L. S., Larhammar, M., Memic, F., Wootz, H., Schwochow, D., Rubin, C.-J., et al. (2012). Mutations in DMRT3 Affect Locomotion in Horses and Spinal Circuit Function in Mice. *Nature* 488, 642–646. doi:10.1038/nature11399

Aoi, S., Katayama, D., Fujiki, S., Tomita, N., Funato, T., Yamashita, T., et al. (2013). A Stability-Based Mechanism for Hysteresis in the Walk-Trot Transition in Quadruped Locomotion. *J. R. Soc. Interf.* 10, 20120908. doi:10.1098/rsif.2012.0908

Biewener, A. A., and Blickhan, R. (1988). Kangaroo Rat Locomotion: Design for Elastic Energy Storage or Acceleration? *J. Exp. Biol.* 140, 243–255. doi:10.1242/jeb.140.1.243

Blickhan, R. (1989). The spring-mass Model for Running and Hopping. *J. Biomech.* 22, 1217–1227. doi:10.1016/0021-9290(89)90224-8

Cavagna, G. A., Heglund, N. C., and Taylor, C. R. (1977). Mechanical Work in Terrestrial Locomotion: Two Basic Mechanisms for Minimizing Energy Expenditure. *Am. J. Physiology-Regulatory, Integr. Comp. Physiol.* 233, R243–R261. doi:10.1152/ajpregu.1977.233.5.r243

Chance, M. R. A., and Russell, W. M. S. (2009). Protean Displays: A Form of Allaesthetic Behaviour. *Proc. Zoolog. Soc. Lond.* 132, 65–70. doi:10.1111/j.1469-7998.1959.tb05513.x

Clemente, C. J. (2014). The Evolution of Bipedal Running in Lizards Suggests a Consequential Origin May Be Exploited in Later Lineages. *Evolution* 68, 2171–2183. doi:10.1111/evo.12447C

Cnops, T., Gan, Z., and Remy, C. D. (2015). "The basin of Attraction for Running Robots: Fractals, Multistep Trajectories, and the Choice of Control," in 2015 IEEE/RSJ International Conference on Intelligent Robots and Systems (IROS), Hamburg, Germany, 1586–1591. doi:10.1109/IROS.2015.7353579

Danner, S. M., Wilshin, S. D., Shevtsova, N. A., and Rybak, I. A. (2016). Central Control of Interlimb Coordination and Speed-dependent Gait Expression in Quadrupeds. *J. Physiol.* 594, 6947–6967. doi:10.1113/JP272787

Domenici, P., Blagburn, J. M., and Bacon, J. P. (2011). Animal Escapology I: Theoretical Issues and Emerging Trends in Escape Trajectories. *J. Exp. Biol.* 214, 2463–2473. doi:10.1242/jeb.029652

DSCC (2015). in *Spring-mass Walking with ATRIAS in 3D: Robust Gait Control Spanning Zero to 4.3 KPH on a Heavily Underactuated Bipedal Robot* (Columbus, OH: American Society of Mechanical Engineers (ASME)). doi:10.1115/dscc2015-9899

Eilam, D., and Shefer, G. (1997). The Developmental Order of Bipedal Locomotion in the Jerboa (Jaculus Orientalis): Pivoting, Creeping, Quadrupedalism, and Bipedalism. *Dev. Psychobiol.* 31, 137–142. doi:10.1002/(sici)1098-2302(199709)31:2<137:aid-dev6>3.0.co;2-l

Farley, C. T., Glasheen, J., and McMahon, T. A. (1993). Running Springs: Speed and Animal Size. *J. Exp. Biol.* 185, 71–86. doi:10.1242/jeb.185.1.71

Farley, C. T., and Taylor, C. R. (1991). A Mechanical Trigger for the Trot-Gallop Transition in Horses. *Science* 253, 306–308. doi:10.1126/science.1857965

Fehlberg, E. (1969). *Low-order Classical Runge-Kutta Formulas with Stepsize Control and Their Application to Some Heat Transfer Problems*, 315. Marshall, AL: National aeronautics and space administration.

Full, R. J., and Koditschek, D. E. (1999). Templates and Anchors: Neuromechanical Hypotheses of Legged Locomotion on Land. *J. Exp. Biol.* 202, 3325–3332. doi:10.1242/jeb.202.23.3325

Full, R. J., and Tu, M. S. (1991). Mechanics of a Rapid Running Insect: Two-, Four- and Six-Legged Locomotion. *J. Exp. Biol.* 156, 215–231. doi:10.1242/jeb.156.1.215

Gan, Z., Jiao, Z., and Remy, C. D. (2018a). On the Dynamic Similarity between Bipeds and Quadrupeds: a Case Study on Bounding. *IEEE Robot. Autom. Lett.* 3, 3614–3621. doi:10.1109/lra.2018.2854923

Gan, Z., Yesilevskiy, Y., Zaytsev, P., and Remy, C. D. (2018b). All Common Bipedal Gaits Emerge from a Single Passive Model. *J. R. Soc. Interf.* 15, 20180455. doi:10.1098/rsif.2018.0455

Geyer, H., Seyfarth, A., and Blickhan, R. (2006). Compliant Leg Behaviour Explains Basic Dynamics of Walking and Running. *Proc. R. Soc. B.* 273, 2861–2867. doi:10.1098/rspb.2006.3637

Happold, D. C. D. (1967). Biology of the Jerboa, Jaculus Jaculus Butleri (Rodentia, Dipodidae), in the sudan. *J. Zoolog.* 151, 257–275. doi:10.1111/j.1469-7998.1967.tb02114.x

Hassard, B., Brian, D., Hassard, N., Kazarinoff, N., Wan, Y., Society, L. M., et al. (1981). "Theory and Applications of Hopf Bifurcation," in *Cambridge Tracts in Mathematics* (Cambridge, United Kingdom: Cambridge University Press).

Hereid, A., Kolathaya, S., Jones, M. S., Van Why, J., Hurst, J. W., and Ames, A. D. (2014). "Dynamic Multi-Domain Bipedal Walking with Atrias through SLIP Based Human-Inspired Control," in *Proceedings of the 17th International Conference on Hybrid Systems: Computation and Control* (New York, NY: ACM), 263–272. doi:10.1145/2562059.2562143

Hildebrand, M. (1977). Analysis of Asymmetrical Gaits. *J. Mammalogy* 58, 131–156. doi:10.2307/1379571

Hildebrand, M. (1967). Symmetrical Gaits of Primates. *Am. J. Phys. Anthropol.* 26, 119–130. doi:10.1002/ajpa.1330260203

Hildebrand, M. (1989). The Quadrupedal Gaits of Vertebrates. *BioScience* 39, 766–775. doi:10.2307/1311182

Hof, A. L. (1996). Scaling Gait Data to Body Size. *Gait & Posture* 4, 222–223. doi:10.1016/0966-6362(95)01057-2

Hoyt, D. F., and Taylor, C. R. (1981). Gait and the Energetics of Locomotion in Horses. *Nature* 292, 239–240. doi:10.1038/292239a0

Hwangbo, J., Lee, J., Dosovitskiy, A., Bellicoso, D., Tsounis, V., Koltun, V., et al. (2019). Learning Agile and Dynamic Motor Skills for Legged Robots. *Sci. Robot* 4, eaau5872. doi:10.1126/scirobotics.aau5872

Hyun, D. J., Lee, J., Park, S., and Kim, S. (2016). Implementation of trot-to-gallop transition and subsequent gallop on the mit cheetah i. *Int. J. Robotics Res.* 35, 1627–1650. doi:10.1177/0278364916640102

Hyun, D. J., Seok, S., Lee, J., and Kim, S. (2014). High speed trot-running: Implementation of a hierarchical controller using proprioceptive impedance control on the mit cheetah. *Int. J. Robotics Res.* 33, 1417–1445. doi:10.1177/0278364914532150

Ian, S., and Golubitsky, M. (1993). *Fearful Symmetry, Is God a Geometer?* London: Penguin Books.

Lee, D. V., Bertram, J. E. A., Anttonen, J. T., Ros, I. G., Harris, S. L., and Biewener, A. A. (2011). A Collisional Perspective on Quadrupedal Gait Dynamics. *J. R. Soc. Interf.* 8, 1480–1486. doi:10.1098/rsif.2011.0019

Marlow, B. J. (1969). A Comparison of the Locomotion of Two Desert-living Australian Mammals, Antechinomys Spenceri (Marsupialia: Dasyuridae) and Notomys Cervinus (Rodentia: Muridae). *J. Zoolog.* 157, 159–167. doi:10.1111/j.1469-7998.1969.tb01695.x

Mathis, A., Mamidanna, P., Cury, K. M., Abe, T., Murthy, V. N., Mathis, M. W., et al. (2018). Deeplabcut: Markerless Pose Estimation of User-Defined Body Parts with Deep Learning. *Nat. Neurosci.* 21, 1281–1289. doi:10.1038/s41593-018-0209-y

McGeer, T. (1990). Passive Dynamic Walking. *Int. J. Robotics Res.* 9, 62–82. doi:10.1177/027836499000900206

Minetti, A. E., Ardigò, L. P., Reinach, E., and Saibene, F. (1999). The Relationship between Mechanical Work and Energy Expenditure of Locomotion in Horses. *J. Exp. Biol.* 202, 2329–2338. doi:10.1242/jeb.202.17.2329

Moore, T. Y., Cooper, K. L., Biewener, A. A., and Vasudevan, R. (2017). Unpredictability of Escape Trajectory Explains Predator Evasion Ability and Microhabitat Preference of Desert Rodents. *Nat. Commun.* 8, 440. doi:10.1038/s41467-017-00373-2

O'Connor, S. M. (2009). *The Relative Roles of Dynamics and Control in Bipedal Locomotion* (Ann Arbor, Michigan: University of Michigan). Ph.D. thesis.

Schöner, G., Jiang, W. Y., and Kelso, J. A. S. (1990). A Synergetic Theory of Quadrupedal Gaits and Gait Transitions. *J. Theor. Biol.* 142, 359–391. doi:10.1016/S0022-5193(05)80558-2

Schröpfer, R., Klenner-Fringes, B., and Naumer, E. (1985). Locomotion Pattern and Habitat Utilisation of the Two Jerboas *Jaculus Jaculus* and *Jaculus Orientalis* (Rodentia, Dipodidae). *Mammalia* 49, 445–454. doi:10.1515/mamm.1985.49.4.445

Seyfarth, A., Geyer, H., and Herr, H. (2003). Swing-leg Retraction: a Simple Control Model for Stable Running. *J. Exp. Biol.* 206, 2547–2555. doi:10.1242/jeb.00463

Shen, Z. H., and Seipel, J. E. (2012). A Fundamental Mechanism of Legged Locomotion with Hip Torque and Leg Damping. *Bioinspir. Biomim.* 7, 046010. doi:10.1088/1748-3182/7/4/046010

Siekmann, J., Godse, Y., Fern, A., and Hurst, J. (2020). *Sim-to-real Learning of All Common Bipedal Gaits via Periodic Reward Composition*. *arXiv preprint arXiv: 2011.01387*.

Westervelt, E. R., Grizzle, J. W., Chevallereau, C., Choi, J. H., and Morris, B. (2018). *Feedback Control of Dynamic Bipedal Robot Locomotion*. Boca Raton, FL: CRC Press.

Conflict of Interest: The authors declare that the research was conducted in the absence of any commercial or financial relationships that could be construed as a potential conflict of interest.

frontiers | Frontiers in Bioengineering and Biotechnology

ORIGINAL RESEARCH
published: 12 May 2022
doi: 10.3389/fbioe.2022.826336

Competing Models of Work in Quadrupedal Walking: Center of Mass Work is Insufficient to Explain Stereotypical Gait

Delyle T. Polet[1,2*†] *and John E. A. Bertram*[2]

[1]Biological Sciences, University of Calgary, Calgary, AB, Canada, [2]Cell Biology and Anatomy, Cumming School of Medicine, University of Calgary, Calgary, AB, Canada

OPEN ACCESS

Edited by:
Denis J. Marcellin-Little, University of California, Davis, United States

Reviewed by:
Peter Gabriel Adamczyk, University of Wisconsin-Madison, United States
Yaroslav I. Molkov, Georgia State University, United States

***Correspondence:**
Delyle T. Polet
dpolet@rvc.ac.uk

†Present Address:
Delyle T. Polet, Structure and Motion Lab, Comparative Biomedical Sciences, Royal Veterinary College, Hatfield, United Kingdom

Specialty section:
This article was submitted to Biomechanics, a section of the journal Frontiers in Bioengineering and Biotechnology

Received: 30 November 2021
Accepted: 29 March 2022
Published: 12 May 2022

Citation:
Polet DT and Bertram JEA (2022) Competing Models of Work in Quadrupedal Walking: Center of Mass Work is Insufficient to Explain Stereotypical Gait. Front. Bioeng. Biotechnol. 10:826336. doi: 10.3389/fbioe.2022.826336

The walking gaits of cursorial quadrupedal mammals tend to be highly stereotyped as a four-beat pattern with interspersed periods of double and triple stance, often with double-hump ground reaction force profiles. This pattern has long been associated with high energetic economy, due to low apparent work. However, there are differing ways of approximating the work performed during walking and, consequently, different interpretations of the primary mechanism leading to high economy. A focus on Net Center of Mass (COM) Work led to the claim that quadrupedal walking is efficient because it effectively trades potential and kinetic energy of the COM. Individual Limbs COM Work instead focuses on the ability of the limbs to manage the trajectory of the COM to limit energetic losses to the ground ("collisions"). By focusing on the COM, both these metrics effectively dismiss the importance of rotation of the elongate quadrupedal body. Limb Extension Work considers work required to extend and contract each limb like a strut, and accounts for the work of body pitching. We tested the prescriptive ability of these approximations of work by optimizing them within a quadrupedal model with two approximations of the body as a point-mass or a rigid distributed mass. Perfect potential-kinetic energy exchange of the COM was possible when optimizing Net COM Work, resulting in highly compliant gaits with duty factors close to one, far different than observed mammalian gaits. Optimizing Individual Limbs COM Work resulted in alternating periods of single limb stance. Only the distributed mass model, with Limb Extension Work as the cost, resulted in a solution similar to the stereotypical mammalian gait. These results suggest that maintaining a near-constant limb length, with distributed contacts, are more important mechanisms of economy than either transduction of potential-kinetic energy or COM collision mitigation for quadrupedal walking.

Keywords: quadrupedal model, trajectory optimization, work minimization, mammal, pendular recovery

1 INTRODUCTION

The walking gait of many quadrupedal mammals is highly stereotyped. Hildebrand found that most mammals use a lateral or diagonal sequence gait, where each leg touches down individually in a "four-beat" pattern (Hildebrand, 1976). A minimum of two limbs are always on the ground, interspersed with periods of triple limb stance at transfer of support (and four-limb stance at the

slowest gaits). At slow speeds, quadrupedal mammals rarely use "two-beat" gaits, where fore and hind limbs transfer support simultaneously.

Many cursorial mammals exhibit a bimodal or "double hump" ground reaction force profile in walking (Jayes and Alexander, 1978; Bobbert et al., 2007; Farrell et al., 2014; Basu et al., 2019). This has been explained as a work-minimizing strategy in humans (Tucker, 1975), and in canids (Usherwood et al., 2007; Polet and Bertram, 2019). The double-hump profile can be a diagnostic feature of walking in humans (Hubel and Usherwood, 2015) and horses (Biknevicius et al., 2004).

The ubiquity of this gait suggests a common cause, and energetic economy has been offered as a potential explanation. While gait may arise from the organization of spinal circuitry (Guertin, 2013) and periodic responses to sensory cues (e.g. Fukuoka et al., 2015), these neuronal controls likely serve some adaptive function themselves. By investigating the extent to which gait emerges from energetics, we can better understand the adaptive context of motor control, and how other biological and mechanical factors fill in the gaps left by an energetic perspective.

Many factors contribute to energetic cost in locomotion, but positive muscular work is likely a primary contributor (van der Zee et al., 2019; Riddick and Kuo, 2020). Muscular work is often impossible to measure and difficult to estimate. While whole body metabolic power can be measured through gas exchange, this requires specialized equipment and long-duration trials. In contrast, kinetic and kinematic measurements can be collected relatively easily over a handful of strides. From these measurements, various measures of work can be calculated, often with the goal of approximating a metric that correlates to muscular work.

The most commonly used metric of work in locomotion is Net Center of Mass Work (Net COM Work, or NCW). This sums the fluctuations in gravitational potential (E_p) and kinetic energy (E_k) of the center of mass, which are equivalent to Net COM Power:

$$\text{Net COM Work} = \int_0^T |\mathbf{F}_{\text{net}} \cdot \mathbf{V}_{\text{COM}}|^+ \text{dt} \tag{1}$$

$$\equiv \int_0^T |\dot{E}_p + \dot{E}_k|^+ \text{dt}, \tag{2}$$

where $\mathbf{F}_{\text{net}}$ is the net ground reaction force (GRF), $\mathbf{V}_{\text{COM}}$ is the center of mass velocity and $|\cdot|^+$ is the positive part function. This metric can be measured easily in steady gaits with force plates knowing only the average horizontal velocity of the animal. **Eq. 2** establishes the connection between NCW and pendular recovery (Cavagna et al., 1977): when pendular recovery is high, NCW is low and vice versa. Likewise, center of mass work has been parameterized in the "collision angle" framework (Lee et al., 2011), comparing the angle between $\mathbf{F}_{\text{net}}$ and $\mathbf{V}_{\text{COM}}$ implied in the dot product of **Eq. 1**.

One issue with NCW is that it cannot account for simultaneous positive and negative work. During transfer of support, one limb pushes forward, performing positive work, while the other limb pushes backward, performing negative work. These contributions largely cancel out, generating no apparent NCW, but contribute to the total cost of locomotion (Donelan et al., 2002a,b). A simple fix to NCW is the Individual Limbs COM Work (ILCW), which considers each limb's instantaneous contribution to the center of mass work:

$$\text{ILCW} = \int_0^T \sum_i |\mathbf{F}_i \cdot \mathbf{V}_{\text{COM}}|^+ \text{dt}, \tag{3}$$

where $\mathbf{F}_i$ is the ground reaction force of limb i. Due to frequent periods of simultaneous limb contact on the same force platform, separating ground reaction forces for each limb can be difficult in quadrupedal gait. However, use of center of pressure measurements (Jayes and Alexander, 1978), or multiple plates (Bertram et al., 1997) can alleviate these difficulties.

By focusing on center of mass energetics, these metrics have effectively ignored body rotation. Indeed, some influential models of quadrupedal locomotion assume that effects of rotation are small contributors to cost (Cavagna et al., 1977; Ruina et al., 2005; Lee et al., 2011; Usherwood and Self Davies, 2017). NCW and ILCW can be calculated when the body undergoes extreme rotation, but would be expected to have lower fidelity to muscular work if rotational energies are large. Indeed, Ruina and Bertram (2003) describe how simple passive systems can exhibit finite NCW, when no work is actually performed (**Figure 1**). In these cases, Net System Work (NSW; total changes in translational and rotational kinetic, and gravitational potential energy) is zero, but NCW increases as gravitational potential and translational kinetic energy convert to rotational kinetic energy.

Another metric can better account for rigid body rotation. Recognizing that ground reaction forces from individual legs are largely aligned with the leg axis of cursorial mammals (Jayes and Alexander, 1978), it is convenient to model the leg as a strut extending and contracting along its axis (Fischer and Blickhan, 2006; Lee et al., 2008). In this framework, one can calculate the Limb Extension Work (LEW):

$$\text{Limb Extension Work} = \int_0^T \sum_i |F_i \cdot \dot{l}_i|^+ \text{dt}, \tag{4}$$

where F_i is ground reaction force from leg i along the leg axis and l_i is the instantaneous length of leg i. This has also been called "radial leg work" by some authors (Lee et al., 2008, 2014). This metric is relatively difficult to measure in animals, as it requires not only separate ground reaction forces, but also synchronized kinematic measurement of limb length. There may also be some ambiguity about the appropriate limb "length" to use, due to the complexities of limb attachment (e.g. as through the muscular sling of the forelimbs). Finally, it also neglects the work of forces not aligned with the leg axis–either using the limb as a lever (Gray, 1944) or taking advantage of hypothesized leg linkages (Usherwood, 2020b, 2022). However, the axial force assumption remains a useful approximation and simplification (at least for large

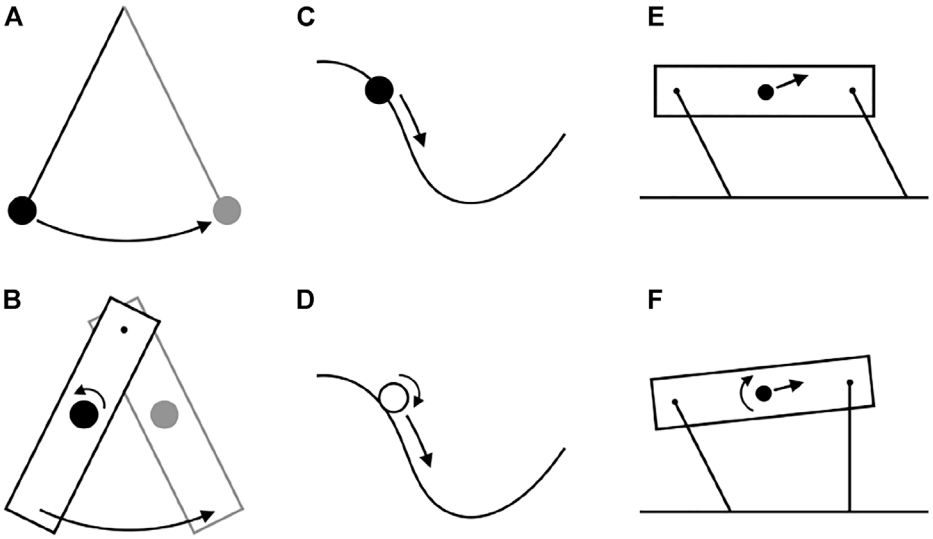

FIGURE 1 | Some examples of conservative systems with differing pendular recovery. Some systems have perfect pendular recovery (top row) while others have low pendular recovery (bottom row) because of energy passively transferred to rotational kinetic energy. **(A)** The classic point mass pendulum exhibits perfect exchange between center of mass kinetic and gravitational potential energy **(B)** A physical pendulum does not. **(C)** A bead on a frictionless wire also has perfect pendular recovery, while **(D)** a ball rolling down a hill does not. **(E)** A quadruped, modelled as a 4-bar linkage with massless legs, can get perfect pendular recovery during vaulting by performing a walking trot. **(F)** The same quadruped gets lower pendular recovery using a four-beat walk.

parasagittal mammals; Fischer and Blickhan, 2006), especially in a modelling context.

All the above metrics have been used in a modelling or prescriptive framework. Cavagna et al. (1977) noticed that the walking gaits of quadrupeds, like bipeds, exhibit out-of-phase kinetic and potential energies of the center of mass. Because the resulting NCW is low (**Eq. 2**), this "pendular" mode of walking has been put forward as the mechanism of low cost in quadrupedal walking (Cavagna et al., 1977; Full and Koditschek, 1999; Fischer and Lilhe, 2011). Alexander and Jayes (1978) optimized **Equation 3** in bipedal and quadrupedal models. Usherwood and Self Davies (2017) used **Eq. 3** with a point mass model to predict the limb phase relationships used by slow-moving mammals. Usherwood et al. (2007) used a collisional approximation of **Eq. 3** in a model with pitch rotational inertia and enforced vaulting phases matching a 4-bar linkage. Alexander (1980), Polet and Bertram (2019) and Polet (2021) used **Eq. 4** to determine whether the walking gaits used by quadrupedal mammals optimized work.

If economy is truly an *objective* of locomotion, and these metrics approximate muscular work well in general for quadrupedal gait, then optimizing the metric should result in a gait similar to the natural one employed. Moreover, to make interpretations about energy saving (or loss mitigating) mechanisms in locomotion, then the simple work metric should ideally be *prescriptive* as well as *descriptive*. The template theory of locomotion (Full and Koditschek, 1999) takes this one step further, positing that the motor control system uses low-order (potentially point-mass) models of the organism to plan behaviour and coordinate muscle activation. From this point of view, low-order models are not merely useful for our understanding of the mechanics of locomotion, but may be used by the organism itself. To what extent can the work metrics above serve as *prescriptive* and *predictive* objectives to be minimized in locomotion?

The "mechanism" of typical quadrupedal walking is important for understanding functional implications. Did the strategy evolve because it stabilizes the organism (Cartmill et al., 2002), or because it is energetically most economical (Hoyt and Taylor, 1981)? If the gait is economical, is that because it efficiently trades kinetic for potential energy (**Eq. 2** Cavagna et al., 1977; Griffin et al., 2004; Fischer and Lilhe, 2011), because it produces limb impulses that most effectively manage collisions between the center of mass and the ground (**Eq. 3** Bertram, 2016), or because it minimizes aspects of muscle work that are not adequately captured by these heuristics?

To better understand the energetic role of stereotypical quadrupedal walking, we test three competing and increasingly complex work-based cost functions (**Eqs 1**, **3**, **4**) under two dynamic models with and without rotational dynamics. We evaluate the ability of these three cost functions to predict duty factors exceeding 0.5, the alternating hind-fore contact pattern, and double-hump ground reaction force profiles typical of walking in cursorial mammals. In forming these reductionist models of locomotion, we prefer if the simpler formulation captures the salient effect of interest- in this case, alternating periods of double and triple limb stance with double-hump ground reaction forces.

2 MATERIALS AND METHODS

2.1 Model Dimensions and Empirical Data

The model is two-dimensional in the sagittal plane, and follows the design of Polet and Bertram (2019) and Polet (2021). The

body consists of a single rigid trunk, with massless prismatic actuators as legs. The forelimbs attach to the trunk at the shoulder (glenoid) while the hindlimbs attach to the body at the hips (acetabulum). We base the model on an adult Warmblood horse (*Equus ferus caballus*), as a "stereotypical" cursorial quadruped. The maximum hindlimb length ($l_{H\max}$) is set to the empirical length in standing (pes to hips) of 1.38 m. This value was derived from **Figure 1** in Bobbert et al. (2007) by scaling to the reported withers height of 1.7 m. The glenoacetabular distance (GAD; hips to shoulders) and maximum forelimb length (manus to shoulders in standing) were set to be equal to the empirical hindlimb length, in order to focus on the effects of the work metrics (rather than complications arising from differences in these lengths). Another model, with more accurate forelimb length and GAD, was also explored using the LEW cost for comparison. In this case, the forelimb length and GAD were measured in the same way as hindlimb length, and found to be 1.14 and 1.63 m respectively.

As the data for this study were recorded at a walking speed of 1.6 m s^{-1}, the non-dimensional speed used in the simulation was $U' \equiv U/\sqrt{gl_{Hmax}} = 0.43$, where U is average horizontal speed, and $g = 9.81$ m s^{-2} is gravitational acceleration. Note that here and elsewhere, we use the prime symbol to denote normalized variables.

The COM is placed along the axis connecting glenoid to acetabulum, at 0.57 times the GAD from the hips, matching the relative impulse produced by the forelimbs by three horses studied by Bobbert et al. (2007). For the distributed mass model, the Murphy number (4 × pitch moment of inertia / body mass / GAD^2) is set to the empirical value for a dutch warmblood horse of 0.82 (Buchner et al., 1997; Polet, 2021). The point-mass model omitted rotational dynamics but maintained limb length constraints.

Empirical ground reaction forces were extracted from **Figure 1** of Bobbert et al. (2007) using WebPlotDigitizer (Rohatgi, 2019). The time between successive touchdowns of the limbs yielded a mean stride time of 1.16 s, and thus a mean stride length D of 1.86 m. The stride length normalized to hind limb length was $D' = 1.34$.

2.2 Optimization and Simulation

2.2.1 Problem Specification

Simulations of symmetrical gaits used a contact-invariant method described by Polet and Bertram (2019), simplified to consider only symmetrical gaits as described by Polet (2021). The actuator force for limb i (F_i) acts along an axis between foot and attachment point to the trunk (hips or shoulders). It is constrained to push only ($F_i \geq 0$) and is constrained to be active only when limb length is less than a given value, *via* the complementarity condition

$$F_i\,(l_{i\max} - l_i) \geq 0. \tag{5}$$

Actuator force is instantaneously reflected in ground reaction force, and sliding friction is infinite. Decision parameters include the footfall locations of the left limbs; as the gaits are symmetrical, these are translated by $D/2$ for the right limbs. In the optimization formulation, time is normalized to stride period ($t' = t/T$), and simulations occur over the half cycle. States include the kinematics (positions and velocities) of the planar rigid trunk, and the prismatic actuator forces. To enforce gait symmetry, initial kinematics (at $t' = 0$) are constrained to equal final kinematics (at $t' = 0.5$), while left-side forces at $t' = 0$ are constrained to equal their associated right-side forces at $t' = 0.5$ [e.g. $F_{LH}\,(0) = F_{RH}(0.5)$].

The left-hind (LH) limb is given as the "reference limb" and is constrained to produce zero force at $t = 0$. The right-hind (RH) limb must therefore lift off in the first half cycle (its force must be zero at $t = 0.5$). Either the left-front (LF) or the right-front (RF) limb must touch down in the first half cycle (or always produce zero force); but since the model is planar, either limb can be swapped with no change to the solution dynamics. So, to simplify the formulation, we constrain the left-front limb to touch down in the first half cycle (or always produce zero force). To allow for the left front limb to lift off before touchdown in the first half cycle, we specify left-front actuator force through a trailing (caudal) footfall (F_{LFt}) as well as a leading (rostral) footfall (F_{LFl}) separated by D, with $F_{LFt} = 0$ at $t' = 0.5$ and $F_{LFl} = 0$ at $t' = 0$. Consequently, the forces of the right-front limb act through at most one footfall in the first half cycle, and do not have any constraints on force at $t' = 0$ or 0.5.

A limb exclusion constraint, given as

$$F_{LFt} \int_0^t F_{LFl}\,(\tau)\mathrm{d}\tau = 0, \tag{6}$$

ensured that the forces of the left-front limb acting through the trailing footfall (F_{LFT}) were never active once the forces through the leading footfall (F_{LFL}) exceeded zero. This requires adding $\int_0^t F_{LFl}\,(\tau)\mathrm{d}\tau$ as an additional state variable.

Periodicity is enforced by constraining all kinematics (apart from horizontal COM position) to be equal at $t' = 0$ and $t' = 0.5$, and constraining left limb forces at $t' = 0$ to be equal to associated right limb forces at $t' = 0.5$.

As constraint violation is only evaluated in SNOPT and GPOPS-II at node points, certain constraints could be violated at intermediate points. If the mesh was too sparse, the constraint **Eq. 6** could be violated between points, leading to brief periods of five-limb contact. This was fixed by adding an additional complementarity constraint for the simulations minimizing NCW,

$$F_{LFt}\dot{F}_{LFl} = 0. \tag{7}$$

Like other complementarity conditions, the path constraints **Eqs 5**–**7** were smoothed using the relaxation parameter method described by Manchester and Kuindersma (2017), which involved augmenting the objective with relaxation parameter and slack variable complementarity penalties.

The predominant cost in the objective is work, using one of **Eqs 1**, **3**, **4**. The absolute values for each cost function were transformed using slack variables, as described by Polet and Bertram (2019), following Betts (2010). A force rate penalty of

$\sum_i \int_0^T c_1 \dot{F}_i^2 \mathrm{d}t$ was added to regularize the cost function and avoid non-smooth force profiles typical of work-minimizing solutions. The scaling factor c_1 was kept at 0.00003, matching Polet (2021) and 100 times smaller than the value used by Polet and Bertram (2019).

In summary, the actuator force rate of change were given as control variables, along with slack variables and relaxation parameters. States were the three planar degrees of freedom of the trunk and its time derivatives, actuator forces and $\int_0^t F_{LFl}(\tau)\mathrm{d}\tau$. Decision parameters were the footfall locations of the left limbs. Solutions are constrained to start at a horizontal position 0 and end at $D/2$ in time $T/2$, and hip and shoulders were constrained to remain above ground. The body pitch (relative to the horizontal) was constrained between $\pm \pi/2$. Actuator forces were constrained to be positive (pushing forces with no suction into the ground). All other variables were left with large enough bounds to be effectively unbounded.

2.2.2 Optimization Routine

Optimizations were transcribed using GPOPS-II (v 2.3, Patterson and Rao, 2014) and meshes were refined using the *hp*-adaptive method described by Patterson et al. (2015) and with gradient estimation using central differencing. The resulting nonlinear program was solved using SNOPT (v 7.5, Gill et al., 2005, 2015).

Initial random guesses were created according to the method described in Polet and Bertram (2019). 250 random initial guesses were used per test case. From these guesses, an initial optimization was performed using low relaxation parameter penalties, and a maximum of 500 SNOPT iterations and two mesh iterations. The output from this optimization was downsampled to 16 evenly-spaced grid points, and served as the input to the next round of optimization. In this round, relaxation parameter penalties were increased tenfold, and up to 1000 SNOPT iterations and three mesh iterations were allowed. If mesh tolerances were not satisfied after the three mesh iterations were used, the output was downsampled again and used as a guess for a final round of optimization with up to eight mesh iterations.

If the solution satisfied mesh tolerance, and SNOPT indicated successful convergence, the solution was subjected to an additional mesh refinement step, which interpolated additional collocation points midway between existing points. This refined mesh served as the input guess for an additional round of optimization.

These final solutions were then evaluated for mesh error below tolerance, satisfactory convergence with SNOPT, and satisfaction of complementarity conditions at grid points. Any solutions that did not satisfy these criteria were rejected. Of the remaining solutions, the one that minimized the total objective (work, force rate penalty, and relaxation parameter penalties) overall was selected as the "pseudoglobal" optimum.

3 RESULTS

3.1 Ground Reaction Force Traces

Figure 2 shows the results of simulations at a moderate walking speed ($U' = 0.43$). Animations of these simulations can be found in **Supplementary Videos S1, S2**. Regardless of whether a distributed mass or point-mass model is used, optimization of a Net COM Work cost function results in duty factors close to 1 (**Figures 2A,B**) with highly compliant leg actuation. Simultaneous contact results in a near-constant net vertical ground reaction force, reducing oscillation of the center of mass. In the distributed mass model, the forward bias of the center of mass results in lower peak forces in the hindlegs relative to the forelegs.

Minimizing Individual Limbs COM Work results in alternating periods of single-stance vaulting, with double-hump GRF profiles (**Figures 2C,D**). While peak forces do not change between the point mass and distributed mass models, the duty factor is extended in the forelimbs for the distributed mass case. This results in higher impulse for the forelimbs, as required to enable cyclical body pitching (Polet and Bertram, 2019).

Under a point mass model, the ILCW and Limb Extension Work are equivalent, and correspond to the solution in **Figure 2C**. However, LEW differs from ILCW under a distributed mass model (**Figure 2F**). The solution uses alternating periods of double and triple stance with double-hump ground reaction forces and duty factors close to 0.5–uniquely matching the empirical solution (**Figure 2E**) in these respects. The addition of a larger force rate penalty (matching Polet and Bertram, 2019) and more realistic forelimb and glenoacetabular lengths (from Bobbert et al., 2007) result in better empirical agreement, with smoother force peaks (**Supplementary Figure S1**; **Supplementary Video S3**).

3.2 Power Traces

3.2.1 Solution Optimizing Net COM Work

Power plots give a sense of how costly each solution is under the alternative cost functions. In **Figure 3** (as in **Figures 4**, **5**), only the optimal solution with the distributed mass model is shown for the given cost function.

By maintaining a virtually constant, vertical net ground reaction force equal to body weight (**Supplementary Video S1**), Net COM Power can be maintained at 0 for the duration of the cycle (**Figure 3A**, solid line). However, there are slight oscillations of total system power (dash line), as rotational kinetic energy varies throughout the cycle. This form of kinetic energy is ignored by NCW.

Despite exhibiting zero NCW, the solution minimizing this cost exhibits pronounced Individual Limbs COM Work (**Figure 3B**, net positive work 0.78 mgl_H, **Table 1**), because limbs produce considerable forwards and backwards forces that provide simultaneous positive and negative power. Because little pitching is observed in this solution, the Limb Extension Power is almost equivalent to Individual Limb COM Power (**Figure 3C**).

Optimizing NCW results in highly compliant gait, consistent with previous bipedal energetic models. A flat "Groucho walk" can maintain NCW of zero (Bertram et al., 2002; Kuo, 2007). However, a NCW cost function should be in some ways indeterminate. NCW of zero results in perfect exchange of COM Kinetic and Gravitational Potential Energies. An infinite number of trajectories could simulate this exchange, with the sufficient

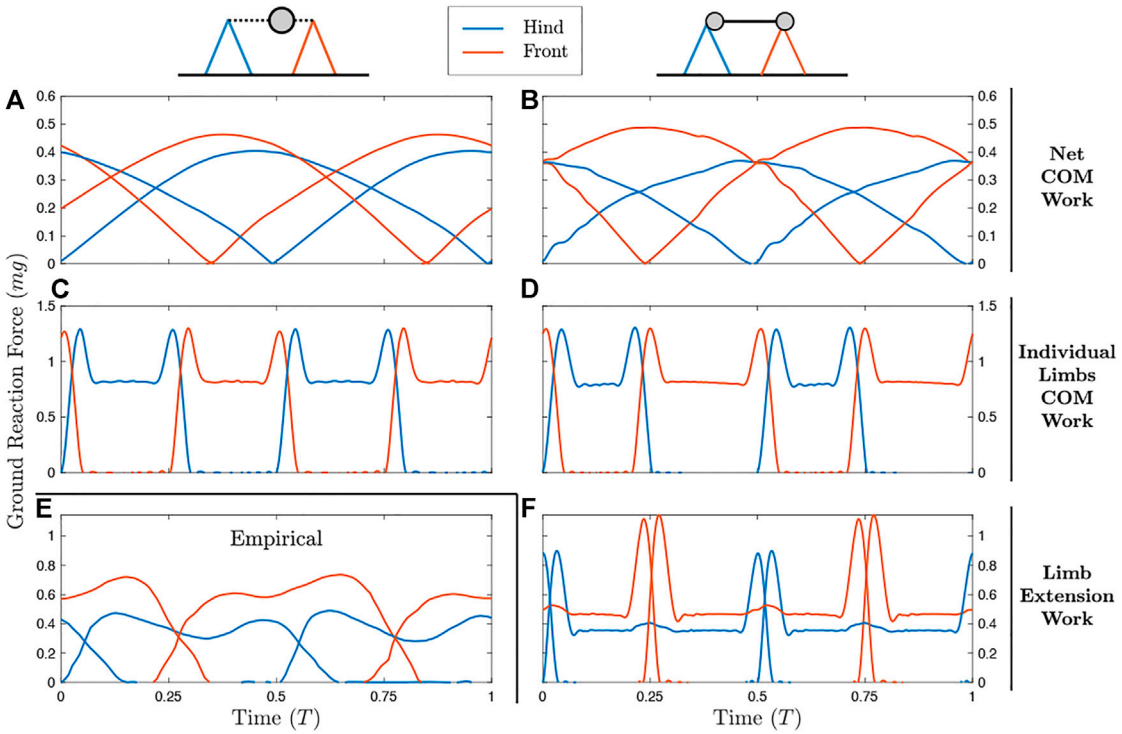

FIGURE 2 | Ground reaction forces (GRFs) for the point mass model (left column) and distributed mass model (right column) with different measures of work (rows). Diagrams show approximate placement of point mass (left) and radii of gyration (right). **(A,B)** Optimizing on Net COM Work results in duty factors close to one and single-peak GRFs. **(C,D)** The Individual Limbs COM Work objective results in alternating periods of single-stance vaulting, with double-hump GRFs. **(E)** Empirically, horses in a medium walk display double-hump GRFs with alternating periods of double and triple support. These features are reproduced only in **(F)** the distributed mass model with Limb Extension Work as the objective. For the planar model results, left and right limb contact can be swapped with no change to the model results, and so only hind and forelimbs are distinguished.

condition of mimicking a bead travelling on a frictionless surface between $x = 0$ and $x = D$ in a set time (**Figure 1C**). Why then is the resulting gait completely flat? Here, the small force-rate penalty becomes the deciding factor. By using high duty factor with a flat gait, the force rate penalty is kept at a low value.

3.2.2 Solution Optimizing Individual Limbs COM Work

When Individual Limbs COM Work is optimized, the Net COM Power fluctuates but remains small (**Figure 4A**, solid line), with total positive COM work of 0.02 mgl_H. However, if changes in rotational dynamics are also considered, then the system exhibits enormous instantaneous changes in total energy (dash line), and total Net System Work of 0.51 mgl_H.

This solution exhibits four peaks in Individual Limb COM power, corresponding to transfers of support (**Figure 4B**). A positive peak in one limb is met with a negative peak in the other; these largely cancel, resulting in low NCW (**Figure 4A**); similar to power curves in human walking (Donelan et al., 2002b). The majority of ILCW is performed during these periods of simultaneous positive and negative work.

This strategy consumes almost 9 times the positive actuator (limb extension) work as the strategy that minimizes Limb Extension Work (1.16 mgl_H compared to 0.13 mgl_H, **Table 1**). The ILCW strategy involves substantial pitching. While this pitching allows the COM to approximate single-stance vaulting over the fore and hind limbs sequentially, it results in a pronounced downward velocity of the hips or shoulders immediately prior to the moment of limb contact (**Supplementary Video S2**). This requires substantial negative work for the touchdown limb, and substantial positive work from the supporting limb (**Figure 4C**) to generate angular momentum redirecting the COM into a vaulting arc over the opposite limb.

3.2.3 Solution Optimizing Limb Extension Work

The solution that optimizes Limb Extension Work (LEW) results in regular oscillations of COM energy (**Figure 5A**), with peaks corresponding to transfer of support and 4 times the net positive COM work as the ILCW solution (0.09 compared to 0.02 mgl_H, **Table 1**). Accounting for changes in rotational kinetic energy (**Figure 5A**, dash line) results in a 55% reduction of the Net System Work (**Table 1**), due to a loss of rotational kinetic energy while translational kinetic energy increases (and *vice versa*). It is not clear, however, whether there is passive "transduction" between these forms (as in a ball rolling down a hill, **Figure 1D**), or whether it is a fully active process (determined by actuator work).

The solution that minimizes LEW exhibits substantial Individual Limbs COM Power throughout the entire cycle (**Figure 5B**). Peaks in power correspond to transfer of support, while flat regions of steady power correspond to portions of the passive vaulting phase. Power

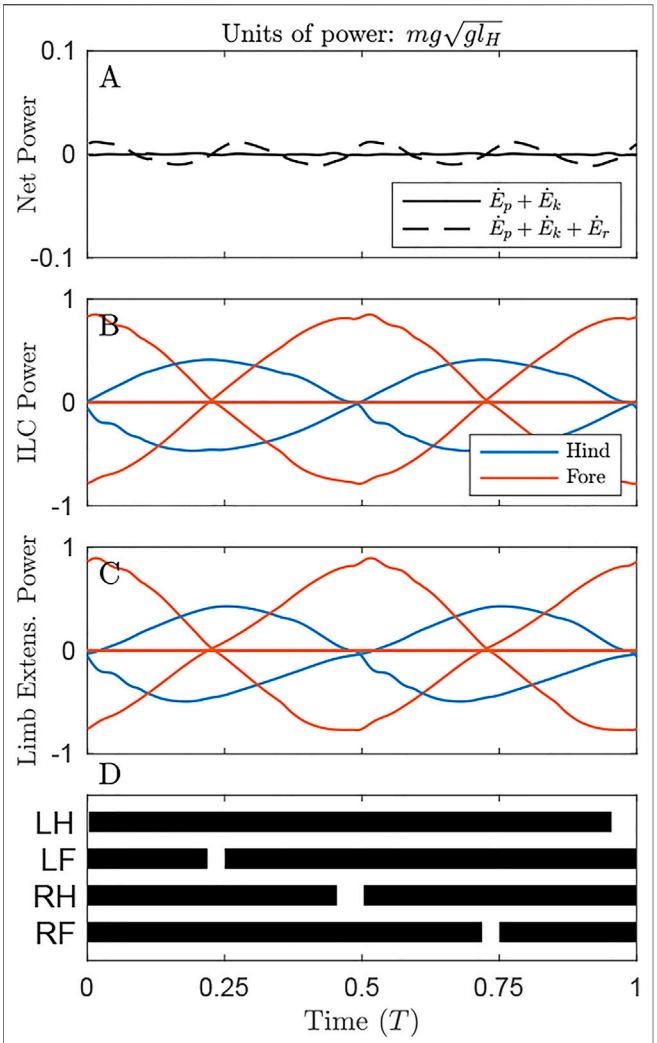

FIGURE 3 | Power through time for the solution minimizing Net COM Work, under the distributed mass model, showing the origination of cost under different metrics. **(A)** Net power on the COM remains zero throughout the cycle (solid line), but system energy fluctuates slightly due to pitching of the body (dash line) **(B)** Individual Limbs COM Power and **(C)** Limb extension power are large, owing to substantial compression and extension of the limbs due to **(D)** large duty factors as shown in the gait diagram, leading to long periods of quadruple stance. Here and in the gait diagrams of **Figures 4**, **5**, stance is plotted when GRF exceeds 0.02 body weights for a given limb.

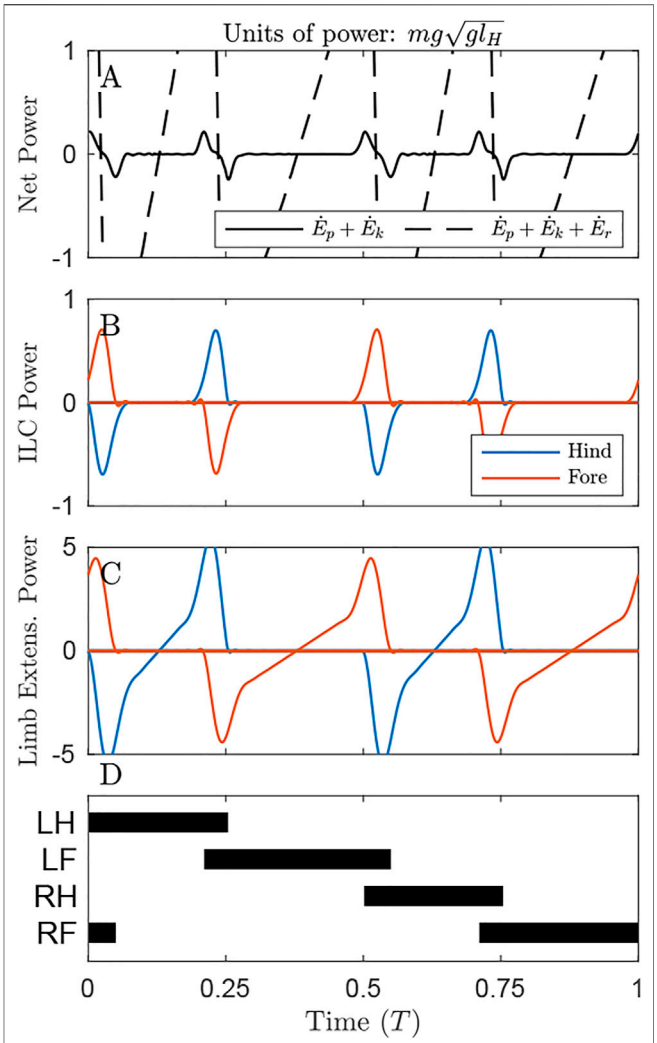

FIGURE 4 | Power through time for the solution minimizing Individual Limbs COM Work under the distributed mass model. **(A)** There is a small oscillation of the Net COM Power (black line), but very large oscillations in the system energy changes (dash line) due to pronounced pitching **(Supplementary Video S1)**. **(B)** Individual Limbs COM Power (ILCP) exhibits positive and negative peaks at transfer of support. Some power is inevitable due to redirecting the COM from a downward to upward trajectory. **(C)** The Limb Extension power is considerable, even during periods where ILCP is zero. Note that the *y*-axis here is 5 times that of **Figures 3C**, **5C**. **(D)** The gait involves alternating periods of single and double stance.

switches from negative in early stance to positive in late stance, after transfer of support has occurred on the opposite set of limbs and has redirected the center of mass velocity from downward to upward (**Supplementary Video S1**). The positive work performed, as measured with the Individual Limbs method, is 0.41 mgl_H, more than four times the minimal value of 0.09 mgl_H (**Table 1**; **Figure 5B**).

The optimal strategy for minimizing LEW exhibits prolonged passive phases of double-stance vaulting (**Figure 5C**), where the legs and torso act as a 4-bar linkage (**Supplementary Video S2**, Usherwood et al., 2007). These are punctuated by short phases of near-simultaneous positive and negative work, representing transfer of support. A supporting limb begins pushing, generating positive power, immediately prior to the touchdown limb generating negative power to absorb added energy and finish redirecting the hip or shoulder onto a vaulting path. The different heights of these power peaks are due to the mass bias. The forelimbs, being closer to the center of mass, exhibit higher peak power than the hindlimbs.

4 DISCUSSION

Alternative metrics of work provide different insights into the energetics of locomotion. While these approximations are useful,

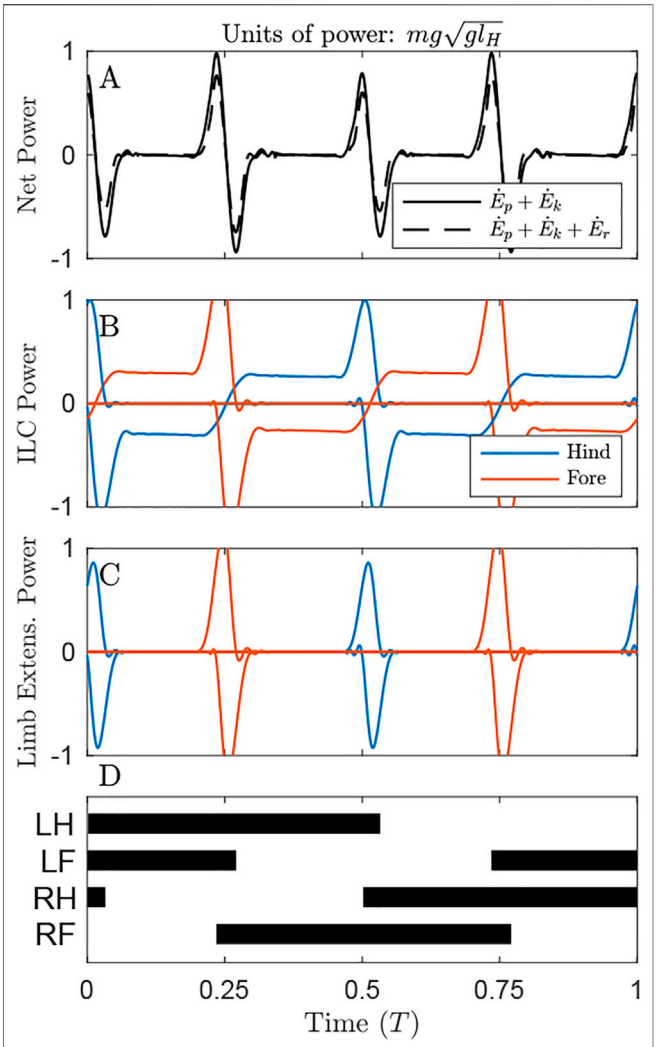

FIGURE 5 | Power through time for the solution optimizing Limb Extension Work, under the distributed mass model. **(A)** Oscillations in Net COM Power (NCP, black line) and Net System Power (NSP, dash line) occur primarily at transfer of support. Accounting for changes in rotational energy results in a slight reduction of peak NSP compared to NCP at transfer of support. **(B)** Throughout the cycle, the gait exhibits continuous Individual Limbs COM Power, because the COM trajectory does not precisely follow the arc of each limb in stance. **(C)** Limb Extension Power exhibits peaks at transfer of support. These peaks are almost twice the value observed in **Figure 3C**, but the total positive work is lower since there are substantial periods of zero-cost passive vaulting. **(D)** The gait diagram shows a typical singlefoot walk with alternating periods of triple and double limb stance, with phase offset of 0.25. Note that left and right limbs can be swapped with no change to gait energetics in this planar model.

they each implicitly ignore certain aspects of the dynamics and energetics of gait. Simplifying the system can be useful, and the metrics provide a way of quantifying gait and pointing to similarities between disparate organisms (Cavagna et al., 1977; Lee and Harris, 2018). It is tempting to point to a descriptive parameter as a prescriptive target of locomotion (or approximation of that target). Our tests on the prescriptive ability of these metrics leads to important insights about what they do– and do not– tell us about the determinants of organismal movement.

TABLE 1 | Positive work under various candidate cost functions, for simulations optimizing each cost function under a distributed mass model.

		Cost function optimized		
		NCW	**ILCW**	**LEW**
Total Positive Work (mgl_H)	NCW	0.000	0.02	0.09
	NSW	0.002	0.51	0.04
	ILCW	0.78	0.09	0.41
	LEW	0.74	1.16	0.13
Percent Recovery		99.4	94	75

Net COM Work is the simplest metric of work to measure in practice. Changes in COM energy mean that something is performing work on it– most likely muscle tendon units. However, the converse is not necessarily true: observing no change in COM energy does not mean that something is not performing work on it. Simultaneous positive and negative work can be performed.

The solutions shown in **Figures 2A,B** and **Figure 3** demonstrates the limitations of NCW. These solutions keep NCW at zero. Apparent fluctuations of potential and kinetic energy are exactly out of phase. Were such a gait observed in nature, an interpretation may be that it efficiently trades kinetic and potential energy of the center of mass [e.g. Griffin and Kram, 2000)]. However, the alternate metrics say something different. Both ILCW and LEW of this gait are high (**Table 1**), because it requires continuous simultaneous positive and negative work from individual limbs to manage the trajectory of the center of mass as if it were a bead on a wire, acting only under the influence of gravity (**Figure 1C**).

Like the mass on a track analogy, NCW does not account for rotational dynamics. If we calculate the Net System Work (NSW) for this solution (including changes in rotational kinetic energy), we see another way that NCW can overlook key system dynamics (**Table 1**). The NSW is 0.002 mgl_H - still small, but appreciable compared to the zero NCW that the solution exhibits.

While the solutions optimizing NCW (**Figures 2A,B**) do not match a stereotypical singlefoot gait in force shape or duty factor (**Figure 2E**), they do match the gait in sequence of footfalls. The optimal solution does exhibit the stereotypical Hind-Fore-Hind-Fore contact pattern, with phase offset around 0.25. Notably, many primates and small mammals exhibit walking ground-reaction force patterns that are similar-single peaks with out-of-phase forelimb and hindlimb contacts, and a relatively compliant gait (Cartmill et al., 2002; Schmitt and Lemelin, 2002; d'Août et al., 2004; Schmidt, 2005; Webb et al., 2011). However, unlike the solution here, the NCW in these animals is appreciable, and percent recovery is often less than 50% (Ogihara et al., 2012; Demes and O'Neill, 2013). It therefore seems that, while these animals could keep NCW close to zero, their preferred gait is driven by other considerations.

There is another cost function implicit to these solutions that may be especially important at small sizes: muscle activation.

Internal damping (Garcia et al., 2000; Weihmann, 2020), peak power (Hubel and Usherwood, 2015), and force generation (Kram and Taylor, 1990) have all been proposed as relatively costly for small animals. All these costs, while controversial in their physiological mechanisms, have a basis in more frequent muscle activation. In the present optimization framework, a force-rate penalty was imposed to regularize the solution, and has been linked with cost of muscle activation (van der Zee and Kuo, 2021). This penalty is likely responsible for the phase offset of 0.25 and the single-hump ground reaction forces in the minimal NCW solutions. Still other, non-energetic aspects may be as or more important determiners of locomotion at small sizes-for example, stability in arboreal habitats (Shapiro and Young, 2010).

Individual Limbs COM Work has been offered as an alternative to NCW that can capture simultaneous positive and negative work (Donelan et al., 2002a). However, it too is poorly prescriptive for quadrupedal walking. Whether or not rotational dynamics are included in the model, optimal ILCW calls for alternate periods of single stance while walking (**Figures 2C,D**). In the distributed mass model, this is achieved by extreme pitching, which results in extremely high actuator work (1.16 mgl_H, **Table 1**) and NSW (0.51 mgl_H), while the NCW is kept at a low value (0.02 mgl_H).

While the present use of ILCW results in poor fidelity to walking in quadrupedal animals, Usherwood et al. (2007) and Usherwood and Self Davies (2017) used ILCW– with a distributed mass and point mass respectively– and achieved decent agreement with observed locomotion. This may be due to imposed constraints in the latter formulations. Usherwood et al. (2007) enforced periods of simultaneous hind and forelimb contact, while Usherwood and Self Davies (2017) constrained duty factor to match empirical data. Applying these constraints to our ILCW model would result in a more natural-looking gait, but would not– as Usherwood and Self Davies (2017) point out– explain why a given duty factor or simultaneous hind-fore contact are preferred.

Our results, from a less constrained optimization problem, show that optimizing ILCW cannot simultaneously explain the duty factors, phasing and ground reaction forces employed by walking quadrupedal animals. A key reason is the influence of pitch rotation, which ILCW ignores. In many natural gaits, including quadrupedal walking, the pitching energies appear small. However, Polet (2021) showed that pitching energies may be kept small because they would otherwise be expensive. While the individual limbs method may correspond closely to Limb Extension Work in most natural gaits, which do not exhibit much pitching, it does not explain why those gaits are non-pitching gaits.

Only the distributed mass model with optimal LEW resulted in a four-beat gait with duty factors close to 0.5 and double-hump GRF profiles (**Figure 2F**)– the stereotypical cursorial quadruped pattern. The pattern appears expensive both from the perspective of NCW and ILCW. It exhibits larger NCW than the other solutions (**Table 1**), and the percent recovery is relatively low at 75%– though this value more closely matches locomotion in dogs, who have percent recoveries between 50 and 70% in walking (Griffin et al., 2004). The ILCW is large (**Figure 5B**) even during passive stance phase with zero actuator power (**Figure 5C**), because the center of mass velocity is seldom oriented perpendicular to any leg in stance (**Supplementary Video S1**). It is only by considering the work of extending the leg that the natural, four-beat strategy becomes economical.

The pattern emerges as a tradeoff between cost of transfer of support–which favours more evenly distributed contacts (Ruina et al., 2005; Polet, 2021)– and cost of pitching the body–which favours simultaneous contact of the hind and forelimbs. For a Murphy number less than one– as occurs in dogs, horses, and likely most mammals– the four-beat singlefoot gait tends to be favoured (Polet, 2021).

The dynamics at transfer of support are, however, nontrivial. It is not immediately clear why, for example, even footfalls are optimal (even with a mass biased toward the forelimbs). We invoke three heuristics to explain why the four-beat singlefoot walk optimizes LEW:

1) Distributed contacts lowering collisional costs. As discussed by Ruina et al. (2005), contacts at regular intervals allow the contact velocity to be relatively consistent. As the cost of redirecting this velocity will be roughly proportional to its magnitude squared, keeping all contact velocities approximately equal lowers the total cost.
2) The pre-touchdown pushoff. Work-minimal bipedal walking benefits from pushing off with the support limb immediately prior to contact of the touchdown limb. The same strategy can be observed here, with a double-peak in the ground reaction force close to transfer of support (**Figure 2F**), and positive peak axial power coming immediately before negative peak power (**Figure 5C**). How the limb on the opposite end of the body might affect this transfer of support is not trivial, but the following effect is apparent (point three).
3) Work-free reaction at the opposite stance leg. Transfer of support causes a large peak force at one end of the body. When the radius of gyration is smaller than the moment arm– that is, the Murphy Number is less than one (Usherwood, 2020a; Polet, 2021)– the other end of the body will pitch downward. This downward pitching need not cost any extra work, however, as the opposite limb can simply increase its applied force to avoid changing length. This is observed as slight increases in force in midstance, at the moment the opposite pair of legs undergoes transfer of support (**Figure 2F**), consistent with the horse-inspired Murphy number of 0.82. When transfer of support at one of the hind legs occurs at midstance for the foreleg (and *vice versa*), the foreleg is vertical and in an optimal position to resist the applied force.

It is not immediately clear, however, how all these effects intermingle at the instant of contact. The interpretations above deserve more scrutiny under a formal collisional mechanical analysis.

4.1 Implications for Interpreting Biological Gait

It is often tempting to use simple metrics of biological locomotion to infer an underlying priority of the motor control system. The

results here point to where the metrics might fail in the analysis of quadrupedal walking. A very widespread approach is to consider the changes in center of mass kinetic and potential energy as an identifier both of gait type and relative economy. Cavagna et al. (1977) noted that many walking animals– from primates, to birds, to dogs– exhibit out-of-phase kinetic and potential energy exchange during walking.

Since a point-mass pendulum exhibits similar out of phase potential and kinetic exchange, this kind of locomotion has been called "pendular" and the degree to which the total system energy remains constant is often parameterized as "pendular recovery" (Biknevicius et al., 2013; Shimada et al., 2017). The comparison has led to a conflation of out-of-phase kinetic and potential energy exchange– equivalently, low Net COM Work– and economical walking (Griffin and Kram, 2000; Reilly et al., 2007; Biknevicius et al., 2013; Shimada et al., 2017). Further, various authors have pointed to transduction of COM kinetic and gravitational potential energy as the primary mechanism allowing animals to walk with low energetic cost by reducing muscular work (Cavagna et al., 1977; Fischer and Lilhe, 2011; Pontzer et al., 2014; Bryce and Williams, 2017; Clayton and Hobbs, 2017).

The results of the present analysis challenge these ideas. Exact transduction of potential and kinetic energy is possible with the quadrupedal apparatus, but is rarely used in nature. Optimizing on NCW results in a solution that is unlike the passive vaulting gaits cited as "pendular" (Cavagna et al., 1977; Griffin et al., 2004; Fischer and Lilhe, 2011). Furthermore, tracking $\dot{E}_P + \dot{E}_K$ can lead to over- or underestimating the system energy changes (**Table 1**), as rotational energy changes are neglected.

Instead, we argue that the natural fluctuations in kinetic and potential COM energy are not the mechanism of quadrupedal walking, or even high walking economy, but a biproduct of optimizing a different cost function. The benefit of the "pendular strategy" is not really the passive transduction of kinetic energy into gravitational. Rather, it is the ability for the legs to remain straight, and the muscles to do little to no work, while the body translates forward (Tucker, 1975; Griffin et al., 2004). Indeed, the reduction of gravity (which ought to provide less opportunity for transduction between these modes) changes energetic cost little in bipedal walking and results in a slight reduction in cost (Farley and McMahon, 1992; Hasaneini et al., 2017). Quadrupeds can emulate perfect transduction of gravitational and kinetic energy; the apparent energy "savings" in this case are not savings at all, but require costly simultaneous positive and negative work.

Nevertheless, we believe that NCW– and its related parameterizations, pendular recovery and the "collision angle" (Lee et al., 2011)– can be usefully applied to gait analysis in two key ways. The first is as a gait classification scheme. Pendular recovery and collision angles have been used to identify subtle changes in gait within elephants (Ren and Hutchinson, 2008), birds (Usherwood et al., 2008), primates (Demes and O'Neill, 2013) and numerous other taxa (Lee and Harris, 2018). The second is to identify what portions of the stride could be most costly (Donelan et al., 2002b; Lee et al., 2011). As **Figure 5** shows, the portions of stride corresponding to large fluctuations in Net COM Power also correspond to peaks in Limb Extension Power. However, the correspondence does not hold in all gaits (**Figures 3**, **4**), and identifying costly portions of a stride does not mean that eliminating those portions would result in a reduction of cost (Kuo and Donelan, 2010; Simpson et al., 2019). As the number of limbs increases, it becomes harder to isolate the work of individual limbs, and NCW can be the only measurable form of work remaining (Zani et al., 2005; Lee et al., 2011). Our present results, however, promote caution in interpreting NCW as representative of energetic cost.

Individual Limbs COM Work is a tempting fix to NCW metrics. Simultaneous positive and negative work can be somewhat identified, while measuring the value *in vivo* remains practical even if more difficult (requiring, in principle, only limb-specific ground reaction forces and kinematic integration constants, e.g., average horizontal speed). It has been readily applied as an optimization paradigm (Alexander and Jayes, 1978; Usherwood and Self Davies, 2017), as it is simpler than computing axial limb work with associated rotational dynamics. However, the results here demonstrate that 1) it can be far removed from LEW (and muscle work: Sasaki et al., 2009) and that 2) its prescriptive solutions are not always biologically realistic (unless highly constrained: Usherwood et al., 2007; Usherwood and Self Davies, 2017).

None of the cost functions predicted gait well in a point mass model. Even though the most natural solution exhibits relatively small rotational energies compared to kinetic and potential energies of the center of mass (**Figure 5A**), rotational dynamics are a prerequisite to obtaining the solution. In this model, rotational dynamics are exploited to provide sequential passive phases of vaulting, while distributing contacts. Forces are applied work-free in the stance leg to accommodate transfer of support at the other end of the body. The model hints at other subtle ways to simultaneously reverse kinetic and rotational momentum at contact, but further analysis is required to understand the dynamics of this transition.

The combination of axial limb work with pitching dynamics in a planar model is more complex than the other cases considered here, and is difficult to measure, yet is still a useful simplification. This combination alone resulted in a four-beat walking gait, similar in many respects to the gaits employed by many quadrupedal mammals. The similarity between the optimal and natural gait could be interpreted as pointing to a biological mechanism. Specifically, it suggests that the four-beat vaulting gait is an emergent strategy from optimizing muscle work (per unit distance) during locomotion, and that axial limb work captures the dominant marginal cost for quadrupeds that use a vaulting walking gait.

However, the evidence provided here is indirect. By comparing metabolic expenditure to axial limb work empirically in different conditions, for example walking at a range of speeds, we would be able to test whether axial limb work is a good proxy for cost. Establishing muscle work or metabolic cost of transport as an optimization criterion of mammalian locomotion will require perturbation studies across many species in many conditions, similar to ongoing studies in human gait selection (Abram et al., 2019; Wong et al., 2019; Schroeder et al., 2021).

The models presented here are deliberately reductionist, and neglect several effects. Notably, lateral motions of the body are ignored, and these would be especially important for distinguishing symmetrical gaits that differ from a phase offset of 0.5 (i.e., Left-Left-Right-Right contact, vs. Left-Right-Left-Right). The gait diagram in **Figure 5D**, for example, is a diagonal sequence gait, while horses use a lateral sequence gait in walking. In the present model, there is no energetic difference between these gaits, and the optimizer in this case happened on the diagonal sequence by chance. However, the use of diagonal sequence gaits by some species, and lateral sequence by others, is a longstanding problem (Hildebrand, 1967) and the energetic consequences can only be resolved in 3D models (e.g., Usherwood and Self Davies, 2017).

The LEW results point to other areas where the model can be improved. LEW is an abstraction of joint work, which itself is an abstraction of muscle work. The cost of locomotion is not exactly proportional to axial limb work during locomotion. Ground reaction forces are not entirely leg-axial during quadrupedal walking in general (Jayes and Alexander, 1978; Usherwood, 2020b), and various antagonist muscles co-contract (Fischer and Lilhe, 2011). Isometric contraction and muscle (de) activation (Kushmerick and Paul, 1977; van der Zee and Kuo, 2021) are metabolically costly, and passive dissipation contributes to the work of locomotion (Zelik and Kuo, 2010). The model offers no explanation for why different mammals exhibit different limb phase relationships (Loscher, 2015), or why some mammals do not exhibit a double-hump ground reaction force profile (Webb et al., 2011; Demes and O'Neill, 2013). It also required stride length as an input, since there is low cost for frequent steps due to massless legs and low muscle (de)activation cost. Further refinement of the model presented here may provide clues as to which features of mammal morphology and physiology are responsible for their patterns of locomotion.

5 CONCLUSION

Simple metrics are used to quantify work in quadrupedal locomotion, and are often posited as determinants of the strategy employed. Here we tested the prescriptive ability of Net COM Work (NCW), Individual Limbs COM Work (ILCW) and Limb Extension Work (LEW) to predict the four-beat walking strategy typical of cursorial quadrupedal mammals. Optimizing NCW results in a highly compliant gait where the COM remains at a near constant height and velocity, while optimizing ILCW results in phases of single stance. Only optimizing LEW with distributed mass results in a gait that matches the stereotypical quadruped pattern.

Optimizing on NCW shows that perfect transduction of COM potential and kinetic energy are possible, but at the cost of extremely high limb work. While the compliant gait that emerges compares favourably to the gait of small mammals in footfall sequence and force shape, we believe this is due to the force-rate penalty imposed in our simulations for numerical regularization. This may have biological significance, as costs similar to force-rate likely become important as size decreases. ILCW has a poor correspondence to LEW in a distributed mass model, as the center of mass does not exactly follow the arcing trajectory of the limbs in passive stance during singlefoot walking. While NCW and ILCW serve as useful descriptive tools in gait analysis, they have limited prescriptive power. ILCW in particular has been used in predictive modelling frameworks with reasonable fidelity to natural gait. However, in a less constrained framework, as in the present study, the fidelity of its predictions are meagre.

Our results suggest that the stereotypical walking pattern in cursorial mammals does not optimally manage transduction of potential and kinetic energy, nor does it minimize the work that individual limbs do on the center of mass. Rather, it lowers the cost of positive muscle work by keeping LEW low. This is likely accomplished by a combination of 1) passive vaulting phases where the limbs remain straight and do no work (even if ILCW and NCW may be non-zero), interspersed with 2) distributed contacts minimizing translational collisional losses, assisted by 3) pre-footstrike pushoffs and 4) work free reaction at the limb in stance during transfer of support of the opposite pair, due to a low Murphy number.

DATA AVAILABILITY STATEMENT

The general optimization code is available at https://doi.org/10.5281/zenodo.5593594. The main overhead scripts for this paper are included as Supplemental Data. The raw data supporting the conclusion of this article will be made available by the authors, without undue reservation.

AUTHOR CONTRIBUTIONS

The study was conceived by DP and JB. DP designed the optimization models and performed the simulation and analysis. DP wrote and JB revised the manuscript.

FUNDING

This work was funded by NSERC (Grant Number 05305, Energy optimization and locomotion control: task, strategy and mechanisms, awarded to JB).

ACKNOWLEDGMENTS

We are grateful to Andy Ruina, Ryan Schroeder, and Jim Usherwood, who provided useful feedback on earlier versions of the manuscript.

SUPPLEMENTARY MATERIAL

The Supplementary Material for this article can be found online at: https://www.frontiersin.org/articles/10.3389/fbioe.2022.826336/full#supplementary-material

REFERENCES

Abram, S. J., Selinger, J. C., and Donelan, J. M. (2019). Energy Optimization Is a Major Objective in the Real-Time Control of Step Width in Human Walking. *J. Biomech.* 91, 85–91. doi:10.1016/j.jbiomech.2019.05.010

Alexander, R. M., and Jayes, A. S. (1978). Optimum Walking Techniques for Idealized Animals. *J. Zoolog.* 186, 61–81. doi:10.1111/j.1469-7998.1978.tb03357.x

Alexander, R. M. (1980). Optimum Walking Techniques for Quadrupeds and Bipeds. *J. Zoolog.* 192, 97–117. doi:10.1111/j.1469-7998.1980.tb04222.x

Basu, C., Wilson, A. M., and Hutchinson, J. R. (2019). The Locomotor Kinematics and Ground Reaction Forces of Walking Giraffes. *J. Exp. Biol.* 222, jeb159277. doi:10.1242/jeb.159277

Bertram, J. E. A. (2016). "Concepts in Locomotion," in *Understanding Mammalian Locomotion: Concepts and Applications* (Hoboken, NJ: John Wiley & Sons), 111–141. doi:10.1002/9781119113713.ch5

Bertram, J. E. A., D'antonio, P., Pardo, J., and Lee, D. V. (2002). Pace Length Effects in Human Walking: "Groucho" Gaits Revisited. *J. Mot. Behav.* 34, 309–318. doi:10.1080/00222890209601949

Betts, J. T. (2010). "Practical Methods for Optimal Control and Estimation Using Nonlinear Programming," in *Advances in Design and Control* (Philadelphia, Pennsylvania, USA: Society for Industrial and Applied Mathematics). doi:10.1137/1.9780898718577

Biknevicius, A. R., Mullineaux, D. R., and Clayton, H. M. (2004). Ground Reaction Forces and Limb Function in Tölting Icelandic Horses. *Equine Vet. J.* 36, 743–747. doi:10.2746/0425164044848190

Biknevicius, A. R., Reilly, S. M., McElroy, E. J., and Bennett, M. B. (2013). Symmetrical Gaits and center of Mass Mechanics in Small-Bodied, Primitive Mammals. *Zoology* 116, 67–74. doi:10.1016/j.zool.2012.05.005

Bobbert, M. F., Alvarez, C. B. G., van Weeren, P. R., Roepstorff, L., and Weishaupt, M. A. (2007). Validation of Vertical Ground Reaction Forces on Individual Limbs Calculated from Kinematics of Horse Locomotion. *J. Exp. Biol.* 210, 1885–1896. doi:10.1242/jeb.02774

Bryce, C. M., and Williams, T. M. (2017). Comparative Locomotor Costs of Domestic Dogs Reveal Energetic Economy of Wolf-like Breeds. *J. Exp. Biol.* 220, 312–321. doi:10.1242/jeb.144188

Buchner, H. H. F., Savelberg, H. H. C. M., Schamhardt, H. C., and Barneveld, A. (1997). Inertial Properties of Dutch Warmblood Horses. *J. Biomech.* 30, 653–658. doi:10.1016/S0021-9290(97)00005-5

Cartmill, M., Lemelin, P., and Schmitt, D. (2002). Support Polygons and Symmetrical Gaits in Mammals. *Zool. J. Linn. Soc.* 136, 401–420. doi:10.1046/j.1096-3642.2002.00038.x

Cavagna, G. A., Heglund, N. C., and Taylor, C. R. (1977). Mechanical Work in Terrestrial Locomotion: Two Basic Mechanisms for Minimizing Energy Expenditure. *Am. J. Physiology-Regulatory, Integr. Comp. Physiol.* 233, R243–R261. doi:10.1152/ajpregu.1977.233.5.r243

Clayton, H. M., and Hobbs, S.-J. (2017). The Role of Biomechanical Analysis of Horse and Rider in Equitation Science. *Appl. Anim. Behav. Sci.* 190, 123–132. doi:10.1016/j.applanim.2017.02.011

D'Aout, K., Vereecke, E., Schoonaert, K., De Clercq, D., Van Elsacker, L., and Aerts, P. (2004). Locomotion in Bonobos (*Pan paniscus*): Differences and Similarities between Bipedal and Quadrupedal Terrestrial Walking, and a Comparison with Other Locomotor Modes. *J. Anat.* 204, 353–361. doi:10.1111/j.0021-8782.2004.00292.x

Demes, B., and O'Neill, M. C. (2013). Ground Reaction Forces and center of Mass Mechanics of Bipedal Capuchin Monkeys: Implications for the Evolution of Human Bipedalism. *Am. J. Phys. Anthropol.* 150, 76–86. doi:10.1002/ajpa.22176

Donelan, J. M., Kram, R., and Kuo, A. D. (2002a). Mechanical Work for Step-to-step Transitions Is a Major Determinant of the Metabolic Cost of Human Walking. *J. Exp. Biol.* 205, 3717–3727. doi:10.1242/jeb.205.23.3717

Donelan, J. M., Kram, R., and Kuo, A. D. (2002b). Simultaneous Positive and Negative External Mechanical Work in Human Walking. *J. Biomech.* 35, 117–124. doi:10.1016/S0021-9290(01)00169-5

Farley, C. T., and McMahon, T. A. (1992). Energetics of Walking and Running: Insights from Simulated Reduced-Gravity Experiments. *J. Appl. Physiol.* 73, 2709–2712. doi:10.1152/jappl.1992.73.6.2709

Farrell, B. J., Bulgakova, M. A., Beloozerova, I. N., Sirota, M. G., and Prilutsky, B. I. (2014). Body Stability and Muscle and Motor Cortex Activity during Walking with Wide Stance. *J. Neurophysiol.* 112, 504–524. doi:10.1152/jn.00064.2014

Fischer, M. S., and Blickhan, R. (2006). The Tri-segmented Limbs of Therian Mammals: Kinematics, Dynamics, and Self-Stabilization-A Review. *J. Exp. Zool.* 305A, 935–952. doi:10.1002/jez.a.333

Fischer, M. S., and Lilhe, K. E. (2011). *Dogs in Motion*. Dortmund, Germany: VDH Service GmbH.

Fukuoka, Y., Habu, Y., and Fukui, T. (2015). A Simple Rule for Quadrupedal Gait Generation Determined by Leg Loading Feedback: A Modeling Study. *Sci. Rep.* 5, 8169. doi:10.1038/srep08169

Full, R. J., and Koditschek, D. E. (1999). Templates and Anchors: Neuromechanical Hypotheses of Legged Locomotion on Land. *J. Exp. Biol.* 202, 3325–3332. doi:10.1242/jeb.202.23.3325

Garcia, M., Kuo, A., Peattie, A., Wang, P., and Full, R. (2000). "Damping and Size: Insights and Biological Inspiration," in Adaptive Motion of Animals and Machines, Montreal, Canada, 7.

Gill, P. E., Murray, W., and Saunders, M. A. (2005). SNOPT: An SQP Algorithm for Large-Scale Constrained Optimization. *SIAM Rev.* 47, 99–131. doi:10.1137/s0036144504446096

Gill, P. E., Murray, W., Saunders, M. A., and Wong, E. (2015). *User's Guide for SNOPT 7.5: Software for Large-Scale Nonlinear Programming*. San Diego, La Jolla, CA: Center for Computational Mathematics Report CCoM 15-1, Department of Mathematics, University of California.

Gray, J. (1944). Studies in the Mechanics of the Tetrapod Skeleton. *J. Exp. Biol.* 20, 88–116. doi:10.1242/jeb.20.2.88

Griffin, T. M., and Kram, R. (2000). Penguin Waddling Is Not Wasteful. *Nature* 408, 929. doi:10.1038/35050167

Griffin, T. M., Main, R. P., and Farley, C. T. (2004). Biomechanics of Quadrupedal Walking: How Do Four-Legged Animals Achieve Inverted Pendulum-like Movements? *J. Exp. Biol.* 207, 3545–3558. doi:10.1242/jeb.01177

Guertin, P. A. (2012). Central Pattern Generator for Locomotion: Anatomical, Physiological, and Pathophysiological Considerations. *Front. Neurol.* 3, 183. doi:10.3389/fneur.2012.00183

Hasaneini, S. J., Schroeder, R. T., Bertram, J. E. A., and Ruina, A. (2017). The converse Effects of Speed and Gravity on the Energetics of Walking and Running. *bioRxiv* 2017, 201319. doi:10.1101/201319

Hildebrand, M. (1976). "Analysis of Tetrapod Gaits: General Considerations and Symmetrical Gaits," in *Neural Control of Locomotion. Vol. 18 of Advances in Behavioral Biology*. Editors R. M. Herman, S. Grillner, P. Stein, and D. Stuart (New York: Plenum Press New York), 203–236. doi:10.1007/978-1-4757-0964-3_9

Hildebrand, M. (1967). Symmetrical Gaits of Primates. *Am. J. Phys. Anthropol.* 26, 119–130. doi:10.1002/ajpa.1330260203

Hoyt, D. F., and Taylor, C. R. (1981). Gait and the Energetics of Locomotion in Horses. *Nature* 292, 239–240. doi:10.1038/292239a0

Hubel, T. Y., and Usherwood, J. R. (2015). Children and Adults Minimise Activated Muscle Volume by Selecting Gait Parameters that Balance Gross Mechanical Power and Work Demands. *J. Exp. Biol.* 218, 2830–2839. doi:10.1242/jeb.122135

Jayes, A. S., and Alexander, R. M. (1978). Mechanics of Locomotion of Dogs (*Canis familiaris*) and Sheep (*Ovis aries*). *J. Zoolog.* 185, 289–308. doi:10.1111/j.1469-7998.1978.tb03334.x

Kram, R., and Taylor, C. R. (1990). Energetics of Running: A New Perspective. *Nature* 346, 265–267. doi:10.1038/346265a0

Kuo, A. D., and Donelan, J. M. (2010). Dynamic Principles of Gait and Their Clinical Implications. *Phys. Ther.* 90, 157–174. doi:10.2522/ptj.20090125

Kuo, A. D. (2007). The Six Determinants of Gait and the Inverted Pendulum Analogy: A Dynamic Walking Perspective. *Hum. Move. Sci.* 26, 617–656. doi:10.1016/j.humov.2007.04.003

Kushmerick, M. J., and Paul, R. J. (1977). Chemical Energetics in Repeated Contractions of Frog Sartorius Muscle at 0° C. *J. Physiol.* 267, 249–260. doi:10.1113/jphysiol.1977.sp011811

Lee, D. V., Bertram, J. E. A., Anttonen, J. T., Ros, I. G., Harris, S. L., and Biewener, A. A. (2011). A Collisional Perspective on Quadrupedal Gait Dynamics. *J. R. Soc. Interf.* 8, 1480–1486. doi:10.1098/rsif.2011.0019

Lee, D. V., and Harris, S. L. (2018). Linking Gait Dynamics to Mechanical Cost of Legged Locomotion. *Front. Robot. AI* 5, 111. doi:10.3389/frobt.2018.00111

Lee, D. V., Isaacs, M. R., Higgins, T. E., Biewener, A. A., and McGowan, C. P. (2014). Scaling of the Spring in the Leg during Bouncing Gaits of Mammals. *Integr. Comp. Biol.* 54, 1099–1108. doi:10.1093/icb/icu114

Lee, D. V., McGuigan, M. P., Yoo, E. H., and Biewener, A. A. (2008). Compliance, Actuation, and Work Characteristics of the Goat Foreleg and Hindleg during Level, Uphill, and Downhill Running. *J. Appl. Physiol.* 104, 130–141. doi:10.1152/japplphysiol.01090.2006

Lee, D. V., Todhunter, R. J., Foels, W. S., Jo Williams, A., Lust, G., and Bertram, J. E. A. (1997). Multiple Force Platform Analysis of the Canine Trot: A New Approach to Assessing Basic Characteristics of Locomotion. *Vet. Comp. Orthop. Traumatol.* 10, 160–169. doi:10.1055/s-0038-1632588

Loscher, D. M. (2015). *Kinematische Anpassungen zur Kollisionsreduktion im Schritt vierfüßiger Lauftiere*. Berlin, Germany: Dr. rer. Nat., Freie Universität Berlin.

Manchester, Z., and Kuindersma, S. (2017). "Variational Contact-Implicit Trajectory Optimization," in *International Symposium on Robotics Research (ISRR)* (Puerto Varas, Chile: ISRR).

Ogihara, N., Makishima, H., Hirasaki, E., and Nakatsukasa, M. (2012). Inefficient Use of Inverted Pendulum Mechanism during Quadrupedal Walking in the Japanese Macaque. *Primates* 53, 41–48. doi:10.1007/s10329-011-0265-3

Patterson, M. A., Hager, W. W., and Rao, A. V. (2015). A *ph* mesh Refinement Method for Optimal Control. *Optim. Control. Appl. Meth.* 36, 398–421. doi:10.1002/oca.2114

Patterson, M. A., and Rao, A. V. (2014). GPOPS-II. *ACM Trans. Math. Softw.* 41, 1–37. doi:10.1145/2558904

Polet, D. T., and Bertram, J. E. A. (2019). An Inelastic Quadrupedal Model Discovers Four-Beat Walking, Two-Beat Running, and Pseudo-elastic Actuation as Energetically Optimal. *PLOS Comput. Biol.* 15, e1007444. doi:10.1371/journal.pcbi.1007444

Polet, D. T. (2021). The Murphy Number: How Pitch Moment of Inertia Dictates Quadrupedal Walking and Running Energetics. *J. Exp. Biol.* 224, jeb228296. doi:10.1242/jeb.228296

Pontzer, H., Raichlen, D. A., and Rodman, P. S. (2014). Bipedal and Quadrupedal Locomotion in Chimpanzees. *J. Hum. Evol.* 66, 64–82. doi:10.1016/j.jhevol.2013.10.002

Reilly, S. M., McElroy, E. J., and Biknevicius, A. R. (2007). Posture, Gait and the Ecological Relevance of Locomotor Costs and Energy-Saving Mechanisms in Tetrapods. *Zoology* 110, 271–289. doi:10.1016/j.zool.2007.01.003

Ren, L., and Hutchinson, J. R. (2008). The Three-Dimensional Locomotor Dynamics of African (*Loxodonta africana*) and Asian (*Elephas maximus*) Elephants Reveal a Smooth Gait Transition at Moderate Speed. *J. R. Soc. Interf.* 5, 195–211. doi:10.1098/rsif.2007.1095

Riddick, R. C., and Kuo, A. D. (2020). Mechanical Work Accounts for Most of the Energetic Cost in Human Running. *bioRxiv* 2020, 2020. doi:10.1101/2020.09.22.309161

Rohatgi, A. (2019). *WebPlotDigitizer*. Available at: https://automeris.io/WebPlotDigitizer.

Ruina, A., and Bertram, J. E. A. (2003). "Problems with Some Historical Locomotion Energy Accounting," in Proceedings of the 27th Meeting of the American Society of Biomechanics, Toledo, OH.

Ruina, A., Bertram, J. E. A., and Srinivasan, M. (2005). A Collisional Model of the Energetic Cost of Support Work Qualitatively Explains Leg Sequencing in Walking and Galloping, Pseudo-elastic Leg Behavior in Running and the Walk-To-Run Transition. *J. Theor. Biol.* 237, 170–192. doi:10.1016/j.jtbi.2005.04.004

Sasaki, K., Neptune, R. R., and Kautz, S. A. (2009). The Relationships between Muscle, External, Internal and Joint Mechanical Work during normal Walking. *J. Exp. Biol.* 212, 738–744. doi:10.1242/jeb.023267

Schmidt, M. (2005). Quadrupedal Locomotion in Squirrel Monkeys (Cebidae: *Saimiri sciureus*): A Cineradiographic Study of Limb Kinematics and Related Substrate Reaction Forces. *Am. J. Phys. Anthropol.* 128, 359–370. doi:10.1002/ajpa.20089

Schmitt, D., and Lemelin, P. (2002). Origins of Primate Locomotion: Gait Mechanics of the Woolly Opossum. *Am. J. Phys. Anthropol.* 118, 231–238. doi:10.1002/ajpa.10048

Schroeder, R. T., Croft, J. L., and Bertram, J. E. A. (2021). Evaluating the Energetics of Entrainment in a Human-Machine Coupled Oscillator System. *Sci. Rep.* 11, 15804. doi:10.1038/s41598-021-95047-x

Shapiro, L. J., and Young, J. W. (2010). Is Primate-like Quadrupedalism Necessary for fine-branch Locomotion? A Test Using Sugar Gliders (*Petaurus breviceps*). *J. Hum. Evol.* 58, 309–319. doi:10.1016/j.jhevol.2009.12.002

Shimada, H., Kanai, R., Kondo, T., Yoshino-Saito, K., Uchida, A., Nakamura, M., et al. (2017). Three-dimensional Kinematic and Kinetic Analysis of Quadrupedal Walking in the Common Marmoset (*Callithrix jacchus*). *Neurosci. Res.* 125, 11–20. doi:10.1016/j.neures.2017.06.005

Simpson, C. S., Welker, C. G., Uhlrich, S. D., Sketch, S. M., Jackson, R. W., Delp, S. L., et al. (2019). Connecting the Legs with a spring Improves Human Running Economy. *J. Exp. Biol.* 222, jeb202895. doi:10.1242/jeb.202895

Tucker, V. A. (1975). The Energetic Cost of Moving about. *Am. Sci.* 63, 413–419.

Usherwood, J. R. (2022). Legs as Linkages: An Alternative Paradigm for the Role of Tendons and Isometric Muscles in Facilitating Economical Gait. *J. Exp. Biol.* 225, jeb243254. doi:10.1242/jeb.243254

Usherwood, J. R. (2020a). An Extension to the Collisional Model of the Energetic Cost of Support Qualitatively Explains Trotting and the Trot-Canter Transition. *J. Exp. Zool.* 333, 9–19. doi:10.1002/jez.2268

Usherwood, J. R., and Self Davies, Z. T. (2017). Work Minimization Accounts for Footfall Phasing in Slow Quadrupedal Gaits. *eLife* 6, 630–650. doi:10.7554/eLife.29495

Usherwood, J. R., Szymanek, K. L., and Daley, M. A. (2008). Compass Gait Mechanics Account for Top Walking Speeds in Ducks and Humans. *J. Exp. Biol.* 211, 3744–3749. doi:10.1242/jeb.023416

Usherwood, J. R. (2020b). The Possibility of Zero Limb-Work Gaits in Sprawled and Parasagittal Quadrupeds: Insights from Linkages of the Industrial Revolution. *Integr. Org. Biol.* 2, obaa017. doi:10.1093/iob/obaa017

Usherwood, J. R., Williams, S. B., and Wilson, A. M. (2007). Mechanics of Dog Walking Compared with a Passive, Stiff-Limbed, 4-bar Linkage Model, and Their Collisional Implications. *J. Exp. Biol.* 210, 533–540. doi:10.1242/jeb.02647

van der Zee, T. J., and Kuo, A. D. (2021). The High Energetic Cost of Rapid Force Development in Muscle. *J. Exp. Biol.* 224, jeb233965. doi:10.1242/jeb.233965

van der Zee, T. J., Lemaire, K. K., and van Soest, A. J. (2019). The Metabolic Cost of *In Vivo* Constant Muscle Force Production at Zero Net Mechanical Work. *J. Exp. Biol.* 222, jeb199158. doi:10.1242/jeb.199158

Webb, A. A., Kerr, B., Neville, T., Ngan, S., and Assem, H. (2011). Kinematics and Ground Reaction Force Determination: A Demonstration Quantifying Locomotor Abilities of Young Adult, Middle-Aged, and Geriatric Rats. *JoVE* 2011, 2138. doi:10.3791/2138

Weihmann, T. (2020). Survey of Biomechanical Aspects of Arthropod Terrestrialisation - Substrate Bound Legged Locomotion. *Arthropod Struct. Develop.* 59, 100983. doi:10.1016/j.asd.2020.100983

Wong, J. D., Selinger, J. C., and Donelan, J. M. (2019). Is Natural Variability in Gait Sufficient to Initiate Spontaneous Energy Optimization in Human Walking? *J. Neurophysiol.* 121, 1848–1855. doi:10.1152/jn.00417.2018

Zani, P. A., Gottschall, J. S., and Kram, R. (2005). Giant Galaápagos Tortoises Walk without Inverted Pendulum Mechanical-Energy Exchange. *J. Exp. Biol.* 208, 1489–1494. doi:10.1242/jeb.01554

Zelik, K. E., and Kuo, A. D. (2010). Human Walking Isn't All Hard Work: Evidence of Soft Tissue Contributions to Energy Dissipation and Return. *J. Exp. Biol.* 213, 4257–4264. doi:10.1242/jeb.044297

Conflict of Interest: The authors declare that the research was conducted in the absence of any commercial or financial relationships that could be construed as a potential conflict of interest.

Publisher's Note: All claims expressed in this article are solely those of the authors and do not necessarily represent those of their affiliated organizations, or those of the publisher, the editors and the reviewers. Any product that may be evaluated in this article, or claim that may be made by its manufacturer, is not guaranteed or endorsed by the publisher.

frontiers | Frontiers in Bioengineering and Biotechnology

ORIGINAL RESEARCH
published: 25 May 2022
doi: 10.3389/fbioe.2022.806314

Computational Modeling of Gluteus Medius Muscle Moment Arm in Caviomorph Rodents Reveals Ecomorphological Specializations

Lukas Löffler†, *Jan Wölfer*†, *Flavia Gavrilei and John A. Nyakatura* **

AG Vergleichende Zoologie, Institut für Biologie, Humboldt-Universität zu Berlin, Berlin, Germany

OPEN ACCESS

Edited by:
John R Hutchinson, Royal Veterinary College (RVC), United Kingdom

Reviewed by:
Robert Brocklehurst, Harvard University, United States
Marguerite A Butler, University of Hawaii at Manoa, United States

***Correspondence:**
John A. Nyakatura
john.nyakatura@hu-berlin.de

†*These authors have contributed equally to this work.*

Specialty section:
This article was submitted to Biomechanics, a section of the journal Frontiers in Bioengineering and Biotechnology

Received: *31 October 2021*
Accepted: *29 March 2022*
Published: *25 May 2022*

Citation:
Löffler L, Wölfer J, Gavrilei F and Nyakatura JA (2022) Computational Modeling of Gluteus Medius Muscle Moment Arm in Caviomorph Rodents Reveals Ecomorphological Specializations. Front. Bioeng. Biotechnol. 10:806314. doi: 10.3389/fbioe.2022.806314

Vertebrate musculoskeletal locomotion is realized through lever-arm systems. The instantaneous muscle moment arm (IMMA), which is expected to be under selective pressure and thus of interest for ecomorphological studies, is a key aspect of these systems. The IMMA changes with joint motion. It's length change is technically difficult to acquire and has not been compared in a larger phylogenetic ecomorphological framework, yet. Usually, proxies such as osteological in-levers are used instead. We used 18 species of the ecologically diverse clade of caviomorph rodents to test whether its diversity is reflected in the IMMA of the hip extensor M. gluteus medius. A large IMMA is beneficial for torque generation; a small IMMA facilitates fast joint excursion. We expected large IMMAs in scansorial species, small IMMAs in fossorial species, and somewhat intermediate IMMAs in cursorial species, depending on the relative importance of acceleration and joint angular velocity. We modeled the IMMA over the entire range of possible hip extensions and applied macroevolutionary model comparison to selected joint poses. We also obtained the osteological in-lever of the M. gluteus medius to compare it to the IMMA. At little hip extension, the IMMA was largest on average in scansorial species, while the other two lifestyles were similar. We interpret this as an emphasized need for increased hip joint torque when climbing on inclines, especially in a crouched posture. Cursorial species might benefit from fast joint excursion, but their similarity with the fossorial species is difficult to interpret and could hint at ecological similarities. At larger extension angles, cursorial species displayed the second-largest IMMAs after scansorial species. The larger IMMA optimum results in powerful hip extension which coincides with forward acceleration at late stance beneficial for climbing, jumping, and escaping predators. This might be less relevant for a fossorial lifestyle. The results of the in-lever only matched the IMMA results of larger hip extension angles, suggesting that the modeling of the IMMA provides more nuanced insights into adaptations of musculoskeletal lever-arm systems than this osteological proxy.

Keywords: moment arms, locomotion, modeling, hind limb, Caviomorpha, hip joint

1 INTRODUCTION

The torque a muscle generates, for example, during vertebrate locomotion, is defined as the product of the muscle force acting along the muscle's line of action (MLoA) and the length of the muscle moment arm (Pedotti et al., 1978; Murray et al., 2002; Pandy and Andriacchi, 2010). This moment arm is the perpendicular and, thus, the shortest distance from the considered MLoA to the joint's center of rotation (CoR) of the joint the muscle is acting on (**Figure 1**). Muscle moment arms have been recognized to instantaneously change in accordance with joint movements due to the associated changes of the MLoA relative to the CoR (e.g., Lieber and Shoemaker, 1992, 1997). Hence, the functioning of this instantaneous muscle moment arm (IMMA) can only be understood by determining its length throughout relevant joint poses. For example, this can be achieved with the help of computational musculoskeletal modeling of scanned bone models (Charles et al., 2016; Regnault et al., 2021). However, its technical sophistication and the multivariate nature resulting from the IMMAs' dependency on complex 3D joint poses over time complicate the analysis of IMMAs in more inclusive, phylogenetically

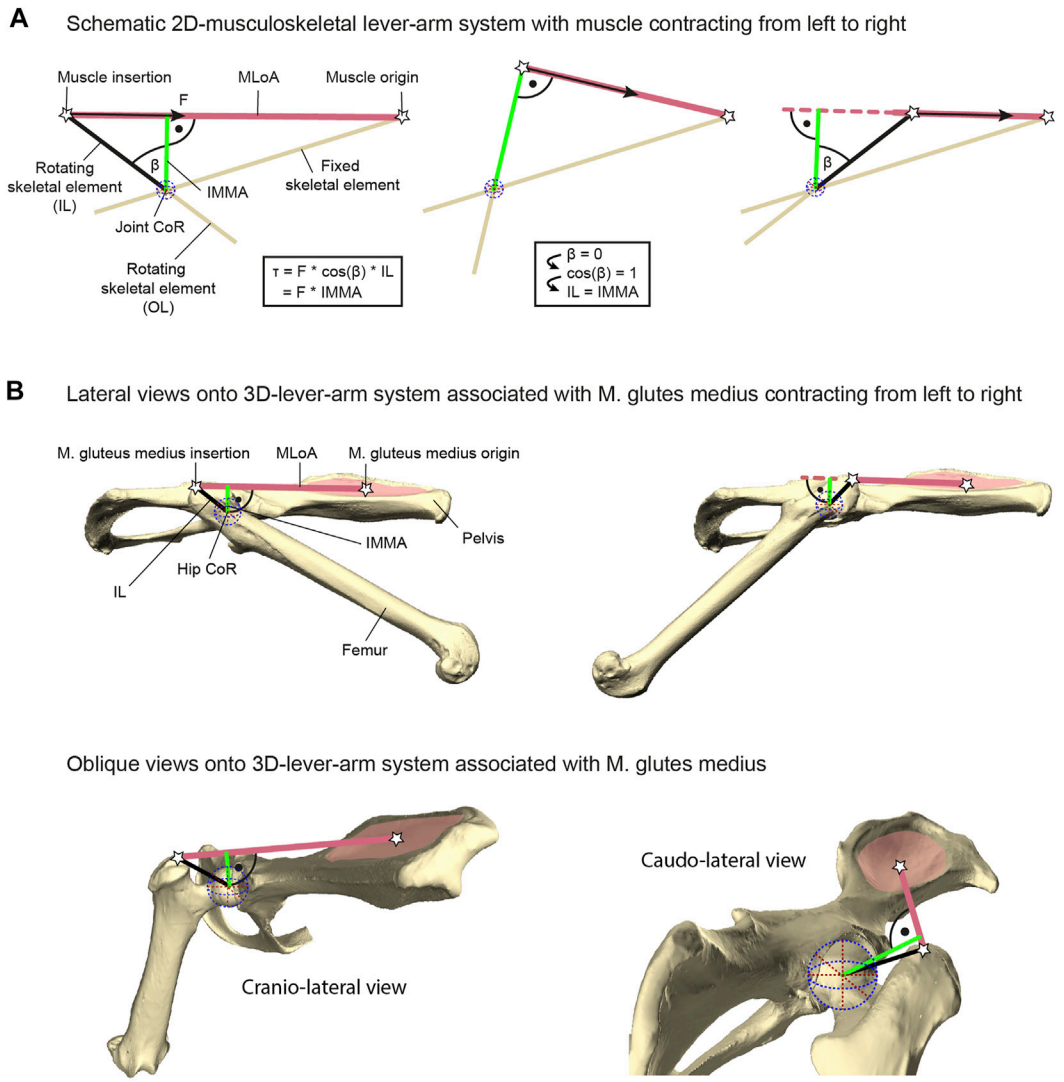

FIGURE 1 | Explanation of lever-arm system components exemplified with the herein studied M. gluteus medius system. **(A)** Geometric properties of a schematic musculoskeletal lever-arm system as typically illustrated in a 2D plane, including the instantaneous muscle moment arm (IMMA), osteological in-lever (IL), osteological out-lever (OL), center of rotation (CoR), and the muscle's line of action (MLoA). The skeletal element that includes the IL is modeled as being rotated due to muscle contraction with respect to a reference element fixed in space (left to right). The equation on the left shows different ways of computing the joint torque (τ) generated by the muscle's force (F) and applies to all poses throughout joint motion. **(B)** 3D-lever-arm system associated with the M. gluteus medius exemplified using the surface models of the right femur and right half of the pelvis from the scans of *C. pilorides* (Desmarest's hutia). Upper panels display lateral views onto the 3D model setup with a hip extended by 30° (left) and 140° (right) at 0° abduction (compare with left and right panels of **(A)**, respectively). Lower panels display oblique views onto the model setup with a hip extension of 120° at 0° abduction to highlight the actual 3D nature of the lever-arm system associated with the M. gluteus medius. For further explanation, see text.

broader datasets. Perhaps this is one reason why computational modeling has usually been used for in-depth analyses of the limb biomechanics of only one or just a few species (e.g., Hutchinson et al., 2005; Bates et al., 2012; Regnault and Pierce, 2018). Allen et al. (2021) were recently the first to analyze the IMMA in an explicitly phylogenetic comparative setting to allow evolutionary inferences about how changes in muscle topography (i.e., the attachment sites of the muscles on the bones) affect the IMMA of the pelvic muscles in 13 bird-line archosaur species. These authors ultimately averaged the IMMA values in their comparative analysis, hence not taking into consideration how the IMMA's length varied with changes in a joint pose (Allen et al., 2021).

In contrast to the challenging determination of IMMAs, osteological muscle in-levers are typically used to provide information on musculoskeletal function in comparative analyses of ecomorphological specialization (see, e.g., Ward and Sussman 1979; Boyer et al., 2013). Osteological in-levers are defined as the distance between the attachment site of a muscle and the CoR of the joint the muscle is acting on (Hildebrand and Goslow, 1995). From a pragmatic standpoint, osteological in-levers can readily be analyzed using dry skeletal collection material and/or well-preserved fossil specimens not only in 2D (e.g., Vizcaino and Milne, 2002; Marshall et al., 2021) but also in 3D (e.g., Mielke et al., 2018; Wölfer et al., 2019), and without further knowledge of joint movements. The IMMA and the osteological in-lever are geometrically related. A larger osteological in-lever increases the distance between the MLoA and the CoR and hence will ultimately lead to an increase in all IMMAs. Thus, as is the case for the IMMAs, increasing in-lever length while keeping everything else constant results in a larger torque (Zajac, 1992; Payne et al., 2006; Moore et al., 2013; Marshall et al., 2021). Importantly, a longer muscle moment arm will also result in a decline in angular velocity at the joint given a constant contraction speed (Hutchinson et al., 2005; Channon et al., 2010). The osteological in-lever and the IMMA are exactly the same in a single joint pose, precisely when the in-lever is at a 90° angle to the MLoA (**Figure 1A**). Consequently, the in-lever also represents the largest possible IMMA. For all other poses, the IMMA is a penalized value of the in-lever length, that is, the in-lever length multiplied by the cosine of the angle between itself and the IMMA (a factor x with $0 \leq x < 1$; see equation in **Figure 1A**). This demonstrates that the in-lever alone misses important geometric information for the assessment of potential muscle torque. Its reliability to approximate the IMMA will depend on the functionally relevant joint range of motion in the taxa of interest.

Given the crucial role in musculoskeletal function, IMMAs can be expected to be under selective pressure and to reflect ecomorphological specialization (cf. Allen et al., 2021). In this study, we therefore aim at obtaining insight into how IMMA length changes reflect different functional demands specific to different locomotor lifestyles using a broad ecomorphological sample. Second, we will assess whether our methodologically more sophisticated IMMA analysis provides additional functional information that would be left unrecognized by utilizing a single, easily accessible, yet simplifying osteological proxy. In order to do so, we use musculoskeletal modeling of the lever-arm system associated with the M. gluteus medius and the broadest phylogenetic sample for IMMA analysis thus far, focusing on the Caviomorpha (Mammalia: Rodentia). The M. gluteus medius, a hip extensor muscle, has been demonstrated to be a main contributor to hip extension and partly to hip abduction during locomotion (e.g., Goslow et al., 1981; Larson and Stern, 2009). Also, the muscle shows clearly recognizable attachment sites on the pelvis and femur necessary to model the MLoA.

We chose the monophyletic and taxonomically diverse Caviomorpha (Fabre et al., 2012) because they exhibit a remarkable morphological disparity which was previously linked to the vast diversity of lifestyles and, specifically, locomotor behaviors (e.g., Elissamburu and Vizcaíno, 2004; Morgan, 2009; Morgan and Álvarez, 2013; Candela et al., 2017). Caviomorphs underwent radiation after the arrival of their most recent common ancestor in South America, which was isolated back then, starting more than 41 million years ago (mya) according to available fossil data (Pierre-Olivier et al., 2011). Today, the group is also distributed across the Caribbean islands and Central and North America (Wilson and Mittermeier, 2011). Four major lineages (Cavioidea, Erethizontoidae, Chinchilloidea, and Octodontoidea) are recognized, comprising about 250 extant species (Wilson and Mittermeier, 2011). Their ecological diversity encompasses subterranean/fossorial (e.g., tuco-tucos of the genus *Ctenomys*), semi-fossorial (e.g., the plains vizcacha *Lagostomus maximus*), semi-aquatic (e.g., nutrias of the genus *Myocastor* and capybaras of the genus *Hydrochoerus*), terrestrial (e.g., guinea pigs of the genus *Cavia*), cursorial (e.g., maras of the genus *Dolichotis*), ricochetal (*Chinchilla*), and scansorial/arboreal lifestyles (e.g., new world porcupines of the family Erethizontidae and hutias of the subfamily Capromyinae) (Nowak 1999; Wilson and Mittermeier, 2011). Caviomorpha also display a noticeable disparity in body size, with the smallest members of Octodontoidea being ~50 g and the capybara weighing up to ~50 kg (Wilson and Mittermeier, 2011).

We will use 18 caviomorph species representing the phylogenetic diversity of lineages within the Caviomorpha and categorize them into three locomotor categories: scansorial, cursorial, and fossorial (**Figure 2**). The former two categories can be considered to include all "overground species," and the latter two categories comprise all "terrestrial species." Generally, independent of lifestyle, we expect the maximum IMMA in the last third of possible extension, when maximum force is needed for powerful hip extension prior to lift-off for leaps or during the late stance in rapidly accelerating locomotor bursts (e.g., Aerts, 1998). We expect cursorial and scansorial (i.e., overground) species to emphasize powerful extension over the fossorial species because it is expected to be equally crucial for high-speed terrestrial locomotion, leaping, and climbing up an incline. However, cursorial and scansorial lifestyles should be reflected differently in terms of the M. gluteus medius IMMA; scansorial species can be expected to exhibit the largest IMMAs of our sample over a large portion of hip extension, as, for these species, maximum torque during climbing should be more important than fast joint excursions (which would be compromised by

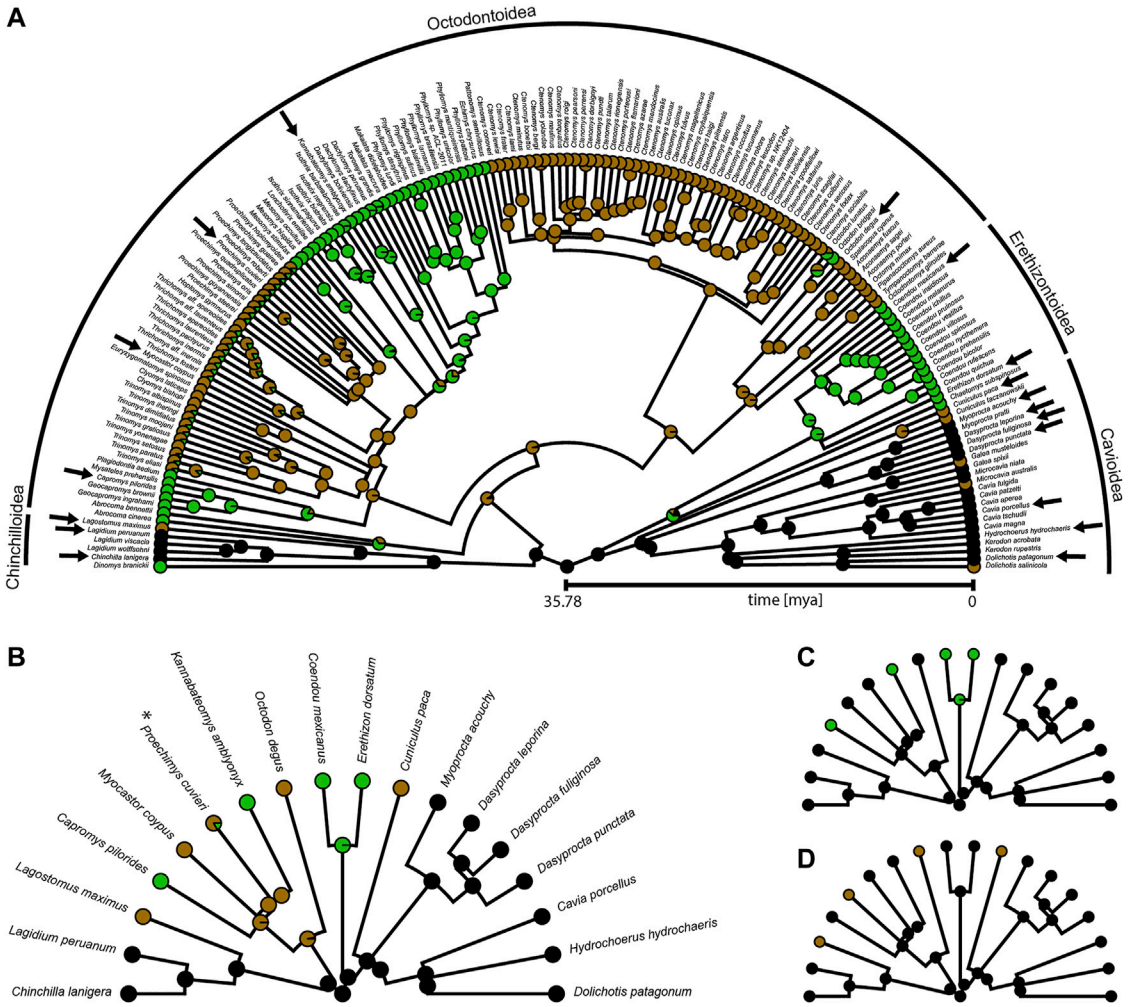

FIGURE 2 | Phylogeny of Caviomorpha with reconstructed lifestyles. Pie charts at tips and nodes indicate posterior probabilities of lifestyles. **(A)** Original phylogeny containing all available species from Hedges et al. (2015). Cursorial category in black, fossorial category in brown, and scansorial category in green. Arrows indicate species included in our dataset. **(B)** Phylogeny and mapping from **(A)** after pruning to match our dataset for fitting an Ornstein-Uhlenbeck (OU) model with three optima (see text). Color coding as in **(A)**. Asterisk indicates the species that was used instead of *P. mincae* (see text). **(C)** Pruned phylogeny and mapping for fitting an OU model with two optima. Terrestrial category in black and scansorial category in green. The original mapping with all species before pruning is provided in **Supplementary Figure S1A**. **(D)** Pruned phylogeny and mapping for fitting an OU model with two optima. Overground category in black and fossorial category in brown. The original mapping with all species before pruning is provided in **Supplementary Figure S1B**.

overly large IMMAs, see Allen et al., 2021). Cursorial species, on the other hand, might display some sort of compromise between large torque generation for fast acceleration and angular velocity for fast hip extension at maximum running speed. Fossorial caviomorphs dig with their forelimbs as most digging mammals (Hildebrand and Goslow, 1995; Nowak, 1999; Wilson and Mittermeier, 2011), but the role of the hind limbs is usually uncertain or not described. Caviomorphs of the genus *Ctenomys* also use their teeth to break up hard soil (Wilson and Mittermeier, 2011), but they were not considered in this study. Given this information, we do not expect to find adaptations of the IMMA for powerful hip extension in these species. As the studied fossorial species are not completely subterranean but search for food overground and must be able to quickly flee from predators, they might also share similarities in the IMMA length changes with the cursorial species. This might justify the hypothesis that they, together as a "terrestrial" category, are distinguishable from the scansorial species.

Our comparative functional modeling approach uses 3D bone models of the pelvis and the femur of each specimen to derive the IMMA from a simple musculoskeletal model while exploring the entire range of hip extension (i.e., femur retraction relative to the pelvis within the parasagittal plane) for three femoral abduction angles (**Figure 3**). Considering the IMMA over the entire range of motion throughout anatomically possible hip extension will allow a more nuanced evaluation of the functional implications for each

locomotor category. In addition to locomotor lifestyle comparisons throughout hip extension *via* exploratory statistics, we will also apply macroevolutionary model comparison *via* likelihood evaluation (Butler and King, 2004) to selected joint poses. For this purpose, we will make use of the largest accessible caviomorph phylogeny to reliably reconstruct caviomorph lifestyle evolution. To compare the IMMA results with those of a simple proxy, the distal osteological in-lever of the M. gluteus medius relative to the hip joint will be measured as well for all species and similarly compared among locomotor categories.

2 MATERIALS AND METHODS

2.1 Specimen Sampling

Femora and pelves were collected from a single specimen of 18 species in total housed in the collections of Naturhistorisches Museum Vienna (NMW), Austria, and Museum für Naturkunde Berlin (MfN), Germany (**Supplementary Table S1**). The bones were scanned with a surface laser scanner *via* the software "Scantools" (Kreon "Skiron" laser scanner for MicroScribe, Solution Technologies, Inc., Oella, United States) or, if too small for surface laser scanning, using a µCT scanner (Phoenix Nanotom M, General Electric, Boston, United States) with the software VGSTUDIO MAX (Volume Graphics, Heidelberg, Germany). Minor defects of the meshed surface models were repaired using the software MeshLab version 1.3.3 (Cignoni et al., 2008) and Geomagic Wrap 2017 (3D Systems, Rock Hill, United States).

2.2 Functional Modeling Approach of IMMAs

The functional modeling approach was conducted using Autodesk Maya 2019 (Autodesk, San Rafael, United States). Surface models of a specimen's femur and pelvis were imported, and the same reference pose was created for each specimen in a separate scene by aligning its pelvis to the coordinate system of Autodesk Maya (**Figure 3**). The symphyseal surface (facies symphysialis) was used for the cranio-caudal orientation of the pelvis (Popesko et al., 1992). For all the specimens of which only one of the hip bones were scanned, a realistic degree of tilt had to be estimated. This was carried out by inclining the pubic bone's inner surface to form a smooth parabolic transition (pictured from a cranial perspective) to the imagined contralateral pubic bone to which it is connected *via* the symphysis. However, scans originating from NMW collections mostly included at least the contralateral pubic bone and parts of the ischium, which made this estimation obsolete. The configuration in which the long-axis of the protracted femur and the cranio-caudal orientation of the pelvis were aligned in Autodesk Maya's side view was defined as the extension angle of 0° (**Figure 3**). Similarly, the abduction angle of 0° was defined by the configuration when the long-axis of the protracted femur and the cranio-caudal orientation of the pelvis's pubic symphysis were parallel in Autodesk Maya's top view. Both abduction and extension angles being 0° were determined as the reference pose.

To model hip extension and to allow comparison of standardized IMMA measurements across all 18 species, the measurement series was conducted in three different setups of hip abduction for each model (**Figure 3**): 0° abduction (i.e., true parasagittal limb movement), 30° abduction, and 60° abduction. Starting from an extension angle of 0°, the extension was then modeled in 10° increments up to 180°. This resulted in $19 \times 3 = 57$ poses per specimen in which the IMMA was measured.

The IMMA in each pose was measured in the following way. A "locator" was positioned each at the muscle origin and the muscle insertion of the M. gluteus medius. A recognizable landmark of both attachment sites was chosen for each "locator" position to facilitate easy and replicable placements in all specimens. For the muscle origin, a landmark was defined at the center of the attachment of the M. gluteus medius' deep part (**Figure 1**). The position of this attachment site can vary quite distinctly as, for example, it was shown to be the case in squirrels (Sokolov, 1964). Comparable publications providing muscle maps for various caviomorph rodents (especially those studied here) were not available to our knowledge, but a map for *Hydrochoerus hydrochaeris* was published by Garcia-Esponda and Candela (2010). Based on their drawings, we approximated the center of the M. gluteus medius origin within the center of the dorsal fossa of the outer wing of the ilium (**Figure 1**). For the muscle insertion, the trochanter major's most proximal point was chosen. The functions of Autodesk Maya were used to visualize the line of action of the muscle connecting both "locators." To simplify the models in this comparative study, it was decided to use a straight line of action crossing insertion and origin "locators" since the exact positioning of other surrounding muscles was mostly unknown in all 18 caviomorph species. Therefore, information for the implementation of "*via* points" and "wrapping surfaces" to guide more realistic muscle lines of action (Hutchinson et al., 2005) could not be provided. A sphere was fitted into the caput femoris and a new "locator" point-constrained into its center, now marking the CoR. Then, this "locator" position was set as a reference point to Maya's "nearest point on curve" function using the node editor. Another "locator" was set as the function's output, thereby visualizing the result as the projected point on the line of action. The projection could either fall on the MLoA or outside (extending the straight MLoA further beyond the "locators" marking the muscle attachment sites), depending on the degree of extension (**Figures 1**, **3**). To finally obtain IMMA lengths, the distance between the CoR and the projected point on the line was measured using the "distance between" function.

Measurements in Maya units had to be converted to the metric system. To accomplish this, the femoral length and width of the condyle of the eight femora from the MfN collections in Berlin were measured using a ruler in centimeters and divided by the corresponding digital measurement of the length of the 3D bone model in Autodesk Maya (Maya units). Afterward, all 16 ratios (**Supplementary Table S1**) were averaged and all measurements in Maya were multiplied by this mean value (1.017). All length

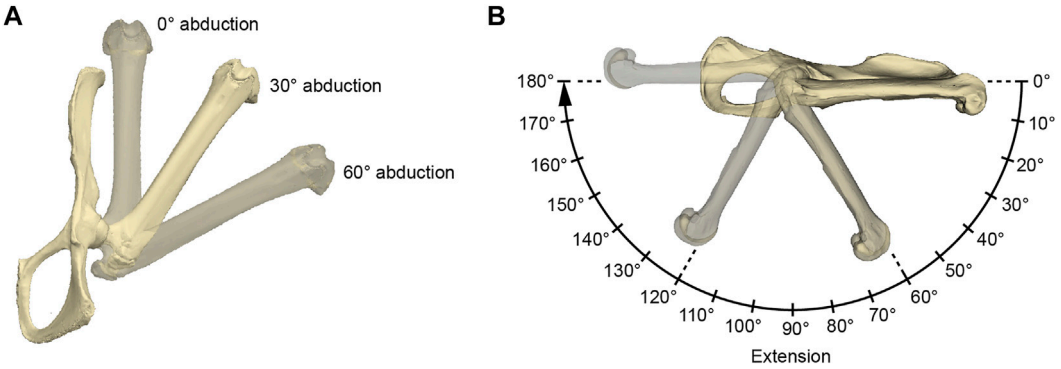

FIGURE 3 | Illustration of the acquired hip joint angles. **(A)** Three abduction angles were used for each measurement series of extension angles **(B)**. The here depicted extension angle is 0°. **(B)** Procedure of a single measurement series. The 0° rotational angle in the 0° abduction setting as in **(A)** was used as the reference pose. The IMMAs were measured every 10° resulting in 19 values per abduction setting and 54 values per specimen in total. For further explanation, see text.

measurements in centimeters are provided in **Supplementary Table S2**.

2.3 Body Mass Proxy

We aimed at accounting for body mass in the subsequent analyses as it is a typical confounding factor compared to locomotor ecology. The body masses of the analyzed specimens were not available. Since Wölfer et al. (2019) showed that the anteroposterior diameter of the femoral midshaft (called just femoral diameter in the following) is strongly correlated to body mass and bears almost no lifestyle signal in the related rodent taxon Sciuromorpha, we used it here to approximate the effect of body mass. The femoral diameter was measured three times on each surface scan using Geomagic Wrap 2017 (3D Systems, Rock Hill, South Carolina, United States) and then averaged (**Supplementary Table S3**).

2.4 Graphical Comparison of Extension Poses Among Lifestyles

We used R version 4.1.2 (R Core Team, 2021) for this and all subsequent analyses. The packages "readxl" (Wickham and Bryan, 2019), "tidyverse" (Wickham et al., 2019), and "ggpubr" (Kassambara, 2020) were used for data preparation and visualization. For each of the three abduction angles, the mean and the standard error of the IMMA of each lifestyle category were plotted for all 19 extension angles for graphical comparison. To account for the effect of body mass on the IMMA, we divided all values of a species by its femoral diameter which we call the normalized IMMA in the following. The measurement series at 30° abduction was believed to be the most realistic representation of the actual utilized joint range due to limited bone collisions and similar values of hip abduction found in *in vivo* studies of small- to medium-sized mammals (Jenkins, 1971). Therefore, this abduction setting was focused on the subsequent macroevolutionary model comparison analysis.

2.5 Macroevolutionary Modeling Approach

Based on the graphical comparison of the lifestyles' mean normalized IMMAs, we compared different macroevolutionary models *sensu* Butler and King (2004) for the IMMA of three different extension angles approximately referring to the early stance, mid-stance, and late stance of a limb contact during cyclic locomotion: 40°, 80°, and 120° (Fischer et al., 2002). We considered the Brownian motion (BM) model (Felsenstein, 1985; Grafen, 1989) and the Ornstein–Uhlenbeck (OU) model (Hansen, 1997) as plausible macroevolutionary models for IMMA evolution. We interpreted the BM model with its constant stochastic rate of change as a non-adaptive null model of phenotypic drift. The OU model was used to represent adaptive evolution in which selection acts on the trait. The strength of selection is determined by the adaptive rate α and the distance of the trait from a hypothetical primary (interspecific) optimum θ specific to a particular selective regime (lifestyle category in our case). In addition to selection, random perturbations on the trait are modeled with a rate σ, representing the joint effect of not only all non-adaptive factors but also adaptive factors with minor influence compared to the selective regime (Hansen, 1997). The expected trait value is a weighted sum of the ancestral state and the past optima a species evolved toward (Hansen, 1997). Kopperud et al. (2020) added the option to include a direct effect on the trait in the R package "slouch." We used this option to include the femoral diameter of a species to model it as exerting an instantaneous effect on the mean IMMA of the species. The α and σ values were transformed into the phylogenetic half-life (the time it takes for a species on average to evolve halfway to the optimum) and stationary variance (interspecific variance that remains constant after a certain time depending on the relative strength of α and σ) (Hansen, 1997).

We here defined three OU models that we considered plausible from a morphofunctional standpoint. The first model contained three optima (OU3), one for each lifestyle category. Two further models with two optima (OU2) each were further

defined. The first OU2 model assumed a shared optimum between cursorial and fossorial species (called the terrestrial category; $OU2_{terr}$). The second OU2 model assumed a shared optimum between cursorial and scansorial species (called the overground category; $OU2_{over}$).

For each of the three OU models, we proceeded as follows. The lifestyle categories were reconstructed for macroevolutionary modeling using stochastic character mapping (Huelsenbeck et al., 2003) and the R packages "geiger" (Pennell et al., 2014) and "phytools" (Revell, 2012). We took the phylogeny from Hedges et al. (2015) which was pruned to an ultrametric tree of 169 caviomorph species (**Figure 2**). Lifestyle information was obtained from species descriptions in Wilson and Mittermeier (2011) and Nowak (1999) (**Supplementary Table S4**). Using the OU3 model as a guideline, we characterized each species by the lifestyle that was described as most dominant, choosing among the three categories: cursorial (specialized in running and foraging overground), fossorial (digging burrows and foraging overground), and scansorial (climbing trees and bushes, but perhaps also traveling on the ground). For many species or genera, lifestyle information was either not available, ambiguous, or a mixture of our categories. Hence, to include uncertainty for those tips, we decided to define the prior probability of each of the three lifestyle categories on the basis of the lifestyles of the closest relatives (**Supplementary Table S4**). In the case of the OU2 models, the prior probabilities of the two lifestyles now collapsed into a single lifestyle were simply added up. All transition rates among lifestyle categories were assumed to be different, and 1000 character maps were generated using the "make.simmap" function of the package "phytools" (**Figure 2**; **Supplementary Figure S1**).

We then trimmed all 1000 phylogenies including their stochastic character maps using the "drop.tip.simmap" function of the package "phytools" to match the species of our dataset. For this purpose, we substituted the name of the sampled species *Proechimys mincae* with the name *P. cuvieri*, as the former was not represented in the phylogeny. This was justified by the fact that it constituted the only sampled species of this genus. We then used the likelihood distribution of lifestyle categories at each node to determine the most likely lifestyle at each node. The branches were then assigned the most likely lifestyle of the preceding node using the "slouch.fit" function of the package "slouch" as part of the model fitting process (**Supplementary Figure S2**).

For model fitting, the IMMA and the femoral diameter were natural-log-transformed. The "slouch.fit" function works interactively by manually defining a range of half-lives and stationary variances of which all combinations are assessed in terms of their likelihood. The maximum likelihood combination was used to compute all regression statistics, but the two-unit support regions (i.e., the minimum and maximum values that were recovered two log-likelihood below the maximum likelihood) of the half-life and the stationary variance were provided as well as the standard errors for the optima and slopes. The likelihood of the four models was compared using the Akaike information criterion corrected for small sample sizes (AICc) and Schwarz information criterion (SIC), which penalize the maximum likelihood according to model complexity (see Burnham and Anderson, 2002).

2.6 Analysis of Osteological In-Lever

The lengths of the osteological in-levers of the femur (**Supplementary Table S3**) were obtained using the "distance measurement tool" in Maya. The osteological in-lever was defined as the distance from the insertion of the M. gluteus medius to the CoR. The macroevolutionary modeling procedure explained earlier for the IMMAs of the three selected joint poses was also applied to the in-lever data to compare their results.

3 RESULTS

3.1 Convergent Evolution of Scansorial and Fossorial Lifestyles From a Cursorial Common Ancestor

The cursorial lifestyle was the most likely state at the root of the phylogeny (**Figure 2**). The fossorial lifestyle evolved six times independently, always from a cursorial ancestor within Caviomorpha. The scansorial lifestyle was most likely acquired five times independently, twice from a cursorial ancestor and three times from a fossorial ancestor.

3.2 Differences in IMMAs Among Lifestyles Depend on Extension Angle

The normalized IMMA measurements averaged per locomotor category show different sigmoidal curve progressions throughout extension while lifestyle differences themselves depend on the abduction angle (**Figure 4**). At 0° abduction, the curves start with a comparatively large normalized IMMA value and have a rather shallow slope until a plateau is reached at around 130° hip extension. At 30° and 60° abduction, the curves start with lower values, reaching a similar peak as during 0° abduction, but a bit earlier at an extension angle around 100–120°. In comparison to 0° abduction, the curves tend to fall off again in model setups of 30° and 60° abduction. This effect is larger at 60° than at 30° abduction. In the range of extension angles that are anatomically possible (as judged by bone collisions during modeling in Maya) among all species, scansorial species always show a larger mean normalized IMMA length than the other lifestyle categories. Cursorial species tend to be similar on average to the fossorial species at smaller extension angles but fall in between them and the scansorial species at larger extension angles, resulting in the slightly steeper slope of their mean IMMA curve progression (**Figure 4**). The scansorial species generally display the largest standard error, which might be due to their lowest sample size, but also due to their larger variability (**Supplementary Figure S3**).

The range of anatomically possible extension angles is widest at 30° abduction, slightly reduced at low extension angles of 0° abduction, and drastically narrowed down at 60° abduction (**Figure 4**). Notably, at 30° abduction, which we believed to be the most plausible joint range for caviomorph locomotion, we observed the specimen of the fossorial species *O. degus* to display

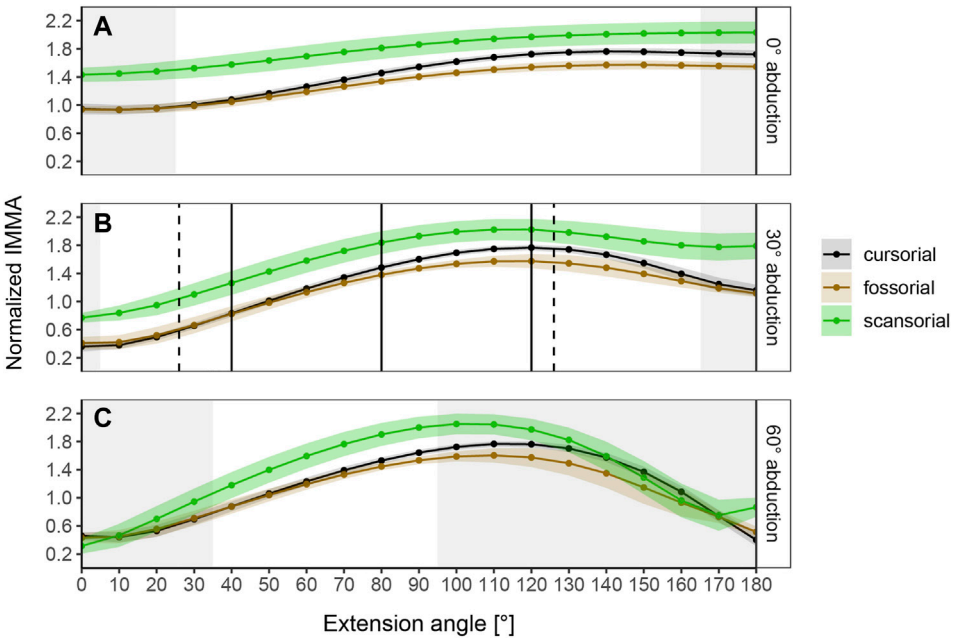

FIGURE 4 | Curve progressions of normalized IMMA lengths averaged (±S.E.) per lifestyle category. The normalized IMMA was obtained by dividing the IMMA [cm] by the anteroposterior diameter of the femoral midshaft of the species. Gray areas depict extension angles that are anatomically impossible due to bone collisions in at least one specimen of the dataset. **(A)** Measurement series at 0° abduction. **(B)** Measurement series at 30° abduction. Solid black vertical lines mark the three extension angles (40°, 80°, and 120°) used for macroevolutionary modeling. Dashed vertical lines mark the touchdown (26°) and lift-off (126°) extension angles of the small caviomorph rodent *G. musteloides* (*in vivo* data from Fischer et al., 2002). **(C)** Measurement series at 60° abduction.

TABLE 1 | Fitted macroevolutionary models ranked according to Akaike information criterion (AICc) in ascending order.

IMMA 40° extension			IMMA 80° extension			IMMA 120° extension			Osteological in-lever		
Model	**SIC**	**AICc**	**Model**	**SIC**	**AICc**	**Model**	**SIC**	**AICc**	**Model**	**SIC**	**AICc**
$OU2_{terr}$	5.52	6.07	$OU2_{terr}$	−15.69	−15.14	$OU2_{terr}$	−17.97	−17.42	$OU2_{terr}$	−22.03	−21.48
OU3	7.96	10.26	OU3	−14.71	−12.42	OU3	−18.07	−15.77	OU3	−22.47	−20.18
BM1	12.39	11.43	$OU2_{over}$	−9.5	−8.96	$OU2_{over}$	−15.01	−14.46	$OU2_{over}$	−19.81	−19.26
$OU2_{over}$	12.81	13.36	BM1	−7.4	−8.36	BM1	−11.23	−12.19	BM1	−12.75	−13.71

IMMA, instantaneous muscle moment arm; SIC, Schwarz information criterion.

its peak IMMA at a smaller extension angle of 80° compared to other fossorial species (**Supplementary Figure S3**).

3.3 Most Likely Macroevolutionary Model Depends on Extension Angle

The regression models revealed that all IMMAs scale positively with the femoral diameter (**Table 2**), justifying the normalization. The IMMA at 40° extension scaled with negative allometry (b = ~0.8), whereas the other two IMMAs at 80° and 120°, respectively, scaled close to isometry (b = ~1).

According to the AICc, which was preferred over SIC to rank the models, the $OU2_{terr}$ model is always the most likely one, followed by the OU3 model (**Table 1**). The SIC values show only minor discrepancies and an overall similar ranking. The likelihood difference of the remaining models was large enough to consider them comparably implausible. The $OU2_{terr}$ model always estimated a larger optimal value for the IMMA of the scansorial group compared to that of the terrestrial group (the combination of fossorial and cursorial species; **Table 2**). In all OU3 models, the optimal IMMA values for a given femoral diameter were estimated to decrease from scansorial to cursorial and finally fossorial species (**Table 2**; **Figure 5**). Overall, this supported our exploratory findings; however, **Figure 4** suggests that fossorial and cursorial species share a similar mean IMMA at 40° extension. This discrepancy between the mean normalized IMMA and the IMMA optima of these two groups at 40° extension might result from the fact that normalization was executed using femoral diameter, whereas a regression exponent of 0.8 instead of 1 was recovered (**Table 2**). The AICc difference between the $OU2_{terr}$ and the OU3 model decreased with increasing extension angle (**Table 1**).

For the three extension angles, these two most likely models (but also all other fitted models) recovered a very small

TABLE 2 | Summary statistics of the two most likely macroevolutionary models per trait (**Table 1**).

Model	θ ± S.E.	b ± S.E.	hl (ML {2-USR})	v_y (ML {2-USR})
IMMA 40° extension				
$OU2_{terr}$	Scansorial: 0.14 ± 0.1 Terrestrial: −0.26 ± 0.06	0.81 ± 0.09	≤0.001{~0; 36.51}	0.04 {0.02; 0.08}
OU3	Cursorial: −0.23 ± 0.06 Fossorial: −0.31 ± 0.09 Scansorial: 0.13 ± 0.1	0.84 ± 0.09	≤0.001{~0; 38.39}	0.03 {0.02; 0.108}
IMMA 80° extension				
$OU2_{terr}$	Scansorial: 0.6 ± 0.06 Terrestrial: 0.36 ± 0.03	0.98 ± 0.05	4.03 {~0; 39.6}	0.01 {0.01; 0.03}
OU3	Cursorial: 0.38 ± 0.04 Fossorial: 0.3 ± 0.05 Scansorial: 0.59 ± 0.06	0.97 ± 0.05	4.56 {~0; 32.48}	0.01 {0.01; 0.02}
IMMA 120° extension				
$OU2_{terr}$	Scansorial: 0.75 ± 0.05 Terrestrial: 0.56 ± 0.03	1.12 ± 0.05	≤0.001 {~0; 31.01}	0.01 {0.01; 0.02}
OU3	Cursorial: 0.59 ± 0.03 Fossorial: 0.5 ± 0.05 Scansorial: 0.74 ± 0.05	1.1 ± 0.04	≤0.001 {~0; 21.11}	0.01 {<0.01; 0.02}
Osteological in-lever				
$OU2_{terr}$	Scansorial: 0.76 ± 0.05 Terrestrial: 0.6 ± 0.03	1.08 ± 0.04	2.42 {~0; 17.85}	0.01 {<0.01; 0.02}
OU3	Cursorial: 0.63 ± 0.03 Fossorial: 0.54 ± 0.04 Scansorial: 0.75 ± 0.04	1.07 ± 0.04	0.12 {~0; 13.24}	0.01 {<0.01; 0.01}

2-USR, two-unit support region; b, direct regression coefficient for the effect of the anteroposterior diameter of the femoral midshaft; hl, phylogenetic half-life; IMMA, instantaneous muscle moment arm; ML, maximum likelihood estimate; θ, optima at zero diameter, that is, regression intercepts; v_y, stationary variance.

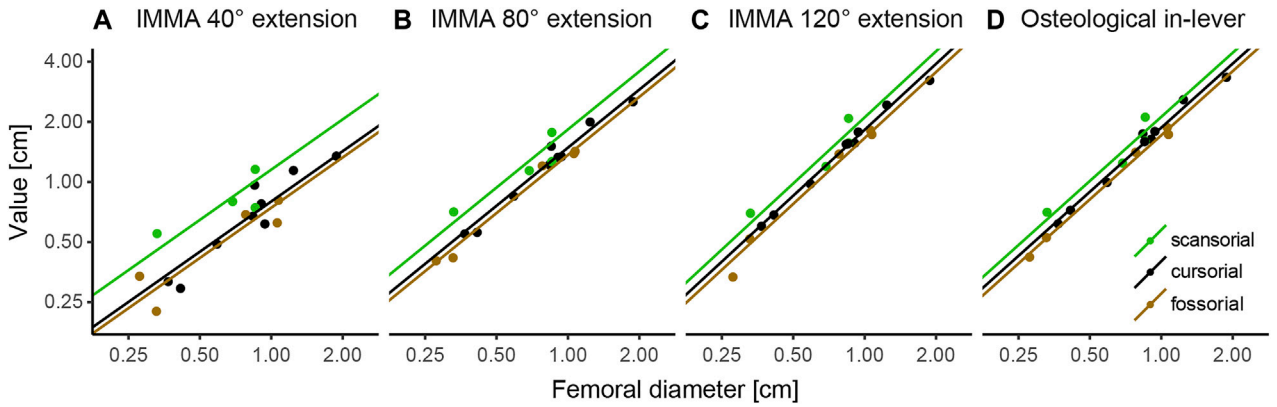

FIGURE 5 | Regression plots of instantaneous muscle moment arms (IMMAs) and osteological in-lever vs. femoral diameter. IMMAs were taken from three different extension angles **(A–C)** at 30° abduction. **(D)** Osteological in-lever. Lines indicate the regression slopes with varying intercepts (i.e., the primary optima for a given femoral diameter) among lifestyle categories as estimated by the most likely macroevolutionary model (**Table 1**). The coordinate axes were log-transformed.

phylogenetic half-life and also a small stationary variance, indicating the relatively strong selective pressure induced by lifestyle and relatively minor influences of other evolutionary factors. The maximum likelihood estimate of the phylogenetic half-life was usually less than 1000 years for the extension angles of 40° and 120°, and from 4 to 4.6 million years (my) for the angle of 80°. This suggests almost instantaneous adaptation since the root of Caviomorpha was dated 35.78 mya and all investigated lineages evolved in their lifestyle longer than 15 my (**Figure 2**). However, the maximum likelihood values have to be interpreted with caution, as the two-unit support regions suggest plausible half-lives of up to ~40 my for the most likely models (**Table 2**). In this extreme case, a caviomorph lineage from the root to the present would have only evolved on average about halfway to its optimum.

3.3.1 Comparison Between In-Lever and IMMAs

The model ranking of the osteological in-lever according to AICc was most similar to that of the IMMA at an extension angle of 120° (**Table 1**), which becomes also apparent from the similarity of intercepts in the regression plots of **Figure 5**. This seems plausible as the peaks of the average IMMA curve progressions were observed around this extension angle, and thus, the IMMA values here were the closest to the osteological in-lever.

4 DISCUSSION

In this study, we modeled the IMMAs of the M. gluteus medius, a primary hip extensor, over the entire range of anatomically possible hip extension in a phylogenetically informed comparative framework. The general assumption of selective

pressure shaping muscle moment arms was tested using a comparison of moment arms in a broad sample of caviomorph rodents with diverse locomotor specializations. Although many studies investigated moment arms in diverse tetrapod muscles, a comparison between existing studies is not easily made due to differences in methodologies (e.g., Lieber and Boakes, 1988; Payne et al., 2006; MacFadden and Brown, 2007; Channon et al., 2010; Charles et al., 2016). Only very few studies looked into instantaneous moment arms from a phylogenetic point of view (e.g., Allen et al., 2021). We will first discuss general IMMA patterns that affect the torque generation of the M. gluteus medius at the hip joint, then proceed to lifestyle-specific findings, then compare our IMMA results to the osteological in-lever results, and finally discuss limitations and future directions.

4.1 M. Gluteus Medius IMMA Benefits Large Extension Angles

Our modeling of IMMAs revealed that caviomorph species, regardless of locomotor category, display a sigmoidal change in the M. gluteus medius' IMMA with an increase of the extension angle relative to the pelvis, independent of each tested abduction angle (**Figure 4**). Perhaps, this is a consequence of an overall relatively consistent anatomical geometry of the hip across all Caviomorpha (and perhaps Mammalia) which presumably cannot be dramatically altered without deleterious effects on other functionalities of the hind limb locomotor system. All species (except for *O. degus*) exhibit large IMMAs at extension angles that can be expected to occur at the late stance phase (>90°; cf. Rocha-Barbosa et al., 1996; Fischer et al., 2002). This might benefit fore-aft acceleration, which usually occurs during the second half of the stem phase (Witte et al., 2002; Lammers et al., 2006; Zumwalt et al., 2006; Walter and Carrier, 2009; Hesse et al., 2015; Granatosky et al., 2020; Wölfer et al., 2021). However, the hip joint angle does not necessarily increase constantly during the stem phase, but its length change could depend on the gait. For example, a study by Rocha-Barbosa et al. (2005) on the limb kinematics of the guinea pig *Cavia porcellus* demonstrated that during trot—a symmetrical gait usually used at moderate running speeds (Hildebrand and Goslow, 1995)—the mean extension angles at touchdown, mid-stance, and lift-off were 58°, 67°, and 115°, respectively, indicating constant hip extension. In the modeling approach of our work, the M. gluteus medius IMMA of *C. porcellus* steadily increased in this range, exemplifying the benefit explained previously. However, during gallop—a synchronous gait usually used at high running speeds (Hildebrand, 1977)—the mean extension angles at the three time points were 91°, 85°, and 116°, respectively (Rocha-Barbosa et al., 2005). This suggests no constant extension, but a retention or even slight flexion during the first half of the stem phase, which could also be observed for other small-sized mammals (see Fischer et al., 2002). In this case, initiating stance with an already large extension angle relative to the pelvis and maintaining that angle during the early stance might assist positive torque generation (promoting hip extension) to counter the negative torque (promoting hip flexion) that is generated by the center of mass of the body on the hip joint as this center is most likely located in front of the hind limbs. On the contrary, in symmetrical running gaits such as the trot, this might not be necessary, as one fore- and one hind limb both simultaneously touch the ground to support the center of mass in between them (Hildebrand, 1985).

Not only the hip joint kinematics were found to be variable in small mammals, but also their net hip torque patterns, with different curve progressions and net torque maxima occurring at different times during stance, which could be partly linked to the preferred gait of the species (Witte et al., 2002). For example, Witte et al. (2002) observed the caviomorph species *Galea musteloides* to constantly increase the net positive hip joint torque and hip extension throughout stance while using symmetrical gaits, supporting the benefit of powerful acceleration during late stance. However, another species (*Tupaia glis*, belonging to the mammalian order Scandentia) primarily characterized by synchronous gaits first displayed a negative hip joint torque associated with hip flexion at the beginning of stance (Witte et al., 2002). This would support the additional need for high muscle-generated torques in the hip during early stance to prevent even higher net negative torques that would collapse the hip joint. Thus, gait choice is also a critical confounding factor that needs to be considered when discussing differences among lifestyles.

4.2 Functional Significance of M. Gluteus Medius IMMAs for Different Lifestyles

The most likely low phylogenetic half-life that we always recovered for the most likely models suggests the IMMA to be functionally significant throughout hip extension and under selective pressure from the considered lifestyles. Despite the overall similarities in normalized IMMA curve progressions, our results indicate that the geometry of the hip does not strictly constrain IMMA adjustments but allows for independent adjustments at different extension angles. This is reflected, for example, in the diversity of the shapes of the sigmoidal IMMA curve progression among species (e.g., **Supplementary Figure S3**). But it is also visible in the fact that differences in the average IMMA between fossorial and cursorial species increased with increasing extension angle (**Figure 4**).

In general, our expectations based on considerations of the differential functional demands associated with cursorial, scansorial, and fossorial lifestyles in caviomorphs were met by our results. We documented larger M. gluteus medius IMMAs on average in scansorial caviomorphs in comparison with fossorial and cursorial species, which were more similar. This was also supported by the $OU2_{terr}$ model always ranking the highest with scansorial species displaying the largest optimum. At larger extension angles, cursorial caviomorph species fell in between fossorial and scansorial species, reflected also in the OU3 model becoming more likely, perhaps because this phase is most important for acceleration, as hypothesized, however, apparently only at larger extension angles.

The cursorial lifestyle was found to be the ancestral state in Caviomorpha. We expected to find a trade-off in the IMMAs between the capacity for the generation of hip extensor torque and faster hip extension. This was based on previous analyses of the geometrically related osteological in-lever. Smith and Savage (1956), for example, argued that the gluteal muscle complex of cursorial mammals should be specialized for high angular velocity, which would imply that a relatively short trochanter and, thus, short IMMAs are beneficial. On the other hand, a relatively long trochanter major and thus gluteal muscle osteological in-lever had previously also been associated with cursorial locomotion (Polly, 2007; Croft and Anderson, 2008). Interestingly, we observed particularly shorter M. gluteus medius IMMAs in our models at little hip extension in cursorial species when compared to scansorial species (but not when compared to fossorial species). This indicates an optimization for increased angular velocity during little hip extension. However, another explanation for a relatively small IMMA could be that especially small cursorial species are expected to exploit fast synchronous gaits, for example, to escape predators (Hildebrand, 1977). As discussed earlier, the stem-phase during synchronous gaits might be initiated by already fairly large extension angles, perhaps mitigating the selective pressure on high torques for fast accelerations at smaller extension angles. Closer to the maximum anatomically possible hip extension of cursorial species (i.e., at values that can be expected during the late stance of Caviomorpha; cf. Rocha-Barbosa et al., 1996; Fischer et al., 2002), the gluteal IMMAs appeared to fall on average between those of scansorial and fossorial species, respectively. This might hint at the trade-off between torque generation and angular acceleration in the hip of cursorial species mentioned earlier.

We found that the scansorial lifestyle is a derived condition within Caviomorpha. Scansorial locomotion requires powerful hip extension during climbing and locomotion on inclines when a larger proportion of the body's mass rests on the hind limbs and additionally needs to be pushed upward against gravity (e.g., Preuschoft, 2002; Lammers et al., 2006; Hesse et al., 2015; Wölfer et al., 2021). Particularly, Channon et al. (2010) described strong hip extension by gluteal muscles as beneficial for the highly arboreal locomotion of gibbons. A similar adaptation of hip extensors would be necessary to facilitate powerful hip extension during launches for leaps from one support to the next in the discontinuous arboreal habitat of scansorial species (Aerts, 1998; Scholz et al., 2006). Indeed, the optimal IMMAs of the scansorial caviomorphs always scored as the largest optima, and this trend was also retrieved graphically after normalization with femoral diameter. These findings agree with those of Wölfer et al. (2019) who investigated the osteological in-lever of the M. gluteus medius in Sciuromorpha (squirrel-related rodents) and also found tree-dwelling species to display longer in-levers on average compared to fossorial/terrestrial species (though particularly for species of larger body masses). The outstandingly large IMMA optimum at the extension angle of 40° (1.5 times larger than that of the terrestrial species) suggests an importance of powerful torques at early stance. This coincides with the fact that scansorial species typically exploit symmetrical gaits with small extension angles during early stance (e.g., Biknevicious et al., 2013; Hesse et al., 2015; Karantanis et al., 2017). Additionally, independent of gait, it might compromise the crouched posture that is usually utilized during climbing on narrow substrates to bring the center of mass closer to the substrate and thus avoid large fatal toppling moment (Nakano, 2002; Schmidt and Fischer, 2011).

The fossorial lifestyle is also most likely a derived condition within Caviomorpha. As expected, the fossorial species of our study do not seem to rely as much on powerful hip extension on average. This is reflected in smaller IMMA optima at larger extension angles (80° and 120°) with respect to the ancestral cursorial condition. However, it is unclear, why, for example, the optimum at 40° extension (and thus in general for smaller angles) was retained and not reduced during evolution. We assume that relatively fast locomotion is still under selection for the species included in this study as they forage above ground (Wilson and Mittermeier, 2011) and should experience similar predation pressure as the remaining species in our study. However, this again cannot explain the overall reduced optima at larger extension angles. The reduced potential for powerful hip extension appears to be consistent with the primary use of the forelimbs to break loose hard soil during digging activities (Wilson and Mittermeier, 2011) and would suggest the forelimbs are adapted to powerful retractions. However, the scapula and the humerus of caviomorph rodents are mostly characterized by a phylogenetic instead of a functional signal (Morgan 2009; Morgan and Álvarez, 2013). Perhaps, an IMMA analysis of the forelimb retractors reveals a functional signal that is not present in the bone morphology as shown here. Additionally, contradicting our results, Wilson and Geiger (2015) compared femoral indices among caviomorph rodents with different lifestyles and concluded that the potential force-output of the M. gluteus medius should be largest in fossorial caviomorphs. This discrepancy might be a consequence either of different species samples, different measurements (they used a proxy for the in-lever), or different normalization approaches (they used the distance between proximal and distal femoral condyles, whereas we used femoral midshaft diameter).

4.3 IMMA Length Changes Are Preferable Over Osteological In-Lever due to Nuanced Insights Into Torque Optimization

Evolutionary model comparison of osteological M. gluteus medius in-levers of the analyzed specimens almost perfectly reproduced the results we obtained for the IMMA at 120° of modeled hip extension. This is plausible because this extension angle was characterized by the largest average IMMA of each lifestyle category (**Figure 4**), which thus is closest to the length of the osteological in-lever (**Figure 1A**). It indicates that for the hip joint, the in-lever only approximates the IMMA well at large extension angles. However, it failed to detect the similarity between cursorial and fossorial species and the pronounced dissimilarity between the former and scansorial species at lower values of hip extension, as suggested by the $OU2_{terr}$

model. As shown earlier, this might hint at similar selective pressures from cursorial and fossorial locomotion as opposed to larger extension angles. On the other hand, the even more increased moment arm lengths in the early stance phase appear to present a significant adaptation of scansorial species to climbing on inclines. Therefore, high extensor torques are probably still achievable in the relatively little extended hip joint of scansorial species climbing in a crouched posture, which is not detectable from an osteological analysis alone. The realization of large IMMAs in this case is most likely only possible due to a position of the origin of the M. gluteus medius relatively farther from the hip joint. Smith and Savage (1956) pointed to pelvis morphology reflecting a specialization for the rapid extension of the thigh (as expected for cursorial species) or slower, but more powerful extension (as expected for scansorial species). In our dataset, we indeed observed considerable shape differences among pelves, especially concerning the wing of ilium, which most certainly affects the position of the attachment site for the M. gluteus medius. A broader quantitative study of caviomorph pelvis shape is necessary to confirm this.

4.4 IMMA Measurements Are Only a First Step to Capture the Dynamics of Lever-Arm Systems

Importantly, the comparative analysis of IMMAs is not the be all and end all of musculoskeletal function. Here, we have focused on one of many parameters that determine the functioning of a lever-arm system, but selection will ultimately act on this system as an integrated whole. For example, our results therefore do not necessarily mean that caviomorph rodents associated with the scansorial locomotor category are in fact generating a comparatively more powerful torque *in vivo*, since the muscle properties of every specimen could not be investigated in this comparative modeling approach and remain unknown (Channon et al., 2010; Charles et al., 2016). For instance, despite relatively small IMMAs at small extension angles, it may be possible for cursorial caviomorph rodents to generate a more powerful muscle moment than their fossorial counterparts simply by generating a larger muscle force, for example, through a larger cross-sectional area or a higher degree of muscle activation (Crook et al., 2010). Relatedly, a study that investigated muscle architectural parameters in the hind limb extensors of a striding and a jumping caviomorph rodent found such differences in muscle properties (Rosin and Nyakatura, 2017). The observed differences in the shape of the wing of ilium of the pelvis mentioned earlier could point at differences in muscle size that most likely are associated with a different potential for torque generation.

Another aspect that was not considered in this study is the out-lever, that is, the distance from the CoR to the point where the lever-arm system exerts a force on its environment (e.g., the autopodia; Hildebrand and Goslow, 1995; Smith and Savage, 1956). Cursorial species, for example, are often characterized by a relatively small mechanical advantage (i.e., the in-lever to out-lever ratio) of the M. gluteus medius, which is interpreted to be beneficial for fast limb rotation but disadvantageous for torque generation (Smith and Savage, 1956). However, these out-levers are usually measured on a single limb configuration with particular predefined angles for all joints distal to the lever-arm system of interest. This disregards the dynamic change of all joint angles during a stride cycle (see Fischer et al., 2002). Previous studies have already incorporated the dynamical change of the out-lever of specific muscles and highlighted the functional importance of dynamic gearing (change of the mechanical advantage) during the stem phase (e.g., Carrier et al., 1994; Carrier et al., 1998). Thus, in order to gain a deeper insight into the adaptability of these dynamics to different lifestyles, the next crucial step would be to simultaneously model the IMMA and the corresponding instantaneous out-lever.

Finally, our IMMA measurements only considered the M. gluteus medius, an important but not the only hip extensor of quadrupedal mammals. As the selection is assumed to act on the joint force-output of all extensor muscles, integrating other contributing pelvic muscles potentially adds additional nuance to the results in this current work (Hoy et al., 1988; Allen et al., 2021). Nevertheless, our phylogenetically informed analysis underscores that IMMAs of single muscular components can already be informative with regard to the functional demands selective regimes impose during evolution.

4.5 Current Limitations

The modeling of IMMA length changes presented here relied on a virtual abstraction of the hip extension process. We focused on hip extension along the parasagittal plane at three separately predefined abduction angles associated with the transversal plane. We believed one of these abduction angles (30°) to be the most plausible for locomotion. These simplified the actual *in vivo* hip joint movements which most likely combine hip extension with changes in hip abduction and hip adduction. Perhaps, femoral long-axis rotation plays a certain role (Nyakatura and Fischer, 2010; Fischer et al., 2018) and even translations could be considered. Methods to assess all six degrees of freedom in *in vivo* joint movement exist (e.g., Brainerd et al., 2010), but as of yet, neither large-scale nor exemplary comparative analyses on rodents as studied herein have been conducted to our knowledge. Furthermore, compromises had to be made for modeling the MLoA. The MLoA modeled here without considering individual muscle architecture benefits a simplified approach for comparative analysis of many specimens (18 in our case), but this comes at the expense of more realistic individual results that a specifically adjusted line of action with "*via* points" and "wrapping objects" would allow (cf., Hutchinson et al., 2005; Bishop et al., 2021; Demuth et al., 2022).

The approach that we undertook is also laden with certain statistical caveats that need to be tackled in the future. Functional modeling of IMMAs in a virtual environment is still time-consuming and most likely the reason why it has regularly only been applied to a single or few species (e.g., Channon et al., 2010; Regnault and Pierce, 2018) or using averaged values when analyzed within a phylogenetic framework (Allen et al., 2021). Although in this study a comparatively large interspecific IMMA dataset was used to explore lifestyle adaptations, only a single specimen per species was involved.

We had to assume that the sampled specimen is close to the species mean and that the interspecific variability exceeds the intraspecific variability. These caveats also limited the interspecific sample size and rendered it necessary to narrow down the diverse locomotor ecologies in our study to just three relatively course locomotor categories. Thus, eventual anatomical differences existing between locomotor behaviors within a category (e.g., between ricochetal and striding cursorial caviomorphs; Rosin and Nyakatura, 2017) were not possible to identify in our comparative modeling approach. This may have resulted in less striking mean results per locomotor category in favor of a general overview. Finally, the limited number of species also hindered the use of more complex multivariate statistical analyses that are necessary to account for the correlation among IMMAs of different joint poses. Establishing automation algorithms for the functional modeling procedure could provide the opportunity to overcome these limitations.

5 CONCLUSION

Taken together, the current study demonstrates nuanced insights into how the functional significance of instantaneous M. gluteus medius moment arms differs between locomotor lifestyles of caviomorph rodents. It also highlights that ecomorphological specializations at smaller hip extension angles could not have been identified by the use of the simple osteological in-lever. Our findings thus underpin the importance of functional modeling for the understanding of the adaptive significance of lever-arm systems. However, future studies on other joint systems are needed to assess its general importance and in which cases osteological measurements can still be sufficient. This is especially relevant for fossils that often lack skeletal elements and, thus, potentially essential lever-arm components for functional modeling.

Several key limitations to our modeling approach are discussed. Despite new functional and evolutionary insights, a future investigation of other aspects of musculoskeletal function (such as muscle activation patterns, muscle architecture, and muscle fiber type composition) would be necessary for a comprehensive understanding of the implications of moment arm values on actual joint torque, as multiple studies have pointed out (e.g., MacFadden and Brown, 2007). This should be accompanied by the simultaneous study of instantaneous out-levers to the point of contact to the support to obtain a deeper understanding of the dynamics of force-output throughout the locomotor cycle. Furthermore, for a more comprehensive understanding of how locomotion affects hind limb retraction in caviomorph rodents, not only other gluteal muscles should be subjected to a comparative modeling approach but also muscles of the ischiopubic complex, such as the M. semimembranosus and the M. biceps femoris (Smith and Savage, 1956).

DATA AVAILABILITY STATEMENT

The original contributions presented in the study are included in the article/**Supplementary Material**, further inquiries can be directed to the corresponding author. Additionaly, the related Maya files for the assessment of the instantaneous muscle moment arms of all 18 species are made available in an open access data repository (Löffler et al., 2022).

AUTHOR CONTRIBUTIONS

JN conceived the study. LL and FG acquired the data. LL and JW analyzed the data. LL, JW, and JN interpreted the data and drafted the manuscript. All authors contributed to its final version.

FUNDING

The study was conducted using budgetary funds of JN.

ACKNOWLEDGMENTS

We are grateful for help from O. E. Demuth with setting up the Maya files for IMMA analysis. We thank the curators who granted access to mammalian collections. We thank M. Butler and R. Brocklehurst for their comments that immensely helped us improve upon a previous draft of this manuscript. We also thank the members of the JN lab for their helpful discussions.

SUPPLEMENTARY MATERIAL

The Supplementary Material for this article can be found online at: https://www.frontiersin.org/articles/10.3389/fbioe.2022.806314/full#supplementary-material

REFERENCES

Aerts, P. (1998). Vertical Jumping in *Galago senegalensis*: The Quest for an Obligate Mechanical Power Amplifier. *Phil. Trans. R. Soc. Lond. B* 353 (1375), 1607–1620. doi:10.1098/rstb.1998.0313

Alfieri, F., Nyakatura, J. A., and Amson, E. (2021). Evolution of Bone Cortical Compactness in Slow Arboreal Mammals. *Evolution* 75 (2), 542–554. doi:10.1111/evo.14137

Allen, V. R., Kilbourne, B. M., and Hutchinson, J. R. (2021). The Evolution of Pelvic Limb Muscle Moment Arms in Bird-Line Archosaurs. *Sci. Adv.* 7 (12), eabe2778. doi:10.1126/sciadv.abe2778

Amson, E., and Bibi, F. (2021). Differing Effects of Size and Lifestyle on Bone Structure in Mammals. *BMC Biol.* 191, 1–18. doi:10.1186/s12915-021-01016-1

Antoine, P. O., Marivaux, L., Croft, D. A., Billet, G., Ganerød, M., Jaramillo, C., et al. (2011). Middle Eocene Rodents from Peruvian Amazonia Reveal the Pattern and Timing of Caviomorph Origins and Biogeography. *Proc. Biol. Sci.* 279, 1319–1326. doi:10.1098/rspb.2011.1732

Bates, K. T., Maidment, S. C. R., Allen, V., and Barrett, P. M. (2012). Computational Modelling of Locomotor Muscle Moment Arms in the Basal Dinosaur *Lesothosaurus diagnosticus*: Assessing Convergence between Birds and Basal Ornithischians. *J. Anat.* 220 (3), 212–232. doi:10.1111/j.1469-7580.2011.01469.x

Biknevicius, A. R., Reilly, S. M., McElroy, E. J., and Bennett, M. B. (2013). Symmetrical Gaits and Center of Mass Mechanics in Small-Bodied, Primitive Mammals. *Zoology* 116 (1), 67–74. doi:10.1016/j.zool.2012.05.005

Bishop, P. J., Cuff, A. R., and Hutchinson, J. R. (2021). How to Build a Dinosaur: Musculoskeletal Modeling and Simulation of Locomotor Biomechanics in Extinct Animals. *Paleobiology* 47 (1), 1–38. doi:10.1017/pab.2020.46

Boyer, D. M., Seiffert, E. R., Gladman, J. T., and Bloch, J. I. (2013). Evolution and Allometry of Calcaneal Elongation in Living and Extinct Primates. *PloS One* 8 (7), e67792. doi:10.1371/journal.pone.0067792

Brainerd, E. L., Baier, D. B., Gatesy, S. M., Hedrick, T. L., Metzger, K. A., Gilbert, S. L., et al. (2010). X-ray Reconstruction of Moving Morphology (XROMM): Precision, Accuracy and Applications in Comparative Biomechanics Research. *J. Exp. Zool A. Ecol. Genet. Physiol.* 313 (5), 262–279. doi:10.1002/jez.589

Burnham, K. P., and Anderson, D. R. (20022002). *Model Selection and Multimodel Inference: A Practical Information-Theoretic Approach*. New York: Springer Science and Business Media.

Butler, M. A., and King, A. A. (2004). Phylogenetic Comparative Analysis: A Modeling Approach for Adaptive Evolution. *The Am. Naturalist* 164 (6), 683–695. doi:10.1086/426002

Candela, A. M., Muñoz, N. A., and García-Esponda, C. M. (2017). The Tarsal-Metatarsal Complex of Caviomorph Rodents: Anatomy and Functional-Adaptive Analysis. *J. Morphol.* 278 (6), 828–847. doi:10.1002/jmor.20678

Carrier, D. R., Gregersen, C. S., and Silverton, N. A. (1998). Dynamic Gearing in Running Dogs. *J. Exp. Biol.* 201, 3185–3195. doi:10.1242/jeb.201.23.3185

Carrier, D. R., Heglund, N. C., and Earls, K. D. (1994). Variable Gearing During Locomotion in the Human Musculoskeletal System. *Science* 265, 651–653. doi:10.1126/science.8036513

Channon, A. J., Crompton, R. H., Günther, M. M., and Vereecke, E. E. (2010). Muscle Moment Arms of the Gibbon Hind Limb: Implications for Hylobatid Locomotion. *J. Anat.* 216 (4), 446–462. doi:10.1111/j.1469-7580.2009.01209.x

Charles, J. P., Cappellari, O., Spence, A. J., Wells, D. J., and Hutchinson, J. R. (2016). Muscle Moment Arms and Sensitivity Analysis of a Mouse Hindlimb Musculoskeletal Model. *J. Anat.* 229 (4), 514–535. doi:10.1111/joa.12461

Cignoni, P., Callieri, M., Corsini, M., Dellepiane, M., Ganovelli, F., and Ranzuglia, G. (2008). *MeshLab. An Open-Source Mesh Processing Tool*. Salerno: Sixth Eurographics Italian Chapter Conference.

Croft, D. A., and Anderson, L. C. (2008). Locomotion in the Extinct Notoungulate *Protypotherium*. *Palaeontol. Electronica* 11 (1), 1–20.

Crook, T. C., Cruickshank, S. E., McGowan, C. M., Stubbs, N., Wilson, A. M., Hodson-Tole, E., et al. (2010). A Comparison of the Moment Arms of Pelvic Limb Muscles in Horses Bred for Acceleration (Quarter Horse) and Endurance (Arab). *J. Anat.* 217 (1), 26–37. doi:10.1111/j.1469-7580.2010.01241.x

Demuth, O. E., Wiseman, A. L., van Beesel, J., Mallison, H., and Hutchinson, J. R. (2022). Three-Dimensional Polygonal Muscle Modelling and Line of Action Estimation in Living and Extinct Taxa. *Sci. Rep.* 12 (1), 1–16.

Elissamburu, A., and Vizcaíno, S. F. (2004). Limb Proportions and Adaptations in Caviomorph Rodents (Rodentia: Caviomorpha). *J. Zoolog.* 262 (2), 145–159. doi:10.1017/s0952836903004485

Fabre, P.-H., Hautier, L., Dimitrov, D., and P Douzery, E. J. (2012). A Glimpse on the Pattern of Rodent Diversification: A Phylogenetic Approach. *BMC Evol. Biol.* 12 (1), 88. doi:10.1186/1471-2148-12-88

Fischer, M. S., Lehmann, S. V., and Andrada, E. (2018). Three-Dimensional Kinematics of Canine Hind Limbs: *In Vivo*, Biplanar, High-Frequency Fluoroscopic Analysis of Four Breeds During Walking and Trotting. *Sci. Rep.* 8, 16982. doi:10.1038/s41598-018-34310-0

Fischer, M. S., Schilling, N., Schmidt, M., Haarhaus, D., and Witte, H. (2002). Basic Limb Kinematics of Small Therian Mammals. *J. Exp. Biol.* 205 (9), 1315–1338. doi:10.1242/jeb.205.9.1315

García-Esponada, C. M., and Candela, A. M. (2010). Anatomy of the Hindlimb Musculature in the Cursorial Caviomorph *Dasyprocta Azarae* Lichtenstein, 1823 (Rodentia, Dasyproctidae). Functional and Evolutionary Significance. *Mammalia* 74 (4), 407–422.

Goslow, G. E., Seeherman, H. J., Taylor, C. R., McCutchin, M. N., and Heglund, N. C. (1981). Electrical Activity and Relative Length Changes of Dog Limb Muscles as a Function of Speed and Gait. *J. Exp. Biol.* 94 (1), 15–42. doi:10.1242/jeb.94.1.15

Granatosky, M. C., McElroy, E. J., Lemelin, P., Reilly, S. M., Nyakatura, J. A., Andrada, E., et al. (2020). Variation in Limb Loading Magnitude and Timing in Tetrapods. *J. Exp. Biol.* 223 (2), jeb201525. doi:10.1242/jeb.201525

Hansen, T. F. (1997). Stabilizing Selection and the Comparative Analysis of Adaptation. *Evolution* 51 (5), 1341–1351. doi:10.1111/j.1558-5646.1997.tb01457.x

Hargaden, M., and Singer, L. (2012). "Anatomy, Physiology, and Behavior," in *The Laboratory Rabbit, Guinea Pig, Hamster, and Other Rodents*. Editors M. A. Suckow, K. A. Stevens, and R. P. Wilson (American College of Laboratory Animal Medicine), 575–602. doi:10.1016/b978-0-12-380920-9.00020-1

Hedges, S. B., Marin, J., Suleski, M., Paymer, M., and Kumar, S. (2015). Tree of Life Reveals Clock-Like Speciation and Diversification. *Mol. Biol. Evol.* 32 (4), 835–845. doi:10.1093/molbev/msv037

Hesse, B., Nyakatura, J. A., Fischer, M. S., and Schmidt, M. (2015). Adjustments of Limb Mechanics in Cotton-Top Tamarins to Moderate and Steep Support Orientations: Significance for the Understanding of Early Primate Evolution. *J. Mammal. Evol.* 22 (3), 435–450. doi:10.1007/s10914-014-9283-4

Hildebrand, M. (1977). Analysis of Asymmetrical Gaits. *J. Mammalogy* 58 (2), 131–156. doi:10.2307/1379571

Hildebrand, M. (1985). "Chapter 3. Walking and Running," in *Functional Vertebrate Morphology*. Editors M. Hildebrandt, D. M. Bramble, K. F. Liem, and D. B. Wake (Cambridge, London: Harvard), 38–57. doi:10.4159/harvard.9780674184404.c3

Hildebrand, M., and Goslow, G. E. (1995). *Analysis of Vertebrate Structure*.

Hoy, M. G., Zajac, F. E., and Gordon, M. E. (1988). A Musculoskeletal Model of the Human Lower Extremity: The Effect of Muscle, Tendon, and Moment Arm on the Moment-Angle Relationship of Musculotendon Actuators at the Hip, Knee, and Ankle. *J. Biomech.* 23 (2), 157–169. doi:10.1016/0021-9290(90)90349-8

Huelsenbeck, J. P., Nielsen, R., and Bollback, J. P. (2003). Stochastic Mapping of Morphological Characters. *Syst. Biol.* 52, 131–158. doi:10.1080/10635150390192780

Hutchinson, J. R., Anderson, F. C., Blemker, S. S., and Delp, S. L. (2005). Analysis of Hindlimb Muscle Moment Arms in Tyrannosaurus Rex Using a Three-Dimensional Musculoskeletal Computer Model: Implications for Stance, Gait, and Speed. *Paleobiol* 31, 676–701. doi:10.1666/04044.1

Jenkins, F. A. (1971). Limb Posture and Locomotion in the Virginia Opossum (*Didelphis marsupialis*) and in Other Non-Cursorial Mammals. *J. Zoolog.* 165 (3), 303–315. doi:10.1111/j.1469-7998.1971.tb02189.x

Karantanis, N.-E., Rychlik, L., Herrel, A., and Youlatos, D. (2017). Arboreal Gaits in Three Sympatric Rodents *Apodemus agrarius*, *Apodemus flavicollis* (Rodentia, Muridae) and Myodes Glareolus (Rodentia, Cricetidae). *Mamm. Biol.* 83 (1), 51–63. doi:10.1016/j.mambio.2016.12.004

Kassambara, A. (2020). *Ggpubr: 'ggplot2' Based Publication Ready Plots*. R package version 0.4.0. Available at: https://CRAN.R-project.org/package=ggpubr.

Kilbourne, B. M. (2017). Selective Regimes and Functional Anatomy in the Mustelid Forelimb: Diversification Toward Specializations for Climbing, Digging, and Swimming. *Ecol. Evol.* 7, 8852–8863. doi:10.1002/ece3.3407

Kopperud, B. T., Pienaar, J., Voje, K. L., Orzack, S. H., and Hansen, T. F. (2020). *Slouch. Stochastic Linear Ornstein-Uhlenbeck Comparative Hypotheses. R Package*. version 2.1.4. Available at: https://CRAN.R-project.org/package=slouch.

Lammers, A. R., Earls, K. D., and Biknevicius, A. R. (2006). Locomotor Kinetics and Kinematics on Inclines and Declines in the Gray Short-Tailed Opossum *Monodelphis domestica*. *J. Exp. Biol.* 209, 4154–4166. doi:10.1242/jeb.02493

Larson, S. G., and Stern, J. T. (2009). Hip Extensor EMG and Forelimb/Hind Limb Weight Support Asymmetry in Primate Quadrupeds. *Am. J. Phys. Anthropol.* 138, 343–355. doi:10.1002/ajpa.20935

Lieber, R. L., and Boakes, J. L. (1988). Muscle Force and Moment Arm Contributions to Torque Production in Frog Hindlimb. *Am. J. Physiol.* 254, C769–C772. doi:10.1152/ajpcell.1988.254.6.C769

Lieber, R. L. (1997). Muscle Fiber Length and Moment Arm Coordination During Dorsi- and Plantarflexion in the Mouse Hindlimb. *Acta Anat. (Basel)* 159 (2-3), 84–89. doi:10.1159/000147970

Lieber, R. L., and Shoemaker, S. D. (1992). Muscle, Joint, and Tendon Contributions to the Torque Profile of Frog Hip Joint. *Am. J. Physiology-Regulatory, Integr. Comp. Physiol.* 263, R586–R590. doi:10.1152/ajpregu.1992.263.3.r586

Löffler, L., Wölfer, J., Gavrilei, F., and Nyakatura, J. A. (2022). Data From: Computational Modeling of Gluteus Medius Muscle Moment Arm in Caviomorph Rodents Reveals Ecomorphological Specializations, Dryad, Dataset. doi:10.5061/dryad.7d7wm37xm

Macfadden, L. N., and Brown, N. A. T. (2007). Biarticular Hip Extensor and Knee Flexor Muscle Moment Arms of the Feline Hindlimb. *J. Biomech.* 40, 3448–3457. doi:10.1016/j.jbiomech.2007.05.021

Marshall, S. K., Superina, M., Spainhower, K. B., and Butcher, M. T. (2021). Forelimb Myology of Armadillos (Xenarthra: Cingulata, Chlamyphoridae): Anatomical Correlates with Fossorial Ability. *J. Anat.* 238, 551–575. doi:10.1111/joa.13326

Mielke, F., Amson, E., and Nyakatura, J. A. (2018). Morpho-Functional Analysis Using Procrustes Superimposition by Static Reference. *Evol. Biol.* 45, 449–461. doi:10.1007/s11692-018-9456-9

Moen, D. S., Morlon, H., and Wiens, J. J. (2015). Testing Convergence versus History: Convergence Dominates Phenotypic Evolution for over 150 Million Years in Frogs. *Syst. Biol.* 65, 146–160. doi:10.1093/sysbio/syv073

Moore, A. L., Budny, J. E., Russell, A. P., and Butcher, M. T. (2013). Architectural Specialization of the Intrinsic Thoracic Limb Musculature of the American Badger (*Taxidea taxus*). *J. Morphol.* 274, 35–48. doi:10.1002/jmor.20074

Morgan, C. C., and Álvarez, A. (2013). The Humerus of S Outh A Merican Caviomorph Rodents: Shape, Function and Size in a Phylogenetic Context. *J. Zool.* 290, 107–116. doi:10.1111/jzo.12017

Morgan, C. C. (2009). Geometric Morphometrics of the Scapula of South American Caviomorph Rodents (Rodentia: Hystricognathi): Form, Function and Phylogeny. *Mamm. Biol.* 74, 497–506. doi:10.1016/j.mambio.2008.09.006

Murray, W. M., Buchanan, T. S., and Delp, S. L. (2002). Scaling of Peak Moment Arms of Elbow Muscles with Upper Extremity Bone Dimensions. *J. Biomech.* 35, 19–26. doi:10.1016/s0021-9290(01)00173-7

Nakano, Y. (2002). The Effects of Substratum Inclination on Locomotor Patterns in Primates. *zmorph_anthropol* 83, 189–199. doi:10.1127/zma/83/2002/189

Nowak, R. M. (1999). *Walker's Mammals of the World*. 6 edn., 2. Baltimore: The John Hopkins University Press.

Nyakatura, J. A., and Fischer, M. S. (2010). Three-Dimensional Kinematic Analysis of the Pectoral Girdle During Upside-Down Locomotion of Two-Toed Sloths (Choloepus Didactylus, Linné 1758). *Front. Zool* 7, 21. doi:10.1186/1742-9994-7-21

Pandy, M. G., and Andriacchi, T. P. (2010). Muscle and Joint Function in Human Locomotion. *Annu. Rev. Biomed. Eng.* 12, 401–433. doi:10.1146/annurev-bioeng-070909-105259

Payne, R. C., Crompton, R. H., Isler, K., Savage, R., Vereecke, E. E., Gunther, M. M., et al. (2006). Morphological Analysis of the Hindlimb in Apes and Humans. II. Moment Arms. *J. Anat.* 208, 725–742. doi:10.1111/j.1469-7580.2006.00564.x

Pedotti, A., Krishnan, V. V., and Stark, L. (1978). Optimization of Muscle-Force Sequencing in Human Locomotion. *Math. Biosciences* 38, 57–76. doi:10.1016/0025-5564(78)90018-4

Pennell, M. W., Eastman, J. M., Slater, G. J., Brown, J. W., Uyeda, J. C., FitzJohn, R. G., et al. (2014). Geiger v2.0: An Expanded Suite of Methods for Fitting Macroevolutionary Models to Phylogenetic Trees. *Bioinformatics* 30, 2216–2218. doi:10.1093/bioinformatics/btu181

Polly, P. D. (2007). "Limbs in Mammalian Evolution," in *Fins into Limbs. Evolution, Development, and Transformation*. Editor B. K. Hall (Chicago: University of Chicago Press), 245–268.

Popesko, P., Rajtová, V., and Horák, J. (1992). *A Colour Atlas of the Anatomy of Small Laboratory Animals. Volume oneRabbit and guinea Pig*. London: Wolfe Publishing.

Preuschoft, H. (2002). What Does "Arboreal Locomotion" Mean Exactly and What Are the Relationships Between "Climbing", Environment and Morphology? *Zmorph_Anthropol.* 83, 171–188. doi:10.1127/zma/83/2002/171

R Core Team (2021). *R: A Language and Environment for Statistical Computing*. Vienna, Austria: R Foundation for Statistical Computing. URL Available at: https://www.R-project.org/.

Regnault, S., Fahn-Lai, P., and Pierce, S. E. (2021). Validation of an Echidna Forelimb Musculoskeletal Model Using XROMM and diceCT. *Front. Bioeng. Biotechnol.* doi:10.3389/fbioe.2021.751518

Regnault, S., and Pierce, S. E. (2018). Pectoral Girdle and Forelimb Musculoskeletal Function in the Echidna (*Tachyglossus aculeatus*): Insights into Mammalian Locomotor Evolution. *R. Soc. Open Sci.* 511, 181400. doi:10.1098/rsos.181400

Revell, L. J. (2012). Phytools: An R Package for Phylogenetic Comparative Biology (And Other Things). *Methods Ecol. Evol.* 3, 217–223. doi:10.1111/j.2041-210X.2011.00169.x

Rocha-Barbosa, O., De Castro Loguerico, M. F., Renous, S., and Gasc, J-P. (2005). Limb Joint Kinematics and Their Relation to Increasing Speed in the Guinea Pig *Cavia porcellus*. (Mammalia: Rodentia). *J. Zool.* 266, 293–305.

Rocha-Barbosa, O., Renous, S., and Gasc, J.-P. (1996). Comparison of the Fore and Hind Limbs Kinematics in the Symmetrical and Asymmetrical Gaits of a Caviomorph Rodent, the Domestic guinea Pig, *Cavia porcellus* (Linné, 1758) (Rodentia, Caviidae). *Ann. Sci. nat., Zool. Biol. Anim.* 17, 149–165.

Rosin, S., and Nyakatura, J. A. (2017). Hind Limb Extensor Muscle Architecture Reflects Locomotor Specialisations of a Jumping and a Striding Quadrupedal Caviomorph Rodent. *Zoomorphology* 136, 267–277. doi:10.1007/s00435-017-0349-8

Schmidt, A., and Fischer, M. S. (2011). The Kinematic Consequences of Locomotion on Sloped Arboreal Substrates in a Generalized (*Rattus norvegicus*) and a Specialized (*Sciurus Vulgaris*) Rodent. *J. Exp. Biol.* 214, 2544–2559. doi:10.1242/jeb.051086

Scholz, M. N., D'Août, K., Bobbert, M. F., and Aerts, P. (2006). Vertical Jumping Performance of Bonobo (*Pan paniscus*) Suggests Superior Muscle Properties. *Proc. R. Soc. B.* 273, 2177–2184. doi:10.1098/rspb.2006.3568

Smith, J. M., and Savage., R. J. G. (1956). Some Locomotory Adaptations in Mammals. *Zoolog. J. Linn. Soc.* 42, 603–622. doi:10.1111/j.1096-3642.1956.tb02220.x

Sokolov, A. S. (1964). The Structure of Hind Extremity Muscles in Sciuridae. Тр. Зоол. Ин-та Ан СССР. 33, 283–318. (In Russian).

Vizcaíno, S. F., and Milne, N. (2002). Structure and Function in Armadillo Limbs (Mammalia: Xenarthra: Dasypodidae). *J. Zoolog.* 257 (1), 117–127. doi:10.1017/s0952836902000717

Walter, R. M., and Carrier, D. R. (2009). Rapid Acceleration in Dogs: Ground Forces and Body Posture Dynamics. *J. Exp. Biol.* 212, 1930–1939. doi:10.1242/jeb.023762

Ward, S. C., and Sussman, R. W. (1979). Correlates Between Locomotor Anatomy and Behavior in Two Sympatric Species of *Lemur*. *Am. J. Phys. Anthropol.* 50, 575–590. doi:10.1002/ajpa.1330500409

Westneat, M. W. (2003). A Biomechanical Model for Analysis of Muscle Force, Power Output and Lower Jaw Motion in Fishes. *J. Theor. Biol.* 223, 269–281. doi:10.1016/s0022-5193(03)00058-4

Westneat, M. W. (1994). Transmission of Force and Velocity in the Feeding Mechanisms of Labrid Fishes (Teleostei, Perciformes). *Zoomorphology* 114, 103–118. doi:10.1007/bf00396643

Wickham, H., Averick, M., Bryan, J., Chang, W., McGowan, L., François, R., et al. (2019). Welcome to the Tidyverse. *Joss* 4, 1686. doi:10.21105/joss.01686

Wickham, H., and Bryan, J. (2019). *Readxl: Read Excel Files. R Package*. Version 1.3.1. Available at: https://CRAN.R-project.org/package=readxl.

Wilson, D. E., and Mittermeier, A. (2011). Handbook of the Mammals of the World. *Lagomorphs and Rodents* 6, 1. Lynx Ediciones.

Wilson, L. A., and Geiger, M. (2015). "Diversity and Evolution of Femoral Variation in Ctenohystrica," in *Evolution of the Rodents*. Editors P. G. Cox and L. Hautier, 510–538.

Witte, H., Biltzinger, J., Hackert, R., Schilling, N., Schmidt, M., Reich, C., et al. (2002). Torque Patterns of the Limbs of Small Therian Mammals During Locomotion on Flat Ground. *J. Exp. Biol.* 205, 1339–1353. doi:10.1242/jeb.205.9.1339

Wölfer, J., Amson, E., Arnold, P., Botton-Divet, L., Fabre, A. C., Heteren, A. H., et al. (2019). Femoral Morphology of Sciuromorph Rodents in Light of Scaling and Locomotor Ecology. *J. Anat.* 234, 731–747. doi:10.1111/joa.12980

Wölfer, J., Aschenbach, T., Michel, J., and Nyakatura, J. A. (2021). Mechanics of Arboreal Locomotion in Swinhoe's Striped Squirrels: A Potential Model for Early Euarchontoglires. *Front. Ecol. Evol.* 9. doi:10.3389/fevo.2021.636039

Wölfer, J., and Nyakatura, J. A. (2019). Weighing Homoplasy Against Alternative Scenarios with the Help of Macroevolutionary Modeling: A Case Study on Limb Bones of Fossorial Sciuromorph Rodents. *Ecol. Evol.* 9, 11025–11039. doi:10.1002/ece3.5592

Zajac, F. E. (1992). How Musculotendon Architecture and Joint Geometry Affect the Capacity of Muscles to Move and Exert Force on Objects: A Review with Application to Arm and Forearm Tendon Transfer Design. *J. Hand Surg.* 17, 799–804. doi:10.1016/0363-5023(92)90445-u

Zumwalt, A. C., Hamrick, M., and Schmitt, D. (2006). Force Plate for Measuring the Ground Reaction Forces in Small Animal Locomotion. *J. Biomech.* 39, 2877–2881. doi:10.1016/j.jbiomech.2005.10.006

Conflict of Interest: The authors declare that the research was conducted in the absence of any commercial or financial relationships that could be construed as a potential conflict of interest.

frontiers | Frontiers in Bioengineering and Biotechnology

ORIGINAL RESEARCH
published: 03 June 2022
doi: 10.3389/fbioe.2022.807777

Fore-Aft Asymmetry Improves the Stability of Trotting in the Transverse Plane: A Modeling Study

Mau Adachi [1], Shinya Aoi [2], Tomoya Kamimura [3], Kazuo Tsuchiya [2] and Fumitoshi Matsuno [1]**

[1]Department of Mechanical Engineering and Science, Graduate School of Engineering, Kyoto University, Kyoto, Japan, [2]Department of Aeronautics and Astronautics, Graduate School of Engineering, Kyoto University, Kyoto, Japan, [3]Department of Electrical and Mechanical Engineering, Nagoya Institute of Technology, Nagoya, Japan

Quadrupedal mammals have fore-aft asymmetry in their body structure, which affects their walking and running dynamics. However, the effects of asymmetry, particularly in the transverse plane, remain largely unclear. In this study, we examined the effects of fore-aft asymmetry on quadrupedal trotting in the transverse plane from a dynamic viewpoint using a simple model, which consists of two rigid bodies connected by a torsional joint with a torsional spring and four spring legs. Specifically, we introduced fore-aft asymmetry into the model by changing the physical parameters between the fore and hind parts of the model based on dogs, which have a short neck, and horses, which have a long neck. We numerically searched the periodic solutions for trotting and investigated the obtained solutions and their stability. We found that three types of periodic solutions with different foot patterns appeared that depended on the asymmetry. Additionally, the asymmetry improved gait stability. Our findings improve our understanding of gait dynamics in quadrupeds with fore-aft asymmetry.

Keywords: fore-aft asymmetry, quadrupedal trotting, transverse dynamics, gait stability, simple model

OPEN ACCESS

Edited by:
John R. Hutchinson, Royal Veterinary College (RVC), United Kingdom

Reviewed by:
Delyle T. Polet, Royal Veterinary College (RVC), United Kingdom
Guoyuan Li, NTNU Ålesund, Norway

***Correspondence:**
Mau Adachi
astpluto@gmail.com
Fumitoshi Matsuno, matsuno.fumitoshi.8n@kyoto-u.ac.jp

Specialty section:
This article was submitted to Biomechanics, a section of the journal Frontiers in Bioengineering and Biotechnology

Received: *02 November 2021*
Accepted: *16 March 2022*
Published: *03 June 2022*

Citation:
Adachi M, Aoi S, Kamimura T, Tsuchiya K and Matsuno F (2022) Fore-Aft Asymmetry Improves the Stability of Trotting in the Transverse Plane: A Modeling Study. Front. Bioeng. Biotechnol. 10:807777. doi: 10.3389/fbioe.2022.807777

1 INTRODUCTION

Quadrupedal mammals have fore-aft asymmetry in their body structure. For example, their fore and hind legs have not only different skeletal structures but also different masses and properties of muscles (Payne et al., 2005a, b; Williams et al., 2008a, b). During their locomotion, while the fore legs generate more braking forces than the hind legs, the hind legs do more propulsive forces than the fore legs (Lee et al., 1999; Bertram and Gutmann 2008). Furthermore, the fore and hind legs have different connections to the body; while the fore legs are suspended by muscles through the scapula, the hind legs are connected to the pelvis *via* skeletal articulation (Hildebrand and Goslow, 2001). In addition, the front part of the bodies of horses and dogs is heavier than the hind part because the front part has a head and neck and the thorax has higher density and larger mass than the abdomen (Buchner et al., 1997; Jones et al., 2018). To compensate for the asymmetric mass distribution, the forelegs generally support more of the body weight than the hind legs (Rollinson and Martin, 1981; Merkens et al., 1993; Lee et al., 1999). Additionally, horses, which have a long neck to increase fore-aft asymmetry, use not only their forelegs but also their thoracic muscles to support their weight (Payne et al.,. 2005b). These asymmetric body structures affect their walking and running dynamics. However, the effects of fore-aft asymmetry on quadrupedal locomotion remain largely unclear. To date, these effects have been investigated in the sagittal plane using both biological approaches (Lee et al., 2004;

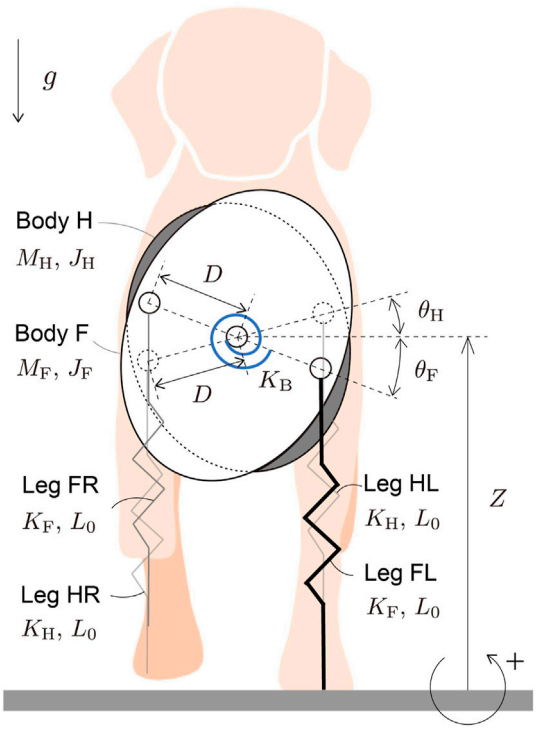

FIGURE 1 | Our model composed of two rigid bodies and four massless springs. The bodies are connected at their COM by a joint with a torsional spring.

Lee, 2010) and modeling approaches (Zou and Schmiedeler, 2006; Yamada et al., 2022). For example, in a modeling study using a simple model, researchers demonstrated that the forward offset of the center of mass (COM) position reduces the stability of bounding gait in the sagittal plane (Zou and Schmiedeler, 2006). The effects of asymmetry are crucial not only in the sagittal plane but also in the transverse plane. However, few studies have investigated the effects in the transverse plane; thus, the effects remain unclear.

In this study, we investigate the effects of fore-aft asymmetry on trotting in the transverse plane using a simple model. Although quadrupedal mammals use various gaits, such as walking, trotting, and galloping, depending on their locomotion speed, trotting is widespread among quadrupedal mammals (Muybridge, 1957; Alexander and Jayes, 1983). In trotting, their four legs are used in two pairs, that is, the diagonal fore and hind legs, and these two pairs of legs touch the ground alternately (Hildebrand, 1965, 1968). During such trotting, quadrupedal mammals basically keep their bodies parallel to the ground unlike other gaits (Muybridge, 1957; Heglund et al., 1974; Dunbar et al., 2008). Although the diagonal touchdown generates moments to rotate the fore and hind parts of the body in opposite directions not only in the sagittal plane but also in the transverse plane, which makes it difficult to maintain their posture during trotting, quadrupedal mammals stabilize their body using trunk muscles (Schilling and Carrier, 2009). In our previous work (Adachi et al., 2020), we used a simple fore-aft symmetrical model in the transverse plane, which had two segmented bodies connected by a torsional joint with a torsional spring and four spring legs, and found that the appropriate stiffness in the body and legs produced stable trotting. However, the fore-aft asymmetry makes differences between the moments by the diagonal touchdown, which changes the gait characteristics and stability. To investigate the effects of fore-aft asymmetry on transverse dynamics in trotting, we extend our previous model to incorporate fore-aft asymmetry and examine the asymmetry effects on trotting from a dynamic viewpoint.

2 MATERIALS AND METHODS

2.1 Model

Each leg of a quadrupedal mammal has only 10% or less of the total mass (Buchner et al., 1997; Amit et al., 2009; Kilbourne and Hoffman, 2013). The main function of the legs is to produce reaction forces from the ground to support the body and can be represented by a spring (e.g., Full and Koditschek, 1999). Because stabilization of the body posture is crucial to generate stable gait, we focused on the dynamics of the body posture in the transverse plane and used massless springs for the legs in our model. Specifically, the model consists of two rigid bodies and four massless springs (**Figure 1**). The two rigid bodies represent the fore and hind parts of the body (Bodies F and H, respectively), and are connected by a joint at their COM. The four massless springs represent the legs (Legs FL, FR, HL, and HR). Legs *i*L and *i*R (i = F, H) are connected to Body i on the left and right sides, respectively. Because mediolateral ground reaction forces (GRFs) are much smaller than vertical forces during trotting of quadrupedal mammals (Merkens et al., 1993; Gillette and Angle, 2008), we ignore the horizontal dynamics of our model, as in previous studies (Berkemeier, 1998; De and Koditschek, 2018) and focus on the vertical and rotational movements of the bodies. Z is the vertical position of the COM of the bodies. θ_i (i = F, H) is the angle of Body i relative to the horizontal line. L_{ij} (i = F, H, j = L, R) is the length of Leg ij. The mass and moment of inertia around the COM of Body i (i = F, H) are M_i and I_i, respectively. The body joint has a torsional spring with a spring constant of K_B that produces the body torsional movement. The body spring is at the equilibrium position when the bodies have the same posture ($\theta_F = \theta_H$). The spring constants of the forelegs (Legs FL and FR) and hind legs (Legs HL and HR) are K_F and K_H, respectively. All the legs have the same nominal length L_0. The distance between the COM of the bodies and the root of the leg spring is D for both the fore and hind bodies. The gravitational acceleration is g.

When Leg ij (i = F, H, j = L, R) is in the air, it remains vertical and maintains the nominal length ($L_{ij} = L_0$). When the tip touches the ground, the leg spring starts to compress to receive a GRF. When its length returns to the nominal length ($L_{ij} = L_0$) after compression, the tip leaves the ground. Because touchdowns and liftoffs occur at the nominal length, our model is energy conservative.

The equations of motion of the model are given by

$$(M_{\mathrm{F}}+M_{\mathrm{H}})\ddot{Z}+\sum_{i\in\mathcal{I},\ j\in\mathcal{J}}F_{ij}+(M_{\mathrm{F}}+M_{\mathrm{H}})g=0 \tag{1a}$$

$$I_i\ddot{\theta}_i+\sum_{j\in\mathcal{J}}F_{ij}D_j\cos\theta_i+K_{\mathrm{B}}\left(\theta_i-\varphi_i\right)=0\quad i=\mathrm{F,H}, \tag{1b}$$

$\mathcal{I}=\{\mathrm{F,H}\}$, $\mathcal{J}=\{\mathrm{L,R}\}$, $\varphi_{\mathrm{F}}=\theta_{\mathrm{H}}$, $\varphi_{\mathrm{H}}=\theta_{\mathrm{F}}$, $D_{\mathrm{L}}=D$, $D_{\mathrm{R}}=-D$, and

$$F_{ij}=\begin{cases}K_i\left(L_{ij}-L_0\right) & \text{stance phase}\\ 0 & \text{swing phase}\end{cases}\quad i=\mathrm{F,H},\ j=\mathrm{L,R},$$

where $L_{ij}=Z+D_j\sin\theta_i$. Leg ij touches the ground when its tip reaches the ground and leaves the ground when its length returns to the nominal length. These conditions are both given by

$$R_{ij}(\mathrm{Q})=Z+D_j\sin\theta_i-L_0=0\quad i=\mathrm{F,H},\ j=\mathrm{L,R}, \tag{2}$$

where $Q=[Z\ \theta_{\mathrm{F}}\ \theta_{\mathrm{H}}\ \dot{Z}\ \dot{\theta}_{\mathrm{F}}\ \dot{\theta}_{\mathrm{H}}]^{\mathrm{T}}$.

To generalize the dynamics of the model, we non-dimensionalize the governing equations using the mass scale $M_{\mathrm{F}}+M_{\mathrm{H}}$, length scale D, and time scale $\sqrt{D/g}$. The dimensionless equations of motion are given by

$$\ddot{z}+\sum_{i\in\mathcal{I},\ j\in\mathcal{J}}f_{ij}+1=0 \tag{3a}$$

$$\mu_i\ddot{\theta}_i+\sum_{j\in\mathcal{J}}d_jf_{ij}\cos\theta_i+k_{\mathrm{B}}\left(\theta_i-\varphi_i\right)=0\quad i=\mathrm{F,H}, \tag{3b}$$

$$z=(Z-L_0)/D,\ \tau=t/\sqrt{D/g},$$

$$f_{ij}=\begin{cases}k_i\left(z+d_j\sin\theta_i\right) & \text{stance phase}\\ 0 & \text{swing phase}\end{cases}\quad i=\mathrm{F,H},\ j=\mathrm{L,R},$$

$\mu_i=I_i/((M_{\mathrm{F}}+M_{\mathrm{H}})D^2)$, $k_i=K_iD/((M_{\mathrm{F}}+M_{\mathrm{H}})g)$ $(i=\mathrm{F,H})$, $k_{\mathrm{B}}=K_{\mathrm{B}}/((M_{\mathrm{F}}+M_{\mathrm{H}})gD)$, $d_{\mathrm{L}}=1$, $d_{\mathrm{R}}=-1$, and hereafter, $\dot{\star}$ indicates the derivative of variable $\star$ with respect to τ. The dimensionless condition for the touchdown and liftoff of Leg ij is given by

$$r_{ij}(q)=z+d_j\sin\theta_i=0\quad i=\mathrm{F,H},\ j=\mathrm{L,R}, \tag{4}$$

where $q=[z\ \theta_{\mathrm{F}}\ \theta_{\mathrm{H}}\ \dot{z}\ \dot{\theta}_{\mathrm{F}}\ \dot{\theta}_{\mathrm{H}}]^{\mathrm{T}}$.

2.2 Gait Assumptions

During trotting, the four legs work in two pairs. Specifically, the diagonal legs (Legs FL and HR, and Legs FR and HL) are paired. These two pairs touch the ground alternately. In this study, we focus on the motions during which one pair of legs touches and leaves the ground and then the other pair does the same. We assume that each leg touches the ground only once in a single gait cycle. Additionally, when one leg of a pair touches the ground, it never leaves the ground until the other leg of that pair touches the ground, that is, a double stance phase exists for each pair. We define the following four phases: flight (F), fore stance (FS), hind stance (HS), and double stance (DS) phases. In the flight phase, all the legs are in the air. In the fore (hind) stance phase, only the fore (hind) leg of a pair is in contact with the ground. In the double stance phase, both legs of a pair are in contact with the ground.

Because the model is left-right symmetric, the motion during which one pair touches and leaves the ground, and the motion during which the other pair touches and leaves the ground can be expressed using the same expression when the left and right sides of the model are reversed. Specifically, we use $q^+=B_{\mathrm{LR}}q^-$ at the apex (i.e., at $\dot{z}=0$ in the flight phase), where $B_{\mathrm{LR}}=\mathrm{diag}(1,-1,-1,1,-1,-1)$. In this study, $\star^+$ and $\star^-$ indicate the states immediately after and before reversing, respectively. Therefore, we focus on the touchdowns and liftoffs for only one pair of legs, specifically using the pair of legs FL and HR.

The motion from one apex to the next apex is obtained from the phase transitions between the four phases (i.e., flight, fore stance, hind stance, and double stance phases), as illustrated in **Figure 2**. These phase transitions occur when the corresponding conditions (Conditions 1–12 in **Figure 2**) are satisfied. For example, the transition from the flight phase to the double stance phase occurs when Condition 2 is satisfied, when Conditions 4 and 5 are sequentially satisfied, or when Conditions 8 and 9 are sequentially satisfied. We use $r_{\mathrm{A}}=0$ to represent the condition where the COM reaches an apex, $r_{\mathrm{F}}=0$ to represent the condition where the fore leg of the pair touches and leaves the ground, $r_{\mathrm{H}}=0$ to represent the condition where the hind leg of the pair touches and leaves the ground, and $r_{\mathrm{D}}=0$ to represent the condition where both legs of the pair simultaneously touch and leave the ground. Specifically, Condition i ($i=1,\ldots,12$) is given by

$$r_i(q)=\begin{cases}r_{\mathrm{A}}(q)=0 & i=1,\ 12\\ r_{\mathrm{D}}(q)=\{r_{\mathrm{F}}(q)\}^2+\{r_{\mathrm{H}}(q)\}^2=0 & i=2,\ 3\\ r_{\mathrm{F}}(q)=0 & i=4,\ 6,\ 9,\ 11\\ r_{\mathrm{H}}(q)=0 & i=5,\ 7,\ 8,\ 10,\end{cases} \tag{5}$$

where $r_{\mathrm{A}}(q)=\dot{z}$, $r_{\mathrm{F}}(q)=r_{\mathrm{FL}}(q)$, and $r_{\mathrm{H}}=r_{\mathrm{HR}}(q)$.

Based on these phase transitions, the motion from one apex to the next apex can be explained using nine sequences (Sequences 1–9), as illustrated in **Figure 2**. In Sequence 1, both legs of the pair touch the ground simultaneously and then leave the ground simultaneously (flight–double stance–flight). In Sequence 2, both legs of the pair touch the ground simultaneously, but the hind leg then leaves the ground earlier than the fore leg (flight–double stance–fore stance–flight). In Sequence 3, both legs of the pair touch the ground simultaneously, but the foreleg then leaves the ground earlier than the hind leg (flight–double stance–hind stance–flight). In Sequence 4, the foreleg touches the ground earlier than the hind leg, but both legs then leave the ground simultaneously (flight–fore stance–double stance–flight). In Sequence 5, the foreleg touches the ground earlier than the hind leg, but the hind leg then leaves the ground earlier than the foreleg (flight–fore stance–double stance–fore stance–flight). In Sequence 6, the fore leg of the pair touches and then leaves the ground earlier than the hind leg (flight–fore stance–double stance–hind stance–flight). Sequences 7–9 are then obtained by exchanging the behavior of the fore and hind legs shown in Sequences 4–6, respectively.

2.3 Search of the Periodic Solutions and Stability Analysis

We search the periodic solutions using a Poincaré map by taking a Poincaré section immediately after the reversal of the left and right sides of the model at the apex ($\dot{z}=0$). Therefore, we define the state on the Poincaré section as

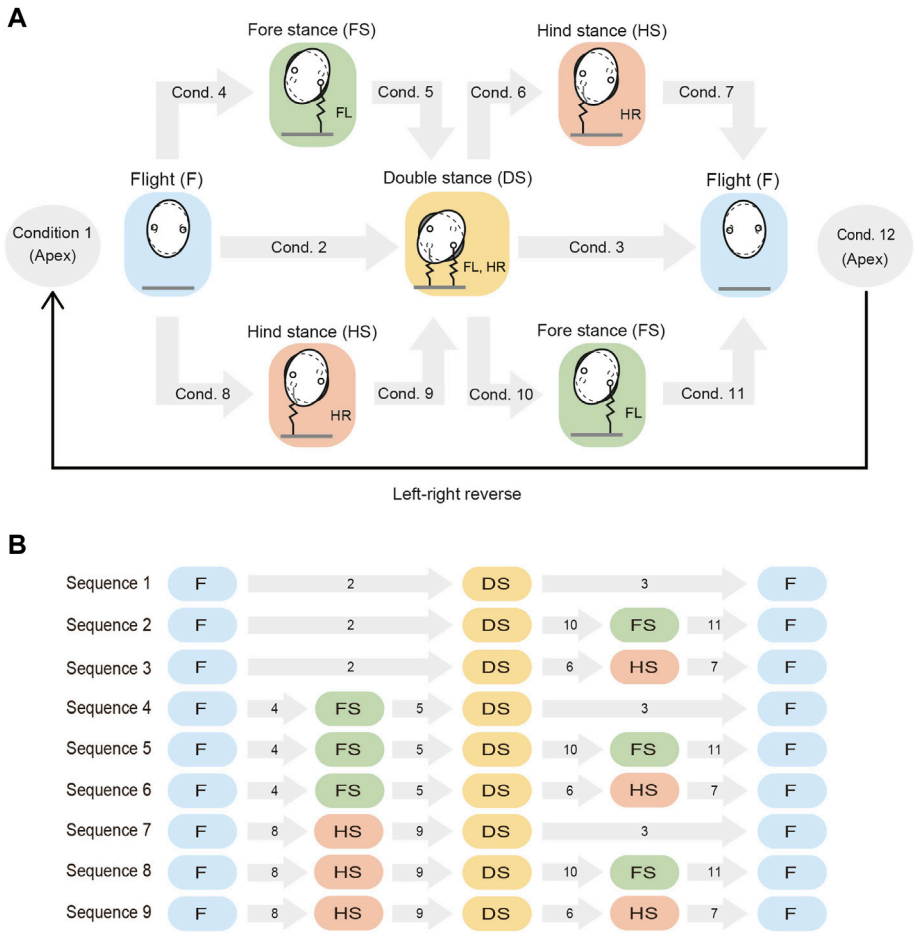

FIGURE 2 | Phase transitions from an apex to the next apex. **(A)** Possible phases and the associated phase transitions. The phase transitions occur when conditions 1–12 are satisfied. The left and right sides of the model are then reversed at the next apex. **(B)** Nine sequences (Sequences 1–9) explain the phase transitions from an apex to the next apex. Each gray arrow with a number indicates the condition of the phase transition. Conditions 1 and 12 are not shown because they are common to all sequences.

$x = [z\ \theta_F\ \theta_H\ \dot{\theta}_F\ \dot{\theta}_H]^T$. The Poincaré map is then denoted by $x_{i+1} = P(x_i)$, where x_i is the state immediately after the reversal at the ith apex. A fixed point x^* on the Poincaré section, which satisfies $x^* = P(x^*)$, corresponds to a periodic solution. We search the periodic solutions numerically by solving the following:

$$S(x^*) = x^* - P(x^*) = 0, \tag{6}$$

where we determine z^* by comparing the simulation results and measured data of animals as described in **Section 2.4**.

We add a perturbation δx_i to the obtained solutions immediately after the reversal at the ith apex. The linearization of the Poincaré map P around x^* yields

$$\delta x_{i+1} = J\delta x_i, \tag{7}$$

where J is the Jacobian matrix of P. If all eigenvalues of J are located inside (inside and on) the unit circle on the complex plane, the periodic solution is asymptotically (marginally) stable; otherwise, the solution is unstable. Because the model is energy conservative, no asymptotically stable solutions exist. Therefore, we simply refer to marginally stable as stable. We define $\Lambda = \max_{i=1,\ldots,5}|\lambda_i|$, where λ_i $(i = 1, \ldots, 5)$ are the eigenvalues of J. If $\Lambda = 1$ is satisfied, the periodic solution is stable; otherwise, the solution is unstable.

2.4 Asymmetric Properties

Although we used the same physical parameters between the fore and hind bodies in the model in our previous study (Adachi et al., 2020), quadrupedal mammals, such as dogs and horses, generally have different physical properties between the fore and hind bodies. In particular, different body masses, moments of inertia, and leg stiffnesses greatly affect the locomotion dynamics. Because the difference of the mass between the fore and hind bodies has no effect on the equations of motion **Eq. 3**) of our model in the transverse plane (only the total mass has effects), we focus on the differences in the moments of inertia (μ_F and μ_H) and leg stiffnesses (k_F and k_H). To highlight the fore-aft asymmetry between these parameters, we define the averaged values of the

moments of inertia and leg stiffnesses between the fore and hind bodies as μ_0 and k_0, respectively, and represent these four properties using asymmetric parameters ε_μ and ε_k as follows:

$$\mu_F = (1 + \varepsilon_\mu)\mu_0 \tag{8a}$$

$$\mu_H = (1 - \varepsilon_\mu)\mu_0 \tag{8b}$$

$$k_F = (1 + \varepsilon_k)k_0 \tag{8c}$$

$$k_H = (1 - \varepsilon_k)k_0. \tag{8d}$$

$\varepsilon_\mu = \varepsilon_k = 0$ corresponds to the symmetrical model used in our previous work (Adachi et al., 2020). Because the fore body of most quadrupedal mammals is typically heavier than the hind body (Rollinson and Martin, 1981) and the forelimbs support greater loads than the hind limbs (Merkens et al., 1993; Lee et al., 1999, 2004; Witte et al., 2004), we use ε_μ, $\varepsilon_k \geq 0$.

In this study, we use two types of physical parameter sets based on large breed dogs (e.g., German Shepherd), which have a short neck, and warmblood horses, which have a long neck. For dogs, we use $M_F + M_H = 35$ kg and $I_F + I_H = 0.43$ kgm^2 based on Amit et al. (2009) and Jones et al. (2018) and $D = 0.10$ m based on the distance between the left and right hip joints of the hind limbs (Carrier et al., 2005; Belhaoues et al., 2020), which yields $\mu_0 = 0.62$. For horses, we use $M_F + M_H = 538$ kg and $I_F + I_H = 37.5$ kgm^2 based on Buchner et al. (1997) and $D = 0.22$ m based on Gómez et al. (2009), which yields $\mu_0 = 0.72$. We also estimate ε_μ based on Buchner et al. (1997), Amit et al. (2009), and Jones et al. (2018) and ε_k based on Herr et al. (2002), which results in $\varepsilon_\mu = 0.12$ and $\varepsilon_k = 0.21$ for dogs and $\varepsilon_\mu = 0.14$ and $\varepsilon_k = 0.25$ for horses.

For the symmetric model ($\varepsilon_\mu = \varepsilon_k = 0$) in our previous study (Adachi et al., 2020), the ratio of the leg and body-torsional spring constants, that is, $\kappa = k_B/k_0$, mainly determined the characteristics of the periodic solutions. In this study, we use κ instead of k_B. We determine k_0 and κ by comparing the simulation results and measured data of dogs and horses. Specifically, we first use the symmetric model ($\varepsilon_\mu = \varepsilon_k = 0$, $\mu_0 = 0.62$ in the dog model and 0.72 in the horse model) to determine k_0, κ, and $z^\star$ so that the half cycle duration $\tau^\star$ (duration from an apex to the next apex), magnitude of the vertical movement δ_z, and duty ratio averaged among the four legs β_0 of the periodic solution minimize $V = c_1(\tau^\star - \bar{\tau}^\star)^2 + c_2(\delta_z - \bar{\delta}_z)^2 + c_3(\beta_0 - \bar{\beta}_0)^2$, where c_1, c_2, and c_3 are the coefficients and $\bar{\tau}^\star$, $\bar{\delta}_z$, and $\bar{\beta}_0$ are the measured data of $\tau^\star$, δ_z, and β_0, respectively, during fast trotting in animals (Froude number is about 1.3; 3.5 m/s for dogs and 4.5 m/s for horses). In particular, we use $\bar{\tau}^\star = 1.9$ [0.2 s (Heglund et al., 1974; Maes et al., 2008)], $\bar{\delta}_z = 0.11$ [0.011 m (Farley et al., 1993; Blickhan and Full, 1993)], and $\bar{\beta}_0 = 0.46$ (Fischer and Lilje, 2016; Maes et al., 2008) for the dog model and $\bar{\tau}^\star = 1.7$ [0.25 s (Heglund et al., 1974; Heglund and Taylor, 1988)], $\bar{\delta}_z = 0.11$ [0.024 m (Blickhan and Full, 1993; Farley et al., 1993)], and $\bar{\beta}_0 = 0.4$ (Dutto et al., 2004; Bullimore and Burn, 2006) for the horse model. Because $\bar{\tau}^\star$ is larger than $\bar{\delta}_z$ and $\bar{\beta}_0$, we use $c_1 = 0.1$ and $c_2 = c_3 = 1$. Using the obtained values of k_0, κ, and $z^\star$, we then introduce asymmetry (ε_k, ε_μ) in the model ($\varepsilon_\mu = 0.12$ and $\varepsilon_k = 0.21$ in dogs and $\varepsilon_\mu = 0.14$ and $\varepsilon_k = 2.5$ in horses). **Table 1** summarizes the parameters of the dog and horse models.

TABLE 1 | Parameters of dog and horse models. μ_0, ε_μ, and ε_k are determined based on the measured data of animals and k_0, κ, and $z^\star$ are determined through the optimization of simulation.

Parameter	Value	
	Dog	Horse
$M_F + M_H$ (kg)	35[a]	538[d]
I_F (kgm^2)	0.26[a]	23.4[d]
I_H (kgm^2)	0.17[a]	14.1[d]
D (m)	0.1[b]	0.22[e]
K_F/K_H	1.27[c]	1.33[c]
μ_0	0.62	0.72
ε_μ	0.12	0.14
k_0	1.5	2.2
ε_k	0.21	0.25
κ	0.20	0.21
$z^\star$	0.06	0.06

a: Amit et al. (2009); Jones et al. (2018), b: Carrier et al. (2005); Belhaoues et al. (2020), c: Herr et al. (2002), d: Buchner et al. (1997), e: Gómez et al. (2009).

3 RESULTS

3.1 Effects of Asymmetry on the Gait Pattern

We obtained a periodic solution uniquely through the optimization in the symmetric model for dogs ($\mu_0 = 0.62$, $\varepsilon_\mu = \varepsilon_k = 0$), which yielded $k_0 = 1.5$, $\kappa = 0.2$, and $z^\star = 0.06$. By changing ε_μ and ε_k based on the symmetric periodic solution, we uniquely obtained the periodic solution for each set of (ε_μ, ε_k). **Figure 3** shows the time profiles of typical periodic solutions. Regardless of ε_μ and ε_k, the curve of z is sinusoidal and those of θ_F and θ_H are parabolic. When $\varepsilon_\mu = \varepsilon_k = 0$, the magnitudes of θ_F and θ_H were identical and flight–double stance phase transition directly occurred (**Figure 3A**), which resulted in Sequence 1. When increasing ε_μ with $\varepsilon_k = 0$, the magnitude of z remained almost unchanged, whereas that of θ_F decreased and that of θ_H increased (**Figure 3B**). This made the stance phase durations of the hind legs longer than those of the forelegs and resulted in the appearance of the hind stance phase between the flight and double stance phases, which resulted in Sequence 9. By contrast, when we increased ε_k with $\varepsilon_\mu = 0$, the magnitude of θ_F increased and that of θ_H decreased (**Figure 3C**), which is opposite to the result when we increased ε_μ in **Figure 3B**. This made the stance phase durations of the fore legs longer than those of the hind legs and resulted in the appearance of the fore stance phase between the flight and double stance phases, which means Sequence 5. Furthermore, we found a proportional relationship between ε_μ and ε_k ($\varepsilon_\mu = a\varepsilon_k$, $a = 0.69$), which never changed the profiles of θ_F and θ_H from those in the symmetric model ($\varepsilon_\mu = \varepsilon_k = 0$) and maintained Sequence 1 (**Figure 3D**). Sequence 5 appeared for $\varepsilon_\mu < a\varepsilon_k$ and Sequence 9 appeared for $\varepsilon_\mu > a\varepsilon_k$ (**Figure 3E**). The estimated values of the asymmetric parameters in the dog model ($\varepsilon_\mu = 0.12$ and $\varepsilon_k = 0.21$) satisfied $\varepsilon_\mu < a\varepsilon_k$ and thus generated Sequence 5. We compared the locomotion characteristics (half gait cycle duration, vertical displacement of COM, roll amplitude of the hind body, maximum vertical GRFs of the fore and hind legs, and duty ratios of the fore and hind legs) between simulation results using the estimated parameters of dogs and the measured data of dogs in **Table 2**. The locomotion characteristics of the

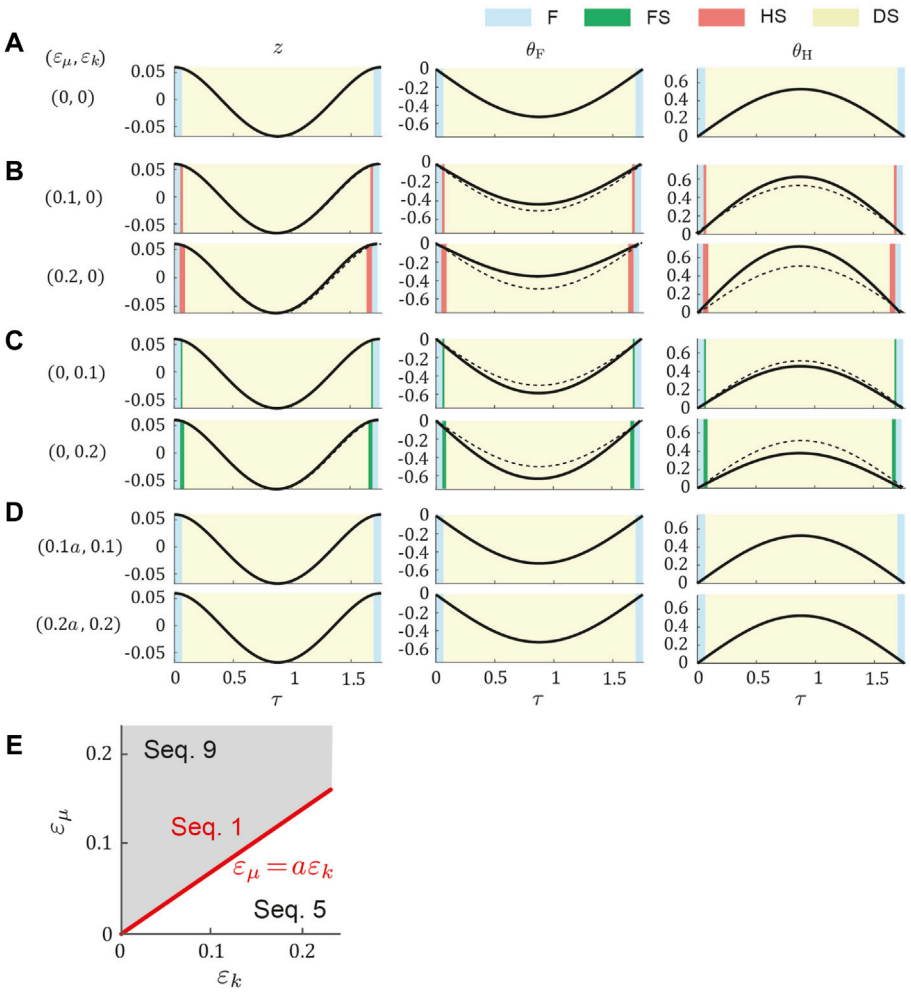

FIGURE 3 | Gait dependence on ε_k and ε_μ in dog model. Time profile of periodic solution **(A)** for the symmetric model ($\varepsilon_k = \varepsilon_\mu = 0$) and those for two values of **(B)** ε_μ with $\varepsilon_k = 0$, **(C)** ε_k with $\varepsilon_\mu = 0$, and **(D)** ε_k with $\varepsilon_\mu = a\varepsilon_k$. Cyan, green, pink, and yellow regions indicate flight (F), fore stance (FS), hind stance (HS), and double stance (DS), respectively. Dotted lines indicate the periodic solution of the symmetric model. **(E)** Gait dependence on ε_k and ε_μ.

TABLE 2 | Comparison of locomotion characteristics between models and animals using dimensionless values.

	Dog		Horse	
	Model	**Animal**	**Model**	**Animal**
Half cycle duration	1.75	1.9[a]	1.54	1.7[f]
Vertical COM displacement	0.12	0.11[b]	0.11	0.11[b]
Hind roll amplitude (deg)	29	6[c]	20	5[g]
Fore maximum GRF	1.1	1.5[d]	1.2	1.2[h]
Hind maximum GRF	0.7	0.8[d]	0.6	0.8[h]
Fore duty factor	0.47	0.48[e]	0.45	0.42[i]
Hind duty factor	0.46	0.44[e]	0.44	0.38[i]

a: Heglund et al. (1974); Maes et al. (2008), b: Farley et al. (1993); Blickhan and Full (1993), c: Fischer et al. (2018), d: Voss et al. (2010), e: Fischer and Lilje (2016); Maes et al. (2008), f: Heglund et al. (1974); Heglund and Taylor (1988), g: Byström et al. (2021), h: Merkens et al. (1993); Witte et al. (2004), i: Dutto et al. (2004); Bullimore and Burn (2006).

simulation results are consistent with those of the measured data except for the roll amplitude of the hind body.

Similar to the dog model, we obtained a periodic solution and $k_0 = 2.2$, $\kappa = 0.21$, and $z^* = 0.06$ through the optimization in the symmetric model for horses ($\mu_0 = 0.72$, $\varepsilon_\mu = \varepsilon_k = 0$). When changing ε_μ and ε_k, we also achieved Sequences 1, 5, and 9 depending on $\varepsilon_\mu \lessgtr a\varepsilon_k$, where $a = 0.69$ (see **Supplementary Appendix SA**). The estimated values of the asymmetric parameters in the horse model ($\varepsilon_\mu = 0.14$ and $\varepsilon_k = 0.25$) also satisfied $\varepsilon_\mu < a\varepsilon_k$ and generated Sequence 5. We compared the simulated locomotion characteristics using the estimated parameters of horses with the measured data of horses in **Table 2**. The locomotion characteristics of the simulation results of the horse model are also consistent with those of the measured data except for the roll amplitude of the hind body.

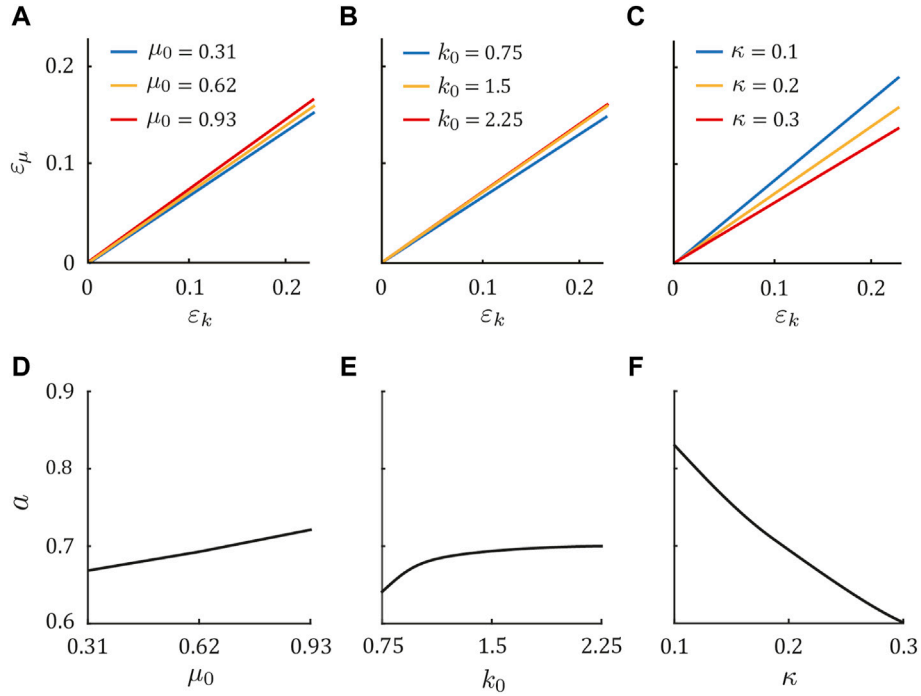

FIGURE 4 | Gait dependence on physical parameters in the dog model. Condition of ε_k and ε_μ ($\varepsilon_\mu = a\varepsilon_k$) to achieve Sequence 1 for three values of **(A)** μ_0, **(B)** k_0, and **(C)** κ, while holding the other parameters constant at $\mu_0 = 0.62$, $k_0 = 1.5$, and $\kappa = 0.2$. Sequences 5 and 9 appeared when $\varepsilon_\mu < a\varepsilon_k$ and $\varepsilon_\mu > a\varepsilon_k$, respectively. Dependence of a on **(D)** μ_0, **(E)** k_0, and **(F)** κ.

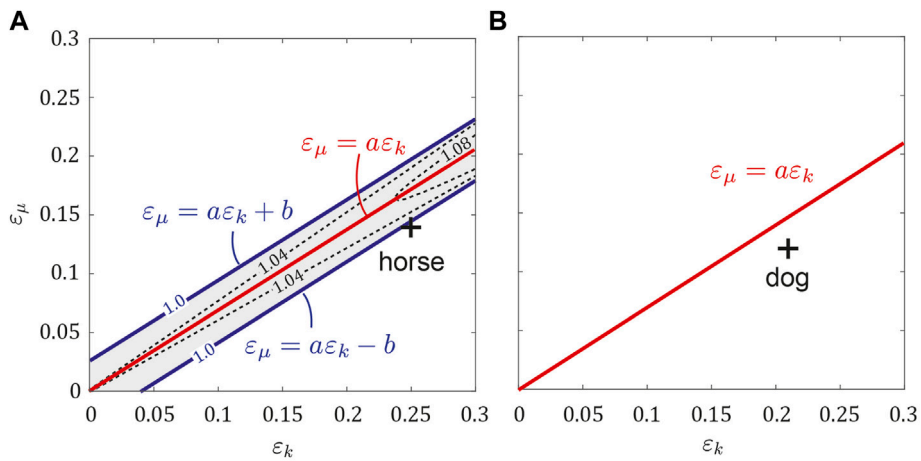

FIGURE 5 | Stability of periodic solutions for ε_μ and ε_k. Contour of the maximum eigenvalue Λ in the **(A)** horse model and **(B)** dog model. White and gray regions indicate the stable and unstable regions, respectively. $\varepsilon_\mu = a\varepsilon_k \pm b$ corresponds to the boundary of $\Lambda = 1$. $b > 0$ in the horse model, whereas $b = 0$ in the dog model. Crosses indicate the estimated values of ε_μ and ε_k in animals.

Next, we investigated the phase transition of the periodic solution by independently changing μ_0, k_0, and κ by ± 50% from the dog parameter set ($\mu_0 = 0.62$, $k_0 = 1.5$, and $\kappa = 0.2$) in **Figure 4**. In the same manner as the above results, Sequences 1, 5, and 9 appeared for $\varepsilon_\mu = a\varepsilon_k$, $\varepsilon_\mu < a\varepsilon_k$, and $\varepsilon_\mu > a\varepsilon_k$, respectively. Although the coefficient a changed slightly when μ_0 and k_0 increased (**Figures 4A,B,D,E**), it largely decreased as κ increased (**Figures 4C,F**). These tendencies were also observed in the horse model (see **Supplementary Appendix SB**).

3.2 Effects of Asymmetry on Gait Stability

We investigated the stability of the obtained periodic solutions for ε_k and ε_μ using the horse parameter set (μ_0, k_0, κ) = (0.72, 2.2, 0.21) by calculating the maximum eigenvalue Λ of the Jacobian

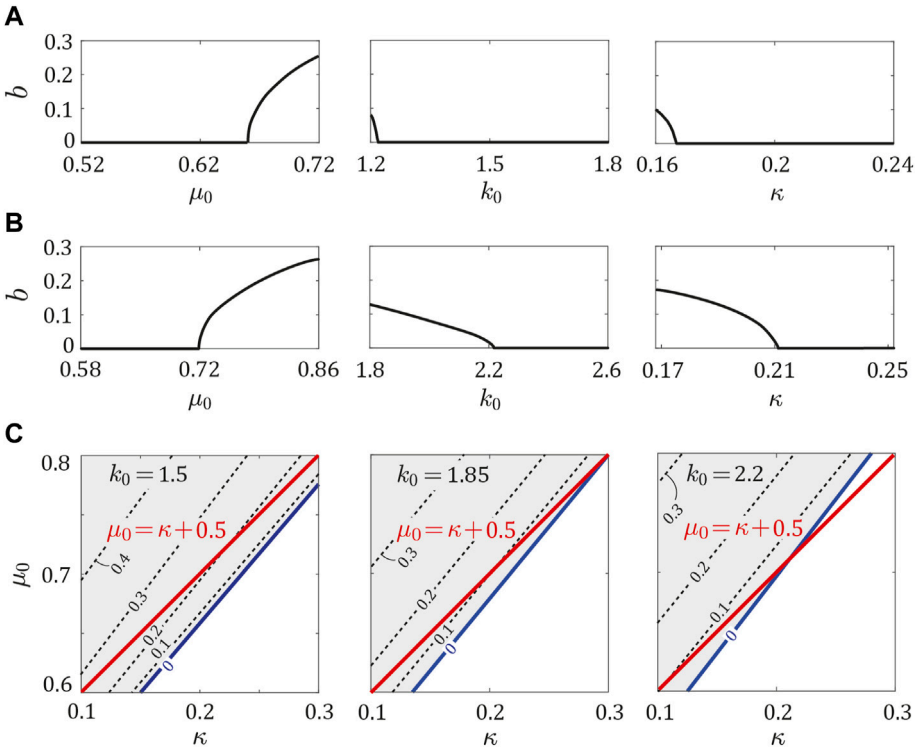

FIGURE 6 | Dependence of b on μ_0, k_0, and, κ. b vs., μ_0, k_0, and, κ using the parameter sets for **(A)** dogs and **(B)** horses, while holding the other parameters constant at (μ_0, k_0, κ) = (0.62, 1.5, 0.2) for dogs and (0.72, 2.2, 0.21) for horses. **(C)** Contour of b around $\mu_0 = \kappa + 0.5$ for $k_0 = 1.5$, 1.85, and 2.2. Red and blue lines indicate $\mu_0 = \kappa + 0.5$ and boundary of $b = 0$ and $b > 0$, respectively. White and gray regions indicate $b = 0$ and $b > 0$, respectively.

matrix of the Poincaré map (**Figure 5A**). When $\varepsilon_\mu = a\varepsilon_k$ was satisfied (including $\varepsilon_k = \varepsilon_\mu = 0$), Λ was much larger than 1 and the periodic solutions were highly unstable (the instability increased as ε_k increased). As the distance of (ε_k, ε_μ) from $\varepsilon_\mu = a\varepsilon_k$ increased, Λ decreased. The solutions became stable with $\Lambda = 1$ when (ε_k, ε_μ) moved across two parallel lines $\varepsilon_\mu = a\varepsilon_k \pm b$, where $b = 0.02$. This means that the trotting of the symmetric horse model was unstable, whereas fore-aft asymmetry stabilized it. The estimated asymmetric parameters of horses ($\varepsilon_\mu = 0.14$ and $\varepsilon_k = 0.25$) satisfied $\varepsilon_\mu < a\varepsilon_k - b$, which indicates that the trotting of horses was stable. By contrast, the periodic solutions for the dog parameter set (μ_0, k_0, κ) = (0.62, 1.5, 0.2) were always stable for $0 \leq \varepsilon_\mu \leq 0.3$ and $0 \leq \varepsilon_k \leq 0.3$, including the symmetric case $\varepsilon_k = \varepsilon_\mu = 0$ (**Figure 5B**). This result corresponds to $b = 0$ in the above horse model. Therefore, trotting of dogs was also stable with respect to the estimated asymmetric parameters of dogs ($\varepsilon_\mu = 0.12$ and $\varepsilon_k = 0.21$).

Next, we investigated the stability of the periodic solutions in the asymmetric model (ε_k, $\varepsilon_\mu \geq 0$) by independently changing μ_0, k_0, and κ from the parameter sets of dogs and horses. We found that $\varepsilon_\mu = a\varepsilon_k \pm b$ determined the stability for both cases in the same manner as that for the above results. Specifically, if $b = 0$, the periodic solutions were stable regardless of ε_μ and ε_k. By contrast, if $b > 0$, while the periodic solutions were unstable when $\varepsilon_\mu = \varepsilon_k = 0$, they became stable when $\varepsilon_\mu \geq a\varepsilon_k + b$ or $\varepsilon_\mu \leq a\varepsilon_k - b$. Therefore, although large asymmetry was necessary as b increased, fore-aft asymmetry stabilized the periodic solutions. We examined whether b depended on μ_0, k_0, and κ in the same manner as a in **Figure 4**. Specifically, we investigated b by independently changing μ_0, k_0, and κ by ± 20% from the parameter sets for dogs ($\mu_0 = 0.62$, $k_0 = 1.5$, and $\kappa = 0.2$) and horses ($\mu_0 = 0.72$, $k_0 = 2.2$, and $\kappa = 0.21$) in **Figures 6A,B**, respectively. In both parameter sets for dogs and horses, when μ_0 exceeded a certain value, b increased from 0. When k_0 or κ fell below a certain value, b increased from 0.

In our previous study (Adachi et al., 2020) using the symmetric model ($\varepsilon_\mu = \varepsilon_k = 0$), we demonstrated that k_0 hardly affected the stability of the periodic solutions, and μ_0 and κ mainly determined the stability. Specifically, the periodic solutions were stable when $\mu_0 \leq \kappa + 0.5$ and unstable when $\mu_0 > \kappa + 0.5$. We investigated b around this stability boundary ($\mu_0 = \kappa + 0.5$) with $k_0 = 1.5$, 1.85, and 2.2 in **Figure 6C**, where $k_0 = 1.5$ and $k_0 = 2.2$ correspond to the dog and horse parameters, respectively. For each value of k_0, the boundary between $b = 0$ and $b > 0$ existed around $\mu_0 = \kappa + 0.5$.

4 DISCUSSION

4.1 Effects of Fore-Aft Asymmetry on the Transverse Dynamics of Trotting

Regardless of the dog and horse models, we found periodic solutions, which had several types of phase transitions

depending on the asymmetric parameters ε_μ and ε_k. Specifically, Sequences 1 (flight–double stance–flight), 5 (flight–fore stance–double stance–fore stance–flight), and 9 (flight–hind stance–double stance–hind stance–flight) appeared when $\varepsilon_\mu = a\varepsilon_k$, $\varepsilon_\mu < a\varepsilon_k$, and $\varepsilon_\mu > a\varepsilon_k$, respectively (**Figure 3**), where a depended on the physical parameter set (μ_0, k_0, and κ) as shown in **Figure 4**. For us to understand the mechanism for generating these sequences, understanding the relationship between the averaged angle of the fore and hind bodies ($\theta = (\theta_F + \theta_H)/2$) and torsional angle ($\phi = (\theta_F - \theta_H)/2$) is crucial. Sequence 1 requires simultaneous touchdowns and liftoffs by the paired fore and hind legs. In our previous study (Adachi et al., 2020) using the symmetric model ($\varepsilon_\mu = \varepsilon_k = 0$), we demonstrated that Sequence 1 appeared only when $\theta = 0$, that is, the fore and hind bodies always rotated in the opposite direction ($\theta_F = -\theta_H$). In the present study, we demonstrated that even if the model had asymmetric properties ε_μ and ε_k, the relationship $\varepsilon_\mu = a\varepsilon_k$ produced $\theta_F = -\theta_H$ ($\theta = 0$), which resulted in Sequence 1. This relationship was analytically obtained using perturbation theory (see **Supplementary Appendix SC**). By contrast, because $\varepsilon_\mu \neq a\varepsilon_k$ caused $\theta_F \neq -\theta_H$ ($\theta \neq 0$), other sequences appeared. In particular, when θ and ϕ had the same sign, the rotation of the fore body ($\theta_F = \theta + \phi$) became larger than that of the hind body ($\theta_H = \theta - \phi$), which induced Sequence 5. When θ and ϕ had opposite signs, the rotation of the hind body became larger than that of the fore body, which induced Sequence 9.

In previous studies (Zou and Schmiedeler 2006; Yamada et al., 2022), the researchers used a single rigid body for their simple models to investigate quadrupedal bounding in the sagittal plane and demonstrated that the fore-aft asymmetry of the CoM position of the body reduced gait stability. However, our results demonstrate that even if the trotting of the fore-aft symmetric model with $\varepsilon_\mu = \varepsilon_k = 0$ in the transverse plane was unstable, it was stabilized by introducing ε_μ and ε_k to satisfy $\varepsilon_\mu < a\varepsilon_k - b$ or $\varepsilon_\mu > a\varepsilon_k + b$ (**Figure 5**), where b also depended on the physical parameter set (μ_0, k_0, and κ) as shown in **Figure 6**; that is, fore-aft asymmetry did not reduce gait stability, but rather improved it in the transverse plane. These different effects of asymmetry on gait stability were mainly caused by different effects on the entire dynamics. Specifically, because in previous studies (Zou and Schmiedeler, 2006; Yamada et al., 2022), researchers used a single rigid body in the model and incorporated fore-aft asymmetry in the single body, the asymmetry directly affected the entire dynamics. By contrast, we used two segmented bodies in our model and incorporated fore-aft asymmetries as different properties between the bodies. The fore-aft asymmetries indirectly affected the entire dynamics via the torsional body joint that connected the two bodies.

In this study, the boundary between $b = 0$ and $b > 0$ existed near $\mu_0 = \kappa + 0.5$ in the μ_0-κ plane (**Figure 6**), which corresponds to the stability boundary ($\mu_0 \leq \kappa + 0.5$: stable, $\mu_0 > \kappa + 0.5$: unstable) in the symmetric model ($\varepsilon_k = \varepsilon_\mu = 0$), as achieved in (Adachi et al., 2020). When $\mu_0 < \kappa + 0.5$, the introduction of ε_μ and ε_k to the symmetric model never changed the stability, and the periodic solutions remained stable, which resulted in $b = 0$ for the stability condition $\varepsilon_\mu \gtrless a\varepsilon_k \pm b$ in **Figure 5**. By contrast, when $\mu_0 > \kappa + 0.5$, the introduction of ε_μ and ε_k made the periodic solutions stable for $\varepsilon_\mu \gtrless a\varepsilon_k \pm b$ ($b > 0$). Therefore, we expect that the boundary between $b = 0$ and $b > 0$ is identical to $\mu_0 = \kappa + 0.5$ in the μ_0-κ plane. However, our results had some differences between them, as shown in **Figure 6**. This is mainly because we obtained the periodic solutions numerically based on the non-linear governing equations, whereas in our previous work (Adachi et al., 2020), we obtained them approximately by linearizing the governing equations.

4.2 Biological Relevance of Our Findings

Our results showed that the fore-aft asymmetry improves gait stability during trotting. Although our model incorporated only passive forces using springs, unstable gait can be stabilized by additional control inputs. However, when the system has passive stability, it needs less control inputs and sensory feedbacks. This results in low energy consumption, which is therefore beneficial for quadrupedal animals.

Because the front part of the body is generally heavier and has larger moment of inertia in the transverse plane than the hind part in quadrupeds (Rollinson and Martin, 1981), the forelegs need to generate more impulse than the hind legs to achieve trotting by inhibiting body pitching. In fact, the stance phase durations of the fore legs are basically longer than those of the hind legs during trotting in quadrupeds (Merkens et al., 1993; Lee et al., 1999; Weishaupt et al., 2004; Robilliard et al., 2007; Fischer and Lilje, 2016). These characteristics appeared only in the periodic solutions with Sequence 5 in our model.

In this study, we used the parameter set estimated in dogs. The average and difference of the moments of inertia between the fore and hind bodies were both relatively small ($\mu_0 = 0.62$ and $\varepsilon_\mu = 0.12$) and $\mu_0 < \kappa + 0.5$ was satisfied (i.e., the periodic solution of the symmetric model was stable). As a result, we achieved $b = 0$ and the periodic solutions were stable even when we introduced the asymmetries ε_μ and ε_k. Additionally, $\varepsilon_\mu < a\varepsilon_k$ was satisfied for the estimated values in dogs, which yielded Sequence 5 (**Figure 5B**). These characteristics are consistent with those of trotting in dogs (Lee et al., 1999, 2004; Lee, 2010; Fischer and Lilje, 2016). By contrast, horses have a longer neck than dogs (Loscher et al., 2016) and the estimated average and difference of the moments of inertia were both larger than those of dogs ($\mu_0 = 0.72$ and $\varepsilon_\mu = 0.14$). The periodic solution of the symmetric horse model with $\varepsilon_\mu = \varepsilon_k = 0$ was unstable. However, that was stabilized by making the fore legs stiffer ($\varepsilon_k = 0.25$, **Figure 5A**). Researchers have suggested that horses enhance the elasticity of their fore legs using their thoracic muscles, such as serratus ventralis thoracis, and generate a large difference in stiffness between their fore and hind legs (Payne et al., 2005b).

4.3 Limitations of Our Study and Future Work

In this study, we investigated the effects of fore-aft asymmetry on quadrupedal trotting in the transverse plane using a simple model. Our results demonstrated that asymmetry improves

gait stability. In addition, many locomotion characteristics of the simulation results were consistent with those of the measured data of animals, as shown in **Table 2**. However, our model does not necessarily explain all phenomena of trotting in animals and has limitations. For example, the roll amplitude of the hind body in our models was larger than that of the measured data of animals (**Table 2**). This discrepancy could be due to the different joint structure at the leg roots. Specifically, although we used smooth rotational joints, quadrupeds have muscles around the joints, which prevent large leg abduction (Schilling et al., 2009). In the future, we would like to incorporate this effect of the muscles around the leg roots to our model.

Secondary, our horse model showed Sequence 5 (flight–fore stance–double stance–fore stance–flight), where the fore leg of the pair touches the ground earlier and leaves it later than the hind leg. Although horses show Sequence 5 during trotting (Weishaupt et al., 2004), they basically show Sequence 6 (flight–fore stance–double stance–hind stance–flight), where the fore leg of the pair touches and leaves the ground earlier than the hind leg (Hildebrand, 1965). One possible reason for this discrepancy is the absence of pitching dynamics in our model. Lee (Lee, 2010) demonstrated that the disturbance of trotting in dogs that results from changing the ground inclination and added mass position changes their foot pattern through the regulation of balance in pitching. Additionally, quadrupeds whose COM is located in an extremely forward position (which corresponds to large ε_μ in this study), such as gnus, do not use trotting, but do use walking and cantering (Pennycuick, 1975). This is mainly because it is difficult for them to keep the body pitching parallel to the ground with the extreme fore-aft asymmetry. To investigate these characteristics in quadrupedal locomotion, we would like to introduce pitching dynamics in our model in the future.

5 CONCLUSION

In this study, we examined the effects of fore-aft asymmetry on trotting by quadrupedal mammals in the transverse plane using a simple model. Our results demonstrated that the asymmetry gives different foot patterns and improves gait stability. Our findings improve our understanding of gait dynamics in quadrupeds with fore-aft asymmetry.

DATA AVAILABILITY STATEMENT

The raw data supporting the conclusion of this article will be made available by the authors, without undue reservation.

AUTHOR CONTRIBUTIONS

SA, TK, KT, and FM contributed to the design of this study. MA conducted the numerical simulation and analysis in consultation with SA, TK, KT, and FM, MA, and SA wrote the manuscript, and all the authors reviewed and approved it.

FUNDING

This work was supported in part by Mori Manufacturing Research and Technology Foundation.

SUPPLEMENTARY MATERIAL

The Supplementary Material for this article can be found online at: https://www.frontiersin.org/articles/10.3389/fbioe.2022.807777/full#supplementary-material

REFERENCES

Adachi, M., Aoi, S., Kamimura, T., Tsuchiya, K., and Matsuno, F. (2020). Body Torsional Flexibility Effects on Stability during Trotting and Pacing Based on a Simple Analytical Model. *Bioinspir. Biomim.* 15, 055001. doi:10.1088/1748-3190/ab968d

Alexander, R. M., and Jayes, A. S. (1983). A Dynamic Similarity Hypothesis for the Gaits of Quadrupedal Mammals. *J. Zoolog.* 201, 135–152. doi:10.1111/j.1469-7998.1983.tb04266.x

Amit, T., Gomberg, B. R., Milgram, J., and Shahar, R. (2009). Segmental Inertial Properties in Dogs Determined by Magnetic Resonance Imaging. *Vet. J.* 182, 94–99. doi:10.1016/j.tvjl.2008.05.024

Belhaoues, F., Breit, S., Forstenpointner, G., and Gardeisen, A. (2020). Sexual Dimorphism in Limb Long Bones of the German shepherd Dog. *Anat. Histol. Embryol.* 49, 464–477. doi:10.1111/ahe.12550

Berkemeier, M. D. (1998). Modeling the Dynamics of Quadrupedal Running. *Int. J. Robotics Res.* 17, 971–985. doi:10.1177/027836499801700905

Bertram, J. E. A., and Gutmann, A. (2008). Motions of the Running Horse and Cheetah Revisited: Fundamental Mechanics of the Transverse and Rotary Gallop. *J. R. Soc. Interf.* 6, 549–559. doi:10.1098/rsif.2008.0328

Blickhan, R., and Full, R. J. (1993). Similarity in Multilegged Locomotion - Bouncing like a Monopode. *J. Comp. Physiol.* 173, 509–517. doi:10.1007/bf00197760

Buchner, H. H. F., Savelberg, H. H. C. M., Schamhardt, H. C., and Barneveld, A. (1997). Inertial Properties of Dutch Warmblood Horses. *J. Biomech.* 30, 653–658. doi:10.1016/s0021-9290(97)00005-5

Bullimore, S. R., and Burn, J. F. (2006). Dynamically Similar Locomotion in Horses. *J. Exp. Biol.* 209, 455–465. doi:10.1242/jeb.02029

Byström, A., Hardeman, A. M., Serra Bragança, F. M., Roepstorff, L., Swagemakers, J. H., van Weeren, P. R., et al. (2021). Differences in Equine Spinal Kinematics between Straight Line and circle in Trot. *Sci. Rep.* 11, 12832. doi:10.1038/s41598-021-92272-2

Carrier, D. R., Chase, K., and Lark, K. G. (2005). Genetics of Canid Skeletal Variation: Size and Shape of the Pelvis. *Genome Res.* 15, 1825–1830. doi:10.1101/gr.3800005

De, A., and Koditschek, D. E. (2018). Vertical Hopper Compositions for Preflexive and Feedback-Stabilized Quadrupedal Bounding, Pacing, Pronking, and Trotting. *Int. J. Robotics Res.* 37, 743–778. doi:10.1177/0278364918779874

Dunbar, D. C., Macpherson, J. M., Simmons, R. W., and Zarcades, A. (2008). Stabilization and Mobility of the Head, Neck and Trunk in Horses during Overground Locomotion: Comparisons with Humans and Other Primates. *J. Exp. Biol.* 211, 3889–3907. doi:10.1242/jeb.020578

Dutto, D. J., Hoyt, D. F., Cogger, E. A., and Wickler, S. J. (2004). Ground Reaction Forces in Horses Trotting up an Incline and on the Level over a Range of Speeds. *J. Exp. Biol.* 207, 3507–3514. doi:10.1242/jeb.01171

Farley, C. T., Glasheen, J., and McMahon, T. A. (1993). Running Springs: Speed and Animal Size. *J. Exp. Biol.* 185, 71–86. doi:10.1242/jeb.185.1.71

Fischer, M. S., Lehmann, S. V., and Andrada, E. (2018). Three-dimensional Kinematics of Canine Hind Limbs: *In Vivo*, Biplanar, High-Frequency Fluoroscopic Analysis of Four Breeds during Walking and Trotting. *Sci. Rep.* 8, 16982. doi:10.1038/s41598-018-34310-0

Fischer, M. S., and Lilje, K. E. (2016). *Dogs in Motion*. Cowbridge, United Kingdom: The Pet Book Publishing Company Ltd.

Full, R. J., and Koditschek, D. E. (1999). Templates and Anchors: Neuromechanical Hypotheses of Legged Locomotion on Land. *J. Exp. Biol.* 202, 3325–3332. doi:10.1242/jeb.202.23.3325

Gillette, R. L., and Angle, T. C. (2008). Recent Developments in Canine Locomotor Analysis: a Review. *Vet. J.* 178, 165–176. doi:10.1016/j.tvjl.2008.01.009

Gómez, M. D., Valera, M., Molina, A., Gutiérrez, J. P., and Goyache, F. (2009). Assessment of Inbreeding Depression for Body Measurements in Spanish Purebred (Andalusian) Horses. *Livestock Sci.* 122, 149–155. doi:10.1016/j.livsci.2008.08.007

Heglund, N. C., Taylor, C. R., and McMahon, T. A. (1974). Scaling Stride Frequency and Gait to Animal Size: Mice to Horses. *Science* 186, 1112–1113. doi:10.1126/science.186.4169.1112

Heglund, N. C., and Taylor, C. R. (1988). Speed, Stride Frequency and Energy Cost Per Stride: How Do They Change with Body Size and Gait? *J. Exp. Biol.* 138, 301–318. doi:10.1242/jeb.138.1.301

Herr, H. M., Huang, G. T., and McMahon, T. A. (2002). A Model of Scale Effects in Mammalian Quadrupedal Running. *J. Exp. Biol.* 205, 959–967. doi:10.1242/jeb.205.7.959

Hildebrand, M., and Goslow, G. E. J. (2001). *Analysis of Vertebrate Structure*. 5th edition. New York: Wiley.

Hildebrand, M. (1968). Symmetrical Gaits of Dogs in Relation to Body Build. *J. Morphol.* 124, 353–359. doi:10.1002/jmor.1051240308

Hildebrand, M. (1965). Symmetrical Gaits of Horses. *Science* 150, 701–708. doi:10.1126/science.150.3697.701

Jones, O. Y., Raschke, S. U., and Riches, P. E. (2018). Inertial Properties of the German Shepherd Dog. *PLOS ONE* 13, e0206037. doi:10.1371/journal.pone.0206037\\}

Kilbourne, B. M., and Hoffman, L. C. (2013). Scale Effects between Body Size and Limb Design in Quadrupedal Mammals. *PLOS ONE* 8, e78392. doi:10.1371/journal.pone.0078392

Lee, D. V., Bertram, J. E., and Todhunter, R. J. (1999). Acceleration and Balance in Trotting Dogs. *J. Exp. Biol.* 202, 3565–3573. doi:10.1242/jeb.202.24.3565

Lee, D. V., Stakebake, E. F., Walter, R. M., and Carrier, D. R. (2004). Effects of Mass Distribution on the Mechanics of Level Trotting in Dogs. *J. Exp. Biol.* 207, 1715–1728. doi:10.1242/jeb.00947

Lee, J. Y., and Lee, S. J. (2010). Hemodynamics of the Omphalo-Mesenteric Arteries in Stage 18 Chicken Embryos and "Flow-Structure" Relations for the Microcirculation. *Microvasc. Res.* 80, 402–411. doi:10.1016/j.mvr.2010.08.003

Loscher, D. M., Meyer, F., Kracht, K., and Nyakatura, J. A. (2016). Timing of Head Movements Is Consistent with Energy Minimization in Walking Ungulates. *Proc. R. Soc. B.* 283, 20161908. doi:10.1098/rspb.2016.1908

Maes, L. D., Herbin, M., Hackert, R., Bels, V. L., and Abourachid, A. (2008). Steady Locomotion in Dogs: Temporal and Associated Spatial Coordination Patterns and the Effect of Speed. *J. Exp. Biol.* 211, 138–149. doi:10.1242/jeb.008243

Merkens, H. W., Schamhardt, H. C., Osch, G. J. V. M., and Bogert, A. J. (1993). Ground Reaction Force Patterns of Dutch Warmblood Horses at normal Trot. *Equine Vet. J.* 25, 134–137. doi:10.1111/j.2042-3306.1993.tb02923.x

Muybridge, E. (1957). *Animals in Motion*. New York: Dover Publications.

Payne, R. C., Hutchinson, J. R., Robilliard, J. J., Smith, N. C., and Wilson, A. M. (2005a). Functional Specialisation of Pelvic Limb Anatomy in Horses (*Equus caballus*). *J. Anat.* 206, 557–574. doi:10.1111/j.1469-7580.2005.00420.x

Payne, R. C., Veenman, P., and Wilson, A. M. (2005b). The Role of the Extrinsic Thoracic Limb Muscles in Equine Locomotion. *J. Anat.* 206, 193–204. doi:10.1111/j.1469-7580.2005.00353.x

Pennycuick, C. J. (1975). On the Running of the Gnu (*Connochaetes taurinus*) and Other Animals. *J. Exp. Biol.* 63, 775–799. doi:10.1242/jeb.63.3.775

Robilliard, J. J., Pfau, T., and Wilson, A. M. (2007). Gait Characterisation and Classification in Horses. *J. Exp. Biol.* 210, 187–197. doi:10.1242/jeb.02611

Rollinson, J., and Martin, R. D. (1981). Comparative Aspects of Primate Locomotion with Special Reference to Arboreal Cercopithecines. *Symp. Zool. Soc. Lond.* 48, 377–427.

Schilling, N., and Carrier, D. R. (2009). Function of the Epaxial Muscles during Trotting. *J. Exp. Biol.* 212, 1053–1063. doi:10.1242/jeb.020248

Schilling, N., Fischbein, T., Yang, E. P., and Carrier, D. R. (2009). Function of the Extrinsic Hindlimb Muscles in Trotting Dogs. *J. Exp. Biol.* 212, 1036–1052. doi:10.1242/jeb.020255

Voss, K., Galeandro, L., Wiestner, T., Haessig, M., and Montavon, P. M. (2010). Relationships of Body Weight, Body Size, Subject Velocity, and Vertical Ground Reaction Forces in Trotting Dogs. *Vet. Surg.* 39, 863–869. doi:10.1111/j.1532-950x.2010.00729.x

Weishaupt, M. A., Wiestner, T., Hogg, H. P., Jordan, P., and Auer, J. A. (2004). Vertical Ground Reaction Force-Time Histories of Sound Warmblood Horses Trotting on a Treadmill. *Vet. J.* 168, 304–311. doi:10.1016/j.tvjl.2003.08.007

Williams, S. B., Wilson, A. M., Daynes, J., Peckham, K., and Payne, R. C. (2008a). Functional Anatomy and Muscle Moment Arms of the Thoracic Limb of an Elite Sprinting Athlete: the Racing Greyhound (*Canis familiaris*). *J. Anat.* 213, 373–382. doi:10.1111/j.1469-7580.2008.00962.x

Williams, S. B., Wilson, A. M., Rhodes, L., Andrews, J., and Payne, R. C. (2008b). Functional Anatomy and Muscle Moment Arms of the Pelvic Limb of an Elite Sprinting Athlete: the Racing Greyhound (*Canis familiaris*). *J. Anat.* 213, 361–372. doi:10.1111/j.1469-7580.2008.00961.x

Witte, T. H., Knill, K., and Wilson, A. M. (2004). Determination of Peak Vertical Ground Reaction Force from Duty Factor in the Horse (*Equus caballus*). *J. Exp. Biol.* 207, 3639–3648. doi:10.1242/jeb.01182

Yamada, T., Aoi, S., Adachi, M., Kamimura, T., Higurashi, Y., Wada, N., et al. (2022). Center of Mass Offset Enhances the Selection of Transverse Gallop in High-Speed Running by Horses: a Modeling Study. *Front. Bioeng. Biotechnol.* 10, 825157. doi:10.3389/fbioe.2022.825157

Zou, H., and Schmiedeler, J. P. (2006). The Effect of Asymmetrical Body-Mass Distribution on the Stability and Dynamics of Quadruped Bounding. *IEEE Trans. Robot.* 22, 711–723. doi:10.1109/tro.2006.875477

Conflict of Interest: The authors declare that the research was conducted in the absence of any commercial or financial relationships that could be construed as a potential conflict of interest.

Publisher's Note: All claims expressed in this article are solely those of the authors and do not necessarily represent those of their affiliated organizations, or those of the publisher, the editors and the reviewers. Any product that may be evaluated in this article, or claim that may be made by its manufacturer, is not guaranteed or endorsed by the publisher.

Advantages of publishing in Frontiers

OPEN ACCESS
Articles are free to read for greatest visibility and readership

FAST PUBLICATION
Around 90 days from submission to decision

HIGH QUALITY PEER-REVIEW
Rigorous, collaborative, and constructive peer-review

TRANSPARENT PEER-REVIEW
Editors and reviewers acknowledged by name on published articles

Frontiers
Avenue du Tribunal-Fédéral 34
1005 Lausanne | Switzerland

Visit us: www.frontiersin.org
Contact us: frontiersin.org/about/contact

REPRODUCIBILITY OF RESEARCH
Support open data and methods to enhance research reproducibility

DIGITAL PUBLISHING
Articles designed for optimal readership across devices

FOLLOW US
@frontiersin

IMPACT METRICS
Advanced article metrics track visibility across digital media

EXTENSIVE PROMOTION
Marketing and promotion of impactful research

LOOP RESEARCH NETWORK
Our network increases your article's readership